Extended Abstracts Booklet

2025 Physical Behavior of Materials Principal Investigators' Meeting

May 21-23, 2025
Hilton Washington DC/Rockville Hotel & Executive Meeting Center
Rockville, Maryland

U.S. DEPARTMENT *of* ENERGY

Office of Science

FOREWORD

This booklet is a collection of extended abstracts submitted to 9th Physical Behavior of Materials Principal Investigators meeting. This meeting is sponsored by Division of Materials Sciences and Engineering (MSE) of the Department of Energy, Office of Basic Energy Sciences (BES), and is held on May 21-23, 2025.

The Principal Investigators meeting brings together all the principal investigators who are supported by the Physical Behavior of Materials program to share their latest exciting scientific discoveries, facilitate exchange of ideas and promote new collaborations. For BES and the participating investigators, the meeting serves the purpose of providing an overview and assessment of the whole program, which helps BES to identify new research areas and future directions for the program. The meeting brings together leading experts in topical areas of research supported by our program and is designed to stimulate and inspire new ideas.

The Physical Behavior of Materials program supports transformative and innovative research activities at the crossroads of materials science and condensed-matter physics. This program supports both fundamental and use-inspired basic scientific research, to advance our knowledge of electronic, electromagnetic, magnetic, and thermal behavior of materials, including light-matter interactions that are relevant to BES mission. The program has a rich portfolio in many ground breaking, exciting, and high-risk high-reward projects in both experimental and theoretical areas.

The meeting format includes oral presentations and 2 poster sessions. This meeting brings together over 100 scientists and is organized to include 25 regular presentations and 53 poster presentations. BES appreciates the contributions of all Physical Behavior of Materials investigators by presenting their latest findings. We are also grateful to the outstanding support of the Oak Ridge Institute for Science and Education, and Teresa Crockett of MSE.

Shawn Chen, Ph.D.
Athena S. Sefat, Ph.D.
Program Managers,
Physical Behavior of Materials Program
Division of Materials Sciences and Engineering
Office of Basic Energy Sciences
Department of Energy

May 2025

Table of Contents

DOE-BES, Division of Materials Sciences and Engineering,
Virtual Program PI Meeting
Physical Behavior Principal Investigators Meeting
May 21-23, 2025

Hilton Washington DC/Rockville Hotel & Executive Meeting Center,
1750 Rockville Pike, Rockville, Maryland

Meeting Chairs:
Kirstin Alberi (NREL), Kenneth Burch (Boston College)

Tuesday, May 20, 2025

*** Dinner (On your own) ***

Wednesday, May 21, 2025

7:30 – 8:30 am	Registration & *** Breakfast ***
8:30 – 8:40 am	**Welcome, *Meeting Chairs***
8:40 – 9:10 am	**"Division and Program Updates"** Andrew Schwartz, *Director, Division of Materials Sciences and Engineering* Refik Kortan, *Program Manager, Physical Behavior of Materials*

Session I	***Chair: Kenneth Burch (Boston College)***
9:10 – 9:40 am	Michael Flatte *(University of Iowa)* *"Quantum Transduction with Abundant Elements for Cleaner Energy"*
9:40 – 10:10 am	Fazel Tafti *(Boston College)* *"Electron Hydrodynamics in 3D Quantum Materials"*
10:10 – 10:30 am	*** Break ***

Session II	***Chair: Kirstin Alberi (NREL)***
10:30 – 11:00 am	Xiaoyang Zhu *(Columbia University)* *"Polaronic Electron Crystals in 2D Moiré Materials"*

11:00 – 11:30 am	Geoffroy Hautier *"Understanding and designing phosphide solar absorbers with high carrier lifetime"*
11:30 – 12:00 pm	Chunhui Du (*Georgia Tech*) *"Nanoscale Quantum Sensing and Imaging of Topological Magnets"*
12:00 – 1:30 pm	** Working Lunch (*poster introductions: session I*) **
Session III	***Chair: Igal Brener (Sandia National Laboratory)***
1:30 – 2:00 pm	Zubin Jacob *(Purdue University)* *"Opening New Frontiers of Epsilon-Near-Zero Optics"*
2:00 – 2:30 pm	Vadym Apalkov *(Georgia State University)* *"Quantum Nanoplasmonics Theory"*
Session IV	***Chairs: Kirstin Alberi (NREL), Kenneth Burch (Boston College)***
2:30 – 5:30 pm	**Poster Session I**
5:30 – 6:30 pm	*** Dinner *(Scientific Highlights of the Day: Discussion and Input from Attendees)* ***
Session V	***Chair: Puru Jena (Virginia Commonwealth University)***
6:30 – 7:00 pm	David Cahill *(University of Illinois)* *"Ionic Heat of Transport of Liquid and Solid Electrolytes"*
7:00 – 7:30 pm	Morgan Stefik *(University of South Carolina)* "*Understanding the Role of Defects to Accelerate Wadsley-Roth Niobates for Long-Duration Energy Storage*
Session VI	***Chairs: Kirstin Alberi (NREL), Kenneth Burch (Boston College)***
7:30 – 9:30 pm	Continuation of Poster Session I

Thursday, May 22, 2025

7:30 – 8:30 am	*** Breakfast ***
Session VII	***Chair: Chris Van de Walle (UCSB)***
8:30 – 9:00 am	Ali Javey *(LBNL)* *"Making Semiconductor Monolayers Perfectly Bright"*
9:00 – 9:30 am	Matthew McCluskey *(Washington State University)* *"Defects in Oxide Semiconductors and Ternary Alloys"*
9:30 - 10:00 am	Akanksha Krishnakumar Menon, *(Georgia Institute of Technology)* *"Understanding Thermo-Chemo-Mechanical Transformations in Thermal Energy Storage Materials and Composites"*
10:00 – 10:30 am	*** Break ***
Session VIII	***Chair: Chia-Ling Chien (Johns Hopkins University)***
10:30 – 11:00 am	Yaroslav Mudryk *(Ames National Laboratory)* *"Extraordinary Responsive Magnetic Rare Earth Materials"*
11:00 – 11:30 am	Takeshi Egami *(ORNL)* *"Structure and Dynamics of Liquid and Glass in Real Space and Time"*
11:30 – 12:00 pm	Krzysztof Gofryk *(INL)* *"Exotic Magneto-Elastic Phenomena in Actinide Materials in High Magnetic Fields"*
12:00 – 1:30 pm	** Working Lunch (*poster introductions: session II*) **
Session IX	***Chair: Shanhui Fan (Stanford University)***
1:30 – 2:00 pm	Janice Musfeldt (*University of Tennessee)* *"Complex chalcogenides under pressure"*
2:00 – 2:30 pm	Kenan Gundogdu *(North Carolina State University,)* *"Investigation of Origin of High-Temperature Superfluorescence in Lead-Halide Perovskites"*
Session X	***Chairs: Kirstin Alberi (NREL), Kenneth Burch (Boston College)***
2:30 – 5:30 pm	**Poster Session II**

5:30 – 6:30 pm	*** Dinner *(Scientific Highlights of the Day: Discussion and Input from Attendees)* ***
Session XI	***Chair: Jinsong Huang (University of North Carolina)***
6:30 – 7:00 pm	Moungi Bawendi *(Massachusetts Institute of Technology)* *"Using Photon Correlations to Study Fundamental Quantum Optical Properties of Perovskite-Based Nanocrystals"*
7:00 – 7:30 pm	Mikhail Zamkov *(Bowling Green State University) "Semiconductor nanoshell quantum dots for energy conversion applications "*
Session XII	***Chairs: Kirstin Alberi (NREL), Kenneth Burch (Boston College)***
7:30 – 9:30 pm	Continuation of Poster Session II

Friday, May 23, 2025

7:30 – 8:30 am	*** Breakfast ***
Session XIII	***Chair: Chia-Ling Chien (Johns Hopkins University)***
8:30 – 9:00 am	Mona Jarrahi (*UCLA*) *"Plasmonic Photoconductive Nanostructures for High-Power Terahertz Wave Generation"*
9:00 – 9:30 am	Kun Wang *(University of Miami Coral Gables)* "*Probing and Understanding the Spatial and Energy Distributions of Plasmonic Hot Carriers via Single-Molecule Quantum Transport*"
9:30 – 10:00 am	Svetlana Kilina *(North Dakota State University)* "*Data-Driven and Computationally Assisted Design of Near-Infrared Emissive Metal-Organic Complexes with Earth-Abundant Metals*"
10:00 – 10:15 am	*** Break ***
Session XIV	***Chair: Mona Jarrahi (UCLA)***
10:15 – 10:45 am	Thomas Autrey *(PNNL)* *"Enabling Reversible Hydrogen Storage and Transfer with Graphene-based Carbon–Boron–Nitrogen Materials"*
10:45 - 11:15 am	Yiying Wu *(Ohio State University)* *"Interface Design and Machine Learning for Dye-Sensitized Solar Fuels and Halide Perovskites"*
11:15 – 11:45 am	Dali Sun *(North Carolina State University)* "Elucidating Chirality-induced Magnetism and Magnetoelectric Functionalities in Layered Chiral Hybrid Metal Halide Perovskites"
11:45 – 12:00 pm	Closing Remarks by Meeting Chairs and PM

Session I

Quantum Transduction with Abundant Elements for Cleaner Energy

M. E. Flatté (PI), D. R. Candido (Co-I), D. Paudyal (Co-I)

Keywords: quantum transduction, oxides, phosphates, abundant rare earth elements

Research Scope

The current leaders in solid-state microwave to optical quantum transduction are electro-optic approaches (i.e. lithium niobate) and rare-earth ion approaches (e.g. erbium-doped yttrium orthovanadate). The main challenges with rare-earth quantum transduction are the coupling strength, the optical loss (due to impurities in the materials), and the cost/accessibility of the required materials (especially yttrium – the erbium is used in very small quantities (ppm) by comparison). The scope of this project is to calculate the properties of materials with abundant rare-earth elements such as cerium orthovanadate, including ground-state magnetism, low-temperature ferromagnetic resonance, magnetic excitations and optical properties. Cerium is an abundant element. We hypothesize that these calculations and advances in theories simulating these materials will identify rare-earth materials with abundant elements as providing (1) comparable or superior fidelity and efficiency of microwave-optical quantum transduction, and (2) comparable or superior quantum memory density with comparable or longer coherence times to current materials that contain yttrium. Transduction will be emphasized as the coherence times required are shorter and the vanadium spin bath may limit these times. This project will establish a fundamental understanding of rare-earth hosts with abundant elements.

Recent Progress

We have developed an effective *ab initio* method[1] to calculate the crystal field coefficients of an erbium ion experiencing different local site symmetries in several wide-band-gap oxides, and then evaluated the crystal field splittings of these Er^{3+} ions for their ground and excited states. The optical transitions between the ground state (Z) and excited state (Y) manifolds of the environmentally shielded 4f states of these erbium ions have wavelengths ~ 1.5μm and thus have potential applications to quantum communications and quantum memories. These results are in excellent agreement with recent low-temperature measurements, provided the inadequate calculation of the 4f shell screening is adjusted by reducing

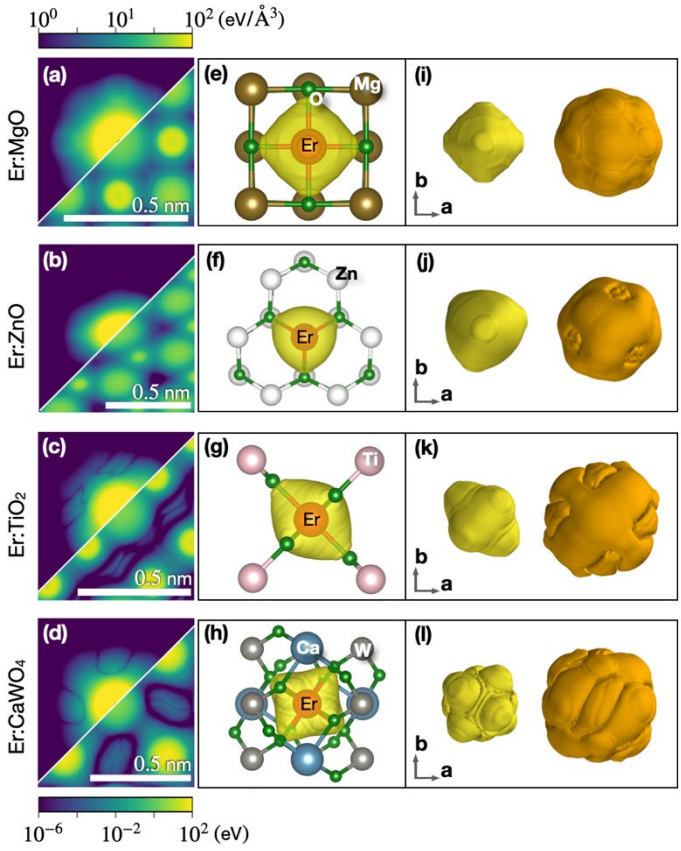

Fig. 1. (a)-(d) Two-dimensional views of the crystal field potential and the same potential multipled by the 4f electron probability density of Er (upper diagonal, in eV/cubic Angstrom). (e)-(h) show the crystal structure surrounding the doped Er ion and the probability density of the 4f electrons at 1.58 eV/cubic Angstrom (yellow isocontour). (i)-(l) illustrate the probability density by plotting at 10^{-2} (left) and 10^{-6} (right) eV/cubic Angstrom isocontours, omitting the crystal.

the radial extent of the 4f wavefunctions by approximately a factor of 2.

The *ab initio* density functional theory (DFT) calculations were performed using the Vienna Ab-initio simulation package (VASP). Augmented plan wave pseudopotentials and Perdew-Burke-Ernzerhof functionals were used. A sufficient plane wave cut off energy (500 eV) and Γ centered k-mesh (maximum of 10x10x10) were used for the Brillouin zone sampling. The 4f electrons were frozen in the core and the 6s, 5p and 5d electrons were considered in the valence shell. From non-spin-polarized calculations the self-consistent charge densities and local potentials were generated to produce the crystal field parameters considering the local potentials as crystal fields.

To study the crystal field splittings we focused on the oxides MgO, ZnO, TiO_2, $CaWO_4$ and $PbWO_4$, with variable point group symmetry. MgO, ZnO and TiO_2 have cubic, hexagonal, and rutile (tetragonal) crystal structures. Once the crystal field coefficients are obtained the lanthanide ion energy spectrum was calculated using the qlanth code[2], which includes terms representing the following interactions and relativistic corrections: spin-orbit, electrostatic repulsion, spin-spin, crystal field and spin-other-orbit as described in Ref. 3. qlanth now reproduces the crystal field parameters of Ref. 4 with an agreement better than 30 cm^{-1} throughout all lanthanides.

We have further developed the theory of microwave to optical quantum transduction using the enhancement of a magnetic material[4]. This is a new method for converting single microwave photons to single optical sideband photons based on spinful impurities in magnetic materials. This hybrid system is advantageous over previous proposals [5] because (i) the implementation allows much higher transduction rates (1000 times faster at the same optical pump Rabi frequency) than state-of-the-art devices, (ii) high-efficiency transduction is found to happen in a significantly larger space of device parameters (in particular, over 1 GHz microwave detuning), and (iii) it does not require mode volume matching between optical and microwave resonators. We identified the needed magnetic interactions as well as potential materials systems to enable this speed-up using erbium dopants for telecom compatibility. This is an important step towards realizing high-fidelity entangling operations between remote qubits and will provide additional control of the transduction through perturbation of the magnet.

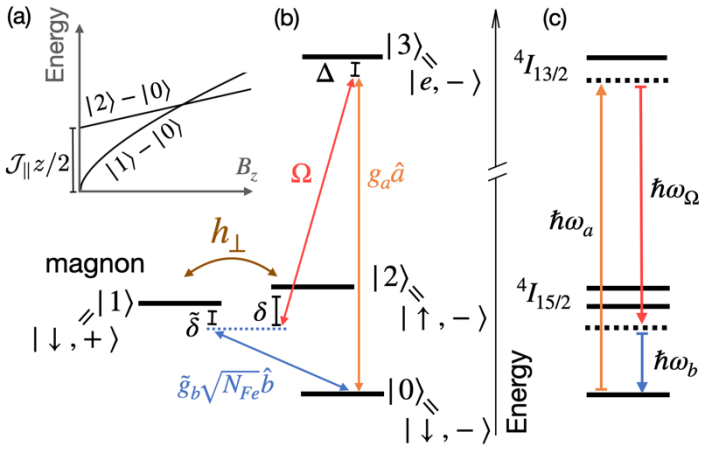

Fig. 2 (a) Crossing between the magnon excitation and the erbium spin flip versus Bz. (b) Full energy-level diagram, including the erbium excited state, and the transitions due to the couplings to an optical cavity, to an optical pump, to a magnon via spin exchange, and to a magnon via the microwave cavity. Detunings are indicated by δ's and Δ. (c) frequencies of the optical cavity resonance, microwave resonator, and optical pump.

In addition to these two key results a number of additional studies have been completed, including ab initio treatments of the stoichiometric cerium containing vanadates and phosphates, and erbium-doped gallium oxide. We have also shown that the two different sites for Er in yttrium oxide have

different formation energies, suggesting that careful control during the synthesis process may allow for preferential occupancy of the site with or without inversion symmetry.
These results establish the foundation of quantum studies of rare earth materials based on abundant elements, such as cerium.

Future Plans

This project opens up new opportunities for exploring the coupling of erbium spins to optical and microwave fields for quantum transduction and communication. The establishment of this theoretical foundation also connects with additional work on energy transfer within rare earth shells, which is important for efficient light emission at room temperature. We anticipate continuing to explore the fundamental connection between the properties of these lanthanides and nonlinear optical properties, for both quantum and classical applications. We have identified a key limiting feature of *ab initio* simulations – the poor reproduction of the screening of the 4f shell. This provides a key focus for future work to try to further establish the properties of crystal field parameters of rare earths on a fundamental *ab initio* basis. Preliminary work with local orbital codes indicates that perhaps those codes describe the screening better. This will be explored in the future.

References

Put the list of references here using Times New Roman 10 pt. Please limit to no more than 5 papers. Provide full citation, including title and full author list.

1. Y. Limbu, Y. Shi, J. Sink, T. O. Puel, D. Paudyal, and M. E. Flatté, *Ab initio calculations of erbium crystal field splittings in oxide hosts*, submitted to Physical Review Letters. arXiv: 2501.03348
2. J. D. L. Ferro, qlanth: *A Hamiltonian for the lanthanides*, github 2024.
3. W. T. Carnall, G. L. Goodman, K. Rajnak, and R. S. Rana, *A systematic analysis of the spectra of the lanthanides doped into single crystal LaF_3*, J. Chem. Phys. 90, 3443-3457 (1989).
4. T. O. Puel, A. T. Turflinger, S. P. Horvath, J. D. Thompson, and M. E. Flatté, *Enhancement of Microwave to Optical Spin-Based Quantum Transduction via a Magnon Mode*, Physical Review Research (in press). arXiv:2411.12870
5. L. A. Williamson, Y.-H. Chen, and J. Longdell, Phys. Rev. Lett. 113, 203601 (2014).

Publications

Put the list of publications in the recent 2-years SUPPORTED BY BES here. **If more than 10 publications, list only the 10 most relevant.**

1. K. Maleki and M. E. Flatté, *Crystal fields, exchange, and dipolar interactions and noncollinear magnons of erbium oxide*, submitted to Physical Review B. arXiv:2504.07234.
2. Y. Limbu, H. Paudyal, M. E. Flatté, and D. Paudyal, *Stability, electronic quantum states, and magnetic interactions of Er^{3+} ions in Ga_2O_3*, submitted to Physical Review Materials. arXiv:2503.12194.
3. H. Paudyal, Y. Limbu, M. E. Flatté, and D. Paudyal, *Singly occupied 4f antiferromagnetic insulators: CePO4 and $CeVO_4$*, submitted to Physical Review B. arXiv:2503.12186.
4. Y. Limbu, Y. Shi, J. Sink, T. O. Puel, D. Paudyal, and M. E. Flatté, *Ab initio calculations of erbium crystal field splittings in oxide hosts*, submitted to Physical Review Letters. arXiv: 2501.03348
5. Y. Limbu, Y. Shi, J. Sink, T. O. Puel, D. Paudyal, and M. E. Flatté, *Ab initio calculations of erbium crystal field splittings in oxide hosts: role of the 4f radial wave function*, submitted to Physical Review B. arXiv:2501.03353
6. A. C. Lourenco, D. R. Candido, and E. I. Duzzioni, *Genuine k-partite correlations and entanglement in the ground state of the Dicke model for interacting qubits*, submitted to Physical Review B. arXiv:2405.12916.
7. T. O. Puel, A. T. Turflinger, S. P. Horvath, J. D. Thompson, and M. E. Flatté, *Enhancement of Microwave to Optical Spin-Based Quantum Transduction via a Magnon Mode*, Physical Review Research (in press). arXiv:2411.12870
8. K. Rubi, D. R. Candido, M. Dumen, S. Zeng, E. L. Q. N. Ammerlaan, F. Bangma, M. K. Chan, M. Goiran, A. Ariando, S. Chakraverty, W. Escoffier, U. Zeitler, and N. Harrison, *Unconventional quantum oscillations and evidence of nonparabolic electronic states in quasi-two-dimensional electron system at complex oxide interfaces*, Physical Review Research **6**, 043231 (2024).

9. C. Bhandari, C. Sahin, D. Paudyal, M. E. Flatté, *Distinguishing erbium dopants in Y2O3 by site symmetry: ab initio theory of two spin-photon interfaces*, Physical Review Materials **7**, 126201 (2023).

Electron Hydrodynamics in 3D Quantum Materials

Fazel Tafti (Boston College)

Keywords: Hydrodynamics, electron-phonon interactions, crystal growth, semimetal, electrical transport

Research Scope

Improving the electrical conductivity of metals is an essential research direction in materials science, with important applications in improving energy efficiency of circuits and devices. An emerging field in condensed matter physics is electron hydrodynamics, where the conductivity of a metal is improved to such an extent that nearly eliminates impurity scattering, allowing electrons to scatter only from each other or from phonons. The goal of this project is to achieve such a limit, not by prost-processing a good metal and make it better, but by design 3D quantum materials with exceptional conductivity.

To achieve such a high conductivity, the project uses four material design principles: (i) short metallic bonds, (ii) large coordination ratios, (iii) strong electron-phonon interactions, and (iv) small Fermi surface. The short metallic bonds are known to drive electron hydrodynamics in graphene, a 2D system which is by far the best candidate for electron hydrodynamics [1]. Large coordination numbers lead to a phonon bunching effect that minimizes anhamonic phonon-phonon decays [2]. Strong el-ph interactions ensure a transfer of momentum between electron and phonon reservoirs, conserving total el-ph momentum and leading to an el-ph hydrodynamic fluid [3]. Finally, a small Fermi surface helps minimizing impurity scattering and mobility per carrier. These principles are derived from observations in $PdCoO_2$ and WP_2, two 3D semimetals with near-hydrodynamic transport properties [4,5].

The project's objectives are (i) growing crystals of candidate materials that satisfy the above four design criteria, (ii) characterizing their electrical transport properties in the lab and at the National High Magnetic Field Lab (NHMFL), and (iii) testing the signature predictions of a hydrodynamic electron fluid such as size dependence of electrical resistivity. The last objectives will require fabrication of mesoscopic devices in collaboration with the group of Dr. Moll at the Max Planck Institute for Structure and Dynamics (MPSD).

Recent Progress

We grew crystals of four compounds with chemical formula MX_2, where M = Nb or Ta and X = Si or Ge. These materials are semimetals with small Fermi surfaces according to quantum oscillation experiments performed at NHMFL [6]. We found that the germanides ($NbGe_2$ and $TaGe_2$) have a much higher transport mobility than quantum mobility (Fig. 1a). The transport mobility is determined by resistivity and Hall measurements while quantum mobility is determined by quantum oscillations. In contrast, the silicides ($NbSi_2$ and $TaSi_2$) have comparable transport and quantum oscillations (Fig. 1a). We also found an enhanced effective mass of electrons in the germanides compared to silicides (Fig. 1b). The findings indicate that the higher transport mobility of germanides is related to some form of interactions that enhance the effective mass of electrons. Since MX_2 compounds are non-magnetic and devoid of f-electrons, the most likely suspect would be el-ph interactions.

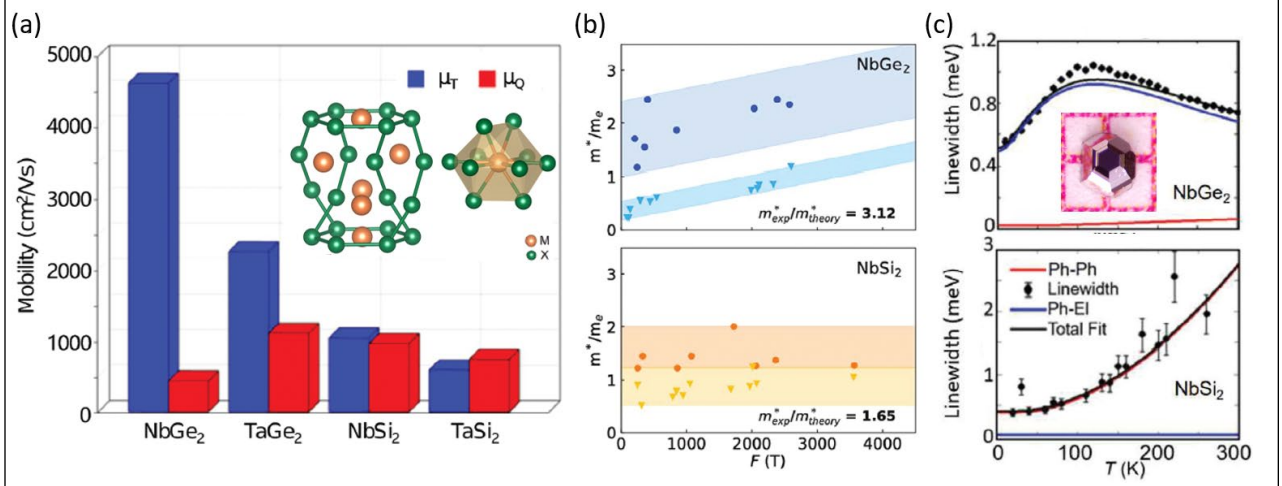

Figure 1: (a) Transport mobility (blue) and quantum mobility (red) are compared between the germanides ($NbGe_2$ and $TaGe_2$) and silicides ($NbSi_2$ and $TaSi_2$). (b) The effective mass of $NbGe_2$ is enhanced by a factor of 3.12 over the calculated mass from DFT, whereas the experimental and theoretical effective masses are comparable in $NbSi_2$. (c) Temperature dependence of the phonon peak width follows a Fermi function in $NbGe_2$ but a Bose function in $NbSi_2$.

The above hypothesis was confirmed by Raman scattering measurements shown in Fig. 1c. We found that the temperature dependence of phonon peak widths in germanides, measured by Raman scattering, follows a Fermi function, whereas that of silicides follows a Bose function (Fig. 1c). This observation shows that electron-phonon interactions are strong in the germanides and weak in silicides. This behavior is also referred to as phonon drag.

These results were published in the journal of Advanced Materials. This work shows that enhanced electron-phonon interactions and phonon drag processes could enhance electrical conductivity and help achieving a hydrodynamic regime in 3D materials [6]. In other works, we showed a similar high conductivity in the magnetic system HoBi [7], found signatures of Majorana fermions in an oxide material [8], discovered colossal magnetoresistance is correlated semimetals [9,10], studied structural transitions under pressure in a metastable compound [11], and found enhanced magnetism in a 2D system due to excitons [12].

Future Plans

Moving forward, we are going to extend the realm of phonon-assisted electron hydrodynamics by growing crystals of new candidate materials, including $OsGe_2$ YS, and $TaSe_3$. These materials were identified based on the four chemical design principles mentioned earlier. They are all semimetals with small Fermi surfaces and considerable el-ph interactions. We will also attempt the growth of large crystals of the silicides and germanides for neutron scattering investigation of

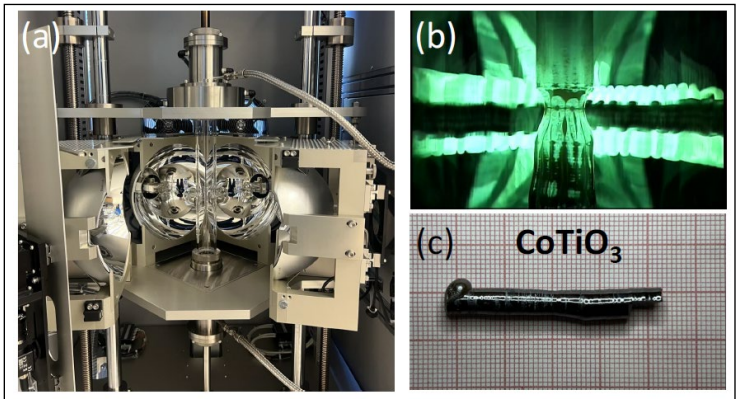

Figure 2: (a) Picture of the 4-lamp optical floating zone furnace. (b) Infra-red image of the melting zone during crystal growth. (c) A large crystal of $CoTiO_3$ grown in the PI's lab.

phonons. Such large crystals will be grown using a floating-zone optical furnace recently installed in the Tafti Lab (Figs. 2a,b). A picture of a large oxide crystal grown by this technique is shown in Fig. 2c.

Additionally, the PI started student exchanges with the MPSD for the fabrication of mesoscopic devices using the focused ion beam (FIB) technique. Using this method, we will fabricate micron-scale transport devices that enables us to measure the size dependence of electrical resistivity. An important applicable property of hydrodynamic materials is the enhancement of conductivity by reducing their sizes. Figure 3 shows a mesoscopic device fabricated by the PI's student at MPSD in the summer of 2024. This particular device has 10 contact terminals, which enable measuring non-local transport phenomena – another applicable phenomenon found in the hydrodynamic regime.

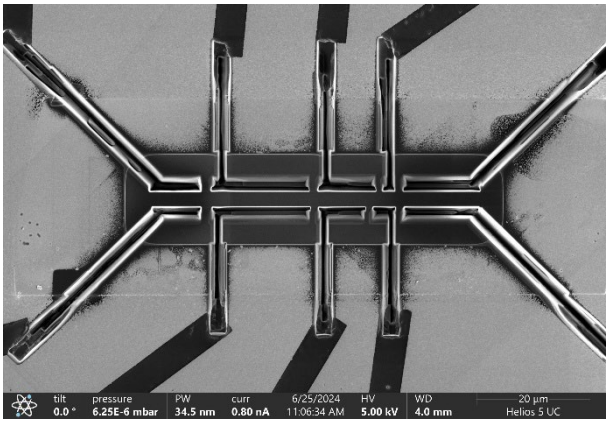

Figure 3: A mesoscopic device with 10 contact terminals ideal for measuring non-local electrical transport.

References

1. D. A. Bandurin, I. Torre, R. K. Kumar, M. B. Shalom, A. Tomadin, A. Principi, G. H. Auton, E. Khestanova, K. S. Novoselov, I. V. Grigorieva, L. A. Ponomarenko, A. K. Geim, and M. Polini, *Negative local resistance caused by viscous electron back ow in graphene*, Science **351**, 1055 (2016).

2. L. Lindsay, D. A. Broido, and T. L. Reinecke, *First-Principles Determination of Ultrahigh Thermal Conductivity of Boron Arsenide: A Competitor for Diamond?*, Physical Review Letters **111**, 025901 (2013).

3. A. Levchenko and J. Schmalian, *Transport properties of strongly coupled electron phonon liquids*, Annals of Physics **419**, 168218, (2020).

4. M. D. Bachmann, A. L. Sharpe, A. W. Barnard, C. Putzke, M. Konig, S. Khim, D. Goldhaber-Gordon, A. P. Mackenzie, and P. J. W. Moll, *Super-geometric electron focusing on the hexagonal Fermi surface of $PdCoO_2$*, Nature Communications **10**, 5081, (2019).

5. J. Gooth, F. Menges, N. Kumar, V. Sub, C. Shekhar, Y. Sun, U. Drechsler, R. Zierold, C. Felser, and B. Gotsmann, *Thermal and electrical signatures of a hydrodynamic electron fluid in tungsten diphosphide*, Nature Communications **9**, 4093, (2018).

Publications

6. Vincent M. Plisson, Xiaohan Yao, Yaxian Wang, George Varnavides, Alexey Suslov, David Graf, Eun Sang Choi, Hung-Yu Yang, Yiping Wang, Marisa Romanelli, Grant McNamara, Birender Singh, Gregory T. McCandless, Julia Y. Chan, Prineha Narang, Fazel Tafti, Kenneth S. Burch, *Engineering Anomalously Large Electron Transport in Topological Semimetals,* Advanced Materials **37**, 2310944 (2024)

7. J. Gaudet, H.-Y. Yang, E. M. Smith, T. Halloran, J. P. Clancy, J. A. Rodriguez-Rivera, Guangyong Xu, Y. Zhao, W. C. Chen, G. Sala, A. A. Aczel, B. D. Gaulin, F. Tafti, C. Broholm, *Spin-orbital order and excitons in magnetoresistive HoBi,* Phys. Rev. B **107**, 104423 (2023)

8. Joshuah T. Heath, Faranak Bahrami, Sangyun Lee, Roman Movshovich, Xiao Chen, Fazel Tafti, Kevin Bedell, *Signatures of a Majorana-Fermi surface in the Kitaev magnet $Ag_3LiIr_2O_6$,* Communications Physics **6**, 348 (2023)

9. Ying-Fei Li, Emily M. Been, Sudhaman Balguri, Chun-Jing Jia, Mira B. Mahendru, Zhi-Cheng Wang, Yi Cui, Su-Di Chen, Makoto Hashimoto, Dong-Hui Lu, Brian Moritz, Jan Zaanen, Fazel Tafti, Thomas P. Devereaux, Zhi-Xun Shen, *Colossal magnetoresistance from spin-polarized polarons in an Ising system,* PNAS **121**, e2409846121 (2024)

10. Sudhaman Balguri, Mira B. Mahendru, Enrique O. González Delgado, David E. Graf, Jose A. Rodriguez-Rivera, Adam A. Aczel Michael, J. Graf, Andreas Rydh, Kyle Fruhling, Xiaohan Yao, Thomas J. Hicken, Hubertus Luetkens,

Jonathan Gaudet, Fazel Tafti, *Two types of colossal magnetoresistance with distinct mechanisms in $Eu_5In_2As_6$,* Phys. Rev. B **111**, 115114 (2025)
11. G. Fabbris, E. H. T. Poldi, S. Sinha, J. Lim, T. Elmslie, J. H. Kim, A. Said, M. Upton, M. Abramchuk, F. Bahrami, C. Kenney-Benson, C. Park , G. Shen, Y. K. Vohra, R. J. Hemley, J. J. Hamlin, F. Tafti, D. Haskel, *Electronic structure of the honeycomb iridate Cu2IrO3 at high pressures,* Phys. Rev. B **111**, 075153 (2025)
12. Xin-Yue Zhang, Thomas K. M. Graham, Hyeonhu Bae, Yu-Xuan Wang, Nazar Delegan, Jonghoon Ahn, Zhi-Cheng Wang, Jakub Regner, Kenji Watanabe, Takashi Taniguchi, Minkyung Jung, Zdeněk Sofer, Fazel Tafti, David D. Awschalom, F. Joseph Heremans, Binghai Yan, and Brian B. Zhou, *Enhanced magnetization by defect-assisted exciton recombination in atomically thin $CrCl_3$,* Phys. Rev. Materials **8**, 104402 (2024)

Session II

Polaronic Electron Crystals in 2D Moiré Materials

Xiaoyang Zhu, Columbia University, New York, NY 10027

Keywords: quantum phases, moiré superlattice, two dimensional semiconductors, dynamics

Research Scope

This project aims to quantitative probe and understand many-body interactions responsible for electron ordering in emerging two-dimensional (2D) moiré materials. A focus is on electron-phonon coupling and polaron formation. While moiré materials have rapidly evolved, little is known about the many-body potential landscape responsible for correlated electron states. In their atomic counterparts, collective oscillations, i.e. phonons, are quantitatively related to inter-atomic force constant matrices. In the PI's approach, a correlated electron phase in a moiré interface is perturbed by a pump pulse to launch coherent oscillations via Raman mechanisms, the result is monitored by a probe pulse from oscillations in optical responses. At high excitation power, the experiment probes dynamics of melting and recrystallization of the electron crystals. These experiments will provide quantitative insight into the nature of correlated electrons, the potential energy landscape for ordering, and their interactions with phonons. There are three major goals: 1) Determine the melting and recrystallization dynamics of ordered electron states in transition metal dichalcogenide (TMDC) moiré bilayers; 2) Probe two collective oscillations, the amplitude (Higgs) mode and the phase (Nambu-Goldstone) mode of the ordered electrons; and 3) Extending the dynamic probes to the ordered exciton phases in TMDC moiré structures.

Recent Progress

We made advances in establishing the polaronic nature of Mott states in the WS_2/WSe_2 moiré system [1], in mechanistically distinguishing different Mott states based on distinct melting and reordering rates [2], in revealing a general mechanism of acoustic phonon modulation of moiré states [3], and in discovering a zoo of correlated states in the twisted MoTe2 bilayer moiré system [4].

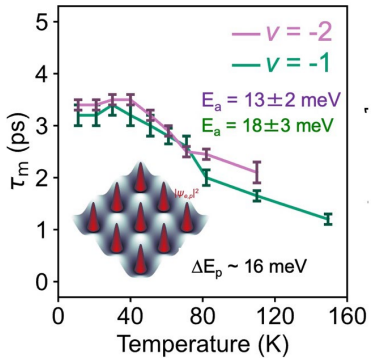

Fig. 1. Thermally activated melting of the v = -1 and v= -2 hole-doped Mott states at the WS_2/WSe_2 moiré interface, with the shown activation energies. DFT calculation confirms the polaronic nature of the Mott state. with polaron binding energy of 16 meV. *Phys. Rev. Lett. 132*, 126501 (2024).

Two-dimensional moiré materials have emerged as the most versatile platform for realizing quantum phases of electrons. Here, we explore the stability origins of correlated states in WSe_2/WS_2 moiré superlattices. We find that ultrafast electronic excitation leads to partial melting of the Mott states on time scales five times longer than predictions from the charge hopping integrals and that the melting rates are thermally activated, with activation energies of 18±3 and 13±2 meV for the one- and two-hole Mott states, respectively, suggesting significant electron-phonon coupling. DFT calculation of the one-hole Mott state confirms polaron formation and yields a hole-polaron binding energy of 16 meV. These findings reveal a close interplay of electron-electron and electron-phonon interactions in stabilizing the polaronic Mott insulators at transition metal dichalcogenide moiré interfaces.

Despite the central importance of Mott states in moiré physics, little is known about their underlying nature. Here, we use pump-probe spectroscopy to show distinct time-domain

signatures of correlated insulators at fillings of one (ν = -1) and two (ν = -2) holes per moiré unit cell in the angle-aligned WSe_2/WS_2 system. Following photo-doping, we find that the disordering time of the ν = -1 state is independent of excitation density (n_{ex}), as expected from the characteristic phonon response time associated with a polaronic state. In contrast, the disordering time of the ν = -2 state scales with n_{ex}^-0.5 in agreement with plasmonic screening from free holons and doublons. These states display disparate reordering behavior dominated either by first order (ν = -1) or second order (ν = -2) recombination, suggesting the presence of Hubbard excitons and free carrier-like holons/doublons, respectively. Our work delineates the roles of electron-phonon (e-ph) versus electron-electron (e-e) interactions in correlated insulators on the moiré landscape and establishes non-equilibrium responses as mechanistic signatures for distinguishing and discovering quantum phases.

Van der Waals (vdW) structures host a broad range of physical phenomena. New opportunities arise if different functional layers may be remotely modulated or coupled in a device structure. Here we demonstrate the in-situ coherent modulation of moiré excitons and correlated Mott insulators in transition metal dichalcogenide (TMD) moirés with on-chip terahertz (THz) waves. Using common dual-gated device structures of a TMD moiré bilayer sandwiched between two few-layer graphene (fl-Gr) gates with hexagonal boron nitride (h-BN) spacers, we launch coherent phonon wavepackets at ~0.4-1 THz from the fl-Gr gates by femtosecond laser excitation. The waves travel through h-BN spacer, arrive at the TMD bilayer with precise timing, and coherently modulate the moiré excitons or Mott states. These results demonstrate that the fl-Gr gates, often used for electrical control, can serve as on-chip opto-elastic transducers to generate THz waves for coherent control and vibrational entanglement of functional layers in moiré devices.

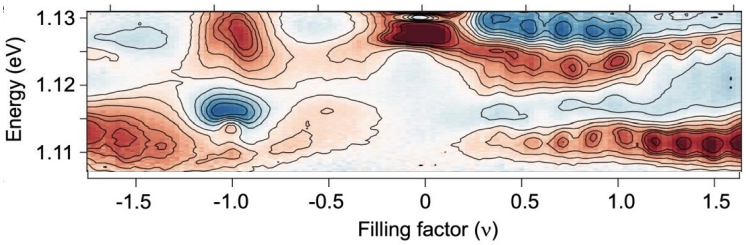

Fig. 2. Pump-probe spectroscopic sensing of correlated quantum phases in twisted $MoTe_2$ bilayer. This provides hitherto the most sensitive technique in detecting a range of quantum phases in moiré systems. *Nature*, https://doi.org/10.1038/s41586-025-08954-8 (2025).

The fractional quantum anomalous Hall (FQAH) effect was recently discovered in twisted $MoTe_2$ bilayers ($tMoTe_2$). Experiments to date have revealed Chern insulators from hole doping at v = -1, -2/3, -3/5, and -4/7 (per moiré unit cell). In parallel, theories predict that, between v = -1 and -3, there exist exotic quantum phases, such as the coveted fractional topological insulators (FTI), fractional quantum spin Hall (FQSH) states, and non-abelian fractional states. Here we employ transient optical spectroscopy on $tMoTe_2$ to reveal nearly 20 hidden states at fractional fillings that are absent in static optical sensing or transport measurements. A pump pulse selectively excites charge across the correlated or pseudo gaps, leading to the disordering (melting) of correlated states. A probe pulse detects the subsequent melting and recovery dynamics via exciton and trion sensing. Besides the known states, we observe additional fractional fillings between v = 0 and -1 and a large number of states on the electron doping side (n > 0). Most importantly, we observe new states at fractional fillings of the Chern bands at v = -4/3, -3/2, -5/3, -7/3, -5/2, and -8/3. These states are potential candidates for the predicted exotic topological phases. Moreover, we show that melting of correlated states occurs on two distinct time scales, 2-4 ps and 180-270 ps, attributed

to electronic and phonon mechanisms, respectively. We discuss the differing dynamics of the electron and hole doped states from the distinct moiré conduction and valence bands.

Future Plans

During the next funding period, the PI and team will continue time-domain studies of moiré quantum matter, including 1) the exploration of magnetic ordering and topological states in $MoTe_2$ using circularly polarized light; 2) the direct time domain view of trion formation from ultrafast charge injection into WSe2 monolayer and bilayers.

Publications

1. Eric A. Arsenault, Yiliu Li, Birui Yang, Xi Wang, Heonjoon Park, Edoardo Mosconi, Enrico Ronca, Takashi Taniguchi, Kenji Watanabe, Daniel Gamelin, Andrew Millis, Cory R. Dean, Filippo de Angelis, Xiaodong Xu, X.-Y. Zhu. *Two-dimensional moiré polaronic electron crystals*, Phys. Rev. Lett. 132, 126501 (2024).
2. Yiliu Li, Eric A Arsenault, Birui Yang, Xi Wang, Heonjoon Park, Yinjie Guo, Takashi Taniguchi, Kenji Watanabe, Daniel Gamelin, James C Hone, Cory R Dean, Sebastian F Maehrlein, Xiaodong Xu, Xiaoyang Zhu, *Coherent Modulation of Two-Dimensional Moiré States with On-Chip THz Waves,* Nano Lett. 24, 12156–12162 (2024).
3. Eric A Arsenault, Yiliu Li, Birui Yang, Takashi Taniguchi, Kenji Watanabe, James C Hone, Cory R Dean, Xiaodong Xu, X.-Y. Zhu, *Time-Domain Signatures of Distinct Correlated Insulators in a Moiré Superlattice*, Nature Commun. 16, 549 (2025).
4. Yiping Wang, Jeongheon Choe, Eric Anderson, Weijie Li, Julian Ingham, Eric A Arsenault, Yiliu Li, Xiaodong Hu, Takashi Taniguchi, Kenji Watanabe, Xavier Roy, Dmitri Basov, Di Xiao, Raquel Queiroz, James C Hone, Xiaodong Xu, X.-Y. Zhu, *Hidden States and Dynamics of Fractional Fillings in twisted $MoTe_2$ Bilayers,* Nature https://doi.org/10.1038/s41586-025-08954-8 (2025).

Understanding and designing phosphide solar absorbers with high carrier lifetime

Geoffroy Hautier,[1] David P. Fenning,[2] Ismaila Dabo,[3] Andriy Zakutayev,[4] Sage Bauers,[4] Jifeng Liu,[1] and Kirill Kovnir[5]

1 Thayer School of Engineering, Dartmouth College, 2 Department of Nanoengineering, UC San Diego, 3 Carnegie Mellon University, 4 National Renewable Energy Laboratory, 5 Department of Chemistry, Iowa State University

Keywords: High-throughput screening, phosphides, photovoltaic, semiconductors, non-radiative lifetime

Research Scope

Semiconductors are central to opto-electronic and energy applications. They are the building blocks of many devices. Finding new semiconductors with favorable opto-electronic properties would have important implications for technologies such as light-emitting diodes (LEDs), solar cells and photoelectrochemical devices. In the field of photovoltaics (PV), the search for new semiconductors acting as solar absorbers is still ongoing. While silicon-based solar cells dominate today's PV market, alternative materials used in thin-film solar cells could have remarkable prospects because their manufacturing involves less embedded energy. Thin-film solar cells can also offer excellent band gap tunability and compatibility with flexible substrates, enabling tandem devices in combination with silicon and building-integrated PV systems. A few materials have been well-studied for use as absorber layers in thin-film solar cells, including CdTe, $Cu(In,Ga)Se_2$ (CIGS), $Cu_2ZnSn(S,Se)_4$ (CZTS) and lead halide perovskites. Among them, CdTe and CIGS have enabled >23% efficient solar cells and have been commercialized. Unfortunately, both CdTe and CIGS rely on critical elements (Te, In and Ga), raising concerns for terawatt-scale deployment. Over the last decade, the research focus of thin-film PV has been largely directed towards emerging technologies based on the earth-abundant materials CZTS, and, in particular, lead halide perovskites. However, CZTS significantly lags behind CdTe and CIGS in power conversion efficiency due to intrinsic defects that are very difficult (or impossible) to mitigate, while halide perovskites offer exceptional properties but continue to suffer from important stability issues.

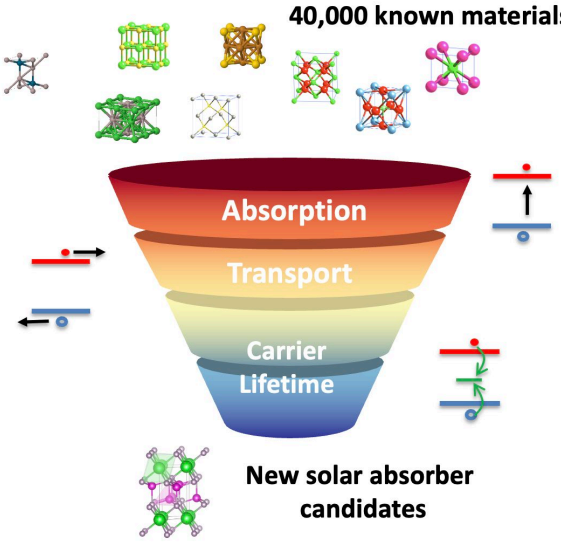

Figure 1: Computational materials screening approach

The properties of interest for high performance opto-electronic semiconductor are well known and computable with modern first principles techniques. The band gap sets the absorption/emission wavelength, carrier transport is controlled by effective masses and phonon/defect scattering, and very importantly, the non-radiative lifetime is controlled by defects which can act as recombination center through the Shockley-Read-Hall (SRH) process. The importance of carrier capture by defects has been recently highlighted by the high performance of halide perovskites

which has been linked to their intrinsic "defect-tolerance". Armed with these developments in first principles computations, our program targets the development of a computationally-driven search for new semiconductors especially for thin film PV applications. It combines high-throughput computational screening to identify promising materials (see **Figure 1**) followed-up by experimental realization and characterization as thin films, powders and both single- and colloidal crystals. One of the unique components of our approach is that we take into account intrinsic defects and focus our search on materials that are likely to be "defect-tolerant".

Recent Progress

We have used our computational screening approach to search among 40,000 inorganic materials from the Inorganic Crystal Structure Database (ICSD). We have identified a series of materials combining promising absorption in the visible, carrier transport and long carrier lifetime. By also taking into account criteria on earth-abundance, cost and air stability, we singled-out $BaCd_2P_2$, a compound known for over 40 years but long-since "forgotten." Our deeper computational analysis shows that the computed nonradiative recombination lifetime in $BaCd_2P_2$ is longer than or comparable to those in established high-efficiency absorbers such as perovskites. Experimentally, we have synthesized $BaCd_2P_2$ powder samples, showing that this material exhibits bright photoluminescence (PL) on par with semiconductor-grade GaAs and has a carrier lifetime of up to 30 ns measured by Time-Resolved Microwave Conductivity (TRMC) (see **Figure 2**). Very recent photoconductivity studies on $BaCd_2P_2$ single crystals further demonstrated a carrier lifetime >500 ns. This carrier lifetime is already longer or in par with well-established solar absorbers such as CdTe, as well as single crystalline GaAs. Very importantly, $BaCd_2P_2$ is extremely air- and moisture-stable and will not have the air sensitivity issues of perovskites. To our knowledge, this is the first time computational screening has been used to successfully identify a promising solar absorber with attractive carrier lifetime. Notably, $BaCd_2P_2$ can be described as a Zintl compound with chemistry and structure quite dissimilar to known high-performance solar absorbers stressing the power of high-throughput screening in searching out-of-the-box.

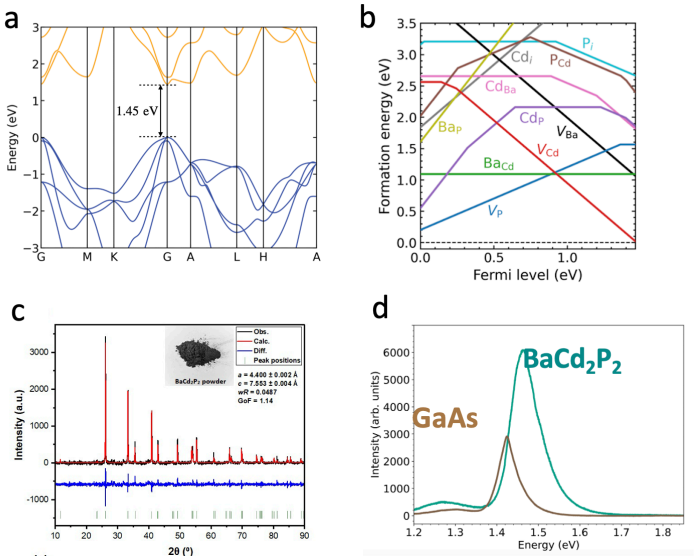

Figure 2: $BaCd_2P_2$ as a promising solar absorber with adequate band structure (a), favorable defects without deep defects low-lying in formation energy (b). The synthesis (c) and photoluminescence (d) of this promising material are provided as well.

The discovery of $BaCd_2P_2$ unveils a broad class of AM_2X_2 (A=Ca, Sr, Ba, M=Zn, Cd, Mg X=N, P, As, Sb, Bi) Zintl absorbers. Using first principles computations, we have shown that across these chemistries the $BaCd_2P_2$ *P*-3*m*1 crystal structure is often thermodynamically stable and that a large range of band gaps from 0 to 2.6 eV can be obtained through chemical tuning. We

have synthesized a large set of these materials as powders and performed PL measurements. Some of these materials have been grown as single crystal as well. Reaching higher band gap (e.g., 1.8 eV) would be of interest for tandem cells and we have shown that mixing Mg on the Cd or Zn site would be effective in increasing the band gap. Additionally, we have predicted the existence of not-yet-made quaternary versions of the *P*-3*m*1 structure that we confirmed experimentally via synthesis, structure and optical characterization.

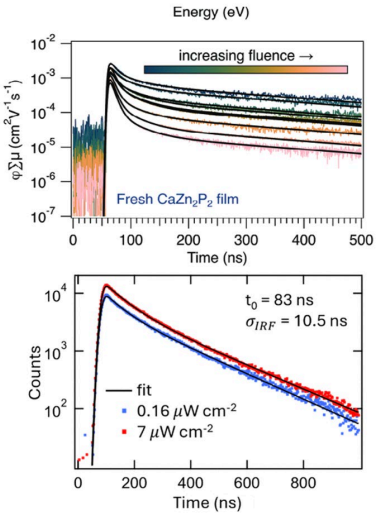

Figure 3: (up) TRMC measurements for $CaZn_2P_2$ thin film (down) TR-PL on $BaCd_2P_2$ nanoparticles.

Solar absorber materials can be used in thin film PV devices but also in photoelectrochemical devices. Absorbed light is used then to enable chemical reactions such as water splitting into hydrogen and oxygen. The Zintl AM_2P_2 could be of interest here in view of their promising opto-electronic properties. We have performed extensive (photo-)electrochemical characterization of $CaCd_2P_2$. We found that $CaCd_2P_2$ is a stable photoelectrode for water oxidation under AM1.5g solar simulation, without any extrinsic photocorrosion barrier layer, unlike traditional III-Vs, Si, CdTe, or perovskites. These Zintl phases could break the long standing paradigm that a photoelectrode is either stable or a high-performing semiconductor.

Ultimately both characterization needs and possible devices call for growing these Zintl phosphides in thin film form. We have successfully synthesized $CaZn_2P_2$ and $SrZn_2P_2$ thin films using reactive sputtering. The dense crystalline films are of good quality and importantly application-wise they are obtained at very moderate growth temperatures (200°C). TMRC indicates encouraging carrier lifetime on par with the $BaCd_2P_2$ powder around the 10's of ns (see **Figure 3**). Additionally, halide perovskites are often synthesized from solution processes as nanocrystals, but phosphides have also a good track-record in this field. Our team synthesized $BaCd_2P_2$ quantum dots, the first of any Zintl phase. We demonstrated nanoconfinement shifting the band gap to higher values up to 1.8 eV for 3 nm particles, potentially a promising candidate for tandem cells on Si. We also performed time-resolved photoluminescence (TRPL) and photoluminescence quantum yield (PLQY) experiments (see **Figure 3**). The TRPL confirms again attractive long carrier lifetime (83 ns in average) and the PLQY indicates a 21% efficiency on par with early results in halide perovskites. This confirms the exceptional non-radiative properties of the AM_2P_2 Zintl phases across different chemistries (Zn vs Cd) or growth method (nanoparticles or thin films).

Figure 4: computed carrier lifetime from first principles for known phosphides versus their computed band gap (HSE). The color indicates stability in air.

Building on our successful computationally-driven identification of the AM_2X_2 Zintl family, we have improved our computational screening approach by using a recently developed single-shot HSE approach which significantly improves the modeling of the charge transition levels of defects. We have built an updated database of known phosphides and their defects including more than 4,000 charged defect computations (see **Figure 4**). We have identified a series of new phosphides of interest and followed-up with further computations. These materials have been selected because of their expected stability and ease of synthesis (ZnP_2, $SrIn_2P_2$, MgP_4, $RbZn_4P_3$, …). Our team synthesized these phases and we are characterizing these materials by PL and TRMC. We are also using this data to identify what drives defect-tolerance in phosphides.

Future Plans

On the short-term, there are still significant opportunities in better understanding the AM_2P_2 Zintl family and the reason for their exceptional properties. With the high synthesis control we have achieved on Cd and Zn-based powders and single-crystals, we will compare the different ACd_2P_2 and AZn_2P_2 materials and rationalizing their difference in PL and TRMC including using first principles computations. Additionally, while many new phosphides have been synthesized, their full characterization is still ongoing and will help us compare with theoretical results both at the screening (single-shot HSE) and full HSE level.

On the longer-term, the development of a successful workflow for the computationally-driven detection of new semiconductor opens many avenues. The improvement of the computational methods (e.g., including carrier capture proxies at the screening level) and the acceleration of the synthesis and characterization steps are promising directions as well as the extension of our targeted chemical landscape to yet-to-be-made phosphides (e.g., relying on emerging databases of predicted materials) or other chemistries (e.g., arsenides, sulfides).

Publications

1. Pike, A., Yuan, Z., Kassa, G., Hasan, M. R., Goswami, S., Dugu, S., Quadir, S., Zakutayev, A., Bauers, S., Kovnir, K., Liu, J., & Hautier, G. A Map of the Zintl AM_2Pn_2 Compounds: Influence of Chemistry on Stability and Electronic Structure. In Revision in in Chemistry of Materials (2025) https://doi.org/10.48550/arXiv.2502.08801
2. Hautzinger, M., Quadir, S., Feingold, B., Seban, R., Thornton, A., Dutta, N., Norman, A., Leahy, I., Muhammed, H., Kovnir, K., Reid, O., Larson, B., Luther, J., Beard, M., & Bauers, S. R. S*ynthesis and Characterization of Zintl-Phase $BaCd_2P_2$ Quantum Dots for Optoelectronic Applications*. ACS Nano. 19, 12345–12353 (2025)
3. Claes, R., Poncé, S., Rignanese, G.-M., & Hautier, G. *Phonon-limited electronic transport through first principles.* Nature Reviews Physics, **7**, 73–90 (2025)
4. Sarkar, A.; Nepal, N.; Coban, Y.; Pike, A.; Harycki, S.; Viswanathan, G.; Gundlach-Graham, A.; Wang, L.-L.; Hautier, G.; Kovnir, K. *$BaCu_{4/3}Si_{2/3}P_2$ and $BaCu_{2-(x+y)}Zn_xSi_yP_2$: Expanding The Semiconducting Landscape in the ThCr2Si2-type Family*. Submitted to Inorg. Chem. (2025)
5. Abusa, Y.; Greenfield, J.; Viswanathan, G.; Goswami, G. Ross, E.; Yox, P.; Oppong, R.; Ojo, I.; Liu, J.; Ozarowski, A.; Kovnir, K. *A competition between 2D and 3D magnetic orderings in novel mixed valent copper frameworks*. Chem. Sci. **2025**, *accepted*.
6. Yuan, Z.; Dahliah, D.; Hasan, M. R.; Kassa, G.; Pike, A.; Quadir, S.; Claes, R.; Chandler, C.; Xiong, Y.; Kyveryga, V.; Yox, P.; Rignanese, G.-M.; Dabo, I.; Zakutayev, A.; Fenning, D. P.; Reid, O. G.; Bauers, S.; Liu, J.; Kovnir, K.; Hautier, G. *Discovery of the Zintl-Phosphide $BaCd_2P_2$ as a Long Carrier Lifetime and Stable Solar Absorber*. Joule, **5**, 1412-1429 (2024).

7. Quadir, S., Yuan, Z., Esparza, G. L., Dugu, S., Mangum, J. S., Pike, A., Hasan, M. R., Kassa, G., Wang, X., Coban, Y., Liu, J., Kovnir, K., Fenning, D. P., Reid, O. G., Zakutayev, A., Hautier, G., & Bauers, S. R. *Low-Temperature Synthesis of Stable $CaZn_2P_2$ Zintl Phosphide Thin Films as Candidate Top Absorbers.* Advanced Energy Materials, **14**, 2402640 (2024)
8. Sarkar, A.; Porter, A.P.; Viswanathan, G.; Yox, P.; Earnest, R.A.; Wang, J.; Rossini, A.J.; Kovnir, K. *$BaCuTP_2$ (T = Al, Ga, In): A Semiconducting Black Sheep in the $ThCr_2Si_2$ Intermetallic Family*. J. Mater. Chem. A, **12**, 10481-10493 (2024).
9. Yuan, Z., Dahliah, D., Claes, R., Pike, A., Fenning, D. P., Rignanese, G.-M., & Hautier, G. *Assessing Carrier Mobility, Dopability, and Defect Tolerance in the Chalcogenide Perovskite $BaZrS_3$*. PRX Energy, **3**, 033008 (2024)
10. Yuan, Z.; Xiong, Y.; Hautier, G. *First-Principles Study of Intrinsic and Hydrogen Point Defects in the Earth-Abundant Photovoltaic Absorber Zn_3P_2*. J. Mater. Chem. A, **11** (38), 20592–20600 (2023).

Nanoscale Quantum Sensing and Imaging of Topological Magnets

Chunhui (Rita) Du, Georgia Institute of Technology

Keywords: Topological materials, quantum sensing, scanning single-spin quantum magnetometry, quantum magnetism, hybrid quantum systems.

Research Scope

The major research focus of this program is to utilize optically active solid-state spin defects [1, 2, 3] to achieve nanoscale quantum sensing and imaging of two-dimensional (2D) magnetism, probing the fundamental physics underlying the interplay between spin, charge, and twist lattice engineering in emergent quantum states of matter. Specifically, we propose to utilize scanning nitrogen-vacancy (NV) microscopy to visualize stacking engineered spatially dependent magnetic phase transitions within moiré supercells of twisted van der Waals (vdW) magnets [2]. We are also interested in using hexagonal boron nitride (hBN)-based wide-field quantum microscopy to image field-free deterministic magnetic switching of room-temperature 2D magnet in an all-vdW spin-orbit torque (SOT) system [3]. Our "stretch" goal is to develop hybrid quantum systems consisting of quantum magnets and solid-state spin defects to realize novel quantum entanglement between distant spin qubits.

The proposed research will make important contributions to the burgeoning field of quantum materials and promote the role of topological materials in designing next-generation, transformative quantum information sciences and technologies. By developing the cutting-edge quantum sensing techniques using 3D and 2D spin defects and demonstrating their operations under a broad range of experimental conditions, we propose to provide versatile solid-state quantum sensing platforms, which could be extended naturally to a large family of untapped material systems and benefit the material science community in the long run by expediting progress towards future quantum technological innovations.

Recent Progress

Over the past years, Dr. Du and colleagues have been intensively working on developing state-of-the-art cryogenic scanning NV quantum microscopy for the proposed research [2]. Our measurement system consists of a home-built confocal and a custom-designed atomic force microscope operating in a cryostat as shown in Fig. 1. The variable temperature insert is placed inside the bore of a three-axis superconducting vector magnet. The microscope head is positioned at the bottom of the insert. A window on top of the cryostat provides optical access for NV measurements. A diamond cantilever is glued to a quartz tuning fork for force-feedback atomic force microscopy operations [1, 2]. A sample holder with imprinted coplanar waveguides is fixed onto a stack of piezo-based positioners and scanners to perform engagement with the diamond cantilever and scanning measurements. The ultimate spatial resolution of scanning NV microscopy with single-spin sensitivity is mainly determined by the NV-to-sample distance, which can reach

tens of nanometers capable of resolving nanomagnetism in cutting-edge condensed matter systems.

We have demonstrated scanning NV quantum sensing of moiré magnetism hosted by twisted chromium triiodide CrI_3 [2]. For the first time, we observed spatial and thermodynamic phase separations of the co-existing ferromagnetic (FM)-antiferromagnetic (AFM) states within and across individual moiré cells of small-angle twisted CrI_3 (Fig. 1). By measuring temperature dependent spin fluctuations at the coexisting FM-AFM regions in twisted CrI_3, we explicitly show that the Curie temperature of the FM state is higher than the Néel temperature of the AFM one by ~10 K. Our mean-field calculations attribute such a spatial and thermodynamic phase separation to stacking order modulated interlayer exchange coupling at the twisted interface of moiré superlattices. The presented results highlight twist engineering as a promising tuning knob to realize on-demand control of not only the nanoscale spin order of moiré quantum matter but also its dynamic magnetic responses, which may find applications in developing transformative vdW electronic and magnetic devices.

We also introduce spin ensembles embedded in 2D hBN crystals to achieve wide-field quantum imaging of field-free deterministic magnetic switching of room-temperature two-dimensional

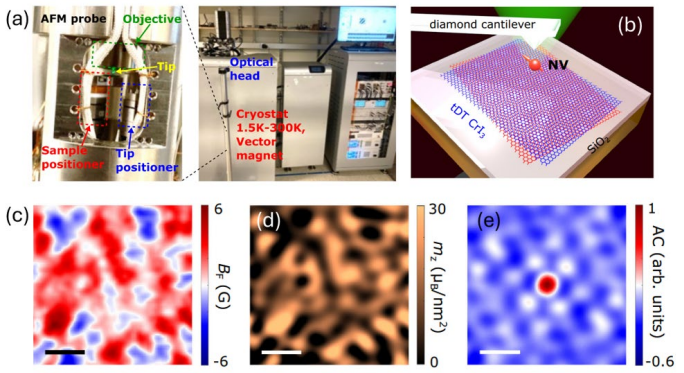

Figure 1. Scanning NV imaging of moiré magnetism. (a) The cryogenic scanning NV microscope in Du lab. (b) Schematic illustration of scanning NV measurements of twisted CrI_3. (c) Nanoscale scanning NV imaging of magnetic stray fields emanating from a surveyed sample area of twisted double trilayer CrI_3 device. (d)-(e) Reconstructed magnetization and normalized autocorrelation (AC) maps of the stray field pattern. Scale bar is 200 nm. Presented results were recently published by Dr. Du in *Nat. Commun.* **15**, 5712 (2024) [2].

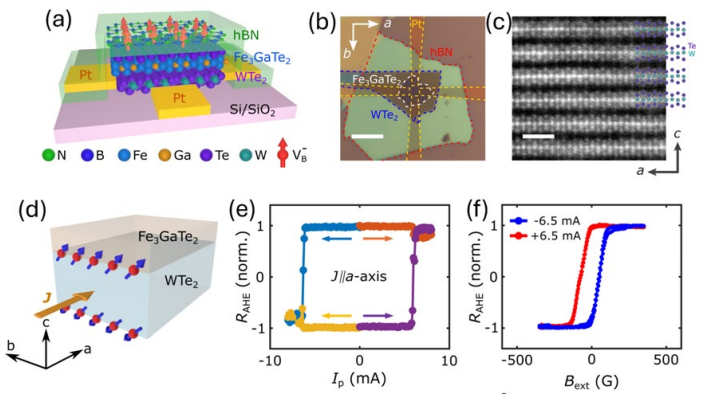

Figure 2. hBN-based wide-field quantum imaging. (a). Schematic of the WTe_2/Fe_3GaTe_2/hBN vdW heterostructure for quantum imaging and electrical SOT switching measurements. (b) Optical microscopy image of a prepared WTe_2/Fe_3GaTe_2/hBN device. The scale bar is 10 µm. (c) Cross-sectional HAADF-STEM image of a prepared device viewed along the *b*-axis of WTe_2. (d) Generation of out-of-plane and in-plane polarized spin currents when an electrical charge current *J* flows along the low-symmetry crystallographic axis of WTe_2. (e) Normalized anomalous Hall resistance of Fe_3GaTe_2 measured as a function of electrical write current pulse I_p applied along the *a*-axis of WTe_2. (f) Variations of measured Fe_3GaTe_2 anomalous Hall loops in response to positive and negative electric current pulses (I_p = 6.5 mA) applied along the *a*-axis of WTe_2.

magnet Fe_3GaTe_2 (Fig. 2) [3]. Out-of-plane polarized spin currents are generated by the spin source material WTe_2 with reduced crystallographic symmetry, which exerts unconventional SOTs on proximal perpendicular Fe_3GaTe_2 magnetization. We show that robust deterministic magnetic switching can be realized in few-layer thick vdW magnet Fe_3GaTe_2 without the assistance of an external magnetic field. Nanoscale magnetic imaging was achieved by utilizing optically active spin defects in the hBN encapsulation layer. Using wide-field quantum magnetometry techniques, we directly visualized the microscopic Fe_3GaTe_2 stray field profile as a function of electrical switching currents (Fig. 3), revealing how the observed magnetic switching evolves from deterministic to indeterministic behavior due to the interplay between out-of-plane spins, in-plane spins, and Joule heating. Our study enriches the current understanding of SOT-induced magnetization dynamics in vdW heterostructures, providing valuable information for future design of energy-efficient 2D spin memory devices. Considering the extensive usage of hBN in preparing vdW nano-electronics, we share the optimism that the demonstrated vdW quantum sensing platform could be extended readily to a broad family of 2D stacking systems, opening new avenues for investigating nanoscale electromagnetic behaviors in 2D quantum matter.

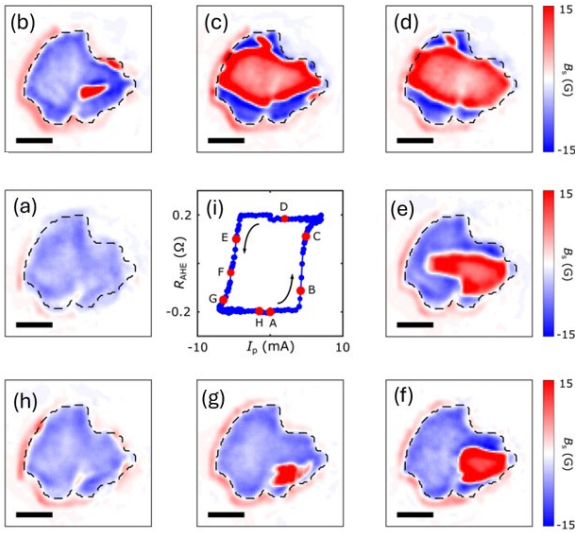

Figure 3. Visualizing field-free deterministic magnetic switching of Fe_3GaTe_2. (a)-(h) hBN-based quantum imaging of microscopic evolutions of Fe_3GaTe_2 magnetic domains during the field-free deterministic magnetic switching process. The scale bar is 4 μ m. (i) Anomalous Hall resistance of Fe_3GaTe_2 measured as a function of electrical write current pulse I_p in absence of an external magnetic field.

Future Plans

We will continue our efforts on using cutting-edge quantum sensing techniques to investigate nanoscale electromagnetic behaviors of emergent quantum materials. The material systems we are interested in include chiral antiferromagnet Mn_3Sn [1], intrinsic topological magnets $MnBi_2Te_4$ $(Bi_2Te_3)_n$ [4] and moiré quantum matter [2]. We will utilize cryogenic scanning NV microscopy to perform quantum sensing of microscopic magnetic, electrical and thermal behaviors in the proposed materials, exploring the interplay between electronic correlations, topology, and unconventional magnetism in topological materials. Taking advantage of out-of-plane polarized spin currents generated from the low crystal-symmetry spin source material WTe_2 [3], we propose to experimentally realize field-free deterministic magnetic switching in noncollinear antiferromagnet Mn_3Sn.

In parallel, we also plan to study the nontrivial topological states of even-layer $MnBi_2Te_4$, which is predicted to be an axion insulator candidate with the antiferromagnetic ground state. So far, direct experimental evidence of axion insulators remains elusive because its vanishingly small Hall response is technically challenging to be distinguished from the counterpart in trivial normal

insulators. We plan to apply a vertical electric field to generate finite, quantized magnetization in even-layer $MnBi_2Te_4$ and use scanning NV magnetometry to image the topological magnetoelectric effect induced magnetic moment, providing the smoking gun evidence of the axion insulating state in $MnBi_2Te_4$.

References

1. S. Li, M. Huang, H. Lu, N. J. McLaughlin, Y. Xiao, J. Zhou, E. E. Fullerton, H. Chen, H. L. Wang, and C. H. R. Du, *Nanoscale Magnetic Domains in Polycrystalline Mn_3Sn Films Imaged by a Scanning Single-Spin Magnetometer*, Nano Letters **23**, 5326 (2023).
2. S. Li, Z. Sun, N. J. McLaughlin, A. Sharmin, N. Agarwal, M. Huang, S. H. Sung, H. Lu, S. Yan, H. Lei, R. Hovden, H. Wang, H. Chen, L. Zhao, and C. H. R. Du, *Observation of Stacking Engineered Magnetic Phase Transitions within Moiré Supercells of Twisted van der Waals Magnets*, Nature Communications **15**, 5712 (2024).
3. X. Zhang, J. Zhou, C. Hu, K. Deng, C. Wang, N. Agarwal, H. Jin, Faris A. Al-Matouq, S. Xu, R. S. Trivedi, S. Li, S. Rathi, H. Lu, Z. Jiang, V. Taufour, R. Hovden, L. Zhao, R. Cheng, X. Xu, J.-H. Chu, C. H. R. Du, and H. L. Wang, *Visualizing Field-free Deterministic Magnetic Switching of all–van der Waals Spin-Orbit Torque System Using Spin Ensembles in Hexagonal Boron Nitride*, arXiv:2502.04561 (2025).
1. Y. Deng, Y. Yu, M. Z. Shi, Z. Guo, Z. Xu, J. Wang, X. H. Chen, Y. Zhang, *Quantum Anomalous Hall Effect in Intrinsic Magnetic Topological Insulator $MnBi_2Te_4$*, Science **367**, 895–900 (2020).

Publications

1. S. Li, M. Huang, H. Lu, N. J. McLaughlin, Y. Xiao, J. Zhou, E. E. Fullerton, H. Chen, H. L. Wang, and C. H. R. Du, Nanoscale *Magnetic Domains in Polycrystalline Mn_3Sn Films Imaged by a Scanning Single-Spin Magnetometer*, Nano Letters **23**, 5326 (2023).
2. N. J. McLaughlin, S. Li, J. A. Brock, S. Zhang, H. Lu, M. Huang, Y. Xiao, J. Zhou, Y. Tserkovnyak, E. E. Fullerton, H. L. Wang, and C. H. R. Du, *Local Control of a Single Nitrogen-Vacancy Center by Nanoscale Engineered Magnetic Domain Wall Motion*, ACS Nano **24**, 25689 (2023).
3. M. Huang, J. Green, J. Zhou, V. Williams, S. Li, H. Lu, D. Djugba, H. L. Wang, B. Flebus, N. Ni and C. H. R. Du, *Layer-dependent Magnetism and Spin Fluctuations in Atomically Thin van der Waals Magnet $CrPS_4$*, Nano Letters **23**, 8099 (2023).
4. S. Li, Z. Sun, N. J. McLaughlin, A. Sharmin, N. Agarwal, M. Huang, S. H. Sung, H. Lu, S. Yan, H. Lei, R. Hovden, H. Wang, H. Chen, L. Zhao, and C. H. R. Du, *Observation of Stacking Engineered Magnetic Phase Transitions within Moiré Supercells of Twisted van der Waals Magnets*, Nature Communications **15**, 5712 (2024).
5. S. Li, S. P. Kelly, J. Zhou, H. Lu, Y. Tserkovnyak, H. L. Wang, and C. H. R. Du, *Observation of On- and Off-resonant Interaction between a Solid-state Spin Qubit and a Superconducting Resonator*, arXiv. 2412.18896 (2024).
6. X. Zhang, J. Zhou, C. Hu, K. Deng, C. Wang, N. Agarwal, H. Jin, Faris A. Al-Matouq, S. Xu, R. S. Trivedi, S. Li, S. Rathi, H. Lu, Z. Jiang, V. Taufour, R. Hovden, L. Zhao, R. Cheng, X. Xu, J.-H. Chu, C. H. R. Du, and H. L. Wang, *Visualizing Field-free Deterministic Magnetic Switching of all–van der Waals Spin-Orbit Torque System Using Spin Ensembles in Hexagonal Boron Nitride*, arXiv:2502.04561 (2025).
7. Z. Sun, G. Ye, C. Zhou, M. Huang, N. Huang, X. Xu, Q. Li, G. Zheng, Z. Ye, C. Nnokwe, L. Li, H. Deng, L. Yang, D. Mandrus, Z. Y. Meng, K. Sun, C. H. R. Du, R. He, and L. Zhao, *Dimensionality Crossover to a Two-Dimensional Vestigial Nematic State from a Three-dimensional Antiferromagnet in a Honeycomb van der Waals Magnet*, Nature Physics **20**, 1764 (2024).

Session III

Opening New Frontiers of Epsilon-Near-Zero Optics

Alexandra Boltasseva, Purdue University (Principle Investigator)
Zubin Jacob, Purdue University (Co-Investigator)
Vladimir M. Shalaev, Purdue University (Co-Investigator)

Keywords: Epsilon-near-zero, nonlinear, transparent conducting oxides, transition metal nitrides

Research Scope

This project focuses on discovering novel platforms to enhance the generally weak interaction of light and matter by exploring novel interaction regimes. Specifically, we explore epsilon-near-zero (ENZ) materials whose real part of the dielectric permittivity approaches zero, taking a holistic approach to understanding and controlling ENZ properties in transparent conducting oxides (TCOs) and transition metal nitrides (TMNs). We study the enhancement of nonlinear optics in ENZ regime and preform optical characterization of ENZ materials focusing on ultrafast and extreme modulation of optical parameters. We also study the control of various emission processes in the presence of homogeneous and structured ENZ media. Our major results can be broadly categorized into two divisions i) investigation of material properties for ENZ applications and ii) the dynamic control and tunability of light using ENZ.

Recent Progress

Epsilon-near-zero materials host a plethora of exciting phenomena including field enhancement, wavelength expansion, and the slow-light effect. An important ENZ material platform are transparent conduction oxides that have static and dynamically tunable ENZ properties. This past period, we have focused partly on ENZ phenomena in dynamically pumped TCOs. We studied the role of losses in ENZ dynamics and demonstrated the spatial and spectral fission of light in optically-pumped thin film TCOs. We also discovered a new mechanism of third-harmonic generation in pumped TCOs which exhibits quadratic scaling instead of the standard cubic scaling. Next, we examined the role of dispersion in photonic time crystals – a new state of matter – in a TCO platform showing a significant reduction in stringent experimental requirements. Further, we experimentally demonstrated that the apparent dimensionality of an interacting ensemble of emitters could be modified using a resonant nanophotonic structure.

Spatio-spectral optical fission in time varying subwavelength layers

Transparent conducting oxides are highly-doped semiconductors that exhibit favorable characteristics when compared to metals, including reduced material losses, tunable electronic and optical properties, and enhanced damage thresholds. Here, we report the spatio-spectral fission of an ultra-fast pulse trespassing a thin film of aluminum-doped zinc oxide with a non-stationary refractive index. We experimentally demonstrate and develop a model that by applying phase conservation to this time-varying layer accounts for both space and time refraction leading to a fission both the spectrum and the energy. Our findings represent an example of extreme nonlinear

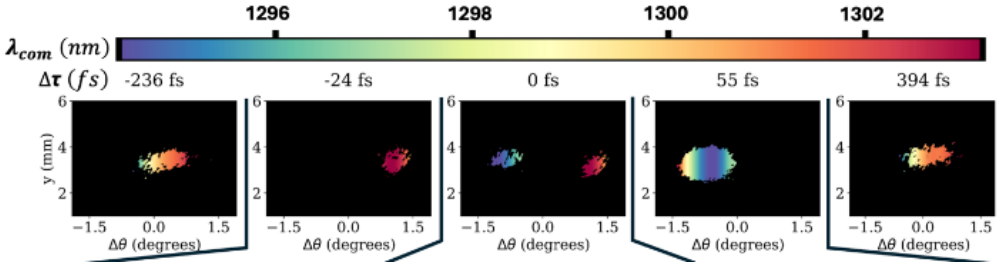

Figure 1. Full spatio-spectral information of transmitted probe pulse as the pump-probe delay is tuned. The probe transmitted beam profiles (with the x-axis recalibrated in deflection angle Δθ) together with the associated spatial spectral distribution for different values of the pump-to-probe time delay (Δτ).

phenomena on subwavelength propagation distances and shed light on the nature of several nonlinear effects recently reported not accounting for the full optical field distribution. Our work provides important insights into transparent conducting oxides' transient optical properties, which are critical for applications such as photonic time crystals, on-chip generation of nonclassical states of light, integrated optical neural networks as well as ultra-fast beam steering and frequency division multiplexing.

Nonlinear Loss Engineering in Near-Zero-Index Bulk Materials

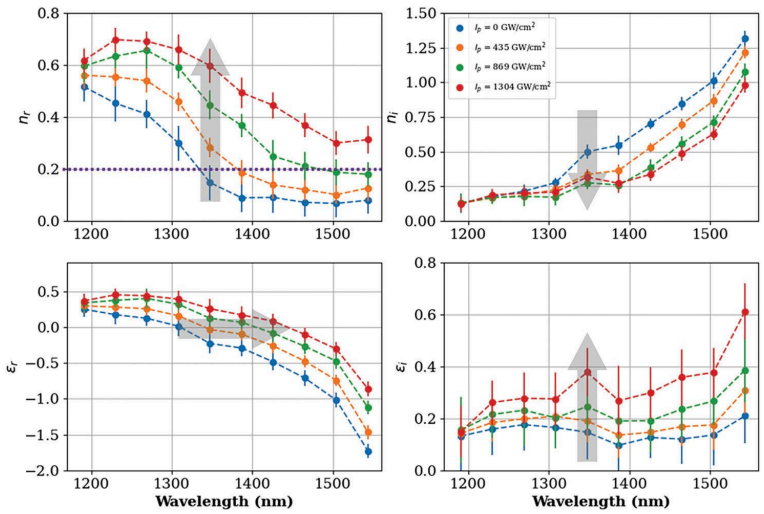

Figure 2. AZO's complex refractive index for various optical pump intensities. The index is retrieved via reflectance and transmittance measurements at various wavelengths and pump powers, while the pump and probe are overlapped temporally. The top panels display the real and imaginary components of index, while the bottom panels display the real and imaginary components of permittivity. Yellow, green, and red dashed lines represent pump intensities of 435 GW cm^{-2}, 869 GW cm^{-2}, and 1304 GW cm^{-2}, respectively.

Here we studied the nonlinear optical absorption properties of aluminum-doped zinc oxide (AZO) thin films in their near-zero-index (NZI) spectral window. We found that the imaginary part of the refractive index is reduced under optical excitation such that the field penetration depth more than doubles (*1*). An optically induced shift of the NZI bandwidth of ≈120nm for a pump intensity of 1.3 TW cm^{-2} is also demonstrated. Looking into the optically induced spectral redistribution of the probe signal, local net gain is recorded, which is ascribed to a nonlinear adiabatic energy transfer. Our study unveils the role of loss in these non-stationary systems building our

understanding of processes such as parametric amplification and its viability for loss compensation.

Third Harmonic Enhancement Harnessing Photoexcitation Unveils Nonlinearities in Zinc Oxide

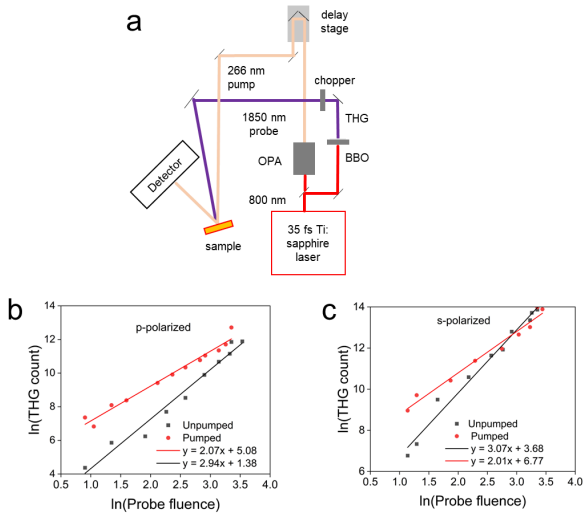

Figure 3. Third harmonic measurement setup b. Power dependence (log-scale) of third harmonic generation without pump and c. with pump.

Nonlinear optical phenomena are at the heart of various technological domains such as high-speed data transfer, optical logic applications, and emerging fields such as non-reciprocal optics and photonic time crystal design (*2*). However, conventional nonlinear materials exhibit inherent limitations in the post-fabrication tailoring of their nonlinear optical properties. Achieving real-time control over optical nonlinearities remains a challenge. We demonstrated (*3*) a novel method to switch third harmonic generation (THG), a commonly occurring nonlinear optical response. Third harmonic generation enhancements up to 50 times are demonstrated in zinc oxide films via the photoexcited state generation and tunable electric field enhancement. The enhanced THG follows a quadratic scaling with incident power, as opposed to the conventional cubic scaling, which demonstrates a previously unreported mechanism of THG. The THG can also be suppressed by modulating the optical losses in the film. We demonstrated that the photoexcitation of states can not only enhance nonlinearities, but can create new processes for THG. Importantly, our method enables real-time manipulation of the nonlinear response of a medium.

Reducing Effective System Dimensionality with Long-Range Collective Dipole-Dipole Interactions

We experimentally demonstrated (*4*) that the apparent dimensionality of an interacting ensemble of emitters is modified by employing a resonant nanophotonic structure. The dimensionality is encoded in the temporal fluorescence decay dynamics. The exponent β that relates to the apparent dimensionality of the interacting system is observed to be a non-integer value. The value of apparent dimensionality on a resonant plasmonic lattice shows a stark contrast value of $d \sim 2.20$, in comparison to $d \sim 3.0$ obtained on glass, an off-resonant TiO_2 dielectric lattice, and an off-resonant plasmonic lattice. Further, we extract the underlying distribution of energy transfer rates

for the interacting emitters' ensemble. The rates indicate a similar dimensionality modification. Our work paves the way for engineering interacting systems with apparent lower dimensionality.

Future Plans

Our future work will branch out from the funded effort in interconnected directions. First, we

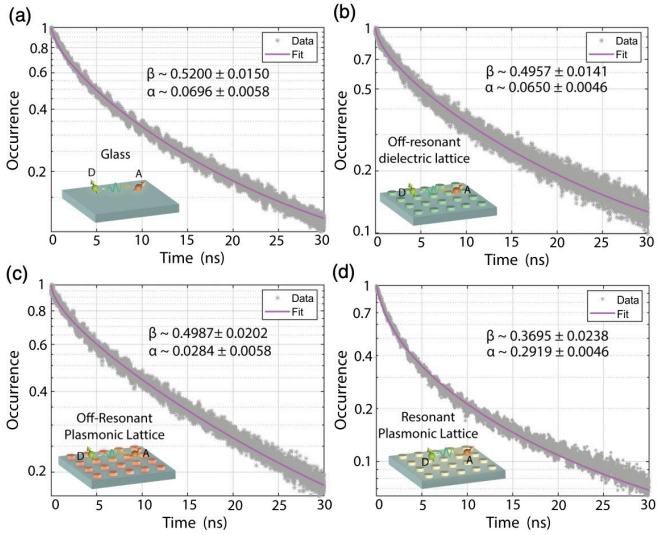

Figure 4. Measured fluorescence lifetime decay when the interacting emitters are in different electromagnetic environments: (a) glass substrate (a homogeneous environment), (b) TiO_2 dielectric lattice (an off-resonant inhomogeneous environment), and (c) a plasmonic lattice (a resonant inhomogeneous environment). The value of $\beta \sim 0.5$ in both inhomogeneous and off-resonant inhomogeneous environments. This is commensurate with a 3D system. In contrast, the faster-than-exponential decay dynamics on a resonant silver (Ag) plasmonic lattice reveals an exponent value of ~0.37. This is commensurate to an effective lower dimension $d \sim 2.20$.

investigate the non-stationary aspects of ENZ behavior. As our recent work suggests, the standard models for nonlinear optics do not hold in a time varying media, for example our observation of quadratic scaling of THG. Additionally, since ENZ materials are an ideal platforms to explore photonic time-crystals in dispersive surface modes, we will explore in more detail thin-film modes such as the Berreman and the ENZ mode, in non-stationary cases. Further, we will explore the localization of the spin and orbital degrees of freedom of light in disordered ENZ media.

References

1. W. Jaffray *et al.*, Nonlinear Loss Engineering in Near-Zero-Index Bulk Materials. *Advanced Optical Materials* **12**, 2301232 (2024).
2. M. G. Ozlu, V. Mkhitaryan, C. B. Fruhling, A. Boltasseva, V. M. Shalaev, Floquet Engineering of Polaritonic Amplification in Dispersive Photonic Time Crystals. *arXiv preprint arXiv:2408.00552* (2024).
3. S. Saha *et al.*, Third Harmonic Enhancement Harnessing Photoexcitation Unveils New Nonlinearities in Zinc Oxide. *arXiv preprint arXiv:2405.04891* (2024).
4. A. K. Boddeti *et al.*, Reducing Effective System Dimensionality with Long-Range Collective Dipole-Dipole Interactions. *Physical Review Letters* **132**, 173803 (2024).

Publications

1. V. Bondarev, A. Boltasseva, J. B. Khurgin, & V. M. Shalaev, *Crystallization of the transdimensional electron liquid*, arXiv preprint arXiv:2503.05165 (2025).
2. C. Fruhling *et al.*, *Time-Refraction Near the Critical Angle and Angular Streaking with Attosecond Resolution*, *Accepted: Optical Materials Express*, 2025.

3. W. Jaffray, S. Stengel, F. Biancalana, C. B. Fruhling, M. Ozlu, M. Scalora, A. Boltasseva, V. M. Shalaev & M. Ferrera, M. *Spatio-spectral optical fission in time-varying subwavelength layers*. Nature Photonics, 1–9 (2024).
4. M. G. Ozlu, V. Mkhitaryan, C. B. Fruhling, A. Boltasseva, & V. M. Shalaev, *Floquet Engineering of Polaritonic Amplification in Dispersive Photonic Time Crystals*. arXiv preprint arXiv:2408.00552 (2024).
5. W. Jaffray, F. Belli, S. Stengel, M. A. Vincenti, M. Scalora, M. Clerici, V. M. Shalaev, A. Boltasseva, & M. Ferrera, *High-order nonlinear frequency conversion in transparent conducting oxide thin films*. Advanced Optical Materials, **12**, 2401249 (2024).
6. P. Das, S. Rudra, D. Rao, S. Banerjee, A. I. K. Pillai, M. Garbrecht, A. Boltasseva, I. V. Bondarev, V. Shalaev, & B. Saha, *Electron confinement–induced plasmonic breakdown in metals*. Science Advances **10**, eadr2596 (2024).
7. X. Wang, X., T. V. Mechelen, S. Bharadwaj, M. Roknuzzaman, F. Bao, R. Rahman, & Z. Jacob, *Exploiting universal nonlocal dispersion in optically active materials for spectro-polarimetric computational imaging*, eLight, **4**, 1-13 (2024).
8. S. Bharadwaj, and Z. Jacob. *Thermal radiation with a twist*. Science **386**, 1348-1349 (2024).
9. A. Boddeti, Yi Wang, X. G. Juarez, A. Boltasseva, T. W. Odom, V. Shalaev, H. Alaeian, and Z. Jacob, *Reducing effective system dimensionality with long-range collective dipole-dipole interactions*, Phys. Rev. Lett. **132**, 173803 (2024).

Quantum Nanoplasmonics Theory

DOE Grant No. DE-SC0007043

Vadym Apalkov (PI)

Department of Physics and Astronomy, Georgia State University, Atlanta, GA 30303

E-mail: vapalkov@gsu.edu

1. Program Scope

Major goals of this Program is in theoretical research devoted to new phenomena in two dimensional (2D) materials and metal nanostructures subjected to strong ultrafast optical fields. We consider such novel and promising 2D systems as graphene (a 2D semimetal), transition metal dichalcogenides (2D semiconductors), and surfaces (2D boundaries) of three-dimensional topological insulators. We focus on effects in the reciprocal space that are related to topological properties of the Bloch wave functions: Topological curvature, Berry phase, valley polarization, etc. These properties are protected by fundamental symmetries of nature: time reversal (T-symmetry) and spatial reflection (P-symmetry), which are in the focus of this Proposal.

2. Recent Progress and Publications

The recent progress covers the period of 2023-2025 and is illustrated by publications [1-9].

2.1 High harmonic generation in graphene quantum dots: elliptically polarized pulse [6]

The nonlinear optical response of low dimensional systems, such as quantum dots (QDs), can be also controlled by tuning the polarization of an optical pulse. The most general polarization is the elliptical one. In this case, for an elliptically polarized pulse, the ellipticity of the pulse can be used as a tuning parameter to change the generation of high-order harmonics in QD system. We considered two general types of graphene QDs: hexagonal and triangular QDs, which have D_{6h} and D_{3h} symmetries, respectively [6]. The QDs were described within the tight-binding model. The radiation spectra of such QDs show strong sensitivity to the ellipticity of an optical pulse when ellipticity is close to one, which corresponds to a circularly polarized pulse. Such sensitivity is observed as a suppression of some high-order harmonics in the radiation spectra. The orders that are suppressed are determined by the symmetry of the QD; for triangular QDs, every third harmonic, while for hexagonal QDs, every sixth harmonic is suppressed.
While for small field amplitudes, the suppression of the corresponding harmonics is realized mainly for a circularly polarized pulse, for large field amplitude, the suppression occurs also for an elliptically polarized pulse with ellipticities that are in some range close to a circularly one. Also, for a hexagonal QD, which has an inversion symmetry, all even-order harmonics are suppressed for all ellipticities of an optical pulse, not only for a circularly polarized pulse.

Interaction of an elliptically polarized pulse with graphene QDs also generates elliptically polarized radiation. The ellipticities of the corresponding high-order harmonics depend on the parameters of the incident pulse, and in some cases, for large enough harmonic orders or for large intensities of the incident pulse, the corresponding polarization ellipse of high-order harmonics is effectively rotated by 90^0 compared to the incident pulse's polarization ellipse.
To address the problem of nonlinear optical response in large-size graphene QDs, we considered disk-shaped QDs within an effective low energy model [7]. The radius of such QDs is up to 20

nm. Our results show nontrivial dependence of both the intensity of high harmonics and their ellipticity on the parameters of an incident elliptically polarized pulse. As a function of the ellipticity of the incident pulse, the maximum intensities of high harmonics are realized at intermediate values of ellipticity around 0.2, where zero ellipticity corresponds to a linearly polarized pulse while the ellipticity of one described a circular polarization. The emission of high harmonics for a disk-shaped QDs is also strongly suppressed for a circularly polarized pulse, which is expected for the system with a continuous rotational symmetry.

2.2 High harmonic generation in graphene quantum dots with vacancy defects [9]

Nonlinear optical properties of QDs can be controlled by varying their size and shape. Quantum dots, or artificial atoms, have another unique property. Namely, due to their finite size, the energy spectra of QDs have size-dependent bandgaps. In this case, for graphene QDs, we can realize the situation when the system can be probed with the optical pulse the frequency of which is below the bandgap, which eliminates the resonant transitions within the system. In this case the nonlinear response is mainly determined by the intensity of an optical pulse and the structure of a QD. One of the ways of controlling the nonlinear response of graphene QDs is to introduce additional defects, such as vacancy defects. The vacancy defects can be of two types: a monovacancy or a divacancy. We studied theoretically the generation of high-order harmonics in hexagonal and triangular graphene QDs with vacancy defects.

For graphene QDs, the effect of the defects on radiation spectra depends on the geometry of a QD, its symmetry, and the type of the edges. The main types of graphene QDs are hexagonal QDs with zigzag edges, triangular QDs with zigzag edges, and triangular QDs with armchair edges.

For an intrinsic hexagonal QD, the system has an inversion symmetry, which results in strong suppression of even-order high harmonics. Introducing one vacancy into the system breaks the inversion symmetry and generates strong even harmonics for both linearly and circularly polarized incident pulses. The second vacancy can be added into the system in such a way that it can restore the system's inversion symmetry, which results in suppression of even-order harmonics that is similar to the intrinsic case. For a circularly polarized pulse, another effect can be also observed. Namely, due to D_{6h} symmetry of a hexagonal QD, the harmonics of orders 3m, where m is an integer, are suppressed in the field of a circularly polarized pulse. In this case, both mono- and di-vacancies break the D_{6h} symmetry, resulting in strong enhancement of 3m-order harmonics. Similar breaking of QD D_{3h} symmetry for triangular QDs by mono- and di-vacancies results in the enhancement of 3m-order high harmonics in such QDs placed in the field of a circularly polarized pulse. Such an effect is visible for triangular QDs with both zigzag and armchair edges. For triangular QDs with armchair edges, there is another symmetry-related effect. Namely, such QDs have a local inversion symmetry, which is similar to the symmetry present in the bulk of QDs. Such local symmetry suppresses generation of even-order harmonics in intrinsic QDs and, similar to hexagonal QDs, when one vacancy is added to the system, the local inversion symmetry becomes broken and the generation of even harmonics is strongly enhanced. Also, when the second vacancy is added to the QD, which restores the local inversion symmetry, then the even-order harmonics become suppressed again.

Thus, the defects in graphene QDs can break the symmetry of the system, which can strongly enhance the generation of some high-order harmonics that are symmetry-forbidden in the intrinsic systems. Such an effect is visible even if a single vacancy is added to the graphene system.

2.3 Ultrafast field-driven valley polarization of transition metal dichalcogenide QDs [5].

Another type of graphene-like QD systems are based on transition-metal dichalcogenide (TMDC) monolayers. We considered large size TMDC QDs of a disk shape. The high harmonics generation can be tuned by changing either the size of such QDs or the parameters of a pulse, i.e., its amplitude, frequency, and polarization. The strongest high harmonics are generated for a linearly polarized pulse, while for a circularly polarized pulse, the high-order harmonics are strongly suppressed. Such a suppression, observable as a function of ellipticity of an incident pulse, shows a very sharp dependence near the ellipticity of 1 (a circularly polarized pulse) for the third-order harmonics, while for the higher order harmonics, i.e., the fifth and the higher, the intensities of the corresponding harmonics smoothly decrease with the ellipticity of the incident pulse. Also, an elliptically polarized pulse generates elliptically polarized high harmonics with the ellipticities that are usually less than the ellipticity of the incident pulse.

The radiation spectra of TMDC QDs also depend on a QD size. The strongest dependence is realized for the frequency of the pulse that is less than the QD bandgap. In this case, the optical response is determined by the properties, e.g., the density of states, of the valence band and the conduction band states near their edges. The number of such states strongly depends on the QD size, which results in strong dependence of the radiation spectra on a QD radius.

With increasing the QD size, both the intensity of high harmonics and the cutoff frequency increase, which is due to a larger number of QD levels that contribute to the generation of high order harmonics. When the frequency of the pulse is above the bandgap of the corresponding QD, the cutoff frequency as a function of the QD radius shows the saturated behavior for the radius close to 15 nm. No such saturated behavior is observed for the frequency of the pulse that is below the bandgap.

The radiation spectra also depend on the material of a QD. Out of three TMDC materials studied, WS_2 and WSe_2 QDs generate the strongest high harmonics, while the corresponding intensities of MoS_2 QDs are a few orders of magnitude smaller. At the same time, the cutoff frequencies of radiation spectra have a weak dependence on the QD material.

3. Future Plans

Our future research will be related to studying the nonlinear optical response of bilayer graphene quantum dots of a large size and small quantum dots of two-dimensional topological materials such as graphene and Weyl semimetals. For bilayer graphene QDs, we will study the sensitivity of optical response to the twist angle between the layers. Such an angle can be used as a parameter to control the nonlinear optical response, for example, the high harmonic generation. For small-size QDs of two-dimensional topological materials, we will study the effects of inter-electron interactions on their nonlinear optical properties. We will include the inter-electron interactions through the interaction Hamiltonian, which will be diagonalized numerically within a single particle basis. Then the nonlinear optical response of such a QD placed in the field of an optical pulse will be studied. The main characteristics that will be calculated are the high harmonic generation, and the sensitivity of high frequency radiation to the parameters of an incident pulse, such as its frequency and polarization, for example, dependence on the ellipticity of the incident pulse.

4. Peer-Reviewed Publications Resulting from this Project (2023-2025)

[1] S Gnawali, V Apalkov, "*High harmonic generation governed by edge states in triangular graphene quantum dots*", Physical Review **B 108** (11), 115434 (2023).

[2] Dalton C Hunley, S Azar Oliaei Motlagh, Rupesh Ghimire, Vadym Apalkov, "*Ultrafast pulse pumping of topological nanospaser*", Journal of Physics: Condensed Matter, **35** (31), 315302 (2023).
[3] Vadym Apalkov, "*Interacting Dirac fermions and the rise of Pfaffians in graphene*", Encyclopedia of Condensed Matter Physics, editor-in-chief: T. Chakraborty, second edition, 366-382 (2023).
[4] Vadym Apalkov, "*Ultrafast optics of topological materials*", Encyclopedia of Condensed Matter Physics, editor-in-chief: T. Chakraborty, second edition, 128-137 (2023).
[5] A Mitra, AJ Zafar, SJ Hosseini, V Apalkov, "*Ultrafast high harmonic generation in transition metal dichalcogenide quantum dots*", Physical Review B **109** (15), 155425 (2024).
[6] S Gnawali, V Apalkov, "*High-order harmonic generation in graphene quantum dots in the field of an elliptically polarized pulse*", Physical Review B **109** (16), 165121 (2024).
[7] AJ Zafar, A Mitra, V Apalkov, "*High harmonic generation in graphene quantum dots*", Journal of Physics: Condensed Matter **36** (21), 215302 (2024).
[8] A Mitra, AJ Zafar, V Apalkov, "*Ultrafast field-driven valley polarization of transition metal dichalcogenide quantum dots*", Journal of Physics: Condensed Matter **36** (20), 205302 (2024).
[9] S Gnawali, V Apalkov, "*High harmonic generation in graphene quantum dots with vacancy defects*", Physica B: Condensed Matter, 416793 (2024).

Session V

Ionic Heat of Transport of Liquid and Solid Electrolytes

David G. Cahill and Paul V. Braun, Department of Materials Science and Engineering, Materials Research Laboratory, University of Illinois Urbana-Champaign

Keywords: Peltier heat; ionic transport; solvation; heat of transport; irreversible thermodynamics

Research Scope

The primary goal of our research is to advance scientific understanding of the heat of transport of Li ions—and in the longer term other single and multivalent ions—in liquid and solid electrolytes to the level that ionic thermoelectric effects can be used as a tool for greater general understanding of ionic transport in electrolytes that are important in energy technologies. Coupled transport of charge, heat, and mass will provide unique information on the thermodynamics and kinetics of ionic transport that is complementary to what can be learned from conventional methods of electrochemistry. The outcomes of the research will facilitate the development of electrolytes with high conductivity and improved performance at low temperatures and has the potential of providing a powerful approach for monitoring degradation of electrolytes during extended cycling.

Recent Progress

We carried out systematic measurements of Peltier coefficients of Li salts in a variety of solvents as a function of salt concentration and solvent composition. We related the Peltier coefficient to the entropy of solvation of the Li ion and used the entropy of fusion of the solvent as a baseline for making comparisons between solvents. The entropy of fusion of the solvent and the entropy of solvation are strongly correlated.

We observed a transient in the Peltier heat, i.e., a difference between the Peltier heat at short and long times, that provides a quantitative measurement of the heat transport of the Li salt (Figure 1). The decay-time of this transient signal can also be used to determine the mass diffusivity of the salt. The heat of transport is an order of magnitude smaller than the Peltier heat, 2-5 kJ/mol.

We measured the thermal conductivity of a variety of solvents and solvent

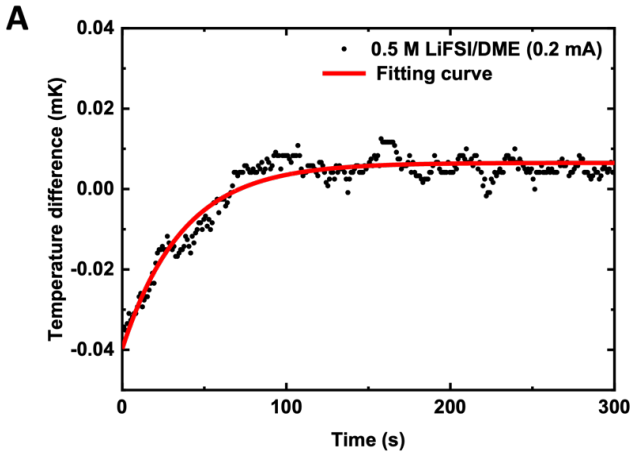

Figure 1. Example of a transient heat current generated by the heat of transport of the salt component of the electrolyte. The magnitude of the transient is determined by the product of the transference number of the anion and the heat of transport of the salt.

mixtures, see Figure 2, and measured several other thermophysical properties of commonly used solvents and solvent mixtures that have not been reported previously, e.g., density, heat capacity, bulk modulus, viscosity, and thermo-optic coefficient. This work was enabled by development of a new approach for determining the thermal diffusivity and thermo-optic coefficients of liquids that we refer to as "immersion thermo-optic phase spectroscopy", I-TOPS. The measurement apparatus includes a temperature-controlled liquid cell that enables measurements of thermal conductivity as a function of temperature.

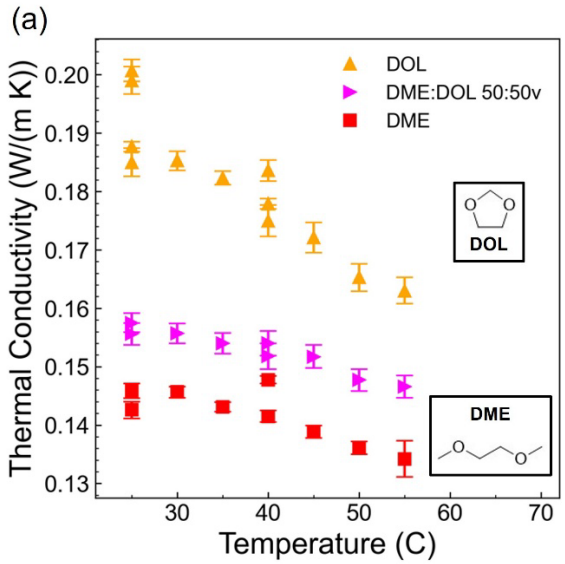

Figure 2. Thermal conductivity of dimethoxy-ethane (DME), 1,3-dioxolane (DOL) and their mixture as a function of temperature.

We constructed an apparatus for sensitive calorimetry and measurements of the thermal conductance, Seebeck coefficient, and electrochemical impedance of solid-state electrochemical cells while operating under a controlled pressure. This is a novel design of a heat flux meter and calorimeter that incorporates two Peltier devices and temperature-controlled liquid heat exchanger on each side of the solid-state cell. For measurements of thermal conductance and Seebeck coefficient, one of Peltier device is operated as a heat source and the second Peltier devices measures the heat flux that pass through the cell. For calorimetry measurements of both reversible and irreversible heats, both Peltier devices are used as heat flux sensors. The noise floor of the heat flux measurements is currently on the order of 10 μW but we believe that there is opportunity for making significant improvements through reductions in the temperature fluctuations of the heat sinks.

Future Plans

We started moving the focus of our work from liquid electrolytes to solid electrolytes in February 2025. Solid-state electrochemical cells typical require the application of a significant pressure (>1 MPa) to maintain good contact between electrodes and electrolytes during cycling. This required a radical change in our approach. While our studies of liquid electrolytes used what is essentially an adiabatic boundary condition, because of the need for an applied pressure, we are instead shifting to an approach that uses boundary conditions where we control heat flux. We have constructed an apparatus that includes a conventional Peltier module on each side of the electrochemical cell that we can use to drive and measure heat fluxes and then measurements of the open-circuit voltage to determine the Seebeck, and equivalently, the Peltier coefficient. Our initial data on the solid electrolyte LPSC (Li_6PS_5Cl) shows that the Peltier coefficient of a symmetric LPSC cell has the opposite sign and is an order of magnitude smaller than a typical liquid electrolyte. Measurements of the Seebeck and Peltier coefficients of solid electrolytes, and changes in the coefficients with long-term cycling, will be the emphasis of our work during the third year of the project.

Publications

1. Zhe Cheng, Yu-Ju Huang, Beniamin Zahiri, Patrick Kwon, Paul V. Braun, and David G. Cahill, *Ionic Peltier Effect in Li ion electrolytes*, J. Phys. Chem. Chem. Phys. **26**, 6708-6716 (2024).

Understanding the Role of Defects to Accelerate Wadsley-Roth Niobates for Long-Duration Energy Storage

Morgan Stefik[1], Hans-Conrad zur Loye[1], Scott Misture[2], Ming Hu[3], Christopher Sutton[1]
[1] Department of Chemistry and Biochemistry, University of South Carolina
[2] Materials Science and Engineering, Alfred University
[3] Department of Mechanical Engineering, University of South Carolina

Keywords: Battery, Niobate, Wadsley-Roth, Diffusion, Machine Learning

Research Scope

This program aims to reduce costs for energy storage by developing novel battery materials with the properties needed for extreme durability. We are investigating Wadsley-Roth (WR) niobates, a family of complex crystal structures with excellent ion and electron transport that each occur along distinct crystalline regions and which have set new charge storage performance records. Recent examples have shown the potential of controlled defects to further enhance transport in this class of materials. There is, however, a knowledge gap in understanding the connections between composition, disorder, and defects upon these transport mechanisms. This program addresses the challenges of improving transport characteristics two ways: first the discovery of new equilibrium WR phases and second studying how non-equilibrium defects can enhance transport.

Our multifaceted and integrative team includes the use of machine learning to accelerate experimental work with an inverse design strategy that identifies promising new WR compositions with the potential for enhanced transport characteristics. Diverse synthetic methods including solid state and sol-gel routes are used to realize these predicted phases with the possibility of including diverse defect structures that may enable novel transport mechanisms. The inclusion of comprehensive atomic scale and nanoscale structure characterizations as well as systematic transport measurements connect experimental transport characteristics to the underlying defect chemistries. From this information, key chemical and structural descriptors will be identified, modeled, and further investigated. The outcome will be the foundational knowledge required to develop new intercalation materials that display exceptional conductivities to enable more durable and energy efficient batteries. This class of materials also promises remarkably high energy densities with fast charge capabilities and have potential to impact major battery applications spanning from grid-level to portable electronics and electric vehicles.

Recent Progress

Our program has established and explained new structure-property relationships with WR materials. Both (1) defect-tailoring studies[1] and (2) isostructural comparisons[2] were published with detailed structural comparisons to explain property differences. These initial studies revealed the need to (3) develop and disseminate a figure-of-merit approach[3] for even-handed comparison of transport metrics for intercalation materials exhibiting second-order phase transitions. The computational effort has grown capability to address lithium ordering where our subsequent submitted (4) isostructural comparison[4] study connected lithium ordering to lithiation-dependent diffusion trends in addition to structure-property relationships. While longevity experiments are ongoing our (5) first published trials showed that extreme durability[5] is possible with such niobates, exhibiting minimal capacity fade with up to 0.25M cycles. Each of these studies is elaborated individually in the following sections.

(1) $TiNb_2O_7$ (TNO) is a promising WR anode material for durable, fast-charging lithium-ion batteries that combine fast lithium diffusion with minimal lithiation strain. Battery performance generally depends on a convolution of defect-sensitive material properties (lithium diffusivity and electrical resistivity) in conjunction with the architecture (feature size, porosity, and charge-transfer surface). All of these attributes connect to synthetic conditions where there is opportunity to improve performance by understanding the interplay of changes during crystallization. Nanostructured TNO was prepared via spray drying, where variable crystallization temperature simultaneously influenced crystal structure/defects while coarsening the architecture. Comprehensive X-ray analysis (WAXS, SAXS, and XRD) and microscopy (SEM) characterized the crystallization and coarsening progress. The galvanostatic lithiation capacities(700−1100°C) were similar at 0.1C (∼300mAh/g); however, sample TNO-800 exhibited the highest capacity at 5C (260 ± 3 mAh/g). Intermittent current interruption (ICI) analysis revealed increasing diffusivity with calcination temperature and a nonmonotonic trend in cell resistance, minimized for TNO-800. Detailed X-ray near-edge structure (XANES), extended X-ray absorption fine structure (EXAFS), and Rietveld analyses identified that crystallization led to progressive point/extended defect elimination and increasing octahedral distortion. With cell resistance including both electrical resistance and charge-transfer resistance, this overall trend reflects competition of generally improving electronic properties with calcination temperature against the coarsening architecture that progressively increases the charge-transfer resistance. The optimal TNO-800 condition exhibited are remarkable 10C capacity of 233±1 mAh/g, which compares favorably with leading TNO precedents. This study highlights the complex convolution of atomic structure and architecture changes that occur during crystallization, which may advance other known battery materials.

(2) Improved understandings of structure−property relationships enable the realization of higher-performance materials. We reported the first single-crystal structures of $Nb_{12}MoO_{33}$ and $Ta_{12}MoO_{33}$ that are consistent with other ($3 \times 4 \times \infty$) WR phases. The lithiation of $Ta_{12}MoO_{33}$ was reported for the first time and enables an isostructural comparison with $Nb_{12}MoO_{33}$. These two compounds have similar unit cell volumes and atomic radii, where the $Ta_{12}MoO_{33}$ unit cell is 0.2 vol % smaller. Despite the similarities in structure, the lithiation capacities, voltage windows, C rate-dependent capacities, and ionic diffusivities are distinctly different. These experimental trends align well with density functional theory calculations showing (a) a lower activation energy for Li transport within $Ta_{12}MoO_{33}$ consistent with its measured 1.5−4.9-fold higher diffusion coefficients (lithiation) and (b) an ∼25% greater measured lithiation stoichiometry for $Nb_{12}MoO_{33}$, which was attributed to the calculated smaller octahedral distortions (compared to $Ta_{12}MoO_{33}$). These findings reveal that smaller channels in $Ta_{12}MoO_{33}$ stabilize the transition state with 5-fold coordination, which both decreases the activation energy for diffusion and limits the overall extent of lithiation. Such structure−property trends help in the search for next-generation battery materials.

(3) Reliable, community-accepted figures of merit are essential for identifying next-generation battery materials with improved transport performance. However, typical measurements yield widely varying voltage-dependent diffusivities and reporting practices are diverse. Some materials (e.g. first-order phase change) have most redox occur at a specific voltage and may be sufficiently represented by singular transport metrics. In contrast, many rapid intercalation materials rather exhibit second-order phase transitions with redox occurring over a broad voltage range. How should such materials be compared to each other? The use of capacity-weighted average values is

suggested where voltage-dependent metrics are consolidated into representative descriptors as figures-of-merit. Examples are elaborated where differential capacity (dQ/dV) is used to derive a weighting function to calculate a diffusion figure-of-merit (D_{Qav}). Furthermore, it is shown that galvanostatic techniques can provide transport values with even capacity-weighting such that their mean value (D_{Tav}) is naturally capacity-weighted. Though equivalent conceptually, the latter approach avoids derivative noise and subjective curve smoothing. Computational diffusion values can similarly include capacity-weighted figures-of-merit. Lastly, diffusivity uncertainty is addressed which is dominated by surface area error due to the second-power dependence. Best-practices can reduce the diffusivity error from~40% to~2% using appropriate BET sorbents or SAXS with thickness measurements. These perspectives improve the comparison of battery materials with a diffusivity figure-of-merit that supports performance-ranking with attention to uncertainty.

(4) The first lithiation of VTa_9O_{25} was reported which enabled a direct isostructural comparison with the better-known VNb_9O_{25}. These WR materials have similar unit cell volumes and atomic radii yet exhibit different voltage windows, C-rate dependent capacities, and transport metrics. Time-dependent overpotential analysis revealed ionic diffusion as the primary bottleneck to high rate-performance in both cases, however, the corresponding lithium diffusivity for VNb_9O_{25} was an order of magnitude faster than that for VTa_9O_{25}. These experimental trends aligned well with density functional theory calculations combined with molecular dynamics that show a factor of six faster diffusion in VNb_9O_{25} as compared with VTa_9O_{25}. Nudged elastic band calculations of the probable hopping pathways indicate that VNb_9O_{25} consistently exhibits a lower activation barrier for lithium diffusion as compared to VTa_9O_{25}. Bader charge analysis reveals a larger net charge on Li in VNb_9O_{25} compared to VTa_9O_{25} which was attributed to the lower polarizability of Nb which stabilizes the transition state and lowers the activation energy for diffusion. This stabilization arises from the stronger coulombic interaction between Li and its coordinated oxygen environment. Furthermore, the parabolic experimental diffusivity trends with increasing lithiation extent were related to trends in lithium ordering that included crowding effects.

(5) The long-term cycling stability of rapid intercalation materials remains understudied despite the relevance to their lifetime cost and market feasibility. Orthorhombic niobium oxide (T-Nb_2O_5) is a rapid ion intercalation material with a theoretical capacity of 201.7 mAh g^{-1} ($Li_2Nb_2O_5$) and good cycling stability due to the minimal unit cell strain during (de)intercalation. Prior reports of T-Nb_2O_5 cycling between 1.3-3.1 V vs. Li/Li^+ noted a 50% loss in capacity after 10k cycles, stemming from a convolved effect of amorphization, dissolution, and/or delamination. Here, cyclic voltammetry (CV) was used to identify the role of the voltage window, state of charge (SOC), and potentiostatic holds on the cycling stability of mesoporous T-Nb_2O_5 thin films. Films cycled between 1.2-3.0 V vs. Li/Li^+ without voltage holds (kinetically limited SOC of $Li_{1.1}Nb_2O_5$) exhibited extreme cycling stability with 90.8% ± 2.1% capacity retention after a quarter million cycles without detectable morphological/crystallographic changes. In contrast, inclusion of 60 s voltage holds (SOC $Li_{2.18}Nb_2O_5$) led to rapid capacity loss with 61.6% ± 2.0% retention after 10k cycles with corresponding x-ray diffraction evidence of amorphization. Cycling with other limited voltage windows identified that most crystallographic degradation occurred at higher extents of lithiation (<1.4 V vs Li/Li^+). These results reveal remarkable stability over specific conditions and suggest that amorphization was associated with high extents of lithiation.

Future Plans

The next phase of this program will (1) complete our analysis of recently discovered WR compounds (including isostructural comparisons of different compounds to develop a deeper understanding of structure–property relationships) and (2) examine the roles of vacancies, transition metal configurational disorder, and stacking faults upon the lithium configuration and the resulting transport metrics. Furthermore, (3) the next series of computational predictions will examine composition spaces intended to increase the extent of transition metal configurational disorder to enable experiments that connect these structures to their resulting properties. Notably out computational team currently has a database of 3K compounds that have been examined as potential WR phases where ~1300 were predicted to be stable. These predicted compounds are being pursued by multiple synthetic approaches within our group. We have ongoing STEM measurements at multiple locations as well as operando and ex situ X-ray measurements including EXAFS and XANES to identify detailed changes in atomic structures.

References/Publications

1. CJ Sturgill, I. Milisavljevic, S. Wechsler, Md. A. A. Muhit, H.C. zur Loye, S. Misture, M. Stefik, *Tailored $TiNb_2O_7$ Particle Size, Defects, and Crystallinity Accelerate Lithiation*, Chemistry of Materials **37**, 624 (2025).
2. Md. A. A. Muhit, S. Wechsler, Z. Bare, C. Sturgill, N. Keerthisinghe, M. Grasser, G. Morrison, C. Sutton, M. Stefik, H.C. zur Loye, *Comparison of Lithium Diffusion in Isostructural $Ta_{12}MoO_{33}$and $Nb_{12}MoO_{33}$: Experimental and Computational Insights from Single Crystals*, Chemistry of Materials **36** 10626 (2024).
3. CJ Sturgill, C. Sutton,; J. Schwenzel, M. Stefik, *Capacity-Weighted Figures-of-Merit for Battery Transport Metrics*, Journal of Materials Chemistry A **13**, 6314 (2025).
4. M. Kumar, Md. A. A. Muhit, CJ Sturgill, M. Stefik, H.C. zur Loye, C. Sutton, *Combined Experimental and Computational Analysis of Lithium Diffusion in Isostructural Pair VNb_9O_{25} and VTa_9O_{25}*, In Preparation (2025).
5. S. C. Wechsler, A. Gregg, M. Stefik, *Highly Reversible Lithiation of Additive Free T-Nb_2O_5 for a Quarter of a Million Cycles*. Advanced Functional Materials **34**, 2312839 (2024).
6. S. C Wechsler, A. Gregg, C. C. Collins, S. K. Balijepalli, M. Stefik, *Nanostructure Retention to 1100°C in Soft-Templated Niobium Tungstates using Dual-carbon Strategy*, New Journal of Chemistry **49**, 5716 (2025).
7. Md. A. A. Muhit, A. Maksimova, S. C. Wechsler, H. B. Kasem, G. Panigrahi, G. Morrison, M. Stefik, H.C. zur Loye, *Crystal Growth, Thermal, Optical and Magnetic Properties of $Mo_2Ta_2O_{11}$*, Solid State Science, Accepted (2025).
8. Z. J. L. Bare, CJ Sturgill, M. Kumar, I. Milisavljevic, H.C. zur Loye, S. Misture, M. Stefik, C. Sutton, *Computational Screening and Experimental Validation of Promising Wadsley-Roth Niobates*, Submitted (2025).

Session VII

Electronic Materials Program

Ali Javey, Joel Ager, Yuan Cao, Daryl Chrzan, Mary Scott, Junqiao Wu

Keywords: 2D semiconductors, optoelectronics, thermal science, excitons, strain

Research Scope

Reduced dimensionality electronic materials, as exemplified by semiconductor superlattices, have been of interest for more than 50 years. The discovery of direct bandgaps at the monolayer limit for 2D transition metal dichalcogenides (TMDCs) has greatly increased the scope of electronic materials with reduced dimensionality. Importantly, these types of 2D semiconductors, and related semiconductors with 1D ordering such as Te, have degrees of freedom (DOFs) not available in semiconductors grown with traditional epitaxial methods. Illustrative examples (**Fig. 1**) are formation of moiré patterns in bilayers of 2D materials, out of plane bending/rippling for 2D materials, and chirality/helicity in materials with 1D order. These DOFs can interact with (and are sometimes caused by) applied strain. Distortions like these have a remarkable potential for altering the electronic and thermal properties of the materials as each of these distortions increases the size of the real space unit cell and thereby reduces the size of the Brillouin zone. The resulting band folding enables previously symmetry-forbidden mixing of electronic states allowing the emergence of correlated electron behavior.

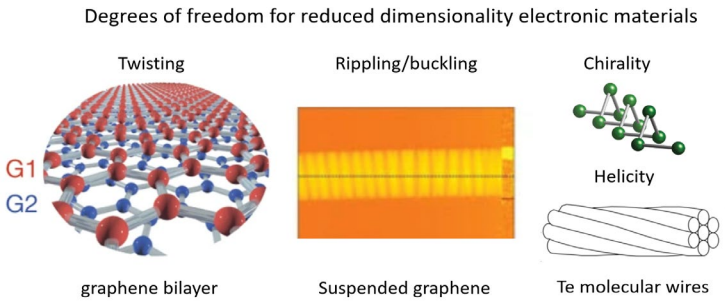

Fig. 1. Degrees of freedom (DOFs) available in reduced dimensionality electronic materials: (a) twist DOF in graphene bilayers. *Nature*, **2018**. (b) Out of plane rippling in suspended graphene. *Nat. Nanotechnol.*, 2009. (c) Chirality/helicity in crystalline tellurium. *Adv. Mat.*, 2021.

In the Electronic Materials Program (EMAT), we are motivated by knowledge gaps regarding the interaction of these DOFs with optical (Thrust 1), electrical (Thrust 2), and thermophysical (Thrust 3) properties of electronic materials *near room temperature* where practical devices operate. We accomplish this through a highly integrated discovery approach, combining materials theory, advanced characterization, synthesis and processing, and even demonstrations of proof of concept. The three research thrusts are linked by the fundamental microstructure-property-performance relationship governed by electron and phonon physics of electronic materials, as well as the tools (e.g., *in-situ* twist and strain MEMs apparatus), theories (e.g., strain design) and materials (e.g., 2D semiconductors and Te molecular wires) common to all three thrusts. All thrusts have a similar overall strategy which includes development of atomistic models that both explain observed behaviors and predict new ones to the exploration of properties in new materials explained by first-principles calculations.

Recent Progress

Over the past two performance periods, EMAT has developed a comprehensive understanding of room temperature radiative and non-radiative recombination processes in 2D monolayers, resulting in the first demonstration of near unity quantum yields in MoS_2 monolayers (Science, 2019; Science, 2021). This knowledge has been extended to other excitonic (and free carrier) material systems across the wavelength spectrum. We discovered an anomalous thickness dependence of PLQY in black phosphorus (BP) (Nature Nanotechnology, 2013). As the thickness decreases from bulk to ~4 nm, a drop in the photoluminescence quantum yield is initially observed due to enhanced surface carrier recombination, followed by an unexpectedly sharp increase in photoluminescence quantum yield with further thickness scaling, which is attributed to a free-carrier to excitonic transition. Furthermore, the surface carrier recombination velocity of black phosphorus is very low; this is due to the presence of self-terminated surface bonds in black phosphorus. By utilizing bulk BP, whose bandgap is ~0.3 eV, we demonstrated highly efficient mid-IR emitters (Nature Comm, 2023; Nano Letters, 2022). Notably, BP-MoS_2 based LED achieved external quantum efficiency (EQE) of 4.4%, surpassing conventional III-V and II-VI semiconductors with similar bandgap (EQE = 0.1–1%). Although LED operation requires high current injection that pronounces oxidation in air, device stability can be dramatically improved by Al_2O_3 passivation and nitrogen sealing. We developed a packaging technology to prevent oxidation of BP-based LEDs in air, resulting in the extrapolated operating lifetime at room temperature of 15,000 hours (Nature Comm, 2023).

We demonstrated bright mid-IR emitters using BP ink as a phosphor coated on a red LED, Fig. 2a. In this device structure, visible light is converted into mid-IR emission, whose EQE is 0.3% (Science Advances, 2023). We demonstrated color tunability of the BP-based ink from mid-IR to near-IR, via size control and alloying, Fig. 2b.

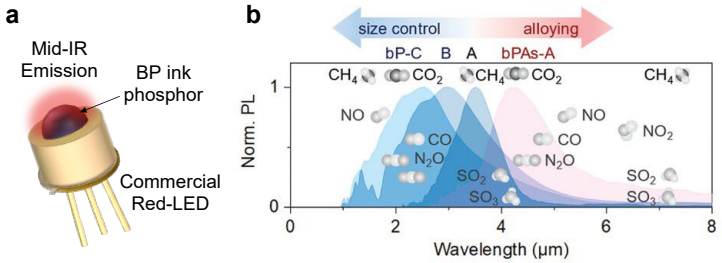

Fig. 2. (a) Color conversion from visible to mid-IR emission using BP ink phosphor coated on red LED. *Sci. Advances* **2023**. (b) Multicolor BP-based inks by using quantum confinement and alloying. *Adv. Mat.* **2024**.

We demonstrated a highly multicolored light-emitting array with 49 different, individually addressable colors on a single chip, Fig 3 (Science Advances, 2023). The array consists of pulsed-driven metal-oxide-semiconductor capacitors, which generate electroluminescence from micro dispensed materials spanning a diverse range of colors and spectral shapes, enabling facile generation of arbitrary light spectra across a broad wavelength range (400 to 1400 nm). When combined with compressive reconstruction algorithms, these arrays can be used to perform spectroscopic measurements in a compact manner without diffractive optics.

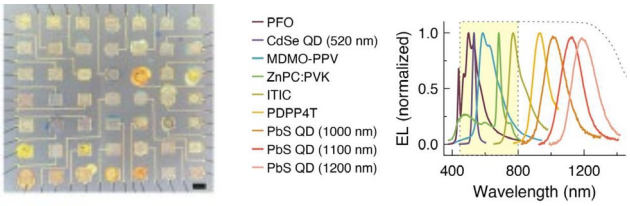

Fig. 3. Optical image of a fabricated 7 × 7 array of devices with a different emitter dispensed on each pixel of the array. Scale bar, 400 μm. Electroluminescence spectra from several materials emitting across the blue to near-infrared range, with emission at all wavelengths in between. *Sci. Advances* **2023**.

In parallel, we advanced the science of large-area processing of the low dimensional materials discussed above. A weak van der Waals (vdW) force in layered materials enables their isolation into thin flakes through mechanical exfoliation while sustaining their intrinsic electronic and optical properties. We introduced a universal roll printing method capable of producing vdW multilayer films on wafer-to-meter scale (Science Advances, 2024). This process uses sequential exfoliation and transfer of layered materials from the powder sources to target substrates through a repeated rolling of a cylindrical metal drum. Uniformly coated films were achieved with a library of vdW powders on various mechanically rigid and flexible substrates. We demonstrated a printable, emissivity-adaptive and albedo-optimized covering (PEAC) based on tungsten-doped VO_2 ($W_xV_{1-x}O_2$) particles and inexpensive recyclable materials (Joule, 2023). A PEAC automatically switches its sky-window emissivity from 0.25 to 0.85 when the surface temperature exceeds a pre-set transition temperature, delivering an albedo optimized for maximal year-round energy saving or thermal comfort.

Future Plans

In our investigation of photophysical properties, we focus on the interplay of twist and strain in excitonic materials, including 2D semiconductors. We use our unique in-situ measurement capabilities, combining MEMS, 4D-STEM, nano-ARPES, and PL, to perform precise measurement of the moiré patterns and evaluate exciton dynamics and recombination pathways at room temperature. In our materials discovery efforts, we will focus on two different wavelength regimes, near-IR/visible and mid-IR, where different non-radiative processes often dominate. By tuning the electronic structure by confinement and strain, we aim to suppress non-radiative recombination channel and create new material systems for mid-IR light emission.

The chirality, atomic chain alignment, strain and buckling DOFs of 1D and 2D materials will be used to control electronic transport properties. We are developing new deterministic synthesis methods to control the alignment of Te molecular chains, thus enabling a new class of quantum structures. We also aim to understand and experimentally realize the controlled out of plane rippling of 2D monolayers and Te molecular wires by the use of our MEMs device.

In our investigation of thermophysical properties, we will examine the thermal transport behavior of the same group of 2D and 1D materials as in the other thrusts. Specifically, we aim at

theoretically understanding and experimentally characterizing the thermal conduction and thermopower of van der Waals materials mediated by twisted stacking (2D materials), screw dislocations and other chiral structures (1D), their dependence on temperature, microstructure, orientation, uniaxial strain, as well as their interplay with electronic, excitonic and photophysical degrees of freedom.

Publications

1. Y. Cai, Z. Wang, J. Wan, J. Li, R. Guo, J. W. Ager, A. Javey, H. Zheng, J. Jiang and J. Wu, "Ion diffusion retarded by diverging chemical susceptibility", Nature Communications 15 (1), 5814 (2024).

2. Y. Liu, L. Jin, T. Pandey, H. Sun, Y. Liu, X. Li, A. Rodriguez, Y. Wang, T. Zhou, R. Chen, Y. Sun, Y. Yang, D. C. Chrzan, L. Lindsay, J. Wu and J. Yao, "Anomalous thermal transport in Eshelby twisted van der Waals nanowires", Nature Materials (2025).

3. N. Higashitarumizu, S. Z. Uddin, D. Weinberg, N. S. Azar, I. K. M. Reaz Rahman, V. Wang, K. B. Crozier, E. Rabani and A. Javey, "Anomalous thickness dependence of photoluminescence quantum yield in black phosphorous", Nature Nanotechnology 18 (5), 507-513 (2023).

4. K. Lee, N. Higashitarumizu, S. Wang, C. Kim, C. Y. Ho, J. W. Oh, G. Zan, M. Madsen, T.-W. Lee, D. C. Chrzan, C. Park and A. Javey, "Meter-scale van der Waals films manufactured via one-step roll printing", Science Advances 10 (36), eadq0655 (2024).

5. V. Wang, S. Z. Uddin, J. Park and A. Javey, "Highly multicolored light-emitting arrays for compressive spectroscopy", Science Advances 9 (16), eadg1607 (2023).

6. N. Higashitarumizu, S. Tajima, J. Kim, M. Cai and A. Javey, "Long operating lifetime mid-infrared LEDs based on black phosphorus", Nature Communications 14 (1), 4845 (2023).

7. J. I. Kim, N. Higashitarumizu, S. Wang, R. Yalisove, M. C. Scott, S. Y. Song and A. Javey, "Multicolor Inks of Black Phosphorus for Midwave-Infrared Optoelectronics", Advanced Materials 36 (30), 2402922 (2024).

8. N. Gupta, S. Wang, N. Higashitarumizu, V. Wang, K. Lee, C. Park and A. Javey, "Large-scale efficient mid-wave infrared optoelectronics based on black phosphorus ink", Science Advances 9 (49), eadi9384 (2023).

9. J. Li, K. Dong, T. Zhang, D. Tseng, C. Fang, R. Guo, J. Li, Y. Xu, C. Dun, J. J. Urban, T. Hong, C. P. Grigoropoulos, A. Javey, J. Yao and J. Wu, "Printable, emissivity-adaptive and albedo-optimized covering for year-round energy saving", Joule 7 (11), 2552-2567 (2023).

10. B. Sari, S. E. Zeltmann, C. Zhao, P. M. Pelz, A. Javey, A. M. Minor, C. Ophus and M. C. Scott, "Analysis of Strain and Defects in Tellurium-WSe2 Moiré Heterostructures Using Scanning Nanodiffraction", ACS Nano 17 (22), 22326-22333 (2023).

Response of Gallium Oxide to Pressure, Temperature, and Alloying

Matthew D. McCluskey, Washington State University (WSU), Pullman, WA
Leah Bergman, University of Idaho (UI), Moscow, ID

Keywords: Gallium oxide, Photoluminescence, Raman, Defects

Research Scope

Improving the efficiency of power devices such as solar-cell inverters is a major component of energy conservation. The physical behavior of materials used in these devices and the link between defects and performance are important considerations for improving reliability [1]. Monoclinic β-Ga_2O_3 is an excellent candidate for next-generation power electronics due to its ultra-wide bandgap of 4.5-4.8 eV, which results in a high breakdown field estimated at 8 MV/cm. Pushing the bandgap higher by alloying with Al could yield even higher breakdown fields. β-Ga_2O_3 also benefits from being relatively cheap to produce and easy to grow in single crystals.

This project investigates the physical behavior of β-Ga_2O_3 and related alloys in response to hydrostatic pressure, nonhydrostatic stress, and temperature. Specific physical properties to be investigated include band structure, vibrational spectra, and defect levels. The pressure response of other materials was also studied. The results of this fundamental work will improve device modeling by providing quantitative insight into how β-Ga_2O_3 behaves under different physical conditions. The research is aligned with the DOE Physical Behavior of Materials program, which supports basic research on the behavior of materials in response to external stimuli.

Recent Progress

<u>Ga_2O_3 under pressure:</u> The effects of pressure on single crystals of Cr-doped gallium oxide (β-Ga_2O_3:Cr^{3+}) and aluminum-gallium oxide [$(Al_{0.1}Ga_{0.9})_2O_3$] were examined by measuring the wavelength shift in the spectral *R* lines. Photoluminescence (PL) spectra of these materials were collected from samples in diamond anvil cells at pressures up to 9 GPa (Fig. 1). The β-Ga_2O_3:Cr^{3+} *R* lines were found to shift linearly under hydrostatic pressure. The $(Al_{0.1}Ga_{0.9})_2O_3$ *R* lines also show a linear shift but the R_1 line shifted less than for β-Ga_2O_3:Cr^{3+}. The ratio of R_2 to R_1 peak areas versus pressure is dominated by nonradiative recombination. Synchrotron x-ray diffraction measurements of $(Al_{0.1}Ga_{0.9})_2O_3$ performed at the Advanced Light Source indicate that its equation of state is similar to that of β-Ga_2O_3 and therefore does not account for the different pressure shift.

β-Ga_2O_3:Cr^{3+} was examined under non-hydrostatic conditions by using mineral oil as a pressure transmitting medium (Fig. 2). The R_1 line is much more sensitive to non-hydrostatic stress than R_2. Spatially resolved PL of a sample at 8 GPa in mineral oil showed significant variations in the R_1 emission wavelength. These results suggest that the R_1 line can serve as a sensitive probe of alloy composition and non-hydrostatic stress, while the R_2 line is insensitive to these perturbations.

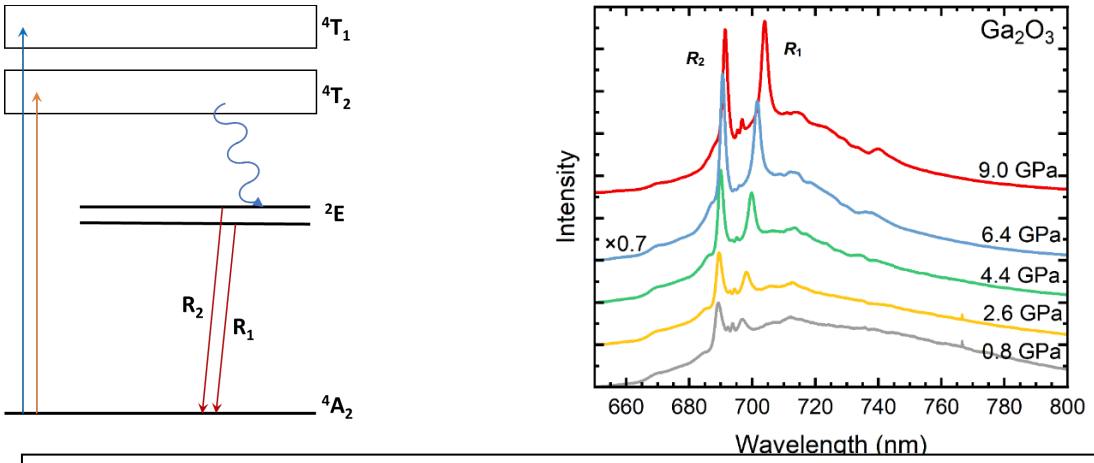

Fig. 1. Left: Electronic transitions of Cr^{3+} in β-Ga_2O_3. Right: PL spectra of β-Ga_2O_3:Cr^{3+} at multiple hydrostatic pressures, offset vertically for clarity.

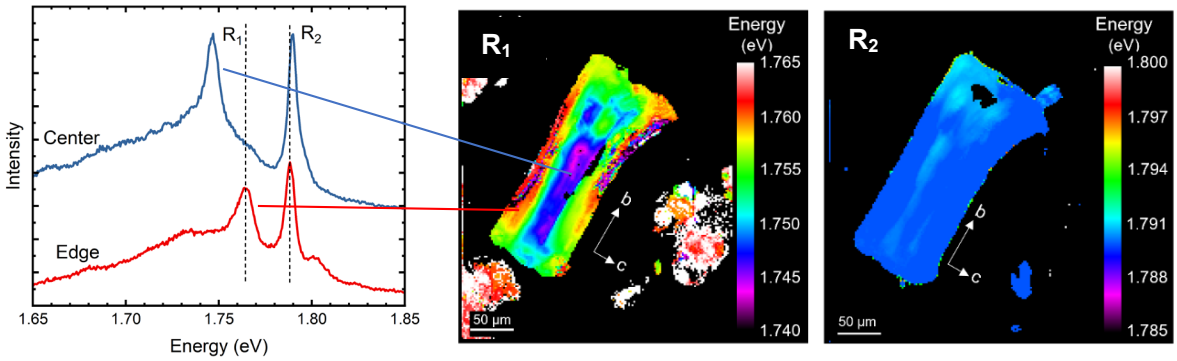

Fig. 2. PL maps of β-Ga_2O_3:Cr^{3+} under non-hydrostatic stress. Energies of the R_1 and R_2 lines are plotted as false-color images. The R_1 line is much more sensitive to non-hydrostatic effects than the R_2 line.

Electron irradiation of Ga_2O_3: Optical and electrical properties of Hf- and Zn-doped β-Ga_2O_3 samples, which are *n*-type and insulating respectively, were altered via high-energy electron irradiation at 2.5 MeV or 0.5 MeV. β-Ga_2O_3:Hf irradiated with 2.5 MeV electrons experienced a color change from blue to yellow (Fig. 3) and a large drop in conductivity due to the creation of gallium vacancies. This irradiation resulted in the absence of free-carrier absorption and the presence of Cr^{3+} emission. PL mapping prior to irradiation revealed optically active ZnO precipitates that formed during growth of β-Ga_2O_3:Zn. These precipitates have a 384 nm (3.23 eV) stacking fault emission in the core; in the outer shell of the precipitate, the PL blue-shifts to 377 nm (3.29 eV) and a broad defect band is observed. After 0.5 MeV electron irradiation, the defect band broadened and increased in intensity. The blue PL band (435 nm) of β-Ga_2O_3 was enhanced

for both Hf- and Zn-doped samples irradiated with 0.5 MeV. This enhancement is attributed to an increase in oxygen vacancies.

Indium gallium oxide alloys: $(In_xGa_{1-x})_2O_3$ microcrystalline alloy films were grown on quartz substrate using Ga and In nitrate precursors followed by annealing at ~1100°C. The composition of the alloys, ascertained from energy-dispersive x-ray spectroscopy (EDS), are shown in Fig. 4, along with the end-members Ga_2O_3 and In_2O_3. Figure 4(a) presents transmission derivative spectra for different alloy compositions. Dips in the spectra correspond to optical bandgaps, plotted in Fig. 4(b), where the inset shows the spectrum for high indium composition (x = 0.7). Two peaks are observed at 4.14 eV and ~3 eV, implying phase separation into Ga-rich and In-rich domains, respectively. For $x \leq 0.46$ [Fig. 4(a)], no second optical gap appears in the spectra, implying that in that range, the alloys exhibit good solubility and are single-phase.

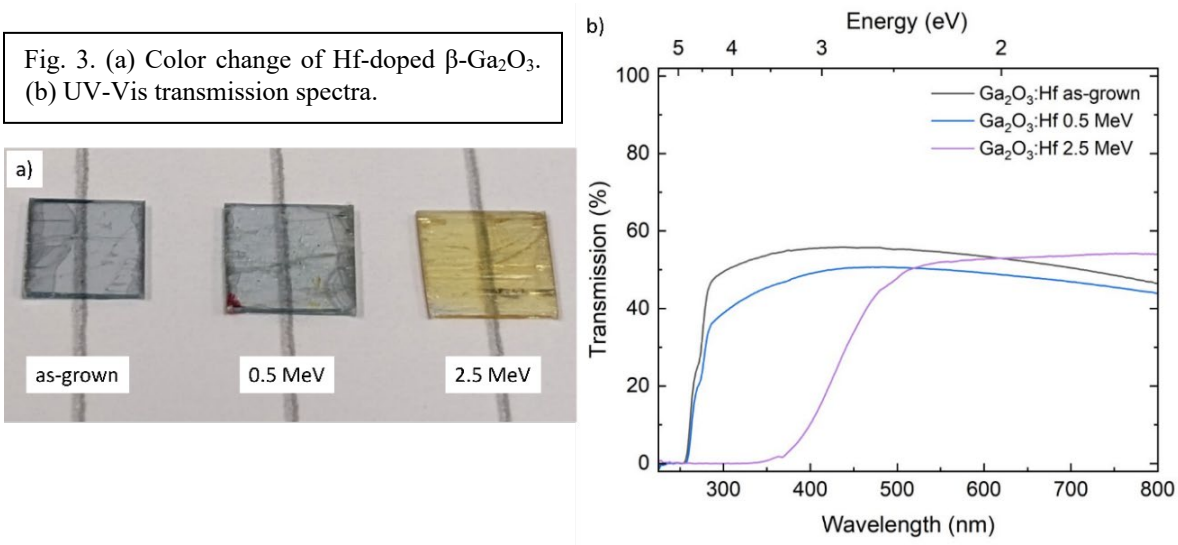

Fig. 3. (a) Color change of Hf-doped β-Ga_2O_3. (b) UV-Vis transmission spectra.

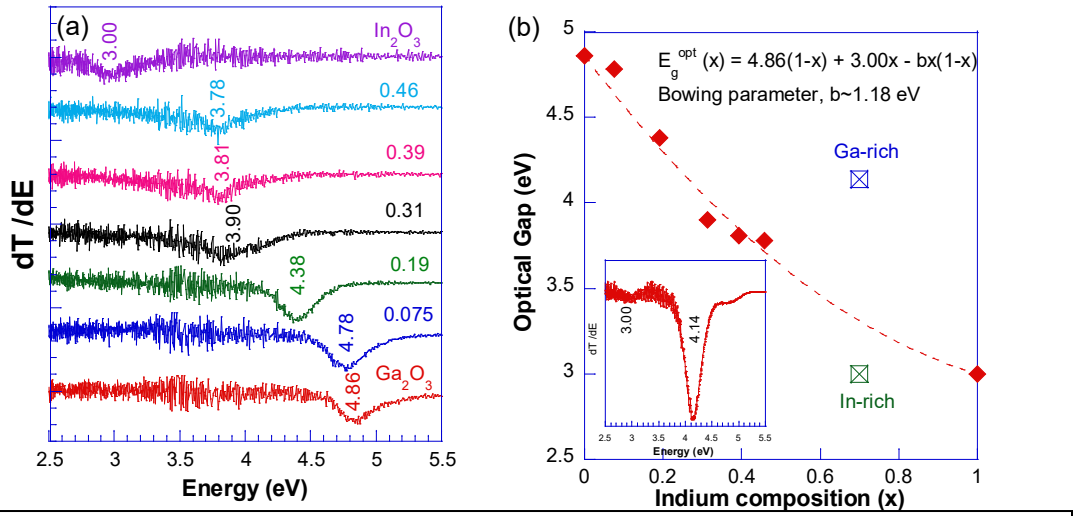

Fig. 4. (a) Transmission derivative spectra for $(In_xGa_{1-x})_2O_3$ thin films. (b) Optical bandgap versus indium composition. Inset: Spectrum of a phase-separated alloy (x = 0.7).

Urbach analysis: Alloy disorder may be enhanced by inhomogeneous distributions of its constituents, leading to randomness of the bond length and angles. Other types of disorder, such as incipient phase separation or incomplete alloying, are also possible. Urbach energy analysis can be used as a measure of deviation from perfect crystallinity. As shown in Fig. 5(a), the slope of the sub-bandgap absorption becomes shallower as the indium content increases. The Urbach energy obtained from the slopes is plotted in Fig. 5(b), along with results from the $Mg_xZn_{1-x}O$ alloy system that we published previously [2]. Both alloys show common behavior, with a relatively constant value up to $x \sim 0.2$ followed by a significant increase for $x > 0.2$.

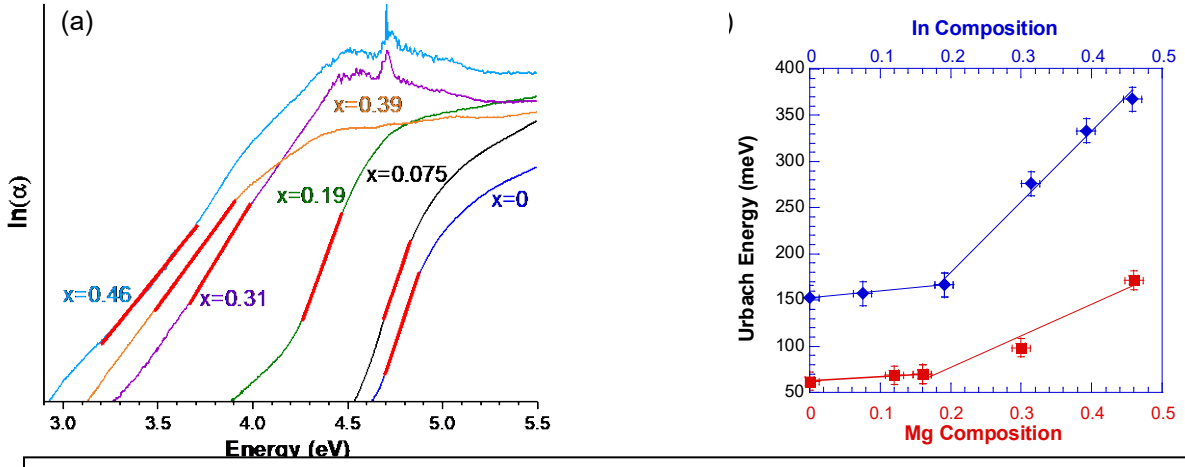

Fig. 5. (a) Spectra for $(In_xGa_{1-x})_2O_3$ thin films, where α is the absorption coefficient. (b) Urbach energy for $(In_xGa_{1-x})_2O_3$ and $Mg_xZn_{1-x}O$ [2] thin films versus composition.

Future Plans

Future work will investigate self-trapped hole (STH) PL as a function of alloy composition. The peak energy of the main PL band, tentatively attributed to STH, is plotted as a false-color map in Fig. 6. X-ray diffraction and scanning electron microscopy will determine crystallographic phase and morphology of $(In_xGa_{1-x})_2O_3$ thin films. Additional tasks include investigating phase separation and metastability, and characterization of Gd-doped Ga_2O_3.

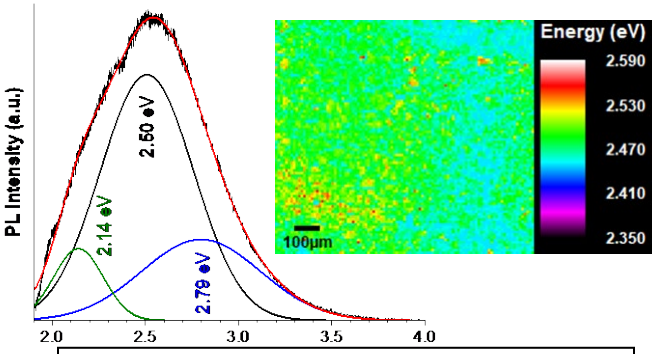

Fig. 6. Representative PL spectrum and map for a $(In_xGa_{1-x})_2O_3$ thin film ($x \sim 0.2$).

References

1. M.D. McCluskey, *Point defects in Ga_2O_3*, J. Appl. Phys. **127**, 101101 (2020).
2. J. Huso, H. Che, D. Thapa, A. Canul, M.D. McCluskey, L. Bergman, *Phonon dynamics and Urbach energy studies of MgZnO*. J. Appl. Phys. **117**, 125702 (2015).

Publications

1. C. Remple, B.L. Dutton, J.B. Varley, J.S. McCloy, and M.D. McCluskey, *Cr is not an acceptor in β-Ga_2O_3*, Phys. Rev. Materials (submitted).
2. J.C. Miller, Y. Wang, Y. Zhang, T.A. Schmedake, and M.D. McCluskey, *Phase transitions of β-$ZnTe(en)_{0.5}$ under hydrostatic pressure*, AIP Advances **15**, 045308 (2025).
3. L.M. Barmore, A.M. Rasmussen, B. Whitfield, and M.D. McCluskey, *Phase transition in heptane under pressure*, J. Phys. Chem. C **128**, 2266 (2024).

4. I. Lukman and L. Bergman, *The nonradiative properties of self-trapped holes in ultra-wide bandgap gallium oxide film*, Phys. Stat. Solidi B **2024**, 2300590 (2024).
5. J. Huso, M.D. McCluskey, J.S. McCloy, A. Bhattacharyya, S. Krishnamoorthy, C.D. Frye, J.B. Varley, and L.F. Voss, *Photoluminescence mapping of laser-damaged β-Ga_2O_3*, MRS Commun. **14**, 427 (2024).
6. J. Huso, M.D. McCluskey, J.S. McCloy, C.D. Frye, J.B. Varley, and L.F. Voss, *Photoluminescence and Raman spectroscopy of wide bandgap semiconductors damaged by deep-UV laser irradiation*, Optical Materials Express **14**, 2929 (2024).
7. C. Remple, J. Huso, M.H. Weber, J.S. McCloy, and M.D. McCluskey, *Electron irradiation effects on the optical properties of Hf and Zn doped β-Ga_2O_3*, J. Appl. Phys. **135**, 185702 (2024).
8. J.E. Stehr, M. Jansson, S.J. Pearton, J.S. McCloy, J. Jesenovec, B.L. Dutton, M.D. McCluskey, W.M. Chen, and I.A. Buyanova, *Color center in β-Ga_2O_3 emitting at the telecom range*, Appl. Phys. Lett. **124**, 042104 (2024).
9. L.M. Barmore, J. Jesenovec, J.S. McCloy, and M.D. McCluskey, *Photoluminescence of Cr^{3+} in β-Ga_2O_3 and $(Al_{0.1}Ga_{0.9})_2O_3$ under pressure*, J. Appl. Phys. **133**, 175703 (2023).
10. M.D. McCluskey, *Resonant interactions involving local vibrational modes in crystals*, J. Appl. Phys. **134**, 201101 (2023).

Understanding Thermo-Chemo-Mechanical Transformations in Thermal Energy Storage Materials and Composites

PI: Prof. Akanksha Menon, Georgia Institute of Technology (GT)

Co-PIs: Prof. Matthew McDowell (GT); Prof. Claudio Di Leo (GT), Dr. Jeffrey Urban (LBNL)

Keywords: Energy Storage, Thermal Cycling, Thermo-Chemo-Mechanics, Salt Hydrates

Research Scope

Thermochemical materials (TCMs) based on salt hydrates exhibit large reaction enthalpies during solid-gas reactions, which makes them promising for energy storage. The overall research goal is to determine how material composition, structure, and mechanical stress co-evolve to determine meso-to-macroscale transformation pathways in thermal energy storage (TES) materials. This fundamental insight can enable the design of new composite architectures with reversible control over the storage process. The current research focuses on:

- Objective 1: Mechanistically understand and probe the dynamic evolution of TES materials under realistic thermal, mechanical, and chemical gradients.
- Objective 2: Elucidate and predict the bidirectional coupling between mechanical stress/damage and thermal/species transport through continuum modeling.
- Objective 3: Design architected composite materials that undergo minimal chemo-mechanical damage during thermal cycling.

Specifically, over the past year we have experimentally characterized the thermophysical properties (thermal diffusivity, mass diffusivity, specific heat) and storage performance (reaction enthalpy) of four salt hydrates – K_2CO_3, $MgSO_4$, $SrBr_2$, and $SrCl_2$. We have also developed new *in situ* techniques (optical microscopy and XRD) to investigate the underlying mechanical degradation mechanisms during charge (dehydration) – discharge (hydration) cycling. These properties serve as inputs to high-fidelity continuum-scale models that resolve the spatial and temporal evolution of stress, damage, heat, and species transport across different length scales (powders and pellets). Finally, we have synthesized different host matrices (hydrogels, mesoporous and microporous materials) that are loaded with salt to provide hygrothermal and mechanical stability under cycling.

Recent Progress

Given the coupled heat and mass transport in salt hydrate TCMs, it is important to understand how the thermal and mass diffusivities vary with pellet density (porosity and tortuosity). To this end, effective diffusion coefficients of the four salts were experimentally measured using the wet cup method in which a vapor pressure driving force causes water vapor to permeate through a salt pellet without inducing a chemical reaction.[1] It was found that in $K_2CO_3 \cdot 1.5H_2O$, as the porosity of the pellet decreases, so does the effective diffusion coefficient as there are fewer pathways for the water vapor to permeate through the pellet. For this hydrated salt, an effective mass diffusivity between 0.5-2 mm^2/s was measured for porosities ranging from 6% to 18%. Thermal diffusivity of the four salts was measured using laser flash analysis – it was found that as the pellet porosity decreases (relative density increases from 82% to 94%), the thermal diffusivity increases from 0.2-0.3 mm^2/s due to there being more contact points for heat transfer. Next, specific heat capacity of the hydrated and dehydrated salts was measured using differential scanning calorimetry. Dehydrated K_2CO_3 and $SrBr_2$ were found to have specific heats of 0.83 J/g-K and 0.3 J/g-K

respectively, which was validated using the Shomate equation and Dulong-Petit law for solid phase heat capacity.

To elucidate chemo-mechanical degradation mechanisms during hydration-dehydration cycling, the structural and morphological evolution of $SrCl_2$ was investigated. A custom-built experimental setup was developed to enable real-time, *in situ* observation of dynamic crack formation and morphological changes under controlled humidity and temperature conditions (Fig. 1a and 1b).

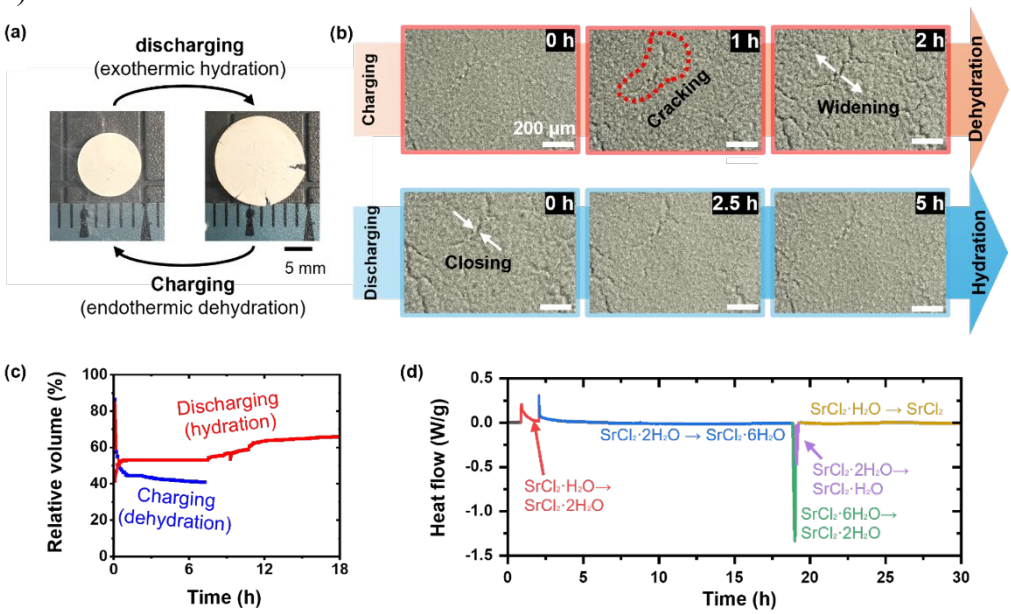

Fig. 1: (a) Volume change of a $SrCl_2$ pellet during hydration-dehydration cycling. (b) In situ optical microscopy images capturing the morphological evolution of the top surface of a $SrCl_2$ pellet during hydration-dehydration. (c) Estimate of the volume changes of the $SrCl_2$ pellet as a function of time during charging (blue line) and discharging (red line). (d) Heat flow of a $SrCl_2$ pellet during hydration and dehydration under controlled conditions of 25 °C and 60 % RH for hydration, and 80 °C and 0.1 % RH for dehydration.

In addition, *in situ* X-ray diffraction (XRD) and simultaneous thermal analysis (STA) were performed to characterize phase transformations, reaction kinetics, and volumetric changes during cycling. It was found that the hydration and dehydration steps have asymmetric kinetics (Fig. 1c and 1d), and that each phase transformation between hydration states exhibits distinct reaction rates.[2] In particular, the early stages of cycling are characterized by abrupt and rapid volume changes. These sudden transformations generate significant mechanical stresses, which in turn drive crack propagation, interfacial sliding, and eventual pulverization of the pellets — compromising their long-term structural integrity and energy storage performance.

To complement the experimental objectives, a continuum thermal-reaction-diffusion model was developed. Parametric studies were conducted to quantify the sensitivity of material properties, such as mass diffusivity, thermal conductivity, and reaction kinetics. A representative simulation, incorporating the aforementioned experimental data, was performed on a pellet to enable a predictive understanding of hydration and dehydration processes in TCMs without mechanical coupling. Specifically, a two-dimensional pellet model for the hydration of $SrBr_2$ (from its monohydrate to hexahydrate state) was used with appropriate temperature and water vapor concentration boundary conditions, and symmetry to reduce computational cost. The temporal evolution of heat flux and the normalized reaction coordinate are shown in Fig. 2 (left). The reaction begins at the top and lateral surfaces, where fixed vapor concentration and

temperature drive hydration. The reaction front propagates inward gradually, with a coarse interface width due to low value of Damkohler number used, as shown in Fig. 2 (left). These simulations lay the groundwork for fully coupled thermo-chemo-mechanical simulations and offer deeper insight into material performance under realistic TES operating conditions.

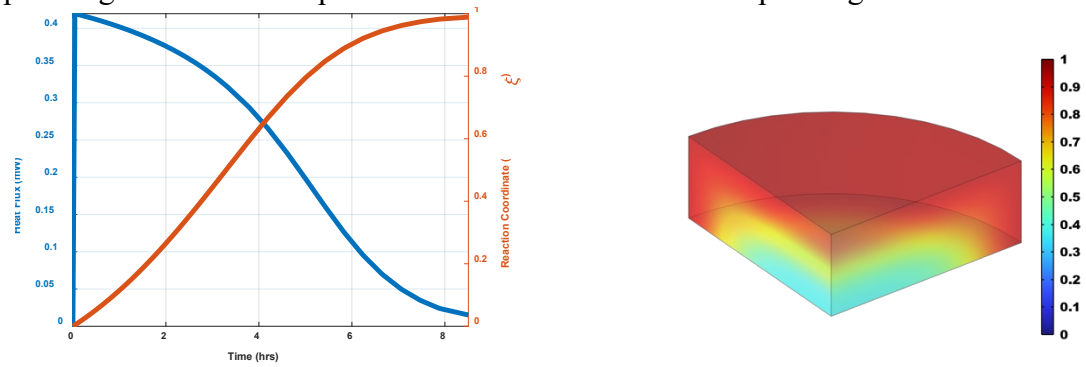

Fig. 2: Hydration of a $SrBr_2$ pellet transitioning from the monohydrate to hexahydrate state: (Left) Temporal evolution of heat flux and the normalized reaction coordinate at the bottom center of the pellet; (Right) Reaction coordinate contour plot of a quarter cylindrical pellet at time = 2.65 hrs.

The experimental characterization and continuum modeling reveal that charge-discharge cycling is limited by mechanical degradation caused by volumetric expansion and contraction. To address this, we fabricated composite architectures by encapsulating salt hydrates into polymer matrices, such as alginate and polyacrylamide, to enhance mechanical stability and cyclability. The alginate matrix was formed using an ionic gelation synthesis in which divalent cations (Ca^{2+} and Sr^{2+}) from the salt hydrates act as crosslinks between the alginate chains.[3] This reaction is initiated to form alginate salt hydrate beads (diameter ~ 0.2-2 mm) by introducing a 1-3 wt. % aqueous alginate solution into an aqueous $SrCl_2$ or $CaCl_2$ solution, as shown in Fig. 3. The polyacrylamide composites were synthesized using an ultraviolet photo-initiator to polymerize acrylamide into chains crosslinked by bis-acrylamide. The salt hydrates were then introduced into the hydrogel structure via diffusion from an aqueous solution. For alginate beads, the salt loading varied from 74 to 83 wt.% of the composite mass, with beads made from the higher solution concentration experiencing shrinkage upon dehydration and salt leakage upon hydration – these suggest that there is an optimal solution concentration and salt loading that balances energy storage capacity and material stability.

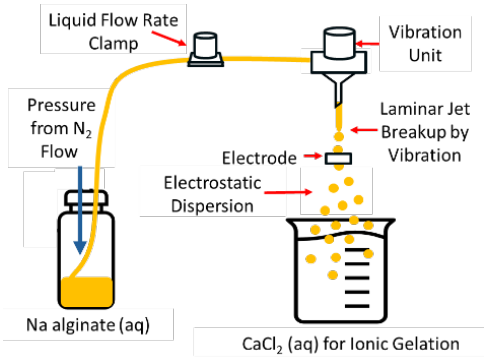

Fig. 3. Schematic showing encapsulation of salt hydrate within an alginate matrix.

Future Plans

From the thermophysical characterization, the Lewis number for some salts was found to be less than unity, indicating that these pellets are thermal transport limited. To improve the heat transfer, we will design composites with thermally conductive fillers (carbon black, graphene nanoplatelets, and multiwalled carbon nanotubes) at volume fractions determined using percolation theory. The thermal conductivity of these samples will be measured using the modified transient plane source technique and laser flash analysis. In addition to pure salts, a composite host matrix comprising both alginate and polyacrylamide will also be developed, based on a ratio that benefits from the

mechanical stability of the polyacrylamide matrix as well as the higher mass diffusion of the alginate matrix.

As a future direction for characterization, we will utilize X-ray computed tomography to investigate the internal morphological evolution of pure salts under repeated cycling. This will allow us to uncover how localized diffusion limitations contribute to stress concentration and fracture initiation within the material. On the modeling side, upcoming work will focus on incorporating mechanics into the thermal–reaction–diffusion framework to capture the influence of stress and deformation on hydration/dehydration of TES materials. The extended model will be validated against experimental data, such as TGA/DSC measurements. Once validated, the model will be applied to investigate how microstructural features, such as porosity, particle size, and interfaces, affect TES performance metrics like energy density, reaction rates, long-term cyclability, and durability. Future efforts will focus on developing effective multiscale models that bridge microstructural behavior with macroscale performance, enabling predictive design of next-generation thermo-chemo-mechanical energy storage systems.

References

1. J. Aarts, H. Fischer, O. Adan, and H. Huinink. “Impact of cycling on the performance of mm-sized salt hydrate particles.” *Journal of Energy Storage*, **2024**, 76, 109806.
2. A. Martin, D. Lilley, R. Prasher, and S. Kaur. “Particle size optimization of thermochemical salt hydrates for high energy density thermal storage.” *Energy & Environmental Materials*, **2024**, 7(2), e12544.
3. P. A. Kallenberger, K. Posern, K. Linnow, F. J. Brieler, M. Steiger, and M. Fröba, "Alginate-Derived Salt/Polymer Composites for Thermochemical Heat Storage," *Advanced Sustainable Systems,* **2018,** 2(7), 1700160.

Publications

1. J. Shin, M. R. Morrell, E. Barbosa, A. K. Menon*, M. T. McDowell*, *Investigating structural and morphological transformations of strontium chloride for thermochemical energy storage* (submitted on 3/14/2025).
2. M. R. Morrell, M. Adams, M. Pomilia, A. K. Menon*, *Characterization of thermophysical properties of salt hydrates for energy storage* (in preparation).
3. S. B. Kaudur, C. V. Di Leo, *Modeling Coupled Thermal-Diffusion-Chemo-Mechanics in Solids: Applications to Thermochemical Energy Storage Materials* (in preparation).

Session VIII

Extraordinary Responsive Magnetic Rare Earth Materials

Yaroslav Mudryk, Anis Biswas, Prashant Singh, and Duane D. Johnson

Ames National Laboratory of US DOE, Iowa State University, Ames, Iowa, 50011-2416

Keywords: Rare-earth materials; Magneto-structural transitions; Theory of 4*f* intermetallic compounds; Spin phenomena; Magneto-functional materials

Research Scope

We focus on magnetic rare-earth compounds with indirect 4*f* exchange interactions, that demonstrate extraordinary responsiveness to external thermodynamic stimuli like temperature (*T*), pressure (*p*), and magnetic field (*H*), and that create a diverse array of intriguing physical phenomena and functionalities. Prominent manifestations include giant magnetocaloric, magnetoresistive, and magnetostrictive effects; spontaneous thermoelectricity; training and acoustic effects; magnetic deflagration; pronounced magnetic anisotropy; phase-separated glass-like states; and exchange bias—each exemplifying the remarkable science and application potential of these materials. These interesting and technologically important behaviors fundamentally originate from the strong coupling between crystal and magnetic lattices.

Our major research goal is to *uncover the underlying electronic, atomic, and microscopic interactions* in novel rare-earth intermetallic materials with extraordinarily strong coupling between the magnetic, electronic, and lattice degrees of freedom that drive remarkable responsiveness to external stimuli. These materials exhibit unique magnetic and electronic behaviors, associated with magneto-structural and magnetic-elastic transformations, that are specific to lanthanides and can lead to future innovations in energy generation, conversion and harvesting, as well as development of spintronic-based devices. The overarching objective is to both understand the composition-structure-property relations of rare earth materials with strong spin-lattice coupling and build fundamental concepts governing their magneto-responsiveness, which *emerges from complex correlations of the atomic and electronic constituents*. We focus on *4f*-electron intermetallic systems - RScT, R_2T, R_7Pd_3 (R is a rare-earth metal, and T is Group 13-15 metal or metalloid) - known to exhibit strong relationships between their crystallographic and electronic structures and magnetic ground states. These compounds, synthesized in bulk and thin film form, show rich physics yet remain simple enough to develop predictive modeling tools gauged against reliable experimental data. Our research focus is on basic understanding of how to predictively tune the interplay between spin and atomic lattices and manipulate magnetic and electronic behaviors of rare earth materials to make them strongly responsive to external stimuli, which is *crucial for guiding the predictive design of advanced energy materials.*

Recent Progress

By making use of our experimental and theoretical expertises, we revealed novel fundamental physical phenomena in rare-earth based intermetallic compounds where magnetism is governed by 4*f* electrons and developed new theoretical approaches for predictive design of magnetic rare earth materials. Three of our recent achievements are highlighted below:

Sm_7Pd_3 - Unusual magnetism in an unlikely place

Materials that exhibit long-range magnetic order while maintaining low or near-zero net magnetization with high magnetic anisotropy are currently the focus of intense investigation due to their significance in both fundamental science and practical applications, like offering higher storage density due to low stray fields. In our recent study, we have identified a remarkable combination of unusual magneto-elastic coupling, nearly zero magnetization, and exceptionally high magnetic coercivity in the binary compound Sm_7Pd_3 [1].

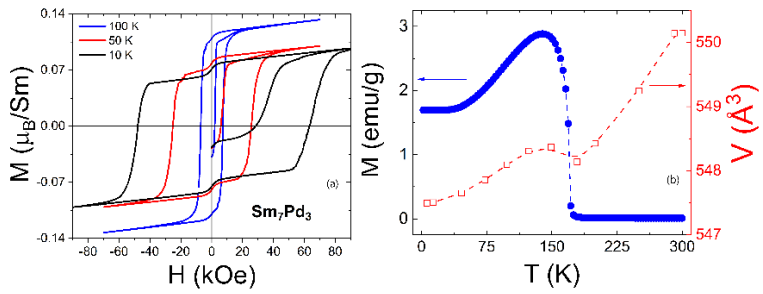

Figure 1. Magnetization of Sm_7Pd_3 compound as a function of applied magnetic field (a) measured below magnetoelastic phase transition (b).

This material also shows large exchange bias effect (EBE), 2.6 kOe, in its bulk polycrystalline form. Finding of a remarkably rich magnetic behavior in Sm_7Pd_3 was unexpected given that all other Sm-Pd compounds exhibit no magnetic ordering. The highly unusual Sm_7Pd_3 magnetic properties dominated by RKKY-type indirect 4*f*-4*d* magnetic interaction are likely interlinked with the existence of strong magneto-elastic coupling, manifested a symmetrically invariant magneto-elastic transition at magnetic ordering temperature, T_C = 169 K (Figure 1), yet the compound retains its non-centrosymmetric hexagonal Th_7Fe_3-type structure down to 6 K. Density functional theory (DFT) calculations indicate the presence of high intrinsic magnetocrystalline anisotropy in Sm_7Pd_3 accounting for the extremely large coercivity (Figure 1) observed in the polycrystalline sample—reaching up to H_C= 130 kOe at 2 K [1].

Physics-Informed Machine Learning for the Discovery of Functional Materials

We demonstrated that physics-informed machine learning (ML), when integrated with experimental validation and density functional theory (DFT)-derived training data, offers powerful predictive capabilities for the design of new functional rare-earth compounds [2]. In this work, we employed ML to pinpoint key quantum-mechanical descriptors—like average *d*- and *f*-bandwidths and formation energies—that govern the magnetic ordering temperature (T_C) in rare-earth-based materials [2]. Trained on a dataset of 220 known compounds, our model achieved strong predictive accuracy, ultimately guiding the experimental discovery of elevated T_C values in pseudo-binary $(Zr_xCe_{1-x})Fe_2$ systems. We recently demonstrated the validity of this model in estimating transition temperatures of another series of rare earth intermetallic compounds: $GdZn_{1-x}Ga_x$ [3]. Complementing the ML approach, DFT electronic structure calculations provided fundamental insights into the mechanisms driving magnetic transitions in these materials. This synergy between data-driven modeling and quantum theory enhances our understanding of the physical features that dictate magnetism, paving the way for more targeted discovery of advanced magnetic materials.

Understanding fundamental magnetism of Eu_2In

Magnetic first-order transitions with giant magnetocaloric effect yet without thermal irreversibility are highly desired for the development of energy efficient magnetic refrigeration technology. The discovery of the novel anhysteretic first-order magneto-elastic transition associated with the giant cryogenic magnetocaloric effect in Eu_2In warranted the continuation of research to explore basic

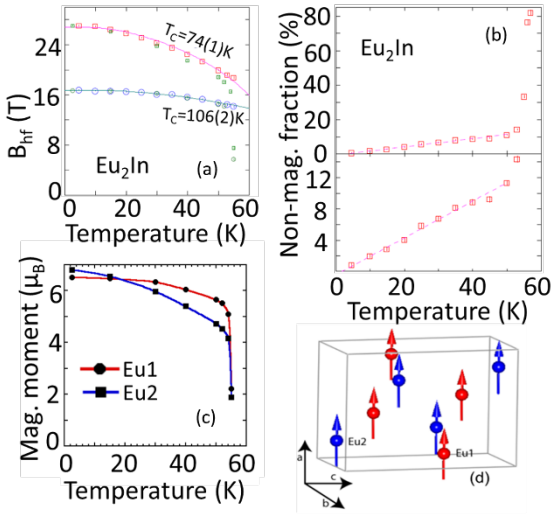

Figure 2. (a) Temperature dependence of the hyperfine fields (B_{hf}) from Mössbauer spectroscopy for two Eu sites in Eu_2In (d). Green symbols show magnetic moments taken from (c), determined by neutron diffraction, and scaled to match the B_{hf}. The non-magnetic phase does not completely disappear at T_C (b) [4].

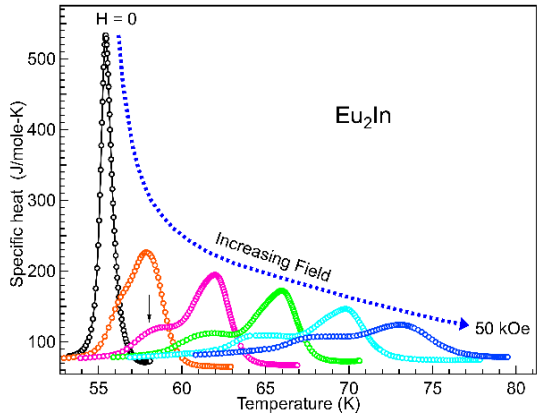

science of electronic, magnetic, and atomic interactions in Eu_2In and related R_2In compounds. A comprehensive research effort involving neutron powder diffraction and Mössbauer spectroscopy established the co-existence of high temperature (HT) and low temperature (LT) phases below T_C (**Figure 2**). We found that the magnetic structure of LT-Eu_2In is ferromagnetically collinear along the *a*-axis, while HT phase remains paramagnetic. The isostructural Eu_2Sn shows very different magnetic behavior, displaying second-order antiferromagnetic ordering at 32 K and a spin-reorientation transition [4].

Future Plans

We aim to develop basic understanding of magneto-responsive behaviors originated from the complex interactions involving 4*f* electrons. Below we describe few key research directions which will be covered in near future.

Magnetoelastic transitions in R_2In compounds

Figure 3. Evolution of specific heat near first-order transition with applied magnetic field in Eu_2In.

We will continue to uncover the underlying mechanisms of phase transformations in R_2In compounds. A key model system of our study will be Eu_2In, which exhibits an anhysteretic first-order transition. Recently, we observed that the sharp peak in the specific heat data of Eu_2In — characteristic of the first-order transition – splits into two distinct peaks when a magnetic field exceeding 10 kOe is applied (Figure 3). Given the L=0 state of Eu(II), and simple magnetic structure of Eu_2In (Figure 2), the splitting is difficult to explain since there is only one transition in magnetic data even at 50 kOe (not shown). To further explore this, we will perform temperature-dependent X-ray absorption spectroscopy (XAS), including both XANES and EXAFS, to probe the local crystal and electronic structures near the transition. These insights will help us understand the origin of the magnetoelastic behavior in the compound.

To underpin the magnetic ground state, we also plan to conduct neutron diffraction studies on Pr_2In and Nd_2In—two other R_2In compounds that display qualitatively similar discontinuous first-order transitions without significant thermomagnetic hysteresis. In addition, we aim to understand how the coexistence of multiple rare-earth elements affects the magnetic ground states and magnetoelastic properties of $(R'_xR''_{1-x})_2In$ compounds. In this regard, we will focus on two series of pseudobinary compounds: $(Er_xYb_{1-x})_2In$ and $(Eu_xPr_{1-x})_2In$.

Predicting stable crystallographic phases of magnetically responsive rare-earth compounds

DFT aided theoretical prediction of phase stability and crystallographic transitions can lead to a discovery of new rare-earth intermetallics with novel magnetoresponsive phenomena. Using R_2In compounds as a model systems of study due to their intriguing magnetoresponsive properties, we found that manipulation of local interactions by substitutional chemistry shows a direct correlation between structural phase change (crystal/lattice symmetry) and local atomic distortion and/or atomic displacement. Computationally, in a first step, we will systematically investigate the role of degree of atomic distortion via change in local chemistry and external parameters (e.g., pressure, temperature) to establish connection among features controlling structural phase transformation in R_2In series. These distortions include several structural aspects including tilting and rotations of a local crystal motifs, as well as variations in bond-lengths and bond-angles that comprise these units. To confirm structural and electronic connection between atomic-scale interactions and magnetoresponsive phase behavior, we will compute electronic indicators, including crystal-field splitting and bandwidth evolution to reveal how changes in the electronic landscape reinforce or oppose lattice instabilities, which will be verified experimentally via compositional tuning and temperature-dependent X-ray powder diffraction.

Understanding magnetic glass states in noncentrosymmetric Sm_7Pd_3

We will continue our investigation into the complex magnetism of Sm_7Pd_3. Our recent findings indicate that this system exhibits an unusual magnetic glassy state near the magnetoelastic transition, likely arising from overlap of both spin and domain freezing. Additionally, we have observed a reversible enhancement in magnetic anisotropy under the application of hydrostatic pressure. To further explore these unconventional magnetic behaviors, we plan to investigate the magnetic properties of Sm_7Pd_3 under high magnetic fields and high pressures, utilizing the advanced experimental facilities at the National High Magnetic Field Laboratory in Florida. Moreover, a collaborative effort is underway with Prof. H. Srikanth's group at the University of South Florida to examine the anisotropic behavior of the material in more detail.

References

[1] A. Biswas, R.K. Chouhan, O. Dolotko, P. Manfrinetti, S. Lapidus, D.L. Schlagel, Y. Mudryk, "Exceptional magnetic and magnetoelastic behavior of rare-earth non-centrosymmetric Sm_7Pd_3," *Acta Materialia*, **265**, 119630 (2023). https://doi.org/10.1016/j.actamat.2023.119630

[2] P. Singh, T. Del Rose, A. Palasyuk, Y. Mudryk, "Physics-informed machine learning prediction of Curie temperatures and its promise for guiding the discovery of functional magnetic materials," *Chemistry of Materials*, **35**, 6304 (2023). https://doi.org/10.1021/acs.chemmater.3c00892

[3] A. Biswas, A. Kumar, P. Singh, T. Del Rose, R. K. Chouhan, B. C. Margato, B. P. Alho, E. P. Nobrega, P. J. von Ranke, P. O. Ribeiro, V. S. R. de Sousa, Y. Mudryk, "The influence of Ga doping on magnetic properties, magnetocaloric effect, and electronic structure of pseudo-binary $GdZn_{1-x}Ga_x$ (x=0-0.1)", *Physical Review Materials*, **8**, 114418 (2024). https://doi.org/10.1103/PhysRevMaterials.8.114418

[4] C. Ritter, D.H. Ryan, A. Provino, G. Lamura, Y. Mudryk, R.K. Chouhan, P. Singh, D.D. Johnson, V.K. Pecharsky, P. Manfrinetti, "Magnetic ordering in Eu_2In and Eu_2Sn", *Journal of Alloys and Compounds*, **980**, 173573 (2024). https://doi.org/10.1016/j.jallcom.2024.173573

Publications [10 out of total 26 articles]

1. P. Singh, T. Del Rose, A. Palasyuk, Y. Mudryk, "Physics-informed machine learning prediction of Curie temperatures and its promise for guiding the discovery of functional magnetic materials," *Chemistry of Materials,* **35**, 6304 (2023). https://doi.org/10.1021/acs.chemmater.3c00892

2. A. Biswas, A. Thayer, O. Dolotko, Y. Mudryk, "Borderline first-order phase transition and large cryogenic magnetocaloric effect in PrNdIn," *Journal of Applied Physics,* **134**(9), 093902 (2023). https://doi.org/10.1063/5.0160429

3. T. Del Rose, R. Choudhary, Y. Mudryk, D. Haskel, A.K. Pathak, G. Bhaskar, J.V. Zaikina, D.D. Johnson, V.K. Pecharsky, "Interplay Between Kondo and Magnetic Interactions in $Pr_{0.75}Gd_{0.25}ScGeH$," *Journal of Alloys and Compounds,* **966**, 171351 (2023). https://doi.org/10.1016/j.jallcom.2023.171351

4. A. Biswas, R.K. Chouhan, O. Dolotko, P. Manfrinetti, S. Lapidus, D.L. Schlagel, Y. Mudryk, "Exceptional magnetic and magnetoelastic behavior of rare-earth non-centrosymmetric Sm_7Pd_3," *Acta Materialia,* **265**, 119630 (2024). https://doi.org/10.1016/j.actamat.2023.119630

5. C. Ritter, D.H. Ryan, A. Provino, G. Lamura, Y. Mudryk, R.K. Chouhan, P. Singh, D.D. Johnson, V.K. Pecharsky, P. Manfrinetti, "Magnetic ordering in Eu_2In and Eu_2Sn", *Journal of Alloys and Compounds*, **980**, 173573 (2024). https://doi.org/10.1016/j.jallcom.2024.173573

6. A. Biswas, A. Kumar, P. Singh, T. Del Rose, R. K. Chouhan, B. C. Margato, B. P. Alho, E. P. Nobrega, P. J. von Ranke, P. O. Ribeiro, V. S. R. de Sousa, Y. Mudryk, "The influence of Ga doping on magnetic properties, magnetocaloric effect, and electronic structure of pseudo-binary $GdZn_{1-x}Ga_x$ (x=0-0.1)", *Physical Review Materials*, **8**, 114418 (2024). https://doi.org/10.1103/PhysRevMaterials.8.114418

7. A. Kumar, P. Singh, A. Doyle, D.L. Schlagel, Y. Mudryk, "Multiple magnetic interactions and large inverse magnetocaloric effect in TbSi and $TbSi_{0.6}Ge_{0.4}$," *Physical Review B,* **109**, 214410 (2024). https://doi.org/10.1103/PhysRevB.109.214410

8. P. Singh, T. Del Rose, Y. Mudryk, V.K. Pecharsky, D.D. Johnson, "Designed metal-insulator transition in low-symmetry magnetic intermetallics," *Physical Review B,* **109**, 064207 (2024). https://doi.org/10.1103/PhysRevB.109.064207

9. A. Kumar, A. Biswas, Y. Mudryk, "Stability of the first-order character of phase transition in $HoCo_2$", *Journal of Applied Physics,* **136**, 203902 (2024). https://doi.org/10.1063/5.0240132

10. A. Bhattacharya, A. Ahmed, A.Dutta, A. Kumar, P. Singh, A. Biswas, Y. Mudryk, I. Das, "Anomalous Hall effect in the polar magnet $Gd_3Ni_8Sn_4$: A candidate for hosting skyrmions", *Physical Review B*, **111**, 104410 (2025). https://doi.org/10.1103/PhysRevB.111.104410

Local Dynamics in Liquid, Glass and Other Disordered Systems

T. Egami, *Univ. of Tennessee and Oak Ridge National Laboratory*, Y. Shinohara, E. Zarkadoula and C. Hua, *Oak Ridge National Laboratory*, W. Dmowski, *Univ. of Tennessee*

Keywords: Local dynamics, liquid, glass, and electrons, neutron and x-ray scattering, correlation function in space and time, electron correlation

Research Scope

The science of disordered matter, such as liquid and glass, is much less developed than that of crystalline materials, even though these materials are important in energy-related applications. The main origin of this slow progress is the dynamic nature and the non-periodicity of their structures, which elude the application of condensed-matter theories predicated by lattice periodicity. The overarching goal of this program is to establish a fundamental understanding of the structure and dynamics of liquid, glass and other disordered systems, and of the microscopic mechanisms that control their properties. To achieve this goal, this project will focus on the following: (1) advance the understanding of the cooperative atomic and spin dynamics in liquids and glasses by direct experimental observation, (2) extend the theory of medium-range atomic order in liquid and glass to elucidate physical properties, including the glass transition, and (3) develop the understanding of local dynamic correlations among electrons, focusing on strongly correlated electron systems, to elucidate physical phenomena, including superconductivity. The outcome of this proposed work will guide us to the development of glass, liquid and other disordered systems with superior properties, and ultimately impact the DOE mission through the development of the general physics of disordered matter.

Recent Progress

1. Local atomic dynamics in liquids and glasses by experiment and simulation

Recently we developed an approach to observe correlated atomic dynamics directly by experiment [1]. In this approach we determine the dynamics structure factor, $S(Q, E)$, by inelastic neutron or x-ray scattering over wide ranges of Q, the momentum transfer, and E, the energy transfer, and Fourier-transform it into the Van Hove function (VHF), $G(r, t)$. Until recently, the experimental determination of the VHF was impractical because of the long time required to collect data on $S(Q, E)$ over wide ranges. But recent progress in instrumentation made it feasible. Using this approach, we demonstrated how atomic dynamics becomes more cooperative as a liquid is supercooled, by using electrostatic levitation and inelastic neutron scattering (INS) [P9]. We also showed that water molecules become dynamically more correlated with decreasing temperature, by demonstrating that the short-range diffusive dynamics becomes different from the long-range diffusion (**Fig. 1**) [P8].

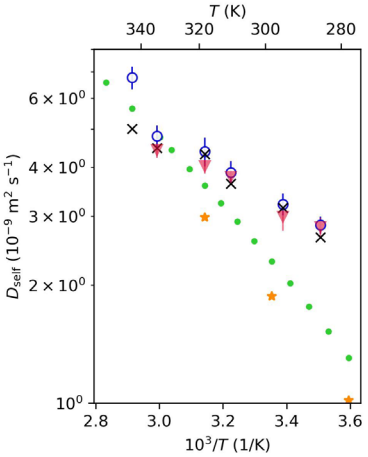

Fig. 1 Local diffusivity measured by the VHF (upper group) is faster than macroscopic diffusivity (lower group)

Computer simulation is a powerful approach to investigate complex many-body problems, such as liquid dynamics. Using simulation, we showed how liquid dynamics differ from those in gas in a fundamental way. By diagonalizing the Hessian matrix, we showed that atoms are dynamically correlated, whereas correlations are weak in gas [P3, P6]. We also demonstrated that the atoms are not totally frozen in metallic glasses, and they are locally mobile down to $T = 0$ K. We applied cyclic shear deformation on a model Cu-Zr metallic glass and identified "lossy atoms" through the analysis of atomic-level energy loss (tan δ). We found that a lossy atom in one cycle is no longer lossy in the next (**Fig. 2**), suggesting that the energy barriers in the mega-basin of the potential energy landscape (PEL) is shallow (only ~ 0.6 meV) and quantum-mechanical zero-point energy is large enough to overcome. This means that atoms are not frozen and locally moving due to zero-point fluctuations, down to $T = 0$ K [P7, P10].

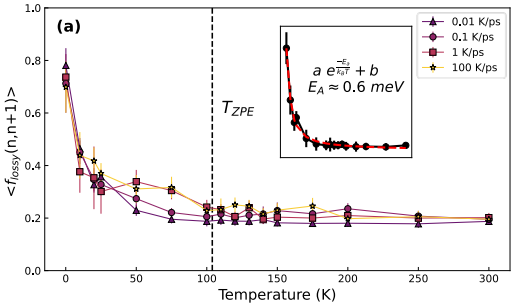

Fig. 2 The probability that a lossy atom is lossy again in the next cycle. <*f*> = 0.2 corresponds to a totally random case [P7].

2. Density wave theory of liquid and glass

The atomic pair-distribution function (PDF), $g(r)$, of metallic liquids and glasses shows extended oscillations beyond the first peak that characterize the medium-range order (MRO). The oscillations decay exponentially with distance with the decay length of ξ_s, which increases with decreasing temperature following the Curie-Weiss law, $\xi_s(T) = C/(T - T_{IG})$ [2]. The current theories of liquid and glass start from an atom and its surrounding neighbors, adding more atoms to create a model, the bottom-up approach. However, it is difficult to explain the MRO that extends many atomic distances by this approach. The MRO plays a central role in controlling the properties of liquid and glass. For instance, it defines the glass transition by freezing at T_g, whereas the SRO in the nearest neighbors does not. The coherence volume, $\xi_s(T)^3$, is proportional to the activation energy of viscosity. It is also directly related to liquid fragility.

We developed a density wave theory that explains the origin of the MRO [P2, P4]. The ξ_s diverges at T_{IG}, although this never happens in reality, because the system freezes at the glass transition. This imaginary state is the density wave (DW) state with long-range order but without periodicity, a quasicrystalline state. The DW state is driven by the pseudopotential (the effective interatomic potential) in reciprocal space, but it is unstable against thermal and other disorder, resulting in the attenuated DW characterized by ξ_s. This theory explains the Curie-Weiss law of ξ_s with high accuracy.

3. Direct observation of electron correlation by inelastic x-ray scattering

Electrons in solids are correlated in space and time because of Coulomb interaction. Even though electron correlation is a principally important subject, it has been studied mainly by theories, such as the density functional theory (DFT) and the Hubbard theory, and there are scant direct studies by experiment. The sole experimental studies are attempts to observe the electronic pair-distribution function (PDF) by diffraction [3]. We measured the $S(Q, E)$ for polycrystalline beryllium by inelastic x-ray scattering (IXS) over the energy range from 1 to 110 eV with the resolution of 0.7 eV, and converted $S(Q, E)$ to $g(r, E)$, the energy-resolved dynamic PDF, by Fourier-transformation from Q to r (Fig. 3).

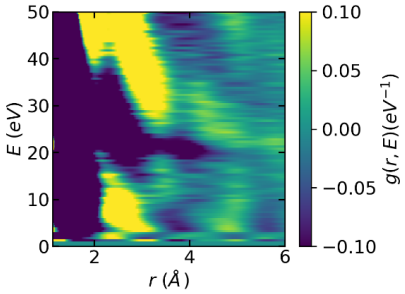

Fig. 3 Energy-resolved dynamic PDF, $g(r, E)$, of polycrystalline beryllium, showing exchange-correlation hole that extends at the plasmon energy

The results lead to two important discoveries:

1. The exchange-correlation hole relevant to the DFT (below 20 eV) is well-defined with the size of 2 Å. The snapshot PDF based upon $S(Q)$ (energy-integrated) includes high-energy portion above the plasma frequency, which is irrelevant to the DFT.
2. At the plasma frequency (~ 20 eV) the exchange-correlation hole extends to 5 Å. In plasmon electrons move collectively, reducing the probability of spatial contact. This demonstrates that electron dynamics affects electron correlation significantly.

The success of this experiment opens up a new opportunity for studying the complex behavior of correlated electrons directly by scattering measurements.

Future Plans

1. Atomic structure and dynamics in complex liquids

In the Periodic Table elements near the left edge are metallic, while those near the right edge are inert or ionic. The elements in the middle, such as Ga, Si, Ge, Sn, and Bi, show complex behavior in the solid and liquid states. They are usually explained as being composed of metallic and non-metallic domains, but we are proposing a new picture, taking liquid Ga as an example. The $S(Q)$ of liquid Ga shows the first peak with a prominent shoulder. The position of the shoulder in Q is close to $2k_F$, where k_F is the Fermi momentum. However, the first peak of the PDF has no shoulder, indicating only one kind of atomic bond and environment. We propose that the structure of liquid Ga is made of two density waves (DWs), one metallic in nature and the other non-metallic and driven by close packing to increase density. The two DWs are strongly overlapping and fluctuating in time. Each atom sees many DWs, so the atomic environment is rapidly fluctuating. This view strongly challenges the current view. We surmise that this picture is valid to liquids of many other elements in the middle of the Periodic Table.

2. Analysis of the convergent beam TEM by the density wave theory

The convergent beam transmission electron microscopy (CB-TEM) is a unique method capable of examining the structure at nanometer-size volume. Currently the data are processed by the fluctuation electron microscopy (FEM) approach [4], but we believe we can extract much more information about the microscopic state of a glass. In collaboration with P. Voyles (U. Wisconsin) we analyze the spatial correlation of the CB-TEM patters of metallic glasses and compare them with the prediction by the density wave theory. This will be a true test of the DW theory.

3. Electron correlations in the cuprates

Earlier we studied the structure of superfluid ^{4}He using the energy-resolved dynamic PDF method [5] and found that the He-He distance in the BE condensate (4 Å) is significantly longer than that in non-condensate (3.6 Å). We explained this in terms of the absence of wavefunction overlap in the BEC [P5].

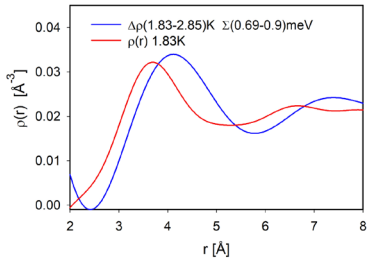

Fig. 4 The PDF in the BEC (blue) and the PDF in non-BEC (red) [P5]

This discovery has a direct implication on the origin of the high-temperature superconductivity (HTSC) of the cuprates, which has been a major mystery for 40 years. In the BCS superconductors Cooper pairs are orthogonal to each other in ***k***-space. However, when the pairing interactions are strong, either by spin or lattice, Cooper pairs are local causing the BCS-BEC crossover. Then, the real space orthogonality of BEC means that the electron repulsion energy between the Cooper pairs is reduced in the HTSC state as in ^{4}He, and this adds to the driving force to superconductivity [P5]. In our estimate, the T_c enhancement by this mechanism can amount to the order of 100K. We propose to prove this hypothesis with the resonant IXS at the oxygen edge, by transforming the data to real space through the energy-resolved dynamic PDF. If successful, this will be a major achievement.

References

1. T. Iwashita, B. Wu, W.-R. Chen, S. Tsutsui, A.Q.R. Baron, and T. Egami, *Sci. Adv.* **3**, e1603079 (2017).
2. C. W. Ryu, W. Dmowski, K. F. Kelton, G. W. Lee, E. S. Park, J. R. Morris and T. Egami, *Scientific Reports*, **9,** 18579 (2019).
3. P. Eisenberger, W. C. Marra and G. S. Brown, *Phys. Rev. Lett*. **45**, 1439 (1980).
4. J. M. Gibson, M. M. J. Treacy and P. M. Voyles, *Ultramicroscopy* **83,** 169 (2000).
5. W. Dmowski, S. O. Diallo, K. Lokshin, G. Ehlers, G. Ferré, J. Boronat and T. Egami, *Nature Commun.* **8,** 15294 (2017).

Principal Publications

P1. T. Egami, W. Dmowski, and C. W. Ryu, Medium-range order resists deformation in metallic liquids and glasses, *Metals* **13,** 442 (2023).

P2. T. Egami and C. W. Ryu, World beyond the nearest neighbors, *J. Phys.*: *Cond. Mat.* **35,** 174002 (2023).

P3. J. Moon, L. Lindsay and T. Egami, Atomic dynamics in fluids: Normal mode analysis revisited, *Phys. Rev. E* **108,** 014601 (2023).

P4. T. Egami and C. W. Ryu, Origin of medium-range atomic correlation in simple liquid: Density wave theory, *AIP Adv.* **13,** 085308 (2023).

P5. T. Egami, Dynamic correlations in disordered systems: Implications on high-temperature superconductivity, *Cond. Matter* **9,** 12 (2024).

P6. J. Moon, S. Thebaud, L. Lindsay and T. Egami, Normal mode description of phases of matter: Application to heat capacity, *Phys. Rev. Res.* **6,** 013206 (2024).

P7. L. Zella, J. Moon and T. Egami, Ripples in the bottom of the potential energy landscape of metallic glass, *Nature Commun.* **15,** 1358 (2024).

P8. Y. Shinohara, T. Iwashita, M. Nakanishi, W. Dmowski, C. W. Ryu, D. L. Abernathy, D. Ishikawa, A. Q. R. Baron, and T. Egami, Real-space local self motion of protonated and deuterated water, *Phys. Rev. E* **109,** 064608 (2024).

P9. Z. Wang, W. Dmowski, H. Wang, R. Ashcraft, D. L. Abernathy, K. F. Kelton, and T. Egami, Real-space atomic dynamics in metallic liquids investigated by inelastic neutron scattering, *Phys. Rev. B* **110,** 024309 (2024).

P10. T. Egami and C. W. Ryu, Perspective: Are glasses really frozen? *J. Appl. Phys.* **137,** 070901 (2025), Journal Highlight.

Electronic Correlations and Topology in Actinide Materials

Krzysztof Gofryk, Idaho National Laboratory

Keywords: Topological insulators, actinides, electronic structure, magnetism, electronic correlations

Research Scope

Strongly interacting electrons in *f*-systems hold great potential for realizing collective quantum behavior, where spin-orbit interactions and topology can lead to emerging phenomena crucial for developing new quantum technologies. Of particular interest is the realization of quantum effects in these correlated materials, where the relativistic shifting of electron energy levels accentuates the spin-orbit coupling effect. These materials typically exhibit stronger coupling than the widely studied *d*-electron systems. However, the role of *f*-electrons and the effect of electronic correlations in forming topologically protected non-trivial states remain unclear. In this project, we conduct comprehensive experimental and theoretical studies of selected *f*-electron correlated systems, focusing on the effects of spin-orbit coupling, electronic correlation, and topology. To understand these phenomena, we perform extensive investigations into the magnetic, thermodynamic, and magneto-transport properties across a wide range of external parameters such as temperature, angle, magnetic fields, and pressure, which allow to tune the *f-spd* hybridization and spin-orbit interactions. The results from these studies provide a fundamental understanding of the interplay between electronic correlation and topology in *f*-electron quantum systems.

Recent Progress

(i) Focus Ion Beam (FIB) micromachining and the study of surface states in SmB_6

Recently, SmB_6 has been identified as a topological Kondo insulator, where a narrow bandgap forms at low temperatures due to the hybridization of conduction and valence bands. This phenomenon is associated with band inversion and the presence of surface states, sparking significant experimental and theoretical research on this material. However, various transport studies have yielded conflicting results, primarily due to the challenge of obtaining high-quality single crystals. To address these challenges, we utilized single-phase micro-sized SmB_6 single crystals extracted from a multi-phase polycrystal sample using plasma Focused Ion Beam (PFIB) techniques. We thoroughly characterized these crystals using back-scattered electron imaging, energy-dispersive spectroscopy, and electron back-scattered diffraction to identify a single-crystal grain of interest, confirm its expected crystallographic structure, and determine its crystallographic orientation. The inductively coupled Xe^+ plasma ion source technique used in this study enables material removal rates up to 50 times faster and provides beam currents several orders of magnitude higher than conventional Ga^+ FIB, allowing for the fabrication of structures of varying sizes with significantly enhanced efficiency. Additionally, the Xe^+ PFIB has been shown to produce 20-40% less surface damage than Ga^+ FIB. The obtained lamellas of SmB_6 (as illustrated

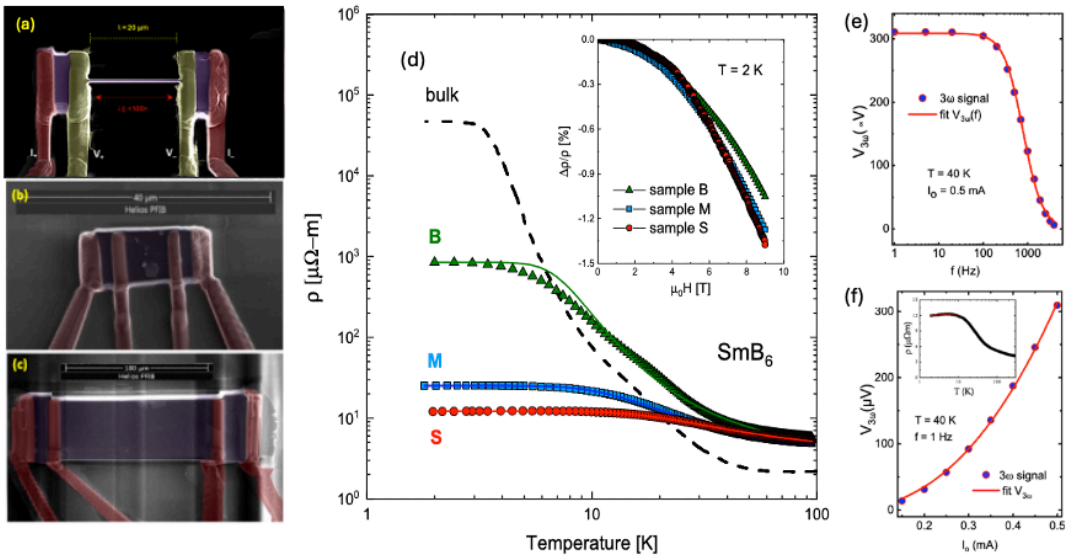

Figure 1: (a-c) different size SmB_6 lamellas with platinum leads deposited on them; (d) the electrical resistivity of the three SmB_6 samples, analyzed by a two-channel model (solid lines). The black dotted line is for the bulk single crystal (Ref.1). Variation of 3ω voltage versus frequency (e) and electrical current (f) of SmB_6 lamella (a) at 40 K. The solid line represents the least-squares fit to 3ω model. The inset shows the temperature dependence of the electrical resistivity of the studied SmB_6 crystal.

in Fig. 1) were subsequently used for detailed low-temperature transport and thermal studies. As depicted in Fig.1d, the electrical resistivity of SmB_6 crystals is found to be dependent on sample size at low temperatures. This observation, characteristic of topological insulators, strongly suggests the presence of topologically protected surface states in this system. A publication detailing these findings is currently under preparation.

Furthermore, using the 3ω technique (see Fig.1e,f), we have investigated the effect of various scattering mechanisms on the thermal conductivity of a micro-sized SmB_6 sample (Fig.1a). The thermal conductivity measured is reduced by an order of magnitude compared to previously reported data on bulk single crystals. We analyzed the low-temperature phonon thermal conductivity of our samples using the Callaway model and demonstrated that phonon boundary scattering plays a primary role in reducing the thermal conductivity of this material. The temperature dependence of thermal conductivity, κ(T), exhibits a double-peak behavior characteristic of resonant scattering. Our work also highlights the successful application of the 3ω method to study the thermal properties of micro-sized samples. This approach is particularly useful for materials where large single crystals are not available or where growing single crystals is impractical. Additionally, this method will play an important role in understanding the thermal conductivity of micro-sized materials, where phonon boundary scattering dominates thermal resistance. This is especially relevant for advanced materials and technologies such as microelectronics, thermoelectrics, and nuclear research. This work has been recently accepted for publication in Applied Physics Letters.

(ii) Strong electronic correlations and topology in PuB_6

Following the discovery of the topological Kondo insulating state in SmB_6, the search for analogous materials among 5*f*-electron compounds has intensified, as actinide materials possess the necessary ingredients for hosting novel topological phenomena. Given that most relevant electronic interactions in 5*f*-electron systems have similar energy scales, combining strong electronic interactions with topology offers a unique way to control topological properties. Consequently, it has been recently proposed theoretically that the intermediate valent PuB_6 is a strong topological insulator with nontrivial $\mathbf{Z}_2$ topological invariants. We address this topic by investigating the low-temperature electronic properties of PuB_6 through synthesis and micro-machining characterization, magnetotransport measurements, and detailed electronic structure calculations. The electrical resistivity indicates the presence of a narrow energy gap at the Fermi level and can be described by a two-conductivity channel model that accounts for both metallic and semiconducting components, similar to other topological insulators (see Fig.2a). The magnetoresistivity exhibits an $H^{1.3}$ dependence, deviating from the H^2 behavior expected for simple metallic systems and aligning more closely with the H^1 dependence observed in various Dirac materials (Fig.2b). This work demonstrates that PuB6 is a compelling candidate for investigating the influence of electronic correlations and topology and supports the theoretical predictions and the model of the presence of an insulating bulk with metallic surface states in this material. This work is currently under review in Physical Review Letters.

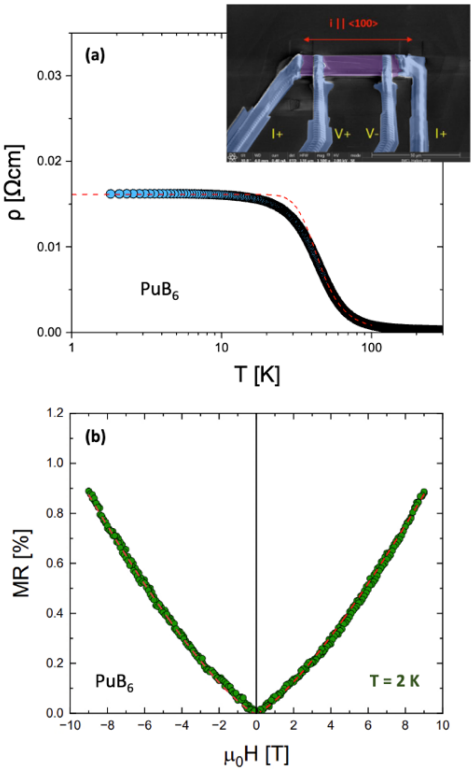

Figure 2: (a) The temperature dependence of the electrical resistivity of the PuB_6 microcrystal. The dashed line is a two-conductance-channel model with an estimated energy gap of $\Delta_\rho = 21$ meV. The inset shows a pFIB lamella of PuB_6 prepared for low-temperature transport measurements. (b) The magnetic field dependence of magnetoresistivity of PuB_6 at T = 2 K. The dashed line represents the relation MR ~ $H^{1.3}$.

Future Plans

- Finalizing publications on the effects of magnetism, electronic correlations, and topology in PuB_6 and $NpTe_2$.
- Electronic study of a new family of topological materials, RNi_3Ga_9 (R = U, Tb, Er). Publication of the results obtained.
- Magnetic and thermodynamic studies of potential topological systems HoSb, USb, and TbSbTe. Publication of the results obtained.
- Angle-Resolved Photoemission Spectroscopy (ARPES) studies of the potential uranium-based topological material, UPS and $UCuAs_2$. Commissioning an ARPES end station dedicated to uranium crystals at the Advanced Light Source (LBNL).

References

1. L. Jiao, S. Roessler, D. Kasinathan, P. F. S. Rosa, C. Guo, H. Yuan, C.-X. Liu, Z. Fisk, F. Steglich, and S. Wirth, Magnetic and defect probes of the SmB_6 surface state," *Science Advances* 4 (2018)
2. Xiaoyu Deng, Kristjan Haule, and Gabriel Kotliar, Plutonium Hexaboride is a Correlated Topological Insulator, *Phys. Rev. Lett.* 111, 176404 (2013).

Publications

1. Sabin Regmi, Iftakhar Bin Elius, Anup Pradhan Sakhya, Milo Sprague, Mazharul Islam Mondal, Nathan Valadez, Volodymyr Buturlim, Kali Booth, Tetiana Romanova, Krzysztof Gofryk, Andrzej Ptok, Dariusz Kaczorowski, and Madhab Neupane, Electronic structure in a rare-earth based nodal-line semimetal candidate PrSbTe, *Phys. Rev. Materials* 8, L041201 (2024)

2. Binod K Rai, Alex Bretaña, Gregory Morrison, Rosalie Greer, Krzysztof Gofryk, and Hans-Conrad zur Loye, Crystal structure and magnetism of actinide oxides: a review, *Reports on Progress in Physics*, 87, 6 (2024)

3. Omar Alejandro Salas, Yohannes W. Getahun, H. Cein Mandujano, Felicia Manciu, Mariana Castellanos, Jorge Lopez, Raquel Garza Hernández, Volodymir B. Buturlim, Krzysztof Gofryk, Dhanpal Bairwa, Suja Elizabeth and Harikrishnan S. Nair, Resilience of the Aurivillius structure upon La and Cr doping in a $Bi_5Ti_3FeO_{15}$ multiferroic, *Dalton Trans*., 53, 6423-6435 (2024)

4. Binod K. Rai, Boris Maiorov, Krzysztof Gofryk, Patrick O'Rourke, Catherine Housley, Henry Ajo, Asraf Sawon, Arjun K. Pathak, Narayan Poudel, Qiang Zhang, Travis J. Williams, Matthias Frontzek, Structure and properties of $NdCuGa_3$ single crystals, *Journal of Magnetism and Magnetic Materials*, 589, 171515 (2024)

5. Narayan Poudel, Daniel Murray, Jason Jeffries, and Krzysztof Gofryk, Boundary scattering in topological Kondo insulator SmB_6, *Applied Physics Letters*, accepted, in press (2025)

Session IX

Complex chalcogenides under pressure

Janice L. Musfeldt, University of Tennessee

Keywords: van der Waals solids, chalcogenides, pressure-driven phase transitions, phase diagrams, vibrational spectroscopies

Research Scope

Our research program focuses on the spectroscopic properties of complex chalcogenides and how external stimuli such as pressure and chemical substitution control the development of new states of matter and functionality. Building on prior advances, we combine synchrotron-based infrared and Raman scattering spectroscopy with diamond anvil cell techniques to reveal charge-structure-function relationships in intercalated chalcogenides, analyze metal-site substitution and the role of local structure on symmetry breaking in magnetic systems, uncover energy transfer processes and phase diagrams in superconducting chalcogenides, and explore the generality of these phenomena and their underlying mechanisms in new settings - such as in chiral materials. What brings these efforts together is our interest in light-matter interactions under extreme conditions and the spectroscopic techniques with which we investigate the new states of matter that emerge from the interplay between charge, orbits, structure, and magnetism. Findings from this comprehensive experimental program will advance theoretical development and energy-related applications.

Recent Progress

Our DoE-supported program *Complex chalcogenides under pressure* is inspired by the opportunity to explore the properties of complex chalcogenides under compression. Specifically, we combine synchrotron-based infrared and Raman scattering spectroscopy and diamond anvil cell techniques with lattice dynamics calculations, an analysis of the energy landscape, a correlation group analysis, and x-ray scattering. Our objective is to reveal charge-structure-function relationships in intercalated chalcogenides, analyze metal-site substitution and the role of local structure on symmetry breaking in magnetic systems, uncover energy transfer processes and phase diagrams in superconducting chalcogenides, and explore the generality of these phenomena and their underlying mechanisms in new settings - such as in chiral materials. Significant discoveries during the past two years include:

- revealing the pressure-temperature phase diagram of $CrSiTe_3$ and how the insulator-to metal transition is triggered by the structural phase transition,
- exploring the unconventional insulator-to-metal transition and colossalmagnetoresistance in $Mn_3Si_2Te_6$ exposing electronic inhomogeneity and phase separation as well as signatures of chiral loop currents,
- unraveling a series of pressure-driven structural phase transitions in the chalco-halide CrSBr,
- uncovering the symmetry progression and signatures of band vs. Mott character in $CdPS_3$, and
- demonstrating giant tunability of the superlattice excitation in chiral $Cr_{1/3}TaS_2$.

A few of these activities are summarized below.

Insulator-metal transition in $CrSiTe_3$ triggered by structural distortion under pressure: $CrSiTe_3$ is a van der Waals ferromagnet that earned widespread recognition for remarkable properties in both single crystal and monolayer form. The discovery of pressure-induced superconductivity above 7.5 GPa and below 4.2 K is one of these exciting developments. One bottleneck to greater understanding of the energy landscape is the limited effort to resolve the pressure-temperature phase diagram. In this work, we combined synchrotron-based infrared spectroscopy and diamond anvil cell techniques to measure the far infrared response of $CrSiTe_3$ under extreme pressure-temperature conditions. The Si-Te stretching mode at 368 cm^{-1} hardens on approach to the structural transition, broadens and develops weak doublet character in the mixed-phase region, and rides on top of a gradually increasing electronic background as the indirect gap begins to close [Fig. 1]. In the end, the pressure-driven insulator-to-metal transition is swift and sharp. What differentiates our work from prior results and revises the entire character of the temperature - pressure (T - P) phase diagram is the finding that the first-order structural phase transition is triggered before the insulator-metal transition [Fig. 1]. In addition to laying the foundation for superconductivity, the trends lead to a nexus of activity that may hide a quantum critical point.

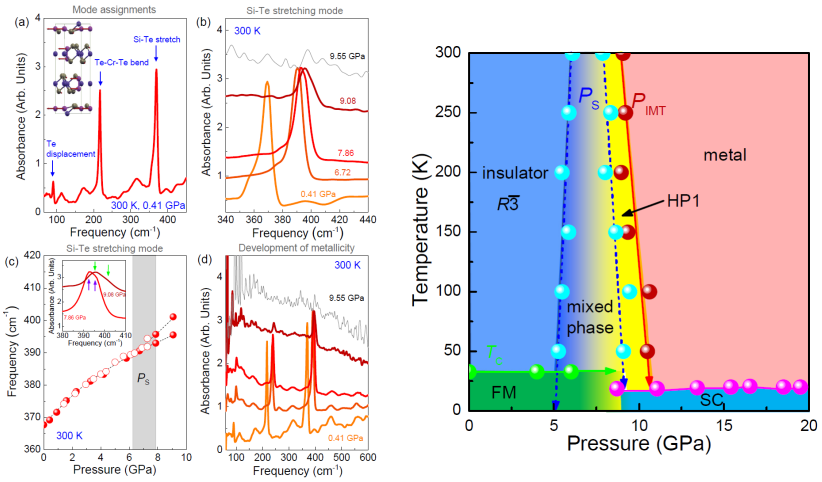

Figure 1: Infrared properties of $CrSiTe_3$ under pressure at room temperature. Similar work at the National Synchrotron Light Source II using both diamond anvil cells and a custom-built cryostat enable us to develop the temperature – pressure (T – P) phase diagram.

Unconventional insulator-to-metal transition in $Mn_3Si_2Te_6$: The nodal-line semiconductor $Mn_3Si_2Te_6$ is generating enormous excitement due to the recent discovery of a field-driven insulator-to-metal transition and associated colossal magnetoresistance as well as evidence for a new type of quantum state involving chiral orbital currents. Strikingly, these qualities persist even in the absence of traditional Jahn-Teller distortions and double-exchange mechanisms, raising questions about exactly how and why magnetoresistance occurs along with conjecture as to the likely signatures of chiral loop currents. Here, we measured the infrared response of $Mn_3Si_2Te_6$ across the magnetic ordering and field-induced insulator-to-metal transitions in order to explore colossal magnetoresistance in the absence of Jahn-Teller and double-exchange interactions. Rather than a traditional metal with screened phonons, the field-driven insulator-to-metal transition leads to a weakly metallic state with localized carriers [Fig. 2]. That our spectral data are fit by a percolation model provides evidence for electronic inhomogeneity and phase separation [Fig. 3]. Modeling also reveals a frequency-dependent threshold field for carriers contributing to colossal magnetoresistance which we discuss in terms of both polaron formation and chiral orbital currents.

These findings enhance the understanding of insulator-to-metal transitions in new settings and open the door to the design of unconventional colossal magnetoresistant materials.

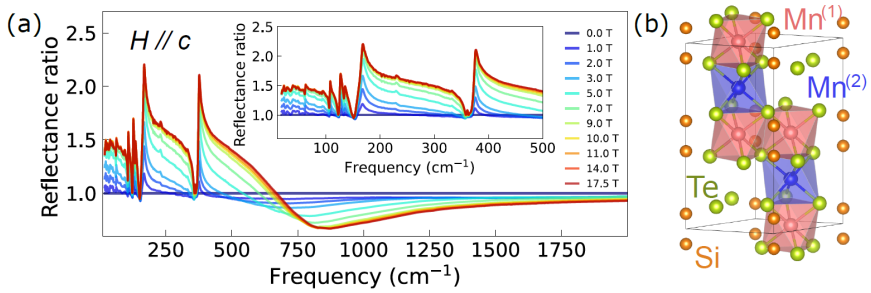

Figure 2: Field-driven insulator-metal transition. (a) Reflectance ratios of $Mn_3Si_2Te_6$ as a function of magnetic field with development of a localized excitation. (b) Crystal structure.

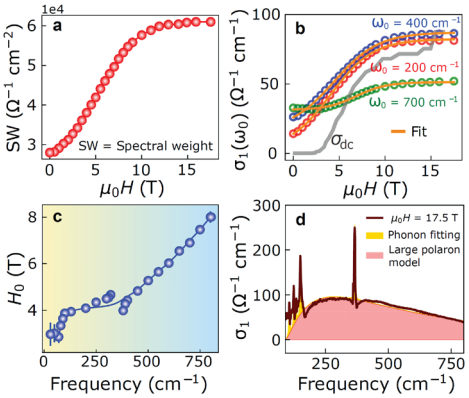

Figure 3: Revealing the properties of localized carriers in $Mn_3Si_2Te_6$. (a) Spectral weight calculated by integrating σ1(ω) over an appropriate frequency window. (b) $\sigma_1(\omega)$ at several different fixed frequencies ω_0 (circles) vs. magnetic field. The dark orange lines are fits to the percolation model. (c) Percolation threshold as a function of frequency, obtained from percolation model fits in panel b. (d) $\sigma_1(\omega)$ at 17.5 T fit with a large polaron model (red area) and typical phonon oscillators (yellow area).

Giant tunability of superlattice excitations in chiral $Cr_{1/3}TaS_2$: Intercalation is an important strategy for enhancing the functionality of van der Waals solids. This is because layered materials such as transition metal dichalcogenides can be endowed with intriguing new properties by filling the van der Waals gap with various ions or molecules which, in addition to their unique chemistry and guest-host interactions, break symmetry in new ways. One barrier to greater control of the collective metal monolayer excitations in these materials is the absence of detailed information about how they evolve under compression. In order to explore superlattice excitations in a series of intercalated chalcogenides, we measured the Raman scattering response of $Cr_{1/3}TaS_2$ under pressure and compared our findings with the behavior of $Cr_{1/3}NbS_2$, $Fe_{1/3}TaS_2$, and $Fe_{1/4}TaS_2$. Overall, we find that the metal monolayer excitations are sharp and strong, spanning a significant portion of the teraHertz range. Analysis reveals that chalcogen layer thickness and size of the van der Waals gap to that of the *A* site ion are sufficient to divide these materials into two classes: the Cr analogs with relatively little distortion of the metal monolayer excitations under compression and the Fe analogs that host substantial symmetry breaking [Fig. 4]. In addition to unraveling these structure-property relations, we combine pressure and strain to demonstrate that the superlattice excitation in $Cr_{1/3}TaS_2$ can be tuned in a nearly linear fashion by approximately 16% in frequency space.

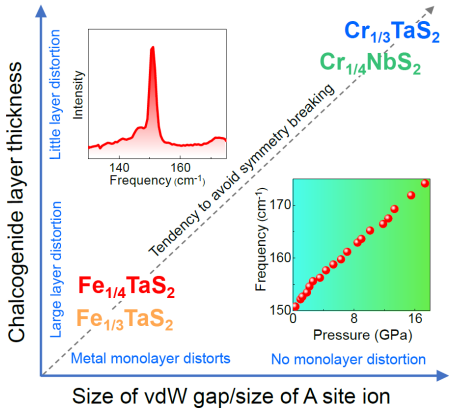

Figure 4: Structure-property relations in intercalated chalcogenides. Schematic to illustrate the structure-property relations in the $M_{1/3}TaS_2$ system in terms of the chalcogenide layer thickness, the size of the van der Waals gap, and the size of the A site ion. The insets display the superlattice mode in $Cr_{1/3}TaS_2$ and how it shifts linearly with pressure.

Future Plans

Going forward, we have several exciting projects designed to reveal the properties of complex chalcogenides under extreme conditions. These include (i) uncovering pressure-driven structural distortions and metallicity in $Mn_3Si_2Te_6$, (ii) unraveling how compression impacts the exciton-polaritons in WS_2 nanotubes as a function of size, (iii) exploring band gap closure and color changes in $CoPS_3$ under pressure, (iv) revealing the series of pressure-driven structural phase transitions in layered ferroelectrics like $CuInP_2S_6$ and other *B*-site substituted systems, and (v) developing structure-property relations in the $Fe_{1/3}TaS_2$, $Fe_{1/4}TaS_2$, $Cr_{1/3}TaS_2$, $Co_{1/3}TaS_2$, and $Cr_{1/3}NbS_2$ family of intercalated chalcogenides. Three PhD students (Brian Taylor, Sambridhi Shah, and Lakshan Silva) lead these projects. Luther Langston recently graduated with a PhD in materials chemistry, but I'm keeping him on to pursue high pressure light emission in CrSBr until the economic situation stabilizes. We are also interested in whether strain is an effective tool for tuning the spectroscopic properties of complex chalcogenides.

Publications

1. J. L. Musfeldt, D. G. Mandrus, and Z. Liu, Insulator-metal transition in $CrSiTe_3$ triggered by structural distortion under pressure, npj 2D Materials and Applications **7**, 28 (2023). https://doi.org/10.1038/s41699-023-00389-x This work was selected as a BNL Science Highlight.

2. Y. Gu, E. T. Ritz, W. R. Meier, A. Blockmon, K. Smith, R. Pokhare Madhogaria, S. Mozaffari, D. Mandrus, T. Birol, and J. L. Musfeldt, Phonon mixing in the charge density wave state of ScV_6Sn_6, npj Quantum Mater. **8**, 58 (2023). https://doi.org/10.1038/s41535-023-00590-7

3. J. L. Musfeldt, S. Singh, S. Fan, Y. Gu, X. Xu, S. -W. Cheong, Z. Liu, D. Vanderbilt, and K. M. Rabe, Structural phase purification of HfO_2:Y through pressure cycling, Proc. Nat. Acad. Sci. **121**, e2312571121 (2024). https://doi.org/10.1073/pnas.231257112

4. Y. Gu, K. A. Smith, S. Amartyajoti, C. De, C.-J. Won, Y. Zhang, L.-F. Lin, S.-W. Cheong, K. Haule, M. Ozerov, T. Birol, C. Homes, E. Dagotto, and J. L. Musfeldt,

Unconventional insulator-to-metal phase transition in $Mn_3Si_2Te_6$, Nature Communications **15**, 8104 (2024). https://doi.org/10.1038/s41467-024-52350-1 This work was selected as an NHMFL Highlight as well as a DoE Highlight.

5. J. L. Musfeldt, Y. Gu, J. T. Haraldsen, K. Du, P. Yapa, J. Yang, D. G. Mandrus, S. -W. Cheong, and Z. Liu, Giant tunability of superlattice excitations in chiral $Cr_{1/3}TaS_2$, npj Quantum Materials **10**, 27 (2025). https://doi.org/10.1038/s41535-025-00734-x

6. J. L. Musfeldt, S. Singh, K. A. Smith, X. Xu, S. -W. Cheong, Z. Liu, D. Vanderbilt, and K. M. Rabe, Pressure-driven polar orthorhombic to tetragonal phase transition in hafnia at room temperature, Chemistry of Materials, **37**, 1820 (2025). https://doi.org/10.1021/acs.chemmater.4c02596

7. L. J. Langston, A. M. Ruiz, C. Boix-Constant, S. Manas-Valero, E. Coronado, J. J. Baldovi, Z. Liu, and J. L. Musfeldt, Pressure-induced structural phase transitions in CrSBr, accepted, npj Quantum Materials.

8. S. Shah, S. Choi, K. A. Smith, Y. Gu, B. Taylor, M. Cothrine, D. Mandrus, Z. Liu, H.-S. Kim, and J. L. Musfeldt, Symmetry progression and band vs. Mott character of $CdPS_3$ under pressure, submitted, APL Materials.

9. T. Matsuoka, H. -S. Kim, S. Samanta, J. L. Musfeldt, and D. Mandrus, MPX_3 van der Waals magnets under pressure (M = Mn, Ni, V, Fe, Co, Cd; X = S, S), Frontiers in Materials **11**, 1362744 (2024). Review article. doi: 10.3389/fmats.2024.1362744

Unconventional Solitonic Superfluorescence in Perovskites

Kenan Gundogdu, NC State University

Keywords: Macroscopic Quantum Coherence, Superfluorescence, Quantum Analog of Vibration Isolation, Quantum Materials, Perovskites.

Research Scope

This research program explores mechanisms that enhance electronic coherence in solids, enabling macroscopic quantum states of matter at high temperatures. Our approach focuses on uncovering the origins of high-temperature superfluorescence in lead-halide perovskites[1, 2]. Gaining a fundamental understanding of this phenomenon is critical for developing strategies to design materials that operate at elevated temperatures and hold promise for applications in Quantum Information Science.

Recent Progress

When an ensemble of quantum particles achieves collective quantum coherence, it can give rise to exotic macroscopic quantum phenomena such as superconductivity, superfluidity, and Bose-Einstein condensation. The ability to create and manipulate these effects is central to emerging quantum technologies. However, thermal dephasing disrupts quantum coherence, limiting these phenomena to cryogenic temperatures.

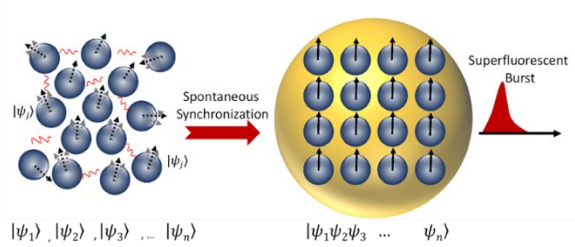

Figure 1: Spontaneous synchronization of incoherent dipoles forming a macroscopic quantum state acting like a giant atom in superfluorescence.

During this reporting period, we discovered a novel mechanism that enables collective electronic coherence at exceptionally high temperatures. Through experimental and theoretical investigations of high-temperature superfluorescence (SF) in lead halide perovskites, we found that SF in these materials originates from a phase transition of polarons into an ordered soliton state. This discovery reveals a new SF mechanism and advances our understanding of how coherent quantum states can form under elevated thermal conditions.

In conventional superfluorescence[3] (Figure 1), an optical pulse generates a population of excited electronic dipoles. These dipoles initially lack coherence but can spontaneously synchronize their phases via interactions with the electromagnetic vacuum, provided their dipole dephasing time is sufficiently long. In contrast, SF in lead halide perovskites does not arise from dipole synchronization. Instead, it results from the phase transition of exciton polarons into a collective

soliton phase. Within this phase, excitons are vibrationally decoupled (Figure 2) from ambient thermal noise, preserving coherence.

We demonstrated that excitonic coherence and superradiance are intrinsic properties of the soliton. Remarkably, while individual excitons outside the soliton rapidly dephase, those within the soliton maintain coherence and exhibit superradiance.

A key distinction between conventional and solitonic SF lies in their origins: conventional SF is a nonequilibrium process driven by vacuum field fluctuations. It cannot occur without the electromagnetic vacuum. In contrast, solitonic SF emerges from exciton-lattice interactions, with the soliton representing a metastable coherent state. Soliton is transient only because of its instability against recombination. Unlike conventional SF in the absence of the electromagnetic vacuum, the soliton would form and remain coherent. This behavior resembles equilibrium phase transitions like superconductivity and superfluidity, governed by critical parameters such as temperature and carrier density.

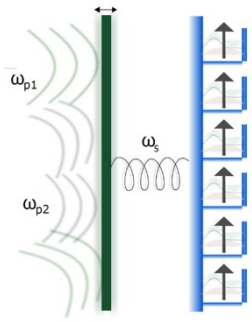

Figure 2: Illustration of how QAVI can promote coherence. Multiple boxes attached to a common lattice distortion mode that protects dipoles from dephasing. This leads to a macroscopic state even at high temperatures.

In this program review, we present the theoretical and experimental work underpinning this discovery and discuss its implications for designing materials that support macroscopic quantum effects at high temperatures.

Experimental Progress:

We tracked the time evolution of solitonic SF and analyzed the stochastic fluctuations in macroscopic coherence during SF emission (Figure 3). Our results show that these are not random oscillations, but collective rocking-mode oscillations that spontaneously develop coherence during soliton formation. Figure 3c presents the autocorrelation and Fourier analysis of these fluctuations. Studying the frequency behavior at varying excitation fluences, supported by theoretical modeling, led to the identification of this solitonic SF mechanism.

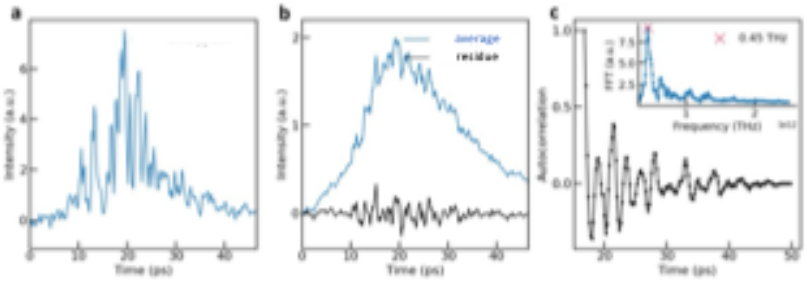

Figure 3 (a,b) Time-resolved SF emission dynamics of PEA:$CsPbBr_3$. Spectral analysis of the fluctuations shows that the fluctuations are not random noise. They correspond the collective rocking oscillations that modulate SF emission.

Theoretical Progress:

We developed a rigorous theoretical model for many-body exciton lattice interactions and analyzed it using a quasiclassical field theoretical formalism[4]. The theory shows that an excited many-body excitonic system in perovskites has two solutions. The first is an incoherent polaron ensemble, and the second is a solitonic collective state. The analysis shows that the solitonic solution becomes the lower energy state (gap formation) beyond a specific threshold excitation density. Since the soliton is the lowest energy state and the solution to the many-body Hamiltonian, it is intrinsically coherent. The gap between the incoherent polaron and coherent soliton states is similar to the energy gap between the collective superconducting state and the Fermi level in BCS theory. We show that the theory explains most experimentally observed spectroscopic features. For instance, the frequency of the rocking oscillations that underlie the fluctuations in Figure 3 blue shifts with the excitation density, which is also predicted by the theory.

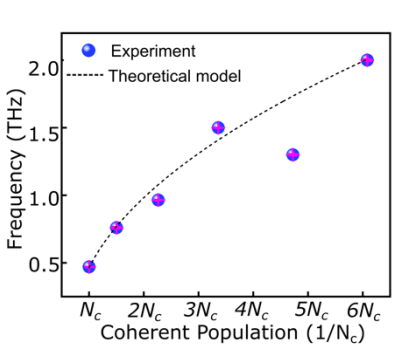

Figure 4 The excitation density-dependent frequency shift of the soliton rocking mode and shifts in the theoretical model.

Future Plans

Our model provides an unprecedented opportunity to investigate the coupling parameters (exciton-lattice interaction terms in the many-body Hamiltonian) and their quantitative extraction using experiments. We will develop the experimental and theoretical framework for extracting these parameters. We will also develop a modified Dicke model that describes solitonic superfluorescence and characterize it experimentally.

References

1. M. Biliroglu, G. Findik, J. Mendes, D. Seyitliyev, L. Lei, Q. Dong, Y. Mehta, V.V. Temnov, F. So, K. Gundogdu, *Room-temperature superfluorescence in hybrid perovskites and its origins*. Nature Photonics **16 (4),** 324-329 (2022).

2. G. Findik, M. Biliroglu, D. Seyitliyev, J. Mendes, A. Barrette, H. Ardekani, L. Lei, Q. Dong, F. So, K. Gundogdu, *High-temperature superfluorescence in methyl ammonium lead iodide.* Nature Photonics **15 (9),** 676-680 (2021).

3. M. Gross, S. Haroche, Superradiance: An essay on the theory of collective spontaneous emission. Physics Reports **93 (5),** 301-396 (1982).

4. R. Friedberg, T. Lee, A. Sirlin, *Class of scalar-field soliton solutions in three space dimensions.* Physical Review D **13 (10),** 2739 (1976).

Publications

1. M. Biliroglu, M. Türe, A. Ghita, M. Kotyrov, X. Qin, D. Seyitliyev, N, Phonthiptokun, M. Abdelsamei, J. Chai, R. Su, U. Herath, A.K. Swan, V.V. Temnov, V. Blum, F. So, K. Gundogdu, *Unconventional Solitonic High-Temperature Superfluorescence from Perovskites, accepted, (2025).*

Session XI

Semiconductor quantum shells for energy conversion applications.

Mikhail Zamkov, The Center for Photochemical Sciences, Department of Physics, Bowling Green State University, Bowling Green, Ohio 43403. zamkovm@bgsu.edu

Keywords: Photovoltaics, Scintillators, Auger, Nanocrystals, Electroluminescence

Research Scope

The project explores a novel nanoscale geometry, called quantum shells, which is designed to suppress two main mechanisms of energy loss in colloidal semiconductor nanocrystals: Auger recombination and surface recombination. The central objective is to establish quantum shells as robust building blocks for optoelectronic materials that maintain high performance under intense optical or electrical excitation. Such resilience is critical for applications in high-brightness LEDs, photodetectors, and X-ray scintillators, where multiexciton populations often lead to severe nonradiative losses. The geometry of quantum shells also offers promise for concentrator photovoltaics, where the reduction of Auger decay could improve carrier extraction and energy conversion efficiency. Meanwhile, a large exciton/biexciton energy splitting observed in these structures provides a key advantage for the realization of single-photon emitters.

Recent Progress

We have demonstrated that the quantum shell architecture offers significant advantages over traditional colloidal nanocrystals across a range of optoelectronic processes, including electroluminescence, optical gain development, up-conversion, and X-ray induced radioluminescence. A brief summary of these findings is provided below.

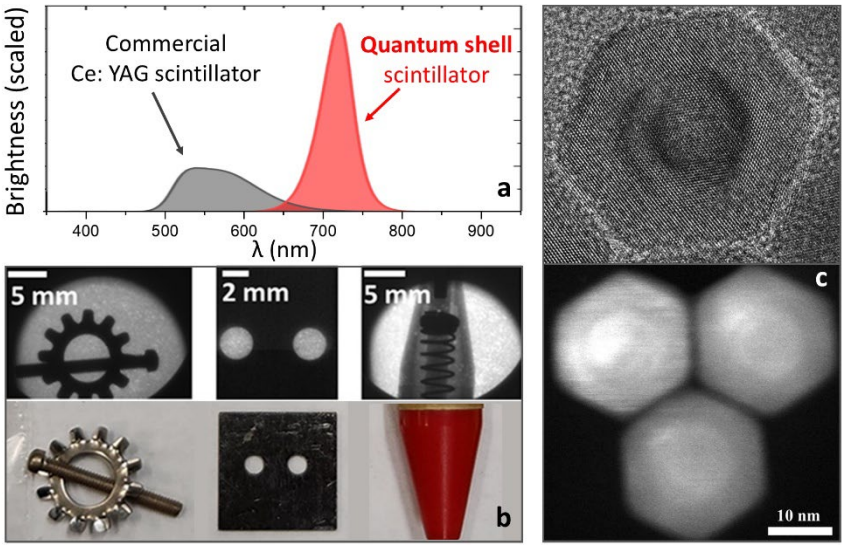

Figure 1. (a) Radio-luminescence of quantum shell scintillator devices versus Ce: YAG commercial standard, normalized for the absorbed X-ray flux. (b). Various objects imaged with the quantum shell scintillators, offering near-record brightness, excellent stability, and fast temporal response. (c). Transmission electron microscope images of CdS-CdSe-CdS core-shell-shell quantum shells.

In a recent study (Ref. 9), we have shown that quantum shells enable one of the highest X-ray scintillation efficiencies reported to date, outperforming conventional colloidal nanocrystals

and even surpassing leading commercial scintillators in both brightness and response speed (Figure 1).

Under hard X-ray excitation, quantum shells exhibited light yields exceeding 70,000 photons/MeV and ultrafast emission decay times below 2.5 nanoseconds, with negligible afterglow. These characteristics make them uniquely suited for high-resolution, high-speed radiation detection. Time-resolved spectroscopy and multiexciton emission modeling revealed that this performance arises from suppressed Auger recombination and unusually long multiexciton lifetimes over 10 ns. The ability to mitigate Auger nonradiative losses while maintaining structural and optical stability under intense X-ray flux further distinguishes quantum shells from other nanocrystal architectures. This development could have a major impact on a wide range of fields, from medical diagnostics to defense and particle physics. For medical applications, this could mean clearer and faster imaging, leading to more accurate diagnoses. In defense, faster and more reliable radiation detection could enhance safety and security measures. The high-resolution imaging capabilities of quantum shells also open up new possibilities in scientific research, allowing for more precise studies of materials.

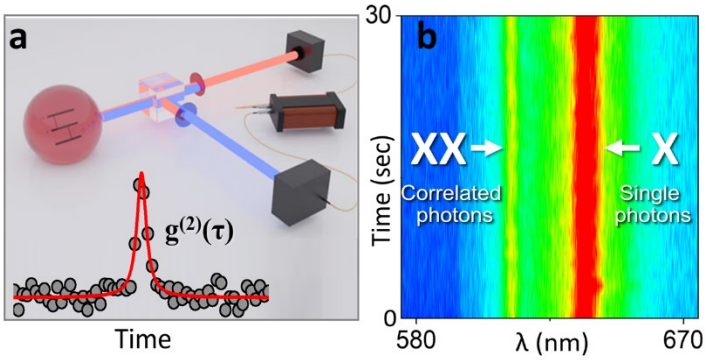

Figure 2. (a). Schematics of radiative biexciton-exciton (XX-X) cascade and spectrally resolved correlation measurements. Insert: Correlation function g2(t) between spectrally isolated XX (start) and X (stop) photons under CW excitation. (b) Single-particle emission trajectory of CdS-CdSe-CdS quantum shells, showing a distinct separation of X and XX states and low spectral diffusion.

Another important milestone was the first demonstration of correlated photon pair emission from colloidal semiconductor nanostructures, achieved using single quantum shells at cryogenic temperatures (10 K). As reported in Ref. 8, we observed exciton–biexciton cascaded photoluminescence, a defining signature of quantum light sources, evidenced by clear photon bunching behavior, shown in Figure 2a (insert). More specifically, our collaborative effort with George C. Schatz (Northwestern University) and Anton Malko (University of Texas, Dallas), we demonstrated that biexciton decay in colloidal quantum shells yields spectrally distinct and temporally correlated photon pairs, with time-correlated emission stable for durations exceeding 200 seconds. Notably, the spectral separation between exciton and biexciton emission in quantum shells is three to five times larger than that observed in conventional 0D nanocrystals. Such a large X-XX splitting is not only critical for the unambiguous identification of correlated photon pairs but also enables effective spectral filtering of the biexciton component, facilitating high-purity single-photon emission. This result establishes quantum shells as a promising platform for quantum light generation, offering either deterministic photon-pair emission or single-photon generation through spectral filtering.

In another project, we have successfully demonstrated broadband, low-threshold lasing emission from a densely packed layer of CdS/CdSe/CdS quantum shells embedded within a photonic nanopillar array, as detailed in Refs 6 and 10. The suppression of multiexciton Auger recombination in quantum shells allowed us to achieve significant spectral tuning of the lasing emission by harnessing multi-exciton states. This, combined with the minimal optical losses of the

nanopillar cavity, resulted in an exceptionally low pump fluence threshold of approximately 4 μJ/cm², one of the lowest reported for colloidal nanomaterials in optical cavity configurations. Lasing threshold gain values were determined to be between 40–80 cm^{-1}, representing a tenfold reduction compared to planar film configurations and highlighting the superior performance of the photonic optical nanocavity. Additionally, our Ref. 7 demonstrates continuous-wave (CW) lasing using ZnS-capped quantum shells on an integrated SiN_x/SiO_x platform, employing a surface-emitting photonic crystal surface-emitting laser (PCSEL) design. This approach enabled effective lasing under both femtosecond and quasi-continuous wave operations across the full red spectrum, with competitive thresholds, no saturation, and impressive stability at high pump rates.

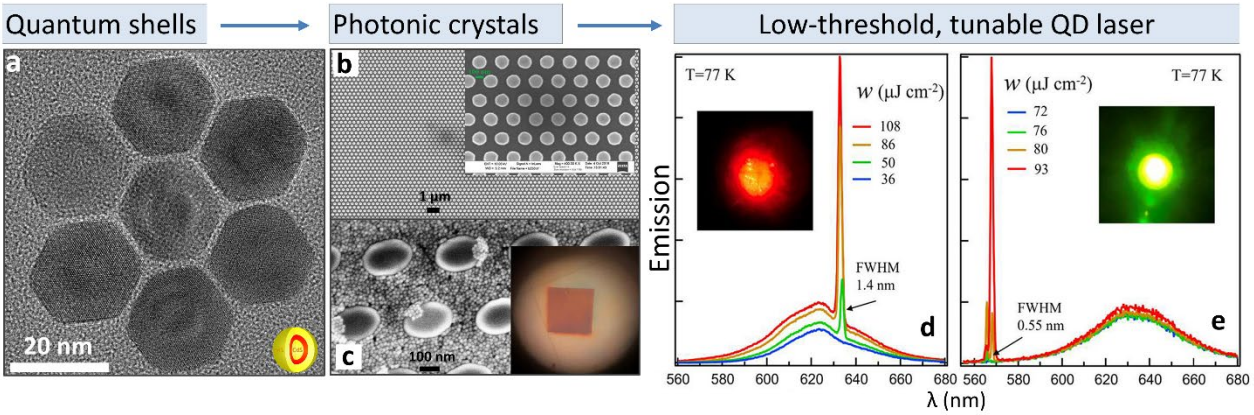

Figure 3. (a) Transmission electron microscope images of CdS-CdSe-CdS core-shell-shell quantum shells. (b) Scanning electron microscope (SEM) image of a photonic crystal nanopillar array with a period of Λ = 335 nm. Scale bar = 1 μm. Inset: Magnified view of the nanopillar arrangement. Scale bar = 100 nm. (c) SEM image of the same nanopillar array after spin-coating with quantum shells. Inset: Optical image of the full nanopillar array following spin-coating. (d, e) Lasing emission spectra recorded at T = 77 K for nanopillar arrays with varying periods: (d) Λ = 365 nm and (e) Λ = 315 nm. Insets: Microphotographs of the corresponding lasing spots under optical excitation.

In our most recent project, we have developed a novel class of quantum shells, termed the quantum cube, which is based on a *cubic* CdS/CdSe/CdS core–shell–shell composition (Figures 4a-4c). This nanostructure offers a unique advantage by incorporating six well-defined 2D CdSe facets, effectively functioning as an assembly of six quasi-independent 2D nanoplatelets.

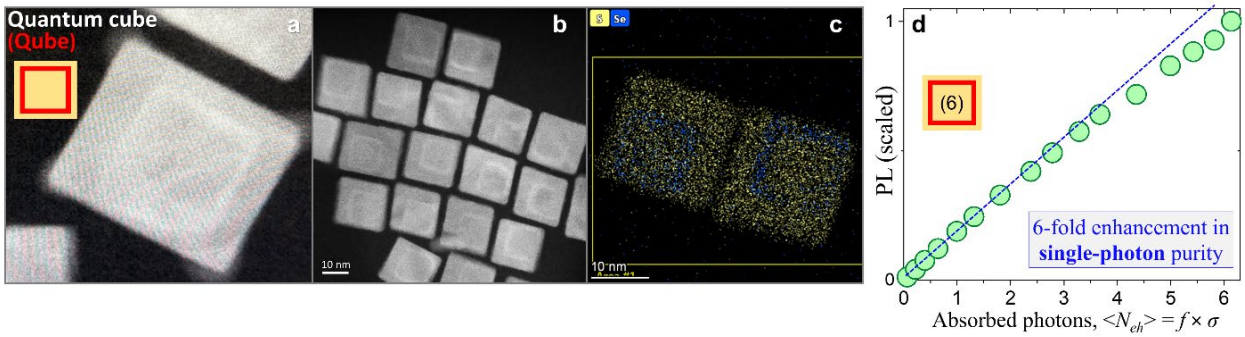

Figure 4. (a–c) Scanning transmission electron microscopy (STEM) images of CdS/CdSe/CdS core–shell–shell quantum cubes, with panel (c) including dark-field energy-dispersive X-ray (EDX) elemental mapping to confirm the layered composition. (d) Power-dependent integrated photoluminescence (PL) intensity of quantum cubes plotted as a function of the average number of absorbed photons per particle (⟨N⟩). The PL response shows minimal saturation up to ⟨N⟩ ≈ 6, consistent with exciton distribution across the six nanoplatelet-like facets and a suppressed biexciton population. A simulated model curve for ideal single-photon emission is shown for comparison (dashed line).

In the multiexciton regime, excitons are spatially distributed across these six cubic facets, with each receiving approximately one-sixth of the total excitation population. This geometry inherently suppresses multiexciton emission pathways (Figure 4d), facilitating the generation of single photons and making the structure particularly promising for quantum light source applications. In addition to its favorable excitonic dynamics, the cubic geometry can also improve material processability by enabling a more controlled self-assembly compared to conventional 2D nanosheets. A manuscript is currently in preparation.

Future Plans

Building on recent advances, we anticipate that the quantum shell architecture will continue to emerge as a compelling alternative to traditional 0D-2D nanocrystals for a broad range of optoelectronic and quantum photonic applications. Our future efforts will focus on both improving fundamental understanding and enabling targeted functionalities of these materials. In particular, we will focus on:

(i) Advancing understanding and application of CdSe-based quantum shells: We aim to further explore the unique advantages of CdSe-based quantum shells in regimes where multiexciton interactions are critical. Our research will expand into new application areas that are only beginning to be explored, including spin-polarized light-emitting diodes (manuscript in preparation), infrared photodetectors, and solution-processed cathodoluminescent materials (manuscript submitted). Concurrently, we will continue advancing our ongoing efforts in established areas such as quantum light emission, X-ray and electron scintillation, and concentrator photovoltaics, leveraging the unique multiexciton dynamics and structural versatility of quantum shells.

(ii) Developing Novel Quantum Shell Material Systems: A second major goal is to expand the quantum shell material library beyond the established CdS/CdSe/CdS system. In particular, we are pursuing two new compositions: ZnS/ZnSe/ZnS and CdS/HgS/CdS with tunable optical properties in the blue and near-infrared (NIR) spectral regions, respectively. These heterostructures are designed to support efficient multiexciton emission and Auger suppression under optical or electrical pumping. Optimization of these systems will be directed toward key applications such as quantum emitters for telecom wavelengths and high-sensitivity NIR photodetectors.

Publications from DOE-sponsored research (10 most significant in the last 2 years)

1. D. Harankahage, J. Cassidy, J. Beavon, J. Huang, N. Brown, D. Berkinsky, K. Zhang, P. Anzenbacher, R. Schaller, L. Sun, M. Bawendi, A. Malko, B. Diroll, and M. Zamkov, *Quantum Shell in a Shell: Engineering Colloidal Nanocrystals for a High-Intensity Excitation Regime*, **J. Am. Chem. Soc. 145**, 13326 (2023).
2. B. T. Diroll, J. P. Cassidy, D. Harankahage, X.-M. Lin, and M. Zamkov, *Large Two-Photon Cross Sections and Low-Threshold Multiphoton Lasing of CdS/CdSe/CdS Quantum Shells*, **Nanoscale 15**, 18415 (2023).
3. M. Zamkov, *Bulk Semiconductor Nanocrystals Transform Solution-Processed Gain Media*, **Nature Nanotechnol. 18**, 1383 (2023).

4. J. Beavon, J. Huang, D. Harankahage, M. Montemurri, J. Cassidy, and M. Zamkov, *Quantum Shells versus Quantum Dots: Suppressing Auger Recombination in Colloidal Semiconductors*, **Chem. Commun. 59**, 11337 (2023).
5. A. A. Marder, J. Cassidy, D. Harankahage, J. Beavon, L. Gutiérrez-Arzaluz, O. F. Mohammed, A. Mishra, A. C. Adams, J. D. Slinker, Z. Hu, S. Savoy, M. Zamkov, and A. V. Malko, *CdS/CdSe/CdS Spherical Quantum Wells with Near-Unity Biexciton Quantum Yield for Light-Emitting Device Applications*, **ACS Mater. Lett. 5**, 1411 (2023).
6. K. Zhao, X. Zhou, X. Li, J. Moon, J. Cassidy, D. Harankahage, Z. Hu, S. M. Savoy, Q. Gu, M. Zamkov, and A. V. Malko, *Green Light from Red-Emitting Nanocrystals: Broadband, Low-Threshold Lasing from Colloidal Quantum Shells in Optical Nanocavities*, **ACS Nano 18**, 10946 (2024).
7. I. Tanghe, K. Molkens, T. Vandekerckhove, D. Respekta, A. Waters, J. Huang, J. Beavon, D. Harankahage, C. Y. Lin, K. Chen, D. Van Thourhout, M. Zamkov, and P. Geiregat, *Two-Dimensional Electron-Hole Plasma in Colloidal Quantum Shells Enables Integrated Lasing Continuously Tunable in the Red Spectrum*, **ACS Nano 18**, 14661 (2024).
8. A. Marder, S. Smith, J. Cassidy, D. Harankahage, Z. Hu, S. Savoy, G. C. Schatz, M. Zamkov, and A. V. Malko, *Heralded Generation of Correlated Photon Pairs from CdS/CdSe/CdS Quantum Shells*, **ACS Nano 18**, 30863 (2024).
9. B. Guzelturk, B. T. Diroll, J. P. Cassidy, D. Harankahage, M. Hua, X.-M. Lin, V. Iyer, R. D. Schaller, B. Lawrie, and M. Zamkov, *Bright, Fast, and Durable Scintillation from Colloidal Quantum Shells*, **Nature Commun. 15**, 4274 (2024).
10. D. Nazar, A. D. Waters, M. M. Kannen, D. Harankahage, J. Huang, and M. Zamkov, *Colloidal Semiconductor Quantum Shells for Solution-Processed Laser Applications*, **Nanoscale 17**, 3698 (2025).

Session XIII

Plasmonic Photoconductive Nanostructures for High-Power Terahertz Wave Generation

Mona Jarrahi, University of California Los Angeles

Keywords: Plasmonics, Quantum well heterostructures, Ultrafast carrier dynamics, Terahertz

Research Scope

The ability to excite surface plasmon waves has enabled many unique opportunities for routing and manipulating electromagnetic waves. It has enabled strong light concentration in the near-field, paving the way for higher resolution imaging and spectroscopy, deep electromagnetic focusing and beam shaping, higher efficiency photovoltaics, photodetectors, modulators, and radiation sources. On the basis of the unique properties of surface plasmon waves, we conduct fundamental studies on metallic multi-spectral plasmonic nanostructures for probing intensity, polarization, and spectral properties of electromagnetic waves from radio frequency (RF) to terahertz (THz) frequencies. The multi-spectral plasmonic nanostructures maximize the intensity and spatial overlap of an optical pump beam with the incident electromagnetic wave to be probed in a photo-absorbing semiconductor substrate. We conduct extensive studies on various polarization-dependent two-dimensional and three-dimensional multi-spectral plasmonic nanostructures fabricated on different photo-absorbing semiconductor substrates to explore their potentials for electromagnetic wave probing and determine fundamental physical limitations of bandwidth and sensitivity of the proposed electromagnetic wave probing technique. We study tradeoff between electromagnetic wave probing bandwidth and sensitivity and its relation with various geometric and material specifications of the analyzed multi-spectral plasmonic nanostructures. These studies offer a deep understanding of behavior of plasmonic nanostructures and nanoscale semiconductor heterostructures in response to external electromagnetic waves in a multi-spectral electromagnetic wave platform. They offer a new perspective on utilizing the unique capabilities of multi-spectral plasmonic nanostructures for probing the intensity, polarization, and spectral properties of electromagnetic waves from RF to THz frequencies. They also enable fundamental physical studies on ultrafast carrier dynamics at nanoscale and discoveries on the interaction of electrons, holes, excitons, photons and semiconductor lattice.

Recent Progress

During the last two years of this research program, we explored the unique capabilities of plasmonic photoconductive nanostructures based on quantum-well semiconductor heterostructures for efficient light-to-terahertz wave conversion. Embedding quantum-well heterostructures in the intrinsic region of PIN photodiode waveguides enables strong, distributed light-matter interaction—enhancing quantum efficiency while mitigating saturation and thermal breakdown effects. Additionally, we conducted comprehensive analytical and experimental studies on ultrafast carrier dynamics in these structures, investigating the fundamental physical limits of conversion efficiency and operational wavelength range. We introduced a comprehensive model to analyze the ultrafast dynamics of interband photo-excited carriers in quantum well PIN structures and to calculate their frequency response. This model characterizes the entire photocarrier transport process, including carrier escape from quantum wells and movement across heterojunction interfaces. Additionally, we outline theoretical methods for calculating carrier escape times from both quantum wells and heterojunction interfaces. The outcomes of this study

show that carrier trapping within quantum wells and at heterostructure interfaces does not impede high-speed photomixing performance at frequencies exceeding 100 GHz, extending even into the terahertz range. With careful optimization of heterostructure layer thickness, doping levels, and photodiode geometry, sub-picosecond carrier transit times and RC time constants can be achieved, facilitating high quantum-efficiency optical-to-terahertz conversion through quantum well PIN heterostructures. Using a GaAs/AlGaAs multiple quantum well PIN heterostructures, we demonstrated interband photomixing as an efficient mechanism for frequency-tunable terahertz generation and detection, achieving significant improvements in power efficiency and sensitivity.

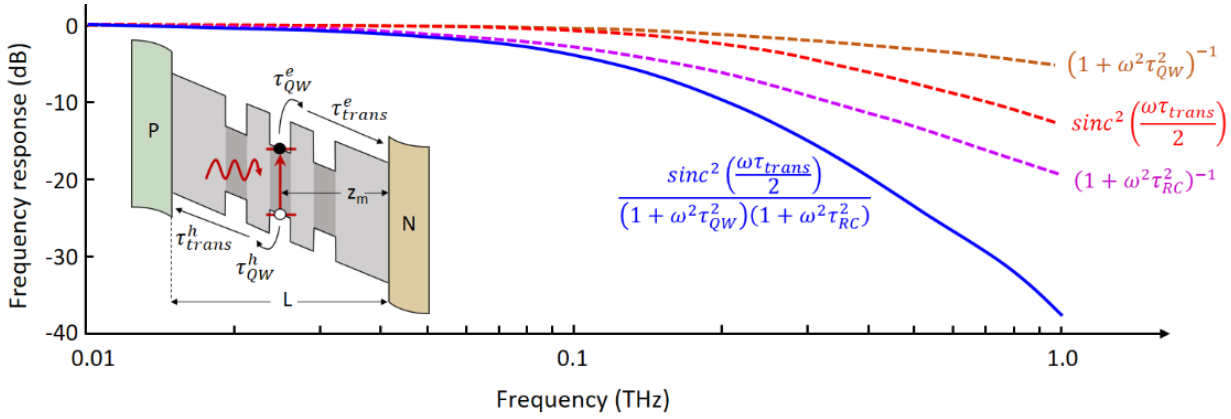

Fig. 1. The theoretically predicted frequency response of the interband photomixing process in the studied GaAs/AlGaAs QW PIN photodiode.

Photomixers utilizing interband photon absorption in QW PIN photodiodes have not been previously explored for terahertz generation and detection due to the misconception that the QW energy barrier restricts the ultrafast carrier dynamics necessary for efficient operation. However, our studies on the ultrafast dynamics of the carriers generated through interband absorption in QW structures reveal substantial potential for realizing monolithically integrated terahertz sources and detectors, seamlessly integrated alongside other optoelectronic components. Under reverse bias, which governs interband photon absorption within the QWs via the quantum-confined Stark effect – the photo-generated carriers escape from the QWs and drift across the intrinsic region (Fig. 1 inset). The resulting induced current can be analyzed using the Shockley-Ramo theorem, which accounts for both conduction and displacement currents. The contribution of photo-generated electrons and holes in the m^{th} QW traveling across the intrinsic region at high frequencies can be approximated as

$$I_{e,m}(\omega) \approx \frac{z_m}{L+W_n+W_p} \times \frac{1}{1+j\omega\tau_{RC}} \times \frac{qSN_m}{1+j\omega\tau^e_{QW}} \times sinc\left(\frac{\omega\tau^e_{trans}}{2}\right) e^{-\frac{j\omega\tau^e_{trans}}{2}} \quad (1)$$

$$I_{h,m}(\omega) \approx \frac{L-z_m}{L+W_n+W_p} \times \frac{1}{1+j\omega\tau_{RC}} \times \frac{qSN_m}{1+j\omega\tau^h_{QW}} \times sinc\left(\frac{\omega\tau^h_{trans}}{2}\right) e^{-\frac{j\omega\tau^h_{trans}}{2}} \quad (2)$$

where z_m is the distance from the m^{th} well to the N-side, L, W_n and W_p are the thicknesses of the intrinsic region, depleted N-region, and depleted P-region, respectively. S denotes the photomixer area, and N_m is the number of photo-generated electrons and holes in the m^{th} QW. τ^e_{QW} and τ^h_{QW} correspond to the electron and hole escape times from the QW respectively, whereas τ^e_{trans} and τ^h_{trans} denote the electron and hole transit times through the intrinsic region. Additionally, τ_{RC}

represents the RC time constant of the photodiode. The total frequency response is obtained by summing the current contributions from all QWs. The overall frequency response is primarily governed by three key time constants: τ_{RC} the photodiode's RC time constant; τ_{trans} the carrier transit time from the QWs to the P/N layers; and τ_{QW} the carrier escape time from the QWs. The values of τ_{QW} and τ_{trans} depend on the reverse bias voltage, as well as the composition and thickness of the heterostructure layers forming the QW PIN photodiode. Meanwhile, τ_{RC} is dictated by the photodiode's geometry, which determines its capacitance and resistance. Figure 1 presents the theoretically predicted frequency response of a reverse-biased QW PIN photodiode with an RC time constant of 1.55 ps, fabricated on the studied GaAs/AlGaAs QW substrate used in our demonstrations. The substrate structure provides estimated saturation velocities of 0.72×10^7 and 0.8×10^7 cm/s for the photo-generated electrons and holes transiting through the depletion region, along with QW escape times of 0.09 and 0.13 ps for electrons and holes, respectively. The contributions of τ_{RC}, τ_{trans}, and τ_{QW} to the frequency response are depicted in purple, red, and brown, respectively, highlighting the negligible impact of τ_{QW} on the frequency roll-off compared to τ_{RC} and τ_{trans}. Thus, careful design of the QW PIN photodiode allows for minimizing τ_{RC} and τ_{trans}, reducing frequency roll-off and extending the photomixer's operational range within the terahertz spectrum. For instance, reducing the thickness of the intrinsic region while maintaining the same QW structures would decrease the carrier transit time while preserving QW properties for stimulated photon generation, amplification, and phase/intensity modulation. Similarly, reducing the photomixer active area and thickness of the P/N layers as well as increasing their doping would lower the RC time constant while maintaining the QW properties.

Leveraging the ultrafast carrier dynamics that support interband photon absorption, an optical pump beam containing two frequency components separated by a terahertz frequency difference can generate a terahertz photocurrent through photomixing. The frequency of the resulting terahertz signal can be tuned by adjusting the optical beat frequency, f_{beat}, with the generated terahertz power scaling quadratically with the induced photocurrent—up to saturation at high reverse bias voltages and optical pump power levels. Similarly, by coupling a received terahertz signal at f_{THz} to a reverse-biased QW PIN photodiode that is simultaneously pumped with a terahertz beat frequency, an intermediate frequency (IF) photocurrent is induced at $|f_{THz} - f_{beat}|$ through photomixing. By tuning the optical beat frequency near the terahertz frequency of interest, the resulting IF signal falls within the radio frequency (RF) range. Using the studied GaAs/AlGaAs QW heterostructures, we experimentally demonstrate interband photomixing in QW PIN photodiodes as an efficient mechanism for frequency-tunable terahertz generation and detection, achieving significant improvements in power efficiency and sensitivity over the state-of-the-art [1, 2]. Our findings have very important technological impacts because while quantum well PIN photodiodes are well-established for photonic integrated circuit implementation, their potential for terahertz generation and detection has yet to be realized in a monolithically integrated terahertz optoelectronic platform. This limitation arises because previous studies have been limited to photomixing schemes utilizing intersubband photon absorption in quantum PIN photodiodes, which require pump photons in the long-wavelength regime (mid-infrared and terahertz), where no monolithically integrated platform exists and there are many challenges preventing the integration of essential system components—such as pump sources, detectors, amplifiers, modulators, and passive optical components—onto the same substrate while operating at room temperature. On the other hand, photomixers utilizing interband photon absorption in quantum well PIN photodiodes have not been previously explored for terahertz generation and detection

due to the misconception that the quantum well energy barrier restricts the ultrafast carrier dynamics necessary for efficient operation. However, our studies on the ultrafast dynamics of the carriers generated through interband absorption in quantum well structures reveal substantial potential for the development of monolithically integrated terahertz sources and detectors, seamlessly integrated alongside other optoelectronic components.

Future Plans

For the next steps of this research program, we plan to continue our investigation on quantum well semiconductor heterostructures embedded in plasmonic nanostructures facilitating strong light matter interaction. We also plan to study thermal characteristics of quantum well heterostructures embedded in plasmonic nanostructures at high optical pump powers and investigate the fundamental physical limitations of optical-to-terahertz conversion efficiency and terahertz detection sensitivity. To suppress the negative impacts of joule heating on the quantum efficiency of plasmonic photoconductors, we plan to investigate distributed and arrayed plasmonic nanostructures.

Publications (March 2023- March 2025)

1. Y. Zhao, S. E. Zumrat, M. Jarrahi, “Terahertz Photonics on a Chip: Monolithically Integrated Terahertz Optoelectronics based on Quantum Well Structures,” arxiv:2411.12046, 2024
2. Y. Zhao, M. Jarrahi, “Ultrafast carrier dynamics in multiple quantum well p-i-n photodiodes,” arXiv:2411.09183, 2024
3. M. S. S. Rahman, T. Gan, M. Jarrahi, A. Ozcan, “Programmable refractive functions,” arXiv:2409.00567, 2024
4. Y. Wang, Y. Li, T. Gan, K. Liao, M. Jarrahi, A. Ozcan, “Diffractive Waveguides,” arXiv:2407.21340, 2024
5. X. Li, D. Mengu, N. T. Yardimci, D. Turan, A. Charkhesht, A. Ozcan, M. Jarrahi, “Terahertz plasmonic focal-plane array with pixel super-resolution,” Nature Photonics, 18, 139–148, 2024
6. J. Li, X. Li, N. T. Yardimci, J. Hu, Y. Li, J. Chen, Y. C. Hung, M. Jarrahi, A. Ozcan, “Rapid Sensing of Hidden Objects and Defects using a Single-Pixel Diffractive Terahertz Processor,” Nature Communications, 14, 6791, 2023
7. Y. Li, J. Li, Y. Zhao, T. Gan, J. Hu, M. Jarrahi, A. Ozcan, “Universal Polarization Transformations: Spatial Programming of Polarization Scattering Matrices Using A Deep Learning-Designed Diffractive Polarization Transformer,” Advanced Materials, 35, 2303395, 2023
8. X. Li, J. Li, Y. Li, A. Ozcan, M. Jarrahi, “High-throughput terahertz imaging: progress and challenges,” Light: Science & Applications, 12, 2023
9. P. K. Lu, M. Jarrahi, “Frequency-domain terahertz spectroscopy using long-carrier lifetime photoconductive antennas,” Optics Express, 31, 9319-9329, 2023

Probing and understanding the spatial and energy distributions of plasmonic hot carriers via single-molecule quantum transport

Kun Wang, University of Miami

Keywords: Single Molecules, Quantum Transport, Hot Carriers, Scanning Probe Microscopy

Research Scope

The overarching goal of this research is to experimentally probe and understand the steady-state distributions of hot carriers (highly energetic electrons and holes) generated in noble metal plasmonic nanostructures (PNs) (Fig. 1). Hot carriers produced in metallic nanostructures during plasmonic excitation are highly dynamic, and understanding their spatial and energy characteristics is essential for advancing many hot carrier-driven applications in molecular electronics, photocatalysis, and optoelectronics.[1] This research aims to develop a novel experimental approach that leverages single-molecule quantum transport properties to access and analyze hot carriers generated in PNs. Central to this project is the utilization of quantum transmission properties of carefully designed single molecules as highly selective energy filters for accessing hot carriers.[2] We employ scanning tunneling microscopy (STM) break junction techniques to construct PN-molecule-tip transport junctions and probe hot carriers in PNs made with different metal materials and geometries.

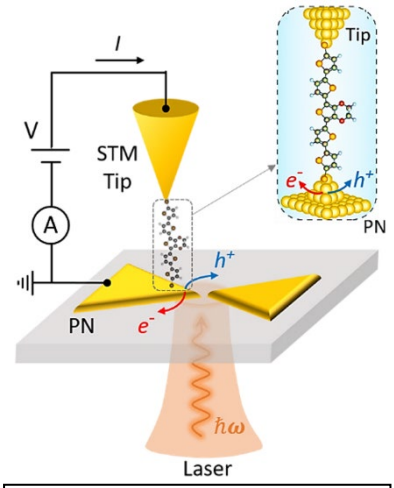

Figure 1. Probing plasmonic hot carriers in a molecular transport junction using STM break junction technique.

During the current research, we mainly focused on the development of the experimental platform, design, synthesis, and characterization of suitable molecular candidates and establishing an appropriate theoretical framework to understand the underlying physical mechanisms.

Recent Progress

The focus of the current research is to search for and design appropriate molecular candidates with desired quantum transmission characteristics via combined theoretical and experimental approaches, with the ultimate goal of establishing the molecular design guideline for favorable molecular systems. The ideal molecular candidates for accessing plasmonic hot carriers are those that possess transmission resonances near the Fermi level of noble metals (e.g., gold) under ambient conditions. It is critical to be able to tune the relative position between the molecular transmission resonances and metal Fermi energy as it will enable the study of hot carriers distributed in different energy windows. Such desired transmission characteristics require an extremely narrow bandgap and frontier molecular orbitals very close to the Fermi level under

ambient conditions. However, molecular materials with such structural and transport features have remained inaccessible to date, despite the extensive exploration of a vast chemical space for over two decades. Existing design paradigms often produce molecules that have relatively large bandgaps and exhibit off-resonant transport with rather low transmission near the Fermi energy (Fig. 2A).[3] In our recent work (*JACS* 2025) [4], we report an important experimental breakthrough by presenting a

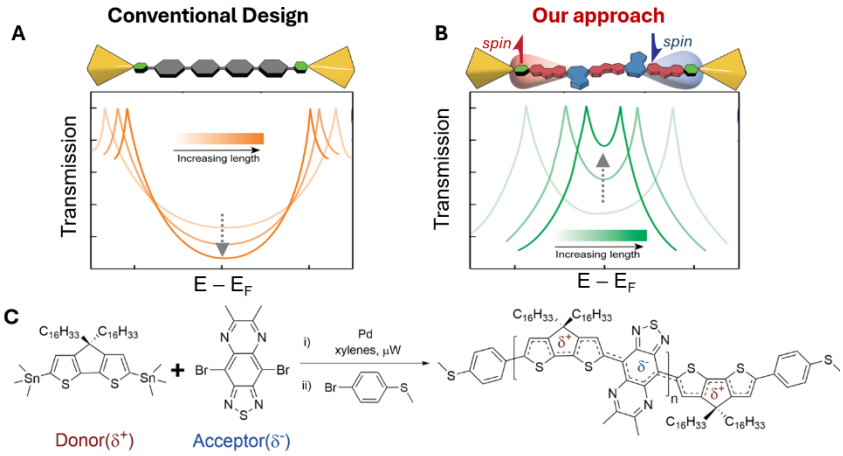

Figure 2. A. Schematics of transmission function of conventional design of π-conjugated molecules in closed shell form. B. Transmission of our newly developed neutral open shell diradical molecular system. C. Synthesis of a model open-shell donor-acceptor molecules that yield remarkably high electron transmission.

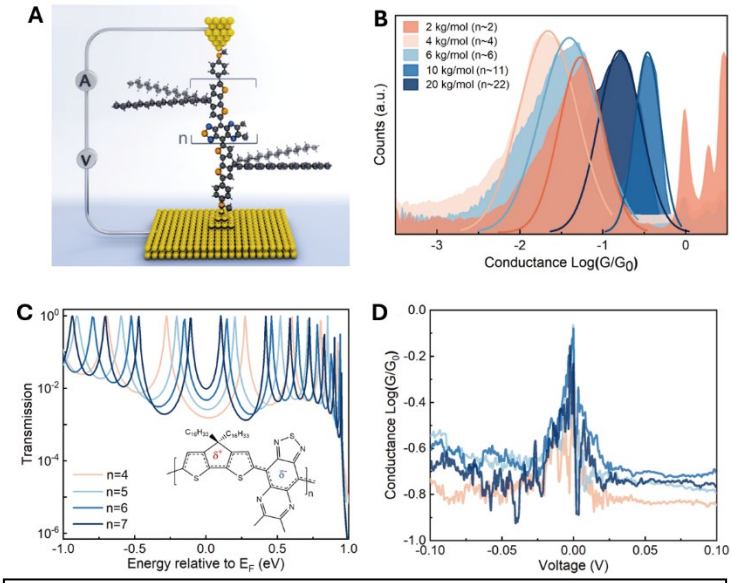

Figure 3. A. Schematic of a single OSDA molecular junction formed in the STM-BJ setup. B. 1D conductance histograms of the single OSDA molecules. C. Transmission function calculated using DFT-NEGF calculations for OSDA oligomers with 4, 5, 6 and 7 repeat units. D. Representative conductance vs. applied bias (G-V) traces for a ~20nm long OSDA molecule.

model molecular system that overcomes the grand challenge that limits the electron transmission efficiency in existing organic molecules. In this study, we showed the first experimental observation of resonant charge transport across a molecular length exceeding 20 nm in air under ambient conditions (Fig. 3). To elaborate on our approach, we integrated emerging chemical design paradigms and quantum transport physics with single-molecule characterization to demonstrate chemically robust, air-stable, and highly tunable molecular wires comprised of neutral open-shell donor-acceptor (OSDA) molecules. This molecular framework, poly(4-(4,4-dihexadecyl-4H-cyclopenta[2,1-b:3,4-b']dithiophen-2-yl)-6,7-dimethyl-[1,2,5]thiadiazolo[3,4-g]quinoxaline, exhibit remarkably high single-molecule conductance close to the ballistic conductance $1G_0$ over distances greater than 20 nm in the low-bias regime. Notably, these molecules show no discernable conductance decay with increasing length, a non-ohmic behavior that is highly favorable yet unattainable with conventional electronic materials. This new molecular platform significantly

exceeds the best-performing organic materials in terms of electron transmission efficiency, chemical stability, and transport length (Fig. 4), making air-robust, highly conductive molecular materials viable for various applications.

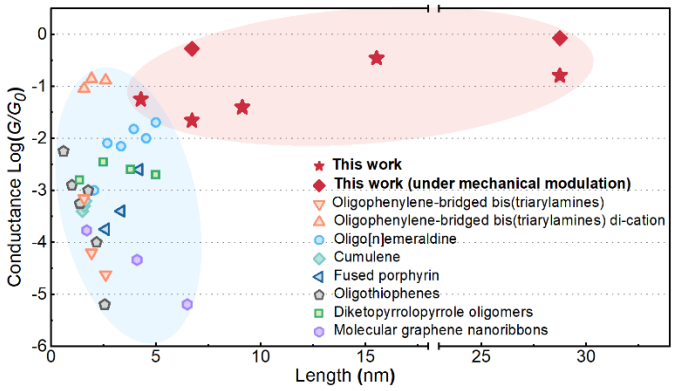

Figure 4. Comparison of the state-of-the-art π-conjugated molecules with our newly developed OSDA molecular systems (red).

Our first principle DFT theoretical calculations further showed that the direct long-range resonant transport arises from the synergistic combination of extended π-conjugation, very narrow bandgap, and open-shell electronic structure (i.e., diradicaloid character), which synergistically enable excellent alignment of frontier molecular orbitals with the electrode Fermi energy in the low-bias regime (Fig. 3C and 3D). Notably, this work provides the first experimental evidence that electronic wires made of single organic molecules can facilitate highly efficient ballistic quantum transport across several tens of nanometers. We established the basis for simultaneously achieving multiple highly desired properties in organic materials, including ultra-high conductance, air-robustness, operability at low bias, and compatibility with ambient conditions. Unlike existing radical systems, these OSDA molecules are neutral in their native "undoped" form and chemically stable in air, making them compatible with solid-state PN devices that will be used in this project.

In addition, to exploit the rich electronic effects arising from metal d-orbitals, we also investigated the design of an emergent dπ-pπ conjugated carbolong metallaaromatics system. The unique feature of these carbolong molecules is the dπ-pπ conjugation from the metal-carbon polydentate chelation. In this study, the monomeric unit contains an osmium metal center that feature Craig-type aromaticity, yielding high structural robustness and excellent transport properties. We investigated a series of carbolong molecules with monomers connected in two geometric orientations: "front-to-back" and "back-to-back". Interestingly, their molecular conductance increases exponentially with the increase of molecular length, which is in contrast to an exponential conductance decay observed in previously reported organometallic systems. In addition, we introduced an effective way to enhance their transport performance via protonation. We showed that after the protonation of the osmium metal centers, two intriguing effects arise: 1. the protonated molecules show higher conductance, and the degree of conductance enhancement increases with the increase of molecular length. 2. current rectification emerged only in protonated molecules, and the rectification ratio also enhances with the increase of molecular length. Such features imply that the bandgap of this dπ-pπ conjugated metallaaromatics system can be tuned by the molecular length while maintaining a high electron transmission. These features are highly desirable for probing hot carriers since they offer opportunities to access hot carriers at different energy windows.

Future Plans

To further advance the project's objectives, we plan to undertake the following activities as next steps:

- Expanding molecular libraries for plasmonic hot carrier studies via optimizing the newly developed OSDA molecular system and continuously investigating new molecular systems and developing strategies to manipulate the molecular transmission feature.
- Integration of suitable molecular candidates with hot carrier characterizations in the STM break junction setup
- Fabrication and optimization of gold plasmonic nanostructures
- Developing temperature control approach and single-molecule thermoelectric measurement.

References

1. M.L. Brongersma, N.J. Halas, and P. Nordlander, *Plasmon-Induced Hot Carrier Science and Technology*, Nature Nanotechnology **10**, 25–34 (2015)

2. H. Reddy, K. Wang, Z. Kudyshev, L. Zhu, S. Yan, A. Vezzoli, S.J. Higgins, V. Gavini, A. Boltasseva, P. Reddy, V.M. Shalaev, and E. Meyhofer, *Determining Plasmonic Hot-Carrier Energy Distributions via Single-Molecule Transport Measurements*, Science **369**, 423-426 (2020)

3. M. Shiri, S. Shen, and K. Wang, *No More Conductance Decay: Toward Efficient Long-Range Transport in Molecular Wires*, ACS Applied Electronic Materials, **6**, 8626–8639 (2024).

4. S. Shen, M. Shiri, P. Mahalingam, C. Tang, T. Bills, A.J. Bushnell, T.A. Balandin, L. Mejía, H. Zhang, B. Xu, I. Franco, J.D. Azoulay, and K. Wang, *Long-Range Resonant Charge Transport Through Open-Shell Donor-Acceptor Macromolecules*, Journal of the American Chemical Society (ASAP article, DOI: https://doi.org/10.1021/jacs.4c18150) (2025).

Publications

1. S. Shen, M. Shiri, P. Mahalingam, C. Tang, T. Bills, A.J. Bushnell, T.A. Balandin, L. Mejía, H. Zhang, B. Xu, I. Franco, J.D. Azoulay, and K. Wang, *Long-Range Resonant Charge Transport Through Open-Shell Donor-Acceptor Macromolecules*, Journal of the American Chemical Society (ASAP article, DOI: https://doi.org/10.1021/jacs.4c18150) (2025).

2. C. Zhai, E.C. Zulueta, A. Mariscal, C. Xu, Y. Cui, X. Wang, H. Wu, C. Doan, L. Wojtas, H. Zhang, J. Cai, L. Ye, K. Wang, and W. Liu, *From Small Changes to Big Gains: Pyridinium-Based Tetralactam Macrocycle for Enhanced Sugar Recognition in Water*, Chemical Science **15**, 19588-19598 (2024).

3. H. Zhang, Y. Zhu, P. Duan, M. Shiri, S.C. Yelishala, S. Shen, Z. Song, C. Jia, X. Guo, L. Cui, and K. Wang, *Energy Conversion and Transport in Molecular-Scale junctions*, Applied Physics Review **11**, 041312 (2024).

4. M. Shiri, H. Zhang, and K. Wang, *No More Conductance Decay: Toward Efficient Long-Range Transport in Molecular Wires*, ACS Applied Electronics Materials **6**, 8626–8639 (2024).

5. R. Ayinla, M. Shiri, B. Song, M. Gangishetty, and K. Wang, *The Pivotal Role of Non-Covalent Interactions in Single-Molecule Charge Transport*, Materials Chemistry Frontiers, **7**, 3524-3542 (2023).

6. Y. Xu, H. Zhang, H. Su, J. Ma, H. Yu, K. Li, J. Shi, X.Q. Hao, K. Wang, B. Song, and M. Wang, *Hourglass-Shaped Nanocages with Concaved Structures Based on Selective Self-Complementary Coordination Ligands and Tunable Hierarchical Self-Assembly*, Small, **19**, 2300009 (2023).

Data-Driven and Computationally Assisted Design of Near-Infrared Emissive Metal-Organic Complexes with Earth-Abundant Metals.

Svetlana Kilina (North Dakota State University), Dmitri Kilin (North Dakota State University), Bakhtiyor Rasulev (North Dakota State University), Wenfang Sun (University of Alabama)

Keywords: photophysical properties, machine learning, emission, transition metal complexes.

Research Scope

Understanding the optical properties of metal-coordinated complexes is essential for their use as photosensitizers and red to near-infrared (NIR) emitters, with potential applications in photocatalysis, photovoltaics, bioimaging, and photodynamic therapy. Despite recent advances, new organic emitters are still needed – ones with fewer stereoisomers, stronger NIR absorption and emission, and lower cost using earth-abundant elements. Our research focuses on identifying design principles for abundant metal complexes (AMCs) by modifying ligand types, ligand substituents, and metal centers to enhance their photophysical properties. The goal is to increase absorption and emission in the NIR spectral region, improve emission quantum yields and radiative lifetime, and reduce nonradiative decay pathways. To achieve this, we are developing an integrated methodology that combines experimental data, quantum chemical calculations (TDDFT), machine learning (ML), and cheminformatics. This approach enables us to uncover the structural features that drive NIR absorption and emission, guiding the rational design of novel NIR-active complexes based on earth-abundant metals, such as Cu(I) and W(0). The optical performance of these complexes is also benchmarked against more widely used Ir(III)- complexes[1] and semiconductor-based[2] NIR emitters.

Recent Progress

We synthesized 27 new homoleptic $Cu(N^N)_2$ and 12 $W(N^N)(CO)_4$. Ligand choice is based on variations in π-conjugation and benzannulation occurred at different positions of the pyridine or phenyl rings, **Fig. 1b**. Following our TDDFT calculations, we confirmed that with the extended π-conjugation on the diamine ligands, the metal-to-ligand charge transfer (MLCT) absorption band

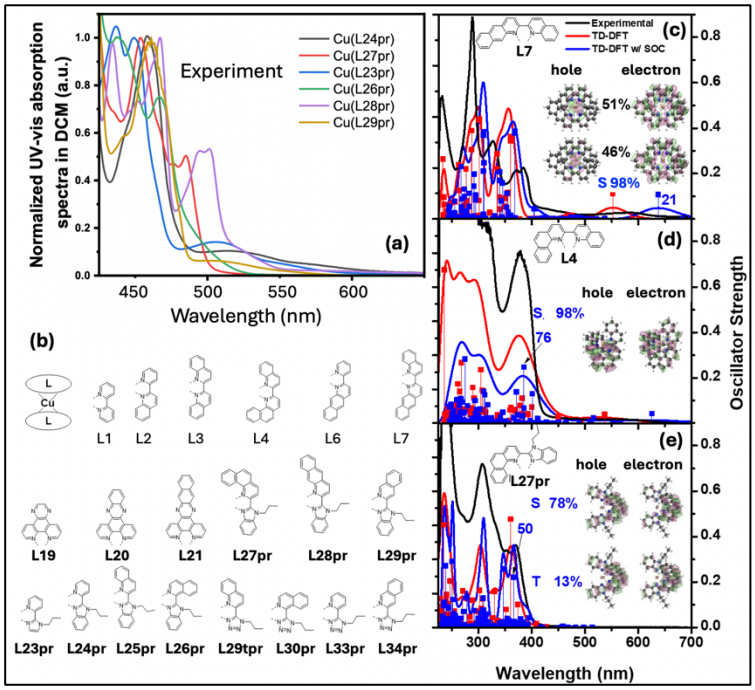

Fig. 1: Structure and UV-Vis absorption spectra of selected Cu(I) complexes measured and calculated in CH_2Cl_2, and electron-hole pairs contributing to the lowest optical transitions showing MLCT.

(the lowest-energy optically bright transitions) in both the Cu(I) and W(0) complexes gradually red-shifted, **Fig. 1a** and **2a** However, for the ligands with the same number of aromatic rings, depending on the position of benzannulation, the MLCT bands were either red or blue-shifted, **Fig. 1c-e**.

The W(L23pr) and W(L24pr) complexes with 2-(pyrid-2-yl)(benz)imidazole ligand show NIR emission in THF, toluene, and dichloromethane solvents, uncovering their potential as NIR-emitters. However, the emission of these complexes is weak. TDDFT shows that using diamine-based L14 and L15 or pyridocarbazole-type (Pycbz) ligands even stronger redshifts absorption and emission bands to NIR. Replacing 1-2 carbonyls with pyridine or bipyridine in W(0) complexes further redshifts the spectra from 600-650 nm to 700-1000 nm, while highly enhancing the optical activity of the lowest transitions, promising efficient emission. TDDFT calculations with included spin-orbit couplings (TDDFT-SOC) show strong triplet (T) and singlet (S) mixing in the lowest optically active transition in Cu(I) with pyridyl-imidazole (L23pr-L29pr), predicting good phosphorescence in these complexes. However, this mixing is minimal in W(0) complexes with similar ligands, resulting in weak emission.

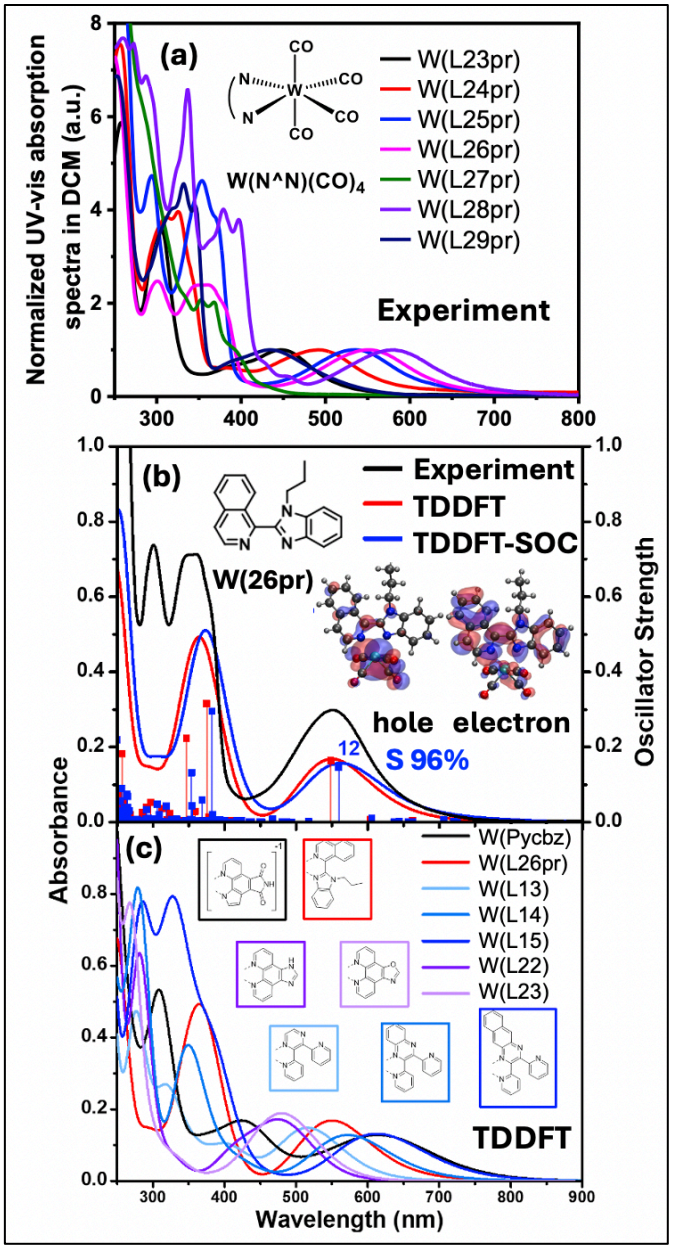

Fig. 2: Structure and UV-Vis absorption spectra of W(0) complexes measured (a)-(b) and calculated (b)-(c) in CH_2Cl_2, and electron-hole pairs showing MLCT character in the lowest optically active transition.

Leveraging these results, based on our previous DFT-based predictions for In(III) complexes[3] and ML model developed by our team for boron-dipyrromethene[4] and Ir(III) complexes[5], we conducted DFT-based calculations for additional 50 hypothetical Cu(I) complexes coordinated by various derivatives of dipyrrin-based ligands (**Fig. 3**). Subsequently, a ML-based Quantitative Structure-Property Relationship (ML/QSPR) model was developed that can reliably predict the absorption wavelength and oscillator strength of Cu(I) complexes, laying the groundwork for high-throughput virtual screening of optical properties of these complexes. To explain the differences in photophysics across structurally diverse individual Cu(I) complexes, the relation between the ML/QSPR models and molecular descriptors was analyzed, revealing contributions of specific properties like polarizability effects, aliphatic chains connected to

heteroatoms, and molecular size and branching to target properties. Furthermore, a large virtual library was developed to screen thousands of hypothetical Cu(I) complexes to find most effective ones to guide future synthesis. Overall, our approach has shown great potential for rational design of novel Cu(I) complexes with optical response at the NIR range of 650-750 nm.

Future Plans

While significant progress has been made toward most project goals, additional effort is needed in predicting and synthesizing new Cu(I) and W(0) complexes with strong NIR emission. To address this, the following steps will be done: **(1)** The developed ML/QSAR models will be improved with using emission descriptors from our DFT calculations and experimental data to screen a virtual library and suggest structural features that contribute best to the target properties.

(2) We also identified an alternative strategy to enhance emission. In Cu(I) complexes with pyrrolidine derivatives, strong singlet–triplet mixing in the lowest MLCT-type transition, along

Fig. 3: The outline of ML modeling procedure and the correlation plot between the observed and predicted values of absorption wavelength and oscillator strength for Cu(I) complexes with dipyrrin-based ligands.

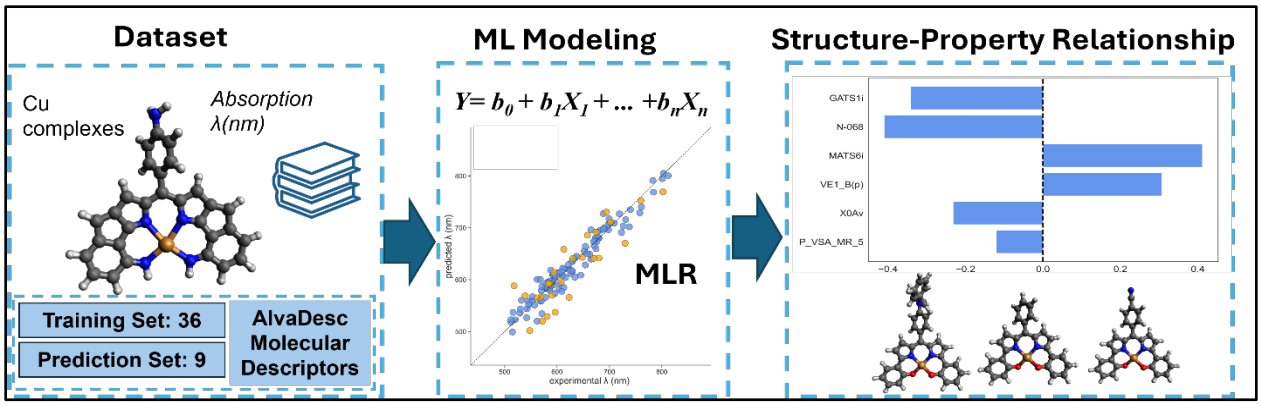

with a small energy gap between these states, create favorable conditions for thermally activated delayed fluorescence (TADF), which is known to significantly enhance internal quantum efficiency and photoluminescence quantum yield (PLQY). We plan to apply the photoexcited dynamics [3] to these Cu(I) complexes to estimate the rates of singlet-to-triplet intersystem crossing and triplet-to-singlet back intersystem crossing, in order to predict the efficiency of TADF in these complexes. If this effect proves efficient, it will offer a promising approach to achieving strong NIR emission in Cu(I) complexes, which our experimental team will synthesize and characterize.

(3) Cu(I) complexes can be chemically modified with chiral substituents, enabling circularly polarized luminescence (CPL) and merging CPL with TADF, leading to novel CP-TADF emitters. Cu(I)-based CP-TADF emitters are rare, especially in the NIR range, but they have significant potential for applications in CP-active organic light-emitting diodes (CP-OLEDs), advanced 3D displays, enantioselective catalysis, spintronics, information encryption, and chiral sensing. Emitters based on Cu(I) complexes offer strong advantages, combining TADF or phosphorescence, adjustable emission, easy synthesis, low cost, and the non-toxic nature of copper. We plan to generate DFT-base data on such emitters and processes these data in ML training and screening to uncover structure-property relationships and navigate rational synthesis of Cu(I)-based CP-TADF emitters.

References

1. X. Sun, H.D. Cole, G. Shi, V. Oas, A. Talgatov, C.G. Cameron, S. Kilina, S.A. McFarland, and W. Sun, *Hypoxia-Active Iridium(III) Bis-terpyridine Complexes Bearing Oligothienyl Substituents: Synthesis, Photophysics, and Phototoxicity toward Cancer Cells*, Inorganic Chemistry **63**, 21323-21335 (2024).
2. H.R. Qu, Y.L. Han, J. Fortner, X.J. Wu, S. Kilina, D. Kilin, S. Tretiak, and Y.H. Wang, *2+2 Cycloaddition Produces Divalent Organic Color-Centers with Reduced Heterogeneity in Single-Walled Carbon Nanotubes*, Journal of the American Chemical Society **146**, 23582-23590 (2024).
3. A. Forde, L. Lystrom, W.F. Sun, D. Kilin, and S. Kilina, *Improving Near-Infrared Emission of meso-Aryldipyrrin Indium(III) Complexes via Annulation Bridging: Excited-State Dynamics*, Journal of Physical Chemistry Letters **13**, 9210-9220 (2022).
4. G.M. Casanola-Martin, J. Wang, J.-g. Zhou, B. Rasulev, and J. Leszczynski, *Chemical Feature-Based Machine Learning Model for Predicting Photophysical Properties of BODIPY Compounds: Density Functional Theory and Quantitative Structure–Property Relationship Modeling*, Journal of Molecular Modeling **31**, 18 (2024).
5. A. Karuth, G.M. Casanola-Martin, L. Lystrom, W. Sun, D. Kilin, S. Kilina, and B. Rasulev, *Combined Machine Learning, Computational, and Experimental Analysis of the Iridium(III) Complexes with Red to Near-Infrared Emission*, The Journal of Physical Chemistry Letters **15**, 471-480 (2024).

Publications

1. X. Sun, H.D. Cole, G. Shi, V. Oas, A. Talgatov, C.G. Cameron, S. Kilina, S.A. McFarland, and W. Sun, *Hypoxia-Active Iridium(III) Bis-terpyridine Complexes Bearing Oligothienyl Substituents: Synthesis, Photophysics, and Phototoxicity toward Cancer Cells*, Inorganic Chemistry **63**, 21323-21335 (2024).
2. H.R. Qu, Y.L. Han, J. Fortner, X.J. Wu, S. Kilina, D. Kilin, S. Tretiak, and Y.H. Wang, *2+2 Cycloaddition Produces Divalent Organic Color-Centers with Reduced Heterogeneity in Single-Walled Carbon Nanotubes*, Journal of the American Chemical Society **146**, 23582-23590 (2024).
3. A. Forde, L. Lystrom, W.F. Sun, D. Kilin, and S. Kilina, *Improving Near-Infrared Emission of meso-Aryldipyrrin Indium(III) Complexes via Annulation Bridging: Excited-State Dynamics*, Journal of Physical Chemistry Letters **13**, 9210-9220 (2022).
4. G.M. Casanola-Martin, J. Wang, J.-g. Zhou, B. Rasulev, and J. Leszczynski, *Chemical Feature-Based Machine Learning Model for Predicting Photophysical Properties of BODIPY Compounds: Density Functional Theory and Quantitative Structure–Property Relationship Modeling*, Journal of Molecular Modeling **31**, 18 (2024).
5. A. Karuth, G.M. Casanola-Martin, L. Lystrom, W. Sun, D. Kilin, S. Kilina, and B. Rasulev, *Combined Machine Learning, Computational, and Experimental Analysis of the Iridium(III) Complexes with Red to Near-Infrared Emission*, The Journal of Physical Chemistry Letters **15**, 471-480 (2024).
6. Y. Han, T. Vazhappilly, D.A. Micha, D.S. Kilin, Relaxation of Photoexcited Electron–Hole Pairs at Si(111) Surfaces with Adsorbed Ag Monolayered Clusters of Increasing Size, The Journal of Physical Chemistry Letters, 16 (2025) 2905-2913.
7. G. Casanola-Martin G, G. Tiffany G, O. Eniodunmo, V. Oas, M. Jabed, W. Sun W, D. Kilin, S. Kilina, and B. Rasulev. *Accelerating the Design of Cu(I) Complexes with Near-Infrared Absorption by Interpretable Machine Learning Approaches*. ChemRxiv. 2025; doi:10.26434/chemrxiv-2025-pcrnp.

Session XIV

Enabling Reversible Hydrogen Storage and Transfer with Graphene-Based Carbon–Boron-Nitrogen Materials.

Tom Autrey, Zbynek Novotny, Peter Rice, Zdenek Dohnálek, Bojana Ginovska, Michel Sassi, Maria Sushko

Pacific Northwest National Laboratory

Research Scope

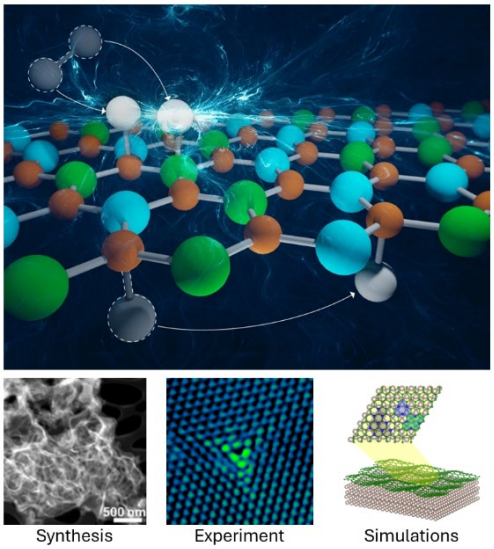

Our research aims to develop a fundamental understanding of how the presence of well-characterized functional sites in two-dimensional materials influences hydrogen activation and transport. We focus on nitrogen doped carbon (CN) and boron–nitride (BN) materials to inform design principles that control hydrogen reactivity and binding energetics, ultimately enabling novel approaches for large-scale energy storage to enhance long-term grid reliability. Although hydrogen is available from several sources, its reversible storage involves complex interfacial interactions. A significant hinderance is our limited understanding of the diverse hydrogen species (H^+, H^-, and H•), their energetics, and dynamics at interfaces. To address this, we combine experimental techniques, ranging from atomic-resolution tools for supported materials to multi-scale analysis for solution-prepared free-standing materials, with computational analysis to investigate these phenomena at atomistic level. Two-dimensional materials, such as CN and BN, are of particular interest due to their lightweight nature, scalability, and earth-abundant element composition. However, practical applications are hindered by kinetic limitations in hydrogen diffusion and surface recombination, which necessitate atomic rehybridization. This program targets key gaps in our knowledge of efficient H_2 activation and reversible storage on CN and BN matrices. Advancing this understanding will support the development of scalable energy storage solutions, contributing to reliable and secure energy technologies.

Recent Progress

Identifying spatially segregated nitrogen dopant sites on graphene/Ru(0001).[Ref. 4] Understanding and controlling doping sites, their coordination environment, and spatial distribution in graphene (Gr) and related 2D materials are critical for tailoring their physical behavior and propensity for hydrogen storage applications. We investigated nitrogen doping in Gr on Ru(0001) using nitrogen ion implantation followed by annealing, successfully tuning the concentrations and distribution of graphitic (GN) and pyridinic (PN) nitrogen sites. Through a combination of high-resolution scanning tunneling microscopy (STM) imaging, X-ray photoelectron spectroscopy (XPS) characterization, and density functional theory (DFT)

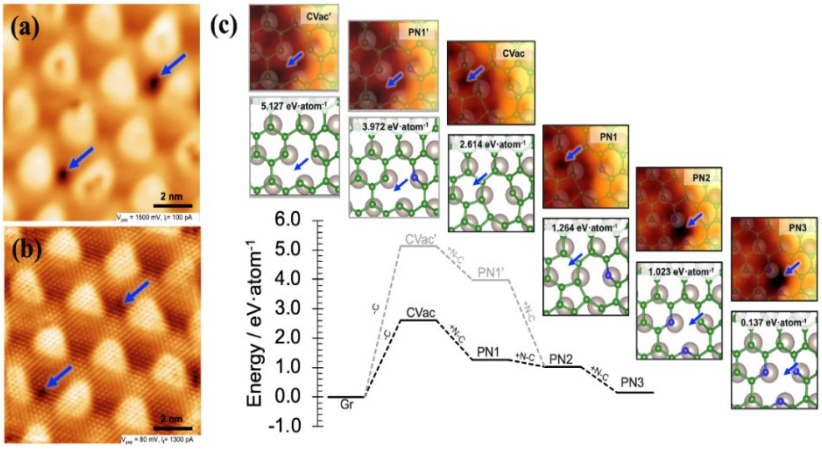

Figure 1. (a) Low- and (b) high-resolution STM images of nitrogen ion irradiated graphene surface annealed to 1100 K. Dark spots in the valley region of the moiré, attributed to pyridinic nitrogen (PN), are highlighted with blue arrows. (c) DFT calculated formation pathway as the number of surrounding PN species is increased from one to three. The graphical inserts indicate the position of each defect, while the simulated STM images for each motif. The blue arrows highlight the position with the darkest STM image contrast. The ball and stick colors correspond to Ru (silver), C (green), and N (blue) atoms.

calculations, we identified the structure and spatial distribution of GN and PN species, see **Figure 1**. A thermodynamic phase diagram was developed, showing the relative stabilities of GN and PN across the Gr moiré. GN was found to be the most stable, favoring the center of the atop region of the moiré, while PN was stabilized by clustering at boundaries between the FCC and HCP regions (blue arrows in Figure 1). The unambiguous assignments provide us with an opportunity to investigate the nature of interaction of both segregated and unsegregated N-motifs with hydrogen to benchmark computational prediction of thermodynamic stability as proposed in the Future Plans.

Synthesis and characterization of segregated N motifs in solution synthesis of N-doped carbon materials. [Ref. 5] We used a combination of experiment and theory to develop a novel approach to characterize a series of 2D carbon materials to gain insight into the mechanism of molecular hydrogen activation at ambient temperatures. The free-standing NC materials are made from a graphitic carbon nitride template and glucose as a carbon source by a hydrothermal synthesis. The precursor complex is annealed at temperatures between 700 ºC (NC700) and 900 ºC (NC900) to modify the ratio of GN and PN functionality. **Figure 2** provides a comparison of the experimental and calculated XPS of C 1s binding energies and provides insights into the arrangement of the N-doped functional groups in the NC700 sample. A key outcome was to provide evidence for the formation of segregated CN3 sites that are predicted to modify the electronic properties of the carbon [1], and are proposed to be key structural

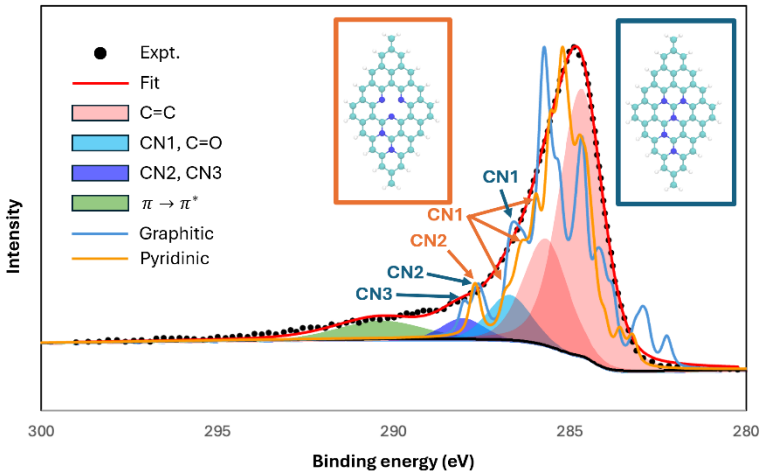

Figure 2. Simulated XPS C 1s spectrum and the fitting of C 1s spectrum of NC700 based on theoretical peak assignment. Peaks at 284.7, 286.2, 288.4, and 290.7 eV correspond to C=C, CN1/C=O, CN2/CN3, and π-π* species, respectively. Carbon atoms are shown as cyan spheres and N atoms as blue spheres in the structures of clusters with pyridinic (orange border) and graphitic (blue border) N.

features leading to the activation of molecular H_2 [2]. The ability to control and identify the N-motifs in these solution-synthesized N-doped carbon materials will assist our studies to evaluate the structure-reactivity relationships to reversible activation of molecular hydrogen.

Thermodynamics of molecular hydrogen activation by defects in hexagonal boron nitride. [Ref. 6] Defects in hexagonal boron nitride (h-BN) that split molecular H_2 heterolytically across adjacent BN sites have been reported in the literature [3], however, there is little insight into the stability or feasibility of forming adjacent defective BN sites in h-BN materials. Our DFT simulations, in combination with *ab initio* thermodynamics, predict that the most likely sites to activate H_2 in the defects of h-BN materials are composed of adjacent N-B-N or B-N-B sites (**Figure 3)**. For small defect sizes, we find that hydrogen preferentially binds to a pair of nitrogen sites, and if no N sites are available, then boron sites would be the next to bind hydrogen. Hydrogen dissociation via Frustrated Lewis Pair (FLP) is found to be favorable only if the defect size is large enough to overcome steric effects. These results provide new insights into hydrogen activation in defective h-BN materials, suggesting both heterolytic and homolytic hydrogen activation. Experimental EPR and NMR works are in progress to confirm both the strongly and weakly bound hydrogen predicted by our computational results.

Future Plans

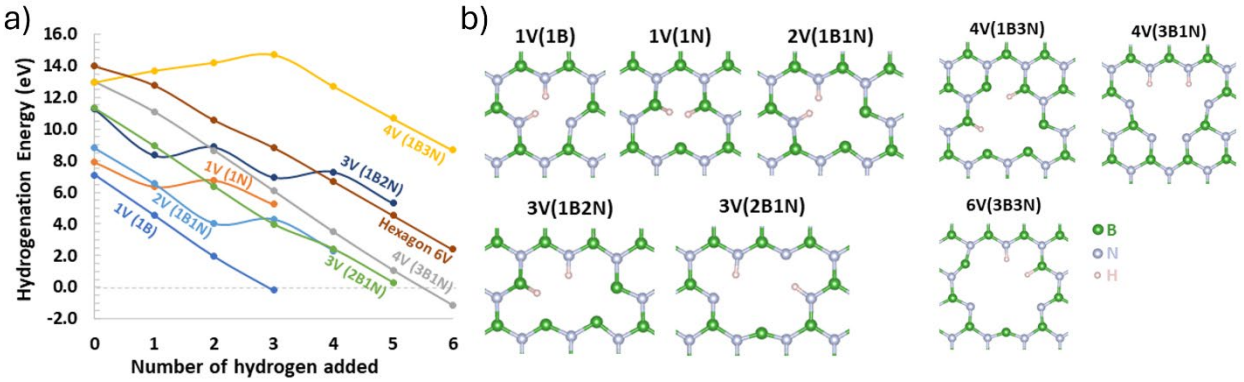

Figure 3. (a) Hydrogenation energy of the defects as a function of hydrogen loading, calculated using the defect-free h-BN as a reference, and (b) visual representation of the most energetically favorable hydrogen configurations for H_2 splitting in defects.

We have made significant progress in our efforts to control and characterize the functionality of nitrogen dopants, i.e., graphitic and pyridinic N, in both free-standing and supported 2D carbon materials. With this insight, we are investigating structure-reactivity relationships between (i) molecular hydrogen and the graphitic and pyridinic N features in 2D graphene materials, and (ii) liquid organic hydrogen carriers (LOHCs), e.g., pyridine and benzene with the same structural features.

Currently, we are investigating the stability and spatial distribution of GN and PN functional groups on highly oriented pyrolytic graphite (HOPG) using nitrogen ion irradiation, similar to the approach used for N-doped Gr on Ru(0001). By performing high-resolution STM imaging, we will progress towards our main goal of understanding GN and PN interactions with hydrogen on both Gr/Ru(0001) and HOPG, aiming to uncover the fundamental descriptors, i.e., paramagnetism, antiferromagnetism, and conduction electrons, and how they are controlling reversible hydrogen adsorption and release from N-doped carbon materials. We aim to understand how nitrogen dopants enhance hydrogen stability and how co-adsorbates, such as water, facilitate hydrogen diffusion on carbon-based materials. Preliminary studies indicate that hydrogen binds to pyridinic N (PN) with stability up to 573 K, while binding to graphitic N is weaker, with full desorption observed below 223 K (Figure 4). We will use temperature programmed desorption, XPS, STM, and DFT to develop a detailed mechanistic understanding of hydrogen stability, its spatial distribution on the surface, diffusion mechanisms, and re-combinative desorption kinetics.

References

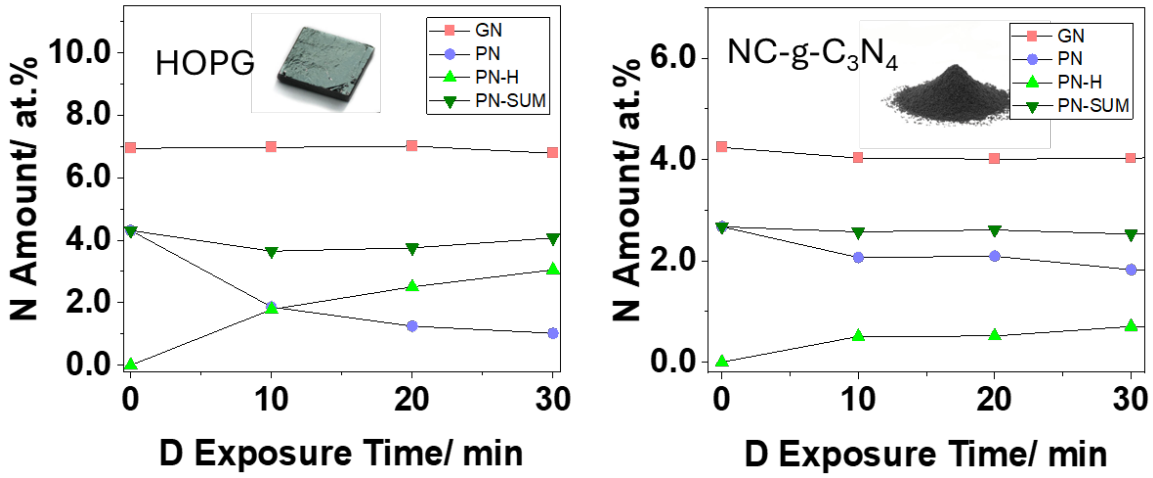

Figure 4. Comparison of *hydrogen atom* affinity for nitrogen motifs in N-doped HOPG and free-standing N-doped carbons (NC-g-C_3N_4) using XPS. Samples are dosed for 30 min with deuterium atoms. In both the model system (HOPG) and the solution-synthesized carbon materials (NC-g-C_3N_4), there is a decrease in the pyridinic nitrogen N 1s peak (398.1±0.1 eV) and the concomitant increase in a new peak at 399.2±0.1 eV assigned to H atom addition to pyridinic nitrogen. As the material is heated to 773 K the N-H bond decrease with the recovery of pyridinic N.

1. P. S. Rice, G. Lee, B. Schwartz, T. Autrey, B. Ginovska. *Leveraging Curvature on N-doped Carbon Materials for Hydrogen Storage*. Small, 2310162 (2024).
2. H. Hu, Y. Nie, Y. Tao, W. Huang, L. Qi, R. Nie. *Metal-free Carbocatalyst for Room Temperature Acceptorless Dehydrogenation of N-heterocycles*. Sci. Adv. 8, (2022). DOI: 10.1126/sciadv.abl9478.
3. H. Chen, C. Xiong, J. Moon, A. S. Ivanov, W. Lin, T. Wang, J. Fu, D. Jiang, Z. Wu, Z. Yang, S. Dai. *Defect-Regulated Frustrated-Lewis-Pair Behavior of Boron Nitride in Ambient Pressure Hydrogen Activation*. J. Am. Chem. Soc. 144, 10688 (2022).

Publications

4. B. S. A. Gedara, P. S. Rice, P. Evans, T. Autrey, B. Ginovska, Z. Dohnálek, Zbynek Novotny. *Identifying Spatially Segregated Nitrogen Dopant Sites on Graphene/Ru(0001)*. Adv. Mater. Interfaces, 2500142 (2025).

5. M. Y. Byun, L. Liu, D. Mejía-Rodríguez, E.D. Walter, Z. Zhu, N. Govind, M.L. Sushko, T. Autrey. *Controlling N speciation in solution synthesis of N-doped carbon materials*. RSC Applied Interfaces. Accepted (2025).
6. M. Sassi, T. Autrey. *First Principles Study of Molecular Hydrogen Activation by Defects in Boron Nitride*. J. Phys. Chem. C. 124, 6657 (2025).
7. P. Bagus, C. Nelin, M. Sassi, D. Baranowski, M. Sharp, T. Autrey, Z. Dohnalek, Z. Novotny. *The XPS of Pyridine: A Combined Theoretical and Experimental Analysis***.** J. Chem. Phys. **162**, (2025).
8. P. S. Rice, G. Lee, B. Schwartz, T. Autrey, B. Ginovska. *Leveraging Curvature on N-doped Carbon Materials for Hydrogen Storage*. Small, 2310162 (2024).
9. W. J. Shaw, M. K. Kidder, S. R. Bare, M. Delferro, J. R. Morris, F. Toma, S. D. Senanayake, T. Autrey, et. al. *Closing the Carbon Cycle: Net-Zero Carbon Emissions for Difficult to Electrify Segments of our Economy*. Nat. Rev. Chem. (2024). DOI: 10.1038/s41570-024-00587-1**.**

Photoelectrochemistry of Organic-Inorganic Metal Halides: from Stability to Chirality

Yiying Wu, The Ohio State University, Columbus, Ohio

Keywords: hybrid semiconductors; photoelectrochemistry; chirality; spin-polarized photocurrent;

Research Scope

This project focuses on conjugated organic-inorganic metal halides (OIMHs) as promising semiconductor materials for fundamental studies of photoelectrochemical (PEC) properties and applications that harness light to drive chemical reactions or generate electricity. Conjugated OIMHs incorporating aromatic quaternary ammonium groups, such as viologens, exhibit enhanced stability in aqueous environments and offer small, tunable bandgaps through charge-transfer excitation. In addition, the project will investigate the PEC properties of chiral OIMHs. Building on the previously observed chirality-induced spin selectivity, we hypothesize that photoexcitation of chiral OIMHs may generate spin-polarized photocurrents, enabling applications in enantioselective recognition and asymmetric organic synthesis. Furthermore, the development of new chiral semiconductors is expected to contribute to broader areas of fundamental materials science, including spintronics.

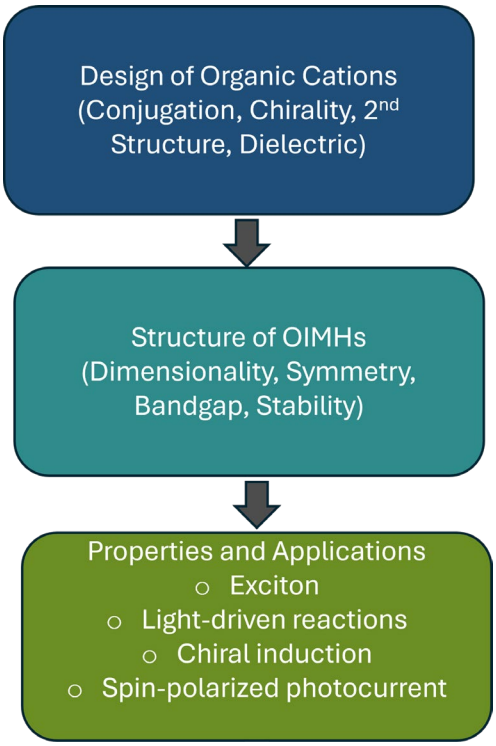

Figure 1. Design of conjugated organic cations controls the structural dimensionality, symmetry, and optoelectronic properties of OIMHs, enabling new opportunities for stable photoelectrochemical energy conversion, spintronic functions, and photoredox catalysis.

Recent Progress

A central theme of this project is to investigate how the design of organic cations impacts the crystal structures, optoelectronic properties, and photoelectrochemical performance of OIMHs (Figure 1). We demonstrated that Zincke reactions provide a general and tunable synthetic platform for growing new conjugated organic cations, highlighting the importance of expanding the synthetic toolbox. We elucidated how secondary structural features of cations, such as hydrogen bonding and dihedral angles, influence the dimensionality, symmetry, and electronic properties of OIMHs. We developed water-stable, chiral, small band gap OIMHs exhibiting broad circular dichroism responses, enabling new opportunities for spintronic and chiral optoelectronic applications. We achieved stable photoelectrochemical operation of conjugated OIMHs in polar electrolytes, overcoming a major barrier to their practical use. Furthermore, we expanded the application scope of OIMHs to include photoredox catalysis and hydrogen generation, highlighting their potential for solar-driven synthesis of valuable chemicals.

1. Chiral Methylbenzylpyridinium-Based Organic–Inorganic Lead Halides for Water-Resistant Photoluminescence Materials

We demonstrated that Zincke reactions provide a general and versatile synthetic strategy to access chiral N-substituted pyridinium salts, specifically (R)/(S)-methylbenzylpyridinium (R/S-MBnP) chloride, and their corresponding 1D chiral OIMHs, (R/S-MBnP)PbX_3 (X = Cl, Br, I). The chirality of both the organic salts and the resulting OIMHs was confirmed by circular dichroism (CD) spectroscopy, and single-crystal X-ray diffraction (XRD) revealed their crystal structures. Photoluminescence (PL) spectra, PL decay lifetimes, and water stability monitored by powder XRD established key optoelectronic and stability properties. This work highlights Zincke reactions as a broadly tunable and powerful synthetic platform for designing conjugated organic cations, offering a critical pathway for expanding the materials library for chiral OIMHs and advancing their PEC applications.

2. Understanding the Composition–Structure Relationship of Hybrid Organic Lead Iodides: Impact of Secondary Structures of Organic Cations

To further understand and control the structure–property relationships in OIMHs, we investigated how the secondary structures of organic cations, driven by noncovalent interactions such as hydrogen bonding, influence the dimensionality and properties of hybrid organic lead iodides. Using alkoxy-ammonium salts as a model system, we systematically studied how NH···O hydrogen bonding induces folding into ring structures, increasing steric hindrance at the ammonium terminus and reducing the material dimensionality. Notably, seven-membered folded rings exhibited the strongest intramolecular hydrogen bonding. The emergence of chirality through folding suggests a novel route for creating symmetry-breaking materials. In a parallel study, we demonstrated that the dihedral angle between adjacent aromatic rings in conjugated cations, such as in 2,2′-dimethyl bipyridinium, critically affects the formation of distinct crystal structures and band gaps. These results establish that secondary structural elements—including hydrogen bonding and torsion angles—provide new handles for tuning the structures and electronic properties of OIMHs.

3. Chiral Viologen-Derived Water-Stable, Small Band Gap Lead Halides: Synthesis, Characterization, and Optical Properties

We developed three pairs of chiral, water-stable OIMHs based on chiral viologen derivatives. These materials feature low-dimensional (1D and 0D) structures with small band gaps (~2 eV). CD spectroscopy of transparent thin films revealed broad CD responses covering most of the visible spectrum. Importantly, even though the chiral center is separated from the pyridinium unit, chirality was successfully transferred into the band gap and exciton absorption regions, likely through chiral crystallization. This design strategy opens new directions for creating low-dimensional chiral semiconductors with potential applications in broadband circular photodetectors and spin-selective PEC devices.

4. Photoelectrochemistry of Methylviologen Lead Iodide: Achieving Stability in Polar Solvents

We established that methylviologen lead iodide ($MVPb_2I_6$) functions as a stable, unprotected photoelectrode in an acetonitrile-based polar electrolyte. Its charge-transfer absorption reduces the band gap to 2.1 eV, making it an effective solar absorber. Stability tests showed only 28% photocurrent decay after 15 hours of continuous operation under 1 sun illumination and applied anodic bias toward iodide oxidation. Energetics were determined via cyclic voltammetry, and degradation pathways were probed through SEM and rotating ring-disk electrode (RRDE)

techniques. This work demonstrates that viologen-based conjugated 1D OIMHs can achieve stability and functionality in polar environments, directly supporting the project's goal of developing practical PEC materials.

5. Photocatalysis of Methylviologen Lead Iodide for Photoredox Organic Transformations and Hydrogen Generation

We further expanded the functional scope of $MVPb_2I_6$ by demonstrating its photocatalytic activity for selective organic transformations and hydrogen evolution (Figure 2). Using $MVPb_2I_6$, we successfully photocatalyzed the reduction of 4-acetylpyridine, taking advantage of the material's suitable conduction and valence band positions and the proton-coupled electron transfer enabled by polar protic solvents. The crystalline structure remained intact after catalytic cycles, indicating excellent robustness. Beyond organic synthesis, $MVPb_2I_6$ also exhibited long-term stability for photocatalytic hydrogen generation under light irradiation. These results establish $MVPb_2I_6$ as a versatile and durable platform for photoredox catalysis and renewable energy applications. Further

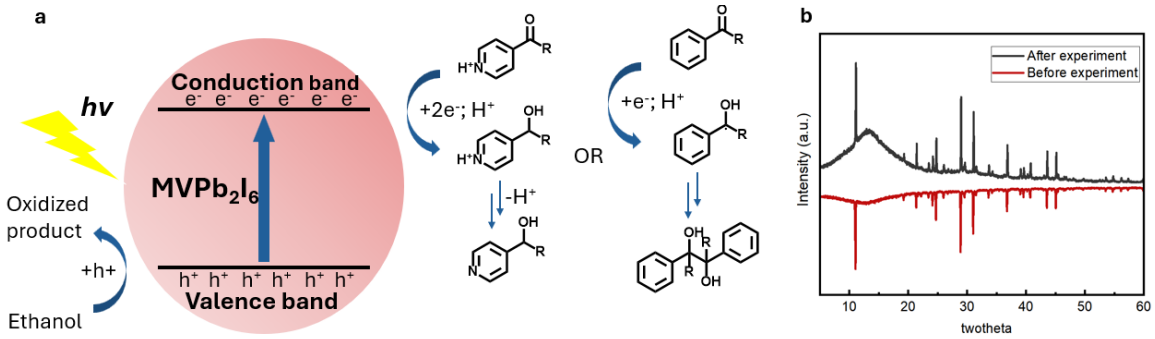

Figure 2. Photocatalytic reduction of aromatic ketone using $MVPb_2I_6$. (a) Schematic reaction mechanism; (b) PXRD of $MVPb_2I_6$ powders before (red) and after (black) photocatalytic reactions.

mechanistic studies and substrate scope expansions are ongoing.

Future Plans

Our next goal is to establish chiral 1D conjugated organic-inorganic metal halides (OIMHs) as a materials platform for spin-polarized photoelectrocatalysis. Traditional semiconductor photoelectrochemistry explores the interaction between light and semiconductor materials to drive electrochemical reactions. However, existing approaches do not control the spin state of photo-generated charge carriers, limiting reaction selectivity and efficiency. Chiral semiconductors provide a pathway to address this gap, offering new opportunities in spin-optoelectronics and spin-selective catalysis.

Publication list during 2022-2025 supported by this grant

1. Wan, R.; Yin, M.; Wang, T.-H.; Moore, C. E.; Wu, Y. Chiral Methylbenzylpyridinium-Based Organic–Inorganic Lead Halides for Water-Resistant Photoluminescence Materials. *Inorg. Chem.* **2025**. https://doi.org/10.1021/acs.inorgchem.4c04989.
2. Chandra Patra, B., Wan, R., Moore, C. E., & Wu, Y. (2024). Impact of Dihedral Angle in Conjugated Organic Cation on the Structures and Properties of Organic-Inorganic Lead Iodides. *Chemistry – A European Journal*, *n/a*(n/a), e202402535. https://doi.org/https://doi.org/10.1002/chem.202402535.
3. Lyu, R., Wan, R., Moore, C. E., & Wu, Y. (2024). Chiral Viologen-Derived Water-Stable Small Band Gap Lead Halides: Synthesis, Characterization, and Optical Properties. *Inorganic Chemistry*, *63*(13), 5885–5896. https://doi.org/10.1021/acs.inorgchem.3c04413.

4. Shao, J., Ao, H., Qin, L., Elgin, J., Moore, C. E., Khalifa, Y., Zhang, S., & Wu, Y. (2023). Design and Synthesis of Cubic K3-2xBaxSbSe4 Solid Electrolytes for K-O2 Batteries. *Advanced Materials*, *n/a*(n/a), 2306809. https://doi.org/https://doi.org/10.1002/adma.202306809.
5. Lyu, R., Cui, Z., Elgin, J., Co, A. C., & Wu, Y. (2023). Photoelectrochemistry of Methylviologen Lead Iodide: Achieving Stability inside a Polar Solvent. *The Journal of Physical Chemistry C*, *127*(32), 15852–15860. https://doi.org/10.1021/acs.jpcc.3c04054.
6. Qin, L., Ao, H., & Wu, Y. (2024). Feasibility of achieving two-electron K–O2 batteries. *Faraday Discuss.*, *248*(0), 60–74. https://doi.org/10.1039/D3FD00085K.
7. Wan, R., Lyu, R., Moore, C. E., & Wu, Y. (2023). Toward Understanding the Composition–Structure Relationship of Hybrid Organic Lead Iodide Compounds: Impact from Secondary Structures of Organic Cations. *The Journal of Physical Chemistry C*, *127*(18), 8880–8886. https://doi.org/10.1021/acs.jpcc.3c01260.
8. Qin, L., Schkeryantz, L., & Wu, Y. (2023). Designing High-Donicity Anions for Rechargeable Potassium Superoxide/Peroxide Batteries. *Angewandte Chemie International Edition*, *n/a*(n/a), e202213996. https://doi.org/https://doi.org/10.1002/anie.202213996.
9. Schkeryantz, L., Nguyen, P., McCulloch, W. D., Moore, C. E., Lau, K. C., & Wu, Y. (2022). K+ Single Cation Ionic Liquids Electrolytes with Low Melting Asymmetric Salt. *The Journal of Physical Chemistry C*, *126*(27), 11407–11413. https://doi.org/10.1021/acs.jpcc.2c03030.
10. Chen, X., Qin, L., Sun, J., Zhang, S., Xiao, D., & Wu, Y. (2022). Phase Transfer-Mediated Degradation of Ether-Based Localized High-Concentration Electrolytes in Alkali Metal Batteries. *Angewandte Chemie International Edition*, *61*(33), e202207018. https://doi.org/https://doi.org/10.1002/anie.202207018.
11. Shao, J., Zheng, J., Qin, L., Zhang, S., Ren, Y., & Wu, Y. (2022). K3SbS4 as a Potassium Superionic Conductor with Low Activation Energy for K–S Batteries. *Angewandte Chemie - International Edition*, e202200606. https://doi.org/10.1002/anie.202200606.

Elucidating Chirality-induced Magnetism and Magnetoelectric Functionalities in Layered Chiral Hybrid Metal Halide Perovskites

Dali Sun, Department of Physics, North Carolina State University
Keywords: Chiral materials, chirality-induced spin selectivity, chiral phonons, magnetism, ferromagnetic resonance, magneto-optical Kerr effect.

Research Scope

2D layered Hybrid Metal Halides (2D-HMHs) are a new class of synthetic semiconductors prepared by low-temperature solution processing with a large chemical and structural 'universe' benefiting from their synthetic versatility. By implanting chiral organic cations into the HMH superstructure, the 2D-chiral-HMH would simultaneously exhibit ferromagnetic, ferroelectric, and magnetoelectric functionalities stemming from a Chirality-Induced Spin Selectivity (CISS) effect that may not be subject to thermal fluctuations. The goal of this program is to elucidate the fundamental origins of chirality-induced magnetism via the CISS effect and electrical control in hybrid chiral materials. To date, we focused our efforts on developing a suite of sensitive detection themes based on spin-orbitronics, ferromagnetic resonance, and magneto-optics to probe the CISS-induced spin transport and magnetoelectric functionalities in hybrid materials.

Recent Progress

[1] "Colossal anisotropic absorption of spin currents induced by chirality" – *Probing chirality-induced spin polarization in chiral materials upon pure spin current excitation.*

The CISS effect, which relates the electron's spin to the chirality of material structure, is of profound importance in contemporary scientific research [1]. This captivating phenomenon, where structural chirality dictates the preference for one electron spin orientation over another, represents a crucial bridge between seemingly disparate realms: the intricacies of quantum spin behavior and the tangible world of non-magnetic chiral materials and devices. Harnessing this fascinating phenomenon and demonstrating the rich interplay of chirality and spin in a variety of emerging chiral semiconductors promises to reveal novel chirality-enabled spin transport properties, paving a new pathway for next-generation, low-power spintronic applications.

Recently, a rapidly rising topic about **anisotropic damping factors** in the field of spintronics has become compelling. The damping factor in a ferromagnet is the most crucial aspect of understanding the spin transport and absorption properties adjacent to non-magnetic materials; and for designing efficient spin transfer torque devices. One key aspect of anisotropic damping is its role in tailoring magnetic switching speeds at which magnetic dynamics of the ferromagnet can be actively controlled [2]. Until now, due to stringent requirements of high-quality, single-crystal epitaxial growth of ferromagnet layers on crystal substrates, the observation of anisotropic damping has been restricted to a few magnetic materials.

CISS implies that the spin preference of chiral structures persists upon injection of pure spin currents and can act as a spin analyzer without the need for a ferromagnet. Here we demonstrate the emergence of **exceedingly large, colossal anisotropic non-local Gilbert**

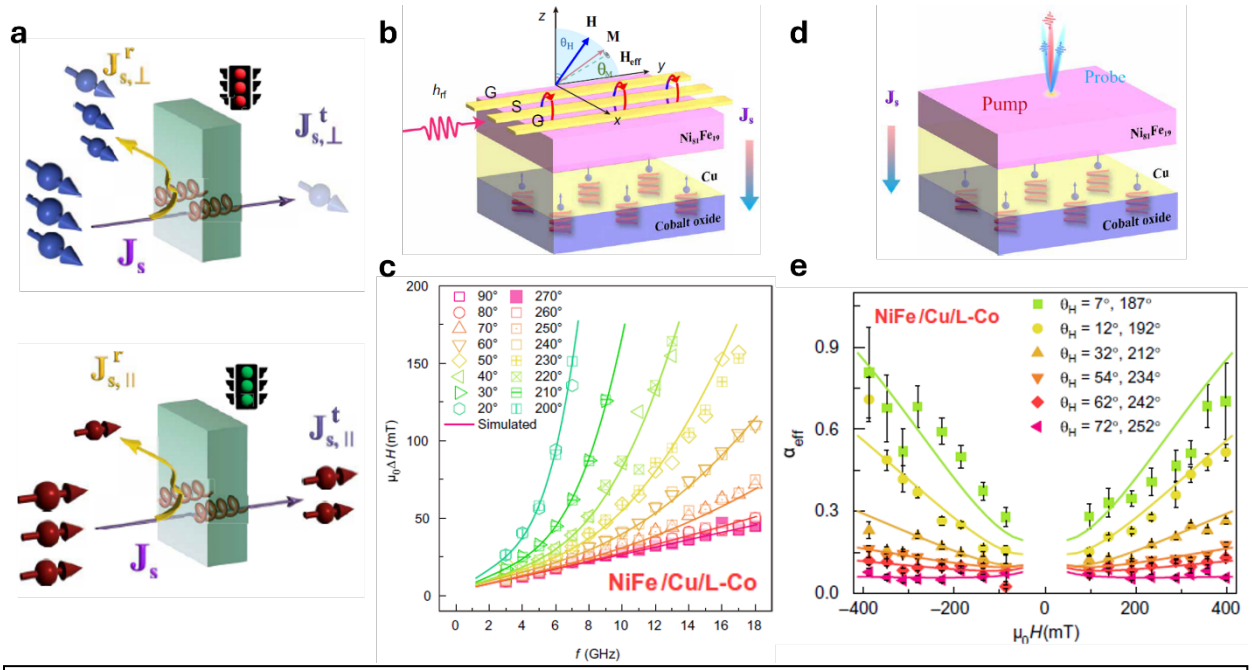

Figure 1. **(a)** Schematics of the colossal anisotropic spin absorption in chiral materials. In a chiral material, injected spin current $\mathbf{J_s}$ flows along the direction of the material's chiral axis. The transmission of $\mathbf{J_s}$ through the interface with spin polarization parallel to the material's chiral axis is greatly enhanced (green traffic light) compared to that with spin polarization perpendicular to the chiral axis (red traffic light), resembling a 'chiral gateway' for spin current transport. **(b)** Schematic of the spin current transport in chiral channel characterized by ferromagnetic resonance measurement. A pure spin current diffuses from the FM, through the Cu layer, and then into the chiral metal oxide. **(c)** Field angle θ_H and frequency dependence of linewidth for NiFe/Cu/L-CuOx. The derived damping factor significantly increases and exhibits a nonlinear behavior when the field angle is rotated toward the chiral axis of L-CoOx. **(d)** Schematic diagram of the spin current transport in chiral channel characterized by the pump-probe time-resolved magnetic-optical Kerr effect (TR-MOKE) technique. (e) The extracted effective damping factor α_{eff} as a function of $\pm H$ at varied field angle θ_H, showing a similar nonlinear response as that in the FMR measurements. Reproduced from Science Advances **10**, adn3240 (2024).

damping factors (experimental value of ~1000% and theoretical value of ~ 3000%) in ferromagnet/chiral metal oxide (chiral-CuO_x) heterostructures, a phenomenon that is absent in the achiral counterpart. We find that the Gilbert damping in a chiral cobalt oxide film exhibits a maximum (minimum) value when the direction of the spin polarization is parallel (perpendicular) to the chiral axis (**Fig. 1a**), whereas an achiral analog of the cobalt oxide film shows isotropic damping. By rotating the magnetization orientation of the FM from the in-plane to the out-of-plane direction, a twofold symmetry of the anisotropic damping manifests and displays a maximum-minimum ratio of ten times (**Fig. 1b-e**). The substantial tunability of the non-local damping factor heralds a paradigm shift in design strategies for improving the performance of spin devices, i.e., faster magnetic switching and larger spin injection efficiency for spin field effect transistors, and terahertz emitters, among others.

A similar concept has been readily applied to the CISS effect in chiral-HMH thin films. Layered-HMH systems provide a unique platform for exploiting chirality-related phenomena due to their ordered, tunable, and diverse structures, which can be engineered for the desired broken symmetry and/or chirality. While the CISS effect has been successfully demonstrated in a variety of chiral-HMH films, the key question is which structural asymmetry (i.e., chirality) directly contributes to the CISS: is from the chiral center of organic cations or the crystal space group

formed by the tilted metal halide octahedral? Here, we seek to address this fundamental question via precise control over chirality and pure spin absorption in selected HOISs. We designed a set of zero-dimensional (0D) HOIS materials: [*S*-MBA]$_4$Bi$_2$Cl$_{10}$ and [*R*-MBA]$_4$Bi$_2$Cl$_{10}$, where MBA is α-methylbenzylammonium. These hybrid solids feature a unique orthogonal alignment between the local chiral axis of individual organic chiral cations and the global screw axis of the entire crystal lattice (**Fig. 2a**). This decoupling of local chiral axis and global screw axis provides an opportunity to disentangle the contributions of the distinct mechanisms responsible for the observed spin absorption behavior. To quantify the chirality-induced anisotropic spin absorption, following our previous approaches, the FMR technique is applied, where externally excited angular momentum is transferred from a FM layer to an adjacent chiral-HMH film. When an enhanced spin absorption in the HMH occurs, the non-local Gilbert damping factor increases which can be directly probed by the linewidth of the FMR peak. By controlling the polarization of the injected spin using an external magnetic field, we studied the anisotropic spin absorption in these heterostructures. We observed a greatly enhanced spin absorption across both the NiFe/Cu/(S/R)-HMH samples. The derived damping factor exhibits a strong non-linear behavior when the spin polarization is tilted towards the chiral axis of the organic cations (i.e., further away from the in-plane screw axis direction) and a stronger damping factor is detected (**Fig. 2c-d**). These findings highlight the critical role of chiral organic cations in the anisotropic spin absorption, driven by their direct interaction with spins, as corroborated by the symmetry analysis for the chiral-HMH structure using continuous chirality measures calculations.

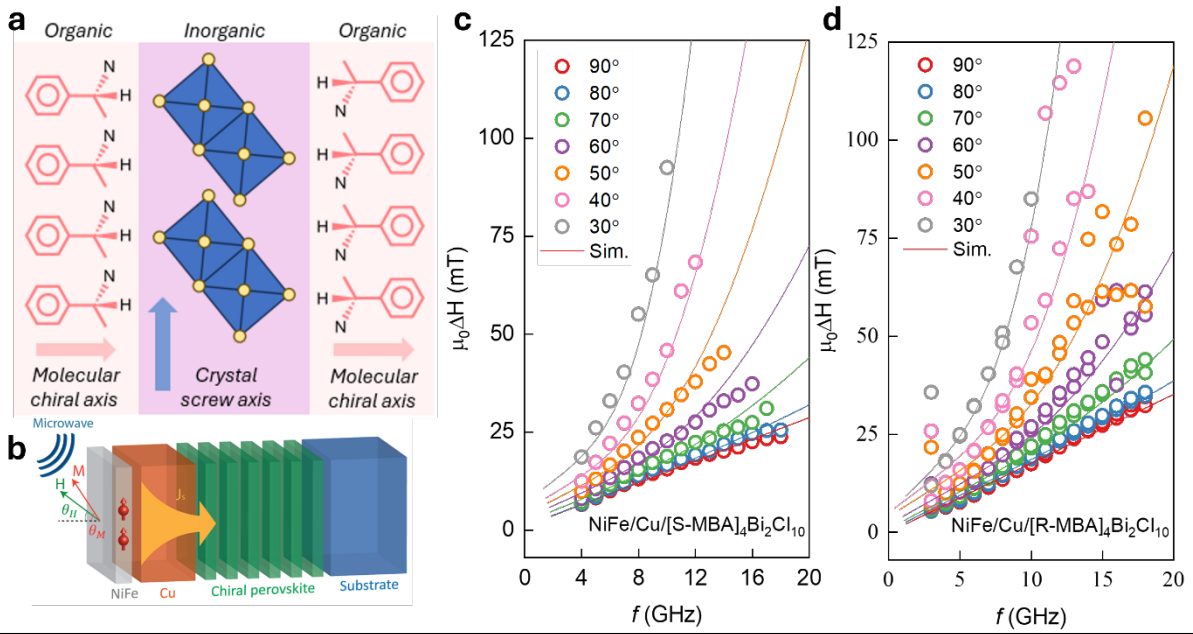

Figure 2. **(a)** Schematic of the zero-dimensional (MBA)$_4$Bi$_2$Cl$_{10}$ HOIS with non-collinear chiral and screw axes. The vertical direction of the schematic diagram is in-plane direction, and the horizontal one is out-of-plane. The $P2_1$ (MBA)$_4$Bi$_2$Cl$_{10}$ HOIS crystal possesses a single in-plane screw axis, whereas the chiral organic cation exhibits a spatially non-collinear chiral axis relative to this screw axis. **(b)** Schematic illustration of the anisotropic spin absorption in NiFe/Cu/chiral-HMH heterostructures measured by FMR. **(c-d)** Field angle θ_H and frequency dependence of linewidth for NiFe/Cu/[*S*-MBA]$_4$Bi$_2$Cl$_{10}$ and NiFe/Cu/[*R*-MBA]$_4$Bi$_2$Cl$_{10}$, respectively. The derived damping factor significantly increases and exhibits a nonlinear behavior when the field angle is rotated toward the chiral axis of organic cations instead of the screw of axis, indicating the chiral organic cations plays the dominant role in determining anisotropic spin absorption.

[2] "Giant interfacial spin Hall angle from Rashba-Edelstein effect revealed by the spin Hall Hanle process" – *Observation of interfacial Rashba effect at the interface of multiferroics/heavy metal heterostructure using developed spin Hall Hanle effect technique.*

Spin-Hall Hanle effect (SHHE) [3] is utilized to study the spin accumulation at the Pt/ferroelectric interface due to the Rashba–Edelstein (REE) effect, where the ferroelectrics are hexagonal ferrites and manganites. We demonstrate REE at Pt/ferroelectric interfaces by showing a positive correlation between polarization and spin Hall angle in the recently elucidated SHHE, in which a Larmor precession of spin polarization in a diffusion process from the interface manifests as magnetoresistance and Hall effect. We show that REE leads to a large enhancement of the effective spin Hall angle of ferroelectric interface Pt/h−$LuFeO_3$, without obvious differences in the spin relaxation time. Our results demonstrate that a ferroelectric interface can produce large spin-charge conversion and that SHHEs are a sensitive tool for characterizing interfacial spin-transport properties. The successful demonstration of giant spin Hall angle from this Rashba effect offers a reliable characterization tool for probing the chirality-induced Rashba/Dresselhaus effect in various chiral insulators/semiconductors.

Future Plans

This is the last year of the grant. Supported by this grant, our group intensively investigated the origins of the CISS effect in layered-HMHs which can be strongly correlated to the presence of chiral phonons. For the first time, we successfully demonstrated the chiral-phonon-activated spin Seebeck (CPASS) effect in chiral-HMH thin films, showing that the conversion angular momentum of chiral phonons into the spin current in the adjacent metallic layer when the heterostructure is subjected to a temperature gradient. Utilizing pure spin current injection produced by ferromagnetic resonance, we reported an anomalous spin current absorption in chiral metal oxides that manifests a colossal anisotropic nonlocal Gilbert damping with a maximum-to-minimum ratio of up to 1000% as well as in the chiral-HMHs. In addition, we showed that the Dzyaloshinskii–Moriya-Interaction (DMI), a chiral antisymmetric interaction that occurs in magnetic systems with low symmetry, can induce hybrid magnonics between two parities. We reported that layered HMH antiferromagnets with an interlayer DMI can lead to a strong intrinsic magnon-magnon coupling strength up to 0.24 GHz. For the continuing of the grant, we will aim to unveil the interplays of spin current, phonon magnetic moment, and chiral phonons in chiral materials with a broken mirror and inversion symmetry including chiral-HMHS, insulators, and multiferroics using the developed electrical and magnet-optics detection themes, fostering groundbreaking research about the generation of spin information from chiral phonons by harnessing thermal energy and structural asymmetry.

References

1. R. Naaman, Y. Paltiel, D. H. Waldeck, *Chiral molecules and the electron spin*. Nat. Rev.Chem. **3**, 250 (2019).

2. L. Chen, S. Mankovsky, S. Wimmer, M. A. W. Schoen, H. S. Körner, M. Kronseder, D. Schuh, D. Bougeard, H. Ebert, D. Weiss, C. H. Back, *Emergence of anisotropic Gilbert damping in ultrathin Fe layers on GaAs(001).* Nat. Phys. **14**, 490–494 (2018).

3. J. Li, A. H. Comstock, D. Sun, and X. Xu, *Comprehensive Demonstration of Spin Hall Hanle Effects in Epitaxial Pt Thin Films*, Phys. Rev. B **106**, 184420 (2022).

2-year publication list supported by this grant

1. J. Li, A. H. Comstock, A. McConnell, X. Li, Y. Yun, D. Sun, and X. Xu, *Giant Interfacial Spin Hall Angle from Rashba-Edelstein Effect Revealed by the Spin Hall Hanle Process*, Phys. Rev. B **108**, L241403 (2023).
2. J. R. Frick, S. Sridhar, A. Khansari, A. H. Comstock, E. Norman, S. O'Donnell, P. A. Maggard, D. Sun, and D. B. Dougherty, *Spreading Resistance Effects in Tunneling Spectroscopy of α-RuCl3 and Ir0.5Ru0.5Cl3*, Phys. Rev. B **108**, 245410 (2023).
3. Y. Li, T. Draher, A. H. Comstock, Y. Xiong, M. A. Haque, E. Easy, J.-C. Qian, T. Polakovic, J. E. Pearson, R. Divan, J.-M. Zuo, X. Zhang, U. Welp, W.-K. Kwok, A. Hoffmann, J. M. Luther, M. C. Beard, D. Sun, W. Zhang, and V. Novosad, *Probing Intrinsic Magnon Bandgap in a Layered Hybrid Perovskite Antiferromagnet by a Superconducting Resonator*, Phys. Rev. Res. **5**, 043031 (2023).
4. A. Negi, A. Rodriguez, X. Zhang, A. H. Comstock, C. Yang, D. Sun, X. Jiang, D. Kumah, M. Hu, and J. Liu, *Thickness-Dependent Thermal Conductivity and Phonon Mean Free Path Distribution in Single-Crystalline Barium Titanate*, Adv. Sci. **10**, 2301273 (2023).
5. Y. Xiong, A. Christy, Y. Dong, A. H. Comstock, D. Sun, Y. Li, J. F. Cahoon, B. Yang, and W. Zhang, *Combinatorial Split-Ring and Spiral Metaresonator for Efficient Magnon-Photon Coupling*, Phys. Rev. Appl. **21**, 034034 (2024).
6. A. Negi, L. Yan, C. Yang, Y. Yu, D. Kim, S. Mukherjee, A. H. Comstock, S. Raza, Z. Wang, D. Sun, H. Ade, Q. Tu, W. You, and J. Liu, *Anomalous Correlation between Thermal Conductivity and Elastic Modulus in Two-Dimensional Hybrid Metal Halide Perovskites*, ACS Nano **18**, 14218 (2024).
7. R. Sun, Z. Wang, B. P. Bloom, A. H. Comstock, C. Yang, A. McConnell, C. Clever, M. Molitoris, D. Lamont, Z.-H. Cheng, Z. Yuan, W. Zhang, A. Hoffmann, J. Liu, D. H. Waldeck, and D. Sun, *Colossal Anisotropic Absorption of Spin Currents Induced by Chirality*, Sci. Adv. **10**, adn3240 (2024).
8. R. Sun, K. S. Park, A. H. Comstock, A. McConnell, Y.-C. Chen, P. Zhang, D. Beratan, W. You, A. Hoffmann, Z.-G. Yu, Y. Diao, and D. Sun, *Inverse Chirality-Induced Spin Selectivity Effect in Chiral Assemblies of π-Conjugated Polymers*, Nat. Mater. **23**, 782 (2024).
9. S. Chen, Z. Tang, M. Fang, R. Sun, X. Zhang, L. Xiao, S. S. Mohajerani, N. Liu, Y. Zhang, A. S. Sarkar, D. Sun, S. Strauf, and E. H. Yang, *Magnetic Switching in Monolayer 2D Diluted Magnetic Semiconductors via Spin-to-Spin Conversion*, Adv. Funct. Mater. 2418647 (2025).

Poster Sessions

Physical Behavior of Materials Principal Investigators' Meeting

Poster Session I

Wednesday, May 21, 2025

1. **Materials, Physics, and Nanostructures for Next Generation Spintronics**

   Chia-Ling Chien, Johns Hopkins University

2. **Phase Transitions in Mesoscopic Systems**

   Raymond Orbach, University of Texas

3. **Quantum Metamaterials**

   David Awschalom, Argonne National Laboratory

4. **Digital Synthesis: A Pathway to Create and Control Novel States of Condensed Matter**

   Anand Bhattacharya, Argonne National Laboratory

5. **Characterization of Functional Nanomachines**

   Michael Crommie, Lawrence Berkeley National Laboratory

6. **A Nonlinear Approach to Weyl Transport**

   Kenneth Burch, Boston College

7. **Measurement of Near-Field Thermal Radiation Between Flat Surfaces with a Nanogap**
   Zhoumin Zhang, Georgia Institute of Technology

8. **Excitons in Low-Dimensional Perovskites**
   William Tisdale, Massachusetts Institute of Technology

9. **Microscopic understanding of thin film growth and substrate engineering of organic charge transfer complexes**
   Pengpeng Zhang, Michigan State University

10. **Probing local, hybrid perovskite photophysics through spatially- and temporally-resolved absorption/emission microscopy**
    Masaru Kuno, University of Notre Dame

11. **Nanocrystal-Based Dyads for Solar to Electric Energy Conversion**
    David Beratan, Duke University

12. **Exploring the Impact of the Local Environment on Charge Transfer States at Molecular Donor-Acceptor Heterojunctions**
    Noel Giebink, University of Michigan

13. **Spin Transport in group IV materials and 2D membranes**
    Hanan Dery, University of Rochester

14. **Spin Functionality Through Complex Oxide Heteroepitaxy**
    Yuri Suzuki, Stanford University

15. **Tunable Excitons and Pseudospins in Transition Metal Dichalcogenide Homobilayers**
    Elaine Li, University of Texas

16. **Construction and Quantum States of Single and Yin-Yang Flat Bands**
    Feng Liu, University of Utah

17. **The synthesis 2D Janus vdW crystals and novel quantum phenomena arising from mirror-symmetry breaking**
    Sefaattin Tongay, Arizona State University

18. **Electron transfer in heterostructures based on two-dimensional materials**
    Hui Zhao, University of Kansas

19. **Mid-Infrared Colloidal Quantum Dots LEDs**
    Philippe Guyot-Sionnest, University of Chicago

20. **Intrinsic charge transport and photoconducting properties of single crystalline halide perovskites**
    Vitaly Podzorov, Rutgers University

21. **Overcoming optical selection rules in materials by extreme localization of light**
    Hayk Harutyunyan, Emory University

22. **Many-Body Localization Phenomena in Nonlinear Photonic Synthetic Lattices**
    Mercedeh Khajavikhan, University of Southern California

23. **Colloidal Group III-Nitride Quantum Dots for Optoelectronic and Photocatalytic Applications**
    Dimitri Talapin, University of Chicago

24. **Quantum Rydberg Photonics**
    Hadiseh Alaeian, Purdue University

25. **Light-Matter Quantum Control: Coherence and Dynamics**
    Jiang Wang, Ames National Laboratory

26. **Metamaterials**
    Thomas Koischny, Ames National Laboratory

Physical Behavior of Materials Principal Investigators' Meeting

Poster Session II

Thursday, May 22, 2025

1. **Design, synthesis, and atomic scale characterization of rare-earth based supramolecular nanographene and nanoribbons**
   Saw Hla, Argonne National Laboratory
2. **Fundamentals of Semiconductor Nanowires**
   Peidong Yang, Lawrence Berkeley National Laboratory
3. **Disorder in Topological Semimetals**
   Kirstin Alberi, National Renewable Energy Laboratory
4. **Light-matter interaction phenomena using subwavelength engineering of material properties**
   Igal Brener, Sandia National Laboratory
5. **Study of Materials and Interface Properties for High-Efficiency Spin Injection**
   Jing Shi, University of California, Riverside
6. **The origin of hysteresis in phase transformation materials**
   Ananya Renuka Balakrishna, University of California, Santa Barbara
7. **Nanostructured Colloidal Self-assembly and Controlled Alignment of Anisotropic Nanoparticles**
   Ivan I. Smalyukh, University of Colorado
8. **Extreme Thermoelectric Behavior in Low-Dimensional Oxide Conductors**
   Joshua Cohn, University of Miami
9. **Properties, Electrochemical Activity, and Stability of Solid Oxide Cell Materials Under Extreme Conditions**
   Scott Barnett, Northwestern University
10. **Magnetization Dynamics and Cooperative Phenomena in Charge and Spin Frustrated Correlated Electron Materials**
    Hariharan Srikanth, University of South Florida
11. **Understanding Compound Phase Transitions in New Heusler Alloy Colossal Magnetocaloric Materials**
    Shane Stadler, Louisiana State University
12. **Optical, Electrical and Magnetic Studies of Hybrid Organic-Inorganic Perovskite Semiconductors**
    Valy Verdeny, University of Utah
13. **Super-Ionic Clusters - Structure, Stability, and Energy Applications**
    Puru Jena, Virginia Commonwealth University

14. **Singlet and Triplet Exciton Interaction and Dynamics in Molecular Crystals**
    Ivan Biaggio, Lehigh University

15. **Weyl Semimetals for High-Thermopower Transverse Thermoelectric Transport**
    Sarah Watzman, University of Cincinnati

16. **Molecular Heterogeneous Multiferroics**
    Shenqiang Ren, State University of New York, Univsersity at Buffalo

17. **Exploring Nonlinear Electrodynamics in Layered Topological Semimetals at Radio Frequencies**
    Ying Wang, University of Wisconsin

18. **EPSCOR Early Career: Forecasting Thermoelectric Performance in 2D Metal-Organic Frameworks Through Ab Initio Atomistic Modeling**
    Laura de Sousa Oliveira, University of Wyoming

19. **Understanding Unique Shallow-trap Physics in Metal Halide Perovskites**
    Jingsong Huang, University of North Carolina, Chapel Hill

20. **Understanding and Controlling Light and Spin Dynamics in Chiral Hybrid Semiconductors**
    Lina Quan, Virginia Polytechnic State University

21. **Sub-Terahertz to Terahertz Metamaterial Coatings for Blackbody Radiation Shielding of Quantum Circuitry**
    Fatima Toor, University of Iowa

22. **RENEW 23, Building a Diverse Workforce in Nanomaterial Characterization and Solid-State Chemistry Sheena M. Reeves, Associate Professor and Interim Head of Chemical Engineering**
    Sheena Reeves, Texas A&M University, Prairie View

23. **Vortex Light-driven Structured Quantum Matter**
    Mahmoud M. Asmar, Kennesaw State University

24. **Enabling Reversible Hydrogen Storage and Transfer with Graphene-based Carbon–Boron–Nitrogen Materials**
    Zbynek Novotny, Pacific Northwest National Laboratory

25. **Uncovering and Surmounting Loss Mechanisms in Nitride Light Emitters**
    Chris Van de Walle, University of California, Santa Barbara

26. **Understanding the role of chemical pressure on thermal expansion tunability in earthabundant materials**
    Joya Cooley, California State University, Fullerton

27. **Nanophotonics-Enhanced Solar Cells**
    Shanhui Fan, Stanford University

Poster

Abstracts

Quantum Rydberg Photonics

PI: Dr. Hadiseh Alaeian, Purdue University

Co-PI: Dr. Alexandra Boltasseva, Purdue University

Co-PI: Dr. Vladimir M. Shalaev, Purdue University

Keywords: Quantum Nonlinear Photonics, Rydberg Excitons, Long-Range Interactions, Blockade Physics, Single-Photon Nonlinearity

Research Scope

This project addresses a fundamental challenge in quantum photonics: realizing robust photon-photon interactions at the single-photon level in a scalable and integrated platform. We propose to pioneer a novel *Rydberg Quantum Nanophotonics* architecture by harnessing the unique properties of Rydberg excitons in cuprous oxide (Cu_2O) thin films and microcrystals. These strongly interacting quasiparticles, recently observed in Cu_2O [1], offer a powerful route to achieving single-photon nonlinearities [2],[3]. By merging the precise control and scalability of nanophotonics with the extraordinary quantum properties of Rydberg states, this platform opens new pathways for manipulating light at the quantum level. A key goal is to develop a CMOS-compatible growth technique for Cu_2O, enabling the fabrication of thin films and microstructures with high optical quality and tunable Rydberg levels [4],[5]. Using advanced optical spectroscopy, we will probe the energy structure, coherence, and lifetimes of these excitonic states while exploring their coupling to engineered plasmonic nanostructures and photonic cavities. Time-resolved and quantum correlation measurements will provide insight into the interaction dynamics, coherence properties, and nonlinear response of the system. Ultimately, we aim to establish a scalable, integrated Rydberg photonic platform by interfacing Rydberg excitons in Cu_2O with custom-designed nanophotonic waveguides. This effort will illuminate the fundamental physics of hybrid Rydberg-nanophotonic systems and lay the groundwork for on-chip quantum nonlinear optics and scalable photonic quantum technologies.

Recent Progress

Since the start of the project, we have worked on the development of a site-controlled technique to grow Cu_2O disks and thin films in a two-dimensional array and on SiN nano-photonic waveguides, respectively [1]. **Figure 1** shows the results of an array of Cu_2O disks grown using the bottom-up growth technique. The averaged photoluminescence spectrum of many sites indicates the consistent emergence of Rydberg excitons up to $n = 6$. This research, supported by this award, presents the first report on the bottom-up fabrication of Cu_2O arrays, which would make the precursor of several follow-on studies, including quantum simulation of driven-dissipative lattice models with long-range interactions and optimization of graph problems.

Besides, in a recent theoretical work, we put forward a proposal for realizing collective quantum effects, including superradiance, when the atom-light interaction is extended beyond the linear

single-photon excitation [2]. These results apply to many experimental platforms, including dark excitons in Cu_2O and other excitonic systems, as well as other quantum emitters.

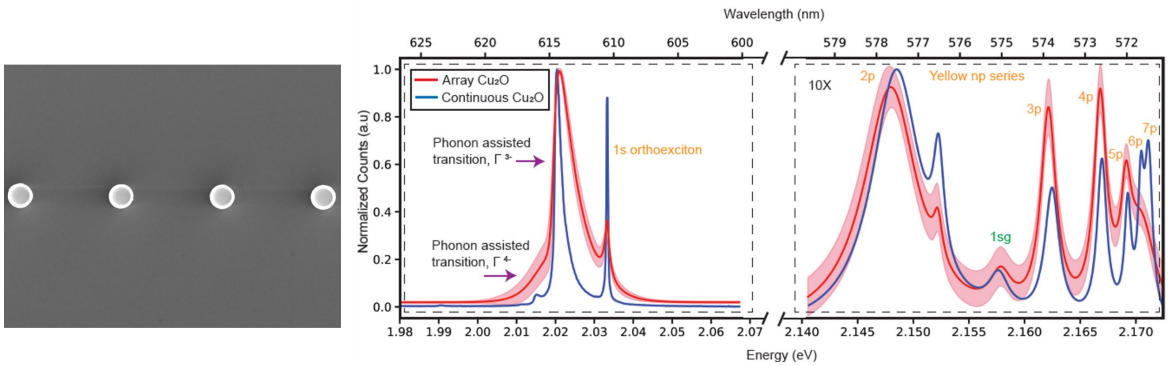

Figure 1. (left) Site-controlled growth of 2D arrays of Cu_2O disks. (right) The averaged photoluminescence spectrum of disks (red lines) shows the consistent emergence of Rydberg excitons in each site. Solid blue lines are the film spectrum for comparison. The figure is from a recently published paper by the team [1].

Future Plans

The team is currently working on the first proposed Rydberg photonic device, i.e., SiN waveguide-coupled Cu_2O films with pre-defined regions of interest as depicted in **Figure 2**. We are working on the non-resonant photoluminescence spectroscopy of the sample to study the coupling of Rydberg excitons to the waveguide by directly illuminating the grown film. The next step is the excitation of Rydberg excitons via direct coupling to the waveguide, which includes both the non-resonant as well as resonant excitations of Rydberg excitons. We will do systematic spectroscopy for various excitation powers and different Rydberg states to study the interaction and ultimately the blockade through lineshift and saturation. To clearly prove the emergence of the blockade, we will conclude this phase by performing photon correlation measurements via a Hanbury-Brown Twiss setup. This will make the first-ever study of interactions and correlation measurements for Rydberg excitons in Cu_2O.

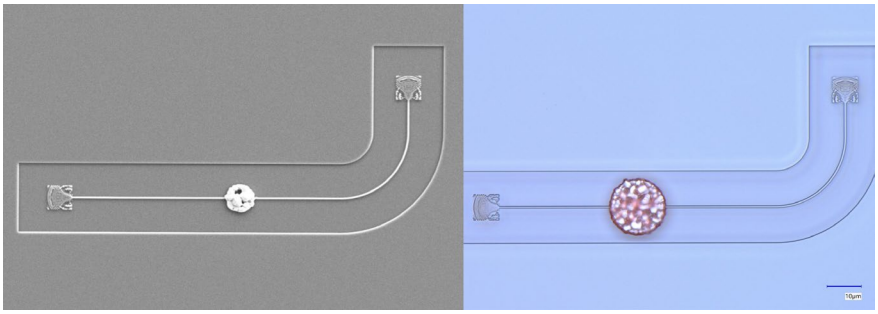

Figure 2. (left) Scanning electron micrograph (SEM) and (right) optical image of the SiN waveguide with the site-selective grown Cu_2O film, i.e. the circular region in the middle.

References

[1] T. Kazimierczuk, D. Fröhlich, S. Scheel, and M. Bayer, *Giant Rydberg excitons in copper oxide Cu_2O*, Nature **514**, 343-347 (2014)

[2] V. Walther, S. O. Krüger, S. Scheel, and T. Pohl, *Interaction between Rydberg excitons in Cu_2O*, Phys. Rev. B **98**, 165201 (2018)

[3] V. Walther, R. Johne, and T. Pohl, *Giant optical nonlinearities from Rydberg excitons in semiconductor microcavities*, Nat. Commun. **9**, 1309 (2018)

[4] S. Steinhauer et al, *Rydberg excitons Cu2O microcrystals grown on a silicon platform*, Commun. Mater. **1**, 11 (2020)

[5] J. DeLange, K. Barua, A. Sundar Paul, H. Ohadi, V. Zwiller, S. Steinhauer, and H. Alaeian, *Highly-Excited Rydberg Excitons in Synthetic Thin-Film Cuprous Oxide*, Sci. Rep. **13**, 16881 (2023)

Publications

[1] K. Barua, S. Peana, A. Deepak Keni, V. Mkhitaryan, V. Shalaev, Y. P. Chen, A. Boltasseva, and H. Alaeian, *Bottom-up Fabrication of 2D Rydberg Exciton Arrays in Cuprous Oxide*, Commun. Mater. **6**, 21 (2025)

[2] A. J. Shah, P. Kirton, S. Felicetti, and H. Alaeian, *Dissipative phase transitions in two-photon Dicke model*, arXiv: **2412.14271** (2024) (https://arxiv.org/abs/2412.14271)

Disorder in Topological Semimetals

Kirstin Alberi[1], Anthony Rice[1], Stephan Lany[1], Mark van Schilfgaarde[1], and Daniel Dessau[2]
[1]National Renewable Energy Laboratory, [2]University of Colorado, Boulder

Keywords: Topological semimetal, electrical transport, disorder

Research Scope

Three dimensional topological semimetals (TSMs) offer exciting opportunities for harnessing new properties and phenomena for the next generation of energy-relevant technologies. Key among them is the potential for widely varying electron charge and spin transport behavior. The expressed properties are strongly tied to the underlying topological phase. Disorder can influence both, representing a variable for intentional tunability as well as a source of unintended effects. However, the roles of disorder are still not well understood. Our goal is to uncover the complex relationships between TSM behavior and disorder. We probe these relationships by controllably introducing defects, impurities and interfaces in epitaxially-grown topological thin films. Our hypothesis is that deliberate manipulation of these forms of disorder will allow us to tune the topological phase and select the material properties.

Recent Progress

Our group studies the role of disorder by intentionally varying it in model Dirac semimetal Cd_3As_2 and Weyl semimetal TaAs thin films grown by molecular beam epitaxy (MBE). Here, we highlight a few of the latest results centers on the mechanisms by which disorder influences carrier transport, the Fermi level, and the topological phase.

Influence of disorder in observing quantum Hall effects in TSMs

Coulomb disorder is one of the greatest determining factors of magnetotransport behavior in TSMs. When screened in the presence of high carrier concentrations typically found in many of these materials, Coulomb disorder introduced by charged point defects leads to linear, non-saturating magnetoresistance (MR), as described by the guiding center diffusion model [1]. Moving the Fermi level, E_F, toward the Dirac point in a simple Dirac semimetal has the potential to shift the magnetotransport in two ways: 1) a transition from weak to strong Coulomb disorder through reduced screening will cause charge puddling and a smearing of E_F, and 2) decreasing the carrier concentration will lower the magnetic field at which the onset of the quantum limit occurs, opening the door for the observation of effects such as the 3D quasi-quantum Hall effect (QQHE). Through our ability to reduce the electron concentration in Cd_3As_2 to $< 10^{17}$ cm^{-3}, we have now observed the competing effects between the 3D QQHE and strong electron scattering via Coulomb

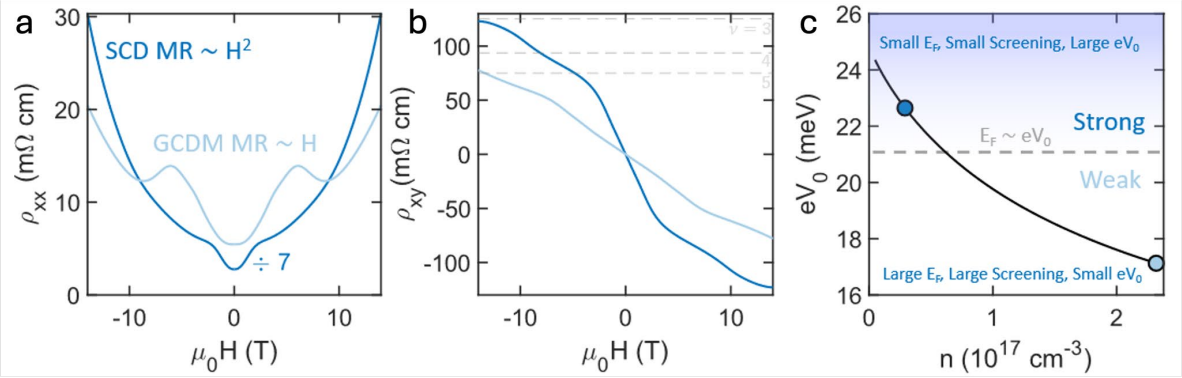

Figure 1. Coulomb disorder drives magnetotransport in semimetals. 2 K a) longitudinal resistivity for high and low carrier density Cd_3As_2 (light and dark, respectively) can be described as a superposition of quantum oscillations (QO) and a disorder-dependent background. The magnitude of the low-density dark trace has been scaled down by 7. At high densities, clear quantum oscillations sit atop a linear magnetoresistance (MR). The guiding center diffusion model (GCDM) has been used to describe the origins of linear MR in many semimetals: charged point defects become screened yielding a smoothly varying disorder potential with magnitude eV_0 which scatters carriers. As the carrier density and chemical potential are reduced, the screening of charged point defects weakens, and the disorder potentials increases. In this strong Coulomb disorder regime (SCD), scattering from charged disorder changes and Landau levels become significantly broaden leading to smooth oscillations on a quadratic-like background. b) The corresponding Hall resistivity exhibits a distinct, step-like kink consistent with the 3D quasi-quantum Hall effect (QQHE) – an effect expected in many low-carrier density semimetals near their quantum limits. Dashed lines represent $1/\nu$ estimates for the low-density sample. Like the 2D quantum Hall effect, a scaling correspondence holds such that $\rho_{xx} \propto |H| \partial H \rho_{xy}$, less the Coulomb disorder dependent background. c) Calculated disorder potential magnitude as a function of carrier density for Cd_3As_2. Reduced densities lead to poor screening of charged defects and an increasing eV_0. The crossover from weak to strong Coulomb disorder occurs when $E_F \sim eV_0$ and results in a unique MR.

disorder [2]. Figure 1 shows (a) longitudinal and (b) Hall resistivity measurements of samples with higher and lower E_F. The bump and plateau-like features in them, respectively, for the sample with low E_F is indicative of the 3D QQHE. Figure 1c also shows regions of the carrier concentration (n) and Coulomb disorder potential (eV_0) where strong Coulomb disorder or the quasi-quantum Hall effect are more pronounced. These results indicate that the Fermi level and charge disorder must both be sufficiently low in gapless Dirac semimetals to observe the 3D QQHE. Importantly, these effects are not limited to Cd_3As_2 and should be accessible in a range of semimetal systems.

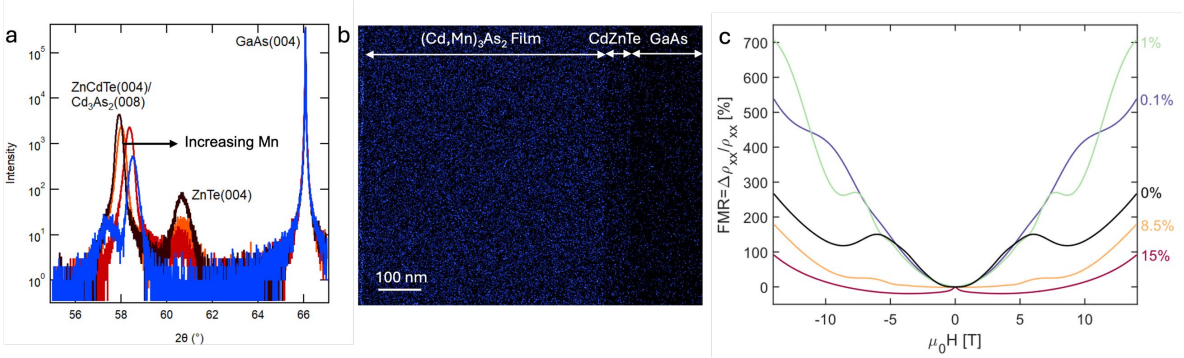

Figure 2. Mn incorporation into Cd_3As_2. a) X-ray diffraction traces of Cd_3As_2 thin films epitaxially grown on ZnCdTe buffer/GaAs (001) substrate structures as a function of Mn incorporation. The peak associated with the $(Cd,Mn)_3As_2$ film shifts to higher 2θ with increasing Mn concentration. b) Elemental map of Mn (in blue) in a $(Cd,Mn)_3As_2$ film grown on a CdZnTe/GaAs structure showing uniform Mn incorporation throughout the film thickness. c) Fractional longitudinal MR as a function of Mn concentration. The onset of distinctive shoulder-like features occurs at lower magnetic fields in samples with higher Mn concentrations (reminiscent of the features in Fig. 1a).

Role of magnetic impurities in the electronic structure and carrier transport in Dirac TSMs

Breaking time reversal symmetry in a Dirac TSM has the potential to transform it into a Weyl TSM. The addition of magnetic impurities is one route to incorporate an effective magnetic field to do so. We have explored the addition of Mn to Cd_3As_2 both computationally and experimentally. Quasi-particle *GW* (QSGW) *ab initio* electronic structure calculations suggest that substitutional incorporation of just a few percent Mn on Cd sites introduces a local moment capable of splitting the Dirac point into a pair of Weyl points displaced in both momentum and energy (see Fig. 2a,b) [3]. Experimentally, Mn is known to be challenging to incorporate in dilute amounts into semiconductors and semimetals. By growing Cd_3As_2 in the (001) orientation, with a higher surface energy, and using As-rich growth conditions to reduce competition between Cd and Mn for incorporation sites, we have been able to add Mn in concentrations up to > 10 at.% (see Fig. 2c,d). Interestingly, initial magnetoresistance measurements indicate that the quantum limit is reached in films with Mn at a lower applied magnetic field than those without Mn. These results are a potential sign that the external field is partially aligning the Mn moments, which then amplifies the overall effective field. Such an approach would allow the topological phase and electronic structure to be transformed dynamically. Further investigation is needed to fully understand the behavior and interaction of Mn in Cd_3As_2.

Getting to p-type doping in Cd_3As_2

The ability to adjust the Fermi level in TSMs opens up the possibility to access new physics that emerge when E_F resides very close to the Dirac or Weyl points, such as the 3D QQHE described above. Extrinsic dopants are a critical tool for directing E_F. Cd_3As_2 is always n-type as-synthesized, and identifying potential hole dopants would be one method for systematically moving E_F toward and even through the Dirac point. We performed a computational study of potential dopants through density functional theory (DFT) calculations, taking into account defect re-distribution as the chemical potentials change as a function of temperature. This capability allowed us to identify potential p-type doping strategies that involve growth at elevated temperatures and subsequent quenching. [4] This work identified potential p-type dopants, including Ge and Au, and we are now at the point of testing Ge doping via MBE growth. Isoelectronic Zn doping has been another route to lowering the carrier concentration in Cd_3As_2. We have spent some time building a DFT model that takes into account short-range ordering of Zn on several nonequivalent symmetry sites in the crystal. This model will aid further exploration of how the addition of isoelectronic Zn dopants influences point defects that determine the Fermi level.

Thin TaAs

While the properties of single crystal bulk Weyl semimetals have been studied in detail, significantly less attention has been paid to the properties of very thin films, where the surface states may dominate the transport properties. Through our ability to epitaxially grow thin films of Weyl semimetals, such as TaAs, we can more readily access and assess surface state transport. TaAs is highly p-type when grown in thin film form, resulting in relatively low mobilities. Signatures of weak antilocalization as a function of film thickness and the density of two-dimensional extended defects produces a picture of transport behavior. A higher density of extended defect boundaries results in a lower hole mobility, indicating that extended defects strongly impact carrier transport, even through surface states. A reduction in thickness below 11 nm also results in the reduction of the number of transport channels from two to one. This change may arise from the coupling of top and bottom surface states as they move closer together [5].

We are currently probing the electronic structure of these films via angle-resolved photoemission spectroscopy (ARPES). Measurements show close agreement between thicker films (>100nm) and single crystals previously reported in the literature. Upon decreasing thickness below ~10nm, a drastic change in Fermi surface connectedness occurs. High-symmetry spectra along X-G-X and M-G-M show some shared features between the bulk and ultrathin films, with the ultrathin films showing some new bands not seen in thicker films, which after comparison with slab-based DFT and bulk QSGW, appear to be of surface origin associated with As-terminated surface states. These finding will be important in guiding the potential use of Weyl semimetals for applications such as next generation interconnects in microelectronics.

Future Plans

Future work in this project will continue to focus on the impact and control of isoelectronic, charged and/or magnetic impurities on the electronic structure, Fermi level and transport behavior in TSMs, including Cd_3As_2 and TaAs as model systems. In particular, this work will include a greater exploration of the behavior of Mn in Cd_3As_2. We also plan to expand our investigation of disorder to carrier transport across interfaces between TSMs and other electronic materials, such as semiconductors and metals.

References

1. J.N. Nelson, I.A. Leahy, A.D. Rice, C. Brooks, G. Teeter, M. van Schilfgaarde, S. Lany, B. Fluegel, M. Lee and K. Alberi, *Direct link between disorder and magnetoresistance in topological semimetals*, Phys. Rev. B **107**, L220206 (2023)
2. I.A. Leahy, A.D. Rice, J.N. Nelson, H. Ness, M. van Schilfgaarde, W. Pan and K. Alberi, *Interplay of quasi-quantum Hall effect and Coulomb disorder in semimetals,* arXiv:2412.05273(2024)
3. H. Ness, I.A. Leahy, A.D. Rice, K. Alberi and M. van Schilfgaarde, *Doping topological Dirac semimetals with magnetic impurities: electronic structure of Mn-doped Cd_3As_2*, submitted
4. C. Brooks and S. Lany, *Pseudo-equilibrium theory for extrinsic doping control of the topological semimetal Cd_3As_2*, submitted
5. I.A. Leahy, A.D. Rice, C.-S. Jiang, G. Paul, K. Alberi and J.N. Nelson, *Anisotropic weak antilocalization in thin films of the Weyl semimetal TaAs*, Phys. Rev. B **110**, 054206 (2024)

Publications

1. J.N. Nelson, I.A. Leahy, A.D. Rice, C. Brooks, G. Teeter, M. van Schilfgaarde, S. Lany, B. Fluegel, M. Lee and K. Alberi, *Direct link between disorder and magnetoresistance in topological semimetals*, Phys. Rev. B **107**, L220206 (2023)
2. J.N. Nelson, A.D. Rice, R. Kurleto, A. Shackelford, Z. Sierzega, P. Hao, B.S. Berggren, C.-S. Jiang, A.G. Norman, M.E. Holtz, J.S. Mangum, I.A. Leahy, K.N. Heinselman, H. Ness, M. van Schilfgaarde, D.S. Dessau and K. Alberi, *Thin film TaAs: Developing a platform for Weyl semimetal devices,* Matter **6**, 1-14 (2023)
3. A.D. Rice, M.O. Liedke, M. Butterling, E. Hirschmann, A. Wagner, N.M. Haegel and K. Alberi, *Vacancy complexes in Cd_3As_2,* APL Materials **11**, 061109 (2023)
4. C. Brooks, M. van Schilfgaarde, D. Pashov, J.N. Nelson, K. Alberi, D.S. Dessau and S. Lany, *Band energy dependence of defect formation in the topological semimetal Cd_3As_2*, Phys. Rev. B **107**, 224110 (2023)
5. C. Brooks and S. Lany, *Heterostructural alloy phase diagram for $(Cd_{1-x}Zn_x)_3As_2$*, Phys. Rev. Mater. **8**, L061201 (2024)
6. I.A. Leahy, A.D. Rice, C.-S. Jiang, G. Paul, K. Albeir and J.N. Nelson, *Anisotropic weak antilocalization in thin films of the Weyl semimetal TaAs*, Phys. Rev. B **110**, 054206 (2024)
7. K. Alberi, C. Brooks, I.A. Leahy and S. Lany, *Tutorial: Defects in topological semimetals*, J. Appl. Phys. **136**, 091102 (2024)

Structured-Light Control of Two-Dimensional Dirac Materials

Mahmoud M. Asmar, Department of Physics, Kennesaw State University
Nancy P. Sandler, Department of Physics and Astronomy, Ohio University

Keywords: Periodically Driven Systems, Vortex Light Beams, Photo-induced Topological States, Light-induced Vortex States, Floquet Engineering.

Research Scope

We present a unified Floquet framework—supported by fermion-doubling-free numerics—that elucidates how structured electromagnetic fields engineer topological phenomena in two-dimensional Dirac materials. (i) Circularly polarized vortex light beams (CP-VLBs) imprint photon-dressed electronic vortices whose states are labeled by a conserved total-angular-momentum. (ii) Departures from CP hybridize states in adjacent Floquet sidebands, producing quasienergy shifts. (iii) In finite samples these vortices coexist with chiral Floquet edge modes; our numerical solver quantifies their spatial extent, disorder resilience, and hybridization across realistic geometries. (iv) Beyond VLBs, one-dimensional intensity gratings create space–time Floquet superlattices in graphene. A high-frequency expansion yields transcendental equations for the photon-dressed spectrum, predicting cascades of minibands, secondary Dirac points, and polarization-controlled gaps. Together, polarization, orbital angular momentum, and spatial intensity modulation constitute complementary knobs for programming electronic vortices, topological edge channels, and Floquet minibands—advancing the vision of optically programmable quantum matter.

Recent Progress

Over the past months, our program has advanced the theory and numerical modelling of how structured electromagnetic fields reshape the electronic spectrum of two-dimensional Dirac materials. The following thrusts underpin this effort.

1. *Photon-dressed electronic vortex states generated by CP-VLBs.* Photon-dressed electronic vortex states emerge when a massive Dirac material is exposed to a CP-VLB. A total angular momentum operator that commutes with the Floquet Hamiltonian assigns a unique eigenvalue to each vortex state, revealing vortex-state branches whose number is controlled by the VLBs orbital angular momentum and with states labeled by their conserved quantum number.[1]

2. *Coexistence of vortex and topological edge states in finite geometries.* For circularly polarized beams, the driven system hosts not only vortex states but also topological edge states. A numerically efficient finite-difference method that avoids fermion doubling—while preserving the system's symmetries and topology[2]—captures both phenomena on equal footing. The solver quantitatively characterizes the spatial extent, robustness to disorder, and degree of hybridization of these photon-dressed states across a wide range of sample sizes and light parameters.

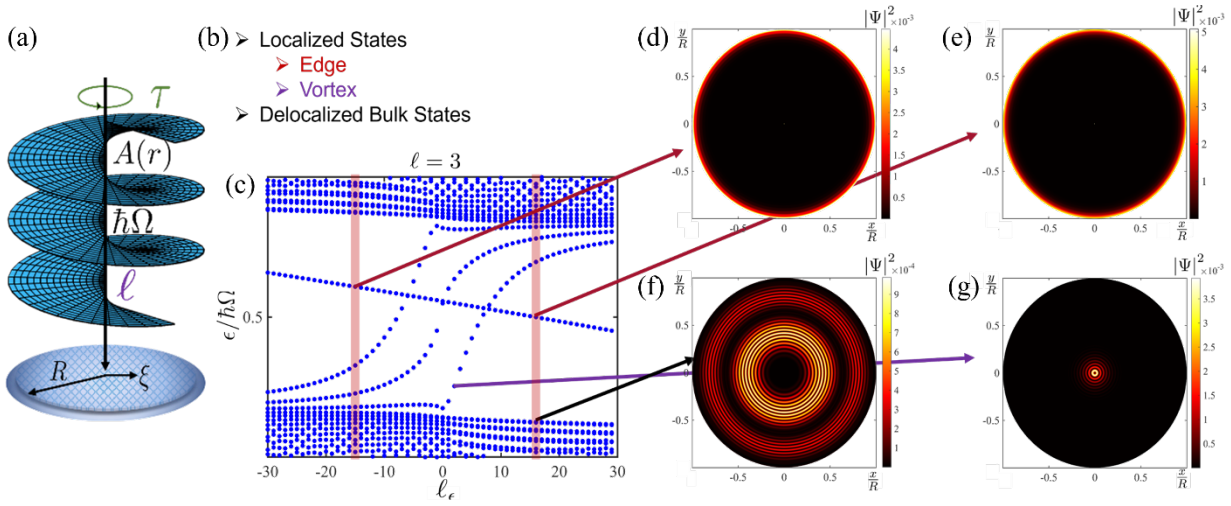

Figure: (a) Schematic of a circularly polarized VLB-driven massive Dirac-like material. (b) Different types of states are present in the VLB-driven system. (c) Quasi-energy spectrum of the VLB-driven system in (a), where the VLB carries an orbital angular momentum *l=3*. (d) and (e) probability density of two edge states, while (f) shows a bulk state, and (g) a vortex state.

3. *Hybridization driven by non-circular polarization.* Introducing even slight deviations from perfect circular symmetry—i.e., employing *non-circular polarization*—destroys total-angular-momentum conservation. Detailed Floquet calculations demonstrate how this non-circular polarization introduces hybridization among neighboring vortex and bulk states sectors, modifying their quasienergies and spatial distribution, making the detection of vortex and edge states increasingly difficult with increasing deviations from the CP condition.

4. *One-dimensional intensity-modulated drives and Floquet minibands.* Optical control extends beyond VLBs: illuminating graphene with a monochromatic beam whose intensity is modulated periodically in one direction creates a space-time dependent Floquet Hamiltonian. Within the high-frequency regime, an effective stroboscopic 1D-space-periodic description emerges. We have analytically derived the transcendental equations that govern the photo-dressed electronic spectrum for such beams, providing a complete description of the photo-induced states and revealing how combined spatial- and time-frequencies define the quasienergy spectrum.

Collectively, these results demonstrate that structured light—whether carrying orbital angular momentum or spatial intensity modulations—offers a versatile platform for engineering vortex textures, topological edge channels, and Floquet minibands on demand.

Future Plans

Building on the findings outlined above, we plan to:

1. Deploy our fermion-doubling-free finite-difference solver to systematically introduce controllable perturbations—light-induced (e.g., polarization changes) as well as material-based (impurities, edge roughness). By systematically monitoring quasienergy shifts, localization lengths, and angular-momentum signatures as controlled disorder is introduced, we will pinpoint the specific defect types and threshold strengths that destabilize vortex modes, topological edge states, or both.

2. Move to a non-perturbative Floquet analysis of TMDs irradiated by circular vortex beams. First, we will extend the total-angular-momentum operator and our fermion-doubling-free solver to the full Floquet basis, retaining every sideband with significant weight. Strong light coupling, intrinsic spin–orbit interaction, and realistic Laguerre-Gaussian/Bessel beam profiles will be incorporated. Exact diagonalization of the valley- and spin-resolved equations will then yield the complete quasienergy spectrum, pinpointing regimes where valley-selective gaps, spin-polarized vortices, and chiral edge states coexist. The outcome will be concrete predictions—circular-dichroism signatures, valley currents, and edge-conductance plateaus—for experimental validation of light-driven TMD physics.
3. Continue our work on intensity-modulated drives, and we will harness spatially structured beams to control two-dimensional materials' electronic and topological properties. We will start with the simplest model: tilting a single beam so its intensity sweeps smoothly from one edge of the monolayer to the other, then replace that beam with more exotic profiles—higher-order Laguerre-Gaussian rings—to create a rich landscape of peaks and nodes. Once the amplitude patterns are analyzed, we will add polarization textures by crossing two or more tilted beams whose polarizations remain fixed but whose interference produces a spatially varying polarization. The Hamiltonians that emerge from these amplitude-and-polarization mosaics vary in both space and time. In the high-frequency limit, we can unravel them analytically with transfer-matrix and effective-Floquet techniques, allowing us to draft a phase diagram that predicts where new bulk gaps open, where edge modes appear, and how the resulting topological channels route charge currents.

References

1. L. Massaro, C. Meese, N. Sandler, and M. Asmar, "*Photon-dressed vortex states in Dirac materials*," Physical Review B **111**, 085402.
2. C. W. J. Beenakker, A. Donís Vela, G. Lemut, M. J. Pacholski, J. Tworzydło, "*Tangent Fermions: Dirac or Majorana Fermions on a Lattice Without Fermion Doubling*," Annalen der Physik **535**, 2300081 (2023).

The Origin of Hysteresis in Phase Transformation Materials

Ananya Renuka Balakrishna, University of California, Santa Barbara

Keywords: Hysteresis, energy barrier, phase transformation, intercalation compounds, magnets

Research Scope

Phase transformation materials undergo an abrupt change in physical property, and in recent years, their use in information storage technology, energy storage devices, and energy conversion concepts has seen tremendous growth. However, when these materials undergo phase transformation, they often display a delay in material response despite a constantly changing applied field. This delay, known as the hysteresis effect, is commonly observed in ferromagnets, shape-memory alloys, and intercalation materials, and limits the rapid and reversible cycling of these materials. This proposal aims to elucidate the fundamental mechanism governing hysteresis in these phase transformation materials.

The proposed effort will focus on one candidate material—the intercalation compound $Li_2Mn_2O_4$ used as electrodes in lithium batteries—with the primary objective being to mitigate structural decay, enhance material reversibility, and reduce voltage hysteresis during phase transformations. Several theories explain voltage hysteresis in intercalation compounds in terms of thermodynamic entropy, surfacial kinetics, and microstructural evolution pathways of the material; however, none of these theories explain the origins in entirety. In this research, we propose to rethink voltage hysteresis as shaped by fundamental material constants and emergent energy barriers, see Fig. 1. This line of thinking has already shed light on understanding hysteresis in other phase-transformation materials, such as shape-memory alloys and magnets. Inspired by these recent successes, we propose to derive the quantitative energy barriers governing reversible phase change in intercalation compounds.

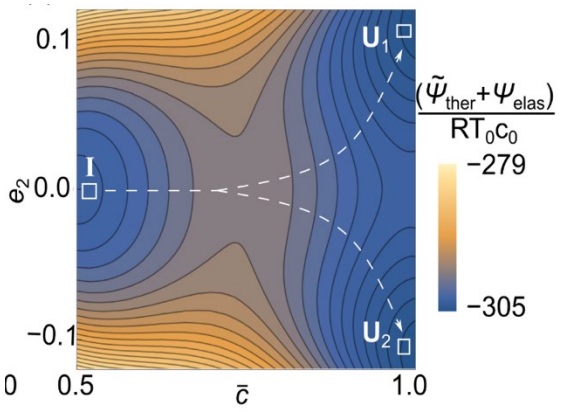

Figure 1: A multi-well energy landscape constructed for a symmetry-breaking phase change in intercalation compound $Li_2Mn_2O_4$. We propose to correlate voltage hysteresis as a delicate interplay between energy barriers (shaped by fundamental material constants) and localized disturbances (e.g., a Li-rich nucleus).

In line with the DOE-BES Physical Behavior of Materials program goals, the findings from this project will provide fundamental insights into the interplay between nucleation barriers and microstructural instabilities governing reversibility and hysteresis in intercalation materials. Additionally, our work will establish a modeling framework that can guide the discovery of the novel intercalation compounds with minimum hysteresis, and in the long run, the theory can be generalized and adapted to other phase change materials including soft magnets, ferroelectrics, and superconductors.

Recent Progress

Major Activity 1: The central aim is to quantify structural transformations in first order phase transformation materials and to establish an algorithmic approach to derive crystallographic design rules necessary to reduce coherency stresses and volume changes during phase change. We are developing new algorithms, founded in the Cauchy-Born theory and Ericksen's multi-well energy landscape,[1-2] to predict structural transformation pathways in first-order phase transformation materials. We recently published our generalized theoretical framework in the Acta Materialia and the JMPS journals (see Refs. [1-2] in the publication list).

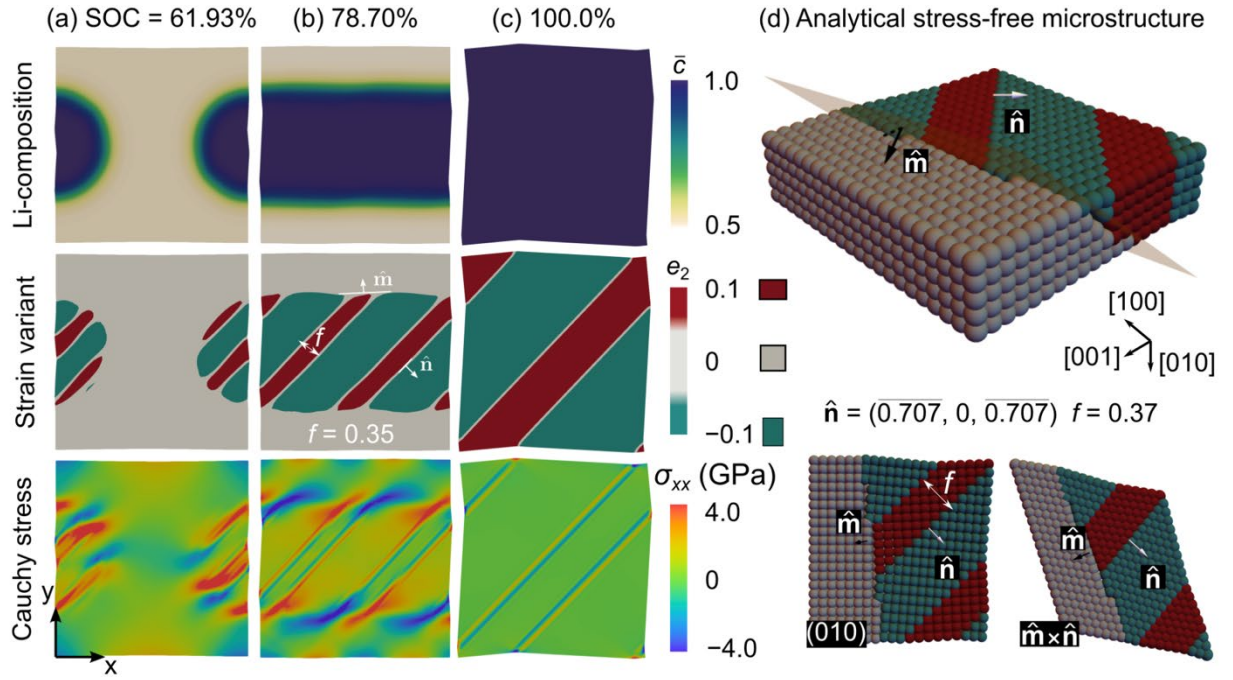

Figure 2: (a-c) A representative calculation from our symmetry-breaking phase-field model that shows how lattice or strain variants evolve during phase change. These simulations are consistent with the (d) analytical solutions of the crystallographic theory and have been validated for a $Li_2Mn_2O_4$ compound. The 3D modeling framework is general and quantifies the elastic energy barrier that emerges during phase change.

Significant Results: Our newly developed variational model predicts symmetry-breaking lattice deformations in crystalline solids. We demonstrate that allowing certain lattice deformations in intercalation compounds—provided they satisfy specific compatibility criteria—can minimize internal stresses and net volume changes. In doing so, we show how precise lattice geometries and structural transformation pathways at the atomic scale can greatly affect material response at the continuum scale. Specifically, compatible microstructures significantly lower the elastic energy barriers that emerge during phase change and contribute to reduced voltage hysteresis and improved material reversibility. These energy barriers and energy-minimizing microstructures, which are characteristic of first-order phase transformations, are difficult to estimate using first-principles calculations but can be effectively captured in our continuum approach. We are generalizing our theoretical framework to materials beyond intercalation compounds, and our material design rules has a potential to open a new route towards material discovery and synthesis.

Major activity 2: We are extending our energy barrier analysis approach to understand the origins of hysteresis in soft magnetic alloys (see Refs. [3-4] in publication list). Specifically, we are developing a nonlinear micromagnetics framework to systematically investigate the interplay between magnetic material constants, residual stresses, and needle domain microstructures (treated as localized disturbances) to collectively lower the energy barrier for magnetization reversal. We correlate this reduced energy barrier with the width of the magnetic hysteresis loop, and derive a mathematical relation between fundamental magnetic constants for minimum hysteresis.

Significant Results: Our findings challenge the widely accepted view that magnetic hysteresis is dependent only on the material's magnetocrystalline anisotropy constant κ_1.[3] Contrary to this norm, we present evidence that magnetoelastic interactions governed by magnetostriction constants λ_{100}, elastic stiffness c_{11}, c_{12}, and applied stresses σ_{11} play an important role in reducing magnetic hysteresis width, despite large κ_1 values. Specifically, we propose a mathematical relationship: $\kappa_1 = a(c_{11} - c_{12})(\lambda_{100} + \beta\sigma_{11})^2$ for which magnetic hysteresis can be minimized (for some constants a, ß). These results provide insights into open problems on the coercivity paradox, permalloy problem, and serve as a quantitative guideline to design new magnets with small hysteresis, which are located beyond the $\kappa_1 \rightarrow 0$ region. This work was published in two publications in Physical Review Materials journal and the MRS communications journal (Refs. [3-4] in publication list).

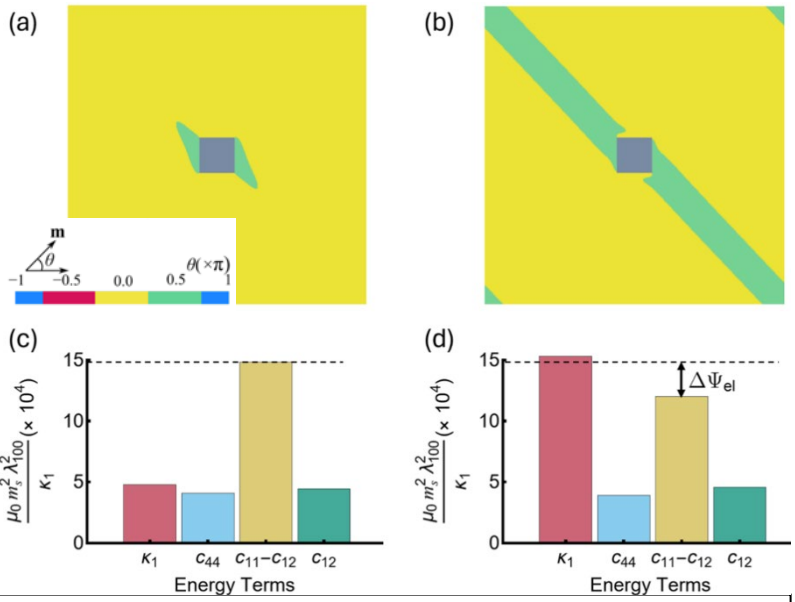

Figure 3: We are extending our energy barrier analysis to investigate origins of magnetic hysteresis. (a-b) We show how emergent micromagnetic domain patterns generate resistance to magnetization reversal and affect hysteresis. (c-d) The energy contributions associated with the growth of a needle domain are reduced during the needle to stripe transition and is associated with a drop in coercivity.

Future Plans

Generalize theory for a wider family of symmetry-lowering transformations: Our chemo-mechanical model describes cubic-to-tetragonal lattice deformations in intercalation compounds, such as $Li_2Mn_2O_4$. This symmetry-breaking transformation generates 3 lattice variants (or 6 twin solutions) that emerge during phase change. The next step is to generalize to predict the generalized cubic-to-monoclinic lattice deformations. This latter symmetry-breaking transformation generates 12 lattice variants and nearly 24 twin solutions that collectively generate rich and complex microstructural patterns during phase change. By generalizing our diffusion-deformation framework, we can investigate how multiple compatibility solutions affect the collective energy barrier during phase change and thereby alter the hysteresis property of the intercalation compound. Additionally, we note that extrinsic electrochemical operating or

boundary conditions, such as particle geometry, anisotropic diffusion kinetics, surface flux, in addition to intrinsic material parameters play a crucial role in stabilizing a Li-rich nucleus. To this end, we will continue integrating surface energy effects (arising from the nanoparticle size of electrodes) and material kinetics to investigate the stability of a Li-rich nucleus in our 3D model.

Unify the continuum theory to predict both twinning and slipping mechanisms: The model describes finite lattice deformations that are reversible and generate twins by using the concept of multiple energy wells. The key constraint is that these energy wells must lie in an Ericksen-Pitteri neighborhood to describe deformations that are reversible. This theory, however, can be generalized to contain infinite energy wells (or computationally 2-3 generations of energy wells) that go beyond the Ericksen-Pitteri neighborhood and therefore generate slip, an irreversible deformation. Our theoretical framework thus far can capture reversible deformations and has the potential to be generalized to also model irreversibility. Furthermore, the twinning and slipping microstructures are inherently three-dimensional and it is important for us to optimize the computational efficiency of our finite element framework. At present our code is parallelized as an openMP format and solved on a CPU node, and our efforts in this regard would be to parallelize parts of the code and solve matrix multiplications on a GPU node. We have identified suitable workshops and courses to train students in this regard and have started optimizing the numerics.

Other disciplines: The distinguishing feature of our work is that we correlate energy barriers, arising from emergent microstructural patterns during phase change in addition to intrinsic thermodynamic and kinetic barriers, with the width of the material hysteresis loop (e.g., voltage hysteresis in intercalation compounds, magnetic hysteresis). This concept can be generalized and not only be adapted to intercalation compounds beyond $Li_2Mn_2O_4$ (e.g., as a next step we are modeling the tetragonal-to-monoclinic deformation in $NaMnO_2$). Furthermore, the model can be extended to other materials undergoing displacive structural transformations, such as the shape-memory alloys, ferroelectrics, and molecular crystals, and as a we are adapting our framework to molecular crystals (see Ref. [5] in publication list).

Summary: Thus far, our contributions include the development of a new chemo-mechanical model that couples Li-diffusion with host-lattice finite deformation. We predict symmetry-breaking lattice deformations that collectively generate crystallographic microstructures (e.g., finely twinned domains) that are not captured in the regular phase-field models for intercalation compounds. By doing so, we provide fundamental insights into the role of lattice geometries and deformation gradients on macroscopic materials properties, such as voltage hysteresis and phase transformation reversibility. We have extended these ideas on hysteresis and energy barriers to soft magnets and have provided quantitative insights into the role of elastic interactions in governing magnetic hysteresis.

References

1. T. Erichsen, B. Pfeiffer, V. Roddatis, and C. A. Volkert. *Tracking the diffusion-controlled lithiation reaction of $LiMn_2O_4$ by in situ TEM*. ACS Applied Energy Materials, **3**(6), 5405-5414 (2020).
2. J. M. Ball and R. D. James, *Fine Phase Mixtures as Minimizers of Energy*, Archive for Rational Mechanics and Analysis **100**, 13-52 (1987).
3. A. Renuka Balakrishna and R. D. James. *Design of soft magnetic materials*. npj Computational Materials, **8** (1), 4 (2022).

Publications

1. T. Zhang, D. Zhang, and A. Renuka Balakrishna, *Coupling Diffusion and Finite Deformation in Phase Transformation Materials,* Journal of Mechanics and Physics of Solids, **183**, 105501 (2024).

2. D. Zhang, and A. Renuka Balakrishna, *Designing Shape-Memory-Like Microstructures in Intercalation Materials*, Acta Materialia, **252**, 118879 (2023).
3. H. Guan, N. Ahani, C. Garcia-Cervera, and A. Renuka Balakrishna, *Hysteresis and Energy Barriers in Soft Magnets*, Physical Review Materials, **9** (4), 044407 (2025).
4. A. Renuka Balakrishna, *Rethinking Hysteresis in Magnetic Materials*, MRS Communications, **14** (5), 835-845 (2024).
5. D. Tiwari, A. Renuka Balakrishna, *A Micromechanical Model for Light-interactive Molecular Crystals,* Journal of Mechanics and Physics of Solids (In revision), arXiv preprint:2501. 14975 (2025).

Properties, Electrochemical Activity, and Stability of Solid Oxide Cell Fuel-Electrode Materials

Scott A Barnett, Northwestern University

Keywords: Electrolysis, Fuel cells, hydrogen, electrode materials, nanoparticle exsolution

Research Scope

This project focuses on high-temperature ionically- and electronically-conducting oxide materials that have applications in solid oxide fuel cells, electrolyzers, and oxygen membranes. These solid oxide cells (SOCs) will play a crucial role in projected net-zero emissions pathways, especially H_2 production by electrolysis and utilization with fuel cells. The present project focuses on fundamental studies of a new class of SOC fuel electrode materials that was discovered under prior DOE-BES funding – oxide materials that exsolve performance-enhancing metallic nanoparticles during device operation. The research aims to: (1) determine the pathways of nanoparticle exsolution and associated oxide phase transformations; (2) measure oxide electronic transport properties; (3) ascertain how electrode electrochemical processes are affected by nanoparticle exsolution and associated oxide phase changes; (4) explore of the stability of the exsolution electrodes relative to electrolyte materials; and (5) explore the factors determining the long-term performance stability.

Recent Progress

Dynamics of phase transitions in $Sr(Ti_{1-x}Fe_x)O_{3-\delta}$ fuel electrodes

New and improved electrode materials are of interest for a next generation of solid oxide cells (SOCs) aiming to achieve improved performance, better long-term stability, and more flexible operation. One area of active interest is the replacement of Ni-based cermet electrodes with Mixed Ionic and Electronic Conducting (MIEC) oxides. $SrTi_{1-x}Fe_xO_{3-\delta}$ (STF) is a promising MIEC fuel electrode into which reducible cations can be substituted to yield exsolution of catalytically active nanoparticles, improving performance. However, questions remain as to which compositions provide the best stability and performance over a range of fuel compositions.

We have studied STF with Fe contents between x = 0.5 and 0.8 in varying H_2/H_2O ratios, observing the phase evolution using *ex situ* and *in situ* x-ray diffraction and *ex situ* TEM-EDS, correlated with impedance spectroscopy observations of electrochemical characteristics and stability. Increasing the Fe-content results in slightly lower initial polarization resistance values. All STF compositions were stable in the perovskite structure for 50:50 H_2/H_2O ratios but decomposed in more reducing fuels (e.g., 91:9 H_2/H_2O) into a Ruddlesden-Popper (R-P) Perovskite, Strontium Oxide, and metallic Fe. The decomposition occurred after an incubation time of ~ 2 – 4 h, and was much slower for lower Fe content. Polarization resistance R_P was fairly stable for 50:50 H_2/H_2O, but showed a rapid increases over the first several hours in highly reducing conditions, suggesting that the R-P transformed oxide was a less active electrode material despite the presence of exsolved Fe.

Figure 1 compares the time dependences of both R_P and the (111) peak intensity from *in situ* XRD data, for $SrTi_{1-x}Fe_xO_{3-\delta}$ (STF) STF-5 and 91:9 H_2/H_2O. The onset of decomposition as indicated by a rapid drop in perovskite (111) peak intensity corresponds closely to with a rapid increase in R_P. The R_P increase appears to result primarily from the perovskite to R–P transformation, because

the R–P phase may have inferior electrochemical properties. The initial fast decrease in R_P in the first hour of testing may be connected to a rapid increase in oxygen vacancies leading to improved ionic conductivity and decreased polarization resistance.

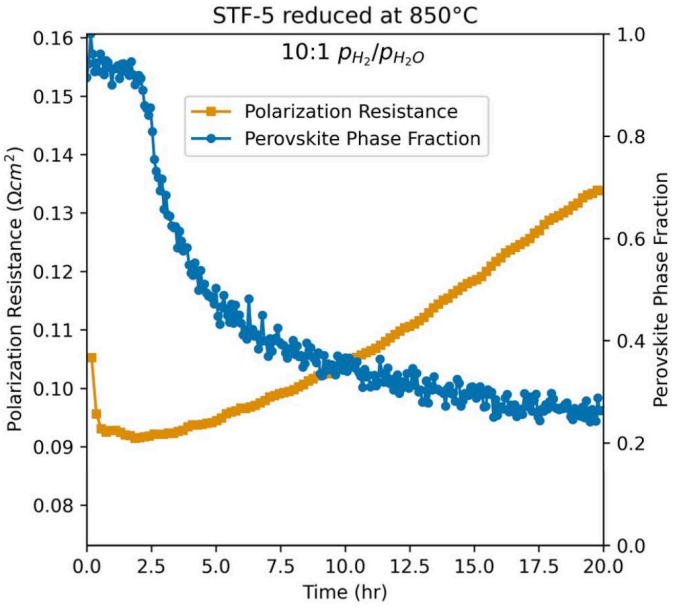

Figure 1. Comparison of polarization resistance and perovskite phase fraction for STF-5 in 91:9 H_2/H_2O.

Surface Amorphization During Reductive Exsolution

Cu-substituted $La_{0.6}Sr_{0.4}Co0_{0.2}Fe_{0.8}O_{3-\delta}$ (LSCF-Cu), a state-of-the-art SOC electrode material, was selected to explore the real-time evolution of surface morphology and chemistry under a reducing atmosphere at elevated temperatures. A novel surface structural transformation is observed where the perovskite surface starts to amorphize while multicomponent metal nanocatalysts form on the amorphous surface. Surprisingly, the resulting amorphous structure can withstand a high-temperature oxidizing atmosphere (650°C) when it has undergone sufficient reduction for an extended period. Figs. 2 displays TEM bright field images of the LSCF-Cu surface, taken after reduction at 450°C for durations of 2 h and 10 h, showing an exsolved nanoparticle and an amorphized surface layer. The amorphous layer thickens from 1.5 to 2.7 nm from 2 to 10 h, and the metallic nanoparticle grows in size. Subsequent exposure of the electrodes to synthetic air at 650°C for 30 hours showed that the exsolved nanoparticles remained without re-dissolving into their matrix. However, the amorphous layer of the samples subjected to 2 h-reduction completely disappeared (Fig. 3 left) whereas that of the sample subjected to 10 h-reduction remained the same thickness (Fig. 3 right). These results highlight that an appropriate duration of reduction is essential for ensuring the stability of the surface amorphous layer. The exsolution reduced the polarization resistance from 0.27 to 0.12 Ωcm^2, and improved the peak power densities at 700ºC from 0.66 to 1.08 W cm^{-2}. That is, the coexistence of the active nanocatalysts and defective amorphous

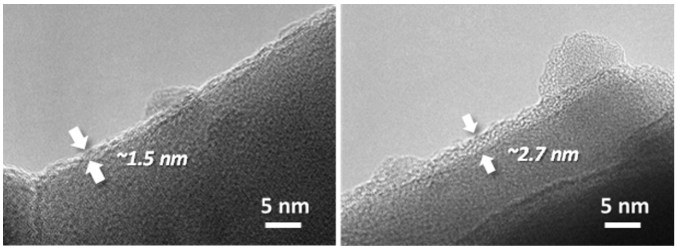

Figure 2. TEM images of LSCF-Cu surfaces after reduction for 2 h (left) and 10 h (right), where a thicker amorphous layer and large exsolved metallic nanoparticle can be seen after the longer reduction. The reduction was conducted in 4% H_2 at 450°C.

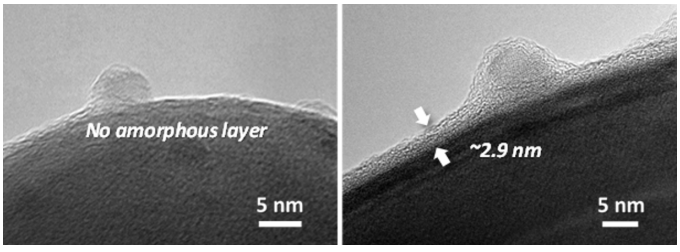

Figure 3. TEM images of LSCF-Cu surfaces after reduction for 2 h (left) and 10 h (right) followed by oxidation at 650°C for 30 h. The nanoparticle is present after oxidation, but the amorphous layer is retained only for the longer reduction time.

surface leads to a nearly 100% enhancement in the electrode resistance over 200 h without significant degradation. These observations provide a new catalytic design strategy for using redox-dynamic perovskite oxide host materials.

A Novel Method for Synthesizing Low-Temperature Electrolysis Catalysts

Hydrogen generation or utilization using low-temperature water electrolysis or fuel cells typically requires relatively large amounts of scarce precious metals. A study has been carried out on the feasibility of using exsolution for producing electrode catalysts for low-temperature proton-exchange-membrane (PEM) cells. The initial work was done using $Sr(Ti_{0.3}Fe_{0.63}Ru_{0.07})O_{3-\delta}$ (STFR), in which exsolution can be used to form Ru-Fe alloy catalyst nanoparticles on the oxide surface. While this material is not an ideal optimized PEM electrode catalyst, the initial results show that exsolution greatly improves activity compared to the non-exsolved oxide, demonstrating proof-of-concept of this novel method for producing PEM electrode catalysts.

Figure 4 shows the results of ambient temperature linear sweep voltammetry for the case of hydrogen evolution reaction (HER) in acidic conditions. In all cases, the electrodes with reductively exsolved STFR required lower applied potentials to achieve a substantial current density, *i.e.,* electrode activity was improved by exsolution. Furthermore, the electrode activity depended strongly upon the reduction conditions, with 700 C for 4 h yielding the lowest potentials. This has been explained by exsolution kinetics and transmission electron microscope observations – higher temperature allows more of the Ru to diffuse out of the STFR particles to reach the surface, resulting in a higher density of Ru-Fe nanoparticles, increasing activity. The slightly lower activity at 800 C may mean that most of the Ru was already exsolved at 700 C, such that the temperature increase to 800 C only serves to coarsen the Ru-Fe nanoparticles, reducing their activity. After a few hundred voltage sweep cycles, the electrode activity generally improved; this provides an initial suggestion that electrode stability is good.

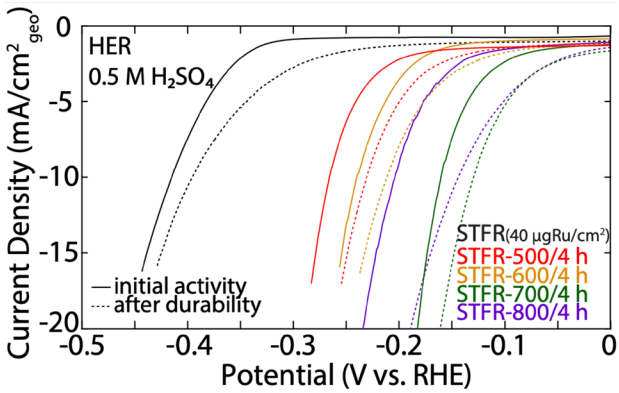

Figure 4. Current density versus potential for electrodes made with STFR with either no exsolution or after reductive exsolution for 4 h at 500, 600, 700, or 800 C. A standard 3-electrode setup was used with the catalyst layer on a glassy carbon disc, a Pt counter electrode, and a Ag/AgCl reference electrode.

This work demonstrates the first ever application of a new class of electrode material, previously developed for high-temperature electrochemical cells, in low-temperature cells. This approach could help mitigate the growing demand on materials sourcing that is caused by scaling up of sustainable hydrogen technologies, and help open a new direction for research on low-temperature electrode catalysts.

Future Plans

The planned research will follow up on the above three areas of the prior work. We will explore new perovskite compositions aiming to mitigate the perovskite to Ruddlesden-Popper phase transition that has been shown to degrade electrode performance. One modification will be to substitute La for Sr on the A-site; this is expected to improve stability by allowing the perovskite

structure to maintain charge neutrality upon oxygen loss and loss of B-site cations during exsolution. The other modification is to explore compositions with Mn instead of Fe on the perovskite B site. Since Mn is much less reducible than Fe, exsolved nanoparticles are expected to contain little Mn; this means less loss of B site cations during exsolution, which should improve perovskite stability and nanoparticle catalytic activity. We will continue to use *in situ* x-ray diffraction as a key tool to explore phase changes under realistic electrode conditions.

Exsolution will be attempted in an oxide system that is being used in state of the art low-temperature PEM electrolyzers: doped SnO_2. Typical systems include Sb-doped SnO_2 and Ta-doped SnO_2, both with Ir surface catalyst particles applied using solution or chemical vapor deposition methods. Our approach will be to synthesize Ir- and Ta-doped SnO_2 and then to develop reduction procedures aimed at selectively exsolving the Ir to form Ta-doped SnO_2 with a high surface density of highly active Ir nanoparticles. The materials will be tested electrochemically and also determine cation stability against dissolution.

References

Publications

N.R. Geisendorfer, P. Pibulchinda, D. Cox and S.A. Barnett, "Electrochemical Characteristics of Sr(Ti0.3Fe0.7)O3–Based Electrodes in Solid Oxide Cells Operated in H2/H2O and CO/CO2 Mixtures," *Journal of the Electrochemical Society* **172** (2025) https://doi.org/10.1149/1945-7111/ada880.

J.M. Reinke and S.A. Barnett, "Mapping phase instability to electrochemical degradation in SrTi1−xFexO3−δ under solid oxide cell fuel-electrode conditions," *Journal of Materials Chemistry A* (2025) https://doi.org/10.1039/d4ta08700c.

J. M. Reinke, R. Li, Z. Yi, L. C. Seitz, and S. A. Barnett, "Exsolution of Catalytically Active Nanoparticles As a Novel Approach for Hydrogen Evolution Reaction Electrode Fabrication," submitted.

S. Jeon, W.G. Jung, H. Bae, S. Ahn, B. Koo, W. Yu, S. Kim, D. Oh, U. Kim, S.A. Barnett, J. Seo, B.J. Kim and W. Jung, "Concurrent Amorphization and Nanocatalyst Formation in Cu-Substituted Perovskite Oxide Surface: Effects on Oxygen Reduction Reaction at Elevated Temperatures," *Adv Mater* (2024) e2404103. https://doi.org/10.1002/adma.202404103.

T.A. Schmauss and S.A. Barnett, "Atomic layer deposition for surface area determination of solid oxide electrodes," *Journal of Materials Chemistry A* **11** (2023) 3695-3702. https://doi.org/10.1039/D2TA09060K.

Digital Synthesis: A pathway to novel states of condensed matter

A. Bhattacharya, Dillon D. Fong, J. S. Jiang, Ulrich Welp (Argonne National Laboratory)

Self-identify keywords to describe your project: superconductivity, magnetism, spintronics, thin film heterostructures, transition metal compounds, molecular beam epitaxy, x-ray scattering.

Research Scope: In our program, we seek to create, explore and understand novel electronic and magnetic states with new functionalities that emerge at interfaces between different materials. These include collective states like interfacial magnetism and superconductivity, as well as topological states of matter, that may have relevance for spintronics and quantum information science. We seek to realize these states in materials synthesized with atomic layer-by-layer control using molecular beam epitaxy and related techniques. A significant part of our research is devoted to understanding growth processes that lead to these interfacial states, and to refine our synthesis conditions. In the research presented here, we focus on the synthesis and emergent properties of two recently discovered oxide superconductors. In the first class of materials, the superconducting nickelates, we use in-situ x-ray diffraction during synthesis with molecular beam epitaxy to understand the processes underlying the growth of the infinite layer perovskite and n = 5 Ruddlesden-Popper phases in epitaxial thin films, and their subsequent topotactic reduction to the square-planar phase to realize superconductivity. Next, we will present our results from ongoing efforts to explore and understand the superconducting state found at interfaces of $KTaO_3$ (KTO). We will describe how we probe the inversion breaking transverse optical TO1 phonons found near the surface of KTO using a unique 'spintronic' THz spectroscopic technique. These are the same phonons that soften to give rise to the 'quantum paraelectric' nature of KTO at low temperatures and may also mediate pairing in the two-dimensional superconducting gas at KTO interfaces. We have also fabricated superconducting coplanar waveguide resonators using the electron gas formed at interfaces of KTO (111), where we find very large sheet kinetic inductance, and as a result also very low phase velocities or 'slow light', which sheds light on the nature of the superfluid in this two-dimensional superconductor.

Recent Progress

Understanding topotactic reduction in superconducting nickelates: Topotactic reduction is critical to a wealth of phase transitions of current interest, including synthesis of the superconducting nickelate $Nd_{0.8}Sr_{0.2}NiO_2$, reduced from the initial $Nd_{0.8}Sr_{0.2}NiO_3/SrTiO_3$ heterostructure. Due to the highly sensitive and often damaging nature of the topotactic reduction, however, only a handful of research groups have been able to reproduce the superconductivity results. A series of in-situ synchrotron-based investigations by our team (Y. Li et al., *Adv. Mater*. 2024) reveal that this is due to the necessary formation of an initial, ultrathin layer at the $Nd_{0.8}Sr_{0.2}NiO_3$ surface that helps to mediate the introduction of hydrogen into the film such that apical oxygens are first removed from the $Nd_{0.8}Sr_{0.2}NiO_3/SrTiO_3$ (001) interface and delivered into the reducing environment. This

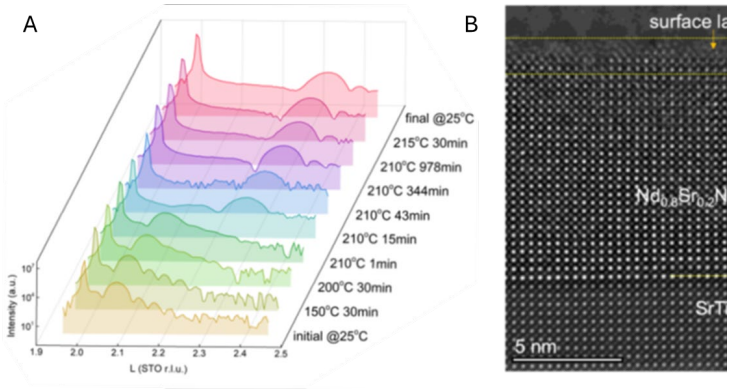

Fig. 1 (A) *In situ* synchrotron X-ray results on the reduction of 11-nm-thick $Nd_{0.8}Sr_{0.2}NiO_3$ / $SrTiO_3$ (001) during reduction with CaH_2 (solid curves). The sharp peak at L = 2 rlu is from the $SrTiO_3$ substrate. (B) Cross-sectional high-angle annular dark-field imaging (HAADF) scanning transmission electron microscopy (STEM) image of the reduced infinite-layer nickelate $Nd_{0.8}Sr_{0.2}NiO_2$, illustrating the presence of a disordered surface layer mediating ion exchange.

allows the square-planar / perovskite interface to stabilize and propagate from the bottom to the top of the film without the formation of interphase defects. Importantly, neither geometric rotations in the square planar structure nor significant incorporation of hydrogen within the films is detected, obviating its need for superconductivity. These findings unveil the structural basis underlying the transformation pathway and provide important guidance on achieving the superconducting phase in reduced nickelate systems.

Superconductivity in an ultrathin multilayer nickelate: We report the appearance of superconductivity in a single unit-cell thick film of $Nd_6Ni_5O_{12}$ (X. Yan et al., *Adv. Mater.* (2024)), exhibiting a transition temperature similar to that of thicker films. In-situ synchrotron x-ray scattering performed during growth of the parent phase, $Nd_6Ni_5O_{16}$, shows that the necessary layer- by-layer deposition sequence does not follow the sequence of the formula unit but an alternate order due to the relative stability of the perovskite unit cell (Fig. 2). We exploit this insight to grow ultrathin $Nd_6Ni_5O_{16}$ heterostructures and conduct in-situ studies of topotactic reduction, finding that formation of the square-planar phase occurs rapidly and is highly sensitive to reduction temperature, with small deviations from the optimum condition leading to inhomogeneity and the loss of superconductivity. The fluorite layer within the unit cell facilitates reduction by initially stabilizing the square-planar phase in the upper half of the unit cell. Our findings provide insight into the growth of the Ruddlesden-Popper nickelates, highlighting the need for in-situ studies of the metastable phases key to superconductivity.

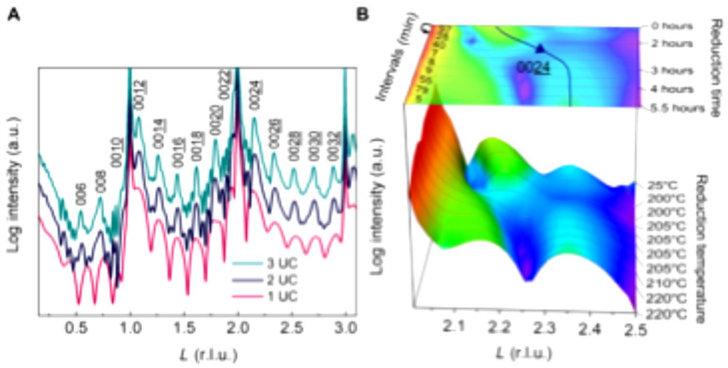

Fig. 2 (A) Measurements of the specular rod for 1-, 2-, and 3-UC-thick $Nd_6Ni_5O_{16}$ films grown on $NdGaO_3$ substrates. (B) Map of specular rods measured for the 1-UC-thick film at different temperatures in the CaH_2 reducing environment. the arrowed profile at the top shows the shift of the 00<u>24</u> reflection.

Tunable 'giant' kinetic inductance of superconducting $KTaO_3$ (111) interfacial 2DEGs: Superconductivity in the electron gas found at $KTaO_3$ (KTO) interfaces is characterized by an unusually low superfluid stiffness J_s, inferred from both transport and microwave measurements. The reason for the low value of superfluid stiffness J_s and the resulting large sheet kinetic inductance $L_{K/\square} \sim 1/J_s$ is not well understood. If we assume that J_s is probing the superfluid density, that would imply that less than 1% of the carriers in the band are participating in the superfluid. This is highly unusual, even in a disordered superconductor where J_s is reduced by scattering. The resultant large kinetic inductance can be potentially useful in device applications. We fabricated coplanar waveguide resonators (Fig. 3) from the two-dimensional superconductor formed at KTO_3 (111) interfaces to characterize the superconductor's $L_{K/\square}$ as a function of carrier density (J. Yang et al., *Nano Letters* 2025). Upon varying the carrier density, in samples with T_c ranging from 0.62 to 1.81 K, we can tune $L_{K/\square}$ between 1.88 and 7.42 nH/□ at the lowest temperatures, exceeding the highest values reported for granular aluminum films. The temperature dependence of $L_{K/\square}$ is consistent with a superconducting gap without nodes. The high $L_{K/\square}$ of superconducting KTO (111) interfacial electron gases combined with the high dielectric constant of KTO results in resonators with exceedingly low phase velocities ("slow light") and small mode volumes. In addition, superconducting KTO (111) interfacial electron gases are robust in magnetic fields well above a Tesla. These features can enable unique device applications in superconducting electronics and quantum information science.

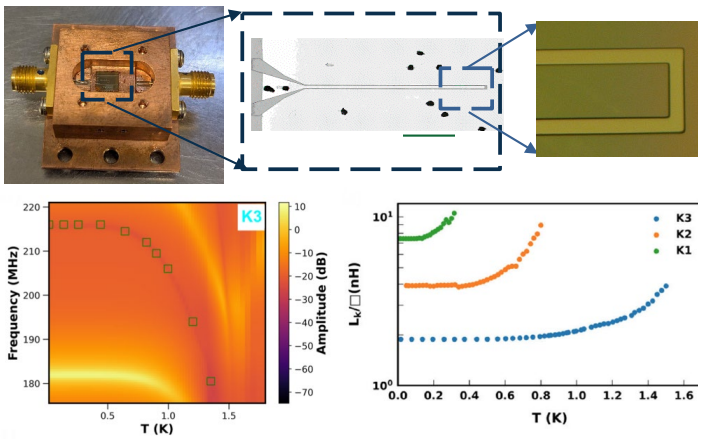

Fig. 3 (Top) Superconducting coplanar waveguide patterned from a $AlO_x/KTaO_3$ (111) 2DEG. (Bottom Left) Temperature evolution of its microwave resonant frequency, which is governed by the kinetic inductance of the resonator. The resonance signal disappears above T_C. (Bottom Right) Temperature evolution of sheet kinetic inductance $L_{K/\square}$of superconducting $KTaO_3$(111) 2DEGs at different doping levels, where higher doping levels lead to higher T_C and lower values of $L_{K/\square}$.

Spintronic THz spectroscopy of surface phonons in $KTaO_3$. With the discovery[Error! Bookmark not defined.] of superconductivity at interfaces of KTO, there has been intense interest in its underlying pairing mechanism. A unique property of the superconductivity at KTO interfaces is its orientation selectivity. For KTO (111) interfaces, the transition temperature can be as high as 2.2 K, for the (110) interface, the maximum T_c is ~ 1.1 K, whereas on the KTO (001) interface, superconductivity was found in ionic liquid gated samples with a $T_c < 0.047$ K (K. Ueno et al., *Nat. Nanotech*. 2011). Since then, other groups have failed to find superconductivity in chemically doped or ionic liquid gated KTO (001) 2DEGs with similar carrier densities down to ~ 20 mK. In a recent paper, we proposed a theory of superconductivity involving inter-orbital interactions that explains this striking orientation selectivity of superconductivity. The proposal relies upon the inversion-breaking TO1 phonon as the 'superconducting glue'. This is the same phonon that softens as $KTaO_3$ is cooled to low temperatures causing it to behave as a 'quantum paraelectric', which is an incipient ferroelectric

thwarted by quantum fluctuations. However, phonons at surfaces can differ from the bulk. With this in mind, we devised a spectroscopic technique – 'spintronic THz spectroscopy' – where THz generated from a magnetic overlayer interacts with the surface phonons, which in turn leaves a signature in the emitted THz spectrum (Z. Chu et al., *Sci. Adv*. 2024). With this technique, we are able to probe the near-surface TO1 phonons in two different quantum paraelectric materials – $SrTiO_3$ and $KTaO_3$, where we find that the surface phonons are distinct from the bulk. These findings are useful for our understanding of ferroelectric fluctuations and their role in superconductivity in these materials.

Future Plans

1. In-situ studies of MBE and PLD growth of nickelates, using coherent x-rays and dynamics of resulting speckle patterns (x-ray photo correlation spectroscopy or XPCS) to track defect dynamics and phase formation during synthesis and topotactic reduction.
2. Explore pathways to tune superconductivity in the nickelates, including strain, interfacial doping and dimensional confinement.
3. Develop new giant spin-Hall effect A15 compounds by tuning the Fermi level via stoichiometry or creating pseudobinary alloys. Many of these are superconducting, and several are predicted to have topological surface states.
4. Carry out high resolution spectroscopy of the superconducting electron gas at KTO interfaces to determine the nature of the superconducting gap.
5. Explore the interaction between magnetism and superconductivity in the KTO interfacial electron gas.

References

1. Danfeng Li, Kyuho Lee, Bai Yang Wang, Motoki Osada, Samuel Crossley, Hye Ryoung Lee, Yi Cui, Yasuyuki Hikita, and Harold Y. Hwang, Superconductivity in an infinite-layer nickelate. *Nature* **572**, 624-627 (2019).
2. Grace A. Pan, Dan Ferenc Segedin, Harrison LaBollita, Qi Song, Emilian M. Nica, Berit H. Goodge, Andrew T. Pierce et al. "Superconductivity in a quintuple-layer square-planar nickelate." *Nature Materials* **21**, 160-164 (2022).
3. Changjiang Liu, Xi Yan, Dafei Jin, Yang Ma, Haw-Wen Hsiao, Yulin Lin, Terence M. Bretz-Sullivan et al. "Two-dimensional superconductivity and anisotropic transport at $KTaO_3$ (111) interfaces." *Science* **371**, 716-721 (2021).
4. Changjiang Liu, Xianjing Zhou, Deshun Hong, Brandon Fisher, Hong Zheng, John Pearson, Jidong Samuel Jiang, Dafei Jin, Michael R. Norman, and Anand Bhattacharya. "Tunable superconductivity and its origin at $KTaO_3$ interfaces." *Nature Communications* **14**, 951 (2023).
5. Mallik, S., G. C. Ménard, G. Saïz, H. Witt, J. Lesueur, Alexandre Gloter, L. Benfatto, Manuel Bibes, and Nicolas Bergeal. "Superfluid stiffness of a $KTaO_3$-based two-dimensional electron gas." *Nature Communications* **13**, 4625 (2022).

Publications

1. Y. Li, C. Liu, H. Zheng, Z. Zhu, X. Yan, H. Cao, K. V. L. V. Narayanachari, B. Paudel, Z. Zhang, B. Fisher, H. Wang, E. Karapetrova, C. Sun, S. Kelly, D. Phelan, Y. Du, B. Buchholz, J. F. Mitchell, A. Bhattacharya, D. D. Fong, H. Zhou, "On the topotactic phase transition in the infinite-layer nickelates", *Adv. Mater.* 2402484 (2024).

2. X. Yan, H. Zheng, Y. Li, H. Cao, D. P. Phelan, H. Zheng, Z. Zhang, H. Hong, A. Bhattacharya, H. Zhou, D. D. Fong, "Superconductivity in an ultrathin multilayer nickelate", *Sci. Adv.* **11,** eado4572 (2025).

3. Z. Chu, J. Yang, Y. Li, K. Hwangbo, J. Wen, Q.i Zhang, S. Hruszkewycz, D. D. Fong, X. Xu, M. R. Norman, A. Bhattacharya, H. Wen, "Revealing subterahertz atomic vibrations in quantum paraelectrics by surface-sensitive spintronic terahertz spectroscopy", *Sci. Adv.* **10,** eads8601 (2024).

4. Junyi Yang, Adem Imamovic, Xinhao Li, Xianjing Zhou, John Pearson, Changjiang Liu, Ulrich Welp, Andrew Higginbotham, Jidong S. Jiang, Dafei Jin, Michael R. Norman, and Anand Bhattacharya, "Tuning Kinetic Inductance with Doping in Superconducting Electron Gases at the $KTaO_3$ (111) Interface", *Nano Letters* (2025). https://doi.org/10.1021/acs.nanolett.4c06029

5. R. Chapai, G. Peterson, M. Smylie, X. Chen, J. S. Jiang, D. Graf, J. F. Mitchell, and U. Welp, "Fermi surface topology and magnetotransport properties of superconducting $Pd_3Bi_2Se_2$", *Physical Review* B, 110, 075152 (2024).

6. Q. Zhang, G. Wan, V. Starchenko, G. Hu, E. M. Dufresne, H. Zhou, H.Jeen, I. C. Almazan, Y. Dong, H. Liu, A. R. Sandy, G. E. Sterbinsky, H. N. Lee, P. Ganesh, D. D. Fong, "Intermittent Defect Fluctuations in Oxide Heterostructures"*, Adv. Mater.* 2305383 (2023).

7. L. Zhang, C. Liu, H. Cao, A. J. Erwin, D. D. Fong, A. Bhattacharya, L. Yu, L. Stan, C. Zou, M. V. Tirrell, H. Zhou, W. Chen, "Redox gating for colossal carrier modulation and unique phase control", *Adv. Mater.* 2308871 (2024).

8. A. Vasdev, G. Sheet, R. Chapai, T. Polakovic, V. Novosad, J. S. Jiang, A. Bhattacharya, J. F. Mitchell, D. Y. Chung, and U. Welp, "Superconducting and spin-wave orders in $Ba_{0.6}K_{0.4}Fe_2As_2$ probed by point contact spectroscopy", *Physical Review B* 110, 094518 (2024).

9. Y. Li, Y. Liu, I.-C. Tung. H. Hong, J. W. Freeland, H. Zhou, H. Wang, and D. D. Fong, "On the Emergence of Ferromagnetism in $LaCoO_3$ Ultrathin Films", *Adv. Funct. Mater.* 2406037 (2024).

10. H. Cao, C. Liu, X. Zhai, D. D. Fong, A. Bhattacharya, M. V. Tirrell, H. Zhou, and W. Chen, "Redox Gating-Induced Modulation of Charge Carrier Density and Lattice Expansion in $LaNiO_3$ Thin Films", *Appl. Phys. Lett.* **125,** 074101 (2024).

Singlet and Triplet Exciton Interaction and Dynamics in Molecular Crystals
Ivan Biaggio, Physics Department, Lehigh University
Keywords: Decoherence, Exciton, Triplet Transport, Spin entanglement, Rubrene

Research Scope

Our research aims at developing a fundamental understanding of excitonic quantum properties such as spin-states, entanglement, and quantum decoherence, how they are affected by transport in a crystal lattice, and how they can be controlled by magnetic fields. A special area of focus is the spin-entangled triplet-pair state that arises from a singlet fission process [1,2], how it is formed, how long the spin-correlation persists, the mechanisms of triplet exciton diffusion and transport, and how they affect quantum decoherence. Current activities include (1) pump&probe transient grating spectroscopy of the singlet-fission processes that lead to entangled triplet pairs in a low-perturbation limit characterized by low excitation density, low repetition rate, and low peak intensity; and (2) the study of geminate triplet-exciton fusion [3] and the related quantum beats [1] to assess the persistence of the spin-entanglement in the presence of extensive diffusion in the crystal lattice in both one and two dimensions and to use as a probe of exciton transport properties such as hopping time and dimensionality.

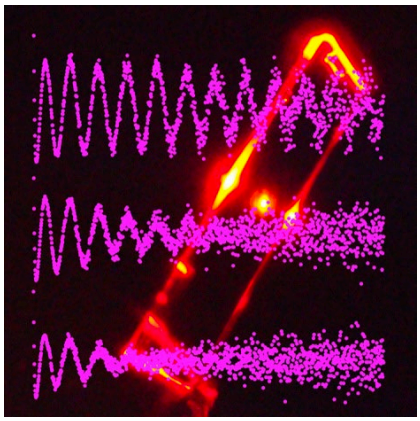

Pictorial representation of the onset of decoherence in the quantum beats in a rubrene crystal during the first 20 ns after photoexcitation, as the magnetic field directions is rotated by just a few degrees. The data is super-imposed on an image of a mm-sized rubrene crystal and the fluorescence it emits

Recent Progress

During the last year our research progressed on a number of fronts, with the discovery of effects that have gone unrecognized until now, and new insights obtained thanks to the development of original theoretical models and their use to analyze new types of experiments. We are currently working on a series of publications describing these effects and models, focusing in particular on the entangled triplet-pair state in molecular crystals. It is worth noting that even though there is a lot of current research on materials for singlet exciton fission, and even though it is known that singlet fission leads to a pair of triplet excitons that should in principle be spin-entangled into an overall singlet state, there is still very little literature about the quantum properties of the entangled triplet pair, which are also of general interest for fundamental quantum mechanics and for quantum information science. We believe that our research is providing a relevant and original contribution to this field. The following paragraphs summarize some recent findings.

Transport induced global decoherence in the high magnetic field limit. We have determined that, in contrast to a generally accepted belief, the wavefunction of triplet excitons can localize on different inequivalent sites in a crystal lattice [4]. As a consequence, exciton hopping between inequivalent sites can and does affect the quantum interference that should give rise to fluorescence quantum beats upon recombination of an entangled triplet-pair, as we demonstrated in rubrene. We also showed that magnetic fields can be used to control the global decoherence caused by this *transport induced dephasing* effect, which enabled us to determine experimentally the excitonic spin energies and the hopping time between inequivalent sites in rubrene crystals from quantum beat measurements. This was published in *Phys. Rev. Lett.* in January 2024 [4].

Evolution of the triplet-pair wavefunction in the low Magnetic Field Limit. Triplet exciton localization on inequivalent sites can also lead to complete suppression of quantum beats when no

magnetic field is applied, and in the low-field limit. In addition, we recognized that in the limit of fast hopping (which is the case, *e.g.*, in tetracene) the averaging effect caused rapid exciton diffusion and its effect on quantum beats must be analyzed in terms of the Hamiltonian of the triplet pair and its variability during exciton hopping, not in terms of the generally accepted D* and E* "crystal" EPR parameters. This leads to a completely different prediction for zero-field and low-field quantum beats than what has been normally expected up to now.

Entanglement lifetime and spin stability in triplet exciton pairs. In materials affected by transport induced dephasing it is possible to restore global spin-coherence by a magnetic field that has the same direction with respect to both inequivalent sites in the crystal lattice [4]. But complete suppression of decoherence can only happen in the high-field limit. To evaluate the stability of spin states it then becomes important to distinguish transport induced dephasing from other effects like spin flips due to spin-orbit coupling that destroy spin entanglement. We showed that magnetic field dependence allows to separately determine the time-constants related to both processes.

Thermally activated behavior of quantum beat amplitude and fluorescence dynamics. As fission-time becomes longer at lower temperatures, the initial fluorescence decay [3] slows down, while the increased spread in the fission time distribution leads to decoherence and a decrease of quantum beat amplitude. These two effects are measurable in two completely different temperature ranges, complementing each other, and showing an extended temperature activated behavior that demonstrates the connection between spin quantum coherence and singlet fission rate.

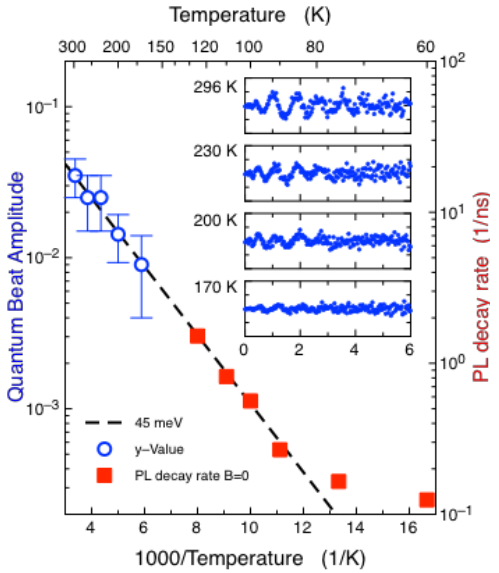

Correlated activation behavior of quantum beat amplitude and fluorescence decay rate in rubrene.

Pump&Probe transient grating uncovers singlet-fission processes in a low perturbation limit. We confirmed the presence of two independent singlet fission mechanisms in rubrene. One is thermally activated and leads to a ~10 ps exponential build-up time of the triplet population at room temperature. The other one is temperature-independent and establishes an initial triplet-population with a characteristic time of 2 ps (see data in the left-most figure below). Spectroscopy [2] of these two transitions led to new insights on the process and its effect on photoluminescence (see next paragraph). In particular, at lower temperatures triplet transport freezes in, causing the triplet states created by the 2 ps fission process that survives at low temperature to remain in a stable superposition with the photoexcited singlet state.

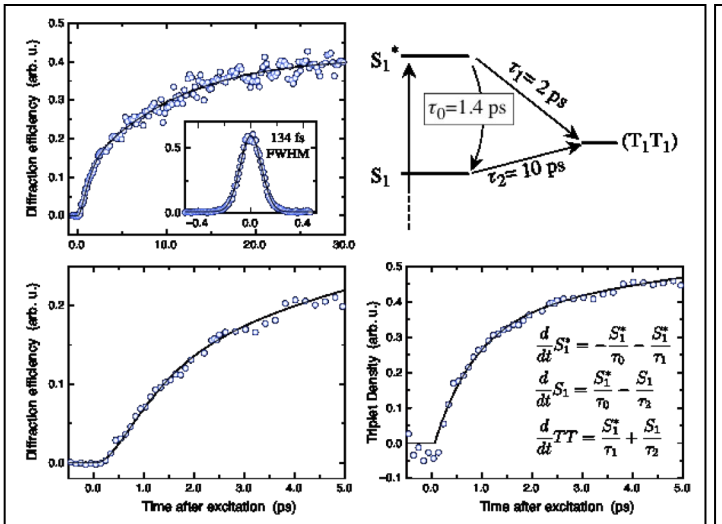

Top: Picosecond transient grating data and models of singlet fission dynamics distinguish an ultrafast <2ps process that likely arises via exothermic fission from excited vibrational states and a ~10 ps process that would be consistent with endothermic fission from the ground vibrational state.

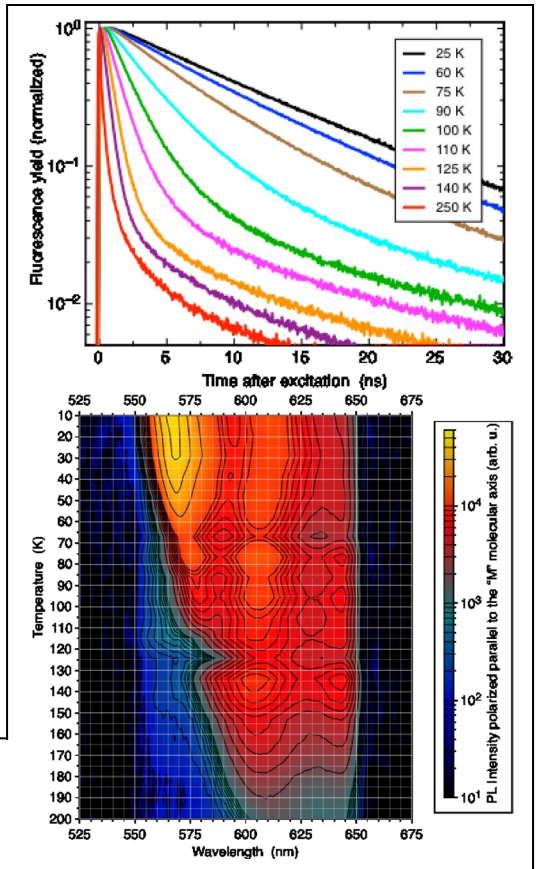

Right: Temperature dependent fluorescence dynamics indicating suppression of triplet transport (top) and corresponding changes in the emission spectrum with the onset of a strong short-wavelength emission (color plot, bottom).

Symmetry breaking and superfluorescence as singlet fission freezes at low temperatures. Separate fluorescence dynamics and spectroscopy experiments demonstrated that as the temperature-activated fission process freezes in, the typical fluorescence power-law dynamics connected to triplet transport and fusion disappears, replaced by the intrinsic radiative lifetime and accompanied by a strong increase in fluorescence quantum yield and shorter wavelength fluorescence (see data in the figure above, right). We expect that the study of the correlation between emitted spectrum, suppression of the activated singlet-fission process, triplet transport, and onset of a dominant radiative emission from photoexcited singlet states will lead to a rich new set of observations and deeper understanding of these phenomena.

Future Plans

Our recent research lead to the development and demonstration of an extensive set of experimental and analysis tools that will allow the use of quantum interference in entangled triplet pairs, detected via fluorescence quantum beats, as an investigative tool to understand triplet exciton transport and the quantum decoherence processes that can be associated with it. There is now a large number of

exciton fission materials where quantum coherence and entanglement has not been studied yet and where the tools we developed should be applied.

As an example, there are several open question regarding the understanding of coherent and incoherent singlet fission processes for which scant experimental data is available. The ability to study fission also with respect to the establishment of the entangled triplet-pair state, not only with respect to the amount of triplet states created in the process, will be an important new research direction, especially when applied to other organic semiconductors characterized by a crystal lattice with inequivalent sites.

The study of the stability of spin-states in organic semiconductors and of the persistence of entanglement and how it varies between materials and as a function of crystal composition and lattice structure is also generally appealing towards establishing quantum properties of the spin states in organic semiconductors, which can be instrumental for possible applications in quantum information science.

It both surprising and interesting that within the large body of literature dedicated to singlet fission, quantum beats from entangled triplet-pair states have only been observed and studied in any depth in essentially just two materials, tetracene and rubrene. In view of the increasing interest in quantum information science it is important to further study spin states in organic semiconductors as a possible new quantum platform. The tools that we have developed and demonstrated are ideally suited for this.

References

1. Eric A. Wolf, Drew M. Finton, Vincent Zoutenbier, Ivan Biaggio, "Quantum beats of a multiexciton state in rubrene single crystals," Appl. Phys. Lett. 112, 083301 (2018).
2. D.M. Finton, E.A. Wolf, V.S. Zoutenbier, K.A. Ward, I. Biaggio, "Routes to singlet exciton fission in rubrene crystals and amorphous films," AIP Advances 9 (9), 095027 (2019).
3. Eric A. Wolf, Ivan Biaggio, "Geminate exciton fusion fluorescence as a probe of triplet exciton transport after singlet fission," Phys. Rev. B Letters 103 (20), L201201 (2021)
4. Gerald Curran III, Zachary Rex, Casper Xallan Wilson, Luke J. Weaver, Ivan Biaggio, "Persistence of spin coherence in a crystalline environment," Phys. Rev. Lett. **133**(5), 056901 (2024).

Publications

1. I. Biaggio, "Fluorescence quantum beats reveal tunable decoherence and the effect of transport in spin-entangled exciton pairs," Optica Open Preprint (9), 26885443 (2024).
2. Gerald Curran III, Zachary Rex, Casper Xallan Wilson, Luke J. Weaver, Ivan Biaggio, "Persistence of spin coherence in a crystalline environment," Phys. Rev. Lett. **133**(5), 056901 (2024).
3. Gerald Curran, Zachary Rex, Casper Xallan Wilson, Luke Weaver, Ivan Biaggio, "Transport-Induced Dephasing (TID) in a Crystalline Environment," APS March Meeting 2024, Anaheim (2024)
4. Zachary Rex, Luke Weaver, Gerald Curran, Casper Xallan Wilson, Ivan Biaggio, "Persistence of Triplet-Exciton Spin Entanglement in -acene Organic Materials," APS March Meeting 2024, Anaheim (2024)
5. Jia H Giam, Irene Figuera, Ivan Biaggio, Ivan Biaggio, "Paths to Singlet Fission in Rubrene," APS March Meeting 2024, Anaheim (2024)
6. G Curran, Z Rex, I Biaggio , "The Entangled Triplet Pair in Rubrene: Quantum Beats," Bulletin of the American Physical Society, Abstract N00.00123, APS March Meeting 2023, Las Vegas (2023)
7. J-H Giam, Z Rex, E Wolf, I Biaggio, "The Entangled Triplet Pair in Rubrene: Transport," Bulletin of the American Physical Society, Abstract N00.00124, APS March Meeting 2023, Las Vegas (2023)
8. Ivan Biaggio and Eric A. Wolf, "Geminate exciton fusion fluorescence as a probe of triplet exciton transport after singlet fission," Frontiers in Optics 2022, Rochester, New York United States, 17–20 October 2022, paper JTu4A.28.
9. Eric A. Wolf, Ivan Biaggio, "Geminate exciton fusion fluorescence as a probe of triplet exciton transport after singlet fission," Phys. Rev. B Letters **103** (20), L201201 (2021)

Opening New Frontiers of Epsilon-Near-Zero Optics

Alexandra Boltasseva, Purdue University (Principle Investigator)
Zubin Jacob, Purdue University (Co-Investigator)
Vladimir M. Shalaev, Purdue University (Co-Investigator)

Keywords: Epsilon-near-zero, nonlinear, transparent conducting oxides, transition metal nitrides

Research Scope

This project focuses on discovering novel platforms to enhance the generally weak interaction of light and matter by exploring novel interaction regimes. Specifically, we explore epsilon-near-zero (ENZ) materials whose real part of the dielectric permittivity approaches zero, taking a holistic approach to understanding and controlling ENZ properties in transparent conducting oxides (TCOs) and transition metal nitrides (TMNs). We study the enhancement of nonlinear optics in ENZ regime and preform optical characterization of ENZ materials focusing on ultrafast and extreme modulation of optical parameters. We also study the control of various emission processes in the presence of homogeneous and structured ENZ media. Our major results can be broadly categorized into two divisions i) investigation of material properties for ENZ applications and ii) the dynamic control and tunability of light using ENZ.

Recent Progress

Epsilon-near-zero materials host a plethora of exciting phenomena including field enhancement, wavelength expansion, and the slow-light effect. An important ENZ material platform are transparent conduction oxides that have static and dynamically tunable ENZ properties. This past period, we have focused partly on ENZ phenomena in dynamically pumped TCOs. We studied the role of losses in ENZ dynamics and demonstrated the spatial and spectral fission of light in optically-pumped thin film TCOs. We also discovered a new mechanism of third-harmonic generation in pumped TCOs which exhibits quadratic scaling instead of the standard cubic scaling. Next, we examined the role of dispersion in photonic time crystals – a new state of matter – in a TCO platform showing a significant reduction in stringent experimental requirements. Further, we experimentally demonstrated that the apparent dimensionality of an interacting ensemble of emitters could be modified using a resonant nanophotonic structure.

Spatio-spectral optical fission in time varying subwavelength layers

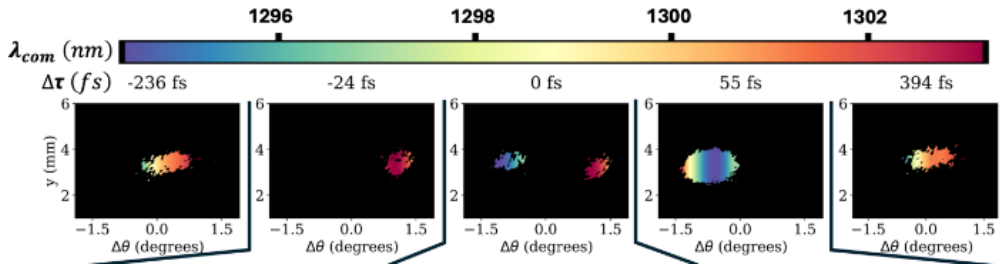

Figure 1. Full spatio-spectral information of transmitted probe pulse as the pump-probe delay is tuned. The probe transmitted beam profiles (with the x-axis recalibrated in deflection angle Δθ) together with the associated spatial spectral distribution for different values of the pump-to-probe time delay (Δτ).

Transparent conducting oxides are highly-doped semiconductors that exhibit favorable characteristics when compared to metals, including reduced material losses, tunable electronic and optical properties, and enhanced damage thresholds. Here, we report the spatio-spectral fission of an ultra-fast pulse trespassing a thin film of aluminum-doped zinc oxide with a non-stationary refractive index. We experimentally demonstrate and develop a model that by applying phase conservation to this time-varying layer accounts for both space and time refraction leading to a fission both the spectrum and the energy. Our findings represent an example of extreme nonlinear phenomena on subwavelength propagation distances and shed light on the nature of several nonlinear effects recently reported not

accounting for the full optical field distribution. Our work provides important insights into transparent conducting oxides' transient optical properties, which are critical for applications such as photonic time crystals, on-chip generation of nonclassical states of light, integrated optical neural networks as well as ultra-fast beam steering and frequency division multiplexing.

Nonlinear Loss Engineering in Near-Zero-Index Bulk Materials

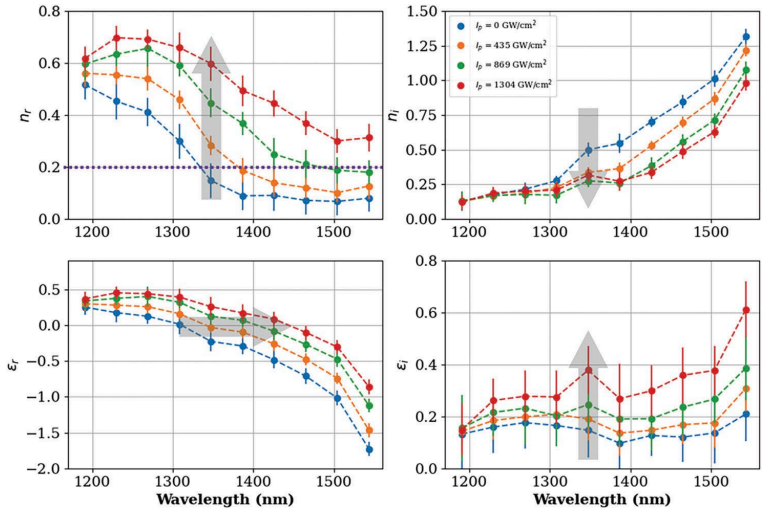

Figure 2. AZO's complex refractive index for various optical pump intensities. The index is retrieved via reflectance and transmittance measurements at various wavelengths and pump powers, while the pump and probe are overlapped temporally. The top panels display the real and imaginary components of index, while the bottom panels display the real and imaginary components of permittivity. Yellow, green, and red dashed lines represent pump intensities of 435 GW cm^{-2}, 869 GW cm^{-2}, and 1304 GW cm^{-2}, respectively.

Here we studied the nonlinear optical absorption properties of aluminum-doped zinc oxide (AZO) thin films in their near-zero-index (NZI) spectral window. We found that the imaginary part of the refractive index is reduced under optical excitation such that the field penetration depth more than doubles (*1*). An optically induced shift of the NZI bandwidth of ≈120nm for a pump intensity of 1.3 TW cm^{-2} is also demonstrated. Looking into the optically induced spectral redistribution of the probe signal, local net gain is recorded, which is ascribed to a nonlinear adiabatic energy transfer. Our study unveils the role of loss in these non-stationary systems building our understanding of processes such as parametric amplification and its viability for loss compensation.

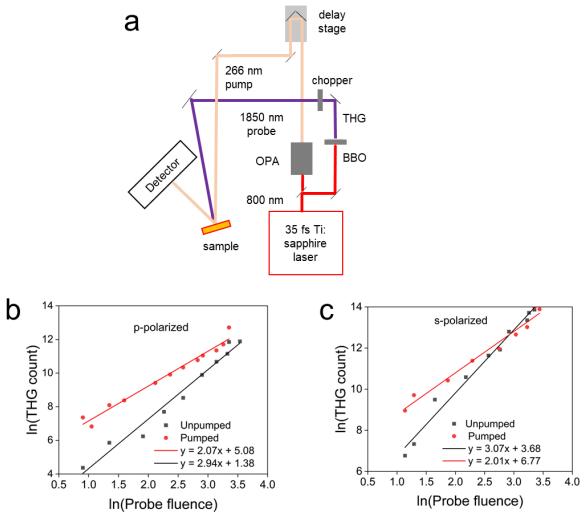

Figure 3. Third harmonic measurement setup b. Power dependence (log-scale) of third harmonic generation without pump and c. with pump.

Nonlinear optical phenomena are at the heart of various technological domains such as high-speed data transfer, optical logic applications, and emerging fields such as non-reciprocal optics and photonic time crystal design (*2*). However, conventional nonlinear materials exhibit inherent limitations in the post-fabrication tailoring of their nonlinear optical properties. Achieving real-time control over optical nonlinearities remains a challenge. We demonstrated (*3*) a novel method to switch third harmonic generation (THG), a commonly occurring nonlinear optical response. Third harmonic generation enhancements up to 50 times are demonstrated in zinc oxide films via the photoexcited state generation and tunable electric field enhancement. The enhanced THG follows a quadratic scaling with incident power, as opposed to the conventional cubic scaling, which demonstrates a previously unreported mechanism of THG. The THG can also be suppressed by modulating the optical losses in the film. We demonstrated that the photoexcitation of states can not only enhance nonlinearities, but can create new processes for THG. Importantly, our method enables real-time manipulation of the nonlinear response of a medium.

Reducing Effective System Dimensionality with Long-Range Collective Dipole-Dipole Interactions

We experimentally demonstrated (*4*) that the apparent dimensionality of an interacting ensemble of emitters is modified by employing a resonant nanophotonic structure. The dimensionality is encoded in the temporal fluorescence decay dynamics. The exponent β that relates to the apparent dimensionality of the interacting system is observed to be a non-integer value. The value of apparent dimensionality on a resonant plasmonic lattice shows a stark contrast value of $d \sim 2.20$, in comparison to $d \sim 3.0$ obtained on glass, an off-resonant TiO_2 dielectric lattice, and an off-resonant plasmonic lattice. Further, we extract the underlying distribution of energy transfer rates for the

interacting emitters' ensemble. The rates indicate a similar dimensionality modification. Our work paves the way for engineering interacting systems with apparent lower dimensionality.

Future Plans

Our future work will branch out from the funded effort in interconnected directions. First, we

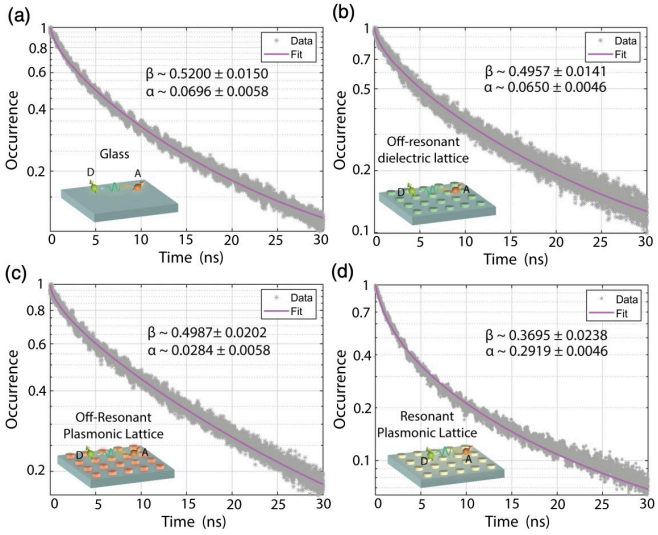

Figure 4. Measured fluorescence lifetime decay when the interacting emitters are in different electromagnetic environments: (a) glass substrate (a homogeneous environment), (b) TiO_2 dielectric lattice (an off-resonant inhomogeneous environment), and (c) a plasmonic lattice (a resonant inhomogeneous environment). The value of $\beta \sim 0.5$ in both inhomogeneous and off-resonant inhomogeneous environments. This is commensurate with a 3D system. In contrast, the faster-than-exponential decay dynamics on a resonant silver (Ag) plasmonic lattice reveals an exponent value of ~0.37. This is commensurate to an effective lower dimension $d \sim 2.20$.

investigate the non-stationary aspects of ENZ behavior. As our recent work suggests, the standard models for nonlinear optics do not hold in a time varying media, for example our observation of quadratic scaling of THG. Additionally, since ENZ materials are an ideal platforms to explore photonic time-crystals in dispersive surface modes, we will explore in more detail thin-film modes such as the Berreman and the ENZ mode, in non-stationary cases. Further, we will explore the localization of the spin and orbital degrees of freedom of light in disordered ENZ media.

References

1. W. Jaffray *et al.*, Nonlinear Loss Engineering in Near-Zero-Index Bulk Materials. *Advanced Optical Materials* **12**, 2301232 (2024).
2. M. G. Ozlu, V. Mkhitaryan, C. B. Fruhling, A. Boltasseva, V. M. Shalaev, Floquet Engineering of Polaritonic Amplification in Dispersive Photonic Time Crystals. *arXiv preprint arXiv:2408.00552* (2024).
3. S. Saha *et al.*, Third Harmonic Enhancement Harnessing Photoexcitation Unveils New Nonlinearities in Zinc Oxide. *arXiv preprint arXiv:2405.04891* (2024).
4. A. K. Boddeti *et al.*, Reducing Effective System Dimensionality with Long-Range Collective Dipole-Dipole Interactions. *Physical Review Letters* **132**, 173803 (2024).

Publications

10. V. Bondarev, A. Boltasseva, J. B. Khurgin, & V. M. Shalaev, *Crystallization of the transdimensional electron liquid*, arXiv preprint arXiv:2503.05165 (2025).
11. C. Fruhling *et al.*, *Time-Refraction Near the Critical Angle and Angular Streaking with Attosecond Resolution*, *Accepted: Optical Materials Express*, 2025.
12. W. Jaffray, S. Stengel, F. Biancalana, C. B. Fruhling, M. Ozlu, M. Scalora, A. Boltasseva, V. M. Shalaev & M. Ferrera, M. *Spatio-spectral optical fission in time-varying subwavelength layers*. Nature Photonics, 1–9 (2024).
13. M. G. Ozlu, V. Mkhitaryan, C. B. Fruhling, A. Boltasseva, & V. M. Shalaev, *Floquet Engineering of Polaritonic Amplification in Dispersive Photonic Time Crystals*. arXiv preprint arXiv:2408.00552 (2024).

14. W. Jaffray, F. Belli, S. Stengel, M. A. Vincenti, M. Scalora, M. Clerici, V. M. Shalaev, A. Boltasseva, & M. Ferrera, *High-order nonlinear frequency conversion in transparent conducting oxide thin films*. Advanced Optical Materials, **12**, 2401249 (2024).
15. P. Das, S. Rudra, D. Rao, S. Banerjee, A. I. K. Pillai, M. Garbrecht, A. Boltasseva, I. V. Bondarev, V. Shalaev, & B. Saha, *Electron confinement–induced plasmonic breakdown in metals*. Science Advances **10**, eadr2596 (2024).
16. X. Wang, X., T. V. Mechelen, S. Bharadwaj, M. Roknuzzaman, F. Bao, R. Rahman, & Z. Jacob, *Exploiting universal nonlocal dispersion in optically active materials for spectro-polarimetric computational imaging*, eLight, **4**, 1-13 (2024).
17. S. Bharadwaj, and Z. Jacob. *Thermal radiation with a twist*. Science **386**, 1348-1349 (2024).
18. A. Boddeti, Yi Wang, X. G. Juarez, A. Boltasseva, T. W. Odom, V. Shalaev, H. Alaeian, and Z. Jacob, *Reducing effective system dimensionality with long-range collective dipole-dipole interactions*, Phys. Rev. Lett. **132**, 173803 (2024).

Light-matter interaction phenomena using subwavelength engineering of material properties

PI: Igal Brener
Team members: Alex Cerjan, Raktim Sarma, Prasad Iyer, Chloe Doiron, Sadvikhas Addamane, Taisuke Ohta, Oleg Mitrofanov
Sandia National Laboratories, Albuquerque, NM 87185, USA

Keywords: Metasurfaces, quantum optics, light-mater interaction, semiconductors, nonlinear optics

Research Scope: Metamaterials and metasurfaces offer exquisite control over local electromagnetic near-field distributions, while also offering mechanisms to control far-field coupling and radiation modes. Our long-term objective is to uncover new optical and material behaviors that will expand our fundamental understanding of nanoscale materials, open up new territory for scientific discovery, and eventually lead to technologically relevant applications. Our activities proceed along two major research themes that will extend our previous breakthroughs in using metasurfaces for nonlinear optical processes and emission control of emitter ensembles: (1) increasing bi-photon rates and realizing new degrees of freedom for spontaneous parametric down-conversion using novel quantum optical metasurfaces, and (2) enabling metasurface-mediated light-matter interactions in sparse quantum dot systems.

Recent Progress

1. Quantum pair generation in nonlinear metasurfaces with mixed and pure photon polarizations: Nonlinear metasurfaces offer a versatile platform for exploring quantum phenomena, such as generating and manipulating entangled photons. In particular, polarization control is crucial for quantum applications such as quantum computation, quantum communication, and quantum simulation. Using our semiconductor nonlinear metasurfaces, designed to enhance photon pair generation via spontaneous parametric down-conversion (SPDC) through high quality-factor (Q) quasi-bound states in the continuum (BIC),[1] we demonstrated that the polarization state of the generated photon pairs can be controlled by adjusting the eigen-polarization of the resonant mode driving the nonlinear interaction.[2]

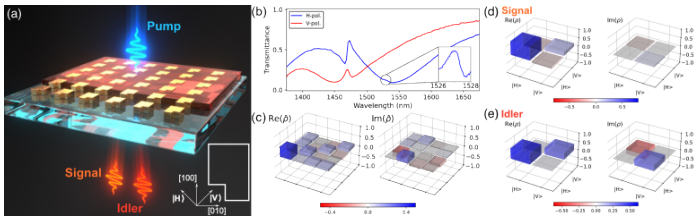

Figure 1: (a) Conceptual diagram of multiplexed entangled photon generation in a multi-resonance semiconductor metasurface. (b) Linear transmittance of the sample. (c) Real and imaginary part of the density matrix $\hat{\rho}$ for photon pairs generated by the MD-qBIC on QOM-A measured using two-photon polarization tomography. (d) Real and imaginary part of the density matrix $\hat{\rho}$ for a signal photon, and (e) for an idler photon, respectively, when photon pairs were generated by the MD-qBIC on QOM-A measured using single-photon polarization tomography.

For this purpose, we performed single and two-photon full tomography measurements of the emitted SPDC photons to characterize the quantum state and the purity of the emitted photons. We showed that the high polarization selectivity of the high-Q resonance enables the generation of pure single-photon polarization states and that the two-photon polarization states exhibit characteristics of mixed and nearly separable states. Furthermore, the single-photon polarization state of the signal photons closely resembles the far-field polarization of the qBICs and exhibits higher purity than the idler photons. These findings highlight the potential of these metasurfaces as heralded single-photon sources with controllable polarization.

We extended our work by using [110]-oriented GaAs metasurfaces with designs similar to those used for [001]-oriented GaAs metasurfaces. We observed not only enhanced SPDC efficiency from q-BIC resonances but also from low-Q modes, (not observable in the [001]-oriented counterparts). This

increase in SPDC efficiency from two spectrally and spatially overlapping yet distinct sources enabled the observation of quantum interference in the spectral domain.

2. Rational Designs to Control of Multiple Bound State in the Continuum and Resulting Polarization Singularities: High quality-factor (Q) modes are essential for enhancing light-matter interactions in all-dielectric photonic systems. While numerous approaches exist for creating high-Q modes, robust methods for simultaneously controlling multiple high-Q modes and their polarization vectors had remained underexplored. Building upon our work on symmetry-guaranteed pairs of bound states in the continuum, we demonstrated the manipulation of singularities arising from pairs of symmetry-protected bound states in the continuum. This was achieved through the creation, annihilation, and placement of polarization singularities via symmetry-breaking operations derived from a design framework rooted in group theory. Experimental results strongly validate theoretical predictions.[3]

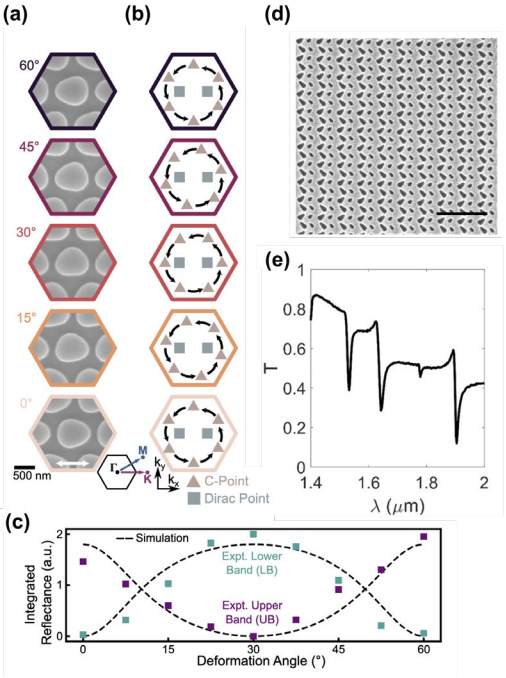

Figure 2: (a) Scanning electron micrographs of silicon metasurfaces where a 180º symmetry breaking deformation is rotated causing (b) points of perfect circular polarization (C-points) to rate in the upper and low bands. (c) Experimentally measure reflectance spectra match computational predictions. (d) Scanning electron micrograph of a quadruply resonant metasurface. (e) Experimentally measured reflectance spectra showing the existence of four high-Q resonances.

While symmetry-guaranteed degeneracies enable pairwise control, their limitation to two high-Q modes is suboptimal for enhancing four-wave mixing. To address this gap, we developed and demonstrated a rational design scheme based on symmetry to simultaneously engineer the optical lifetimes, free-space polarizations, mode profiles, and resonant wavelengths of up to four high-Q resonances. [4] These approaches enable the development of metasurfaces with enhanced performance for applications in classical and quantum optics, including narrowband sensors, modulators, and entangled photon-pair sources. As these design paradigms are rooted in group theory, they may open new pathways for mode control in systems beyond photonics, such as optomechanical and acoustic systems.

3. Semiconductor Metasurfaces with embedded Quantum Dots for Quantum Information Applications: In this period, we focused on developing semiconductor metasurfaces which can serve as sources of quantum light with the overarching aim of developing *a novel metasuface-based platform for Quantum Information systems using photons as qubits*. Semiconductor metasurfaces are well-suited for monolithic integration with of one of the most promising sources of quantum light, semiconductor quantum dots (QDs), while providing solutions to the critical technological challenges faced by the QDs: poor outcoupling efficiency, inhomogeneity of the emission wavelength, and the need for high-precision nanoscale device fabrication approaches. Our metasurface with embedded QDs is illustrated in Fig. 3a. We

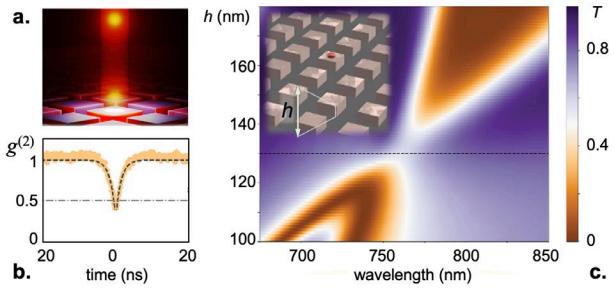

Figure 3: Semiconductor metasurface (MS) with embedded QDs for single-photon emission. (a) Illustration of photon emission from Huygens' MS. (b) Measured $g^{(2)}$ correlation function for photons from a single GaAs QD embedded in the AlGaAs MS, where the Huygens' point is controlled by the height of resonators, h, as illustrated in **c.**

deveoped two designs, with QDs coupled to superpositions of (1) in-plane electric (ED) and magnetic dipole (MD) modes (Huygens' metasurface) [5]; and (2) two degenerate in-plane and out-of-plane ED modes. The Huygens' metasurface design (Fig. 3c) facilitates free-space directional photon outcoupling for QDs with the dipole moment orientation in the metasurface plane, while the second design can facilitate preferential outcoupling for quantum emitters with the orthogonal dipole orientation. Both designs enhance the outcoupling by over one order of magnitude: for the Huygens' design, the outcoupling efficiency can reach up to 35% compared to 1-2% for QDs embedded in a dielectric slab. We experimentally realized the Huygens' design using low-density local droplet etched GaAs QDs and observed an enhancement of up to 20 times without deterioration of single-photon emitter properties (Fig. 3b) [5]. These results demonstrate that semiconductor metasurfaces can drastically improve photon extraction without the need for strict spatial position alignment, while also enabling filtering based on the wavelength and polarization. The metasurface-based platform therefore offers immense opportunities for fundamental studies in QD interactions, and for the development of novel quantum information systems.

4. Establishing Photoelectron-based Imaging of Light-Matter Interactions: Understanding the fundamental and fabrication limitations of metasurface design requires direct imaging of electromagnetic fields that dictate the light-matter interactions. As the response of the metasurface depends the system's symmetry and periodicity, metrology requires an imaging approach with nanoscale resolution, sensitivity to the field within the volume of the meta-atoms, and far-field excitation to reveal the symmetry of the resonances. In the photoemission process, the electromagnetic fields within the material excite electrons with higher field intensity resulting in a greater number of photoelectrons. We leveraged this relationship to image the spatial distribution of the fields within two exemplar metasurfaces via photoelectron emission microscopy (PEEM). In the visible range, we examined a metasurface of TiO_2 meta-atoms. By comparing two-photon photoelectron (2PPE) images to finite-difference time-domain simulations, we determined the inelastic mean free path (IMFP) of the very low-energy (<1 eV) photoelectrons to be ~35 nm. Because this IMFP is comparable to the height of the meta-atoms, the result highlights the sensitivity of photoelectron imaging to optical resonances supported within the meta-atom volume. Extending to the near-infrared wavelength, we showed the polarization-dependent variation of the spectra of a broken symmetry resonator metasurface supporting BICs. Altogether, these results showcase the applicability of photoelectron imaging to examine light-matter interactions in volume-type photonic resonances supported by dielectric nanophotonic structures.

Future Plans

i) Symmetry, chirality, linear and nonlinear optics: We plan to apply our design paradigms to develop metasurfaces for enhancing spontaneous parametric down-conversion and spontaneous four-wave mixing. Furthermore, while our current approaches enable single points of chirality, we are working towards a unified framework for enhancing chiral light-matter interactions allowing the creation of high-Q bands with enhanced chirality across the entire resonance band.

ii) Multiple QD interaction in metasurfaces: We aim to enable precise control of QD emission to facilitate and control the generation of complex quantum states of light by developing material- and photonic design-based approaches to enhance the overall emission efficiency, enable wavelength tuning, and explore QD interaction with metasurface resonances (including BICs).

iii) Enhancing photon pair generation rates using polaritonic metasurfaces: We plan to enhance photon pair generation rates by designing polaritonic metasurfaces coupled to quantum-engineered intersubband transitions supported by polar n-doped GaN/AlN-based heterostructures. We will design the heterostructure to achieve a nonlinear response that is at least 50x larger compared to GaAs. Figure 4 shows preliminary results where we already achieve a nonlinear susceptibility that is 10x larger compared to GaAs. Finally, we will utilize the inverse design techniques that we recently demonstrated for nonlinear metasurfaces to maximize photon pair generation.

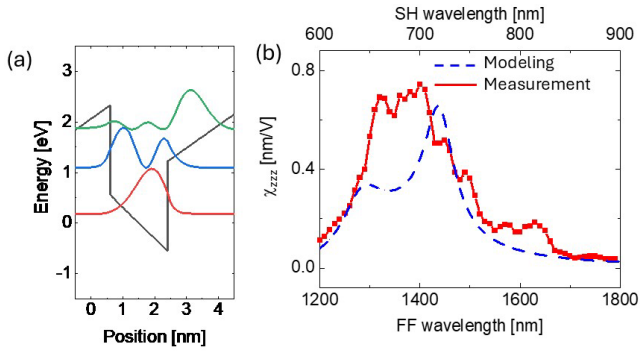

Figure 4: a: k.p band structure calculation of an optimized n-doped GaN/AlN heterostructure **b:** Experimental measurement of the nonlinear susceptibility of (**a**) and comparison to theory. This $\chi^{(2)}$ is 4X higher than GaAs.

iv) Imaging photomic-magnetic and photonic-electronic metasurface systems using photoelectrons: Taking advantage of photoemission being sensitive to magnetic and electronic properties, we aim to enable the intertwined interactions of photonic-driven magnetic lattices and metasurface-supported 2D materials. We plan to work on two-color photoelectron excitation to capture time-resolved phonemena and to extend into infrared photonic systems that are incompatible with lowering the work function via potassium.

References

1. T. Santiago-Cruz, S. D. Gennaro, O. Mitrofanov, S. Addamane, J. Reno, I. Brener and M. V. Chekhova, "Resonant metasurfaces for generating complex quantum states", Science **377**, 991 (2022).

2. J. Noh, T. Santiago-Cruz, V. Sultanov, C. F. Doiron, S. D. Gennaro, M. V. Chekhova and I. Brener, "Quantum Pair Generation in Nonlinear Metasurfaces with Mixed and Pure Photon Polarizations", Nano Lett. **24**, 15356 (2024).

3. C. F. Doiron, I. Brener and A. Cerjan, "Dual-Band Polarization Control with Pairwise Positioning of Polarization Singularities in Metasurfaces", Phys. Rev. Lett **133**, 213802 (2024).

4. S. C. Malek, C. F. Doiron, I. Brener and A. Cerjan, "Robust multiresonant nonlocal metasurfaces by rational design", Nanophotonics **14**, 449 (2025).

5. P. P. Iyer, S. Prescott, S. Addamane, H. Jung, E. Renteria, J. Henshaw, A. Mounce, T. S. Luk, O. Mitrofanov and I. Brener, "Control of Quantized Spontaneous Emission from Single GaAs Quantum Dots Embedded in Huygens' Metasurfaces", Nano Lett. **24**, 4749 (2024).

Two-year list of publications supported by BES (10 most relevant)

1. K. Y. Dixon, T. A. Loring and A. Cerjan, "Classifying Topology in Photonic Heterostructures with Gapless Environments", Phys. Rev. Lett **131**, 213801 (2023). DOI: 10.1103/physrevlett.131.213801
2. P. P. Iyer, N. Karl, S. Addamane, S. D. Gennaro, M. B. Sinclair and I. Brener, "Sub-picosecond steering of ultrafast incoherent emission from semiconductor metasurfaces", Nature Photonics (2023). DOI: 10.1038/s41566-023-01172-6

3. A. Boehm, S. D. Gennaro, C. F. Doiron, T. E. Beechem, M. B. Sinclair, I. Brener, R. Sarma and T. Ohta, “Near-field imaging of optical resonances in silicon metasurfaces using photoelectron microscopy”, APL Photonics **9**, 066103 (2024). DOI: 10.1063/5.0193683
4. C. F. Doiron, I. Brener and A. Cerjan, “Dual-Band Polarization Control with Pairwise Positioning of Polarization Singularities in Metasurfaces”, Phys. Rev. Lett **133**, 213802 (2024). DOI: 10.1103/physrevlett.133.213802
5. P. P. Iyer, S. Prescott, S. Addamane, H. Jung, E. Renteria, J. Henshaw, A. Mounce, T. S. Luk, O. Mitrofanov and I. Brener, “Control of Quantized Spontaneous Emission from Single GaAs Quantum Dots Embedded in Huygens' Metasurfaces”, Nano Lett. **24**, 4749 (2024). DOI: 10.1021/acs.nanolett.3c04846
6. H. Jung, I. Brener, S. J. Addamane, T. S. Luk, C. T. Harris, G. Subramania and O. Mitrofanov, “InAs Terahertz Metalens Emitter for Focused Terahertz Beam Generation”, Adv. Photonics Res. (2024). DOI: 10.1002/adpr.202400125
7. J. Noh, T. Santiago-Cruz, V. Sultanov, C. F. Doiron, S. D. Gennaro, M. V. Chekhova and I. Brener, “Quantum Pair Generation in Nonlinear Metasurfaces with Mixed and Pure Photon Polarizations”, Nano Lett. **24**, 15356 (2024). DOI: 10.1021/acs.nanolett.4c04398
8. J. H. Krakofsky, R. Sarma, I. Brener, A. Alù, J. Lee and M. A. Belkin, “Flat nonlinear optics with intersubband polaritonic metasurfaces”, Nanophotonics (2025).
9. S. C. Malek, C. F. Doiron, I. Brener and A. Cerjan, “Robust multiresonant nonlocal metasurfaces by rational design”, Nanophotonics **14**, 449 (2025). DOI: 10.1515/nanoph-2024-0551
10. S. Stich, J. Mohajan, D. de Ceglia, L. Carletti, H. Jung, N. Karl, I. Brener, A. W. Rodriguez, M. A. Belkin and R. Sarma, “Inverse Design of an All-Dielectric Nonlinear Polaritonic Metasurface”, ACS Nano (2025). DOI: 10.1021/acsnano.4c16934

A Nonlinear Approach to Topological Semimetals

Kenneth S. Burch, Boston College

Keywords: Topological Semimetals, Transport, Weyl, Raman, Nonlinear

Research Scope

This work builds on the PI's discoveries of novel phonon-electron interactions and colossal nonlinearity in topological semimetals (TSM) to understand their dynamics, enabling energy-efficient electronic interconnects, nonlinear optoelectronic, and thermal devices. In the previous reporting period, the PI proved TSM's ultrahigh transport mobilities result from the phonon-electron scattering far exceeding phonon-phonon, such that momentum is conserved in a phonon-electron fluid.[1] This explained how TSM with various symmetries, quantum geometries (Dirac, Weyl, Three-fold fermions), and Fermi surface topologies ($0<E_F<1.5$ eV) possess orders of magnitude larger transport than single particle mobilities. At the nanoscale, this universality disappears with electrical transport enhanced in thin NbAs and MoP, while the mobilities are degraded in Cd_3As_2. These results and fine-tuning the phonon-electron fluid motivate our systematic study of nanoscale TSM. Scattering also controls TSM's nonlinear responses, typically assigned to quantum geometry. Inspired by phonons boosting linear transport, we will employ nanoscale TSM devices to test the phonon-electron fluid's role in nonlinearity. Specifically, the PI will use his unique combination of fabrication and optical techniques to systematically explore the interplay between the phonon-electron fluid and quantum geometry in nanoscale TSM. First, we will explore phonon spectra changes as the materials are thinned and later with lateral confinement along specific crystal directions. In parallel, the electronic evolution will be explored by combining broadband IR spectroscopy and transport measurements. Here, we aim to uncover how the confinement changes in scattering and dispersion alter the electron-fluid (via phonon scattering) and electron transport. With this knowledge, we will be well-positioned to uncover the phonons' role in nonlinear responses.

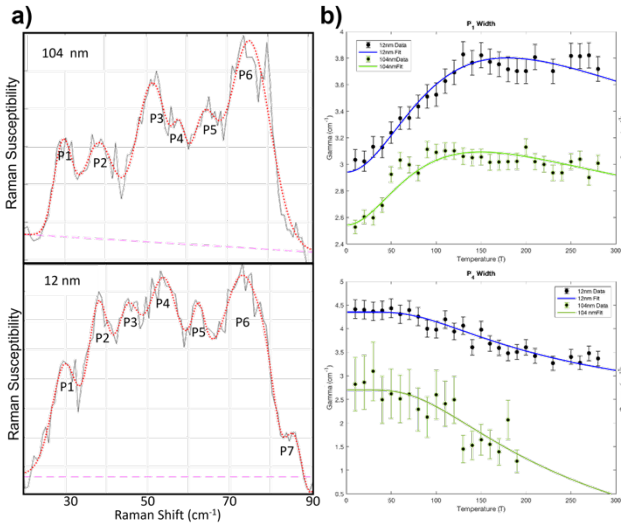

Figure 1: a) Raman spectra for bulk-like (104nm -top) and ultrathin (12nm - bottom) Cd_3As_2 films. b) Linewidth versus temperature for two representative modes, demonstrating phonon-electron scattering.

Recent Progress

The PI has been studying the Raman response of Cd_3As_2 films to understand the role of nanoconfinement on the phonon-electron fluid. Specifically, the temperature dependence of films with thicknesses ranging from 12nm to 104nm have been measured. We focus on the six modes seen below 100 cm^{-1} that provide the strongest and well-isolated signals. Their energies and symmetries match previous studies on bulk (See Figure 1), and do not change substantially upon thinning. Furthermore, as shown in Figure 1b, we find their linewidths versus temperature to be quite anomalous, but in line with our previous TSM results obtained with support from the DOE-PBM program in TSM.[2,3] Specifically, a typical phonon decays via anharmonic scattering into other phonons, producing a linewidth that grows with temperature due to Bose statistics. However, in TSM, the linewidths either grow much more rapidly, saturate, and then are reduced at higher temperatures or are reduced with temperature. This behavior results from the dominance of phonon-electron scattering and is described by the Fermi statistics of the electrons. As seen from the figures, we

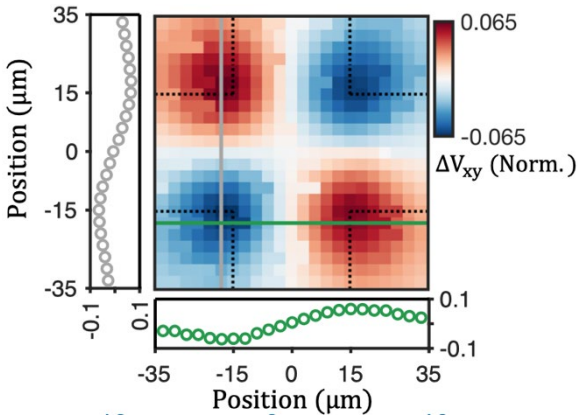

Figure 2: Phonon-electron scattering strength for Bi(top) and Cd3As2 (bottom) for all modes studied.

observe substantial differences between the thin (12nm - blue lines) and bulk-like (104nm – green lines).

Due to the large unit cell of Cd_3As_2, its band structure undergoes substantial changes below 70nm. Thus, we have also measured thin Bi single crystals to test the extent to which these results occur due to MBE growth versus a large unit cell. Indeed, Bi is a TSM that similarly possesses a large discrepancy between its transport and single particle mobilities. Nonetheless, a temperature-dependent study of its phonons has never been reported. To this end, we employ Bi single crystals grown by hot pressing between hBN. This allowed us to study samples of nearly similar thicknesses (15nm and 80nm). Again, the resulting spectra matched previous bulk results.

Following our standard protocol,[1,3] the phonon linewidths for Bi and Cd_3As_2 were fit to separate the electron-phonon, phonon-phonon, and disorder scattering. The resulting electron-phonon coupling strengths for both materials are reported in Figure 2. Here, we find that the scattering of the Bi phonon modes is unaffected by reducing the thickness to 15 nm. However, for Cd_3As_2, we find nanoconfinement results in a substantial enhancement of the phonon-electron scattering for all phonons. The origin of this enhancement remains unclear, but it could result from small changes in the Fermi level and/or the phase space for phonon-electron scattering.

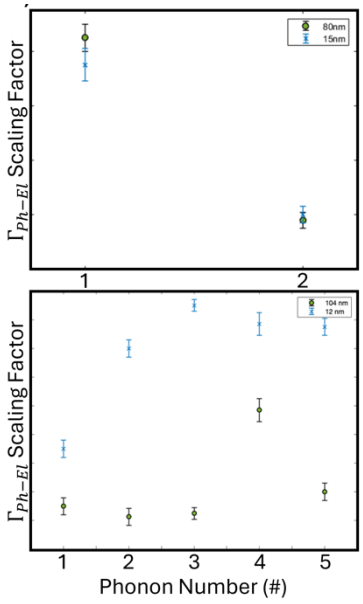

Figure 3: Transverse photoresistance in a Pt cross for different positions of a Mid-IR laser.

Simultaneously, we have optimized the device design to eliminate unwanted thermal signals in nonlinear photocurrent experiments. Specifically, following our previous DOE-PBM-supported work demonstrating the enormous second-order nonlinear responses of TSM,4,5, we have been developing a new means to study current-induced second-order optical responses. These offer two advantages: studying the quantum geometry of inversion symmetric materials and potentially exploring its change around the Fermi surface.

Nonetheless, as with standard second-order responses, these can be plagued by artifacts from contacts or thermal responses due to the Seebeck effect. To this end, we have developed a device geometry that completely eliminates such responses. This was achieved through an iterative process by studying the response of Au and Pt crosses of various shapes, sizes, and device geometries. Interestingly, this also revealed a new optically induced transverse photo-resistance. As shown in Figure 3, by applying a current in the x direction, we find a transverse voltage from shining a mid-IR laser on the substrate. Strangely, this response changes sign as the laser crosses the current or voltage leads. Extensive tests with different wavelengths, substrates, and thicknesses, as well as comparisons with COMSOL simulations, proved these results from current deflection. Specifically, the laser induces a thermal gradient in the substrate, causing a gradient in the device resistance. As a result, the current is deflected away from the gradient, producing the transverse voltage. These results are currently under review at Applied Physics Letters.

Our efforts in studying phonons, fabrication, nanoconfinement, and their role in transport also contributed to a recent work on W5N6 MXENES. Specifically, we helped to demonstrate the absence of resistance enhancement upon reduction to the nanoscale thicknesses. This offers a new route of chemically converted materials for future interconnects. Lastly, our efforts in optimizing heterostructures, device fabrication, and characterization, developed as part of this effort, have contributed to several other studies on the mobility of 2D semiconductors, the role of structure in 2D magnets, and optimization of intercalation into various materials for device applications.

Future Plans

We continue to study the thickness dependence of the Raman response of Cd_3As_2 and Bi thin films. Here, we aim to uncover a clear trend in the role of nanoconfinement, separate from strain or changes in the Fermi level, on the phonon-electron scattering and transport. Simultaneously, we are optimizing the fabrication of these materials into devices for Nonlinear thermal and photocurrent response experiments. The nonlinear photocurrent experiment is also being adapted for low temperatures to study how the phonons affect the nonlinear responses.

References

1. V. Plisson et al., *Engineering Anomalously Large Electron Transport in Topological Semimetals*, Advanced Materials **23**, e2310944 (2024).

2. H.Y. Yang et al., *Evidence of a coupled electron-phonon liquid in NbGe2*, Nature Communications **12**, 5292 (2021).

2. G. Osterhoudt et al., *Evidence for Dominant Phonon-Electron Scattering in Weyl Semimetal WP_2*, Physical Review X **11**, 011017 (2021).

Publications

1. D. Cao et al., *Li Dynamics in Mixed Ionic-Electronic Conducting Interlayer of All-Solid-State Li-metal Batteries*, Nano Letters **24**, 1544 (2024).

2. J.D. Thomsen et al., *Effect of Surface Oxidation and Crystal Thickness on the Magnetic Properties and Magnetic Domain Structures of $Cr_2Ge_2Te_6$*, ACS Nano **18**, 13458 (2024).

3. G. Villalpando et al., *Accessing bands with extended quantum metric in kagome $Cs_2Ni_3S_4$ through soft chemical processing*, Science Advances **10**, eadl1103 (2024).

4. A. Kumar et al., *High-temperature superconductor based mid-infrared detector*, Optics Communications **579**, 131548 (2025).

5. A. Kumar et al., *Downscaling of Non-Van der Waals Semimetallic W_5N_6 with Resistivity Preservation*, ACS Nano **19**, 3362 (2025).

6. T. Zheng et al., *Ultrafast and Highly Mobile Photocarriers in Monolayer WSe2 Doped by α-$RuCl_3$*, Nano Letters **25**, 4054 (2025).

Unequivocal Identification of Spin-Triplet Superconductors with Half Quantum Flux

C. L. Chien

The Johns Hopkins University

Keywords: Spin-triplet superconductors, flux quantization, and half quantum flux

Research Scope

Known superconductors (SCs) are mostly spin-singlet (numerous *s*-wave and some *d*-wave) and few spin-triplet SCs. Spin-triplet SCs, essential for Majorana fermions and fault-tolerant quantum computing, but are rare and difficult to identify with traditional methods. We use phase-sensitive measurements to detect half-quantum flux (HQF) in flux quantization in sub-μm rings to identify triplet SCs. Previously we have observed HQF in polycrystalline β-Bi_2Pd rings. Recently, we have observed HQF in composite rings of Nb connecting the opposite crystalline ends of epitaxial β-Bi_2Pd. With increasing temperature, the half-integer-flux quantization transits to integer-flux quantization. These findings unequivocally demonstrate odd-parity pairing symmetry in spin-triplet β-Bi_2Pd.

Recent Progress

Superconductivity occurs due to Bose-Einstein condensation of Cooper pairs of two electrons, as explicitly displayed in the fundamental constant of flux quantum $\Phi_0 = hc/2e \approx 2 \times 10^{-15}$ T-m^2, where h is the Planck constant, c the speed of light, and $2e$ the Cooper pair charge. The Cooper pairs in superconductors (SCs) may be spin-singlet with spin 0 or spin-triplet with spin 1. The known SCs are overwhelmingly spin-singlet, mostly *s*-wave (e.g., Al, Nb) and some *d*-wave (e.g., cuprates). Spin-triplet SCs, essential for Majorana fermions and fault-tolerant quantum computing, are rare and difficult to identify with traditional methods such as upper critical field exceeding the Pauli limit and NMR Knight shift.

The essential differences between singlet and triplet SCs in gap parity, Cooper spin, and time reversal symmetry lead to distinct features in half quantum flux (HQF), Andreev reflection spectroscopy (ARS), and superconducting tunnel junctions (STJs) for unequivocal identification of singlet and triplet SCs. Here we describe the recent results of HQF in superconducting rings of β-Bi_2Pd.

Singlet SCs (*s*-wave and *d*-wave) have even parity with the same gap values upon inversion. This leads to integer quantum flux (IQF) of $\Phi = n\Phi_0$ (n = 0, 1, 2…), where the resistance minima occur at integer quantum number n, known as the Little-Park effect [1] as has been observed in numerous rings of singlet SCs, both polycrystalline and epitaxial (e.g., Al, Nb, cuprates, etc.). The gap value of triplet SCs

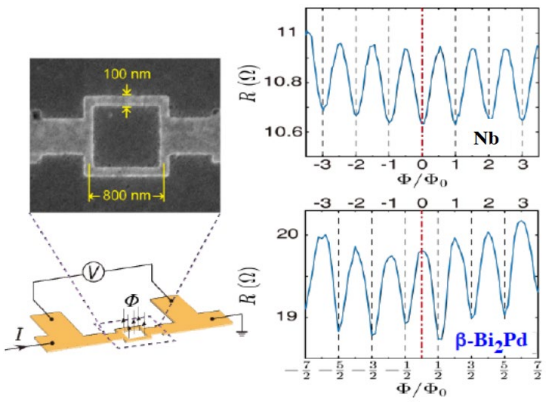

Fig. 1. Integer (Nb) and half-integer (β-Bi_2Pd) flux quantization observed in polycrystalline SC rings, with structures shown on the left. [Li, Xu, Lee, Chu, and Chien, Science **366**,238 (2019)].

with odd parity changes sign upon inversion. Consequently, the resistance minima occur at half quantum flux (HQF) of $\Phi = (n+ ½)\Phi_o$ if there are odd number of sign changes in the gap value in the grain boundaries in a *polycrystalline* ring as opposed to IQF of $\Phi = n\Phi_o$ with an even number of sign changes in the gap values, or no sign change as in epitaxial rings. These characteristics lead to unequivocal identification for triplet SCs as in β-Bi_2Pd [2].

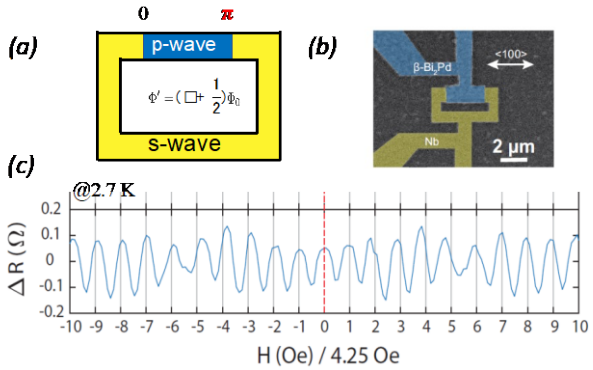

Fig.2: (a) GLB composite ring of triplet (p-wave) connected at the ends with a singlet (s-wave) structures, (b) actual GLB structure of epitaxial β-Bi_2Pd and Nb and (c) the observed half-integer flux (n + ½)Φ_o. [Xu. Li, Chien, Phys. Rev. Lett..**132**, 056001(2024)]

In polycrystalline triplet rings, the total number of sign changes in the gap values are random. The identification of triplet pairing requires *multiple* rings showing both IQF and HQF of similar occurrence. The identification of singlet pairing also requires multiple polycrystalline rings showing only IQF. Recently, we have demonstrated unequivocal identification of any SC, singlet or triplet, using *one composite* ring of an *epitaxial* SC and an *s*-wave SC with only a *single* measurement [3].

Geshkenbein, Larkin and Barone (GLB) [4] first proposed the composite ring structure consisting of a triplet SC and a singlet s-wave SC as shown in *Fig. 2a*, where the triplet SC segment must be a *single crystal* (or *epitaxial*) to preserve the orientation of the odd-parity triplet gap, whereas the singlet SC (e.g., Nb) with an isotropic gap can be polycrystalline. Due to its odd-parity gap, the two ends of the triplet SC with the singlet SC have opposite signs. Thus, the GLB composite ring contains only *one* sign change thus *always* exhibits HQF of $\Phi = (n + 1/2)\Phi_o$, the definitive signature of a triplet SC.

The definitive GLB rings require high resolution lithography of fabricating a μm-sized composite ring structure [3] of an epitaxial triplet SC of β-Bi_2Pd and a polycrystalline singlet SC of Nb (*Fig. 2b*), where we have observed only HQF (*Fig. 2c*). The measured oscillation period of 4.25 Oe is consistent with the expected period from the area of 4.2 x 1.6 μm^2 of the ring. In such a GLB composite ring, one obtains the definitive evidence of HQF of triplet SC with only *one* measurement [3].

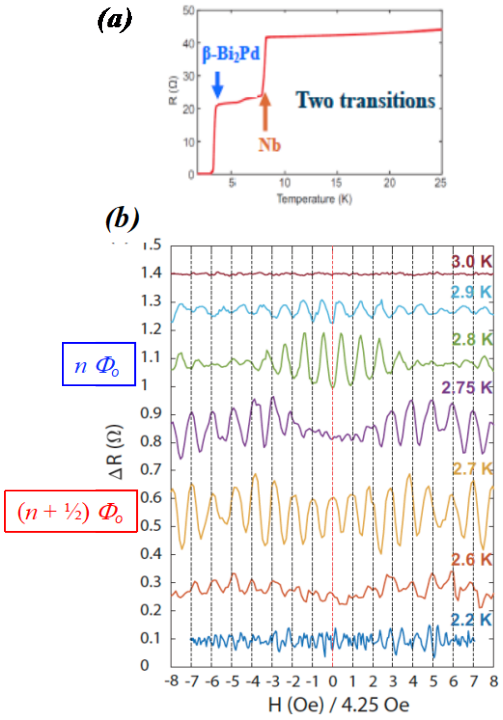

Fig. 3: (a) Two transitions of Nb (8 K) and β-Bi_2Pd (3.4 K) in the GLB composite ring. (b)Flux quantization changes from HQF to IQF a function of temperature [Xu. Li, Chien Phys. Rev. Lett.,**132**, 056001(2024)]

The GLB composite ring consists of two SC shows two superconducting transitions of singlet *s*-wave Nb ($T_C \approx 8$ K) and triplet β-Bi_2Pd ($T_C \approx 3.4$ K) as shown in *Fig.3a*. This combination of a singlet and a triplet also reveals other unusual features. At 2.7 K, just below the T_C of β-Bi_2Pd, HQF has been observed as shown in *Fig. 2c* and *Fig.3b*. At 2.75 K, the resistance minima at half-integers

began to move towards those at integers. At 2.8 K and 2.9 K, the resistance minima are at integers at lower fields but washed out at the higher fields. With increasing temperatures, as the *triplet* pairing with HQF in β-Bi_2Pd fading away, the composite ring acquires *singlet* pairing with IQF due to the proximity effect of Nb.

In summary, notwithstanding the challenges of fabricating GLB composite rings of two SCs with an epitaxial triplet SC, the GLB composite rings reveal its triplet nature by exhibiting only half-quantum flux. The unequivocal identification can be accomplished in one GLB ring with one measurement.

Future Plans

We use HQF in polycrystalline rings and GLB composite rings to identify other triplet SCs, both centrosymmetric and noncentrosymmetric SCs. We are also developing Andreev reflection spectroscopy for identifying triplet SCs and fabricating superconducting tunnel junctions involving spin-triplet SCs.

References

1. W. A. Little and R. D. Parks, "*Observation of Quantum Periodicity in the Transition Temperature of a Superconducting Cylinder*," Phys. Rev, Lett., **9**, 9 (1962).
2. Yufan Li, Xiaoying Xu, M. H. Lee, M. W. Chu, and C. L. Chien, "*Observation of Half-Quantum Flux in Unconventional Superconductor β-Bi_2Pd*," Science, **366**, 238 (2019).
3. Xiaoying Xu, Yufan Li, and C. L. Chien, "*Observation of odd-parity superconductivity with the Geshkenbein-Larkin-Barone composite rings*," Phys. Rev. Lett. **132**, 056001 (2024).
4. V. B. Geshkenbein, A. I. Larkin, and A. Barone, "*Vortices with half magnetic flux quanta in ''heavy-fermion'' superconductors*," Phys. Rev. B **36**, 235 (1987).

Publications supported by DOE

1. Jinsong Xu, Weiwei Lin, Jiaming He, J.-S. Zhou, Danru Qu, Ssu-Yen Huang, and C. L. Chien, "*Vector spin Seebeck effect and spin swapping effect in antiferromagnetic insulators with non-collinear spin structure*," Appl. Phys. Lett. Mater. **11**, 091102 (2023).
2. C. C. Chiang, H. C. Lee, S. C. Lin, D. Qu, M. W. Chu, C. D. Chen, C. L. Chien, and S. Y. Huang, "*Unequivocal identification of spin-triplet and spin-singlet superconductors with upper critical field and flux quantization*," Phys. Rev. Lett. **131**, 236003 (2023).
3. Jinsong Xu, Jiaming He, J.-S. Zhou, Danru Qu, Ssu-Yen Huang, and C. L. Chien, "*Electrical Seebeck-contrast observation of magnon Hall effect in topological ferromagnet $Lu_2V_2O_7$/heavy metal heterostructures*," Phys. Rev. B (Lett) B **109**, L020401 (2024).
4. Xiaoying Xu, Yufan Li, and C. L. Chien, "*Observation of odd-parity superconductivity with the Geshkenbein-Larkin-Barone composite rings*," Phys. Rev. Lett. **132**, 056001 (2024).
5. Yufan Li, Xiaoying Xu, Shu-Ping Lee, and C. L. Chien, "Unconventional periodicities of the Little-Parks effect observed in a topological superconductor," Phys. Rev. B **109**, L060504 (2024).

Thermoelectric Effects and Spin-Mediated Heat Transport in Novel Materials

Joshua L. Cohn, Department of Physics, University of Miami

Keywords: heat transport, thermoelectricity, spin Seebeck, magnons, superconductivity

Research Scope

This program involves experimental transport studies of spin-mediated heat transport and thermoelectric effects in novel materials that elucidate the interaction and exchange of energy between subsystems: magnon-phonon interactions, charge-carrier pairing in an extreme low-carrier density superconductor, spin-charge conversion at magnetic insulator-superconductor interfaces. Some of the materials targeted for study are low-dimensional and have novel thermoelectric or magnetic properties already established in published and preliminary work.

Recent Progress

Anisotropic thermal conductivity of CuO

[Phys. Rev. Mater. **8**, 124403 (2024).]

The monoxide CuO received much attention given its potential to inform the physics of high-Tc superconductors, the quasi-one-dimensional character of its high-energy antiferromagnetic spin dynamics,[1] and more recently, for the discovery of novel, spin-driven ferroelectricity[2] in one of its high-T antiferromagnetic spin phases. CuO and NiO provide rare examples of three-dimensional collinear antiferromagnetic ordered phases with large exchange coupling (J~100 meV) and are of interest for the study of thermal conductivity (κ) by magnons (the wide energy separation between phonon and magnon acoustic spectra limits a direct interaction through hybridization). NiO crystals have internal twin and/or magnetic domain boundaries that suppress κ below 35 K and mask any magnon term. Surprisingly, no work prior to ours had been published on heat conduction in CuO single crystals; κ for other monoxide crystals[Error! Bookmark not defined.] (MnO, NiO, CoO) were studied in the 1950s and 1960s. CuO is commonly employed as a thermal additive, thus reliable thermal conductivity data can also inform applications, e.g. as input in modeling heat exchange in such compound fluids.

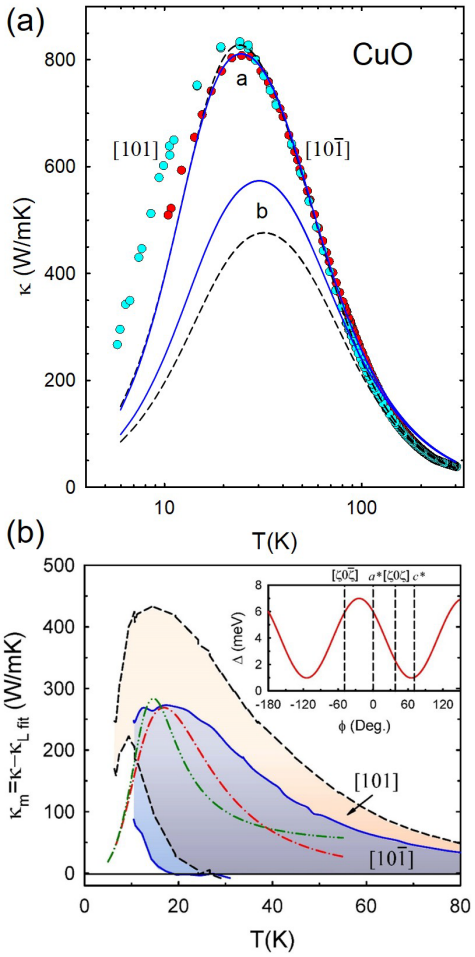

Fig. 1 (a) Thermal conductivity (κ) data (solid circles) for the [10$\bar{1}$] and [101] directions (along and transverse to the spin chains) with two curves for each (labeled a and b) calculated from the anisotropic Callaway model for lattice conductivity. (b) Inferred magnon contributions for the two directions computed by subtracting the model lattice conductivity curves in (b) from the measured data. The shaded regions highlight the range of possible values defined by the boundaries set by the computed curves in (b) The dash-dotted (dash-dot-doted) curve is κ_m computed for the [101] direction using an anisotropic spin gap, $\Delta(\phi)$, shown in the inset, and a sum of rates for magnon-boundary scattering and empirical rates for 4-magnon (magnon-phonon) scattering.

Evidence of a substantial magnon heat conductivity along the [10$\bar{1}$] and [101] (Fig. 1) was revealed in the difference between the measured κ and model calculations of the lattice thermal conductivity that

employed published phonon dispersions and successfully modeled κ for other directions. The magnitude of the magnon κ ($\geq$ 200 W/mK near 20 K) is in reasonable accord with that calculated using the known spin-wave spectrum.

Superconductivity at carrier density 10^{17} cm^{-3} in quasi-one-dimensional $Li_{0.9}Mo_6O_{17}$

[Phys. Rev. B **108,** L100512 (2023).]

This work incorporated low-T ($T \gtrsim 0.4$ K) magnetotransport data (Hall, magnetoresistance, thermopower and Nernst) within the most conducting bc-plane (field along a) for both superconducting (SC) and non-superconducting (non-SC) $Li_{0.9}Mo_6O_{17}$ (LiPB) crystals of this quasi-one-dimensional (q1D) conductor. The principal findings are a clear signature of two-carrier physics [Fig. 2 (a), (b)] and extremely low carrier densities ($n \approx 10^{17} cm^{-3}$) [Fig. 2 (c)], among the lowest known for any superconductor. The interelectron distance at T_c, $d_{ee} \cong n^{-\frac{1}{3}} \approx 22\,nm$, is comparable to or smaller than the relevant superconducting coherence lengths ξ_b~30 nm and ξ_c~10 nm, i.e. Cooper pairs do not substantially overlap. Equivalently, the ratio of critical temperature to effective Fermi temperature, $T_c/T_F \gtrsim 0.1$. Both assessments place LiPB's parameters near the border between BCS superconductivity and Bose-Einstein condensation. An unusual aspect of the transport is the predominance of electron-like carriers along the q1D chains and hole-like character transverse throughout most of the temperature range, suggesting a density-wave-induced reconstruction of the Fermi surface[3] to a semimetallic state at temperatures far above that of the minimum in electrical resistivity ($T_{min} \approx 15 - 30\,K$), the latter a mystery for decades. In non-SC specimens a sharp suppression of mobile carrier density at $T \lesssim 10$ K may indicate a second density-wave gapping of

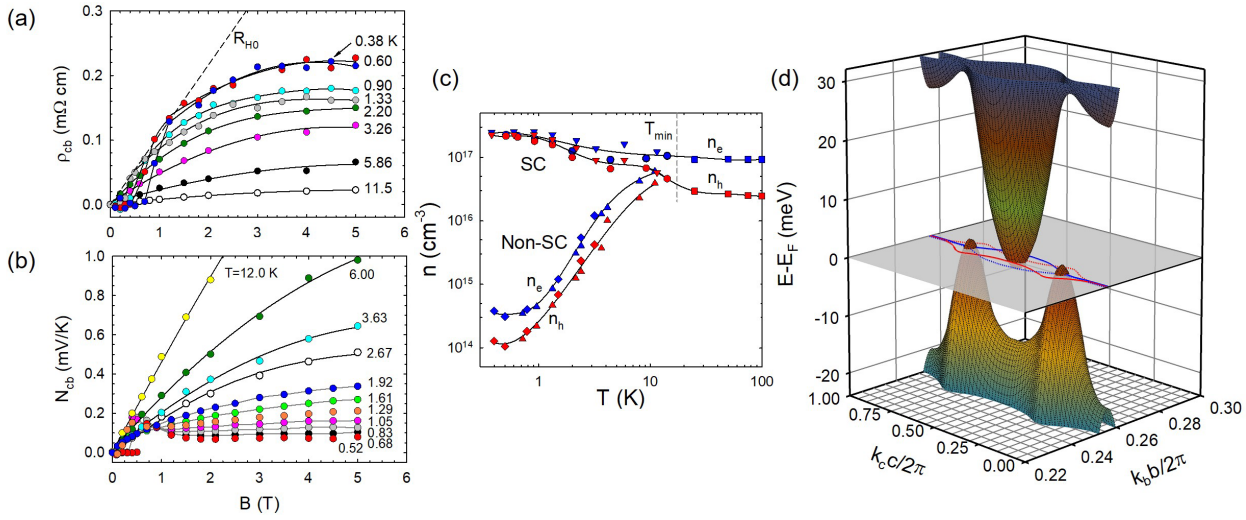

Fig. 2 Hall resistivity (a) and Nernst signal (b) versus magnetic field for SC LiPB with electric and heat currents along the chains (b axis); the non-linearity of these curves indicates contributions from electrons and holes. (c) carrier densities from anisotropic 2-band simultaneous fitting of the Hall and magnetoconductivities. Different symbols represent the two pairs of crystals (for SC and non-SC specimens) with $\boldsymbol{J} \parallel \boldsymbol{b}$ and $\boldsymbol{J} \parallel \boldsymbol{c}$. Solid curves are guides. (d) Energy band scheme and Fermi plane (adapted from Ref. 3) assuming a SDW gap-induced reconstruction to a semimetal with $E_F = 1.5$ meV for both hole and electron bands. Shown in the $E = E_F$ plane is the incomplete nesting of the unreconstructed FS (solid curves: upper sheet -- red, lower sheet -- blue) and their translations by the nesting vector $q_{SDW} = 2k_F \cong \pi/b$ along k_b (dashed curves).

most of the residual Fermi surface that renders the system non-metallic transverse to the conducting chains.

Quasiparticle Spin-Charge Conversion and Spin-Seebeck Effect at Niobium/Cu_2OSeO_3 interfaces

Only recently have ferromagnetic insulator-superconductor (FMI-SC) interfaces been investigated within the spin pumping context. Non-local experiments[4] indicate that competing effects influence the quasiparticle (QP) spin-charge conversion efficiency in FMI-SC interfaces: SC coherence effects and the exchange-field modified QP relaxation. Open questions remain for theory given the complexity of the couplings of different nonequilibrium imbalances (magnon, spin, charge, heat) with the exchange spin-splitting [reflected in the SC density of states—Fig. 3 (a)] and their inclusion in the relevant nonlinear kinetic equations in the SC.

Building on our prior work [PRB **95**, 224407 (2017), PRB **99**, 020403(R) (2019), PRB **101**, 100407(R) (2020)] studying magnon heat conduction and the longitudinal spin Seebeck effect with Pt contacts in Cu_2OSeO_3 [the inset of Fig 3 (b) shows its spin phases] we recently succeeded in fabricating superconducting, 10-20 nm-thick niobium films grown on the (111) polished face of thin Cu_2OSeO_3 crystals. The bulk measurement configuration [Fig. 3 (b)], has the advantage of accurately determining the thermal gradient, simultaneously yielding the thermal conductivity and longitudinal spin Seebeck coefficient (S_{LSSE}).
Figure 3 (c) shows S_{LSSE} versus applied field at two temperatures for a 10-nm Nb/Cu_2OSeO_3 device, $S_{LSSE} = (V_{Nb}/\Delta T)(\ell_{Nb}/\ell_{RuO})$, where ΔT is the temperature difference along the heat flow, and ℓ_{Nb} and ℓ_{RuO} are distances between the Nb voltage contacts (essentially the width of the crystal) and the

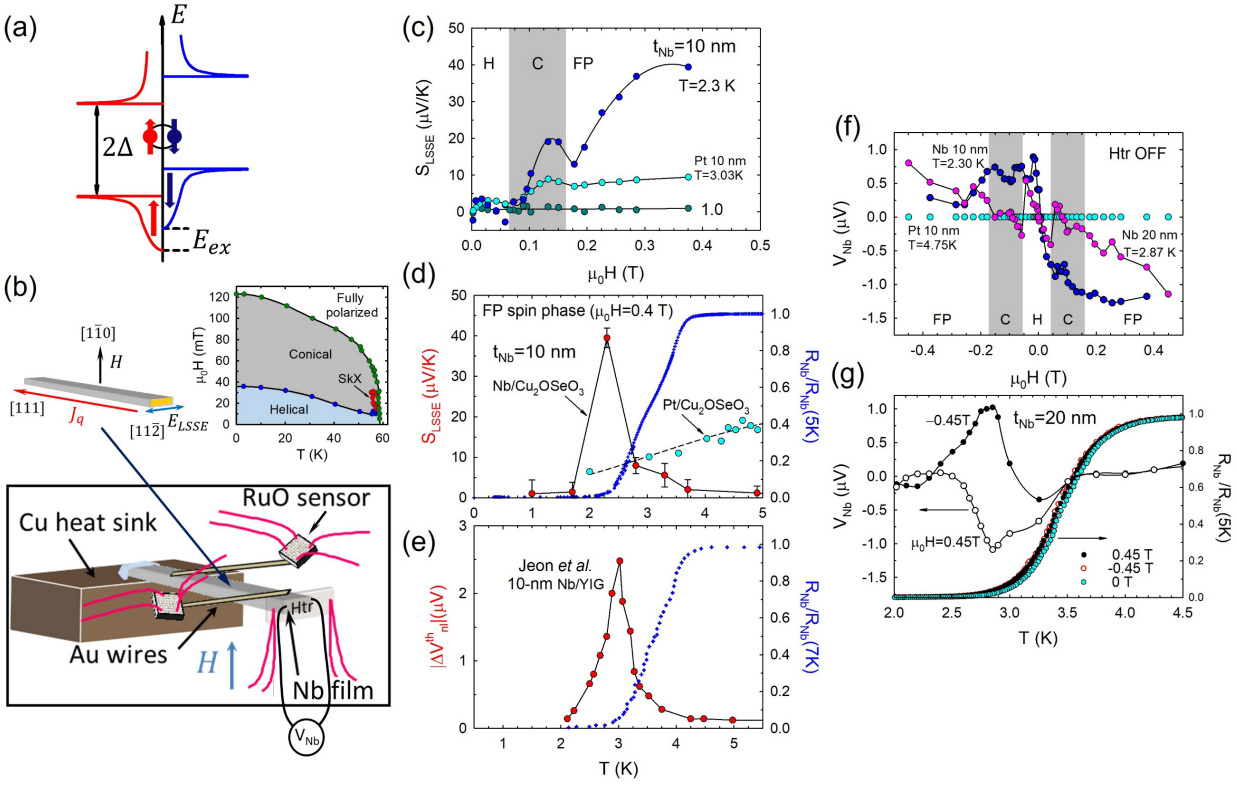

Fig. 3 (a) schematic of the exchange spin-split density of states in a superconducting thin film adjacent to a FM insulator. (b) schematic of the bulk, longitudinal spin Seebeck measurement setup (with thin Nb film deposited on the free end of the crystal beneath the heater) and inset: spin phase diagram for bulk Cu_2OSeO_3. (c) spin Seebeck coefficient for 10-nm Nb/Cu_2OSeO_3 at two temperatures below the superconducting transition compared to measurements at a similar T for 10-nm Pt/Cu_2OSeO_3 from our prior work. (d) Right ordinate: normalized $R(T)$ for the 10-nm Nb/Cu_2OSeO_3. Left ordinate: S_{LSSE} at $\mu_0 H = 0.4\,T$ for the same heterostructures in (c). (e) nonlocal thermally-induced Nb voltage via spin injection and normalized $R(T)$ for 10-nm Nb/YIG (Ref. 4) (f) Heater OFF Nb voltages vs applied field for 10-nm and 20-nm Nb/Cu_2OSeO_3 devices compared to that for 10-nm Pt/Cu_2OSeO_3 at temperatures corresponding to their maximum signals. (g) Right ordinate: $R(T)$ for the 20-nm Nb/Cu_2OSeO_3 device at $\mu_0 H = 0, \pm 0.45\,T$. Left ordinate: Heater OFF Nb voltage at $\mu_0 H = \pm\,0.45\,T$.

RuO sensors, respectively, and Fig. 3 (d) has $S_{LSSE}(T)$ at fixed field ($\mu_0 H = 0.4\,T$) in the fully-polarized spin phase; also shown in both Fig. 3 (c) and (d) is S_{LSSE} for 10-nm Pt/Cu_2OSeO_3 from our prior work. The giant enhancement near the "foot" of the superconducting transition is also observed in the non-local measurements of Ref. 4 for 10-nm Nb/YIG [Fig. 3 (e)]. This enhancement for our 10-nm device is at least a factor of 60 given that its S_{LSSE} maximum is about 6 times that of the Pt device at the same T and the normal-state S_{LSSE} for Nb is about 10 times smaller than that for Pt, scaling as the ratio of their spin-Hall angles, $\theta_{SH}^{Pt}/\theta_{SH}^{Nb} \approx 10$.

A remarkable surprise is our observation of clear, sharp features in the *heater off* $V_{Nb}(H)$ of both 10-nm and 20-nm devices [Fig. 3 (f)] that are coincident with the spin-phase boundaries of Cu_2OSeO_3 (grey shaded regions). This is in marked contrast to the $V_{Pt}(H)$ plot for the 10-nm Pt/Cu_2OSeO_3 device which is **zero and featureless, as to be expected with the heater off and no driving force for a net spin current.** Figure 3 (g) shows the heater off $V_{Nb}(T)$ for the 20-nm device in the fully spin-polarized phase ($\mu_0 H = 0.45\,T$) and the superconducting resistive transition, demonstrating that the signal reverses with applied field (following the magnetization of Cu_2OSeO_3) and that the giant enhancement appears in the foot of the transition.

Future Plans

- LiPB: superconducting-state heat conduction in magnetic field to assess the gap anisotropy; further investigations of the extreme low-carrier density metallic state along the chains of non-superconducting crystals
- Nb/Cu_2OSeO_3 interfaces: control experiments using wide-area crystals, short along [111], to rule out a small ΔT as potential driving force for the heater-off spin Seebeck results (Fig. 3); deposition of thin Al_2O_3 spin-blocking layer between Nb film and Cu_2OSeO_3 to confirm spin injection as the source of the novel observations and to assess the exchange energy (from the expected enhancement of the Nb film T_c).

References

1. H. Jacobsen, S. M. Gaw, A. J. Princep, E. Hamilton, S. Tóth, R. A. Ewings, M. Enderle, E. M. Hétroy Wheeler, D. Prabhakaran, and A. T. Boothroyd, *Spin dynamics and exchange interactions in CuO measured by neutron scattering*, Phys. Rev. B **97**, 144401 (2018).
2. T. Kimura, Y. Sekio, H. Nakamura, T. Siegrist, and A. P. Ramirez, *Cupric oxide as an induced-multiferroic with high-T_C*, Nat. Mater. **7**, 291 (2008).
3. L. Dudy, J. W. Allen, J. D. Denlinger, J. He, M. Greenblatt, M. W. Haverkort, Y. Nohara, O. K. Andersen, *ARPES and NMTO Wannier Orbital Theory of $LiMo_6O_{17}$ – Implications for Unusually Robust Quasi-One Dimensional Behavior*, arXiv:1812.03388.
4. Kun-Rok Jeon, Jae-Chun Jeon, Xilin Zhou, Andrea Migliorini, Jiho Yoon, and Stuart S. P. Parkin, *Giant Transition-State Quasiparticle Spin-Hall Effect in an Exchange-Spin-Split Superconductor Detected by Nonlocal Magnon Spin Transport*, ACS Nano **14**, 15874−15883 (2020).

Publications

1. A. Akopyan, N. Prasai, A. Rebello, J. J. Neumeier, and J. L. Cohn, Anisotropic thermal Conductivity of CuO, Phys. Rev. Mater. **8**, 124403 (2024).
2. J. L. Cohn, C. A. M. dos Santos, and J. J. Neumeier, Superconductivity at carrier density 10^{17} cm^{-3} in quasi-one-dimensional $Li_{0.9}Mo_6O_{17}$, Phys. Rev. B **108**, L100512 (2023).

Controlling thermal expansion with composition in framework oxide materials

Joya A. Cooley, Department of Chemistry and Biochemistry, California State University, Fullerton

Keywords: transition metal oxide, negative thermal expansion, diffraction, chemical pressure

Research Scope

This project aims to systematically manipulate chemical pressure through composition in a framework oxide material exhibiting negative thermal expansion (NTE) toward understanding controlling tunability of thermal expansion. Thermal expansion describes how the dimensions of a material change with temperature. Conventionally, materials exhibit positive thermal expansion (PTE) and expand when temperature is increased, but some materials exhibit negative thermal expansion (NTE) and are useful as thermal compensators. Control of thermal expansion in an end material can be achieved when PTE and NTE materials are composited and the thermal expansion of the final material can be tuned to what is desired; to allow for tuning, understanding the tunability of thermal expansion on an atomic level is key. NTE has been observed above 400 °C in framework oxide $Zn_2V_2O_7$[1] and we endeavor to understand the mechanisms of thermal expansion as we change chemical composition toward design principles for controllable thermal expansion. NTE in materials such as $Zn_2V_2O_7$, called framework oxides, depends on the flexibility of the structure and the transverse vibrations of certain oxygen atoms which are corner shared between polyhedral in the crystal structure. While oxygen is important to the NTE mechanism, other factors within the crystal chemistry can affect the rigidity or flexibility of certain bonds to control thermal expansion. In this project we synthesize, characterize, and use variable temperature X-ray diffraction (VTXRD) and dilatometry understand both intrinsic and bulk thermal expansion of framework oxides. We target solid solutions of $Zn_2V_2O_7$ as $Zn_{2-x}M_xV_2O_7$, where *M* is one of the substituent ions in Table 1. Each substituent imparts a different degree of negative or positive chemical pressure onto the structure, and we can begin with this size difference as a place to understand changes in the structure, thermal expansion, and other properties. The substituents can also give insight into other characteristics that may affect observed properties, such as covalent/ionic character of the bonds, Lewis acidity or basicity, average observed coordination number. Finally, our prior work[3] shows the importance of understanding not only intrinsic thermal expansion using diffraction or other average structure techniques, but also bulk thermal expansion through dilatometry. While knowledge of how to control intrinsic thermal expansion can help develop design principles, understanding the overall changes in bulk thermal expansion will be important to future applications.

Table 1: $Zn_2V_2O_7$ substituent ions

Ion	5-coordinate radius[2]
Ni^{2+}	0.63
Cu^{2+}	0.65
Mg^{2+}	0.66
Co^{2+}	0.67
Zn^{2+}	**0.68**
Mn^{2+}	0.75
Ca^{2+}	1.00*

Recent Progress

Advanced in-house instrumentation: We have obtained a state-of-the-art powder X-ray diffractometer with improved resolution over our previous instrument and the ability to filter some wavelengths to decrease the effect of fluorescence in Co- and Mn-containing. A comparison of the data quality between the previous instrument and new instrument is shown in Figure 1. Additionally, the diffractometer has a furnace attachment which allows us to collect VTXRD data in-house. While VTXRD data collection at synchrotron sources will likely always be our goal because of the exceptionally high resolution, the in-house VTXRD data collection will allow us to understand phase purity and temperature regions of interest to optimize the time we spend during synchrotron data collection allocations.

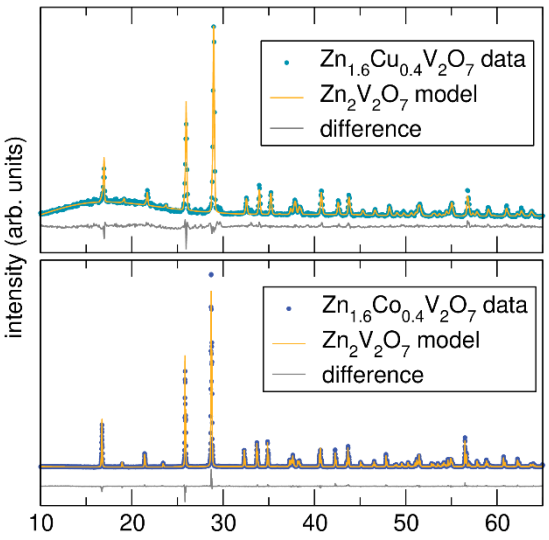

Figure 1: Rietveld refinements of X-ray diffraction data on *M* = Cu (top) and Co (bottom) with maximum successful substitution amounts. Bottom data set show enhanced data quality of new XRD instrument.

Establishing synthetic control over solid solutions containing five of six M substituents:

We have established reproducible ceramic and sol-gel synthetic methods for solid solutions containing five of the six target substituent ions – *M* = Ni, Cu, Mg, Co, and Mn. Rietveld refinements of X-ray diffraction data of the most recent synthetic accomplishments are shown in Figure 1. Synthetic methods have been iteratively tested to understand the maximum solubility of each ion, and maximum substitution amount is in good agreement with maximum solubility established in the literature.

Observing changes in thermal expansion onset and hysteretic behavior:

Recently, we have collected temperature-dependent diffraction data on several solid solutions during two national lab data allocation times at the Stanford Synchrotron Radiation Lightsource. Through our partnership with SSRL, Dr. Kevin Stone at Beamline 2-1 acquired an Anton Parr capillary heating stage for the beamline. Here, we have collected VTXRD data, including while cycling temperature. We are conducting Rietveld refinements to understand how lattice parameters evolve with temperature, and these analyses lead us to interrogate each material more deeply using other probes. We have collected data for solid solutions with *M* = Mn, Ni, Co. *M* = Mn (x = 0.1, 0.2; Figure 2) data show the transition to NTE behavior occurs at 300 °C, which is near 100 °C cooler than the transition to NTE behavior in the parent compound. This substitution of Mn, exhibiting positive chemical pressure, represents the first of our results which shows tunability in the NTE onset temperature, and will allow further study of the phonon densities of states through collaboration to understand the effect of Mn substitution.

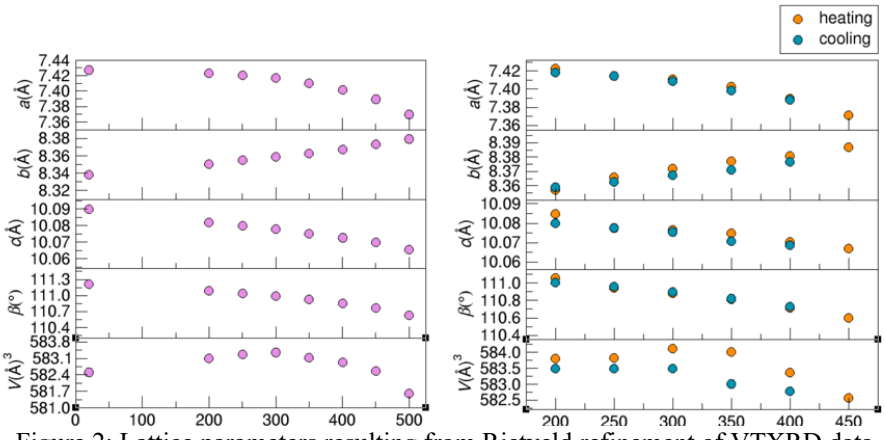

Figure 2: Lattice parameters resulting from Rietveld refinement of VTXRD data for $Zn_{2-x}Mn_xV_2O_7$ with x = 0.1 (left) and x = 0.2 (right).

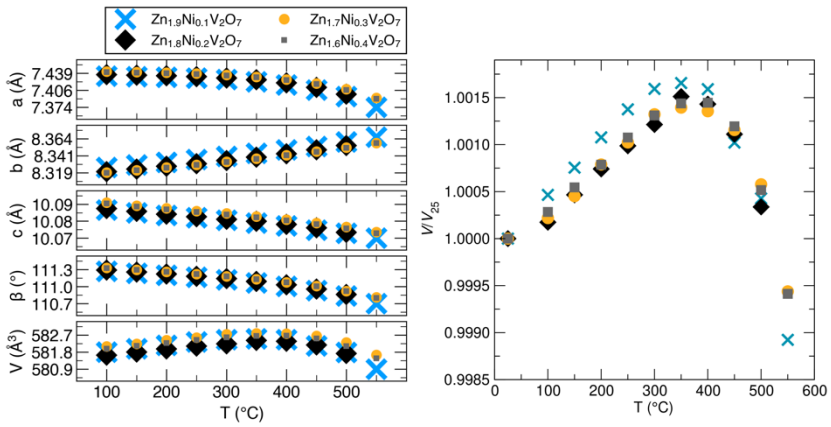

Figure 3: Left: Lattice parameters resulting from Rietveld refinement of VTXRD data from SSRL for four compositions. Right: Volume changes relative to the ambient volume (V_{25}).

Additionally, slight changes in the overall coefficient of thermal expansion in the NTE region relative to the parent compound are observed Mn = 0.2 also shows considerable hysteresis between heating and cooling data, both in the reappearance of the low-temperature α-phase value and the overall unit cell volume with temperature. This result allows us to explore the structural and/or energetic underpinnings of the stabilization of the higher temperature phase at low temperatures.

VTXRD data on samples with *M* = Ni (x = 0.1, 0.2, 0.3, 0.4; Figure 3) have been collected to understand the effect of negative chemical pressure on thermal expansion properties. The trend in the temperature-dependent lattice parameters is overall the same as the parent compound, and samples within the solid solution do not show gross differences from one another. The relative volume change, however, shows that smaller amounts of Ni substitution result in greater changes in the volume. We are using neutron diffraction to understand the true Ni composition and oxygen occupancy to understand if these may be responsible for the trend in properties.

Establishing a hypothesis for the changing phase transition temperature: $Zn_2V_2O_7$ exhibits a structural phase transition from α-$Zn_2V_2O_7$ in space group *C*2/*c* ß-$Zn_2V_2O_7$ in space group *C*2/*m* around 650 °C, and this transition temperature can be changed with substituents on the Zn site.[4] Recently, we have observed similar transitions when M = Mn and Co, in addition to our previously published work where *M* = Mg. Each of these substitutions decreases the temperature at which the phase transition is observed and can be used to tune this transition temperature. We believe that the average observed coordination and Lewis acidity could be responsible for lowering the transition temperature. In α-$Zn_2V_2O_7$, the Zn site is 5-coordinate, and in ß-$Zn_2V_2O_7$ it is 6-coordinate. According to the average observed coordination numbers,[5] Zn prefers to be 5-coordinate. Substituents like Mn and Mg which prefer to be 6-coordinate have lowered the transition temperature, implying that these stabilize the high temperature phase which allows for 6-coordinate polyhedra.

Future Plans

We plan to use several other methods to probe changes to the structure and composition as a function of both substituent concentration and temperature. Specifically, we will employ both ambient and temperature-dependent neutron diffraction to: 1) understand true composition in cases where ions cannot be discerned by synchrotron X-rays (e.g., Zn/Ni mixed occupancy); 2) probe oxygen vacancies, since light elements like O can be detected by neutrons. Since the mechanism of thermal expansion in these types of materials depends primarily on the transverse vibration of 2-coordinate oxygen atoms, the oxygen occupancy is important to probe. We will aim to understand how oxygen occupancy changes with compositional substitution on the Zn site and with temperature. We will also aim to intentionally create oxygen vacancies using deep eutectic solvent synthesis methods to systematically control oxygen vacancies. Following from our previous work which shows major differences between intrinsic and bulk thermal expansion, we will also use dilatometry to quantify bulk thermal expansion of these materials while cycling temperature. Through collaboration, we will also study phonon densities of states for the $Zn_2V_2O_7$ and modifications thereof to understand the anharmonicity through Grüneisen parameters.

References

1. M. V. Rotermel. and T. I. Krasnenko, *Mechanism of thermal expansion of structural modifications of zinc pyrovanadate*, Kristallografiya **62**, 703 (2017).
2. R. D. Shannon, *Revised effective ionic radii and systematic studies of interatomic distances in halides and chalcogenides*, *Acta Cryst.* **A32,** 751(1976).
3. E. T. B. Esteban, J. J. Garcia, S. R. Windover, and J. A. Cooley, *Intrinsic thermal expansion and tunability of thermal expansion coefficient in Ni-substituted* $Co_2V_2O_7$, J. Phys.: Mater. **6**, 045011 (2023).
4. G. Mahler, C. O. Iyare, Jr., C. Avalos, S. Kong, K. Kovnir, and J. A. Cooley, *Tuning thermal expansion and phase transition temperature with Mg substitution in* $Zn_2V_2O_7$, J. Solid State Chem. **347**, 125296 (2025).
5. I. D. Brown, *What factors determine cation coordination numbers?*, Acta Cryst. **B44**, 545 (1988).

Publications

A manuscript is under preparation currently.

Characterization of Functional Nanomachines

PI: Michael F. Crommie[1,2]
Co-PIs: Felix R. Fischer,[1,3] Steven G. Louie,[1,2] Andy M. Minor,[1,4] Alp Sipahigil,[1,5] Feng Wang[1,2]
[1]Materials Sciences Division, Lawrence Berkeley National Laboratory, Berkeley, CA 94720
[2]Physics Department, UC Berkeley, Berkeley, CA 94720
[3]Chemistry Department, UC Berkeley, Berkeley, CA 94720
[4]Materials Science and Engineering Department, UC Berkeley, Berkeley, CA 94720
[5]EECS Department, UC Berkeley , Berkeley, CA 94720
Keywords: nanostructure, nanomechanical, molecular, graphene, quantum

Research Scope: This program is focused on exploring and developing nanostructures (termed "nanomachines") that utilize their mechanical degrees of freedom to convert energy and information from one form to another. Central goals include controlling nanomachine behavior down to *atomic* length scales, understanding how dissipation affects nanomachine activity, and performing energy transduction processes with quantum limited control. The program is focused on two broad thrusts: **(1)** fabrication and characterization of *synthetic molecular* nanomachines, and **(2)** *phase coherent* control of nanomachines. Controlling the behavior of nanomachines down to the atomic scale requires the development of new techniques for assembling molecular nanostructures and for incorporating them into operational devices. At molecular scales the placement of even a single atom can completely change nanomachine function, and so new methods for creating *atomically-precise* nanostructures must be developed. Phase coherent control of nanomachines is necessary for performing broadband energy and information conversion processes. We utilize atomically-thin 2D materials to create new nanostructures that exhibit mechanical, electromagnetic, and quantum phase coherence, and which allow different quantum degrees of freedom to be flexibly coupled. This program has six co-investigators whose expertise span physics, chemistry, materials science, and electrical engineering. The experimental tools utilized within this collaboration range from synthetic chemistry, electron microscopy, and scanned probe techniques (**Fischer, Minor,** and **Crommie**), to optical spectroscopy, silicon-based NEMS, and quantum characterization (**Wang** and **Sipahigil**). **Louie** provides theoretical support through the use of *ab initio* density functional theory-based simulations.

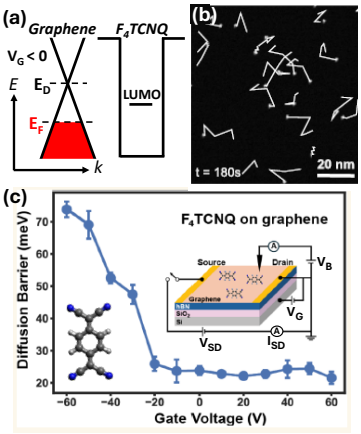

Fig. 1: (a) Graphene and F_4TCNQ electronic structure. (b) STM map of diffusing F_4TCNQ molecules. (c) Experimental diffusion barrier of F_4TCNQ on graphene.[17]

Recent Progress: Here we highlight some of our activities spanning both molecular scale nanomachine behavior as well as phase coherent nanomachine behavior. We will highlight three subprojects involving (1) *molecular diffusion*, (2) *molecular spin systems*, and (3) *phase coherent THz phonon stacks*.

(1) Gate-tunable molecular diffusion on 2D devices: We have developed new techniques to control how molecules move on 2D field-effect transistor (FET) devices.[1,17] This is accomplished by back-gating our devices to tune E_F and then transiently heating them with electrical current. By choosing molecules with frontier orbitals (e.g., HOMO and/or LUMO levels) that lie in the gate-tunable energy range of E_F in our 2D devices we are able to toggle the charge-state of the molecules by tuning E_F above/below the molecular orbital energy (E_{LUMO}) (Fig.1a). We find that the diffusivity of molecules

on single-layer graphene FET devices is highly gate-tunable, allowing the molecular diffusivity to be tuned over six orders of magnitude depending on the substrate temperature.[17]

The molecule used for this work was F_4TCNQ (Fig.1c, inset) since it has a LUMO level that lies energetically very close to the graphene Dirac point (E_D) (Fig.1a). We evaporated F_4TCNQ molecules onto the surface of a graphene FET in UHV and then imaged the molecular behavior using a cryogenic scanning tunneling microscope (STM). Positive gating of our device ($V_G > 0$) shifted E_F above E_{LUMO}, thus causing each F_4TCNQ molecule to accept a single electron and become negatively charged, whereas negative gating ($V_G < 0$) shifted E_F below E_{LUMO} and caused the molecules to return to a charge-neutral state. By heating the graphene device with electrical current we were able to visualize the diffusive motion of F_4TCNQ molecules (Fig. 1b) and to determine how molecular diffusion barriers depend on gate-voltage for the first time (Fig.1c). We observe that the F_4TCNQ diffusion barrier rises steeply as gate-voltage is reduced in the neutral-molecule regime, whereas the diffusion barrier stays low and gate-independent in the charged-molecule regime. Comparison of our data to ab initio simulations using density functional theory shows that this behavior can be explained by a dominance of *purely translational* diffusion pathways in the charged regime and *rotational* diffusion pathways in the neutral regime (Fig. 2). The strong gate-tunability of the diffusion barrier on graphene suggests that graphene could be used as a *diffusion switch*.

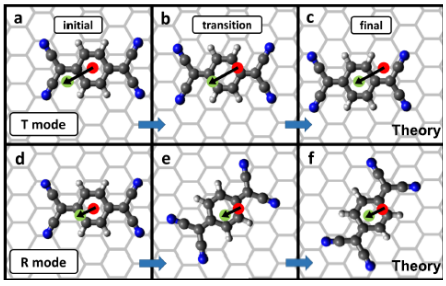

Fig. 2: Calculated translational (top) and rotational (bottom) diffusion pathways for F_4TCNQ molecules on graphene.[17]

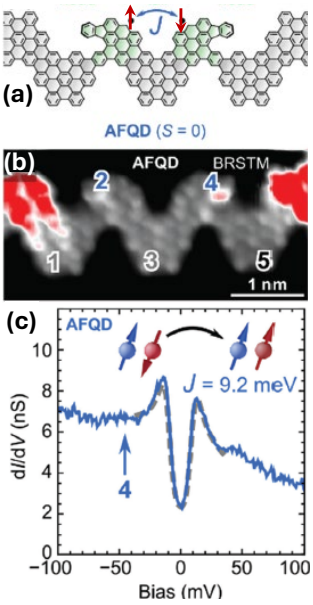

Fig. 3: (a) Structure of spin centers incorporated into a chevron GNR. (b) STM image of GNR having structure shown in (a). (c) STM spectroscopy shows signatures of AF coupling between spin centers in (b).[20]

(2) Atomically-precise synthesis of coupled molecular spin systems: An important goal of our program is to ultimately create molecular nanomachines that can manipulate quantum information. Because spin is so effective at storing quantum information, we are motivated to develop new ways to control spin in covalently-bonded molecular nanostructures, a process requiring the ability to fabricate atomically-precise structures. We recently made a breakthrough in this topic by developing a new method for introducing local spin centers into bottom-up-fabricated graphene nanoribbons (GNRs).[20] GNRs are a good platform for this application because they can be grown as defect-free quasi-1D nanostructures with highly tunable electronic structure. We introduced spin into GNRs by engineering local GNR sublattice asymmetry (i.e., if N_A (N_B) is the number of carbon atoms in the A (B) GNR sublattice, then a spin center with $S = ½ |N_A - N_B|$ will result). Working with our collaborators we fabricated the first molecular precursors that allow local spin-½ centers to be directly incorporated into GNRs using bottom-up growth techniques.[20]

We successfully grew different molecular spin configurations using the chevron GNR platform, including isolated spin centers, ferromagnetically (FM) coupled spin centers, and antiferromagnetically (AF) coupled spin centers.[20] Fig. 3a shows a sketch of the atomic structure of a pair of AF-coupled spin centers in an otherwise nonmagnetic chevron GNR, while Fig. 3b shows an STM image of the

actual experimental system (the spin centers reside at sites **2** and **4**). STM spectroscopy performed on these spin centers revealed the strength of AF-coupling through inelastic spin-flip processes (Fig. 3c).

(3) Phase coherent control of THz phonon response in stacked 2D devices: We discovered that nanomachines fabricated from layered stacks of 2D materials enable flexible phase coherent nanomechanical control up to THz frequencies.[21] Our 2D stacks were made from individual layers of graphene, hBN, and transition metal dichalcogenide (TMD) materials (Fig. 4). Such stacks can be thought of as vertical "ball-and-spring" models, where the different layers are associated with different masses and spring constants. Different layered patterns can thus be engineered to have different vibrational (i.e., phonon) response. The phonons can be driven with short (fs) pulses of light and read-out using high-frequency pump/probe optical spectroscopy (Fig. 4).

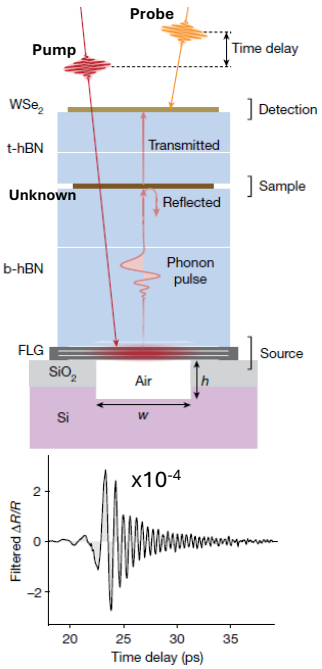

Fig. 4: (Top) Sketch of 2D stack used to probe THz acoustic phonons. (Bottom) Reflectivity signal shows time-resolved THz response.[21]

We demonstrated the efficient generation, detection, and manipulation of THz phonons in such stacks by using few-layer graphene as a broadband phonon transducer to convert fs near-infrared pulses to acoustic-phonon pulses. A monolayer of WSe_2 was used as the readout sensor through strong exciton-phonon coupling (Fig. 4). We demonstrated high-Q THz phononic cavities and showed that a WSe_2 monolayer embedded in hexagonal boron nitride can efficiently block the transmission of THz phonons, thus creating new opportunities for developing phononic metamaterials and ultrafast phase coherent nanomachines.[21]

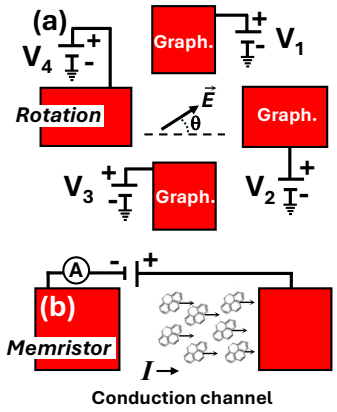

Fig. 5: (a) Proposed device geometry for actuating molecular rotors. (b) Proposed molecular memristor geometry.

Future Plans: Our plans for the future involve the development of new experimental tools and nanomachine structures to help us gain nanomechanical control down to the atomic scale. This will involve the development of new hybrid molecule/device configurations, new excitation modalities, and new techniques to characterize nanomachine mechanical degrees of freedom at ultrafast time scales. Here we describe our plans in greater detail:

(i) E-field-driven molecular rotors: We will develop new classes of 2D nanodevices that allow flexible actuation of molecular rotors via lateral in-plane fields. Graphene electrodes will be patterned onto clean semiconducting TMD substrates using new AFM-based nanolithography techniques to electrically actuate molecular rotors (Fig. 5a). Molecules having large electric dipole moments will be put into the junction region between the electrodes and subjected to large lateral electric fields. Isolated molecules in the junction region should align with the applied field and molecular rotor behavior will be characterized using STM imaging. Because the junction region is surrounded by four electrodes, the E-field will have full 360° rotation capability, thus enabling us to explore how molecule-substrate interactions influence molecular rotor behavior. Individual molecular rotors

investigated previously have been driven randomly by thermal motion or STM tip-pulses, and so our research should result in the first isolated molecular rotors driven fully by external electrodes.

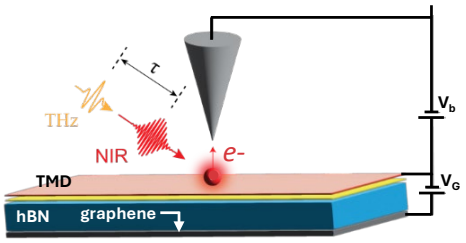

Fig. 6: Scheme to perform ultrafast STM imaging of 2D devices via optical pulses.

(ii) Electromigration-driven memristor functionality using hybrid molecule/2D devices: We will use the device geometry shown in Fig. 5b to explore *combined* electromigration and electrical transport behavior in molecular nanomachine systems. The idea here is to apply sufficiently high current density to the device conduction channel that the interior molecular configuration is mechanically altered by electromigration processes, thus changing the channel conductance (here the molecules will be *translated* (Fig. 5b) rather than rotated like the dipolar molecules above). The resulting hysteretic I-V behavior should result in memristor functionality, thus yielding new building blocks for proposed neuromorphic computing schemes. Our device geometry is unique because it is an open 2D scheme that will allow the internal device structure to be imaged with atomic resolution *while* operating it. We will explore the fundamental *microscopic mechanisms of electromigration* that drive molecular nanomechanical actuation in the presence of applied current (Fig. 5b), as well as how different molecular configurations alter 2D device *conductance*.

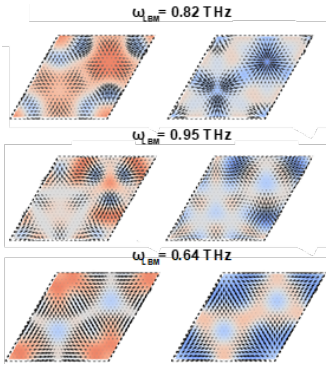

Fig. 7: Predicted real-space amplitudes of WS_2 bilayer moiré phonon modes (S. G. Louie, unpublished).

(iii) Visualizing THz nanomechanical response in 2D devices using ultrafast STM: Ultrafast optical spectroscopy (including near-field techniques) is limited to spatial resolution orders of magnitude larger than the atomic scale. We will beat this limit by *directly imaging* picosecond dynamical processes at *Ångström* length scales by integrating ultrafast optical pump/probe techniques with STM (Fig. 6). This will allow us to *image* how domain walls, point defects, 3D moiré reconstructions, electrostatic doping, and the presence of adsorbates all affect *local* nanoscale lattice vibrations for 2D materials in the ultrafast regime. Examples of lattice vibrations that are of interest here are the breathing and shear modes of TMD bilayer moiré superlattices as shown in Fig. 7 (predicted by S. G. Louie). To accomplish these measurements we will use tailored, near infrared and THz pulses as both photoexcitation (pump) and transient bias voltage (probe) with sub-picosecond duration. Local optically-induced electric fields will be enhanced via plasmonic effects between the tip and substrate, thus facilitating efficient light-sample interactions. Similar STM techniques have been used previously for investigating bulk metal systems, but have never been used to explore the local dynamical properties of 2D devices as proposed here. These investigations should enable a new understanding of how the internal degrees of freedom of coupled 2D nanostructures interact at their natural spatial and temporal scales.

Publications resulting from work supported by this DOE grant over previous two years:

(1) F. Liou, H.-Z. Tsai, Z. A. H. Goodwin, A. S. Aikawa, E. Ha, M. Hu, Y. Yang, K. Watanabe, T. Taniguchi, A. Zettl, J. Lischner and M. F. Crommie, "Imaging Field-Driven Melting of a Molecular Solid at the Atomic Scale", *Advanced Materials* **35**, 2300542 (2023).

(2) R. D. McCurdy, A. Delgado, J. Jiang, J. Zhu, E. C. H. Wen, R. E. Blackwell, G. C. Veber, S. Wang, S. G. Louie and F. R. Fischer, "Engineering Robust Metallic Zero-Mode States in Olympicene Graphene Nanoribbons", *Journal of the American Chemical Society* **145**, 15162 (2023).

(3) E. C. H. Wen, P. H. Jacobse, J. Jiang, Z. Wang, S. G. Louie, M. F. Crommie and F. R. Fischer, "Fermi-Level Engineering of Nitrogen Core-Doped Armchair Graphene Nanoribbons", *Journal of the American Chemical Society* **145**, 19338 (2023).

(4) C. Dai, D. Popple, C. Su, J.-H. Park, K. Watanabe, T. Taniguchi, J. Kong and A. Zettl, "Evolution of nanopores in hexagonal boron nitride", *Communications Chemistry* **6**, 108 (2023).

(5) P. H. Jacobse, M. C. Daugherty, K. n. Čerņevičs, Z. Wang, R. D. McCurdy, O. V. Yazyev, F. R. Fischer and M. F. Crommie, "Five-Membered Rings Create Off-Zero Modes in Nanographene", *ACS Nano* **17**, 24901 (2023).

(6) A. K. Davey, Z. Li, N. Lefton, B. E. Leonhardt, A. Pourghaderi, S. McElhany, D. Popple, C. Dai, S. Kahn, M. N. Dods, A. Zettl, C. Carraro and R. Maboudian, "Enhanced ZIF-8-enabled colorimetric CO2 sensing through dye-precursor synthesis", *Sensors and Actuators B: Chemical* **374**, 132783 (2023).

(7) Y. Lee, Y. W. Choi, K. Lee, C. Song, P. Ercius, M. L. Cohen, K. Kim and A. Zettl, "Tuning the Sharing Modes and Composition in a Tetrahedral GeX2 (X = S, Se) System via One-Dimensional Confinement", *ACS Nano* **17**, 8734 (2023).

(8) W. Shi, S. Kahn, N. Leconte, T. Taniguchi, K. Watanabe, M. Crommie, J. Jung and A. Zettl, "High-Order Fractal Quantum Oscillations in Graphene/BN Superlattices in the Extreme Doping Limit", *Physical Review Letters* **130**, 186204 (2023).

(9) J. Martis, S. Susarla, A. Rayabharam, C. Su, T. Paule, P. Pelz, C. Huff, X. Xu, H.-K. Li, M. Jaikissoon, V. Chen, E. Pop, K. Saraswat, A. Zettl, N. R. Aluru, R. Ramesh, P. Ercius and A. Majumdar, "Imaging the electron charge density in monolayer MoS2 at the Ångstrom scale", *Nature Communications* **14**, 4363 (2023).

(10) Y. Lee, Y. W. Choi, K. Lee, C. Song, P. Ercius, M. L. Cohen, K. Kim and A. Zettl, "1D Magnetic MX3 Single-Chains (M = Cr, V and X = Cl, Br, I)", *Advanced Materials* (**n/a**), 2307942 (2023).

(11) H. Pun Sai, H. Wen Ethan Chi, Z. Xia, H. Chen, R. Fischer Felix and Q. Miao, "Reactivity, Regioselectivity, and Synthetic Application of 2-Pyrenyl Units in Scholl Reactions", CCS Chemistry **5**, 2069 (2023).

(12) M. Sun, H. Amiri, A. B. Tong, K. Shintomi, T. Hirano, C. Bustamante and R. Heald, "Monitoring the compaction of single DNA molecules in Xenopus egg extract in real time", *Proceedings of the National Academy of Sciences* **120**, e2221309120 (2023).

(13) L. M. Wee, A. B. Tong, A. J. Florez Ariza, C. Cañari-Chumpitaz, P. Grob, E. Nogales and C. J. Bustamante, "A trailing ribosome speeds up RNA polymerase at the expense of transcript fidelity via force and allostery", *Cell* **186**, 1244 (2023).

(14) P. M. Pelz, S. M. Griffin, S. Stonemeyer, D. Popple, H. DeVyldere, P. Ercius, A. Zettl, M. C. Scott and C. Ophus, "Solving complex nanostructures with ptychographic atomic electron tomography", *Nature Communications* **14**, 7906 (2023).

(15) S. H. Pun, A. Delgado, C. Dadich, A. Cronin and F. R. Fischer, "Controlled catalyst-transfer polymerization in graphene nanoribbon synthesis", *Chem* **10**, 675 (2024).

(16) K. Slicker, A. Delgado, J. Jiang, W. Tang, A. Cronin, R. E. Blackwell, S. G. Louie and F. R. Fischer, "Engineering Small HOMO–LUMO Gaps in Polycyclic Aromatic Hydrocarbons with Topologically Protected States", *Nano Letters* **24**, 5387 (2024).

(17) F. Liou, H.-Z. Tsai, Z. A. H. Goodwin, Y. Yang, A. S. Aikawa, B. R. P. Angeles, S. Pezzini, L. Nguyen, S. Trishin, Z. Cheng, S. Zhou, P. W. Roberts, X. Xu, K. Watanabe, T. Taniguchi, V. Bellani, F. Wang, J. Lischner and M. F. Crommie, "Gate-Switchable Molecular Diffusion on a Graphene Field-Effect Transistor", *ACS Nano* **18**, 24262 (2024).

(18) M. C. Daugherty, P. H. Jacobse, J. Jiang, J. Jornet-Somoza, R. Dorit, Z. Wang, J. Lu, R. McCurdy, W. Tang, A. Rubio, S. G. Louie, M. F. Crommie and F. R. Fischer, "Regioselective On-Surface Synthesis of [3]Triangulene Graphene Nanoribbons", *Journal of the American Chemical Society* **146**, 15879 (2024).

(19) B. Qie, Z. Wang, J. Jiang, Z. Zhang, P. H. Jacobse, J. Lu, X. Li, F. Liu, A. N. Alexandrova, S. G. Louie, M. F. Crommie and F. R. Fischer, "Synthesis and characterization of low-dimensional N-heterocyclic carbene lattices", *Science* **384**, 895 (2024).

(20) P. H. Jacobse, M. Sarker, A. Saxena, P. Zahl, Z. Wang, E. Berger, N. R. Aluru, A. Sinitskii and M. F. Crommie, "Tunable Magnetic Coupling in Graphene Nanoribbon Quantum Dots", *Small* **20**, 2400473 (2024).

(21) Y. Yoon, Z. Lu, C. Uzundal, R. Qi, W. Zhao, S. Chen, Q. Feng, W. Kim, M. H. Naik, K. Watanabe, T. Taniguchi, S. G. Louie, M. F. Crommie and F. Wang, "Terahertz phonon engineering with van der Waals heterostructures", *Nature* **631**, 771 (2024).

(22) Z.-H. Zhang, K. Godeneli, J. He, M. Odeh, H. Zhou, S. Meesala and A. Sipahigil, "Acceptor-Induced Bulk Dielectric Loss in Superconducting Circuits on Silicon", *Physical Review X* **14**, 041022 (2024).

(23) Y. Lee, Y. W. Choi, L. Li, W. Zhou, M. L. Cohen, K. Kim and A. Zettl, "SiX_2 (X = S, Se) Single Chains and (Si–Ge)X2 Quaternary Alloys", *ACS Nano* **18**, 17882 (2024).

(24) C. Su, E. Janzen, M. He, C. Li, A. Zettl, J. D. Caldwell, J. H. Edgar and I. Aharonovich, "Fundamentals and emerging optical applications of hexagonal boron nitride: a tutorial", *Adv. Opt. Photon*. **16**, 229 (2024).

(25) Y. Lee, U. Choi, K. Kim and A. Zettl, "Recent progress in realizing novel one-dimensional polymorphs via nanotube encapsulation", *Nano Convergence* **11**, 52 (2024).

(26) E. C. Regan, Z. Lu, D. Wang, Y. Zhang, T. Devakul, J. H. Nie, Z. Zhang, W. Zhao, K. Watanabe, T. Taniguchi, S. Tongay, A. Zettl, L. Fu and F. Wang, "Spin transport of a doped Mott insulator in moiré heterostructures", *Nature Communications* **15**, 10252 (2024).

(27) Y. W. Choi, Y. Lee, K. Kim, A. Zettl and M. L. Cohen, "Atomic and Electronic Structures of 1D Phosphorus Nanoring and Nanohelix", *ACS Nano* **19**, 12155 (2025).

Spin Transport in group IV materials and 2D membranes
Hanan Dery

Depts. of Electrical and Computer Engineering and of Physics, University of Rochester

Keywords: moiré superlattice, Wigner lattices, excitons, transition-metal dichalcogenides

Program Scope

During the last two years, this program was focused on a multitude of investigations that study the optical properties of transition-metal dichalcogenide systems, including many-body excitonic complexes [p1, p2], Landau-level composition of excitonic states [p3], emission and formation properties of trions [p4, p5, p6, p7], dynamical screening effects [p8, p9], and excitons in moiré potentials [p10, r1]. In this short document, I will only focus on the progress we have made in the latter topic [r1].

Recent Progress: excitons in fractionally filled moiré superlattices

Long-range Coulomb forces give rise to correlated insulating states when charge particles populate a moiré superlattice at fractional filling factors. Such behavior is characterized by a broken translation symmetry wherein particles spontaneously form a Wigner crystal. Motivated by recent experiments that investigated the correlated states through optical spectroscopy of the exciton resonances, we have developed a theory that captures the correlated insulating state of a fractionally filled moiré superlattice through the energy shift and change in oscillator strength of the exciton absorption resonance [r1]. The theory shows that the experimental findings can only be supported if the electrons reside in a charge-ordered state (i.e., electrons are not randomly distributed among the sites of the moiré superlattice). Furthermore, we have explained why the energy shifts of exciton resonances are qualitatively different in cases that the superlattice is nearly empty compared with a superlattice whose sites are doubly occupied.

Figure 1 shows the experimental findings we will be focusing on [r2]. The raw data was provided by courtesy of Yang Xu, Kin Fai Mak and Jie Shan. Figure 1(a) shows the device structure used in Ref. [r2], where a WSe_2 sensor monolayer is placed a few nm below a moiré superlattice made of angle aligned WSe_2/WS_2 bilayers (bottom panel), where a thin hexagonal boron nitride (hBN) layer is placed between the sensor and bilayers. The circuitry of the device guarantees that the sensor monolayer remains intrinsic, and the electrostatic doping is only introduced in the bilayer system. The moiré potential lowers the optical gap in the WSe_2 part of the bilayer system by ~50 meV compared with the optical gap of the isolated WSe_2 monolayer [r2]. This difference allows one to unambiguously determine that the reflection contrast map in Fig. 1(b) corresponds to the spectral region of the 2*s* exciton state in the sensor monolayer. The reason that the 2*s* state has the most salient response to the moiré superlattice will become clear later. The goal of the model we are about to present is to reproduce the exciton resonances in Fig. 1(b) for each of the fractionally filled states both in terms of their energies and amplitudes.

We consider an exciton moving in a periodic moiré potential $V_M(\mathbf{R},\mathbf{r})$, where $\mathbf{R}$ and $\mathbf{r}$ are its center-of-mass and relative motion position vectors, respectively. The exciton Hamiltonian reads

$$H = -\frac{\hbar^2\nabla_{\mathbf{R}}^2}{2M} - \frac{\hbar^2\nabla_{\mathbf{r}}^2}{2\mu} + V(\mathbf{r}) + V_M(\mathbf{R},\mathbf{r}),$$

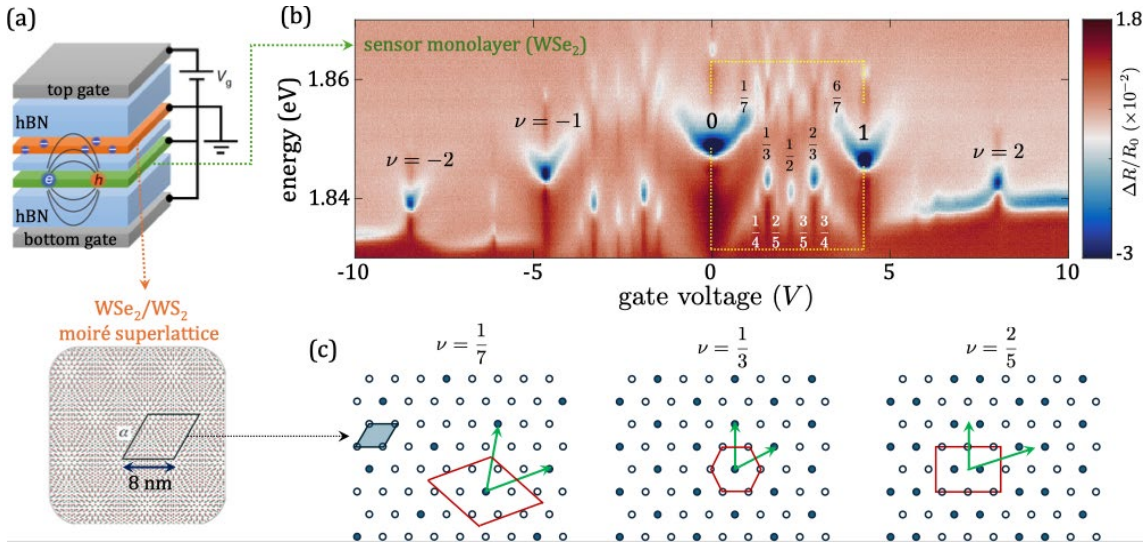

FIG 1. Experimental results of Ref. [r2]. (a) Device structure and electric circuitry. The optically active regions of the stack are the sensor monolayer (charge neutral WSe_2), separated by a thin hBN layer from an electrostatically doped moiré superlattice (WSe_2/WS_2 bilayers; bottom scheme). (b) Gate-dependent reflection contrast at T=1.6 K, shown in the spectral window of the 2*s* exciton state in the sensor monolayer. The resonances are labeled by filling factors of the moiré superlattice at the corresponding gate voltages. The highlighted box between 0 and 4 V is analyzed in Fig. 2, where we compare these results with our theory. (c) Three examples of charge-order configurations at zero temperature of the fractionally filled moiré superlattice. Filled and unfilled circles denote occupied and empty sites, respectively. Also shown are the unit cells and lattice vectors of each example.

where $V(\mathbf{r})$ is the electron-hole Coulomb interaction. $M = m_e + m_h$ and $\mu = m_e m_h/(m_e + m_h)$ are the translational and reduced masses of the exciton. The periodic potential satisfies $V_M(\mathbf{R},\mathbf{r}) = V_M(\mathbf{R} + n_1\mathbf{R}_1 + n_2\mathbf{R}_2, \mathbf{r})$, where $n_{1(2)}$ are integers and $\mathbf{R}_{1(2)}$ are the basis lattice vectors, denoted by the arrows in Fig. 1(c). The periodicity of $V_M(\mathbf{R},\mathbf{r})$ means that the exciton wavefunction has a Bloch form,

$$\Psi_{\mathbf{K}}(\mathbf{R},\mathbf{r}) = \sum_{\mathbf{G}} e^{i(\mathbf{K}+\mathbf{G})\cdot\mathbf{R}} u_{\mathbf{K}}(\mathbf{G},\mathbf{r}) = \sum_{\mathbf{G},\alpha} C_\alpha(\mathbf{G}) e^{i(\mathbf{K}+\mathbf{G})\cdot\mathbf{R}} \phi_\alpha(\mathbf{r}),$$

in which the sum runs over reciprocal lattice vectors $\mathbf{G}$ and exciton states, $\phi_\alpha(\mathbf{r})$, where $\alpha = \{1s, 2s, 2p^{\pm}, \ldots\}$. The constant of motion $\mathbf{K}$ is the translational wavevector of the exciton. After projecting both sides of the Schrodinger Equation on $e^{i(\mathbf{K}+\mathbf{G})\mathbf{R}}$, and considering an exciton in the light cone (K=0), we arrive at a secular equation that can be solved by matrix inversion,

$$\sum_{\mathbf{G}',\beta} \left[\left(\frac{\hbar^2 \mathbf{G}^2}{2M} + \varepsilon_\alpha \right) \delta_{\mathbf{G},\mathbf{G}'} \delta_{\alpha,\beta} + V_{\alpha,\beta}(\mathbf{G} - \mathbf{G}') \right] C_\beta(\mathbf{G}') = E C_\alpha(\mathbf{G}) \ .$$

ε_α is the exciton energy in state α (without the moiré potential), and the Coulomb matrix element between the exciton and the moiré potential is $V_{\alpha,\beta}(\mathbf{G}\text{-}\mathbf{G}') = \langle \beta \mid V_M(\mathbf{G}\text{-}\mathbf{G}',\mathbf{r}) \mid \alpha \rangle$, where $V_M(\mathbf{G},\mathbf{r})$ is the Fourier transform of $V_M(\mathbf{R},\mathbf{r})$. To calculate this matrix element, we assume that the moiré potential assumes the form,

$$V_M(\mathbf{R},\mathbf{r}) = \frac{e^2}{\epsilon} \sum_{\mathbf{R}_M} \left(\frac{1}{\sqrt{d^2 + (\mathbf{R} + \frac{\mathbf{r}}{2} - \mathbf{R}_M)^2}} - \frac{1}{\sqrt{d^2 + (\mathbf{R} - \frac{\mathbf{r}}{2} - \mathbf{R}_M)^2}} \right) .$$

ϵ is the effective dielectric constant of the environment, $\mathbf{R}+\mathbf{r}/2$ is the position of the electron component in the exciton, and $\mathbf{R}\text{-}\mathbf{r}/2$ is that of the hole component. *d* is the distance between the plane

at which the exciton resides in the sensor monolayer and the plane at which electrons reside in the moiré superlattice at positions $\mathbf{R}_M$. Taking the Fourier transform of $V_M(\mathbf{R},\mathbf{r})$ with respect to $\mathbf{R}$, we get after some algebra that the matrix elements of the periodic potential read

$$V_{\alpha,\beta}(\mathbf{G}) = \frac{2\pi e^2}{A_\nu \epsilon}\frac{e^{-dG}}{G}\left[2i\sum_{\mathbf{R}'_M} e^{-i\mathbf{G}\cdot\mathbf{R}'_M}\right]\mathcal{M}_{\alpha,\beta}(\mathbf{G}),$$

where A_ν is the area of the unit cell and the sum runs over electrons positions in one unit cell (e.g., the filled circles in a unit cell of Fig. 1(c)). The term in square bracket is the form-factor of the moiré superlattice, and

$$\mathcal{M}_{\alpha,\beta}(\widetilde{\mathbf{G}}) = \int \phi^*_\alpha(\mathbf{r}) \sin\left(\tfrac{1}{2}\widetilde{\mathbf{G}}\cdot\mathbf{r}\right)\phi_\beta(\mathbf{r}) d^2\mathbf{r}\,.$$

The odd sine function implies that the integration does not vanish only if α and β have different parity. Consequently, the oscillator strengths and energies of the *s*-states, whose properties are probed in optical reflectance experiments, change because they are mixed through the moiré potential with exciton states of {p,d,...} characters. Given that $|\varepsilon_{2s} - \varepsilon_{2p\pm}| \sim 10$ meV whereas $|\varepsilon_{1s} - \varepsilon_{2p\pm}| \sim 120$ meV in hBN-encapsulated TMD monolayers, the 2*s* state exhibits a stronger response to the presence of electrons in the moiré superlattice in these types of experiments. Whereas electrons in the moiré superlattice can also strongly mix *s*-state excitons at higher energies (3*s*, 4*s*,...) with exciton states at nearby energies ($3p^{\pm}$, $3d^{\pm}$, $4p^{\pm}$...), the detection of these larger-radii excitons is difficult on accounts of their weaker oscillator strength.

The calculation results we are about to present only consider the small subspace of 2*s* and $2p^{\pm}$ hydrogen-like exciton states. Figure 2 shows the experimental results with the calculated absorption profile (derived from the eigenstates of the secular Equation). Figure 2(a) is a magnified view of the reflectance spectra in the highlighted box of Fig. 1(b). Figures 2(b) and 2(c) show the theory results when electrons in the moiré superlattice are charge-ordered and disordered, respectively. The results in Figs. 2(a) and (b) match both in terms of the resonance energies and oscillator strengths. With respect to the strongest 2*s* resonances at ν=0 and 1, both experiment and theory show that the next strongest resonances are at ν=1/3 and 2/3 and they emerge ~5 meV below the one at ν=0. The next strongest resonance appears at ν=1/2 and it emerges ~9 meV below the one at ν=0. Next in amplitudes are the resonances at ν=1/4 and 3/4 that emerge ~8 meV below in theory versus ~10 meV in experiment, followed by the ones at ν=2/5 and 3/5 that emerge ~10 meV below in both theory and experiment. The weakest resonance emerges 13 meV below at ν=1/7 and 6/7, in which case there is also a stronger resonance next to the one at ν=0 in both experiment and theory. All in all, these results support the conclusion that particles of the moiré superlattice in Ref. [r2] form a Wigner crystal.

This conclusion is further reinforced by the simulated absorption profile when assuming disordered configuration. The calculated absorption map in Fig. 2(c) is completely different than the one seen in experiment, and this conclusion remains valid whether we average the absorption maps of many random distributions of electrons or consider the absorption profile of a certain random distribution. The absorption map in Fig. 2(c) shows two energy `bands', where the absorption is stronger at the higher energy around zero energy, which blueshifts continuously from ν=0 to ν=1/2 (or from ν=1 to ν=1/2). The second band with weaker absorption emerges ~20 meV below. This band is reminiscent of an impurity band in doped semiconductors, where here it is an exciton that becomes localized next to disorder centers.

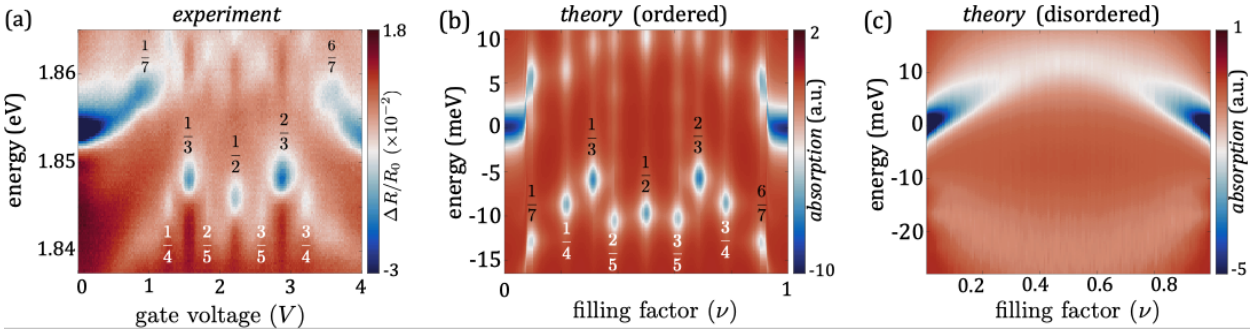

FIG 2. Comparing the measurement results with theory. (a) Experiment: Magnified view of the reflectance spectra in the highlighted box of Fig. 1(b). (b) Theory: Optical absorption in the sensor WSe_2 monolayer, calculated by assuming an ordered state of the electrons in the moiré superlattice (e.g., Fig. 1(c)). The reference level (zero energy) corresponds to the resonance energy of the 2*s* exciton state when the adjacent moiré superlattice is empty. (c) The same as in (b), but by assuming a disordered state of the electrons in the moiré superlattice.

In closing, the presented theory studies how the resonance energy and oscillator strength of excitons depend on the fractionally filled state of a moiré superlattice. Evident differences are found between cases in which the electrons form a Wigner crystal compared with cases in which the electrons are randomly distributed among the unit cells of the moiré superlattice. Comparing the calculated results with recent experiments, we conclude that charge-order states are responsible to the observed behavior in these experiments. Future experiments can further investigate the mixing between the *s* and *p* states of the exciton through the moiré potential, making use of out-of-plane magnetic fields or in-plane electric fields to split the $p^{\pm}$ states, acting as knobs to control the polarization, amplitude, and energy of the exciton resonance.

Future Plans

1. We will perform Monte Carlo simulations to study the effect of temperature when the Wigner crystal melts down. In addition, we plan to incorporate more orbitals and investigate how the resonance energy and oscillator strength of excitons in higher *s* states behave in response to fractional filling of the moiré superlattice.
2. Together with our collaborators in France [p1,p4,p5], and Germany [p8], we will investigate many-body excitonic states in devices that allow for the satellite Q valleys to be filled in WSe_2 monolayers. We have initial promising results from both groups.

References

[r1] J. Kim, H. Dery, and D. Van Tuan, Excitons in fractionally filled moiré superlattices, arXiv:1805.08722 (submitted).

[r2] Y. Xu, S. Liu, D. Rhodes, K. Watanabe, T. Taniguchi, J. Hone, V. Elser, K. F. Mak, J. Shan, Correlated insulating states at fractional fillings of moiré superlattices, Nature 587, 214 (2020).

Publications (2-year list of publications supported by BES)

[p1] H. Dery, C. Robert, S. A. Crooker, X. Marie, and D. Van Tuan, Energy shifts and broadening of excitonic resonances in electrostatically-doped semiconductors, arXiv:2411.11790 (submitted).

[p2] J. Choi, J. Li, D. Van Tuan, H. Dery, and S. A. Crooker, Emergence of composite many-body exciton states in WS_2 and $MoSe_2$ monolayers, Phys. Rev. B 109, L041304 (2024).

[p3] D. Van Tuan and H. Dery, Landau level composition of bound exciton states in magnetic field, arXiv:2501.16564 (to be published).

[p4] V. Jindal, K. Mourzidis, A. Balocchi, C. Robert, P. Li, D. Van Tuan, L. Lombez, D. Lagarde, P. Renucci, T. Taniguchi, K. Watanabe, H. Dery, and X. Marie, Brightened emission of dark trions in transition metal dichalcogenide monolayers, Phys. Rev. B 111, 155409 (2025).

[p5] L. Ren, C. Robert, H. Dery, M. He, P. Li, D. V. Tuan, P. Renucci, D. Lagarde, T. Taniguchi, K. Watanabe, X. Xu, and X. Marie, Measurement of the conduction band spin-orbit splitting in WSe_2 and WS_2 monolayers, Phys. Rev. B 107, 245407 (2023).

[p6] D. Van Tuan and H. Dery, Component exchange theory of trions, Phys. Rev. B 111, 085305 (2025).

[p7] D. Van Tuan and H. Dery, Excitons and trions in monolayer semiconductors with correlated electrons, Phys. Rev. B 108, 085303 (2023).

[p8] A. Ben Mhenni, D. V. Tuan, L. Geilen, M M. Petric, M. Erdi, K. Watanabe, T. Taniguchi, S. Tongay, K. Muller, N. P. Wilson, J. J. Finley, H. Dery, and M. Barbone, Breakdown of the static dielectric screening approximation of Coulomb interactions in atomically thin semiconductors, ACS Nano 19, 4269 (2025).

[p9] D. Van Tuan and H. Dery, Effects of dynamical dielectric screening on the excitonic spectrum of monolayer semiconductors, Phys. Rev. B 110, 125301 (2024).

[p10] D. Van Tuan and H. Dery, Excitons in periodic potentials, Phys. Rev. B 108, L081301 (2023).

Forecasting Thermoelectric Performance in 2D Metal–Organic Frameworks Through *Ab Initio* Atomistic Modeling

Laura de Sousa Oliveira, Department of Chemistry, University of Wyoming, Laramie, Wyoming, USA

Keywords: MOFs, thermoelectrics, semiconductors, electronic calculations, materials discovery

Research Scope

This DOE Early Career project aims to develop fundamental knowledge for predicting key quantitative structure–property relationships (QSPRs) to guide the rational design of thermoelectric metal–organic frameworks (MOFs). While MOFs possess ultralow thermal conductivity due to their high porosity—making them ideal thermal insulators—their typically poor electrical conductivity has limited their use in thermoelectric applications. The challenge lies in overcoming this trade-off and identifying MOF structures that enable efficient electrical transport without sacrificing their inherent thermal insulation. Our four main objectives are to: (1) clarify the role of electron-phonon coupling and quantify electron scattering in MOFs; (2) identify whether polaron hopping is a viable charge transport mechanism alongside band conduction; (3) evaluate the accuracy of tight-binding density functional theory (SCC-DFTB) for modeling electronic properties; and (4) implement machine learning strategies to identify QSPRs and guide high-throughput screening of MOFs, including doped systems.

Recent Progress

The present work outlines a multifaceted approach to investigating charge transport and thermoelectric performance in metal-organic frameworks (MOFs) and related materials. One major component of the effort has focused on the benchmarking and validation of computationally efficient electronic structure methods, notably the self-consistent-charge density functional tight-binding (SCC-DFTB) and extended tight-binding methods (GFNn-xTB). These semi-empirical methods offer the possibility of simulating large MOF systems at a fraction of the computational cost of standard density functional theory (DFT), but its reliability must be thoroughly established. In recent work [1], our team evaluated several MOFs—$Zn_3C_6O_6$, $Cd_3C_6O_6$, Zn-NH-MOF, and the well-known $Ni_3(HITP)_2$ [2]—using multiple computational methods, including DFT with both PBE and HSE06 functionals, and various flavors of tight-binding (GFN1-xTB, GFN2-xTB, and SCC-DFTB with different parameter sets). The analysis demonstrated that while GFNn-xTB is adequate for predicting the overall band structure shape and density of states, it is less reliable for band gap estimations. Importantly, the study shows that $Zn_3C_6O_6$, $Cd_3C_6O_6$, and Zn-NH-MOF all exhibit higher predicted power factors than $Ni_3(HITP)_2$, indicating their promise for thermoelectric applications.

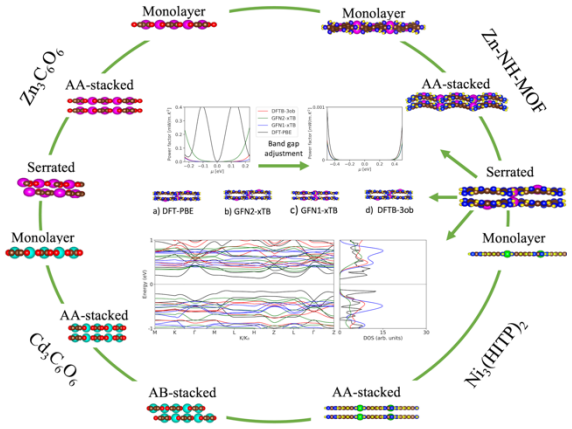

Graphical abstract illustrating the MOF structures and some of the properties evaluated in [1].

A second study [3] extended the analysis to phonon transport properties. DFT-PBE and the same semi-empirical methods employed to evaluate electron transport in the aforementioned study were used to calculate harmonic and anharmonic lattice dynamics for the same set of MOFs. The findings indicated that SCC-DFTB and GNFn-xTB are broadly suitable for evaluating thermal transport and dynamic stability. However, caution and further research are advised for the analysis of thermal conductivity, an important factor in calculating the thermoelectric figure of merit (ZT), in thermally insulating materials, as minor shifts in thermal

conductivity values can substantially affect ZT. The study identified serrated $Zn_3C_6O_6$ and Zn-NH-MOF as particularly stable and promising candidates. Zn-NH-MOF was found to have a notably low thermal conductivity, enhancing its overall ZT despite its power factor being slightly lower than that of $Zn_3C_6O_6$. These findings support the continued use of GFNn-xTB in high-throughput screening and transport modeling for low-dimensional MOFs.

Graphene oxide has long attracted interest for use in electronics due to its unique combination of high surface area, tunable bandgap, and relative ease of processing. Its functional groups can facilitate integration into devices, and partial reduction can yield materials with semiconducting or conductive properties. Achieving controlled porosity, functionalization, and doping in materials like graphene oxide (GO) remains a challenge due to current synthetic limitations, which often result in random porosity and decreased structural stability. Motivated by the potential of covalent organic frameworks (COFs) to mimic and even surpass the electronic properties of graphene oxide (GO), experimental collaborators successfully synthesized a series of 2D covalent organic frameworks (COFs) using Pictet–Spengler polymerization. These COFs incorporate a pyranoazacoronene (PAC) node and resemble doped graphene while maintaining desirable semiconducting characteristics. Computational analysis of this new material class, carried out using DFT and tight-binding methods, revealed structural and electronic features of interest for thermoelectric applications. This work, though focused on COFs rather than MOFs, contributed valuable insight into the electronic behavior of porous carbon-based networks [4].

Complementing the modeling efforts, the project also integrates machine learning to accelerate the discovery and design of porous frameworks with tailored properties. Two machine learning models have been developed to predict the band gap of a dataset comprising 232 COF structures based on the PAC node (with 8 distinct linkers and 29 functional groups). One model employs a random forest (RF) algorithm trained on compositional atomistic features, while the second leveraging a more advanced crystal graph convolutional neural network (CGCNN), which encodes structural information via graph-based representations. Benchmarking showed that the CGCNN significantly outperforms the RF model, underscoring the importance of including detailed structural descriptors in band gap prediction tasks. The RF model's feature set is constructed using atomic property-weighted averages and standard deviations, while the CGCNN incorporates one-hot encoded vectors for each atom type within a crystal graph, with bonding information defining the graph edges. Hyperparameter tuning and validation are ongoing for both models. Ultimately, these tools aim to extract qualitative structure-property relationships and guide the rational design of COFs and potentially MOFs for semiconducting and thermoelectric applications. This work is the subject of a manuscript currently in preparation.

The team also co-authored a review on the covalent integration of polymers and porous organic frameworks [5]. Our contribution focused on the computational modeling and machine learning analysis of porous frameworks, including both MOFs and COFs. This review situates the current project within a broader scientific context and provides a critical assessment of emerging methodologies for understanding and engineering these materials. Overall, the combined use *of ab initio* modeling, semiempirical simulations, and machine learning presents a comprehensive framework for advancing the performance and utility of MOFs and related materials in thermoelectric applications.

On clarifying the role of electron-phonon coupling and quantifying electron scattering processes in MOFs, preliminary progress has been made using AMSET, an *ab initio* scattering and transport code developed at Lawrence Berkeley National Laboratory. A graduate researcher in the group has become proficient with AMSET, starting by performing calculations on a control material, followed by early calculations on serrated $Zn_3C_6O_6$ and Zn-NH-MOF. These initial results identify both acoustic and

polar optical phonon scattering mechanisms and set the groundwork for more detailed investigations into how these interactions affect carrier lifetimes and mobility in porous framework materials.

In parallel, the project aims to evaluate whether polaron hopping constitutes a significant or dominant transport mechanism relative to conventional band conduction, particularly within the context of thermoelectric applications. While no direct computational or experimental work has yet been undertaken to address this question, recruitment efforts are underway to onboard a dedicated postdoctoral researcher who will focus on this aspect of the project in the coming years. This inquiry is expected to shed light on the extent to which charge localization and thermally activated hopping affect the transport efficiency in MOFs and similar low-dimensional materials, especially under conditions relevant to thermoelectric operation.

Future Plans

Over the next phase of the project, our research will continue to target key questions outlined in goals 1, 2, and 4 of the grant. Although some progress has been made on goal 1, goal 2 remains largely unexplored and is a central focus for the upcoming reporting period. The machine learning methodologies developed for goal 4 will be applied to MOF materials, leveraging the recent efforts on COFs; the original use of COFs allows for critical validation of our computational models against experimental data. Another avenue of future exploration includes doping in MOFs and COFs, a topic proposed in the original scope of work but not yet addressed. We plan to systematically investigate how doping impacts electronic and thermal properties, integrating this with our existing structure-property modeling efforts.

Additional efforts will focus on magnetic MOFs, MOF/COF structure prediction, and property characterization. Magnetic MOFs show promise for thermoelectric applications, and could enable multi-functional devices combining thermoelectric, electronic, and magnetic properties. We are conducting an extensive study of more than 15 layered 2D COFs and MOFs, comparing simulated XRD and vibrational data (via SCC-DFTB and GFNn-xTB approaches) against experimental results. Current investigations are focused on reconciling discrepancies between model predictions and emerging experimental data. These structures, comprising 60 to 350 atoms per unit cell with varying stacking configurations, present unique challenges in stability prediction. To further enhance accuracy, especially under realistic conditions, we plan to incorporate semi-empirical molecular dynamics simulations that account for temperature effects and solvent environments.

We are also preparing a comprehensive review paper focused on the state-of-the-art in MOFs for thermoelectric applications, aiming to consolidate recent findings and identify gaps in the field. Collectively, these efforts are aimed at deepening our understanding of structure-property relationships and enhancing the predictive power of our models for complex framework materials.

References

2. L. Sun, B. Liao, D. Sheberla, D. Kraemer, J. Zhou, E. A. Stach, D. Zakharov, V. Stavila, A. A. Talin, Y. Ge, and others, *A microporous and naturally nanostructured thermoelectric metal-organic framework with ultralow thermal conductivity*, Joule **1**, 168 (2017).

Publications

1. M. Mahmoudi Gahrouei, N. Vlastos, R. D'Souza, E. C. Odogwu, and L. de Sousa Oliveira, *Benchmark Investigation of SCC-DFTB Against Standard and Hybrid DFT to Model Electronic Properties in Two-Dimensional MOFs for Thermoelectric Applications*, Journal of Chemical Theory and Computation, **20**, 3976–3992 (2024).

3. M. Mahmoudi Gahrouei, N. Vlastos, O. Adesina, and L. de Sousa Oliveira, *Benchmark Investigation of SCC-DFTB Against Standard DFT to Model Phononic Properties in Two-Dimensional MOFs for Thermoelectric Applications*, J. Chem. Theory Comput. **20**, 10167 (2024).

4. K. Coe-Sessions, A. E. Davies, B. Dhokale, M. J. Wenzel, M. Mahmoudi Gahrouei, N. Vlastos, J. Klaassen, B. A. Parkinson, L. de Sousa Oliveira, and J. O. Hoberg, *Functionalized Graphene via a One-Pot Reaction Enabling Exact Pore Sizes, Modifiable Pore Functionalization, and Precision Doping*, Journal of the American Chemical Society, **146**, 33056–33063 (2024).

5. M. A. Hossain, K. Coe-Sessions, J. Ault, F. O. Gboyero, M. J. Wenzel, B. Dhokale, A. E. Davies, Q. Yang, L. de Sousa Oliveira, X. Li, and others, *Covalent Integration of Polymers and Porous Organic Frameworks*, Frontiers in Chemistry, **12**, 1502401 (2024).

DOE Award # DE-FG02-07ER46426
Light-Matter Interactions in Nanoscale Systems for Energy Applications

PI: Shanhui Fan, Department of Electrical Engineering, Stanford University. Email: shanhui@stanford.edu.
Co-PI: Prof. Mark Brongersma, Department of Material Science and Engineering, Stanford University, Email: markb29@stanford.edu.
Keyword: Light-matter interaction; hot electrons; solar energy harvesting; radiative cooling.
Program Scope
The overall objective of the program is to develop a fundamental understanding of light-matter interaction at nanocale in the context of energy applications. Towards this goal, we undertook substantial efforts on developing radiative cooling concept, on understanding the ultimate limit of solar energy harvesting, and on determining hot-carrier dynamics.
Below we review some of the major progresses made in this report period.
Recent Progress

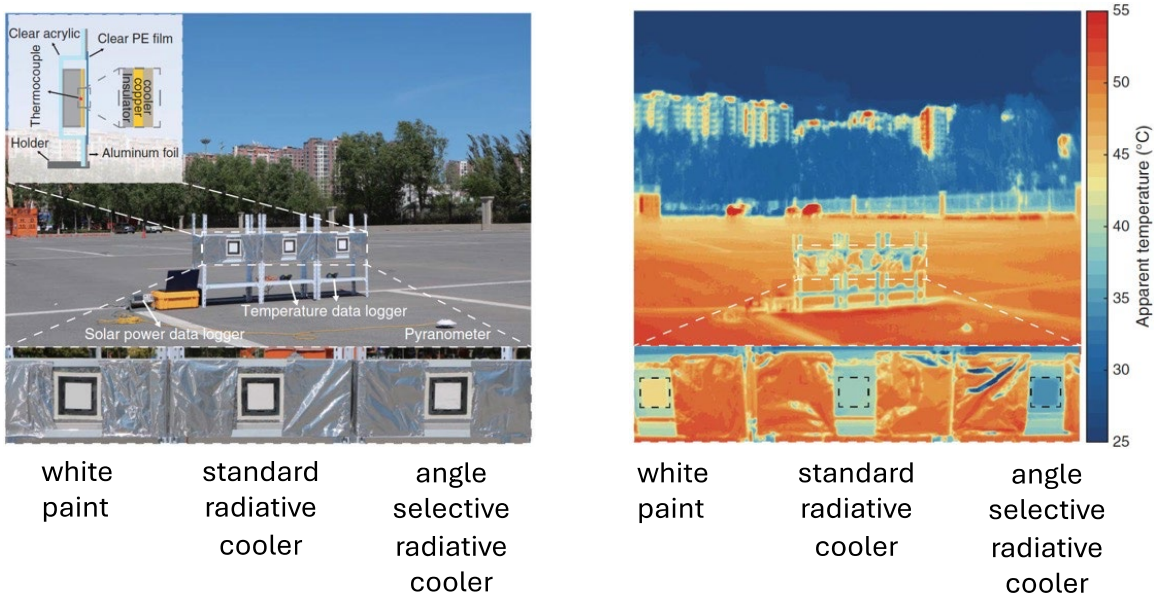

Figure 1 The setup (left panel) and the infrared image (right panel) for our demonstration of sub-ambient radiative cooling of vertical surfaces. The standard radiative cooler failed to achieve sub-ambient temperature when placed the vertical surface due to the thermal emission from the ground. The angle selective radiative cooler doesn't absorb the thermal radiation from the ground and achieves a temperature below that of the ambient air when deployed on a vertical surface.

Sub-ambient radiative cooling of vertical surfaces. Sub-ambient daytime radiative cooling enables temperatures to passively reach below ambient temperature, even under direct sunlight, by emitting thermal radiation toward outer space. This technology holds promise for numerous exciting applications. However, previous demonstrations of sub-ambient daytime radiative cooling require surfaces that directly face the sky, and these cannot be applied to vertical surfaces that are ubiquitous in real-world scenarios such as buildings and vehicles. Here, we demonstrate sub-ambient daytime radiative cooling of vertical surfaces under peak sunlight using a hierarchically designed, angularly asymmetric, spectrally selective thermal emitter. The angular asymmetry of its absorptivity ensures that the emitter does not absorb the thermal radiation emitted from the ground, which is a key requirement to achieve sub-ambient temperature when the emitter is deployed on a vertical surface. Under peak sunlight of 920 watts per square meter, our emitter reaches a temperature that is 2.5°C

below ambient temperature, corresponding to a temperature reduction of 4.3° and 8.9°C compared with a silica-polymer hybrid radiative cooler and commercial white paint, respectively (Figure 1). Our results on angle-asymmetric thermal emitter may point to fundamentally new opportunities in manipulating heat flow.

This work has been published in *Science*[1].

Approaching the ultimate limit of solar energy harvesting with non-reciprocal photovoltaic cells.

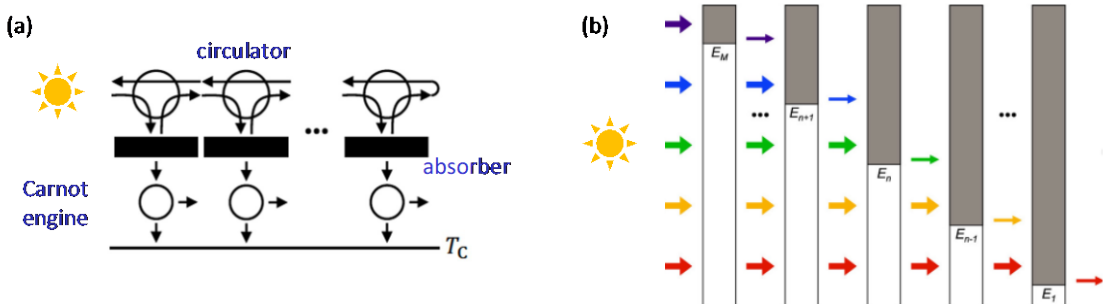

Figure 2: Configurations for reaching the Landsberg limit for the efficiency of solar energy harvesting. (a) A configuration proposed by Ries. (b) Our recently proposed non-reciprocal multiple junction cell. The cell consists of multiple semiconductor layers with varying band gaps. Each layer operates as a non-reciprocal semitransparent absorber.

Understanding the fundamental limits of solar energy conversion and developing device configurations to reach these limits have been of central importance in the study of solar cells. When reciprocity is assumed, the solar energy conversion has an upper bound on its efficiency of 86.6%, known as the multi-color limit. With the use of non-reciprocal components, one can further increase the efficiency beyond the multicolor limit to reach the Landsberg limit of 93.3%. The Landsberg limit represents the ultimate efficiency limit of solar energy harvesting, as can be proven using fundamental thermodynamic considerations.

The multicolor limit can be reached with use of a multi-junction solar cell, which consists of a stack of multilayers of semiconductors with different band gaps. Compared with the multijunction solar cells, however, the existing proposed configurations for reaching the Landsberg limit are far more complicated (Figure 2a). The first proposal consists of an array of circulators and Carnot engines. None of the proposed configurations has the conceptual simplicity of the multijunction solar cell.

Here we propose a non-reciprocal multijunction solar cell that can reach the Landsberg limit (Figure 2b). In this configuration, like the standard multijunction solar cells, the layers are semiconductors with different band gaps, with the larger band gap semiconductor placed closer to the front side of the cell facing the sun. Unlike the standard multijunction solar cells, however, each layer has a non-reciprocal semitransparent absorption/emission property. The absorber absorbs solely from one side but emits solely to the other. We have shown that this configuration, in the ideal limit with infinite number of semiconductor layers, can reach the Landsberg limit. We have also shown the nonreciprocal multijunction cell outperforms its reciprocal counterparts for any number of layers greater than one. We envision the study of non-reciprocal solar cells will open a new direction in the theoretical understanding of fundamental issues associated with solar and thermal energy harvesting.

This work has been published in *Nano Letters*[2].

Determining hot-carrier transport dynamics from terahertz emission. Understanding the ultrafast excitation and transport dynamics of plasmon-driven hot carriers is critical to the development of optoelectronics, photochemistry, and solar-energy harvesting. However, the ultrashort time and length scales associated with the behavior of these highly out-of-equilibrium carriers have impaired experimental verification of ab initio quantum theories. Here, we present an approach to studying plasmonic hot-carrier dynamics that analyzes the temporal waveform of coherent terahertz bursts

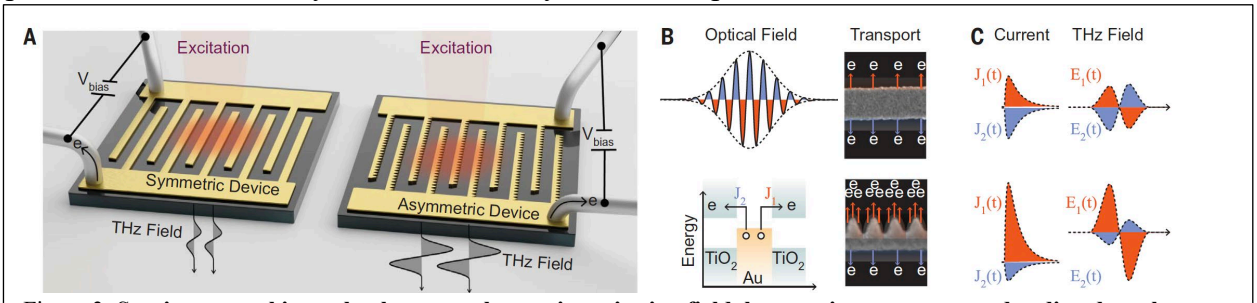

Figure 3: **Spatiotemporal interplay between plasmonic excitation field, hot-carrier transport, and radiated terahertz fields**. (A) Schematics of two arrays of electrically enabled designer plasmonic antennas for studying the spatiotemporal dynamics of hot-electron transport through their THz radiation responses. The external bias voltages are only applied during the photocurrent measurements. (B) Photo-ejection of hot electrons by a NIR pulse across a TiO_2/Au/TiO_2 heterojunction. SEM images depict a symmetric and an asymmetric Au nanostripe that are embedded in a thin TiO_2 film. The symmetric structure liberates an equal number of electrons from the top and bottom junctions, enabled by the electric field of the laser in the downward (orange) and upward (blue) half cycles, respectively. Breaking the geometrical mirror symmetry leads to a higher ejection rate from the top edge owing to the enhanced field concentration at the sharp nanotips. (C) The interfacial transport of hot carriers produces two counterpropagating current pulses, each enabling the radiation of a coherent THz burst. The orientation and amplitude of these current pulses define the polarity and amplitude of emerged THz fields, respectively.

radiated by photo-ejected hot carriers from designer nano-antennas with a broken symmetry (Figure 3). For ballistic carriers ejected from gold antennas, we find an ~11-femtosecond timescale composed of the plasmon lifetime and ballistic transport time. Polarization- and phase-sensitive detection of terahertz fields further grant direct access to their ballistic transport trajectory. Our approach opens explorations of ultrafast carrier dynamics in optically excited nanostructures.
The work has been published in *Science*[3].

A Purcell-enabled monolayer semiconductor free-space optical modulator Dephasing and non-radiative decay processes limit the performance of a wide variety of quantum devices at room temperature. Here we illustrate a general pathway to notably reduce the detrimental impact of these undesired effects through photonic design of the device electrodes (Figure 4). Our design facilitates a large Purcell enhancement that speeds up competing, desired radiative decay while also enabling convenient electrical gating and charge injection functions. We demonstrate the concept with a free-space optical modulator based on an atomically thin semiconductor. By engineering the plasmonic response of a nanopatterned silver gate pad, we successfully enhance the radiative decay rate of excitons in a tungsten disulfide monolayer by one order of magnitude to create record-high modulation efficiencies for this class of materials at room temperature. We experimentally observe a 10% reflectance change as well as 3 dB signal modulation, corresponding to a 20-fold enhancement compared with modulation using a suspended monolayer in vacuum. We also illustrate how dynamic control of light fields can be achieved with designer surface patterns. This research highlights the benefits of applying radiative decay engineering as a powerful tool in creating high-performance devices that complements substantial efforts to improve the quality of materials.

This work has been published in *Nature Photonics*[4].

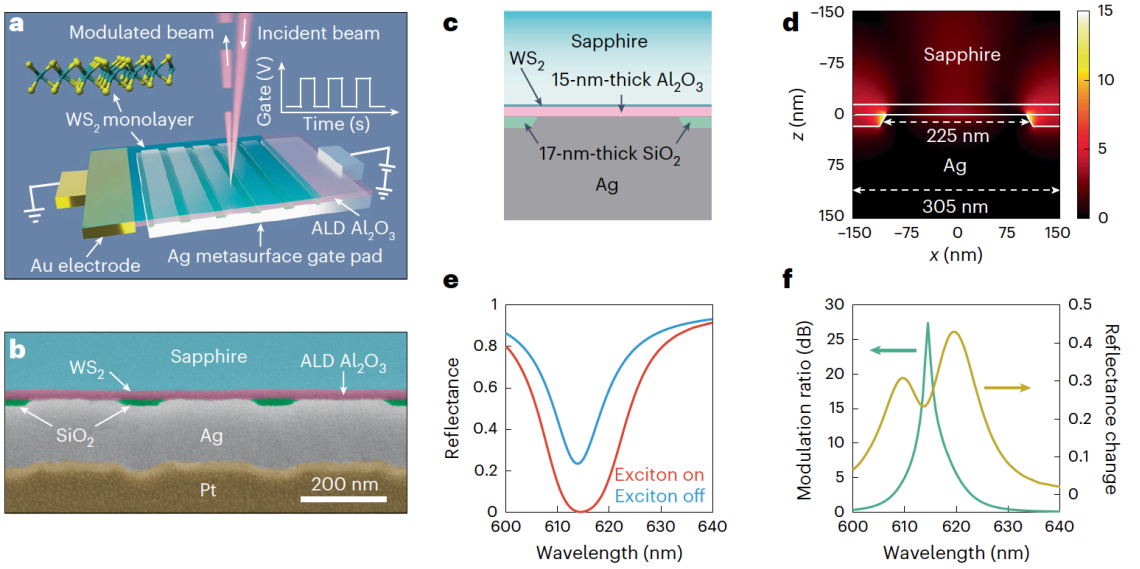

Figure 4: Concept of a monolayer WS_2 free-space optical modulator. (a) Schematic of a monolayer WS_2 free-space optical modulator based on a metal-oxide-semiconductor (MOS) capacitor configuration. The intensity of the reflected beam is modulated by changing the gating voltage between the Au electrode and the Ag metasurface gating pad. (b) Cross-sectional scanning electron microscope image of the fabricated optical modulator. (c) Detailed cross-sectional geometry and (d) the corresponding electric-field distribution of the designed optical modulator in one period under the normally incident plane wave illumination. The incident wavelength is 615 nm. (e) Simulated reflection spectra of the designed optical modulator under TE-polarized plane-wave illumination. The exciton resonance in WS_2 is turned on (orange) and off (blue). (f) Simulated modulation ratio (green) and absolute reflectance change (yellow) of the designed optical modulator.

Future Plans

In the next budget period, we plan to focus on continued efforts towards understanding light-matter interaction in nanophotonic structures in the context of energy applications. In particular, we aim to develop deeper understanding of thermal radiation from systems away from equilibrium. These include systems under time-modulation, as well as with hot-carrier injection. We anticipate that such exploration will provide us with deeper insights of thermodynamics of light, and lead to potential new application opportunities in photonics-based energy harvesting and cooling schemes.

References

F. Xie et al, Science 386, 788 (2024).
Y. Park, B. Zhao, and S. Fan, Nano Letters 22, 448–452 (2022).
M. Taghinejad et al, Science 382, 299-305 (2023).
Q. Li, et al, Nature Photonics 17, 897–903 (2023).

Selected Journal Publications in 2022-2025

Y. Park, B. Zhao, and S. Fan, "Reaching the Ultimate Efficiency of Solar Energy Harvesting with a Nonreciprocal Multijunction Solar Cell," Nano Letters 22, 448–452 (2022).

H. Hu, N. Chen, H. Teng, R. Yu, Y. Qu, J. Sun, M. Xue, D. Hu, B. Wu, C. Li, J. Chen, M. Liu, Z. Sun, Y. Liu, P. Li, S. Fan, F. J. García de Abajo, and Q. Dai, "Doping-driven topological polaritons in graphene/α-MoO3 heterostructures," Nature Nanotechnology 17, 940–946 (2022).

J. Li, X. Wang, D. Liang, N. Xu, B. Zhu, W. Li, P. Yao, Y. Jiang, X. Min, Z. Huang, S. Zhu, S. Fan, and J. Zhu, "A tandem radiative/evaporative cooler for weather-insensitive and hi-performance daytime passive cooling," Science Advances 8, eabq0411 (2022).

S. Fan and W. Li, "Photonics and thermodynamics concepts in radiative cooling," Nature Photonics 16, 182–190 (2022).

Y. Peng, L. Fan, W. Jin, Y. Ye, Z. Huang, S. Zhai, X. Luo, Y. Ma, J. Tang, J. Zhou, L. C. Greenburg, A. Majumdar, S. Fan, and Y. Cui, "Coloured low-emissivity films for building envelopes for year-round energy savings," Nature Sustainability 5, 339–347 (2022).

N. Lee, M. Xue, J. Hong, J. Van De Groep, and M. L. Brongersma, "Multi-Resonant Mie Resonator Arrays for Broadband Light Trapping in Ultrathin c-Si Solar Cells," Advanced Materials 35, 2210941 (2023).

Q. Li, J. -H. Song, F. Xu, J. van de Groep, J. Hong, A. Daus, Y. J. Lee, A. C. Johnson, E. Pop, F. Liu, and M. L. Brongersma., "A Purcell-enabled monolayer semiconductor free-space optical modulator," Nature Photonics 17, 897–903 (2023).

M. Taghinejad, C. Xia, M. Hrton, K. -T. Lee, A. S. Kim, Q. Li, B. Buzelturk, R. Kalousek, F. Xu, W. Cai, A. M. Lindenberg, and M. L. Brongersma, "Determining hotcarrier transport dynamics from terahertz emission." Science 382, 299-305 (2023).

F. Xie, W. Jin, J. R. Nolen, H. Pan, N. Yi, Y. An, Z. Zhang, X. Kong, F. Zhu, K. Jiang, S. Tian, T. Liu, X. Sun, L. Li, D. Li, Y. F. Xiao, A. Alu, S. Fan, and W. Li, "Subambientdaytime radiative cooling of vertical surfaces," Science 386, 788 (2024).

S. T. Ha, Q. Li, J. K. W. Yang, H. V. Demir, M. L. Brongersma, A. I. Kuznetsov,"Optoelectronic Metasurfaces", Science 386, eadm7442 (2024).

S. Doshi, A. Ji, A. I. Mahdi, S. T. Keene, S. P. Selvin, P. Lalanne, E. A. Appel, N. A. Melosh, M. L. Brongersma, "Electrochemically mutable soft metasurfaces," Nature Materials 24, 205–211 (2025).

J. Li, Y. Jiang, B. Li, Y. Xu, H. Song, N. Xu, P. Wang, D. Zhao, Z. Liu, S. Shu, J. Wu, M. Zhong, Y. Zhang, K. Zhang, B. Zhu, Q. Li, W. Li, Y. Liu, S. Fan and J. Zhu, "Accelerated photonic design of coolhouse film for photosynthesis via machine learning," Nature Communications 16, 1396 (2025).

Towards new midinfrared light sources using the intraband transitions of colloidal quantum dots.

Xingyu Shen, Rounak Naphade, Augustin Caillas, Shraman Saha, Philippe Guyot Sionnest, University of Chicago, James Franck Institute, 929 East 57th Street, Chicago, IL 60637

Keywords: midinfrared, nanocrystal, detector, emitters, cascade, luminescence, intraband.

Research Scope

The research scope is to develop midinfrared light emitting devices (LED) using colloidal quantum dots (CQD). The work focuses on cascade intraband electroluminescence, and aims to develop RoHS compliant CQDs as efficient midinfrared emitters. The broader impact is primarily molecular spectroscopy and sensing. We demonstrated the cascade LED process with CQDs emitting at 5 microns and the work continues with trying to increase efficiency, to deepen the understanding of the process, and to broaden the range of materials. This abstract presents two results from the past year: the first report of midinfrared electroluminescence from CdSe quantum dots, and the "brightest" midinfrared CQD film made by solution processing.

Recent Progress

Cascade LED with CdSe CQD emitting at 5 microns: visible CQDs have size-dependent energy gap, narrow emission linewidth, high luminescence efficiencies, and solution processability, and they are widely studied for commercial applications in displays and optoelectronics. Research extends to the infrared with the same strategy, but all the work focused exclusively on emission using the "interband" recombination between electrons and holes.

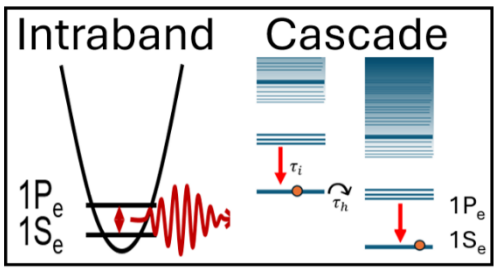

In this grant, the main idea is to explore midinfrared cascade CQD electroluminescence (EL) via intraband transitions. The proposed cascade only requires unipolar transport and high bias across dots. It was first proposed for epitaxial quantum dots, soon after the invention of quantum cascade lasers. It relies on the phonon bottleneck to slow down the $1P_e$-$1S_e$ intraband relaxation enough to facilitate emission. The main unknown is whether electrons transfer effectively from $1S_e$ to $1P_e$ state in a simple CQD film.

The idea worked surprisingly well. We made vertical and lateral devices, using HgSe and HgTe narrow gap. Partially n-doped dots HgSe/CdS CQDs showed the best power conversion efficiency of 0.085% which is close to commercial cascade epitaxial quantum well LEDs which have up to 0.2% at the same wavelength.

The work described here is the midinfrared cascade electroluminescence from wide gap CdSe CQDs. **Figure 1a** shows the device structure, where the CdSe CQD layer is deposited on a gold grating on a sapphire substrate. A ZnO injection layer is then deposited above the CdSe, followed by an evaporated Ge dielectric layer, and a gold reflector on top. The SEM cross section is shown in **Figure 1b**. The grating and Ge layer thickness are designed using Comsol simulations to maximize the normal incidence (from the grating side) absorption at 5 microns. On the basis of Kirchhoff rules, this should also maximize the normal emission outcoupling. **Figure 1c** shows the 5 μm emission spectra. **Figure 1d** shows that it is not a thermal emission since it follows the bias promptly without a phase shift. **Figure 1e** shows the nonlinearity of the voltage with current. The use of ZnO as the injection layer allows to obtain much larger current for the same voltage. Ohmic transport is relatively well understood in CQD films, but the non-ohmic transport shown here likely includes resonant tunnelling between $1S_e$ and $1P_e$. The current onset is indeed approximately when the bias over a dot diameter is equal to the $1S_e$-$1P_e$ energy. **Figure 3f** shows that the increase of emission with current is robust. As a result, the external quantum efficiency shown in **Figure 3g,** and defined as photon per

electron, increases slightly with current. **Figure 3h** shows the power conversion efficiency, and an interesting aspect is that it droops far less than QW devices. Multiple devices showed stable performances.

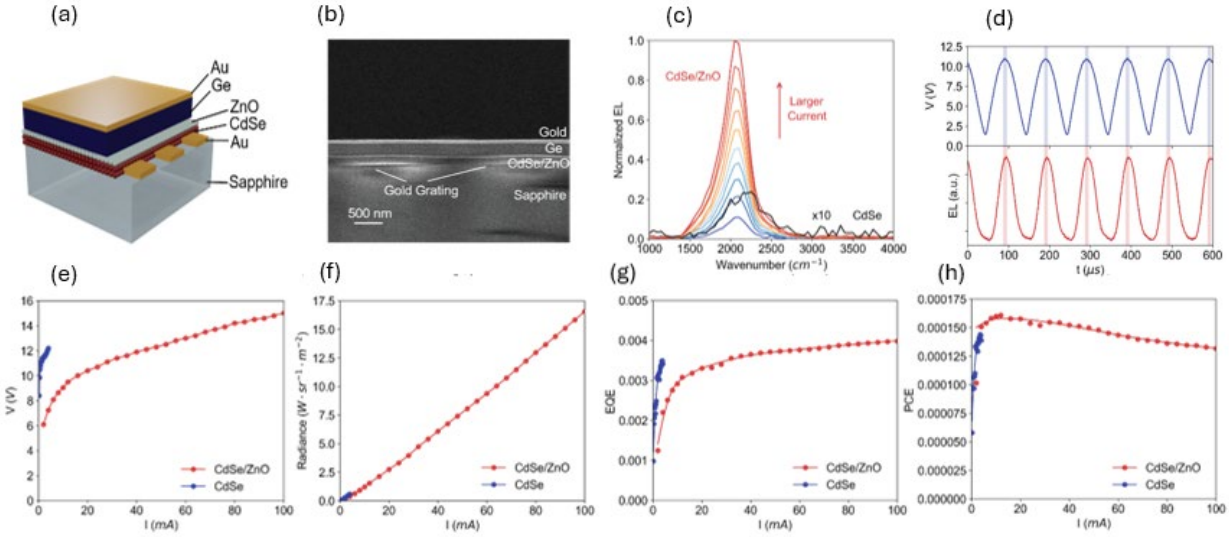

Figure 1: (a) Schematic of the CdSe cascade LED. (b) Cross section.(c) Electroluminescence spectra. (d) Time dependent electroluminescence compared with the oscillating bias. (e) Voltage as a function of current. (f) Radiance as a function of current. (g) EQE. (h) PCE.

This first example of CdSe CQD emitting midinfrared electroluminescence was recently published in ACS nano. Although the power conversion efficiency was only 0.013% and lower than with HgSe/CdS, the result opens the perspective of using many other wide gap CQDs.

Bright midinfrared films with CQDs: The LED efficiency is limited by the low quantum yield of the intraband relaxation. This should be vastly improvable with brighter midinfrared CQDs films, and this is the topic discussed below.

There is concurrently a growing interest in making bright midinfrared emitters. Among semiconductors, intrinsic bulk lead selenide (PbSe) may be the brightest midinfrared phosphor. A 30% internal PLQY has been reported at 3.9 μm at room temperature for epitaxial PbSe. The external PLQY is however poor because bulk semiconductors have high indices of refraction. $1/4n^2$ is commonly used for the extraction efficiency of light from a smooth semi-infinite solid with no reabsorption. For PbSe with n~ 4.8, the extraction efficiency would be $1/4n^2 \sim 1\%$. Optically rough polycrystalline PbSe thin films are commercially available as photoconductors, and brighter PbSe films correlate with better detectors. We tested an Opto-Diode model BXP-35E and the film emits at 4.3 μm. Since the backside is against the housing, PL is only in the forward direction. We used a gold integrating sphere with an InSb detector, and measured an external PLQE of $1 \pm 0.1\%$. That is a "good" external PLQY. With black phosphorous, the Javey group reported 0.3% QY at 3.6 μm and room temperature but we do not know if it is external or internal.

With CQD, we proposed that the non-radiative relaxation from $1P_e$ to $1S_e$ is due to near-field energy transfer to some unwanted infrared absorption.[i] This idea is supported by our study of very thick shell HgSe/CdS which showed a 20-fold increase in PLQY per doped dots ($PLQY^D$) in solution, reaching up to 2%.

Here, we studied the 5 μm emission of films of HgSe and HgSe/CdS CQDs. **Figure 2A** and **2B** shows the TEM images of the HgSe cores and core/shell respectively with a mean diameter of 4.5nm ± 0.5 nm for the HgSe cores, and 7.2nm ± 0.4 nm for the core/shell. Thin smooth films were made by spin-coating the non-polar colloidal solutions on substrates. The films were then processed with ethanedithiol (EdT) for organic ligand exchange followed by PbI_2/DMSO for inorganic ligand exchange. The EdT removes some of the original oleylamine or dodecanethiol ligands, and the

PbI_2/DMSO removes more than 95% of the remaining CH stretch infrared absorption. The films were annealed up to 140ºC for brighter emission.

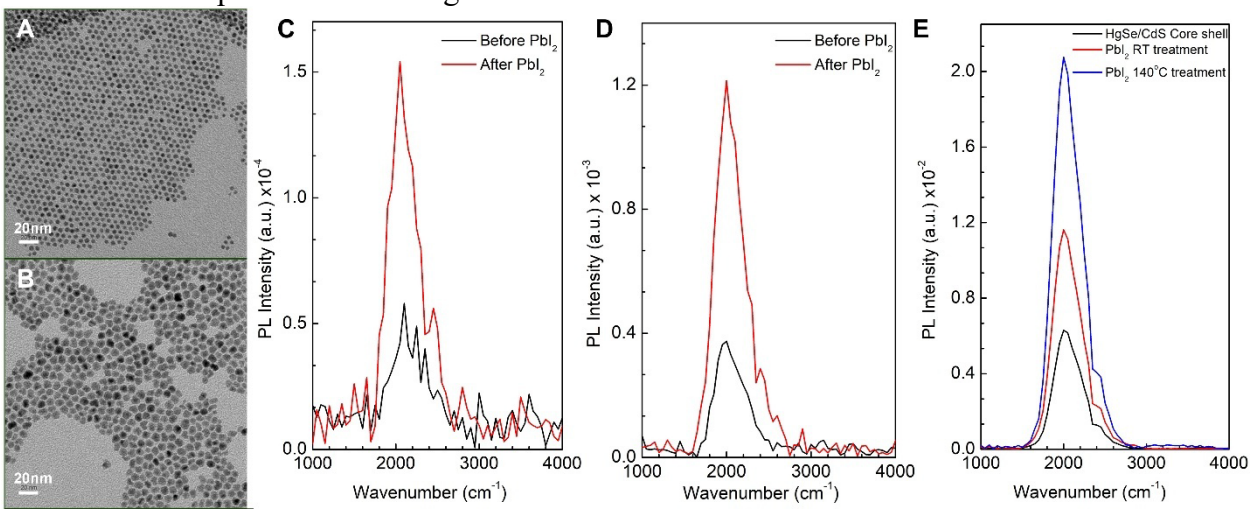

Figure 2: A. TEM of HgSe cores. B. TEM of the HgSe/CdS core/shells. C. PL of HgSe CQD on ZnSe. D. PL of HgSe/CdS on ZnSe. E. PL of HgSe/CdS on a ¼ wave reflector. Note that the scale increases 10-fold for each panel.

The PL is excited by 808 nm, and collected near normal incidence with a 50mm focal length and a numerical aperture of ~0.25. The collimated PL is sent into a step-scan FTIR and focused on an MCT detector. The FTIR/detector relative quantum efficiency as a function of wavenumber is calibrated with a blackbody source of known temperature. The sample external quantum efficiency, PLQE, which is photon emitted divided by photon incident, is then determined by integrating the PL spectrum and dividing by the same for the PbSe reference. **Figure 2C** is the PL of the HgSe cores, for a thin film on a ZnSe substrate where light is emitted front and back. Since only doped dots can emit intraband PL, we calculate the quantum yield per doped dots, $PLQY^D$, as the PLQE divided by the absorption of the 808nm excitation and by the fraction of the doped dots. The fraction of doped dots is determined by a separate measurement of the relative intraband and interband absorption. Most of the HgSe cores are n-doped. The film emits weakly with a 0.009% $PLQY^D$, and this improves to 0.026% after treatment with PbI_2. **Figure 2D** is the PL of the film of HgSe/CdS. It is about 10-fold brighter. The film brightens after PbI_2 treatment, but the absorption shows that this is mostly due to an increased doping. Indeed, after taking the increased doping into account, the $PLQY^D$ is 0.36±0.15% after EdT and 0.25±0.03% after PbI_2. The QY value is consistent with solution data for the same shell thickness. An unexpected result is that the PbI_2 treatment does not improve the quantum yield even though it removes 95% of the C-H vibrational absorptions. $PbBr_2$ and $PbCl_2$ have similar effects with slightly weaker PL.

To make overall brighter films, the CQDs are then deposited on a ¼ wave reflecting substrate. Optical simulations show that the 5 μm absorption in the normal direction increases ~ 10 fold compared to the same CQD film thickness on the ZnSe substrate. **Figure 2E** is the PL of a 200nm film of HgSe/CdS CQDs treated with EdT and then PbI_2 , followed by annealing at 140ºC. The PL signal is indeed more than 10-fold larger than in **Figure 2D** consistent with Kirchhoff rules. In the same instrument measurement units, the PL of the PbSe reference peaks at 0.1. Therefore, the CQD film has an apparent external efficiency of 0.2% at 5 μm, when imaged with a numerical aperture of 0.25, and this is our "brightest" emitter at 5 μm so far.

Also of basic interest, the homogeneous linewidth is about 300 cm^{-1} at 300K and it scales linearly with temperature. Cooling from 423K to 85K, the emission blueshifts by 75cm^{-1} and the quantum yield increases by only ~20%. This is evidence that the PL is not yet limited by multiphonon

relaxation, and it motivates exploring other synthetic approaches for brighter midinfrared PL. This work is currently submitted to JPCL.

Future Plans

The future work aims to improve the efficiency of the cascade LEDs, by understanding the electron transport and the non-radiative processes. The tasks include:

1) Investigation of the cascade phenomenon. This includes modelling the electrical and optical properties of CQD films using microscopic rates that include resonant tunneling. This will be a first attempt to consider resonant tunneling across CQDs under high bias.
2) Investigation of the energy transfer mechanism that quenches the PL, through the direct measurements of the weak broad absorption characteristics of CQD films and matrices. Exploration inorganic matrices and anhydrous processing methods for much brighter films.
3) Synthesis of RoHS compliant CQDs and study of their intraband spectra. This includes III-V indium pnictides (InAs and InSb), silver telluride (Ag_2Te), and chalcopyrite $CuInSe_2$, and their infrared spectro-electrochemistry.

The basic research plans align with the materials science program of the Department of Energy (DOE), and it has the potential to lead to technological advancements in areas like gas sensing and emission monitoring.

References

1. N.S. Wingreen; C.A. Stafford, Intraband quantum-dot cascade laser: proposal for an ultralow-threshold semiconductor laser. IEEE J Quantum Electron, 33(7), 1170 (1997)
2. X Shen, A. Kamath, P Guyot-Sionnest, Mid-Infrared Cascade Intraband Electroluminescence with HgSe–CdSe Core–Shell Colloidal Quantum Dots. Nat Photonics, 17 (12), 1042–1046 (2023)
3. J. Meyer, A.J. Muhowski, L. Nordin, E. Hughes, B. Haidet, D. Wasserman, K. Mukherjee, Bright Mid-Infrared Photoluminescence from High Dislocation Density Epitaxial PbSe Films on GaAs. APL Mater, 9 (11), 111112. (2021)
4. N. Higashitarumizu, S. Wang, S. Wang, H. Kim, J. Bullock, A. Javey, Black Phosphorus for Mid-Infrared Optoelectronics: Photophysics, Scalable Processing, and Device Applications. Nano Lett, 24 (42), 13107–13117 (2024)

Publications from the grant:

1. A Kamath, RD Schaller, P Guyot-Sionnest, Bright fluorophores in the second near-infrared window: HgSe/CdSe quantum dots, Journal of the American Chemical Society 145 (19), 10809-10816 (2023)
2. A Kamath, P Guyot-Sionnest, The “energy gap law” for mid-infrared nanocrystals, The Journal of Chemical Physics 160 (20) (2024)
3. X Shen, P Guyot-Sionnest , Midinfrared Electroluminescence from CdSe Quantum Dots ,ACS nano (2025)
4. R. Naphade, A. Caillas, P. Guyot Sionnest, Relatively bright intraband 5 microns photoluminescence from HgSe/CdS quantum dot films after Lead Halide Treatment. Submitted to JPCL.

Overcoming Optical Selection Rules in Materials by Extreme Localization of Light
Hayk Harutyunyan, Department of Physics, Emory University, Atlanta, GA 30322
Keywords: nanophotonics, metamaterials, nonlinear optics, ultrafast optics, materials physics

Research Scope

The primary scope of this research program is to investigate novel physical phenomena arising from nanoscale confinement in light-matter interactions. Traditionally, optical interactions in nanoscale systems are predominantly dictated by material composition and the geometric attributes of nanostructures. Within this conventional framework, quantum transitions and carrier dynamics rely fundamentally on the electronic structure intrinsic to the constituent materials. Adjustments at the nanoscale—such as structural and geometric modifications—provide additional control mechanisms, influencing electronic transitions via carrier confinement or injection across heterogeneous interfaces. However, conventional methodologies often overlook the influence of specific optical mode characteristics in the mechanisms of photo-assisted transitions.

This program seeks to address this gap by adopting an alternative approach: controlling light-matter interactions through deliberate manipulation of the properties of the excitation light itself. We employ nanostructured materials designed to feature tailored interfaces and nanocavities exhibiting desired optical characteristics. These engineered structures facilitate optical modes with adjustable spatial and temporal features, including field enhancement, localization, field gradients, and optimized quality factors. By leveraging advanced optical spectroscopy techniques, we explore and develop fundamentally new classes of optical interactions at the nanoscale.

Recent Progress

Our recent progress has significantly advanced our understanding of how extreme electromagnetic confinement can be used to manipulate light–matter interactions. We have systematically explored nonlinear photoluminescence (NPL) from spatially confined plasmonic nanostructures, emphasizing how nanoscale confinement fundamentally alters the photophysical mechanisms involved. Specifically, our work leverages metal-dielectric-metal (MDM) gap-mode resonators with precisely engineered nanoscale gaps to investigate the detailed interplay between plasmonic modes and excited carrier distributions. Unlike conventional models that attribute broadband photoluminescence primarily to thermalized "hot" electron distributions approximated by a Fermi–Dirac equilibrium [1-3], our experimental findings clearly demonstrate substantial contributions from non-thermal electronic populations that significantly deviate from thermal equilibrium, Fig. 1a [4]. This deviation

arises from large-momentum electronic transitions enabled by extreme optical field confinement, effectively overcoming the dipole approximation and thus significantly altering conventional recombination dynamics.

In our experimental studies, we fabricated arrays of gold nanowires separated from underlying gold films by ultrathin dielectric spacers with precisely controlled thicknesses. By adjusting spacer thicknesses from 1 nm to 15 nm, we achieved fine control over plasmonic resonance frequencies and spatial field confinement. The resulting gap-mode resonances exhibited pronounced wavelength-dependent nonlinear emission behaviors, characterized by a nonlinear power-law exponent (PLE). We systematically measured this exponent under various excitation conditions, including both up-converted and down-converted emission regimes. Our results indicate that reducing the gap thickness strongly enhances the non-thermal carrier generation due to increased field localization and large-wavevector optical fields, thus promoting intraband transitions typically inaccessible within dipole approximations.

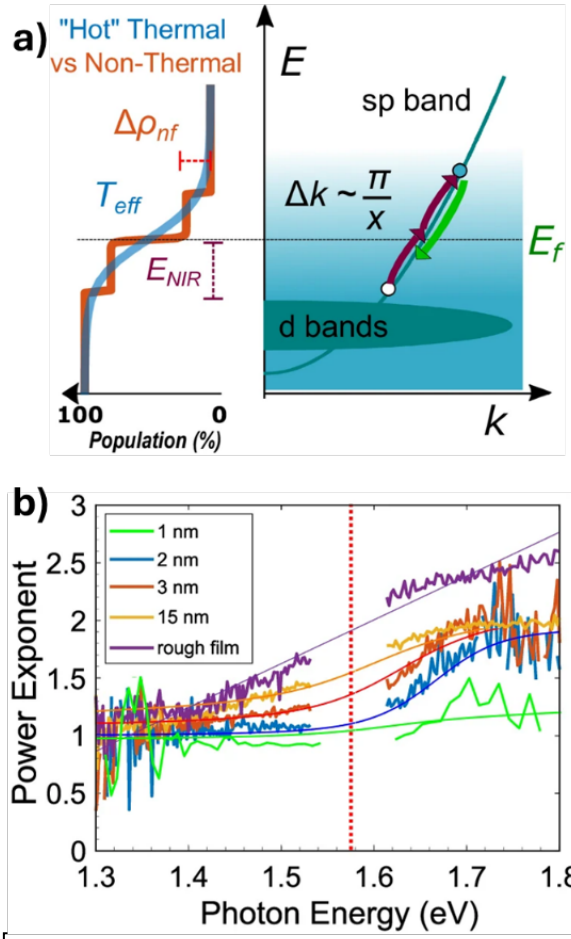

Figure 1. a) Near-infrared intraband multiphoton absorption (upward arrows) and emission (downward arrow) mechanism induced by the wavevector of the localized plasmon mode. The resultant "hot" (thermal) vs non-thermal electron distributions with the corresponding state variables. b) Photoluminescence (PL) power-law exponents (PLE) vs emitted photon energy, for the labeled values of gap spacer thickness in MDM geometry.

By comparing the experimentally determined nonlinear power-law exponent values across different gap sizes and plasmonic resonance conditions, we demonstrated a clear transition from thermal-dominated emission (larger gaps and off-resonance excitation) toward a regime dominated by non-thermal electronic populations at smaller gaps and resonance-matched excitations, Fig. 1b. We also performed complementary finite-difference time-domain (FDTD) simulations to accurately quantify the plasmonic field enhancements and wavevector components within our nanogaps, confirming that field confinement, rather than simple field intensity enhancements alone, drives these significant deviations from the expected thermal emission characteristics.

Further, through detailed analysis of emission spectra under various excitation fluences and detuning conditions, we provided robust evidence supporting a hybrid model combining thermal and non-thermal electronic distributions. Remarkably, the non-thermal contributions dominated the emission characteristics in highly confined nanogaps, substantially altering the scaling of photoluminescence intensity with excitation power, especially in the up-converted emission range. This observation directly challenges the existing models predominantly based on thermalized hot electrons, indicating a necessity to incorporate momentum-dependent non-equilibrium carrier dynamics for accurate description.

These findings significantly advance our understanding of nanoscale plasmonic phenomena, particularly by revealing the fundamental importance of non-Fermi electron distributions under

extreme field confinement conditions. By disentangling thermalized and non-thermal contributions, we have opened new pathways for engineering light–matter interaction in systems where momentum transfer can be substantially larger than in conventional photophysical processes. The demonstrated ability to precisely engineer and exploit non-thermal emission processes paves the way for novel applications in nanophotonics and optoelectronics, including highly efficient photovoltaics, enhanced photocatalysis driven by hot-carrier injection, and advanced nonlinear optical devices relying on non-equilibrium carrier states at nanoscale interfaces. Moreover, the ability to tailor non-vertical transitions in strongly confined geometries points toward possibilities for advanced photonic devices, including spasers and high-performance detectors, and underscores the potential of this research to eventually lead to practical silicon-based lasers.

Future Plans

Our future research directions will expand toward combining electrical and optical excitations to achieve enhanced control of material properties at the nanoscale. Specifically, we aim to explore photon-assisted transport phenomena through quantum tunneling junctions, an emerging platform enabling nanoscale electroluminescence (EL) and optical rectification processes. To overcome the inherent instability and complexity of traditional tunneling junctions, we will focus on fabricated ultra-stable epitaxial junctions exhibiting unprecedented stability and minimal fluctuations in tunneling current. Leveraging these junctions, we plan to systematically investigate photon-assisted tunneling phenomena over a broad spectral range and diverse power conditions. By differentiating between classical and quantum descriptions of optical rectification, and unraveling the interplay of hot-electron currents and thermal effects, we expect to deepen our fundamental understanding of nanoscale light-matter interactions. These ultra-stable junctions not only simplify experimental approaches but also open new avenues for future applications in nanoscale photodetectors, integrated light sources, and multifunctional optoelectronic devices.

References

1. Y. Cai, et al. *Photoluminescence of gold nanorods: Purcell effect enhanced emission from hot carriers*. ACS Nano **12**, 976–985 (2018).
2. T. Haug, P. Klemm, S. Bange, J. M. Lupton, *Hot-Electron Intraband Luminescence from Single Hot Spots in Noble-Metal Nanoparticle Films*. Phys. Rev. Lett. **115**, 67403 (2015).
3. A. R. Bowman,. et al. *Quantum-mechanical effects in photoluminescence from thin crystalline gold films*. Light Sci. Appl. **13**, 91 (2024).
4. R. Lemasters, M. Manjare, R. Freeman, F. Wang, L. G. Pierce, G. Hua, S. Urazhdin, H. Harutyunyan, *Non-thermal emission in gap-mode plasmon photoluminescence*, Nat. Commun., **15**, 4468, (2024)

Publications

1. R. Lemasters, M. Manjare, R. Freeman, F. Wang, L. G. Pierce, G. Hua, S. Urazhdin, H. Harutyunyan, *Non-thermal emission in gap-mode plasmon photoluminescence*, Nat. Commun., **15**, 4468, (2024)
2. G. Yang, M. S. Allen, J. W. Allen, and H. Harutyunyan, *Unlocking Efficient Ultrafast Bound-Electron Optical Nonlinearities via Mirror Induced Quasi Bound States in the Continuum*, Nano Lett., **24**, 1679 (2024)
3. S. B. Anantharaman, J. Lynch, C. E. Stevens, C. Munley, C. Li, J. Hou, H. Zhang, A. Torma, T. Darlington, F. Coen, K. Li, A. Majumdar, P. J. Schuck, A. Mohite, H. Harutyunyan, J. R. Hendrickson, D. Jariwala*, Dynamics of self-hybridized exciton–polaritons in 2D halide perovskites*, Light Sci. Appl., **13**, 1 (2024)
4. J.-S. Park, C. Li, K.-H. Kim, Y. Tang, C. G. E. Murphey, T. S. Teitsworth, S. Kim, H. Harutyunyan, J. F. Cahoon, *Optical Nonlinearity in Silicon Nanowires Enabled by Bound States in the Continuum*, ACS Nano, **17**, 11729 (2023)
5. C. Li, X. Tian, G. Yang, S. U. Dev, M. S. Allen, J. W. Allen, H. Harutyunyan, *Invertible optical nonlinearity in epsilon-near-zero materials*, Phys. Rev. Research, **5**, 013198 (2023)

Project Title: Critical Materials: Atomic Scale Characterization and Manipulation of Rare-Earth Complexes on Material Surfaces

Investigators: Saw Wai Hla[1] (PI), Larry A. Curtiss[1], Xuedan Ma[2,3], Eric Masson[4], Anh T. Ngo[1,5], Volker Rose[6], Tijana Rajh[7], Sergio E. Ulloa[8]

Affiliations:
[1] Materials Science Division, Argonne National Laboratory, Lemont, IL 60439
[2] Nanoscience & Technology Division, Argonne National Laboratory, Lemont, IL 60439
[3] Department of Materials Science, Rice University, Houston, TX 77005
[4] Department of Chemistry and Biochemistry, Ohio University, Athens, OH 45701
[5] Department of Chemical Engineering, University of Illinois at Chicago, Chicago, IL 60608
[6] Advanced Photon Source, Argonne National Laboratory, Lemont, IL 60439
[7] School of Molecular Sciences, Arizona State University, Tempe, AZ 85281
[8] Department of Physics & Astronomy, Ohio University, Athens, OH 45701

Keywords: Rare Earth, Atomic Control, X-rays, STM, Upconversion

Research Scope

This project focuses on developing novel rare-earth materials for energy up-conversion and emission applications. In these materials, multiple rare-earth ions are protected by cages from the surrounding environment, where their separation inside the cages is precisely controlled to achieve desired interactions. These rare-earth complexes have varying sizes and shapes and incorporate different numbers of coordinated rare-earth atoms. The surrounding ligands and counterions are used to fine-tune their electronic structures. The rare-earth complexes here are designed to have distinct advantages over conventional rare-earth molecules or solids in fine-tuning their properties. Using the specially tailored rare-earth cages as basic units, we form 2D clusters and 2D self-networks. Fine-tuning the properties of the individual rare-earth ions in these structures demands systematic control over their coordination and electronic environment at the atomic level. Atomic scale characterization of individual rare earth ions is performed with the most advanced instrumentation: The elemental, chemical, and magnetic properties of rare earth ions in the complexes are determined simultaneously using synchrotron X-ray scanning tunneling microscopy, on one ion-at-a-time basis, while tunneling spectroscopy is used to measure the electronic structure of individual rare earth ions. These experiments provide unparalleled atomic-level information, which is used to develop theoretical frameworks to accurately describe their structural, electronic, and magnetic properties, providing rational blueprints for the design and synthesis of new structures with improved functions.

Recent Progress

Single Molecule Gating[1]: We have successfully demonstrated the atomic-scale control of the electronic structure of a rare-earth complex using a counterion. The complexes are formed by a positively charged lanthanum ion coordinated to a $(pcam)_3$ molecule and a negatively charged triflate counterion trapped underneath via electrostatic interactions on a Au(111) surface. Local gating is performed by adding an additional negatively charged counterion to one side of the complex (Fig.

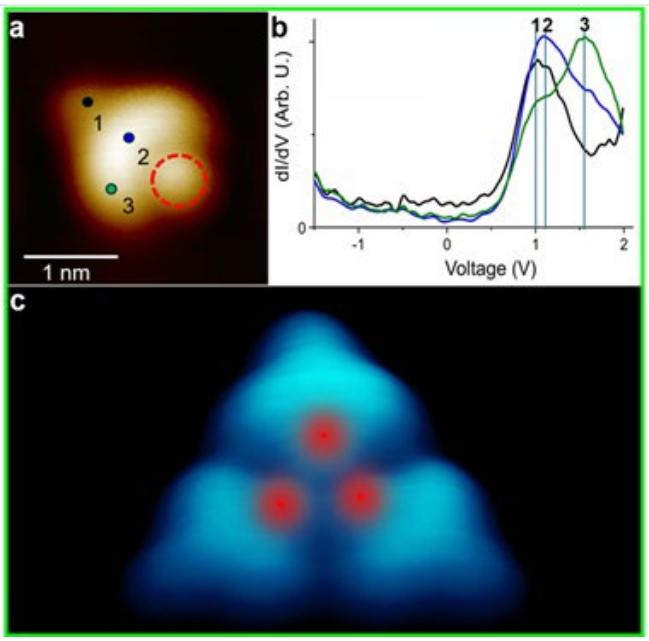

Fig. 1. (a) STM image of a single La-complex. The red circle indicates a counterion. **(b)** dI/dV spectra show a blue shift of orbitals. **(c)** STM image of a cluster consisting of three rare-earth complexes constructed by STM manipulation.

1a). This results in the redistribution of charges within the complex and a positive shift of the frontier orbitals (Fig. 1b) caused by the internal Stark effect of the counterion. This effect is directly captured using tunneling spectroscopy and spectroscopic mapping at 5K. The polarizability of the complex is corroborated by density functional theory and analytical calculations based on experimental findings. Furthermore, the influence of charge polarization on nearby complexes is investigated in a cluster composed of three complexes assembled by STM manipulation (Fig. 1c), which reveals maintaining the charge states as in single complexes. Gating is vital to control the local electronic structure of the rare-earth complexes, and it is a long-standing goal to find an efficient gating process. Our achievement will enable the design of robust rare-earth complex structures for efficient energy conversion behaviors.

2-D Ionic Liquid-Like State of Charged Rare-Earth Clusters on a Metal Surface[2]:

Charged molecular complexes are difficult to form on metal surfaces, and single-molecule studies are usually performed on insulating substrates. Therefore, maintaining net charges in rare-earth complexes on metallic surfaces opens opportunities to investigate their novel behaviors. We have successfully formed 2-D rare-earth clusters having net charges on a metal surface, enabling investigations of their structural and electronic properties on a one-cluster-at-a-time basis. While these ionic complexes are highly mobile on the surface at ~100 K, their mobility is greatly reduced at 5 K, and they reveal stable and self-limiting clusters. In each cluster, a pair of charged rare-earth complexes (Fig. 2a) formed by electrostatic and dispersive interactions acts as a basic unit, and the clusters are chiral. Unlike non-ionic molecular clusters formed on the surfaces, these rare-earth clusters show mechanical stability. Moreover, their high mobility on the surface suggests that they are in a two-dimensional liquid-like state. This finding impacts the design of robust rare-earth complexes for efficient energy conversion behaviors and rare-earth separation in a solid-state environment.

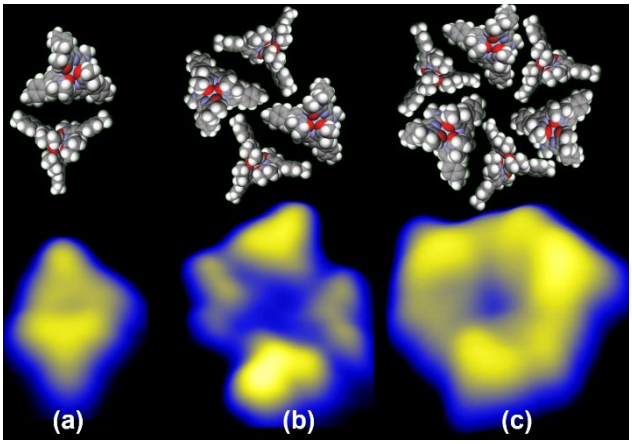

Fig. 2. Models and corresponding STM images of **(a)** two, **(b)** four, and **(c)** six-unit rare-earth clusters.

Single Atom XMCD: X-Ray Characterization of One Atom Magnetism. X-rays are useful for detecting core-level atomic information related to magnetic properties. If X-rays could detect the magnetism of an atom, it would revolutionize material characterization at the ultimate atomic limit. Here, we detect the magnetic properties of just one rare-earth atom inside a molecule using X-rays while simultaneously determining its elemental and chemical states (Fig. 3). Using left and right circular polarized X-rays, core electrons of a europium (Eu) ion inside a molecular host on a nickel (Ni) island are excited at 22 K. The X-ray excited tunnelling current shows cogent $M_{4,5}$ edge signals of a single Eu ion arising from the transitions of $3d_{5/2}$ and $3d_{3/2}$ states to unoccupied 4f orbitals (Fig. 3c, d), while the near-edge X-ray absorption fine structure reveals a 3+ oxidation state of Eu. A single Eu ion's X-ray magnetic circular dichroism (XMCD) measured at the quantum tunnelling regime exhibits a strong ferromagnetic spin alignment with the Ni spins. Thereby, the van Vleck effect[3], discovered almost 100 years ago, is now observed at the ultimate single-atom limit for the first time. Moreover, the opposite spin alignment of molecular orbitals is detected (Fig. 3c, red arrows), revealing a double exchange process as the underlying mechanism. This work demonstrates a comprehensive characterization of magnetic, elemental, chemical, and electronic states of a rare-earth atom inside a molecule and opens a new avenue of materials characterization at the ultimate atomic limit.

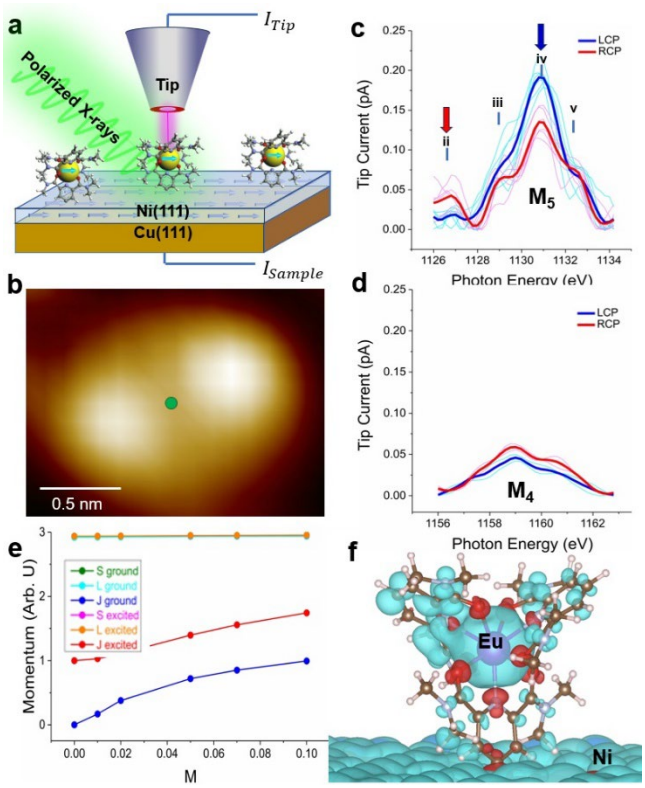

Fig. 3. Single Atom XMCD. (a) A schematic of a single-atom XMCD measurement using SX-STM. **(b)** An STM image of Eu-complex on a Ni-island. The dot at the center indicates where the X-ray signal is measured. **(c, d)** Single-atom STM-XAS signals of M_5 and M_4 edges, respectively. Blue: LCP, and red: RCP. **(e)** Calculated momentum as a function of magnetic exchange interaction, M. **(f)** A 3D spin density plot of Eu-complex on Ni. Red: spin up and blue: spin down.

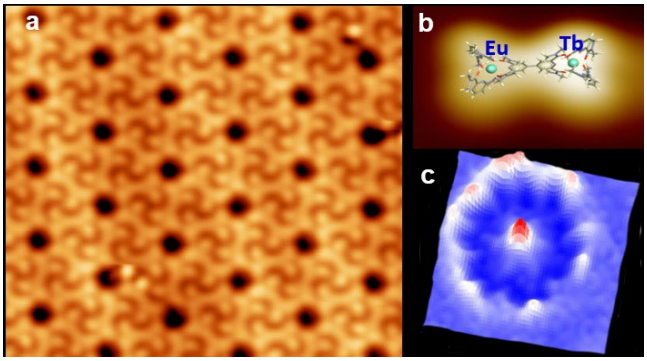

Fig. 4. STM images of **(a)** a 2D network and **(b)** a single complex containing multiple rare-earth ions. **(c)** STS map showing Tb-Eu complex signal in a 2D network.

Synthesis of Multi-Rare-Earth Complexes and Formation of 2D Networks: We have successfully synthesized several molecular complexes containing multiple rare-earth ions such as Ru-Yb, Tb-Eu, and Er-Yb, using solution-based or on-surface synthesis. Some of the complexes, such as Ru-Yb and Er-Yb, are specially designed for photon upconversion processes. We have also successfully formed 2D networks of rare-earth complexes containing Eu-Eu, Tb-Tb, and Eu-Tb (Fig. 4). Their structural and electronic properties are investigated using tunneling microscopy, spectroscopy, X-ray measurements, and DFT and analytical calculations. The optical properties and their interactions in these complexes have also been studied with magneto-optical spectroscopy and low-temperature EPR methods.

Awards and Recognitions: The lead PI, Saw Wai Hla, has won two highly prestigious international awards in 2024 based on the achievements of this project.

1. Falling Walls Science Breakthrough Laureate of the Year 2024 in Physical Sciences by the Falling Walls Foundation, Berlin, Germany.
2. Feynman Prize in Nanotechnology (experiment) in 2024 by Foresight Institute.

Moreover, PI-Hla and Co-PI Rose have also received multiple recognitions within the last two years for their achievements in this project.

3. Physics World Top 10 Breakthrough of the Year 2023 from the Institute of Physics (IoP), UK.
4. Impact Argonne Award (2023) from Argonne National Laboratory.

DOE BES highlight story: For the First Time, Scientists X-Ray a Single Atom. (08/30/2024) https://www.energy.gov/science/bes/articles/first-time-scientists-x-ray-single-atom

Future Plans

Our overarching goal is understanding and controlling the behaviors of rare-earth ions in the complexes and their networks, which would enable tailoring their properties beneficial for different areas such as emission, upconversion, energy harvesting, separation, spintronics, and quantum sciences. Following our success on one-atom-level characterizations of rare-earth ions, as well as atomic control over their environment, and investigations on mixed rare-earth ions within molecular complexes, we are now focusing on their emission properties, especially for the upconversion processes. Moreover, we plan to extend our project by incorporating two additional directions/approaches in the future.

1). Beyond rare-earth: After understanding the atomic-level properties of rare-earth in the molecular hosts, we plan to replace some rare-earth ions with other metals, such as transition metal atoms, for the desired behaviors.

2). AI-driven automatic synthesis: We have successfully demonstrated Artificial Intelligence (AI) controlled STM atomic/molecular manipulation, and a patent has been applied.[4] In addition, the PI Hla has pioneered an on-surface single-molecule synthesis method using STM manipulations in the past.[5] By combining these two schemes, we plan to develop new methods to synthesize novel rare-earth complexes on material surfaces using AI-controlled STM manipulation.

References

[1] D. J. Trainer, K. Z. Latt, X. Cheng, N. K. Dandu, L. A. Curtiss, S. E. Ulloa, A. T. Ngo, E. Masson, & S. W. Hla. *Gating single molecules with counterions.* ACS Nano **19**, 15272-15280 (2025).

[2] D. Trainer, A. T. Lee, S. Sarkar, V. Singh, X. Cheng, N. K. Dandu, K. Z. Latt, S. Wang, T. M. Ajayi, S. Premarathna, D. Facemyer, L. A. Curtiss, S. E. Ulloa, A. T. Ngo, E. Masson, & S. W. Hla.*2D ionic liquid-like state of charged rare-earth clusters on a metal surface.* Adv. Sci. **11**, 2308813 (2024).

[3] Van Vleck, H. J. *On dielectric constants and magnetic susceptibilities in the new quantum mechanics part III – application to dia- and paramagnetism.* Phys. Rev. **31**, 587-613 (1928).

[4] D. J. Trainer, S. Srinivasan, N. P. Guisinger, & S. W. Hla. *Artificial Intelligence driven automated atomic manipulation.* US Patent App.17/733,812. https://patents.google.com/patent/US20230351579A1/en

[5] S. W. Hla, L. Bartels, G. Meyer, & K.-H. Rieder. *Inducing all steps of a chemical reaction with the scanning tunneling microscope tip: Towards single molecule engineering.* Phys. Rev. Lett. **85**, 2777 (2000).

Publications (10 most relevant publications within the last 2 years)

(1). T. M. Ajayi, N. Shirato, T. Rojas, S. Wieghold, X. Cheng, K. Z. Latt, D. J. Trainer, N. K. Dandu, Y. Li, S. Premarathna, S. Sarkar, D. Rosenmann, Y. Liu, N. Kyritsakas, S. Wang, E. Masson, V. Rose, X. Li, A. T. Ngo, & S.-W. Hla. *Characterization of just one atom using synchrotron x-rays.* Nature **618**, 69-73 (2023). https://www.nature.com/articles/s41586-023-06011-w

(2). T. Rajh, E. Masson, K. Z. Latt, A. Smith, A. M. Brugh, N. Dandu, D. Trainer, L. A. Curtiss, A. T. Ngo, & S.-W. Hla. *Light and chemical-doping-induced magnetic behavior of Eu molecular systems.* Inorg. Chem. **62**, 12721-12729 (2023). https://doi.org/10.1021/acs.inorgchem.3c01154

(3). D. W. Facemyer, N. K. Dandu, A. T. Lee, V. R. Singh, A. T. Ngo, & S. E. Ulloa. *Spin and electronic excitations in 4f atomic chains on Au(111) substrates*. Phys. Rev. B. **108**, 085407 (2023). https://doi.org/10.1103/PhysRevB.108.085407

(4). R. Emmanuele, W. Wang, A. Smith, E. Masson, D. J. Gosztola, T. Rajh, S.-W. Hla, & X. Ma. *Amplified spontaneous emission from europium-based molecular complexes coupled to photonic crystal cavities.* Appl. Phys. Lett. **123**, 061106 (2023). https://doi.org/10.1063/5.0160179

(5). S. Wieghold, N. Shirato, X. Cheng, K. Z. Latt, D. Trainer, R. Sottie, D. Rosenmann, E. Masson, V. Rose & S. W. Hla. *X-ray spectroscopy of a rare-earth molecular system measured at the single atom limit at room temperature.* J. Phys. Chem. C **127**, 20064-20071 (2023).
https://doi.org/10.1021/acs.jpcc.3c04806

(6). D. Trainer, A. T. Lee, S. Sarkar, V. Singh, X. Cheng, N. K. Dandu, K. Z. Latt, S. Wang, T. M. Ajayi, S. Premarathna, D. Facemyer, L. A. Curtiss, S. E. Ulloa, A. T. Ngo, E. Masson, & S. W. Hla. *2D ionic liquid-like state of charged rare-earth clusters on a metal surface.* Adv. Sci. **11**, 2308813 (2024). https://doi.org/10.1002/advs.202308813

(7). R. Emmanuele, H. Sai, J.-S. Chen, D. J. Morrow, L. Đorđević, D. J. Gosztola, S. W. Hla, S. I. Stupp, and X. Ma. Lattice symmetry-guided charge transport in 2D supramolecular polymers promotes triplet formation. Adv. Sci. **11**, 2402932 (2024).
https://doi.org/10.1002/advs.202402932

(8). X. Xiao, J. G. Connell, K. Z. Latt, J. Gong, Y. Liu, T. Kim, H.C. Fry, J. E. Pearson, O. S. Wostoupal, M. Li, C. Soldan, Z. Yang, R. D. Schaller, B. T. Diroll, S. W. Hla, and T. Xu. *Light-induced Kondo-like exciton-spin interaction in neodymium(II) doped hybrid perovskite.* Nat. Commun. **15**, 6084 (2024). https://www.nature.com/articles/s41467-024-50196-1

(9). D. W. Facemyer, & S. E. Ulloa. *Probing nonlocal correlations in magnetic rare-earth clusters*. Phys. Rev. B. **111**, 064403 (2025). https://doi.org/10.1103/PhysRevB.111.064403

(10). D. J. Trainer, K. Z. Latt, X. Cheng, N. K. Dandu, L. A. Curtiss, S. E. Ulloa, A. T. Ngo, E. Masson, & S. W. Hla. Gating single molecules with counterions. ACS Nano **19**, 15272-15280 (2025). https://doi.org/10.1021/acsnano.4c12662

Understanding Shallow-trap Physics in Metal Halide Perovskites

PI: Jinsong Huang, University of North Carolina at Chapel Hill

Keywords: perovskite, defect tolerance, shallow traps, energy, sensing

Research Scope

Metal halide perovskites (MHPs) are known for their unique defect tolerance that enables high efficiency perovskite solar cells and light emitting diodes. The point defects in iodide perovskites generally introduce shallow traps or energy levels in conduction band of valance band. Most surface defects of perovskites are still deep but can be effectively passivated to become shallow. Conventional wisdom believes that photogenerated charges in the shallow traps behave like free ones. However, the present theory lacks two critical proof to close the loop: 1) the presence of shallow traps was not proven in pristine perovskites and passivated perovskites, mainly because of lack of appropriate characterization methods; 2) there is no study whether the charge carrier dynamics in shallow traps to verify whether they really behave as shallow traps, or whether they play a role in the defect tolerance of MHPs.

The fundamental understanding of shallow traps in perovskites is crucial for advancing the field of perovskite materials and related devices, such as photodetectors and gamma-ray room-temperature/high temperature semiconductor detectors by reducing the device noise. We aim at understanding the influence of shallow traps on the charges recombination rate, charges carrier lifetime in MHPs, and overall perovskite solar cell and light emitting diode performance upper limits, with a central hypothesis that the shallow traps to be another mechanism for the unusual defect tolerance of MHPs. Utilizing the unique high density of shallow traps and high emission probability of shallow traps in MHPs, we will explore other new applications enabled by the rich emissive shallow traps in MHPs.

Recent Progress

1. Influence of strain on shallow traps in iodide perovskites

We explored bilaterial amine treatment to perovskites, ethylenediamine (EDA) where were shown to improve the efficiency and stability of perovskites[1]. All devices were fabricated with a structure of ITO/ PTAA/ $Cs_{0.08}FA_{0.92}PbI_3$/ C_{60}/ BCP/ Cu. As shown by the *N*-Δt plot in **Fig. 1a**, the pristine device showed only one remission peak at 260±20 ns. After being treated with EDA, the perovskite device had a detrapping time of 420±20 ns, while the reemission peak at 260±20 ns was almost the same. EDA surface treatment increased the shallow trap density by two orders of magnitude times. We conducted cryogenic thermally stimulated photoemission spectroscopy (C-TSPS) measurement which can also detect ultra-shallow traps [2]. As shown in **Fig. 1c**, the TL intensity of re-emitted charges was enhanced by ~75 times after the film was treated by EDA. We hypothesize that the strain is the origin of the new shallow traps based on the observation that devices without strain did not induce new shallow traps. To verify it, we treated the perovskite surface with propylamine (PA) which has a similar molecular structure to EDA but only one amine group at one end. The shallow trap reemission peak did not appear in the device with PA surface treatment (**Fig. 1b**). We also evaluated five other molecules with only one terminal amine group. The results lead to the same conclusion that the surface treatment using molecules with monoamine did not increase the shallow trap density.

Since EDA has amine group at both ends, it can react with the two FA^+ cations in the adjacent lattice cells[3] and generate n'-[2-(aminomethylideneamino)ethyl]methanimidamide (2-EMA) (**Fig. 1d**). After replacing the FA^+ cations in two adjacent unit cells with 2-EMA, it can impose a surface strain to perovskites when its length doesnot match the spacing between the two A-sites, as illustrated

in **Fig. 1e**. PA won't cause surface strain because of the single amine group. We employed Williamson-Hall method on pristine, PA-treated, and EDA-treated films to quantify the strain based on the different scattering vector dependence on the peak broadening in the grazing incidence X-ray diffraction (GIXRD)[4]. The pristine and PA-treated film showed a depth-independent uniform compressive strain of -0.05±0.01% and -0.04±0.01% along the out-of-plane directly respectively (**Fig. 1f**). PA treatment did not change the strain, but the EDA-treated film showed a depth-dependent gradient strain of 0.10% at 10 nm depth, -0.03% at 20 nm depth, and -0.04% at 50 nm depth (**Fig. 1f-g**). Since the only difference of PA and EDA is the number of amine groups, the shallow traps should be caused by the strain introduced by the EDA treatment.

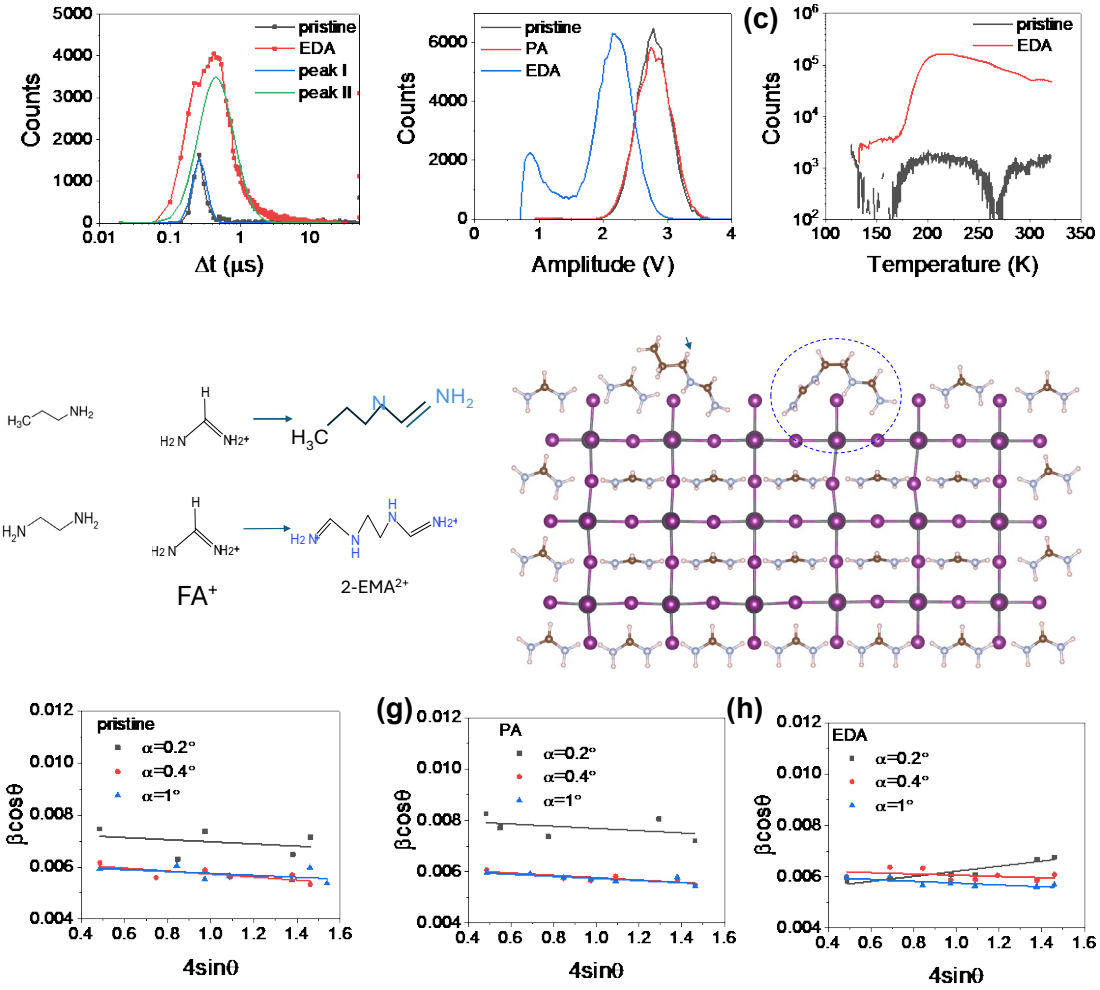

Fig. 1 Shallow trap manipulation by strain. *(**a**) N-Δt plots of the pristine and EDA treated devices, the green and blue lines are the peaks fitting for EDA-treated devices. (**b**) N-A plots of pristine, PA-treated, and EDA-treated devices. (**c**) The cryogenic thermally stimulated photoemission spectra of the pristine and EDA-treated films. Williamson-Hall plot of (**d**) pristine, (**e**) perovskite treated by EDA, (**f**) PA-treated. (**g**) Reaction of EDA, PA with FA+. (**H**) Illustration of the strain generated in EDA treated sample with both ends staying in A-site.*

2. Suppression shallow traps by chloride incorporation

We studied $FAPbBr_xCl_{3-x}$ single crystals which are promising candidates for gamma-ray spectroscopic detectors.[5] The shallow traps in them may cause lower response speed, so it is important to understand the origin of the shallow traps and then eliminate them.

Here, we grew a series of $FAPbBr_xCl_{3-x}$ single crystals with various Cl% from 0 to 15%. The color of the crystals changed with the chlorine fraction (**Fig.2a**). X-ray diffraction (XRD) and bandgap measurement confirmed the incorporation of chloride (**Fig.2b**). We studied the charge collection process for the crystals under gamma-ray event or pulsed laser light, and we noticed a typical signal as shown in **Fig.2c** when $FAPbBr_3$ was used. The amplitude of voltage at the charge sensitive amplifier, which represents the number of collected charges, shows a two-step increasing process, a faster one with larger slope and one slower one. We assign the faster one to be those charges directly collected by the electrode without encounter any charge traps, and the slower one to be the charges that are first trapped and then reemitted. This allows us to directly characterize the shallow traps in these crystals. This slower part does not show up in single crystal silicon devices.

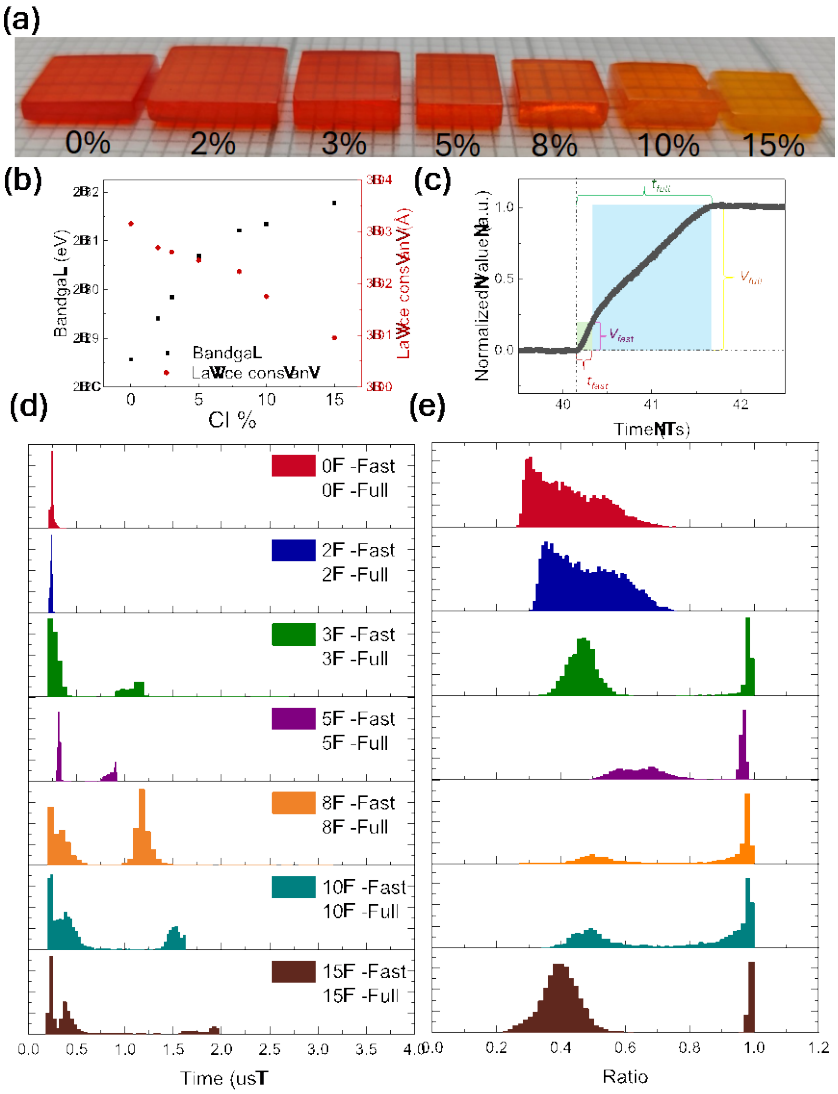

Fig. 2 *(a) Photos of the synthesize $FAPbBr_xCl_{3-x}$ single crystals; (b) Bandgap and lattice constant of the crystals with Cl percentage; (c) A typical signal collected from charge sensitive amplifer when the crystal devices were exposed to a gamma-ray photon or a laser pulse; (d) histogram of the fast and full charge collection time; (f) histogram of the ratio of the fast and full amplitudes (V_{fast}/V_{full}).*

We did this measurement for all $FAPbBr_xCl_{3-x}$ single crystals, and collected the data of thousands of events for each crystal. **Fig. 2d** shows the histogram of the fast and full charge collection time as defined in **Fig.2c**. One can see from **Fig. 2d** that all of these crystals show fast and delayed charge collection. With the increasing of Cl percentage to 2%, full collection time get smaller, indicating shallower traps. This trend was kept when the Cl percentage was increased to 5%, which show the fastest charge collection even with the presence of shallow traps. For Cl%≥3%, some fast and fall even overlap, indicating these events do not encounter any trapping behavior. The mobility calculated from these events should represent the intrinsic carrier mobility, showing 5% Cl results in the highest mobility. The reemission events are smallest for the crystal with 5% Cl. To quantify the density of shallow traps, we did the histogram for the ratio of fast amplitude

versus full amplitude. For events that donot encounter shallow traps, the ratio should be unity. As shown in **Fig.2e**, $FAPbBr_xCl_{3-x}$ with ≥3% have a significant number of events which are not trapped. For $FAPbBr_xCl_{3-x}$ with 5% Cl, the events that are trapped still show a largest average amplitude, which again indicates the smallest density of traps in this composition. This result concludes that: 1) $FAPbBr_3$ are rich in traps, but they are relatively shallow so that most charges are still reemitted; 2) Cl incorporation with optimal 5% not only increases the carrier mobilities but also reduces the shallow trap density. We hypothesize the traps might be bromide vacancies which are filled by chloride, which will be evaluated.

Future Plans

We will identify the nature of the shallow traps in $FAPbBr_3$ using several established methods by our group. In addition, we will continue to study the composition dependent shallow traps, including A, B, X sites. Alloying of the different cations and anions donot only change of the lattice distortion and the associated electronic structures, they also introduce other changes such as heterogeneity of composition in both in-plane and out-of-plane directions. We hypothesis they would have strong impact on the shallow trap densities. We will study the relationship of the shallow trap density and photoluminescence lifetime to find out the possible correlation.

References

1. Wu, W.-Q.; Yang, Z.; Rudd, P. N.; Shao, Y.; Dai, X.; Wei, H.; Zhao, J.; Fang, Y.; Wang, Q.; Liu, Y., Bilateral alkylamine for suppressing charge recombination and improving stability in blade-coated perovskite solar cells. *Science advances* **2019,** *5* (3), eaav8925.
2. Selim, F. A., Advanced thermoluminescence spectroscopy as a research tool for semiconductor and photonic materials: a review and perspective. *Phys. Status Solidi A* **2023,** *220* (10), 2200712.
3. Wang, M.; Shi, Z.; Fei, C.; Deng, Z. J. D.; Yang, G.; Dunfield, S. P.; Fenning, D. P.; Huang, J., Ammonium cations with high pKa in perovskite solar cells for improved high-temperature photostability. *Nature Energy* **2023,** *8* (11), 1229-1239.
4. Yang, B.; Bogachuk, D.; Suo, J.; Wagner, L.; Kim, H.; Lim, J.; Hinsch, A.; Boschloo, G.; Nazeeruddin, M. K.; Hagfeldt, A., Strain effects on halide perovskite solar cells. *Chem. Soc. Rev.* **2022,** *51* (17), 7509-7530.
5. Liang Zhao, Z. S., Ying Zhou, Xiaoming Wang, Yeming Xian, Yifan Dong, Obadiah Reid, Zhenyi Ni, Matthew C. Beard, Yanfa Yan, and Jinsong Huang Surface Defect Passivation Enabled Near Unity Charge Collection Efficiency in Bromide based Perovskite Gamma-Ray Spectrum Devices. *Nature Photonics* **2023,** *18*.

Publications

1. Y. Zhou, H. Zhang, Y. Xian, Z. Shi, J. N. Aboa, C. Fei, G. Yang, N. Li, F. A. Selim, Y. Yan, J. Huang, Enhancing charge-emitting shallow traps in metal halide perovskites by >100 times by surface strain, *Joule* 9, 1–11, (2025)
2. X Tian, SD Stranks, J Huang, VM Fthenakis, Y Yang, F You, Perspectives for sustainability analysis of scalable perovskite photovoltaics, *Energy Environ. Sci.*, ,18, 194-213 (2025)

PROJECT TITLE: Superatomic Clusters – Structure, Stability, and Applications

Jena, Purusottam
Department of Physics, Virginia Commonwealth University, Richmond, VA 23284-2000
pjena@vcu.edu

Keywords: super atoms, ionic clusters, structure, stability, energy materials

Program Scope:

The objective of this project is to provide a fundamental understanding of the structure-property relationships of a novel class of superatomic clusters mimicking the chemistry of atoms and to explore their potential for promoting unusual reactions as well as serving as building blocks of new energy and magnetic materials. Working closely with experimental groups, the goal is not only to validate our theoretical predictions but also to guide experimentalists in the focused discovery of new materials.

The project exploits the unique size- and composition-specific properties of clusters and explores their potential as building blocks of functional materials. Using first-principles theory, our approach is an atom-by-atom rational design of a new class of superatomic clusters such as superalkalis and superhalogens that not only mimic the chemistry of alkali and halogen atoms, respectively, but also are suitable for forming supersalts with unusual properties. The proposed project involves three interrelated thematic areas: (1) *Ligand assisted rational design of highly reactive clusters:* Following the recent discovery that removing a ligand, L from the boron-based clusters such as $B_{12}L_{12}^{2-}$ (L=H, F, CN), one can create a super-electrophilic center capable of binding noble gas atoms at room temperature, we will study their ability to activate H_2, N_2, and CO_2. Similar studies will be carried out for ligand- and core-tailored $Co_6S_8(PEt_3)_6$ clusters. Also proposed is a study of superatom-based catalysts versus single-atom catalysts. (2*) Cluster-based magnetic materials:* Following our recent joint experimental and theoretical work that UAu_6 cluster is magnetic even though neither U nor Au is nonmagnetic, we will explore its potential as the building block of magnetic materials and examine if a material composed of two non-magnetic and metallic elements can form a magnetic semiconductor. We will also study the magnetic properties of chalcogenide $Co_6S_8(PEt_3)_6$ clusters by tailoring the composition of its metal core and the number of ligands. (3) *Super-ions as building blocks of energy materials:* Given that electrolytes in metal-ion batteries are salts composed of metal cations and halogen anions, we will study a wide range of superhalogens as the building blocks of electrolytes in K-ion batteries and their interaction with the electrode surfaces. Similarly, halogens in thermoelectric materials such as $Re_6Se_8I_2$ will be replaced by superhalogens to see if the new cluster degrees of freedom can enhance the figure of merit, ZT, value due to the inherent rich phonon dynamics. Use of superatomic clusters as building blocks will open new opportunities for the design and synthesis of novel materials.

The complexity of the above systems necessitates the use of a multi-scale approach - from molecular orbital theory to supercell band structure theory and *ab-initio* molecular dynamics. Although most studies are carried out using density functional theory (DFT) with a variety of hybrid exchange-correlation functionals, post-Hartree-Fock methods are used, when needed, to validate the accuracy of the DFT-based results. Efficient search algorithms and methodology including machine learning are developed for rational design of metastable phases of cluster-based matter.

Exploration of new frontiers of superatomic clusters as building blocks of energy and magnetic materials can have the potential for advanced technologies. The project lies at the interface

between physics, chemistry, and materials science and is ideal to train graduate and undergraduate students as well as postdoctoral fellows in multi-disciplinary research.

Recent Progress:

We have accomplished much of what was proposed in our renewal proposal in 2023. Over the past two years, we published/in press 33 papers in high-impact journals such as Advanced Energy Materials (impact factor, IF=27.8), ACS Nano (IF=15.8), Small (IF=13), ACS Applied Materials and Interfaces (IF=8.5), etc. Two papers were featured on the cover of Chemical Communications (IF=6.22) and Nanoscale (IF=5.8). In addition, 6 papers are currently under review, and 13 of these papers are published jointly with experimentalists.

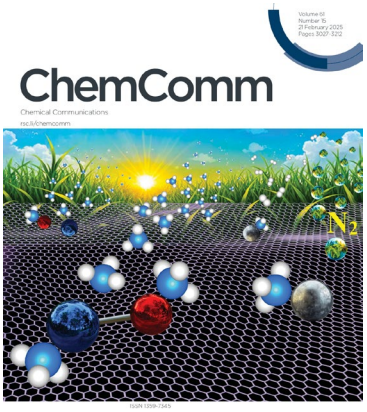

Chem. Commun. **61**, 3127 – 3130 (2025)

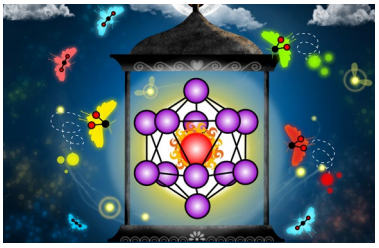

Nanoscale **17**, 8505 – 8514 (2025)

The papers cover a wide range of topics dealing with the role of dimensionality, size, symmetry, and composition on the unique properties of materials at the nanoscale. These include *zero-dimensional clusters* (Janus behavior of Au atoms interacting with fluorine, catalytic potential of modified dodecaboranes and transition metal-embedded Cu cage clusters, single-superatom catalysts, ferromagnetic nickel chalcogenide nanocluster); *two-dimensional systems* (penta-CdO_2 sheet exfoliated from its bulk phase, twisted layers of penta-NiN_2, persistent spin texture non-symmorphic CdTe and ZnTe monolayers, $In_2Si_2S_3X_3$ (X = S, Se, Te) Janus monolayers, realization of ferroelectricity in penta-$PdSe_2$/penta-$PtSe_2$ van der Waals heterostructure, magnetic mono-layers composed of otherwise nonmagnetic elements); *three-dimensional materials with superatomic clusters as building blocks for energy storage* (3D porous metallic carbon allotrope composed of 5-7 nanoribbons as an anode material for sodium-ion batteries, stabilization of interface between the solid-state electrolyte metal anode, advanced electrocatalytic cathodes in high areal capacity and long-life lithium-sulfur batteries, $Na_3La_5Cl_{18}$ solid-state electrolyte with high stability and fast ionic conduction, stabilization of argyrodite LPSCl solid-state battery, high-capacity composite anode for next generation lithium-ion batteries, ductile $Na_3La_5Br_{18}$ solid-state electrolyte with fast Na^+ conduction and high electrochemical and interfacial stability, 3D metallic, ductile, and porous boron nitride anode material for sodium-ion battery). In addition, we explored the potential of dual-atom catalysts for hydrogen production and the production of a 3D metallic and magnetic phase of carbon starting with a molecular precursor.

As the allotted space is limited, we give one example from each of the three thematic areas mentioned above in the research scope, namely, (1) *Ligand assisted rational design of highly reactive clusters,* (2*) Cluster-based magnetic materials,* and (3) *Super-ions as building blocks of energy materials*.

(1) Dodecaborate anions and their derivatives $[B_{12}X_{11}]^{2-}$ (X = H, F, Cl, Br, I, CN) dianions[1] that carry one more electron than needed to satisfy the Wade's rule should not be stable, assuming that the rule applies to fragments as well. While this is the case for X = H, we showed that $[B_{12}X_{11}]^{2-}$ (X = F, Cl, Br, I, CN) dianions are stable with the second electron in $[B_{12}(CN)_{11}]^{2-}$ bound by as much as 3.17 eV. More importantly, the stability of these dianions is found to have a significant effect on the activation of gas molecules such as CO_2 and N_2, providing a path toward the development of new catalysts.

(2) Atomic clusters are known to exhibit properties different from their bulk phase. However, when assembled or supported on substrates, clusters often lose their uniqueness. We showed[2] that while uranium and coinage metals (Cu, Ag, Au) are nonmagnetic in their bulk, UX_6 (X=Cu, Ag, Au) clusters, unlike their nonmagnetic bulk, are not only magnetic but also retain their magnetic character and structure when assembled into a two-dimensional (2D) material. The magnetic moment remains localized at the U site and is found to be $3\mu_B$ in clusters and about $2\mu_B$ in the 2D structure. In 2D UX_4(X=Cu, Ag, Au) monolayers, U atoms are found to be coupled antiferromagnetically through an indirect exchange coupling mediated by the coinage metal atoms. Furthermore, hydrogenation of these monolayers can induce a transition from the antiferromagnetic to the ferromagnetic phase.

(3) The success of all-solid-state batteries (ASSBs) depends on the solid-state electrolyte (SSE) exhibiting high interfacial stability and room-temperature ionic conductivity. However, the current SSEs, especially those with practical ionic conductivities ($\geq 10^{-3}$ S/cm) at room temperature, often develop unstable interfaces at the metal anode, in some cases with even greater severity than with liquid organic electrolytes. Despite persistent efforts, achieving interfacial stability and sufficient ionic conductivity simultaneously represents one of the greatest challenges in ASSBs. The current approaches focus on stabilizing the interface by incorporating secondary interlayers or introducing coatings by surface engineering. The method is often material-specific, and the added interlayers often deteriorate during cycling. Using phase analysis and explicit interface modeling, we demonstrated[3] a strategy to kinetically stabilize the interface between the SSE and metal anode by incorporating selected monoanion clusters in the SSE; they can effectively lower or even halt the reduction kinetics at the interface by promoting on-site formation of interphases that are highly electron insulating. The study provides insight into the kinetic effects to achieve SSEs with superior properties in bulk and at the interface.

Future Plans:

Our future projects will continue to include designing cluster-based materials for energy harvesting, conversion, and storage; highly reactive negatively charged ions and their use in promoting unusual chemical reactions; superatom-based catalysts for production of green hydrogen and conversion of CO_2; magnetism of atomically precise clusters and the effect of ligands in magnetic transition; and understanding the evolution of the structure and properties of clusters. We will continue to work with experimentalists for focused discovery of new cluster-based materials.

References:

1. Kilic, M. E. and Jena, P.: "Catalytic Potential of $[B_{12}X_{11}]^{2-}$ (X = F, Cl, Br, I, CN) Dianions", J. Phys. Chem. Lett. **14**, 8697−8701 (2023)
2. Mohanta, M., Jena, P.: "Magnetism of otherwise nonmagnetic Elements: From clusters to Mono-layers", J. Phys. Chem. C **128**, 12286-12295 (2024)
3. Fang, H. and Jena, P: "Kinetic Effects of Anion Clusters on the Interfacial Stability between Solid-State Electrolyte and Metal Anode", Phys. Rev. X Energy **2**, 043013 (2023)

Publications (2023-25):

1. Hou, C., Shen, Y., Wang, Q., Kawazoe, Y., Jena, P.: "Large second harmonic generation in the penta-CdO_2 sheet exfoliated from its bulk phase", J. Mat. Chem. A **11**, 167-177 (2023)
2. H. Banjade, A. Shah, P. Jena: "Janus behavior of Au atoms interacting with Fluorine", Theo. Chem. Accounts **142**, 9 (2023) DOI10.1007/s00214-022-02946-x, 2023

3. Zhang, C., Sun, J., Shen, Y., Yoshikawa, A., Kawazoe, Y., Wang, Q., and Jena, P. "Extremely large response of phonon coherence to the twisting in layered penta-NiN_2", Small **19**, 2303295 (2023) DOI: 10.1002/smll.202303295
4. Zhu, Z., Tufekci, B. A., Harris, R. M., Deepika, Jena, P., Peterson, K. A., Bowen, K. H. "Electronic Structure and Anion Photoelectron Spectroscopy of Uranium-Gold Clusters (UAu_n^-), (n = 3 – 7)", J. Phys. Chem. A **127**, 34, 7186–7197 (2023)
5. Mohanta, M. K., Jena, P.: "Symmetry-driven persistent spin texture in non-symmorphic CdTe and ZnTe monolayers", Phys. Rev. B **108**, 085432 (2023)
6. Kilic, M. E. and Jena, P.: "Catalytic Potential of $[B_{12}X_{11}]^{2-}$ (X = F, Cl, Br, I, CN) Dianions", J. Phys. Chem. Lett. **14**, 8697−8701 (2023)
7. Sun, W., Ni, D., Hou, C., Wang, Q., Yoshiyuki Kawazoe, Y., Jena, P.: "A new 3D porous metallic carbon allotrope composed of 5-7 nanoribbons as an anode material for sodium-ion batteries". Journal of Power Sources **584**, 233594 (2023)
8. Fang, H. and Jena, P: "Kinetic Effects of Anion Clusters on the Interfacial Stability between Solid-State Electrolyte and Metal Anode", Phys. Rev. X Energy **2**, 043013 (2023)
9. Mohanta, M., Jena, P.: $In_2Si_2S_3X_3$ (X = S, Se, Te) Janus monolayers: from magnetic element-free spin-Hall transistor to sustainable energy generation, J. Mater. Chem. C, **12**, 1888-1896 (2024)
10. Kaid, M. M., Shehab, M. K., Fang, H., Ahmed, A. I., El-Hakam, S. A., Ibrahim, A. A., Jena, P., El-Kaderi, H. M.: "Selective Reduction of Multivariate Metal-Organic Frameworks for Advanced Electrocatalytic Cathodes in High Areal Capacity and Long-Life Lithium-Sulfur Batteries", ACS Applied Materials and Interfaces **16**, 283–2295 (2024)
11. Mohanta, M., Jena, P.: "$In_2Si_2S_3X_3$ (X = S, Se, Te) Janus Monolayers: From Magnetic Element-Free Spin-Hall Transistor to Sustainable Energy Generation", J. Mat. Chem. C **12**, 1888 (2024)
12. Mohanta, M., Jena, P.: "MgTe (110) Semiconductor for Magnetic Element Free Nonballistic Spin-Field-Effect Transistor ", Phys. Rev. B **109** (8), 085415 (2024)
13. Hussain, S. J.; Liu, J.; Du P-H.; Nazir, M. A.; Sun, Q.; Jena, P.: "Novel Solid-State Electrolyte $Na_3La_5Cl_{18}$ with High Stability and Fast Ionic Conduction", ACS Appl. Mat. Interfaces **16**, 14364-14370 (2024)
14. Kilic, M. E.; Jena, P.: "Activation of Small Molecules by Modified Dodecaborate Anions", J. Phys. Chem. A **128**, 1993−2002 (2024)
15. Rabbani, M. G.; Sasse, R. K.; Behera, S.; Jena, P.; Liu, J.; Thallapally, P. K.; Islamoglu, T.; Shehab, M. K.; Farha, O. K.; El-Kaderi, H. M.: "High-Performance Porous Organic Polymers for Environmental Remediation of Toxic Gases", Langmuir **40**, 8024-8034 (2024)
16. Sahoo, R.; Sahoo, P.; Mohanta, M.; Jena, P.; Matte, H. S. S.: "Solution Processing of Spinel Nickel Cobaltite: Exfoliation Mechanism, Dispersion Stability and Applications", Inorg. Chem. **63**, 7838 (2024)
17. Wang, Y., Hao, H., G. Naik, K. G., Vishnugopi, B. S., Fincher, C. D., Yan, Q., Raj, V., Celio, H.; Yang, G., Fang, H., Chiang, Y-M., Perras, F. A., Jena, P., Watt, J., Mukherjee, P. P., Mitlin, D.: "Mechanical Milling - induced Microstructure Changes in Argyrodite LPSCl Solid-State Electrolyte Critically Affect Electrochemical Stability", Adv. Energy. Mat. 2304530 (2024); doi.org/10.1002/aenm.202304530
18. Hou, C.; Shen, Y.; Wang, Q.; Yoshikawa, A.; Kawazoe, Y.; and Jena, P.: "In-plane sliding ferroelectricity realized in penta-$PdSe_2$/penta-$PtSe_2$ van der Waals heterostructure", ACS Nano **18**, 16923-16933 (2024)
19. Mohanta, M., Jena, P.: "Magnetism of otherwise nonmagnetic Elements: From clusters to Mono-layers", J. Phys. Chem. C **128**, 12286-12295 (2024)
20. Kilic, M. E.; Jena, P.: "Catalytic Potential of Supported Superatoms", Small **20**, 2403888 (2024)
21. Long, Z-C.; Shah, A.; Banjade, H.; Liu, K-W.; Xu, H-G.; Zheng, W.; Jena, P.: "Observation of halogen-like behavior of gold in fluorinated bimetallic $CoAuF_{1-2}^-$ and $CuAuF_{1-2}^-$ clusters: Anion photoelectron spectroscopy and density functional theory", J. Chem. Phys. **161**, 124304 (2024)
22. Basumatary, P.; Konwar, D.; Kim, S. H.; Kilic, M. E.; Jena, P.; Han, B.; Yoon, Y. S.: "Design of high-capacity composite anode for next generation lithium-ion batteries", Chem. Eng. Journal **502**, 157941(2024)
23. Hussain, S. J.; Liu, J.; Du, P-H.; Sun, Q.; Jena, P.: "Ductile $Na_3La_5Br_{18}$ as a promising solid-state electrolyte with fast Na^+ conduction and high electrochemical and interfacial stability", ACS Materials Letters 7, 761-769 (2025)
24. Fang, H., M., Therrien, J., Jena. P.: "Metallic and Ferromagnetic Carbon Allotrope discovered using Molecular Precursors", Phys. Rev. Research **7**, 013048 (2025)
25. Kilic, M. E.; Jena, P.: "Single-atom vs Single-superatom as Catalysts for Ammonia Production", Chem. Commun. **61**, 3127 – 3130 (2025)
26. Kilic, M. E.; Jena, P.: "Superatoms as Superior Catalysts: ZrO vs Pd", Small 2409289 (2025) DOI: 10.1002/smll.202409289
27. Sun, W., Wang, Q., Jena, P.: "A new 3D metallic, ductile, and porous boron nitride as a promising anode material for sodium-ion battery", Phys. Chem. Chem. Phys. **27**, 2444–2452 (2025)
28. Mohanta, M.; Jena, P.: "Anomalous spin texture representation in quantum materials: Insights from density functional theory and analytical models", Phys. Rev. B 111 (4), 045140 (2025)

29. Sahoo, R.; Mohanta, M.; Tamudia, D.; Jena, P.; Matte, H. S. S.: "Nickel Silicate Hydroxides embedded in Expanded Graphite as a Stable and Fast-charging Anode for the Next-generation Li-ion Batteries", ACS Applied Materials and Interfaces **17**,14157−14167 (2025)
30. Du, P-H., Wang, Q., Sun, Q., Jena, P.: "Thermal Rectification of Sierpiński Tetrahedron Fractals Assembled from Super-tetrahedral T_2-type Tin Selenide Clusters", Phys. Rev. B Letters **111**, L121406 (2025)
31. Mohanta, M.; Jena, P.: "Activation and electrochemical reduction of carbon dioxide by transition metal atom-doped copper clusters", Nanoscale **17**, 8505 – 8514, DOI: 10.1039/d4nr03795b
32. Vishwanathan, S.; Mohanta, M. K.; Jena, P.; H. Matte, S. S. R.: "Experimental and theoretical insights on interface engineered FeS/rGO as anode for fast-charging lithium and sodium-ion batteries", Small 2410482 (2025)
33. Li, X.; Wu, X.; Dilley, N.; Gholipour-Ranjbar, H.; Fang, H.; Jena, P.; Laskin, J.: "Discovery of a Ferromagnetic Nickel Chalcogenide Nanocluster $Ni_3S_3H(PEt_3)_5$", Small (in press)
34. Fang, H.; Sun, Q.; Jena, P.: "Chemistry of Superatoms and their Applications", Nature Reviews Chemistry (submitted)
35. Cheng, J., Du, P., Sun, Q., Jena, P.: "Densely-Packed Hydrogen in Superhalogen-Based Porous $Mg(XH_4)_2$ (X = B, Al) simulated by combining Machine Learning Potential with Hybrid Grand Canonical Monte Carlo and Molecular Dynamics", Phys. Rev. Lett. (submitted)
36. Zhang, C.; Chen, Y.; Wang, Q.; Jena, P.: "Boson-peak-like anomaly in twisted penta-$PdSe_2$ bilayer", Nano Letters (submitted)
37. Konwar, D.; Kilic, M. E.; Basumatary, P.; Ramchiary, A.; Jena, P.; Yoon, Y. S.: "Bi-doped PtZnP nanoflower anchored on N–rGO support as a bifunctional electrocatalyst for enhanced hydrogen evolution and ethanol oxidation reaction", Adv. Mat. (submitted)
38. Alam, M. K., White, D., Mohanta, M. K., Baker, J., Graves, L. S., Jena, P., Arachchige, I. U.: "Facile Synthesis of Cubic $Ni_{1-x}Cr_x$ Nanoalloys and Their Composition-Dependent Electrocatalytic Activity for the Hydrogen Evolution Reaction", NanoTechnology (Submitted)
39. Raj, V.; Wang, Y.; Naik, K. G.; Feng, M.; Jain, M.; Vishnugopi, M.; Manning, A.; Schorr, N.; Salazar, M.; Heusser, A.; Deng, S.; Kalnaus, S.; Watt, J.; McBrayer, J.; Boyce, B.; Qi, Y.; Mukherjee, P.; Huang, X.; Liu, Y.; Fang, H.; Jena, P.: "Grain Boundary Zirconia-Modified Garnet Solid-State Electrolyte", Nature Mat. (Submitted)

Photon-photon chemical thermodynamics of frequency conversion processes in highly multimode systems

Mercedeh Khajavikhan, Demetrios Christodoulides, University of Southern California

Keywords: frequency conversion, chemical thermodynamics, multimode optical system

Research Scope

Harnessing optical nonlinearity for frequency generation has emerged as a cornerstone of modern photonic science, underpinning transformative technologies such as tunable frequency combs [1], atomic clocks [2], and advanced spectroscopic tools [3]. These innovations have found widespread application across key domains including optical communications, precision metrology, medical imaging, and bio-photonics. However, current studies of frequency conversion dynamics have primarily been restricted to systems with a limited number of transverse modes per frequency component, leaving a largely uncharted landscape in highly multimode nonlinear platforms.

This project seeks to explore this untapped potential by investigating frequency generation in complex multimode optical systems such as multimode fibers, nonlinear waveguide arrays, and optical cavities. These systems offer unprecedented power-handling capabilities and spatiotemporal complexity, yet their nonlinear behavior remains poorly understood and difficult to control. The central challenge lies in the inherently high-dimensional nature of these environments, where nonlinear interactions couple power across a multitude of transverse modes and nonlinear pathways, rendering traditional engineering approaches insufficient.

To address this, we propose a fundamentally new perspective: treating optical frequency conversion in multimode systems as an all-optical thermodynamic process. By framing nonlinear frequency interactions as photonic analogs of chemical reactions—governed by stoichiometry, we aim to develop a predictive and unifying framework for frequency generation in multimode settings. Our theoretical model captures all key nonlinear mechanisms, including sum-frequency generation (SFG), difference-frequency generation (DFG), and four-wave mixing (FWM), and reveals that optical entropy maximization leads naturally to Rayleigh-Jeans equilibria under general excitation conditions.

A central outcome of this work is the derivation of an expression linking stoichiometric coefficients to optical chemical potentials, formally analogous to the extremization of Gibbs free energy in molecular systems. This framework not only enables us to predict the equilibrium distribution of power among modes and frequencies, but also to identify optimal regimes for efficient frequency conversion. Notably, we uncover a novel regime of Rayleigh-Jeans thermalization at near-zero optical temperatures, which promotes irreversible, entropy-driven funneling of optical power into the desired output frequency and mode—a feature highly desirable for high-power applications such as parametric oscillators and frequency comb generators.

By providing a general strategy for understanding and controlling nonlinear dynamics in systems with hundreds or thousands of coupled modes, this project lays the foundation for a new generation of multimode photonic devices. The proposed research has the potential to unlock transformative capabilities in optical frequency conversion, expanding the reach of nonlinear optics into new regimes of power, scalability, and functional complexity.

Recent Progress

Through our analysis, we have found that optical frequency generation in multimode systems can be fundamentally viewed as a thermodynamic process, where interactions among frequency components behave as optical analogs of chemical reactions. To investigate this, we examined an exemplary frequency conversion process within a highly multimoded optical system, using a stoichiometric framework. Specifically, we considered a general four-frequency interaction represented as: $\nu_1\omega_1 + \nu_2\omega_2 \rightleftharpoons \nu_3\omega_3 + \nu_4\omega_4$, where ω_1 and ω_2 act as optical "reactants," ω_3 and ω_4 as "products," and the integer coefficients ν_k are determined by the constraints of energy conservation. This stoichiometric representation captures a wide spectrum of nonlinear frequency generation phenomena, including second-harmonic generation (SHG), sum- and difference-frequency generation (SFG/DFG), and four-wave mixing (FWM). In such systems, optical nonlinearities mediate power exchange among hundreds or even thousands of transverse modes, corresponding to multiple frequency components. This complexity makes it exceedingly difficult to predict or engineer how power is distributed among different frequency species.

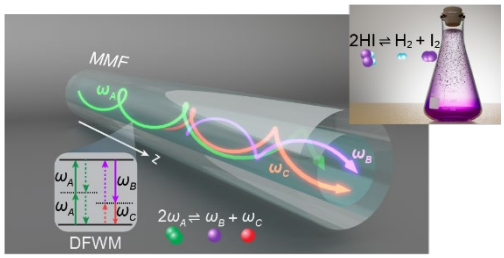

Fig. 1| Schematic of a degenerate four wave-mixing process $2\omega_A \rightleftharpoons \omega_B + \omega_C$, in a $\chi^{(3)}$ graded-index (GRIN) multimode silica fiber. Here, the stoichiometry is analogous to the reversible reaction of hydrogen iodide $2HI \rightleftharpoons H_2 + I_2$.

To address this challenge, we developed a thermodynamic framework [4] that describes the distribution of power among spatiotemporal modes when the equilibrium is attained. Our key result shows that, under thermalization, the average power $\langle J_{k,i} \rangle$ in a transverse mode i at frequency ω_k, with propagation constant $\epsilon_{k,i}$, follows a Rayleigh-Jeans (RJ) distribution: $\langle J_{k,i} \rangle = -T/(\epsilon_{k,i} + \mu_k)$, where T is a global optical temperature shared across the system, and μ_k is the optical chemical potential unique to each frequency component. Importantly, we have rigorously proved that the chemical potentials pertaining to each frequency, are related through: $\nu_1\mu_1 + \nu_2\mu_2 = \nu_3\mu_3 + \nu_4\mu_4$. In this context, the equilibrium conditions for this utterly complex multimode, multi-frequency conversion process have been established: each frequency component attains its own Rayleigh-Jeans distribution, characterized by a global optical temperature but distinct chemical potentials. Meanwhile, the chemical potentials are balanced through the stoichiometric coefficients ν_{1-4}.

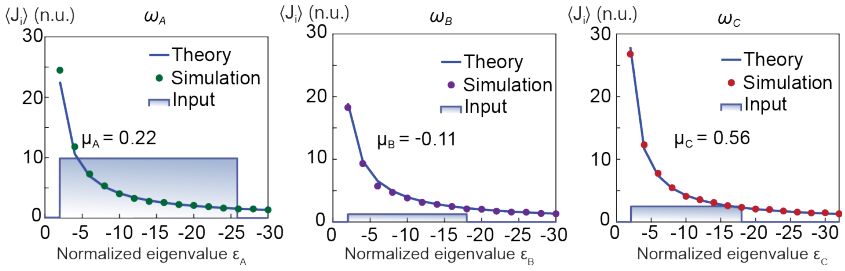

Fig. 2| The ensemble-averaged transverse modal occupancies $\langle J_i \rangle$ at thermal equilibrium for the three frequency components interacting via degenerate four-wave mixing in a GRIN fiber.

To corroborate our theoretical analysis, we investigated a degenerate four-wave mixing process unfolding in a weakly guiding, $\chi^{(3)}$ nonlinear silica multimode fiber, as illustrated in Fig. 1. This frequency conversion process, described by $2\omega_A \rightleftharpoons \omega_B + \omega_C$, is conceptually analogous to the reversible decomposition of hydrogen iodide: $2\mathrm{HI} \rightleftharpoons \mathrm{H_2} + \mathrm{I_2}$, which is characterized by the

stoichiometric coefficients $\nu_1 = 2, \nu_2 = 0, \nu_3 = \nu_4 = 1$. According to our theory, the chemical potentials of the interacting frequency components must satisfy the condition $2\mu_A = \mu_B + \mu_C$. In our example, the wave-mixing process involves three wavelengths, $\lambda_A = 1272$ nm , $\lambda_B = 1306$ nm and $\lambda_C = 1240$ nm, with the fiber supporting a total number of $M_A = 120$, $M_B = 120$ and $M_C = 136$ guided transverse modes at each respective wavelength. The fiber is excited at all three wavelengths with powers $P_A = 800$ kW, $P_B = 50$ kW, $P_C = 100$ kW and the total initial internal energy $U = 1.532 \times 10^4$. Our theory predicts that, at chemical equilibrium, the resulting Rayleigh–Jeans distributions are characterized by the following intensive parameters: $T = 40.1, \mu_A = 0.22, \mu_B = -0.11$ and $\mu_C = 0.56$. To monitor the thermalization dynamics of light in this multimode fiber, we numerically simulated the nonlinear evolution of all supported modes under continuous-wave (CW) or broad pulse conditions. The results, shown in Fig. 2, reveal that the average modal power occupancies settle to Rayleigh–Jeans distributions after approximately 3 meters of propagation, in excellent agreement with our theoretical predictions.

The theory presented herein not only can decipher the complex dynamic behavior of multimode multifrequency photonic systems but also offers a framework for optimizing frequency conversion efficiency. To demonstrate this capability, we investigated second-harmonic generation (SHG), i.e., $2\omega_A \rightleftharpoons \omega_B$ in a $LiNbO_3$ lattice comprising $M = 30$ sites, where ω_A and ω_B represent the frequencies of the fundamental wave (FW) and second-harmonic wave (SH), respectively. The linear eigenvalues for these two frequency components are given by $\epsilon_{A,i} = 2\kappa_A \cos[\pi i/(M+1)]$ and $\epsilon_{B,i} = 2\kappa_B \cos[\pi i/(M+1)] + \Delta$, where $\Delta = 2\beta_A - \beta_B$ is a phase mismatch and $\kappa_A = \kappa_B = 1$. Figure 3a illustrates the conversion efficiency of the SHG process as a function of the input energy U—determined by the initial power distribution among the FW transverse modes—and the phase mismatch Δ. Remarkably, an abrupt transition from 0% to 100% conversion efficiency occurs at $\Delta = 2.1$, marked by the green dot in Fig. 3a. This point corresponds to a near-zero optical temperature state, enabling complete power transfer from the FW to the ground state of the SH. To numerically validate the theoretical predictions of Fig. 3a, we simulate the SHG process at $\Delta = 2.1$ by exciting equally the first two modes of the FW with total normalized power of $P = 1.5$ (the corresponding actual power in LiNbO3 is 12 W). Figure 3b displays the modal occupancies of both the FW and the SH, at the input and after reaching thermal equilibrium at the output. As shown, the two species relax to the theoretically predicted RJ equilibria, with $T = 0.0018$ and $\mu = -2.046$, while the majority of the initial FW power is transferred to the SH ground state, yielding a conversion efficiency of 91%. Finally, Fig. 3c illustrates the evolution of power along the

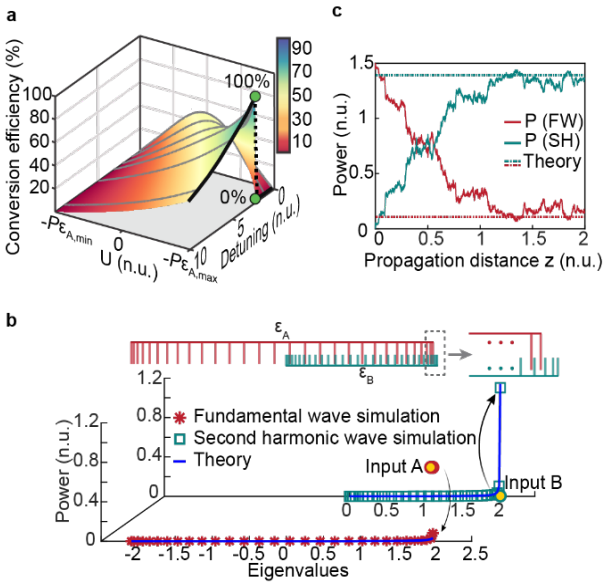

Fig. 3| a) Theoretically obtained conversion efficiency as a function of input energy *U* and phase mismatch *Δ* for a LiNbO3 lattice involving 30 elements. **b)** Numerically simulated equilibrium power distributions at the maximum conversion efficiency point, marked by the green dot in panel b). **c)** Optical power evolution as obtained from numerical simulations.

propagation distance, clearly indicating that in this multimode regime, the energy transfer process is effectively irreversible.

Future Plans

Building on our current framework, which models optical frequency generation in multimode systems under a microcanonical ensemble, our future research will extend this investigation to the canonical ensemble—where the optical system is coupled to a thermal reservoir at a fixed temperature. This shift will enable us to explore whether these all-optical processes can be described using broader thermodynamic variables, such as enthalpy and Gibbs free energy, and to examine the applicability of classical thermodynamic principles—such as Le Chatelier's principle—in nonlinear optical systems [5]. Additionally, we aim to investigate the feasibility of defining and observing optical analogs of exothermic and endothermic frequency conversion processes. Such behavior could be enabled through the controlled injection or extraction of optical "heat" from the thermal reservoir, offering a novel means of managing energy flow in nonlinear multimode platforms.

References

1. D. J. Jones, S. A. Diddams, J. K. Ranka, A. Stentz, R. S. Windeler, J. L. Hall, and S. T. Cundiff, *Carrier-Envelope Phase Control of Femtosecond Mode-Locked Lasers and Direct Optical Frequency Synthesis,* Science **288**, 635-639 (2000).

2. Y. Jun, H. Schnatz, and L. W. Hollberg, *Optical frequency combs: from frequency metrology to optical phase control,* IEEE Journal of Selected Topics in Quantum Electronics **9**, 1041-1058 (2003).

3. P. Guyot-Sionnest, J. H. Hunt, and Y. R. Shen, *Sum-frequency vibrational spectroscopy of a Langmuir film: Study of molecular orientation of a two-dimensional system,* Physical Review Letter **59**, 1597-1600 (1987).

4. F. O. Wu, A. U. Hassan, and D. N. Christodoulides, *Thermodynamic theory of highly multimoded nonlinear optical systems,* Nature Photonics **13**, 776-782 (2019).

5. P. Atkins and J. De Paula, *Physical chemistry* (Macmillan, 2006), Vol. 1.

Publications

1. H. Ren, G. G. Pyrialakos, Q. Zhong, F. O. Wu, M. Khajavikhan, D. N. Christodoulides, "*Photon-photon chemical thermodynamics of frequency conversion processes in highly multimode systems,*" to appear on Light: Science & Applications (2025).

Universal Funneling of Light via Optical Thermodynamics

Mercedeh Khajavikhan, Demetrios Christodoulides, University of Southern California

Keywords: Optical Thermodynamics, Nonlinear optics

Research Scope

This project investigates a novel light-routing mechanism in a judiciously designed nonlinear array, where light launched from any input port universally funnels toward a designated output location. We conceptualize this phenomenon as an all-optical thermodynamic effect, wherein light undergoes a Joule-Thomson-like cooling process followed by thermalization into a tightly localized ground state—a response entirely unattainable in linear conservative systems. The underlying mechanism arises from the engineered lattice potential and the interplay between kinetic and nonlinear Hamiltonian components. This effect is experimentally verified in a time-synthetic fiber-loop platform, where light is faithfully directed toward the center of the lattice by cooling to near-zero optical temperatures and ultimately condensing into a localized ground state. This universal funneling behavior opens new avenues in optical multiplexing, beam steering, and high-power photonic applications, while laying the groundwork for broader implementation of thermodynamic principles in nonlinear optics.

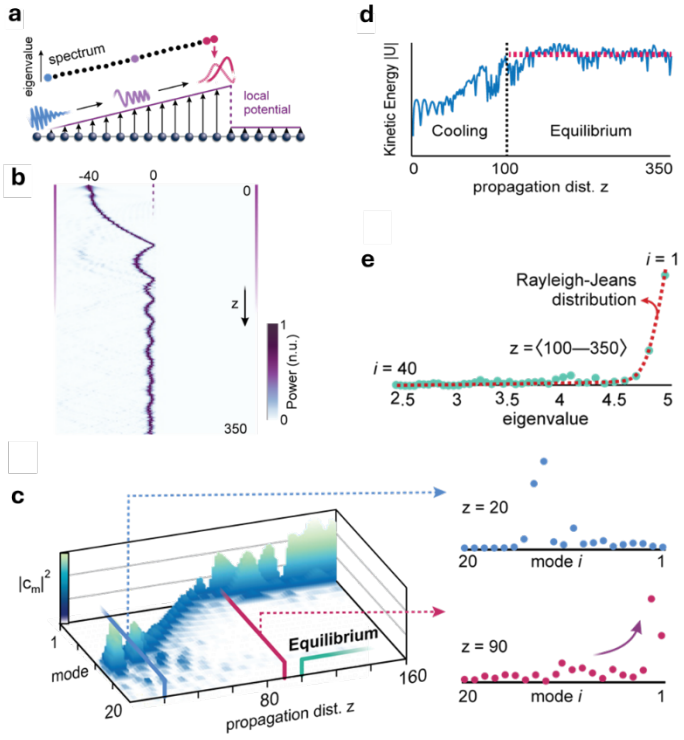

Fig. 4| Analysis of a funneling waveguide array system. **a**) Photonic lattice with lowest-order modes (red) localized at the peak of its weakly triangular potential. **b**) Funneling on an appropriately tuned lattice potential (slope $\delta\Delta = 0.02$ and peak site at 0) from an excitation at the port -40. **c**) Evolution of the corresponding modal amplitudes, indicating that the wave packet undergoes optical cooling, progressively carrying power towards the lower-order modes. **d**) During this process the kinetic energy drops while **e**) a Rayleigh-Jeans distribution manifests at equilibrium.

Recent Progress

Over the past year, this project has made significant advances in understanding and demonstrating a fundamentally new nonlinear light-routing mechanism rooted in optical thermodynamics [1]. Specifically, we have realized and experimentally validated a universal optical funneling process in which light, regardless of its injection site, channels toward a highly localized ground state. This effect, achieved in a nonlinear conservative environment, represents a new paradigm in manipulating

multimode nonlinear light dynamics, departing radically from what is possible in linear or non-Hermitian settings.

The key theoretical insight of this work lies in applying optical thermodynamic principles to an array engineered such that the lowest-order modes are strongly localized on one side, while higher-order (bulk) modes remain extended across the lattice. This configuration is realized by progressively varying the detuning between adjacent sites at a constant rate $\delta\Delta$ (where $\delta\Delta = \Delta_n - \Delta_{n-1}$), resulting in a truncated triangular potential within the 1D structure (Fig. 1a). Our strategy for enabling light funneling (Fig. 1b) focuses on identifying a nonlinear parametric regime that supports irreversible power transfer from higher-order modes into the lowest-order states, effectively climbing the potential ladder. Initially, light injected into the lattice occupies several higher-order modes with a high peak amplitude, characterized by a large nonlinear energy component H_{NL}. As the light propagates along z, it gradually loses energy due to Peierls–Nabarro effects. This gradual reduction in peak amplitude leads to a decrease in H_{NL} and a proportional increase in $|U|$ (Fig. 1d), similar to what is observed during an optical Joule-Thomson expansion [2, 3]. As a result, this nonlinear process facilitates the transfer of power into the lowest-order modes (Fig. 1c), which are spatially weighted toward the right side of the array, driving light closer to the potential peak. Upon reaching the triangular barrier, the abrupt collision triggers multiple reflections that cause the beam to disintegrate into a low-temperature "gas-like" state, where the Hamiltonian energy is almost entirely converted into kinetic energy U, which then remains approximately conserved. Beyond this point, the photon gas enters a second, weakly nonlinear phase, eventually reaching thermal equilibrium, as indicated by the emergence of a Rayleigh–Jeans (RJ) distribution (Fig. 1e), and ultimately concentrating it into the ground with near-zero optical temperature.

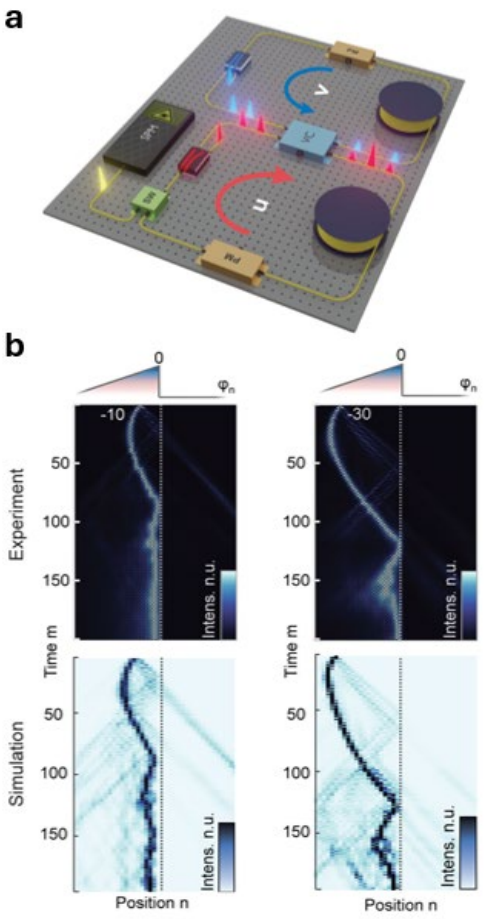

Fig. 5| Experimental demonstration of funneling. **a**) Time-syntehtic mesh lattice system schematic. Nonlinear optical fiber loops are connected by a variable coupler (VC), each containing a phase modulator (PM) to control the lattice potential. A single pulse is injected from a seed pulse module (SPM) into the shorter via an optical switch (SW). The pulses are perpetually monitored by photodetectors. **b**) Comparison of experimental and simulation data during funneling. Injection (at a pulse power of 160 mW) at sites -10 and -30 both result in acceleration towards and eventual trapping within the center of the lattice.

To experimentally demonstrate this mechanism, we built a nonlinear fiber-loop platform (Fig. 2a), which allows one to observe light evolution in discrete time. The setup comprises two unequal-length dispersion-compensating fiber loops coupled via a variable coupler, supporting appreciable Kerr nonlinearity. By incorporating phase modulators in each loop, we realize a triangular on-site phase profile, enabling precise control over the lattice potential. Figure 2b illustrates the experimentally observed light evolution in a triangular potential lattice when a signal is injected at various positions (e.g., $n = -10, -30$). As can be seen, the experimental observations closely align with simulations. When light is injected farther from the center, it preferentially excites higher-order modes that extend toward the edges of the lattice, leading to a slightly slower optical

cooling process. Nevertheless, in all scenarios, the system reliably directs light toward the center of the lattice as expected from a universal router.

Together, these advances represent a pivotal step toward the thermodynamic engineering of light, where macroscopic statistical principles govern and enable new regimes of optical control. This work opens the door to applications in all-optical multiplexing, beam steering, nonlinear beam shaping and power-scalable photonic systems while also offering a rigorous framework for further exploration of non-equilibrium dynamics in multimode nonlinear systems.

Future Plans

Preliminary simulations by our group indicate that the funneling process may be extended into higher-dimensional lattices. While this is expected according to the observation of the Joule-Thomson in a two-dimensional waveguide array, the design requirements of the lattice potential pose a crucial technical challenge in higher-dimensional funneling. Of paramount importance is the implementation of our methodology in the compact and versatile environment of on-chip, one-dimensional waveguide arrays. Harnessing the intrinsically high material nonlinearity of ubiquitous cubic crystalline materials and the effective increase in nonlinearity provided by high-contrast confinement is anticipated to result in a centimeter-long funnel.

References

1. F.O. Wu, A.U. Hassan, D.N. Christodoulides, *Thermodynamic theory of highly multimoded nonlinear optical systems*, Nature Photonics **13** (11), 776–782 (2019).
2. M.S. Kirsch, G.G. Pyrialakos, R. Altenkirch, et al., *Observation of Joule–Thomson photon-gas expansion*, Nature Physics **21**, 1–7 (2025).
3. G.G. Pyrialakos, M. Khajavikhan, and D.N. Christodoulides, *Fundamental mode excitation via Joule–Thomson light expansion in nonlinear optical lattices*, Optics Letters **50** (4), 1349-1352 (2025).

Publications

1. H.M. Dinani, G.G. Pyrialakos, A.M. Berman Bradley, et al., *Universal Routing of Light via Optical Thermodynamics*, submitted to Nature Photonics (2025).
2. H.M. Dinani, G.G. Pyrialakos, A.M. Berman Bradley, et al., *Thermodynamic Light Funneling in Time-Synthetic Photonic Lattices*, accepted for publication in CLEO (2025).

Observation of Joule–Thomson photon-gas expansion

Mercedeh Khajavikhan, Demetrios Christodoulides, University of Southern California

Keywords: Joule-Thomson effect, optical thermodynamics, multimode optics

Research Scope

The recent development of an optical thermodynamic framework has enabled systematic exploration of the complex collective dynamics of multimode nonlinear systems [1]. These developments are positioned to help address several outstanding problems in optics, including the prospect of funneling the light in a multimode system into its ground state. In this thrust, we demonstrate an all-optical Joule–Thomson expansion process mediated by photon–photon interactions whereby the temperature of the optical gas suddenly drops near zero. Our experiments in various configurations of coupled multicore nonlinear waveguide arrangements illustrate how light undergoing expansion-induced cooling can be channeled from arbitrary input states into the fundamental mode with high efficiency. We show that the stability of the post-expansion state is ensured by power and energy conversion and the irreversibility endowed by extremizing the optical entropy.

Within the framework of optical thermodynamics, one of the key quantities describing the state of a photon gas is its optical temperature T. Along with its corresponding chemical potential μ, it dictates how the power or energy is statistically distributed among modes under conditions which maximize the entropy of a system [2,3]. In waveguiding arrangements, the optical temperature inherently characterizes the quality of a beam in the absence of statistical correlations between the modal phases at thermal equilibrium. High optical temperatures indicate that the beam comprises many modes, adversely affecting its coherence properties [4]. On the other hand, low temperatures correspond to a condensation of power into the ground state. In this regime, nonlinear mode mixing effects are substantially reduced, analogous to a zero-temperature gas whose molecules remain almost motionless. Clearly, the prospect of optical “cooling” to significantly enhance the spatial coherence of a beam remains of paramount importance.

In a yet separate vein, a methodology for transforming a beam injected at an arbitrary input channel of a multimoded structure into a coherent, high-quality beam does not yet exist. Under linear conditions, power injected in a single port decomposes into the many, low-quality modes of the structure, while traditional methods of analyzing the nonlinear regime do not render a design methodology. This research thrust successfully employs a thermodynamic approach to overcome the limitations of the linear process, employing the aforementioned optical analog of the Joule-Thomson effect to collapse an optical gas into a zero-temperature state, exhibiting high beam quality owing to predominant occupation of the fundamental mode.

Recent Progress

Our work experimentally demonstrates a Joule-Thomson (JT) expansion process by means of which the optical temperature of the photon gas can abruptly drop very close to zero (Fig. 1a,b). This effect is mediated by purely photon-photon interactions and is a direct byproduct of nonlinearity. We show that, unlike what happens during a sudden expansion of a dense non-ideal molecular gas (Fig. 1a), here, cooling is induced by transforming the nonlinear interaction energy of the photon gas into the kinetic component of its ground state. However, in both physical contexts, the end result is the same: a system initiated in an optically "hot" state (Fig. 1d) can experience a sudden drop in temperature, transitioning into a much "colder" state (Fig. 1e) where mostly the fundamental mode is populated, through a controlled process of energy conversion (Fig. 1c).

Figure 1b illustrates a photonic JT expansion in a nonlinear multicore array. This process involves two distinct nonlinear optical lattices, where the smaller one (which may involve as few as one site) serves as a "throttle" to constrict the influx of light into a much larger optical system comprising M cores, supporting an equal number of supermodes.

Within a thermodynamic framework, a photon-gas description of light emerges when considering the two invariants of motion associated with equation (1) in such conservative systems. These correspond to the optical power $P = \sum_{j=1}^{M} |a_j|^2 = \sum_{n=1}^{M} |c_n|^2$ conveyed in the lattice, where a_j and c_n denote the field and modal occupancy of sites j and mode n respectively, and its total Hamiltonian $H_{\mathrm{tot}} = -U + H_{\mathrm{NL}}$, where $U = -\sum_{n=1}^{M} \varepsilon_n |c_n|^2$ and $H_{\mathrm{NL}} = \frac{1}{2}\sum_{j=1}^{M} |a_j|^4$ are associated with the 'kinetic' and 'potential' energy components respectively. Provided nonlinearity is weak, the total Hamiltonian will be dominated by the kinetic component U, as one would expect for an ideal photon gas. In this regime, the optical temperature associated with thermal equilibrium is fixed by initial conditions on the modal occupancies. Therefore, the process of cooling must be done out of equilibrium with the ideal-gas conditions violated. In this vein, cooling is expected to take place under a controlled exchange of energy between U and H_{NL}, where an ultra-low temperature may be achieved when U reaches the minimum accessible value given the conservation laws of the system, namely $U_{\min} = -\varepsilon_M P$.

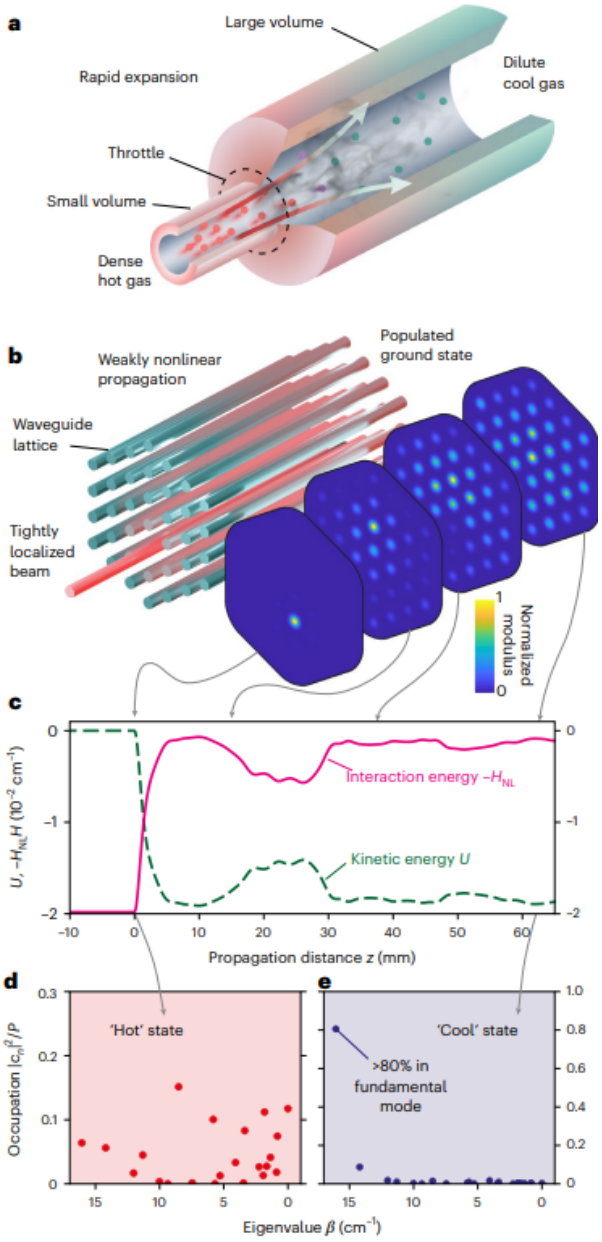

Fig. 1| Optical Joule-Thomson effects. **a)** Dense gas rapidly cooling during expansion into a larger volume. **b)** Analogous expansion of a photon gas into the fundamental mode of a waveguide array. **c)** Energy exchange between linear (kinetic) and nonlinear (interaction) components of the total optical energy. **d)** The "hot" initial state decomposes into all modes, while the "cool" final state is dominated by the fundamental mode.

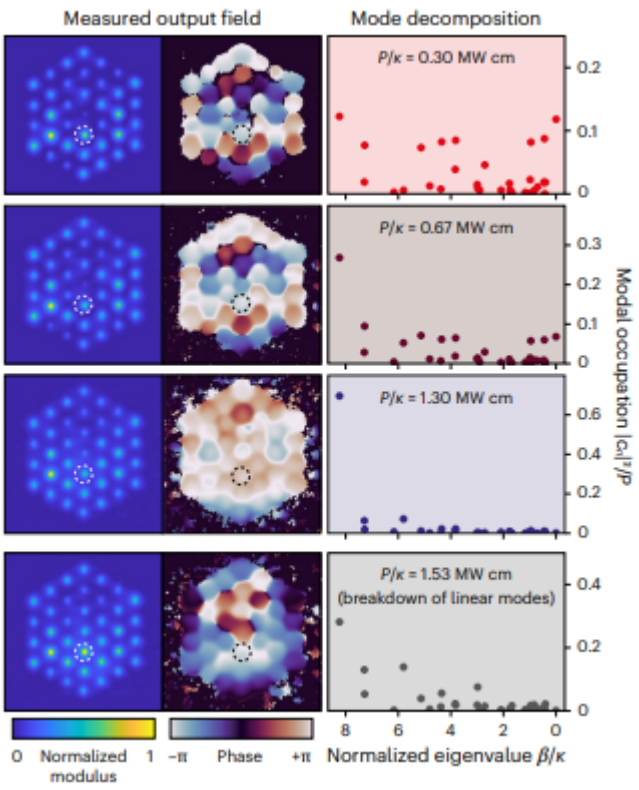

Fig. 2| Joule-Thomson expansion in a triangular lattice. Amplitude and phase profiles (left) and corresponding modal content (right) observed at the output facet of the multicore lattice for different normalized excitation powers. Despite a fixed placement of the initial excitation (indicated by dashed circles), the initially broad population of most lattice modes gradually cools down until approximately 70% of light is channeled into the fundamental mode.

Let i denote the initial excitation plane, at which point the lattice supports a single site, and f denote an equilibrium plane in the expanded lattice. The potential energy before expansion will be $H_{\mathrm{NL},i} = \frac{1}{2}P^2$, which assumes that the pre-expansion kinetic component is $U_i = 0$. After expansion, the potential energy will rapidly drop close to its minimum value, given by $H_{\mathrm{NL},f} \approx \frac{1}{2}\sum_{j=1}^{M}|a_j|^4 = \frac{1}{2}\sum_{j=1}^{M}|P/M|^2 = \frac{P^2}{2M}$, indicating an almost uniform distribution of power among all lattice sites. For sufficiently large lattices ($M \gg 1$), this post-expansion potential energy becomes negligible, transferring entirely to the kinetic component through $U_f \approx -H_{\mathrm{NL},i} = -\frac{1}{2}P^2$. By equating this expression for the post-expansion kinetic energy with its minimum accessible value, we find that a power level of $P = 2\varepsilon_M$ results in complete transfer of power into the fundamental mode, regardless of the underlying lattice properties.

The predictions outlined above have been confirmed experimentally in a range of laser-inscribed photonic lattice configurations in fused silica [5]. Figure 2 depicts the first representative example of our experimental observations in a finite hexagonal domain involving $M = 37$ sites (or supermodes), built on a triangular unit cell with a nearest-neighbour coupling coefficient of $\kappa = 0.3\ \mathrm{cm}^{-1}$. Light was injected into the lattice by means of a single waveguide port, to produce a point-like excitation that simultaneously populated virtually all supermodes. A closer look at the output distributions provides valuable insights into the mechanisms at play. At low power levels, the quasilinear diffraction pattern of the single-site input (obtained at a normalized power of $P/\kappa = 0.30\ \mathrm{MW \cdot cm}$) displays a complex phase pattern with numerous sign flips between adjacent sites (top row of Fig. 2). In this regime, the expansion process has a negligible impact on the photon gas, as illustrated in the red shaded panel of Fig. 2 where the lattice supermodes retain a random-like distribution. As power increases (second row of Fig. 2), the first indications of optical cooling emerge, with optical power progressively moving towards lower-order modes. A further increase in the injected power (third row of Fig. 2) results in a more homogenized light distribution across the waveguide array in both phase and amplitude. At this particular power level ($P/\kappa = 1.3\ \mathrm{MW \cdot cm}$), the output distribution approximately conforms with the smooth amplitude envelope and the flat phase of the ground state, which indicates that the power now almost exclusively resides in the fundamental mode. From experimental data and from our theoretical analysis, we estimate that, post-expansion, the photon gas in the larger array will eventually relax at thermal equilibrium to an RJ distribution with an optical temperature $T = 0.11\ \mathrm{m}^{-1}$ and a chemical potential $\mu = -156\ \mathrm{m}^{-1}$. Beyond the JT limit, as the power increases, we experimentally observed that the

photon-gas model suddenly breaks down and the projection of the reconstructed field distribution onto the linear modes of the system becomes increasingly unreliable (last row of Fig. 2).

Future Plans

While conservation of energy and extremization of entropy guarantee the Joule-Thomson cooling process, the expansion dynamics and a precise description of the breakdown conditions are yet to be determined. To tackle this issue, the optical thermodynamic formalism must be modified to account for strong nonlinear interactions in the photon gas, akin to the methods developed for configurational partition functions in a nonideal classical gas.

References

1. F. O. Wu, A. U. Hassan, and D. N. Christodoulides, *Thermodynamic theory of highly multimoded nonlinear optical systems*, Nature Photonics **13**, 776–782 (2019).
2. K.G. Makris, F.O. Wu, P.S. Jung, and D.N. Christodoulides, *Statistical mechanics of weakly nonlinear optical multimode gases*, Optics Letters **45**, 1651–1654 (2020).
3. P. Aschieri, J. Garnier, C. Michel, V. Doya, and A. Picozzi, *Condensation and thermalization of classsical optical waves in a waveguide*, Phys. Rev. A **83**, 033838 (2011).
4. M.A. Selim, F.O. Wu, G.G. Pyrialakos, M. Khajavikhan, and D.N. Christodoulides, *Coherence propertiesof light in highly multimoded nonlinear parabolic fibers under optical equilibrium conditions*, Optics Letters **48**, 1208–211 (2023).
5. A. Szameit and S. Nolte, *Discrete optics in femtosecond-laser-written photonic structures*, J. Phys. B: Mol. Opt. Phys. **43**, 163001 (2010).

Publications

1. G.G. Pyrialakos, M. Khajavikhan, and D.N. Christodoulides, *Fundamental mode excitation via Joule–Thomson light expansion in nonlinear optical lattices*, Optics Letters **50**, 1349-1352 (2025).
2. M.S. Kirsch, G.G. Pyrialakos, R. Altenkirch, et al., *Observation of Joule–Thomson photon-gas expansion*, Nature Physics **21**, 214–220 (2025).

Metamaterials

Thomas Koschny, Jigang Wang
Ames National Laboratory, Iowa State University, Ames, Iowa

Keywords: Broadband metamaterial, Multi-resonant metasurfaces, Dark-state surface lasers

Research Scope

Metamaterials are artificial materials that enable the realization of novel optical properties unattainable in nature. This project explores the fundamental theoretical understanding, analysis, development, fabrication, and experimental characterization of metamaterials, and investigates their feasibility for innovative applications. Our work targets current, fundamental problems and opportunities in controlling light with matter and matter with light: We will enhance nanoscale light-matter interactions and overcome dissipative loss by coupling to quantum gain, enabling undamping of resonances, amplification, and coherent collective radiation, to devise novel lasers and coherent dark near-field sources. We will control radiation damping, manipulate the radiative electromagnetic vacuum seen by quantum emitters in metasurfaces to obtain fundamental improvements to metasurface-based coherent THz sources and nonlinear photon energy-conversion. We will overcome the inherent bandwidth limitations in resonant metasurfaces, creating arbitrarily large phase and group delay and potentially replacing bulk optics with surfaces. We investigate optical forces at the nanoscale for control of matter with light and create coherent opto-mechanical coupling, exploiting macromolecular mechanical and electromagnetic states in novel metallized DNA-templated meta-molecules. The proposed work will expand our physical understanding of the interaction of light with both classical and quantum matter and will facilitate further development of modern metamaterials. It aligns with the 2007 BES Grand Challenge as well as the recent 2015 BESAC report on how to exploit coherence in light and matter, and leverages major theoretical and experimental expertise within the FWP and interdisciplinary collaboration between FWPs available at Ames Laboratory.

Recent Progress

Breaking the bandwidth limit with multi-resonant metasurfaces: Metasurfaces enable us to implement very generic boundary conditions for light. Broadband, multi-resonant metasurfaces can solve one of the fundamental limitations of conventional, resonant metamaterials. While resonant response is usually required to achieve strong response or negative response functions, it inherently leads to a very narrow operating bandwidth of the material. Technologically relevant signals, however, are always broadband. We have extended our theory on multi-resonant broadband metasurfaces to "beyond linear" phase modulation. We show how specific multi-resonant ultra-thin metasurfaces can enable simultaneously arbitrarily strong and broadband dispersion compensation, in transmission or reflection, pulse (de-)chirping, and compression or broadening, overcoming the fundamental trade-off between conventional, non-resonant (bulky) and modern, singly-resonant (but narrowband) metasurface approaches to quadratic phase manipulation. [1]

We further expanded the theory of broadband multiresonant metasurfaces to function as generalized spatio-temporal "meta-boundaries." This advancement facilitates the realization of theoretically arbitrary broadband (perfectly) reflective boundary conditions, enabling precise shaping of propagating mode profiles in wave-guiding applications. It also allows for the manipulation of bulk versus surface energy transport, control over spatial loss distribution, and enhanced energy localization. [2]

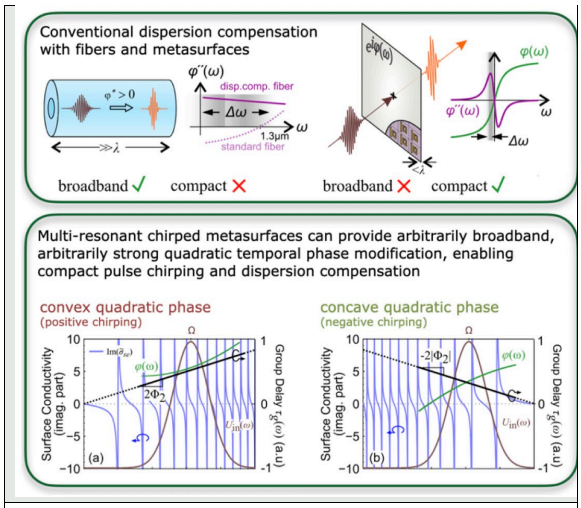

Fig. 1: Broadband, multi-resonant metasurfaces that enable "beyond linear" phase modulation. Conventional dispersion compensation is either broadband or compact. Specific multi-resonant metasurfaces can enable arbitrary broadband, low loss, quadratic dispersion compensation and chirping by an ultra-thin surface. [1]

Resonant meta-atoms from metallized DNA-templated meta-molecules: In collaboration with the Bioinspired Metamaterials FWP, we gathered experimental optical scattering data for individual metallized DNA origami meta-atoms and conducted realistic simulations to analyze their optical scattering properties. Metallized V-shaped DNA origami structures exhibited well-defined, low-loss electric and magnetic resonance modes, despite morphological imperfections arising from the stochastic nature of the self-assembled nano-resonator growth process. [3]

Chiral meta-surface lasers: We have designed and numerically demonstrated a simple, low-cost, and ultracompact chiral resonant metasurface design, which, by strong local coupling to a quantum gain medium (quantum emitters), allow to implement a "cavity-free", ultra-thin metasurface laser, capable of generating tunable circularly polarized coherent lasing output. The lasing output originates from the direct lasing action of a collective resonant eigenmode of the periodic, resonant chiral meta-atoms forming the metasurface. Each meta-atom consists of a twisted pair of metallic (plasmonic) crosses. Strong coupling to the quantum gain medium through the resonant near-field of the meta-atoms compensates the dissipative losses in the plasmonic meta-atoms, eventually causing them to oscillate coherently, i.e., driving the system into a coherent lasing state. The chiral resonators here effectively constitute a subwavelength equivalent of a "resonant cavity" for the laser, allowing for strongly enhanced light-matter interaction and subwavelength size. This approach represents a chiral analog to plasmon lasers ("Spaser"), achieving direct lasing into the resonant modes of sub-wavelength plasmonic chiral meta-atoms with circularly polarized far-field radiation. We have shown that both the geometrical twist-angle of the metallic crosses, as well as the polarization of an incident pump radiation, can be used to control the emission polarization state of the laser from linear to circular and to switch from the right- to left-circularly polarized output, thus providing dynamic lasing-polarization control. The layered, planar design is well suited for easy optical implementation. Our findings can guide further experimental efforts toward realization of polarization controllable, circularly polarized output, ultrathin surface lasers using resonant chiral metasurfaces, unlocking a wide range of photonic applications. [4]

We have also experimentally demonstrated a novel approach for contactless thermal tuning of metasurfaces using spatially addressable laser heating of dielectric Mie-resonant titanate cubes. This method provides a scalable alternative for achieving tunability and active control in metamaterials, and allows extending its applicability to THz and optical metasurfaces. [5]

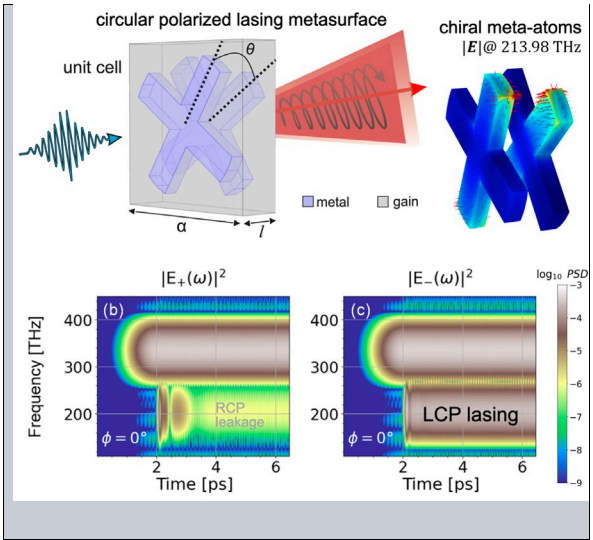

Fig. 2: Design (top) and spectrogram (bottom) of an ultra-thin, cavity-free metasurface laser controllably emitting circularly polarized light when pumped by a linearly polarized pump beam, enabling direct stimulated emission from the quantum gain into the chiral resonant plasmonic mode of tightly-coupled twisted-cross meta-atoms, which then radiate a purely circularly polarized coherent far-field. [4]

Future Plans

Deeply-subwavelength light-matter interactions at the nanoscale: Continue to develop quantitative theory for THz scattering by an AFM-tip SNOM, subject to nanoscale light-matter interactions between tip and sample surface. Accurately model the AFM tip/cantilever, the dominant source for the scattered THz signal, identify its eigenmodes, build circuit models for multi-resonant tip/cantilever assembly subject to loading via near-field coupling with sample modes and THz field above the sample; Identify the cause of the approach curves power-law discrepancy between experiments and models.

Further develop metasurface interaction with quantum gain: Dark-state lasing, and functionalized lasing using beyond-dipolar meta-atoms. Develop tunable chiral metasurface lasers & dark-state chiral metasurface lasers; Develop a rigorous analytical theory to design chiral and general bi-anisotropic resonant meta-molecules from hybridization of planar resonant electric dipoles. Design dark-state lasing-based approaches to coherent sources in unconventional vacua, e.g., surface plasmons, magnons, topological edge modes.

Spatio-temporal broadband multi-resonant metasurfaces: Develop analytical theory, numerical simulations, and practical designs for broadband multi-resonant metasurfaces that can implement general spatio-temporal "meta"-boundaries. Extend our abstract theoretical work to include technologically relevant broadband spatial dispersion and beam shaping & beyond-quadratic phase modulation for group-delay dispersion manipulation and compensation, not only achromatic (over frequency) but also spatially broadband (over wide incidence angle range). *Develop "stackable" metasurfaces* as a possible solution to current problems in practical multi-resonant metasurfaces designs, where multiple, independent resonant meta-atoms would hybridize and, therefore, disturb one another.

Theory for bio-inspired, metallized-DNA origami self-assembled meta-atoms: To enable large-scale metamaterials, improve characterization, and mitigate morphological as well as spatial and orientational disorder. Develop methods to extract optical Green's function and effective material parameters from THz-SNOM experiments on fabricated samples, specifically for DNA-templated

meta-atoms, and compare with simulation of Green's function of real morphology nano-resonators. Explore non-periodicity for mitigation of periodicity artifacts in non-asymptotic effective media. Use optical forces in metallized-DNA meta-molecules to implement opto-mechanical coupling for non-linearity (and, potentially, sensing).

References

1. O. Tsilipakos, T. Koschny, *"Multiresonant metasurfaces for arbitrarily broad bandwidth pulse chirping and dispersion compensation,"* Physical Review B **107**, 165408 (2023).

2. O. Tsilipakos, T. Koschny, *"Shaping the Profile and Dispersion of Waves Guided Between Spatiotemporally Dispersive, Electrically and Magnetically Conductive Metasurface Boundaries,"* IEEE Transactions on Antennas and Propagation **72**, 6472–6480 (2024).

3. M.M. Islam, M.M. Hossen, J. Adjasoo, P.E. Palo, L. Bendickson, N.E. Kallmyer, N.F. Reuel, M. Nilsen-Hamilton, T. Koschny, A.C. Hillier, *"Direct Measurement of Optical Resonance Modes in Gold Meta-Atoms Fabricated by Metallization of Triangle- and V-Shaped DNA Origami Templates,"* The Journal of Physical Chemistry C **127**, 24291–24302 (2023).

4. I. Katsantonis, A.C. Tasolamprou, E.N. Economou, T. Koschny, and M. Kafesaki, *"Ultrathin, Dynamically Controllable Circularly Polarized Emission Laser Enabled by Resonant Chiral Metasurfaces,"* ACS Photonics 2025, 12, 71−78 (2025).

5. L. Zhang, Q. Zhao, A. Jain, T. Koschny, *"Laser Heating of Ferroelectric Cubes for Tunable Electromagnetic Properties in Metamaterials,"* Applied Physics Letters **123**, 211703 (2023).

Publications

1. I. Katsantonis, A.C. Tasolamprou, E.N. Economou, T. Koschny, and M. Kafesaki, *"Ultrathin, Dynamically Controllable Circularly Polarized Emission Laser Enabled by Resonant Chiral Metasurfaces,"* ACS Photonics **12**, 71−78 (2025).

2. O. Tsilipakos, T. Koschny, *"Shaping the Profile and Dispersion of Waves Guided Between Spatiotemporally Dispersive, Electrically and Magnetically Conductive Metasurface Boundaries,"* IEEE Transactions on Antennas and Propagation **72**, 6472–6480 (2024).

3. S. Haeuser, R.H.J. Kim, J.-M. Park, R.K. Chang, M. Imran, T. Koschny, J. Wang, "*Analysis of Near-Field Magnetic Responses on ZrTe5 through Cryogenic Magneto-THz Nano-Imaging,"* Instruments **8**, 21 (2024).

4. R.H.J. Kim, A.K. Pathak, J.-M. Park, M. Imran, S.J. Haeuser, Z. Fei, Y. Mudryk, T. Koschny, J. Wang, *"Nano-compositional imaging of the lanthanum 2 silicide system at THz wavelengths,"* Optics Express **32**, 2356-2363 (2024).

5. L. Zhang, Q. Zhao, A. Jain, T. Koschny, *"Laser Heating of Ferroelectric Cubes for Tunable Electromagnetic Properties in Metamaterials,"* Applied Physics Letters **123**, 211703 (2023).

6. M.M. Islam, M.M. Hossen, J. Adjasoo, P.E. Palo, L. Bendickson, N.E. Kallmyer, N.F. Reuel, M. Nilsen-Hamilton, T. Koschny, A.C. Hillier, *"Direct Measurement of Optical Resonance Modes in Gold Meta-Atoms Fabricated by Metallization of Triangle- and V-Shaped DNA Origami Templates,"* The Journal of Physical Chemistry C **127**, 24291–24302 (2023).

7. O. Tsilipakos, T. Koschny, *"Multiresonant metasurfaces for arbitrarily broad bandwidth pulse chirping and dispersion compensation,"* Physical Review B **107**, 165408 (2023).

8. R.H.J. Kim, J.M. Park, S. Haeuser, C. Huang, D. Cheng, T. Koschny, J. Oh, C. Kopas, H. Cansizoglu, K. Yadavalli, J. Mutus, L. Zhou, L. Luo, M.J. Kramer, J. Wang, *"Visualizing heterogeneous dipole fields by terahertz light coupling in individual nano-junctions,"* Communications Physics **6**, 147 (2023).

9. I. Katsantonis, A.C. Tasolamprou, T. Koschny, E.N. Economou, M. Kafesaki, C. Valagiannopoulos, *"Giant enhancement of nonreciprocity in gyrotropic heterostructures,"* Scientific Reports **13**, 21986 (2023).

10. R.H.J. Kim, J.-M. Park, S.J. Haeuser, L. Luo, J. Wang, *"A sub-2 Kelvin cryogenic magneto-terahertz scattering-type scanning near-field optical microscope (cm-THz-sSNOM),"* Review of Scientific Instruments **94**, 043702 (2023).

Ion Migration and Its Impact on the Stability of Metal Halide Perovskites

Masaru Kuno and Prashant V. Kamat

Keywords: Halide Perovskites, 2D- Perovskite, ion migration, exciton, excited state

Research Scope

The research scope entails (1) understanding the photoremixing phenomenon of mixed-halide perovskites under high excitation intensities and (2) studying cation exchange at two-dimensional (2D)/three-dimensional (3D) perovskite interfaces. This research continues our earlier work to develop a microscopic model for mixed-halide perovskite photosegregation as well as ultimately linking cation exchange/migration at perovskite interfaces with light-induced anion photosegregation.

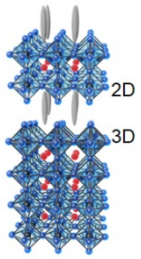

Metal Halide Perovskite

Recent Progress

(1) Improvements to the band gap thermodynamic model of mixed-halide perovskite photosegregation. We have previously developed a microscopic model for photosegregation based on local band gap differences between parent, mixed-halide materials and local iodine-rich domains. This model has successfully explained nearly all reported photosegregation behaviors (*i.e.*, terminal stoichiometry, excitation intensity dependence, existence of an excitation intensity threshold for photosegregation, temperature independent terminal stoichiometries etc…). However, the model has also been shown to be incomplete as observed through departures between measured and predicted excitation-intensity terminal stoichiometries. Departures are best seen as qualitatively different excitation intensity trends -theory showing a concave down dependence with excitation intensity while experiments show a concave up behavior.

We have now addressed this deficiency by improving the model.[3] Improvements now account for the fact that mixed-halide perovskite photosegregation produces a distribution of terminal stoichiometries. Furthermore, only the lowest *x*-value stoichiometries (*i.e.*, a very small subpopulation of I-enriched material) are monitored experimentally in photoluminescence-based photosegregation measurements. This means that theory must be modified to account for experimental biases introduced by a minority phase fraction of highly I-enriched inclusions in a parent, mixed-halide material. Carrier funneling factors to these highly I-enriched domains must also be included. Consideration of both factors has now allowed us to obtain near quantitative agreement between model-predicted terminal photosegregation stoichiometries and those recorded experimentally.

(2) Discovery of pulsed laser-induced photoremixing of mixed-halide perovskite thin films. Previously, the only reported observation of persistent halide photoremixing has been Bach's observation of the phenomenon in $MAPb(I_{1-x}Br_x)_3$ microcrystals (Mao, W., Hall, C.R., Bernardi, S. *et al*. Light-induced reversal of ion segregation in mixed-halide perovskites. Nature Mater. 20, 55-61, 2021). This has been problematic as most data on mixed-halide perovskite photoinstabilities have been acquired with thin films. We have made mixed-halide perovskite microcrystals and have found Bach's photoremixing effect to be highly hit or miss. This has prevented us from conducting a thorough investigation of photosegregation and photoremixing on the same material.

We have recently discovered that photoremixing can be induced in mixed-halide perovskite thin films when a high intensity pulsed laser is used.[2] The pulsed laser photoremixing is highly reproducible and appears general. We have observed reproducible photoremixing in $MAPb(I_{1-x}Br_x)_3$, $FACsPb(I_{1-x}Br_x)_3$, and $FAMACsPb(I_{1-x}Br_x)_3$ thin films. We have also established reproducible photosegregation and photoremixing cycling in these materials. This discovery now allows us to study both photosegregation and photoremixing in the same material and opens up the possibility to develop a more general theoretical understanding of mixed-halide perovskite photoinstabilities.

(3) Verification of cation migration across 2D/3D perovskite interfaces. Although claims have been made that introducing 2D halide perovskite layers into 3D perovskite active layers in solar cells enhances device stability and efficiency, our in-depth studies now show that these 2D/3D interfaces are unstable with regard to cation migration. Cations readily move across 2D/3D $BA_2MAPb_2I_7/MAPbI_3$ interfaces to form new phases.[4,5] Subsequent absorbance and incident photon power conversion efficiency (IPCE) measurements reveal that cation migration is a major contributor to the (eventual) decreased performance of perovskite-based solar cells. This is even when device active layers are passivated with 2D materials (**Figure 1**). Although 2D/3D perovskite devices are more stable than exclusive 3D solar cells at room temperature, cation exchange at 2D/3D interfaces detrimentally affects solar cell performance and stability. Temperature-dependent studies further show increased proclivity for cation migration rate at elevated temperatures. In this case, we find 2D/3D perovskite solar cells to perform worse than comparable 3D solar cells at higher operating temperatures.

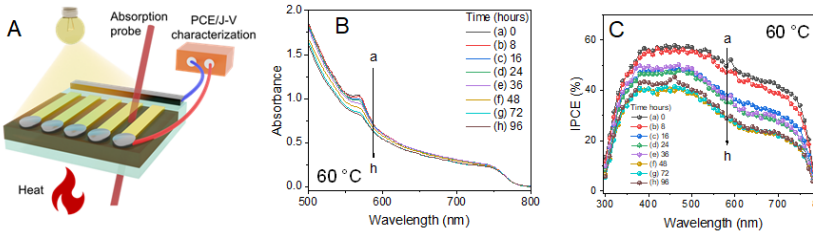

Figure 1. (A) 2D/3D Solar cell architecture allowing absorption measurements between two metal contacts, (B) Absorption spectra of a 2D/3D perovskite film in a solar cell device recorded over time while kept at 60 °C in a N_2-filled glovebox. (C) IPCE (Photoconversion efficiency) spectra of a 2D/3D solar cell recorded over time while kept at 60 °C. The changes in the absorption spectra and IPCE reflect the mixing of cations at 2D/3D interface. From Reference 4.

(4) Elucidating the interaction between migrating ions and hole transport layers. The interface between halide perovskites and corresponding hole transport layers (HTLs) in devices is critical to maintaining solar cell performance. If migrating ions (cations as well as oxidized anions) interact with HTLs, this can adversely affect device performance. We have now conducted a detailed study to characterize the oxidation states of a widely used HTL material, SpiroOMeTAD.[1] Our spectroelectrochemical experiments confirm that charges (*i.e.*, holes) from higher spiro-OMeTAD (viz $Spiro^{+/2+}$) oxidation states quickly transfer to adjacent, lower oxidation states to maintain redox equilibrium. This hole transfer cascade continues until charges are captured by collecting electrodes. Under normal solar cell operational conditions, redox equilibrium is dominated by $Spiro^{+/2+}$ species. This ability by spiro-OMeTAD to undergo multiple (reversible) oxidations while maintaining redox equilibrium makes it a unique HTL material for both solar cell and light emitting diode applications. Preliminary experiments show changes in the morphology of $MAPbI_3$ films as I_2 is expelled under photoirradiation. This is accompanied by corresponding decreases in solar cell performance (**Figure 2**). The increased absorption in the near infrared during photoirradiation confirms HTL layer oxidation. In-situ spectroscopic measurements during solar cell operation allow us to establish the impact of halide ion and cation migration in perovskite solar cells.

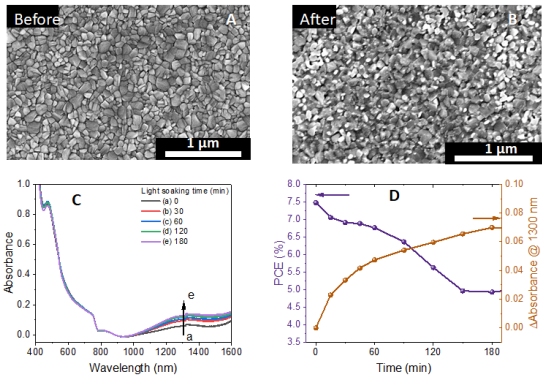

Figure 2. SEM images of $MAPbI_3$ film physically paired with spiro-MeOTAD film, (A)Before and (B) after subjecting to 3 sun (300 mW/cm^2). (C) Absorption changes of the $MAPbI_3$ based solar cell showing the oxidation of Spiro OMeTAD (increased absorption at 1300 nm). (D) Comparison of solar cell performance and SpiroOMeTAD oxidation during photoirradiation. (unpublished results)

Future Plans

We are finalizing the construction and optimization of a widefield infrared photothermal absorption microscopy/spectroscopy technique. A camera, integral to the measurement technique, was purchased using DOE funding. This mid-infrared microscopy/spectroscopy is tied to the proposed work since it will allow us to conduct chemically-specific imaging and spectroscopy of organic cations in hybrid perovskites. This will enable observation of cation migration at interfaces and also during associated anion photosegregation. Materials of interest include the archetype pure halide $MAPbI_3$ system as well as more recent, mixed-cation materials such as $FACsPbI_3$. They also include mixed-anion versions such as $MAPb(I_{1-x}Br_x)_3$ and $FACsPb(I_{1-x}Br_x)_3$.

Strategies to suppress ion migration at 2D/3D perovskite interfaces will be undertaken in two ways. The first involves carefully selecting other spacer cations and alloying with other A-site cations (like FA^+, Cs^+). Bulkier spacer cations in 2D perovskites are expected to slow down the mobility of ions under visible light irradiation. By mapping out processes responsible for ion migration it should be possible to extend the operational stability of 2D/3D perovskite solar cells. The second approach involves introducing a monolayer of carbazole derivative between 2D and 3D interfaces to block the migration of spacer cations. Use of self-assembled monolayers of such hole transport materials has proven effective at stabilizing the performance of perovskite solar cells.

We will also conduct in-situ operando measurements of perovskite solar cells to probe the impact of different cations on their photovoltaic performance. Spectroelectrochemical measurements will enable us to correlate the impact of ion migration with solar cell performance at different applied voltages. Voltage-dependent cation migration will be probed through in-situ emission/emission lifetime measurements as well as with time-resolved, transient absorption spectroscopy. The interaction of migrating ions with hole transport layers will also be probed to obtain a complete understanding of photoinduced processes that lead to perovskite solar cell instability.

References

1. G. Szabó, P. V. Kamat, *Spiro-OMeTAD: Unique redox chemistry driving the hole transport*, ACS Energy Lett. **10**, 330-336 (2025).
2. H. Okrepka, L. Franzini, S. Pagliara, M. Kuno, *Photoremixing of photosegregated formamidinium/cesium lead iodide/bromide thin films under pulsed laser excitation*, ACS Energy Lett. **9**, 5744-5746 (2024).
3. H. Okrepka, Y. Ding, S. Ghonge, A. Ruth, M. Kuno, *Excitation intensity-dependent terminal halide photosegregation stoichiometries in formamidinium/cesium lead iodide/bromide [$FACsPb(I_{1-x}Br_x)_3$] thin films*, J. Phys. Chem. Lett. **15**, 10488-10494 (2024).
4. P. Mathew, J. Cho, P. V. Kamat, *Ramifications of ion migration in 2D lead halide perovskites*, ACS Energy Lett. **9**, 1103-1114 (2024).
5. G. Szabó, P. V. Kamat, *How cation migration across a 2D/3D interface dictates perovskite solar cell efficiency*, ACS Energy Lett. **9**, 193-200 (2024).

Publications

1. G. Szabó, P. V. Kamat, *Spiro-OMeTAD: Unique redox chemistry driving the hole transport*, ACS Energy Lett. **10**, 330-336 (2025).
2. H. Okrepka, L. Franzini, S. Pagliara, M. Kuno, *Photoremixing of photosegregated formamidinium/cesium lead iodide/bromide thin films under pulsed laser excitation*, ACS Energy Lett. **9**, 5744-5746 (2024).
3. H. Okrepka, Y. Ding, S. Ghonge, A. Ruth, M. Kuno, *Excitation intensity-dependent terminal halide photosegregation stoichiometries in formamidinium/cesium lead iodide/bromide [$FACsPb(I_{1-x}Br_x)_3$] thin films*, J. Phys. Chem. Lett. **15**, 10488-10494 (2024).
4. E. Aleksanyan, V. Harutyunyan, A. Badalyan, N. Grigoryan, N. Margaryan, A. Manukyan, A. Kirakosyan, M. Zakaryan, L. Matevosyan, H. Okrepka, V. Trepalin, Y. Ding, M. Zhukovskyi, M. Kuno, A. Aprahamian, K. Manukyan, *Superior stability of $CsPbBr_3$ films under high-energy proton irradiation*, J. Phys. Chem. C. **128**, 40, 16854-16860 (2024).
5. P. Mathew, J. Cho, P. V. Kamat, *Ramifications of ion migration in 2D lead halide perovskites*, ACS Energy Lett. **9**, 1103-1114 (2024).
6. G. Szabó, P. V. Kamat, *How cation migration across a 2D/3D interface dictates perovskite solar cell efficiency*, ACS Energy Lett. **9**, 193-200 (2024).

7. A. Ruth, H. Okrepka, P. V. Kamat, M. Kuno, *A thermodynamic band gap model of mixed-halide perovskite photosegregation*, J. Phys. Chem. C **127**, 18547-18559 (2023).
8. A. Ruth, M. Kuno, *Modeling the photoelectrochemical evolution of lead-based, mixed-halide perovskites due to photosegregation*, ACS Nano **17**, 20502-20511 (2023).
9. N. Hiott, J. Chakkamalayath, P. V. Kamat, *Reversible phase transformation of colloidal 2D lead halide perovskite platelets under photoirradiation*. ACS Materials Letters, 2614-2620 (2023).
10. K. Kniazev, E. Zaitsev, S. Zhang, Y. Ding, L. Ngo, Z. Zhang, G. V. Hartland, M. Kuno, *Hyperspectral and nanosecond temporal resolution widefield infrared photothermal heterodyne imaging*, ACS Photonics, **10**, 2854-

Quantum Coherence of New Quasiparticles in Moiré Superlattices

supported by DOE BES grant # DE-SC0019398

PI : Xiaoqin Elaine Li at the University of Texas-Austin

Keywords: quantum coherence, quasiparticles, superlattices, moiré

Research Scope

When two atomically thin van der Waals (vdW) layers are vertically stacked together, the atomic alignment between the layers exhibits periodical variations, leading to a new type of in-plane superlattices known as the moiré superlattices. In moiré superlattices formed by transition metal dichalcogenide (TMD) monolayers, optical properties are dominated by excitons (i.e. bound electron-hole pairs). Similar to TMD monolayers, exciton binding energy in moiré superlattices is exceptionally large (≥ 200 meV),[1–4] making these quasiparticles stable at room temperature and relevant for various optoelectronic devices. Because the moiré supercell size is typically larger than the exciton Bohr radius (~ 1-2 nm), an exciton is typically viewed as a composite particle moving in a smooth and periodic energy landscape. All fundamental properties of excitons are modified by the moiré potential[5–8] including optical selection rules, spin-valley correspondence, mobility, and, of particular relevance here, quantum dynamics.[9] These properties are controllable with the twist angle, a unique tuning knob of moiré superlattices.

The many complexities associated with excited states in moiré superlattices also offer new and exciting opportunities to discover and engineer quasiparticles. In the proposed program, we will study the quantum dynamics of new exciton resonances and Fermi polarons in TMD atomically thin layers and moiré superlattices using two-dimensional coherent electronic spectroscopy (2DCES). These proposed directions derive from our original discoveries made in the current funding cycle. Specifically, we will investigate three topics as summarized in Fig. 1:

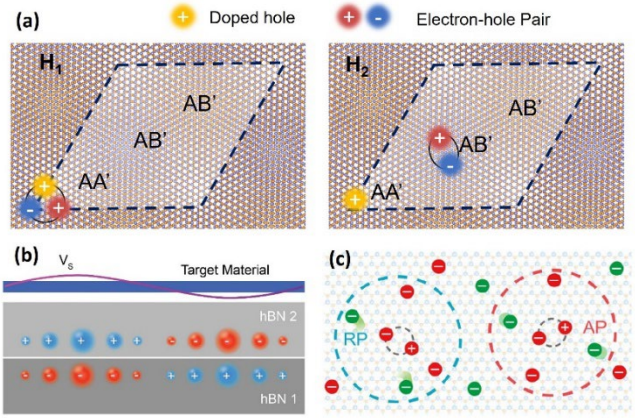

Fig. 1: Summary of three proposed projects. (a) two-types of trions in a twisted homobilayers; (b) excitons confined by a remote moiré potential; (c) attractive and repulsive polarons (AP and RP) in doped TMDs.

- Two types of trions in twisted TMD homobilayers
- Excitons in TMD monolayers and bilayers confined by a remote moiré potential
- Fermi polarons in doped TMD natural and twisted bilayers

Recent Progress

We have made the most progress on the task 1 in the first year. We have studied excitonic resonances in several $MoSe_2$ bilayers near H-stacking angles (i.e., 60°, 59.6°, and 57.5°). Ultra-flat bands have been predicted in these homobilayers.[10] The twist angle can be precisely controlled with

an accuracy better than 0.1 °, enabling us to examine the effects of lattice reconstructions with specific supercell sizes.

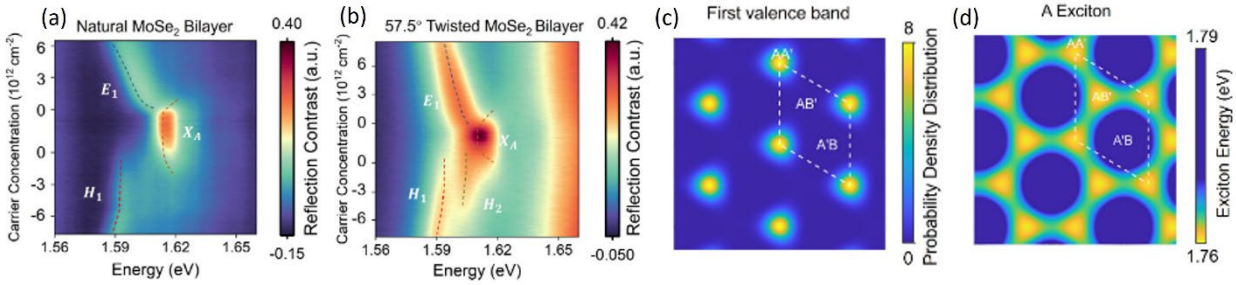

Fig. 2: Optical reflectivity spectra taken as a function of doping in (a) a natural $MoSe_2$ bilayer and (b) a twisted bilayer with $\theta = 57.5°$. (c) calculated spatial distribution of doped holes in the 57.5° twisted bilayer. (d) calculated energy of the lowest energy exciton. The nearly degenerate exciton energy at two locations within the supercell suggests both AA' and AB' are possible locations for optically excited excitons.

By analyzing the optical reflectivity spectra of several $MoSe_2$ bilayers at different doping levels, we identify a new type of positively charged trion, charge-transfer trion H_2, which exhibits a smaller binding energy than tightly bound trions H_1. While tightly-bound trions are observed in all three bilayers (Fig. 2a), charge-transfer trions H_2 are only found in the 57.5° bilayer (Fig. 2b), which shows gradual atomic alignment shifts between the two layers. First-principles calculations indicate that doped holes are localized in a flat moiré band at specific AA' sites within supercells (Fig. 2c) of the 57.5° bilayer while optically excited electron-hole pairs might be situated at either AA' or AB' locations (Fig. 2d and Fig. 1a), resulting in two distinct trion species. These results are summarized in a manuscript that is under review at Nature Materials and has been posted at arXiv:2407.17025. This linear spectroscopy study was initiated under an NSF grant and laid the foundation for the coherent nonlinear spectroscopy studies of quantum coherence of these new quasiparticles funded by this DOE grant.

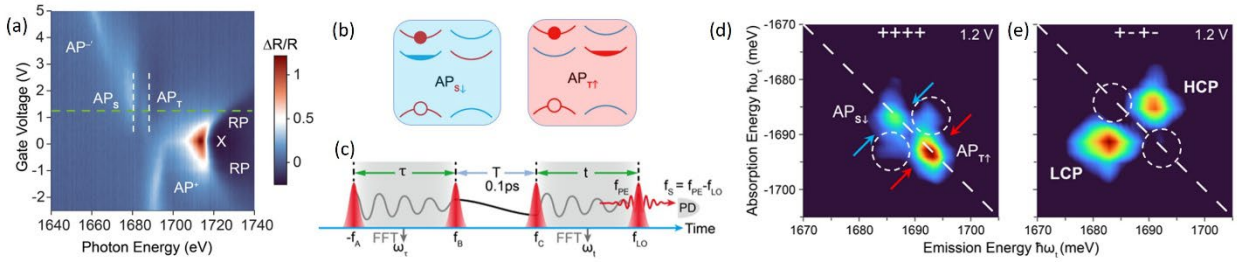

While we have focused our energy on understanding the linear optical spectroscopy measurements on twisted TMD bilayers, we have applied the two-dimensional coherent electronic spectroscopy (2DCES), a unique technique to understand quantum dynamics of quasiparticles, to study doped monolayers. Following our study of Fermi polaron quantum dynamics published in PRX in 2023, we studied polarons in WSe_2 monolayers in the past year as shown in Fig. 4. We first examine the evolution of the linear reflectivity spectrum with doping (Fig. 4a). Both electron and hole doping lead to the formation of Fermi polarons. The distinctions between MoSe2 and WSe2 monolayers are most pronounced for electron doping. In WSe2 monolayers, there are multiple attractive polarons (APs). We focus on a modest electron doping at $8.4*10^{11}$ cm^{-2} indicated by the green horizontal dashed line, where two attractive polarons are present simultaneously, singlet- and triplet attractive polarons ($AP_{S\downarrow}$ and $AP_{T\uparrow}$). These two states correspond to the optically excited electron-hole pairs occupying the same or opposite valley, as illustrated in Fig. 3b. We assign the valley index according to the valley where the electron-hole pair resides. The diagrams in Fig. 3b correspond to singlet- and triplet attractive polarons in the K valley. The single particle energy diagram is somewhat misleading

as it implies the singlet- and triplet states have the same energy. The Coulomb exchange interaction lowers the energy of the singlet state by ~ 7 meV.

To investigate the quantum dynamics and interactions between $AP_{S\downarrow}$ and $AP_{T\uparrow}$, we employ a the collinear (2DCES. Briefly, three laser pulses, each approximately 100 fs long and operating at an 80 MHz repetition rate from a Ti:Sapphire laser, are tightly focused through a microscope objective lens onto a spot roughly 1 μm in diameter. The photon-echo emission is collected via reflection geometry using the same lens and combined with a reference pulse for heterodyne detection. Unless specified otherwise, each beam maintains a power of 10 μW, corresponding to an exciton density of approximately 8×10^{10} cm^{-2}. The high-quality sample and tightly focused beam are essential to distinguish between the singlet and triplet states in the two-dimensional (2D) spectra, thereby revealing their distinct dynamics and coupling mechanisms.

We perform one-quantum rephasing measurements by scanning delays between the first two pulses (τ) and between the third and reference pulses (t), followed by Fourier transformation to obtain absorption ($\hbar\omega_\tau$) and emission ($\hbar\omega_t$) energies, as illustrated in Fig. 3c. To eliminate coherent artifacts from nonlinear interactions during pulse overlaps, the waiting time (T) between the second and third pulses exceeds 0.1 ps. The normalized amplitude spectrum obtained with co-circularly polarized pulses (+ + + +) is shown in Fig. 3d. Two diagonal resonances, $AP_{T\uparrow}$ at 1693 meV and $AP_{S\downarrow}$ at 1686 meV, appear clearly. The absence of cross-peaks indicates that $AP_{S\downarrow}$ and $AP_{T\uparrow}$ do not couple directly, as they occupy separate Fermi seas and do not compete for electrons. Conversely, pronounced cross-peaks appear in the spectrum recorded with cross-circularly polarized pulses (+ − + −, Fig. 3e), indicating coupling due to shared electrons between singlet and triplet polarons in opposite valleys, consistent with previous observations in WS_2. This confirms that polaron interactions represent a universal mechanism across TMDs.

By performing these 2DCES measurements as a function of doping, we have demonstrated that the quantum dynamics of singlet and triplet attractive polarons in a WSe_2 monolayer evolve systematically with increasing electron doping density. At lower doping levels, the dephasing rates of these attractive polarons remain relatively constant; however, at higher doping densities, the dephasing rates increase, likely due to additional decay pathways involving coupling to higher-order many-body states.

Interestingly, the non-radiative valley coherence between the singlet and triplet polarons is maintained longer compared to excitons, primarily due to pure dephasing processes rather than population relaxation. A detailed analysis of valley and polaron pure dephasing reveals correlated energy fluctuations between the coupled singlet and triplet states sharing the same Fermi sea. Significantly, we have identified a long-lived component of attractive polaron valley polarization, originating from a dark-to-bright state conversion. Moreover, the scattering processes involving the dark state differ notably between the singlet and triplet polarons due to electron-electron exchange interactions occurring between the singlet configuration and the opposite-valley Fermi sea. Consequently, the singlet state exhibits a longer-lasting valley polarization compared to the triplet state. Our findings underscore important similarities and differences in polaron dynamics across various transition metal dichalcogenide (TMD) monolayers, setting the stage for future explorations of diverse polaron phenomena predicted in moiré superlattices composed of stacked TMD bilayers.

Future Plans: Having identified the two distinct types of trions this year, we will investigate their distinct quantum dynamics using two-dimensional coherent electronic spectroscopy 2DCES in the next 1-2 years.

References

(1) Splendiani, A.; Sun, L.; Zhang, Y.; Li, T.; Kim, J.; Chim, C.-Y.; Galli, G.; Wang, F. Emerging Photoluminescence in Monolayer MoS2. *Nano Lett.* **2010**, *10* (4), 1271–1275. https://doi.org/10.1021/nl903868w.

(2) He, K.; Kumar, N.; Zhao, L.; Wang, Z.; Mak, K. F.; Zhao, H.; Shan, J. Tightly Bound Excitons in Monolayer WSe2. *Phys. Rev. Lett.* **2014**, *113* (2), 026803. https://doi.org/10.1103/PhysRevLett.113.026803.
(3) Mak, K. F.; Shan, J. Photonics and Optoelectronics of 2D Semiconductor Transition Metal Dichalcogenides. *Nat. Photonics.* **2016**, *10* (4), 216–226. https://doi.org/10.1038/nphoton.2015.282.
(4) Lu, X.; Li, X.; Yang, L. Modulated Interlayer Exciton Properties in a Two-Dimensional Moiré Crystal. *Phys. Rev. B* **2019**, *100* (15), 155416. https://doi.org/10.1103/PhysRevB.100.155416.
(5) Huang, D.; Choi, J.; Shih, C.-K.; Li, X. Excitons in Semiconductor Moiré Superlattices. *Nat. Nanotechnol.* **2022**, *17* (3), 227–238. https://doi.org/10.1038/s41565-021-01068-y.
(6) Perea-Causin, R.; Erkensten, D.; Fitzgerald, J. M.; Thompson, J. J. P.; Rosati, R.; Brem, S.; Malic, E. Exciton Optics, Dynamics, and Transport in Atomically Thin Semiconductors. *APL Materials* **2022**, *10* (10), 100701. https://doi.org/10.1063/5.0107665.
(7) Fang, H.; Lin, Q.; Zhang, Y.; Thompson, J.; Xiao, S.; Sun, Z.; Malic, E.; Dash, S. P.; Wieczorek, W. Localization and Interaction of Interlayer Excitons in MoSe2/WSe2 Heterobilayers. *Nat Commun* **2023**, *14* (1), 6910. https://doi.org/10.1038/s41467-023-42710-8.
(8) Chatterjee, S.; Dandu, M.; Dasika, P.; Biswas, R.; Das, S.; Watanabe, K.; Taniguchi, T.; Raghunathan, V.; Majumdar, K. Harmonic to Anharmonic Tuning of Moiré Potential Leading to Unconventional Stark Effect and Giant Dipolar Repulsion in WS2/WSe2 Heterobilayer. *Nat Commun* **2023**, *14* (1), 4679. https://doi.org/10.1038/s41467-023-40329-3.
(9) Purz, T. L.; Martin, E. W.; Rivera, P.; Holtzmann, W. G.; Xu, X.; Cundiff, S. T. Coherent Exciton-Exciton Interactions and Exciton Dynamics in a MoSe 2 / WSe 2 Heterostructure. *Phys. Rev. B* **2021**, *104* (24), L241302. https://doi.org/10.1103/PhysRevB.104.L241302.
(10) Naik, M. H.; Kundu, S.; Maity, I.; Jain, M. Origin and Evolution of Ultraflat Bands in Twisted Bilayer Transition Metal Dichalcogenides: Realization of Triangular Quantum Dots. *Phys. Rev. B* **2020**, *102* (7), 075413. https://doi.org/10.1103/PhysRevB.102.075413.

Publications

1. "Valley-Mediated Singlet- and Triplet-Polaron Interactions and Quantum Dynamics in a Doped Monolayer", Yue Ni, Di Huang, Danfu Liang, Albert Liu, Xiaohui Liu, Kevin Sampson, Zhida Liu, Jianmin Quan, Kenji Watanabe, Takashi Taniguchi, Dmitry K Efimkin, Jesper Levinsen, Meera M Parish, Xiaoqin Li, Phys. Rev. Lett., 134, 036901, 2025
2. "Fermi Pressure and Coulomb Repulsion Driven Rapid Hot Plasma Expansion in a van der Waals Heterostructure", Junho Choi, Jacob Embley, Daria D Blach, Raül Perea-Causín, Daniel Erkensten, Dong Seob Kim, Long Yuan, Woo Young Yoon, Takashi Taniguchi, Kenji Watanabe, Keiji Ueno, Emanuel Tutuc, Samuel Brem, Ermin Malic, Xiaoqin Li, Libai Huang, Nano Letters, 23, 4399−4405, 2023.
3. Jiamin Quan, Ganbin Chen, Lukas Linhart, Zhida Liu, Takashi Taniguchi, Kenji Watanabe, Florian Libisch, Rui Huang, Xiaoqin Li, "Quantifying Strain in Moiré Superlattice", Nano Lett. 2023, 23, 24, 11510–11516, 2023
4. Di Huang, Kevin Sampson, Yue Ni, Zhida Liu, Danfu Liang, Kenji Watanabe, Takashi Taniguchi, Hebin Li, Eric Martin, Jesper Levinsen, Meera M Parish, Emanuel Tutuc, Dmitry K Efimkin, Xiaoqin Li, "Quantum dynamics of attractive and repulsive polarons in a doped $MoSe_2$ monolayer", PRX, 13, 011029, 2023.
5. Dong Seob Kim, Di Huang, Chunhao Guo, Kejun Li, Dario Rocca, Frank Y Gao, Jeongheon Choe, David Lujan, Ting-Hsuan Wu, Kung-Hsuan Lin, Edoardo Baldini, Li Yang, Shivani Sharma, Raju Kalaivanan, Raman Sankar, Shang-Fan Lee, Yuan Ping, Xiaoqin Li, "Anisotropic excitons reveal local spin chain directions in a van der Waals antiferromagnet", Advanced Materials, 2206585, 2023

Model Construction and Material Realization of Electronic Flat Bands

Feng Liu, University of Utah

Keywords: flat-band models, flat-band materials, electron topology, excitonic insulator

Research Scope

This project, titled "Construction and Quantum States of Single and Yin-Yang Flat Bands", encompasses a comprehensive study of physical mechanisms that lead to formation of exotic many-body quantum electronic states associated with topological flat bands (FBs) in lattice models and FB materials. It consists of three correlated research topics: (1) Orbital design of 2D/3D single and yin-yang flat bands and search of FB materials; (2) Complete population inversion between yin-yang FBs; (3) Fractional excitonic insulator state. The common theme of the proposed research is to improve our fundamental understanding of topological FBs, demonstrate novel and exotic many-body quantum phases arising from single and yin-yang FBs, and discover new classes of topological FB materials.

Our theoretical/computational project will employ a multiscale approach, combining several state-of-the-art theoretical and computational techniques, ranging from single-particle first-principles density-functional-theory (DFT) electronic structure calculations to tight-binding (TB) model Hamiltonian calculations and analyses, and to calculations and solutions of many-body Hamiltonian. Specifically, open-source package of DFT method combined with many-body GW and Bethe-Salpeter equation (e.g. Berkley-GW) and our newly developed in-house package of exact diagonalization (ED) method for solving many-body TB Hamiltonian will be used to study various excitonic states arising from photoexcitation, including fractional excitations, between yin-yang FBs. Topological properties of single-particle electronic states will be analyzed using conventional methods of calculating (spin) Chern numbers, while topology and fractional statistics of many-body quantum states will be analyzed using ED calculations of spectral flow, quasi-hole excitation and particle-cut entanglement spectra.

Our studies will significantly improve our fundamental understanding of the nature and underpinning of many-body quantum states in association with single and yin-yang FBs, in terms of lattice symmetry and dimension, electron-electron Coulomb vs. exchange interaction and screening, and fractional statistics of band population. Both the continuations and new initiatives of the proposed research will significantly not only improve our fundamental understanding of the construction of topological FBs and realization of FBs-enabled many-body quantum states, but also expand the scope of topological FB materials and FB physics. They will provide useful guidelines for future experimental efforts in synthesis and characterization of new 2D and 3D topological FB materials. They will also have direct technological impact on advancing quantum materials and devices for energy applications, to fulfill the mission of the Department of Energy.

Recent Progress

During the last two years, we have published 17 journal papers fully or partially supported by this DOE grant, including 2 Physical Review Letters (one **editor's suggestion**), 1 Nature Communications, 2 Nano Letters (one **journal front cover**), and one invited review article. Three postdoctoral research associates and two graduate students have been fully or partially supported by this DOE project. The PI gave 8 invited talks at national/international conferences, and 18 departmental colloquium/seminar presentations. Below is a brief summary of four topics of research achievements pertaining to this project.

(1) Excitonic Condensate in a Quantum Semiconductor with Flat Valence and Conduction Bands:[1] Excitonic Bose-Einstein condensation (BEC) has drawn increasing attention recently with the emergence of 2D materials. A general criterion for BEC, as expected in an excitonic insulator state, is to have negative exciton formation energies in a semiconductor, as we showed earlier [Sethi et. al., *Phys. Rev. Lett.* 126, 196403 (2021)]. Recently, using exact diagonalization of a multiexciton Hamiltonian modeled in a diatomic kagome lattice, we demonstrate that the negative exciton formation energies are only a prerequisite but insufficient condition for realizing an excitonic BEC. By a comparative study between the cases of a so-called quantum semiconductor with both conduction and valence flat bands (FBs) (Fig. 1a) versus that of a conventional semiconductor with parabolic conduction band (Fig. 1c), we show that the presence and increased FB contribution to exciton formation provides an attractive avenue to stabilize the excitonic condensate, as confirmed by calculations and analyses of multiexciton energies, wave functions, and reduced two-body density matrices (Figs. 1b, d). Our results warrant a similar many-exciton analysis for other known and/or new candidates of excitonic insulators. Our work greatly enriches FB and exciton physics going beyond the state-of-the-art theoretical and computational studies which are largely limited to single exciton calculations. We demonstrate quantum semiconductors of flat valence and conduction band edges as a novel quantum materials platform.

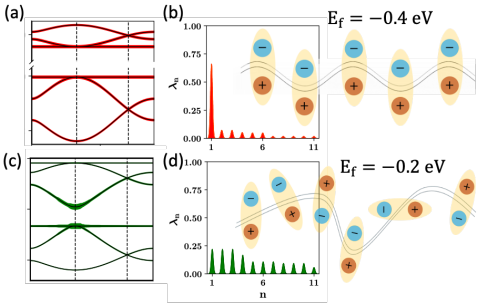

Fig. 1. (a) Band structure of a quantum semiconductor with flat valence and conduction band edges. (b) Plot of one large eigenvalue (λ_n) of exciton two-body density matrix indicating off-diagonal long-range order (ODLRO), characteristic of a highly coherent excitonic BEC state (inset) with the band structure of (a). (c) Band structure of a semiconductor with a parabolic conduction band edge. (d) excitons may still form spontaneously with a negative formation energy (E_f) with (c), but lack ODLRO and hence a coherent excitonic BEC state (inset).

(2) Anomalous bilayer quantum Hall effect:[2] In parallel to the condensed-matter realization of quantum Hall (Chern insulators), quantum spin Hall (topological insulators), and fractional quantum Hall (fractional Chern insulators) effects, we propose that bilayer FB lattices with one FB in each layer constitute solid-state analogs of bilayer quantum Hall (BQH) system, leading to anomalous

BQH effect without a magnetic field (Fig. 2). By exact diagonalization of a bilayer kagome lattice Hamiltonian, as an example, we demonstrate the stabilization of excitonic condensate Halperin's (1,1,1) state at the total filling $\nu_T = 1$ of the two FBs. Furthermore, by tuning the interlayer tunneling and distance between the kagome layers at $\nu_T = 2/3$, we show phase transitions among Halperin's (3,3,0), spin-singlet (1,1,2), and particle-hole conjugate of Laughlin's 1/3 states, as previously observed in conventional BQH systems. Our work opens a new direction in the field of FB physics by demonstrating bilayer FB materials as an attractive avenue for realizing exotic anomalous BQH states including non-Abelian anyons.

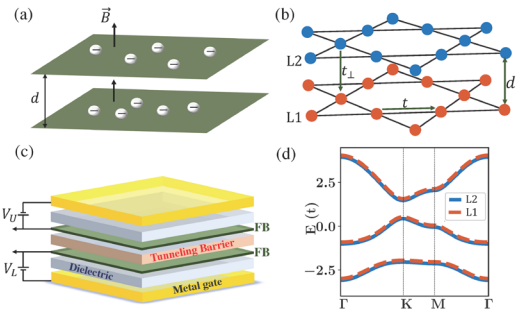

Fig. 2. (a) Schematic of BQH setup containing two layers of 2D electron gas separated by a distance d and a tunneling barrier. (b) Schematic of bilayer kagome lattice with blue and orange colors indicating atoms in layers L1 and L2 respectively. (c) Schematic of possible device configuration that can be used to realize anomalous BQH effect. $V_U(V_L)$ represent gate voltages for upper (lower) layer. FB material is indicated by a green layer with a tunneling barrier in between. (d) Single-particle band structure of bilayer kagome lattice at spin-orbit coupling (SOC) strength $\lambda = 0.3$ and $t_\perp = 0$. The two FBs belonging to individual layers are depicted in blue and orange color respectively.

(3) Growth of Mesoscale Ordered Two-dimensional Hydrogen-Bond Organic Framework with the Observation of Flat Band:[3] Flat bands, presenting a strongly interacting quantum system, have drawn increasing interest recently. However, experimental growth and synthesis of FB materials have been challenging and remained elusive for the ideal form of monolayer materials where the FB arises from destructive quantum interference in 2D lattice models. In 2013, our group made the first theoretical prediction of FBs in 2D monolayer organic frameworks, in a project also funded by the DOE-BES program. Recently, in collaboration with experimentalists, we reported direct observation of topological FB enabled by successful growth of large-scale uniform self-assembled monolayer of hydrogen-bond (H-bond) organic frameworks (HOFs) of 1,3,5-tris(4-hydroxyphenyl) benzene (THPB) on Au(111) substrate. High-resolution scanning tunneling microscopy/spectroscopy (STM/STS) shows mesoscale, highly-ordered and uniform THPB-HOF domains (Fig. 3a), while angle-resolved photoemission spectroscopy (ARPES) highlights a FB over the whole Brillouin zone (Fig. 3b). Furthermore, our density-functional-theory (DFT) calculations and analyses reveal that the observed topological FB arises from a hidden electronic breathing-Kagome lattice without atomically breathing bonds (Figs. 3d, 3e). Our findings demonstrate that self-assembly of HOFs provides a viable approach for the synthesis of 2D organic topological materials, paving the way to explore many-body quantum states of topological FBs.

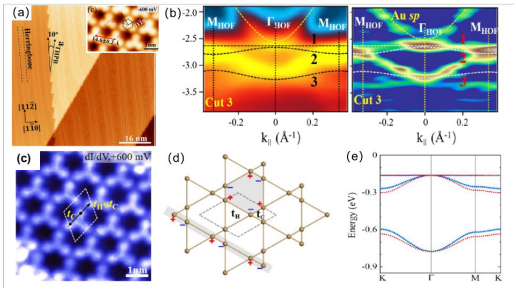

Fig. 3. (a) STM image of self-assembled monolayer 2D HOF of THPB on Au(111) substrate. (b) Observation of FB in HOF-THPB by ARPES. (c) In situ STM image showing hydrogen vs. covalent bonds of different inter-molecular hopping strength. (d) Schematic breathing-Kagome lattice. (e) DFT band structures, in good agreement with ARPES.

(4) Topological Nodal-Point Superconductivity in 2D Ferroelectric Hybrid Perovskites:[4,5] 2D hybrid organic-inorganic perovskites (HOIPs) with enhanced stability, high tunability and strong SOC have shown great potential in vast applications. Interestingly, we have recently extended the already rich functionality of 2D HOIPs to a new territory realizing topological superconductivity and Majorana modes for fault-tolerant quantum computation. We predict that room-temperature ferroelectric BA_2PbCl_4 (BA for benzylammonium) (Fig. 4) exhibits topological nodal-point superconductivity and gapless Majorana modes on selected edges and ferroelectric domain walls when proximity-coupled to an s-wave superconductor and an in-plane Zeeman field, attractive for experimental verification and application. It represents a unique example of a new class of ferroelectric topological superconductors we proposed recently.[5] We envision more exotic topological superconducting states to be found in this class of HOIP materials due to their diverse non-centrosymmetric space groups, which may open a new avenue in the fields of HOIPs and topological superconductivity.

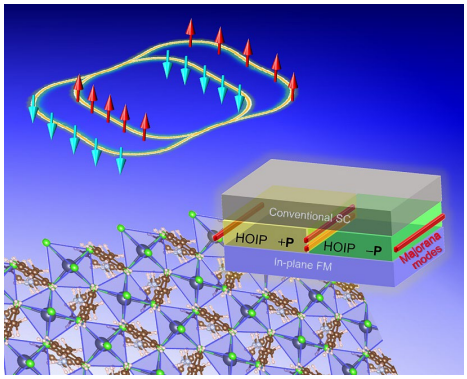

Fig. 4. Ferroelectric hybrid perovskites (the bottom figure shows the structure of a specific material, BA_2PbCl_4) with unique unidirectional SOC texture (top) can offer topological nodal-point superconductivity when the they are coupled to a conventional s-wave superconductor and an in-plane ferromagnet in proximity. The resultant heterostructure exhibits edge and domain-wall gapless Majorana modes (middle).

Future Plans

We plan to expand our current studies in the following areas:

(a) Graph Theorem and Orbital Design of yin-yang flat bands with High Chern Numbers
(b) Quantum Matric, Landau Levels, and Exciton Superfluid Weight of yin-yang flat bands
(c) Catalytic Activity of flat band at Charge Neutrality Point
(d) Continuing the efforts of experimental collaborations.

References

1. G. Sethi, M. Cuma, and Feng Liu, *Excitonic Condensate in Flat Valence and Conduction Bands of Opposite Chirality*, Phys. Rev. Lett. **130**, 186401 (2023).
2. G. Sethi, D. Sheng and Feng Liu, *Anomalous bilayer quantum Hall effect*, Phys. Rev. B **108**, L161112 (2023).
3. M. Pan, X. Zhang, Y. Zhou, P. Wang, Q. Bian, H. Liu, X. Wang, X. Li, A. Chen, X. Lei, S. Li, Z. Cheng, Z. Shao, H. Ding, J. Gao, F. Li, and Feng Liu, *Growth of Mesoscale Ordered Two-Dimensional Hydrogen-Bond Organic Framework with the Observation of Flat Band*, Phys. Rev. Lett. **130**, 036203 (Editor's Suggestion) (2023).
4. X. Li, S. Zhang, X. Zhang, Z. V. Vardeny, and Feng Liu, *Topological Nodal-Point Superconductivity in Two-Dimensional Ferroelectric Hybrid Perovskites*, Nano Lett. **24**, 2705 (2024) (Front Cover).
5. X. Zhang, P. Zhao and Feng Liu, *Ferroelectric topological superconductor: α-In2Se3*, Phys. Rev. B **109**, 125130 (2024).

Publications

1. G. Sethi, M. Cuma, and Feng Liu, *Excitonic Condensate in Flat Valence and Conduction Bands of Opposite Chirality*, Phys. Rev. Lett. **130**, 186401 (2023).

2. G. Sethi, D. Sheng and Feng Liu, *Anomalous bilayer quantum Hall effect*, Phys. Rev. B **108**, L161112 (2023).

3. M. Pan, X. Zhang, Y. Zhou, P. Wang, Q. Bian, H. Liu, X. Wang, X. Li, A. Chen, X. Lei, S. Li, Z. Cheng, Z. Shao, H. Ding, J. Gao, F. Li, and Feng Liu, *Growth of Mesoscale Ordered Two-Dimensional Hydrogen-Bond Organic Framework with the Observation of Flat Band*, Phys. Rev. Lett. **130**, 036203 (Editor's Suggestion) (2023).

4. X. Li, S. Zhang, X. Zhang, Z. V. Vardeny, and Feng Liu, *Topological Nodal-Point Superconductivity in Two-Dimensional Ferroelectric Hybrid Perovskites*, Nano Lett. **24**, 2705 (2024) (Front Cover).

5. X. Zhang, P. Zhao and Feng Liu, *Ferroelectric topological superconductor: α-In2Se3*, Phys. Rev. B **109**, 125130 (2024).

6. X. Zhang, X. Li, Z. Cheng, A. Chen, P. Wang, X. Wang, X. Lei, Q. Bian, S. Li, B. Yuan, J. Gao, F. Li, M. Pan, and Feng Liu, *Large-scale 2D heterostructures from hydrogen-bonded organic frameworks and graphene with distinct Dirac and flat bands*, Nat. Commun. **15**, 5934 (2024).

7. G. Sethi, B. Xia, D. Kim, H. Liu, X. Li and Feng Liu, *Graph theorem for chiral exact flat bands at charge neutrality*, Phys. Rev. B **109**, 035140 (2024).

8. B. Xia, H. Liu and Feng Liu, *Negative interatomic spring constant manifested by topological phonon flat band*, Phys. Rev. B **109**, 054102 (2024).

9. K.-H. Jin, W. Jiang, G. Sethi and Feng Liu, *Topological quantum devices: a review*, Nanoscale **15**, 12787 (2023).

10. D. Kim and Feng Liu, *Realization of flat bands by lattice intercalation in kagome metals*, Phys. Rev. B 107, 205130 (2023).

Magneto-thermopower in Mg3Bi2, a goniopolar Nodal Line Semimetal

Joseph P. Heremans
The Ohio State University

Keywords: Goniopolarity, direction-dependent polarity, transport, thermoelectricity, transverse thermoelectric transport

Research Scope

The quest for efficient thermoelectric materials has gained new momentum with recent theoretical advances predicting magnetic field-enhanced thermopower in topological semimetals. Chakraborty et al. proposed that nodal-line semimetals exhibit a unique two-stage magneto-thermopower response: a two-fold enhancement of the Seebeck coefficient (SSS) at intermediate magnetic fields followed by linear growth with field in the extreme quantum limit regime. This behavior arises when the applied field aligns with the nodal ring, amplifying the density of states through Landau quantization while suppressing parasitic conduction channels. In this work, we investigate single-crystalline Mg3Bi2 – a type-II Weyl nodal-line semimetal (WNLSM) with a closed nodal loop in the ab-plane and intrinsic goniopolarity manifesting as axis-dependent carrier polarity. Our magneto-thermopower measurements under in-plane fields up to 9 T reveal a linear increase in Seebeck coefficient at 20 K. Notably, we observe a sign reversal from electron-like ($S < 0$) to hole-dominated ($S > 0$) behavior, signaling strong electron-hole interactions. However, the predicted two-fold enhancement at lower fields (predicted at $B = 3$ T) remains absent, likely due to the multi-carrier dynamics inherent to type-II WNLSMs. These results highlight the critical role of carrier compensation in realizing theoretical predictions for topological thermoelectrics. While Mg3Bi2's goniopolar anisotropy enables unique transport tunability, its complex Fermi surface obscures the single-carrier regime required for the theoretically predicted Seebeck enhancement. Our findings suggest that type-I nodal-line systems with simpler band structures may better realize the predicted enhancement, guiding future material design for magneto-thermopower enhancement.

Recent Progress

This work focuses on Mg_3Bi_2 which is a goniopolar material. This was put in evidence by work carried out in 2024, which reports the thermopower of the material in and perpendicular to the basal plane **(Figs 1. a, b)** [1]. Additionally, Mg_3Bi_2 hosts a closed nodal loop near the Fermi level around the Γ point in the Brillouin zone [2]. Unlike type-I nodal-line systems, the type-II classification arises from a strong tilting of the linear dispersion along one momentum direction, violating Lorentz symmetry and enabling exotic transport properties. Crucially, spin-orbit coupling (SOC) introduces only a minor gap of 35 meV at the nodal line, preserving the type-II band dispersion and allowing the material to retain its semi-metallic behavior [2]. Experimental validation via angle-resolved photoemission spectroscopy (ARPES) confirms the predicted bulk band structure and reveals drumhead surface states within the nodal loop—a hallmark of topological nodal-line systems [2]. For the above reasons, Mg_3Bi_2 emerged as a candidate to study its thermopower in magnetic fields.

The enhancement of the thermopower in WNLSMs as predicted by the theory has two temperature regimes, below and above the Fermi temperature **(Fig. 2.a)** [3]. The predicted Seebeck enhancement below the Fermi temperature is shown in **Figure 2.b**. There are two critical magnetic field points, the first where $\omega_c\tau = 1$, where ω_c is the cyclotron frequency and τ is the relaxation time,

and the second is the extreme quantum limit above which only one Landau level is occupied. At the first condition, the Seebeck coefficient increases by a factor of two till it reaches the extreme quantum limit, above which, it increases linearly with the magnetic field. As will be explained later, the samples' carrier concentration n and mobility μ were measured first. Since $\omega_c\tau = \mu B$, the applied magnetic field that satisfies the first condition can be derived from the experimental value of μ: the first regime is achieved at 3 T. The extreme quantum limit can be estimated from the value of n to require a field of 30 T, which is beyond our instrument's capability. Therefore, observing a two-fold enhancement in the thermopower would signal a great success for the theory and motivate further studies.

First the magneto-thermopower measurements on Mg_3Bi_2 have been conducted with the field along the c axis as shown in **Fig. 2.c.** On top of that, the magnetoseebeck is also measured with the magnetic field along the ab plane so as to be parallel to one of the directions of the nodal line **(Fig. 2.d)**. This is a crucial point for achieving the theory, where the applied magnetic field must be in the same plane as the nodal ring, which in the case of Mg_3Bi_2 lies around the gamma point in the ab-plane.

Mg_3Bi_2 single crystals were grown using a solid-state synthesis technique, where the precursors were heated at 890 ºC for 48 h, cooled to 660 °C at 2 °C/h, and quenched to room temperature. The first measurement focused on the magnetotransport and shubnikov-de Haas (SdH) with the magnetic field along the c-axis. The crystals exhibit exceptional magnetoresistance (MR) of 5000% at 8 T and 3.2 K, far surpassing polycrystalline samples (**Fig. 1.c**). This colossal MR arises from the material's high electron mobility and low carrier density, as confirmed by Hall effect measurements and SdH analysis. SdH oscillations emerge above 3 T, revealing a single frequency of 29.2 T through Fourier analysis (**Fig. 1.d**). The Onsager relation yields a small Fermi surface cross-sectional area ($S_F = 2.79\times10^{-3}$ Å^{-2}) and Fermi wavevector ($k_F = 0.030$ Å^{-1}), consistent with isotropic electron pockets along the L-M line in the Brillouin zone [4].

The effective cyclotron mass derived from temperature-dependent SdH amplitudes is 0.16 m_e, indicative of light carriers. From Dingle plot, Dingle temperature and scattering were estimated to be 3.3 K and 369 fs, reflecting minimal scattering events and high crystal quality. Mean free path and mobility were found to be 80 nm and 4060 cm^2/Vs, respectively. Because of the existence of both carriers in this material, we conducted a two-band model to analyze our Hall data. We found that at 4.2 K, the carrier concentration of electrons and holes are 1.75×10^{18} and 1.79×10^{18} cm^{-3}, and their corresponding mobility are 1.02×10^4 and 0.83×10^4 cm^2/Vs, respectively. Because the higher mobility of electrons, we expect it to dominate over the holes and represent the observed SdH oscillations [4].

In the second part of the project, the magnetic field was applied along the ab plane (along the nodal ring) up to 9 T. **Figure 2.d** shows the measured Seebeck coefficient as a function of applied magnetic field at 20 K. The signal looks predominantly linear, which doesn't match the predicted behavior in the theory. At zero field, Seebeck is negative, indicating a predominant electron-like behavior. However, with increasing magnetic field, the thermopower turns positive, where it is hole-like. This signals a strong interaction between the electron and hole bands in the material.

There are three possibilities to explain why the enhancement of Seebeck coefficient by a factor of 2 at 3 T was not observed. First, it is possible that the chemical potential was simply too far in energy from the nodal line's energy. This is because of unintentional doping of the samples, presumably due to very slight (~ ppm-levels) deviations from the 3:2 Mg:Bi stoichiometry during sample preparation. Second, type-ll weyl nodal line semimetals differ from type-l in the tilting of the linear dispersion. This tilting enhances the contribution from the nearby hole pockets, making it impossible to negate the effects of the holes in the transport. The predicted theory for enhancing the thermopower in WNLSMs assumes a one-carrier system, thus, a major contribution from a second carrier would be

unfavorable. The third possibility lies in the fact that the theory was developed for a purely linear nodal line, while the nodal line in Mg3Bi2 is warped in k-space, and the influence of this warping is unknown. Future directions would be to focus on type-l nodal line semimetals with simple Fermi surfaces, where the nodal line is far from hole pockets.

Future Plans: This is the last report of this cycle.

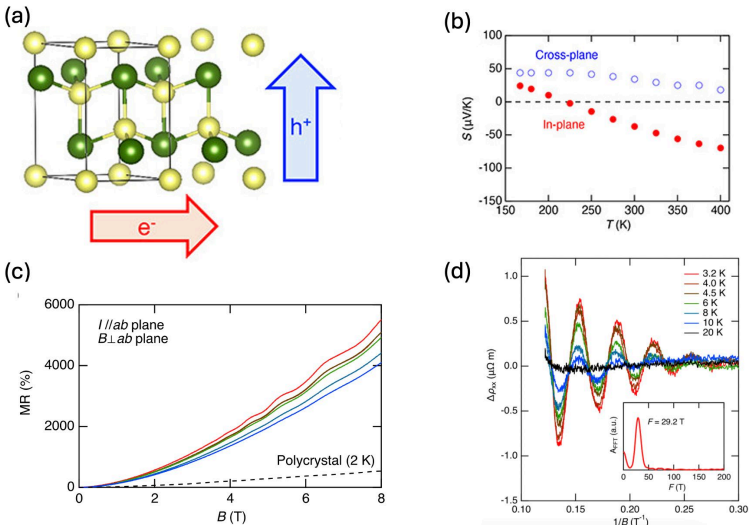

Figure 6: (a) Goniopolarity in Mg_3Bi_2, where the sample is p-type along the cross-plane and n-type along the in-plane *[1]*. (b) Measured thermopower along both directions, confirming the goniopolarity in the material *[1]*. (c) Magnetoresistance for Mg3Bi2 *[4]*. (d) SdH oscillations for Mg3Bi2 *[4]*.

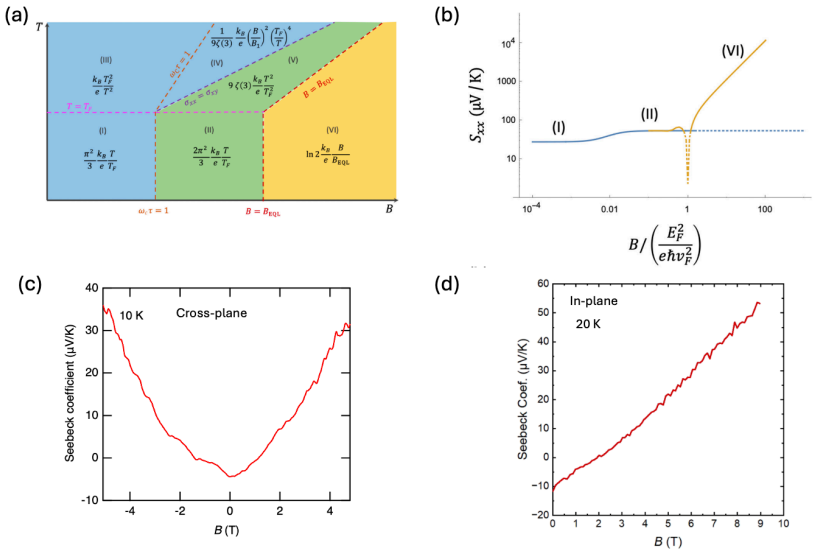

Figure :2 Seebeck thermopower for nodal line semimetals. (a, b) The theoretical calculations for the magneto-thermopower of WNLSMs. (b) Calculations in the case the temperature is below the Fermi temperature *[3]*. (c, d) experimental results of the Seebeck coefficient for Mg_3Bi_2 with magnetic field applied cross-plane and in-plane, respectively.

References:

[1] Y. Goto, H. Usui, M. Murata, J. E. Goldberger, J. P. Heremans, and C.-H. Lee, Band Anisotropy Generates Axis-Dependent Conduction Polarity of Mg3Sb2 and Mg3Bi2, Chem. Mater. **36**, 2018 (2024).

[2] T.-R. Chang et al., Realization of a Type-II Nodal-Line Semimetal in Mg3Bi2, Adv. Sci. **6**, 1800897 (2019).

[3] P. Chakraborty, A. Hui, G. Bednik, and B. Skinner, Magnetothermopower of Nodal-Line Semimetals, PRX Energy **3**, 023007 (2024).

[4] Y. Goto, M. Murata, H. Usui, K. Ono, J. P. Heremans, T. Terashima, and C.-H. Lee, Magnetotransport properties and Shubnikov–de Haas oscillations in a type-II nodal-line semimetal candidate n -type Mg 3 Bi 2 single crystal, Phys. Rev. B **111**, 075163 (2025).

Publications:

1. Y. Goto, M. Murata, H. Usui, K. Ono, J. P. Heremans, T. Terashima, and C.-H. Lee, Magnetotransport properties and Shubnikov–de Haas oscillations in a type-II nodal-line semimetal candidate n -type Mg 3 Bi 2 single crystal, Phys. Rev. B **111**, 075163 (2025).
2. Y. Goto, H. Usui, M. Murata, J. E. Goldberger, J. P. Heremans, and C.-H. Lee, Band Anisotropy Generates Axis-Dependent Conduction Polarity of Mg3Sb2 and Mg3Bi2, Chem. Mater. **36**, 2018 (2024).
3. M. Ochs, G. H. Fecher, B. He, W. Schnelle, C. Felser, J. P. Heremans, and J. E. Goldberger, Synergizing a Large Ordinary Nernst Effect and Axis-Dependent Conduction Polarity in Flat Band KMgBi Crystals, Advanced Materials **36**, 2308151 (2024).
4. M. Ochs, D.-G. Oprea, J. Cardenas-Gamboa, C. E. Moore, J. P. Heremans, C. Felser, M. G. Vergniory, and J. E. Goldberger, KMg4Bi3: A Narrow Band Gap Semiconductor with a Channel Structure, Inorg. Chem. **63**, 20133 (2024).

Quantifying Memory in Spin Glasses

PI: Raymond L. Orbach[1]
Co-PI E. Dan Dahlberg[2]
Co-PI: Samaresh Guchhait[3]
Co-PI: Gregory G. Kenning[4]

[1]Texas Materials Institute, The University of Texas at Austin, Austin, Texas 78712
[2]School of Physics and Astronomy, The University of Minnesota, Minneapolis, Minnesota, 55455
[3]Department of Physics and Astronomy, Howard University, Washington, DC, 20059
[4]Department of Physics, Indiana University of Pennsylvania, Indiana, Pennsylvania, 15705

Key words: memory, rejuvenation, spin-glasses, far-from-equilibrium systems

Research Scope

Rejuvenation and memory, long considered the distinguishing feature of spin glasses, are a property of systems far-from-equilibrium (e.g. granular materials, phase separation in the early universe, and, particularly, glass formers). Recently, they have been proven to result from the growth of multiple length scales. This insight, enabled by simulations on the Janus II supercomputer, has opened the door to a quantitative analysis. We combine numerical simulations with comparable experiments to introduce two coefficients that quantify memory.[1]

Recent Progress

Memory is among the most striking feature of far-from-equilibrium systems, including granular materials, phase separation in the early universe, and, particularly, glass formers. Whether a universal mechanism is responsible for memory in all these materials is unknown, but spin glasses stand out. Memory effects are particularly strong in these systems – perhaps because of the large attainable coherence lengths. More important, their dynamics is now understood in great detail. Indeed, to model protocols where temperature is varied, one must first understand the non-equilibrium evolution at constant temperature. In other words, before tackling memory, rejuvenation and aging should be mastered. These intermediate steps, including the crucial role of temperature chaos, have now been taken for spin glasses.

In the context of spin glasses, rejuvenation is the observation that when the system is aged at an initial temperature $T_{initial}$ for a time $t_{w,initial}$, and then cooled to a sufficiently lower temperature T_{final}, the spin glass reverts to the same state it would have achieved had it been cooled directly to T_{final}. That is, its state is independent of its having approached equilibrium at temperature $T_{initial}$. However, when the spin glass is then warmed back to temperature $T_{initial}$ it appears to return to its aged state, hence memory. Baity et al.[2] has not only demonstrated memory numerically and related rejuvenation to temperature chaos, and also shown that both effects are ruled by multiple length scales, setting the stage for more quantitative studies.

We introduce two coefficients to quantify memory, one experimentally accessible and the other adapted to numerical work. In both experiment and simulations[1,2] we have a three step procedure: (i) the system is quenched to a temperature $T_{initial} < T_g$ (T_g is the glass temperature) and relaxes for a

time $t_{w,initial}$. In simulations, this quench is instantaneous while in experiment it is done at ≈ 10 K/min. A protocol where temperature is kept constant after the initial quench is termed *native*. (ii) The system in then quenched to $T_{final} < T_{initial}$ where it evolves for a time $t_{w,final}$. (iii) The system is raised back to $T_{initial}$, instantaneously in simulations, and at the same rate as cooling in experiment. After a short time at $T_{initial}$ (2^{10} time steps in simulations) the dynamics are compared to the native system, which has spent time $t_{w,initial}$ at $T_{initial}$. The temperature drop $T_{initial} - T_{final}$ is chosen to ensure that temperature chaos (and, hence, rejuvenation) is sizeable. The experiments are performed on a single crystal sample of
CuMn (8 at.%) with $T_g = 41.6$ K. For simulations, $T_c = \approx 1.1$.

Length scales-Memory and rejuvenation are ruled by several length scales of which only one is experimentally accessible: ξ_{Zeeman}, related to the Zeeman effect.[3] In simulations, the basic length scale is the size of glassy domains in a native protocol, ξ_{micro}^{native}. Rejuvenation is regarded as a consequence of temperature chaos. The preexisting correlated spins, formed at $T_{initial}$ and aging time $t_{w,initial}$ to generate the correlation length $\xi(t_{w,initial},T_{initial})$ are "frozen" dynamically at T_{final} and a new correlated state of size $\zeta(t_{w,final},T_{final})$ forms where $t_{w,final}$ is the ageing time at T_{final}. The newly correlated state at T_{final} is *independent* from that formed at $T_{initial}$. Upon heating back to $T_{initial}$, the two correlated states *interfere*, causing a memory loss that is seen both in experiment and simulations. We plot the memory coefficient C ($C = 1$ for perfect memory, $C = 0$ for no memory) below vs $\log_2(t_{w2}/\tau_0)$ where τ_0 is an exchange time ≈ $\hbar/k_BT$:

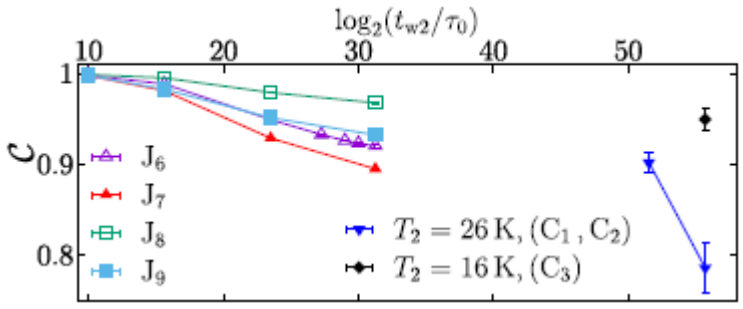

Memory coefficient C as a function of t_{w2}. C_1: $T_1 = 30$ K, $t_{w1} = 1$ hr, $T_2 = 26$ K, $t_{w2} = 1/6$ hr; C_2: $T_1 = 30$ K, $t_{w1} = 1$ hr, $T_2 = 26$ K, $t_{w2} = 3$ hr; C_3: $T_1 = 30$ K, $t_{w1} = 1$ hr, $T_2 = 16$ K, $t_{w2} = 3$ hr. J_6: $T_1 = 1.0$, $t_{w1} = 2^{29.875}$, $T_2 = 0.625$; J_7: $T_1 = 1.0$, $t_{w1} = 2^{29.875}$, $T_2 = 0.7$; J_8: $T_1 = 0.9$, $t_{w1} = 2^{31.25}$, $T_2 = 0.5$; J_9: $T_1 = 0.9$, $t_{w1} = 2^{31.25}$, $T_2 = 0.7$.

Experiment: (C stands for cycle) (i) The temperatures in C_2 are the same as C_1: $T_{initial} = 30$ K, $T_{final} = 26$ K. The figure shows that C decreases as $t_{w,final}$ increases from 1/6 hr in C_1 to 3 hr in C_2. The magnitude of $\zeta(t_{w,final},T_{final})$ at T_{final} is therefore larger for C_2 as compared to C_1. Hence, the interference of $\zeta(t_{w,final},T_{final})$ with $\xi(t_{w,initial},T_{initial})$ is stronger. Concomitantly, memory is therefore smaller for C_2 as compared to C_1. (ii) C_3: The temperature $T_{final} = 16$ K instead of 26 K as in C_1 and C_2, everything else being equal. Because the growth of $\zeta(t_{w,final},T_{final})$ during $t_{w,final}$ at $T_{final} = 16$ K is much slower that at $T_{final} = 26$ K for the same $t_{w,final}$, the interference with $\xi(t_{w,initial},T_{initial})$ created at $T_{initial}$ for $t_{w,initial}$ is smaller, and the memory for C_3 is found to be much larger than for C_1 and C_2.

Simulations: (J stands for jump) J_6 differs from J_7 in that T_{final} is larger for the latter. This would mean that the correlated state at T_{final} grows more rapidly for the latter, so that memory should be smaller for J_7 as compared to J_6. This is seen in the figure. J_8 has a much larger $t_{w,initial}$ than J_6 or J_7, and T_{final} is much smaller. Put together, this results in a much larger memory, as seen in the figure.

Finally, each of the points in the figure are calculated from measured values of ξ_{Zeeman} and ξ_{micro}^{native}, from experiment and simulation, respectively, indeed quantifying memory in spin glasses.

Future Plans

Temperature chaos: Temperature chaos (TC) in spin glasses has been controversial ever since it was first introduced. The simplest description[4] of TC is[4] "…the complete reorganization of the equilibrium configurations by the slightest change in temperature." Concomitantly, extending the analysis to off-equilibrium dynamics,[5] TC "…means that the spin configurations that are typical from the Boltzmann weight at an initial temperature, T_1, are very atypical at a final temperature, T_2, no matter how close the two temperatures are." Yet the experiments and simulations to-date all used temperature differences $T_{initial} - T_{final}$ sufficiently large that full rejuvenation took place through temperature chaos. But what happens for smaller temperature differences? Does temperature chaos suddenly turn on at some value of $T_{initial} - T_{final}$ of sufficient magnitude for rejuvenation? Or is there evidence that it in fact is present "no matter how close the two temperatures are"?

Our procedure to address this open question is the following. First, we propose to cool our single crystal CuMn sample (T_g = 31.5 K) to an initial temperature $T_{initial}$ and age for a time $t_{w,initial}$. This will create a length scale in that the spin glass correlation length will grow to $\xi(t_{w,initial},T_{initial})$. Upon lowering the temperature to T_{final} and ageing for a time $t_{w,final}$, two changes will occur. The first is a reversible behavior that will turn out to be a rather complex quantity to calculate. The second follows from the findings of the simulations.[5] They showed that, upon a change in temperature $\Delta T = T_{initial} - T_{final}$, there is a probability that a portion of the spin glass is maximally decorrelated from that created at $T_{initial}$ (i.e. temperature chaos). Thus, upon a temperature change ΔT, *both* reversible and chaotic behavior are present. We propose to extract the relative magnitudes of the two through the following experimental protocols.

(i) *Amplitude of the chaotic component*

We propose to cool the spin glass from above T_g to $T_{initial}$ and age for $t_{w,initial}$ and measure the effective response time $t_{w,native}^{eff}$. We then drop the temperature to T_{final} and age for $t_{w,final}$ and measure the effective response time $t_{w,Tinitial\rightarrow Tfinal}^{eff}$. This time contains the contribution of both the chaotic and reversible components. The latter becomes very long as ΔT increases. Thus, at some ΔT, the time response $t_{w,Tinitial\rightarrow Tfinal}^{eff}$ will approach time $t_{w,native}^{eff}$ measured at T_{final}. This is the ΔT at which the entirety of the state at T_{final} is maximally decorrelated from that created at $T_{initial}$.

(ii) Amplitude of the reversible component

One knows the amplitude of the maximum barrier height Δ_{max} created by aging the system at $T_{initial}$ for $t_{w,initial}$ by virtue of the Arrhenius relation knowing $t_{w,native}^{eff}$. Upon reduction of the temperature to T_{final}, Δ_{max} increases according to previous measurements. Thus, the reversible component of the effective response time can be calculated after the temperature change, and compared with $t_{w,Tinitial\rightarrow Tfinal}^{eff}$. The difference between $t_{w,Tinitial\rightarrow Tfinal}^{eff}$ and $t_{w,native}^{eff}$ is the contribution to the effective response time from the decorrelated state created upon the temperature drop ΔT.

In this manner, one can separate the reversible component from that of the decorrelated component as a function of ΔT. We expect to find a decorrelated contribution from the smallest ΔT we can reliably measure, showing that, indeed, temperature chaos is present for any finite ΔT, consistent with the predictions of numerical simulations.[4,5]

References

(1) I. Paga, J. He, M. Baity-Jesi, E. Calore, A. Cruz, L. A. Fernandez, J. M. Gil-Narvion, I. G. A. Pemartin, A. Gordillo-Guerrero, D. Iñiguez, A. Maiorano, E. Marinari, V. Martin-Mayor, J. Moreno-Gordo, A. M. Sudupe, D. Navarro, R. L. Orbach, G. Parisi, S. Perez-Gaviro, F. Ricci-Tersenghi, J. J. Ruiz-Lorenzo, S. F. Schifano, D. L. Schlagel, B. Seoane, A. Tarancon, D. Yllanes, Janus Collaboration, *Quantifying Memory in Spin Glasses*, Phys. Rev. Lett. **133**, 256704 (2024).
(2) M. Baity-Jesi, E. Calore, A. Cruz, L. A. Fernandez, J. M. Gil-Narvion, I. Gonzalez-Adalid Pemartin, A. Gordillo-Guerrero, D. Iñiguez, A. Maiorano, E. Marinari, V. Martin-Mayor, J. Moreno-Gordo, A. Muñoz Sudupe, D. Navarro, I. Paga, G. Parisi, S. Perez-Gaviro, F. Ricci-Tersenghi, J. J. Ruiz-Lorenzo, S. F. Schifano, B. Seoane, A. Tarancon, and D. Yllanes, *Memory and rejuvenation effects in spin glasses are governed by more than one length scale*, Nature Physics **19**, 978 (2023).
(3) Y. G. Joh, R. Orbach, G. G. Wood, J. Hammann, and E. Vincent, *Extraction of the Spin Glass Correlation Length*, Phys. Rev. Lett. **82**, 438 (1999).
(4) L. A. Fernandez, V. Martin-Mayor, G. Parisi, and B. Seoane, *Temperature chaos in 3d Ising spin systems is driven by rare events*, Euro. Phys. Lett. **103**, 67003 (2013).
(5) M. Bairy-Jesi, E. Calore, A. Cruz, L. A. Fernandez, J. M. Gil-Narvion, I. Gonzalez-Adalid Pemartin, A. Gordillo-Guerro, D. Iñiguez, A. Maiorano, E. Marinari, V. Martin-Mayor, J. Moreno-Gordo, A. Muñnoz-Sudupe, D. Navarro, I. Paga, G. Parisi, S. Perez-Gaviro, F. Ricci-Tersenghi, J. J. Ruiz-Lorenzo, S. F. Schifano, Beatriz Seoane, A. Tarancon, R. Tripiccione, and D. Yllanes, *Temperature chaos is present in off-equilibrium spin-glass dynamics*, Commun. Phys. **S42005-021-00565-9** (2021).

Publications

(1) I. Paga, Q. Zhai, M. Baity-Jesi, E. Calore, A. Cruz, C. Cummings, L.A. Fernandez, J.M. Gil-Narvion, I. Gonzalez-Adalid Pemartin, A. Gordillo-Guerrero, D. Iñiguez, G.G. Kenning, A.Maiorano, E. Marinari, V. Martin-Mayor, J. Moreno-Gordo, A. Muñoz-Sudupe, D. Navarro, R.L. Orbach, G. Parisi, S. Perez-Gaviro, F. Ricci-Tersenghi, J.J. Ruiz-Lorenzo, S.F. Schifano, D.L. Schlagel, B. Seoane, A. Tarancon, and D. Yllanes, *Superposition Principle and nonlinear response in spin glasses*, Phys. Rev. B **107**, 214436 (2023).
(2) J. He and R. L. Orbach, *Spin glass dynamics through the lens of the coherence length*, Front. Phys. **12,** 1370278 (2024).
(3) Q. Zhai and R. L. Orbach, *Toward Understanding the dimensional crossover of canonical spin-glass thin films*, Front. Phys. **12**, 1488275 (2024).
(4) J. Freedberg, W. Joe Meese, J. He, D.L. Schlagel, E. Dan Dahlberg, and R.L. Orbach, *Memory and rejuvenation in glassy systems*, Phys. Rev. B **110**, L060411 (2024).
(5) K.-T. Tsai, E. D. Dahlberg, and R. L. Orbach, *Extracting free-energy landscape of AgMn spin-glass thin films with 1/f resistance fluctuations*, Phys. Rev. B **110**, 214205 (2024).
(6) I. Paga, J. He, M. Baity-Jesi, E. Calore, A. Cruz, L. A. Fernandez, J. M. Gil-Narvion, I. G. A. Pemartin, A. Gordillo-Guerrero, D. Iñiguez, A. Maiorano, E. Marinari, V. Martin-Mayor, J. Moreno-Gordo, A. M. Sudupe, D. Navarro, R. L. Orbach, G. Parisi, S. Perez-Gaviro, F. Ricci-Tersenghi, j. j. Ruiz-Lorenzo, S. F. Schifano, D. L. Schlagel, B. Seoane, A. Tarancon, D. Yllanes, Janus Collaboration, *Quantifying Memory in Spin Glasses*, Phys. Rev. Lett. **133**, 256704 (2024).
(7) S. Pradhan, D. Harrison, G. G. Kenning, D. L. Schlagel, and S. Guchhait, *Investigation of experimental signatures of spin glass transition temperature*, Front. Phys. **12**, 1482907 (2024).
(8) H. Li, J. He, and R.L. Orbach, *Nature of Temperature Chaos in Spin Glasses*, Phys. Rev. B **111**, 104309 (2025).

Emergent Magnetism and Spin-Dependent Transport Phenomena in Correlated Electron Materials and Heterostructures

Hari Srikanth and Manh-Huong Phan
Department of Physics, University of South Florida, Florida 33620

Keywords: Magnetic oxides; 2D van der Waals materials; Heterostructures; Magnetism; Thermo-spin transport

Research Scope

The advancement of modern technologies is driven by the discovery of new materials with unique properties. Our project aims to investigate the fundamental physics of complex magnetism and emergent spin-mediated phenomena in strongly correlated electron materials and heterostructures. By exploring the interplay between spin, charge, and orbital degrees of freedom, we uncover new magnetic and spintronic functionalities with potential applications in next-generation devices. Our research focuses on a diverse range of material systems, including ferrite oxides, rare-earth iron garnets (REIGs), helimagnets, Heusler alloys, and magnetic heterostructures integrated with two-dimensional (2D) van der Waals (vdW) materials.

We have successfully employed a unique approach that combines DC and AC magnetic susceptibility measurements, neutron diffraction, synchrotron X-ray diffraction with relatively unconventional radio frequency (RF) transverse susceptibility (TS), magnetocaloric effect (MCE), ferromagnetic resonance (FMR), spin Seebeck effect (SSE), spin Hall magnetoresistance (SMR), spin pumping effect (SPE), and anomalous Nernst effect (ANE) experiments to yield new insights into the ground state magnetism and thermo-spin transport in a wide variety of emergent correlated electron systems and heterostructures, leading to important discoveries of the tunable SSE in garnet-based heterostructures, the giant ANE in Heusler alloy systems, the giant positive magnetoresistance in nanostructured helimagnets, surface termination- vs. magnetic proximity-enhanced magnetism in ferrite thin films interfaced with 2D materials, the light-tunable room temperature ferromagnetism in 2D transition-metal dichalcogenide (2D-TMD) heterostructures, and the control of the intrinsic Weyl nodes in Weyl semimetals, among others.

Recent Progress

In addition to elucidating the effects of phase coexistence, dimensionality, strain, and competing magnetic interactions on the ground-state magnetic properties of ferrite nanoparticles (Fe_3O_4, $CoFe_2O_4$, $NiFe_2O_4$, Fe_3O_4@$CoFe_2O_4$) and thin films (Fe_3O_4, $NiFe_2O_4$), as well as REIG films ($Y_3Fe_5O_{12}$ (YIG), $Gd_3Fe_5O_{12}$ (GdIG), $Tm_3Fe_5O_{12}$ (TmIG)), we have explored these effects on thermo-spin transport across the magnetic ordering transitions in these systems. Some of the important findings are highlighted below:

- We provide the first experimental evidence linking magnetic anisotropy, Gilbert damping, and magnon propagation length, and their relationship with the SSE in ferrimagnet (FM)/heavy metal (HM) bilayer systems such as TmIG/Pt (see **Fig. 1**). Our study represents an important step toward the development of efficient spin-caloritronic devices based on voltage-controlled SSE.
- We demonstrate the significant role of phase transitions on thermo-spin transport in FM/HM systems. The SSE signal in the GdIG/Pt system exhibits a sign change across the compensation temperature (T_{Comp}), while the Verwey and Morin transitions (T_V, T_M) have distinct impacts on the biphase iron oxide (BPIO)/Pt system, where BPIO = Fe_3O_4 + α-Fe_2O_3.

Our studies provide good guidance on designing novel materials with enhanced SSEs for spincaloritronic devices.

- Our experiments and DFT calculations consistently demonstrate the surface termination-enhanced magnetic properties of a $NiFe_2O_4$ (NFO) film when interfaced with monolayer graphene (Gr) or hexagonal boron nitride (hBN), suggesting a novel strategy for engineering interfacial magnetic effects in FM/2D material systems for spintronics.
- By stacking different 2D vdW materials (metal vs. semiconductor), we have provided the first demonstration of light-tunable 2D ferromagnetism in 2D-TMD systems, such as VSe_2/MoS_2 and VSe_2/WS_2. Our research not only provides new insights into light-mediated 2D magnetism but also opens the door for exploring interfaces between 2D semiconducting TMD layers and non-magnetic metals, such as graphene.
- We demonstrate that the presence of a WS_2 monolayer reduces the magnetization of BPIO, and, consequently, the overall magnetization of the BPIO/WS_2/Pt system at $T > T_V \sim 120$ K - the Verwey transition temperature of Fe_3O_4. However, the magnetization is enhanced at $T < T_V$. Our findings provide new insights into the complex nature of magnetism at 2D-TMD/FM interfaces, paving the way for the design of 2D-TMD-based heterojunctions with tailored properties for spintronics, opto-spintronics, and valleytronics.
- We have established a correlation between the observed SSE signal, magnetic anisotropy, and Gilbert damping in CoFeCrGa Heusler films. These insights are beneficial for the fabrication of tunable and highly efficient spincaloritronic nanodevices.
- We have introduced a new prototype for an ANE-based thermopile device using topological spin semi-metallic quaternary Heusler alloys, such as FeCrRhSi and FeCrRhGe, for enhanced thermal-to-electrical energy harvesting.
- While controlling intrinsic Weyl nodes in Weyl semimetals remains challenging due to their topological protection, we show that the macroscopic magnetic properties of Co_2MnGa Heusler thin films can be modulated through structural distortions that affect the Weyl nodes. Our study introduces a novel degree of freedom for controlling macroscopic magnetic properties by modulating the intrinsic properties of Weyl nodes via structural distortions, offering new pathways for tuning the magnetic behavior of Weyl semimetals.
- By leveraging reduced dimensionality, strain, and confinement effects, we have discovered the giant positive magnetoresistance effect in nanostructured helimagnetic systems, such as MnP nanocrystalline thin films. Our findings unveil a novel strain-mediated spin helicity phenomenon in nanostructured helimagnets, offering a promising pathway for the development of high-performance magnetic sensors and spintronic devices by strategically utilizing dimensionality, confinement, and strain effects.

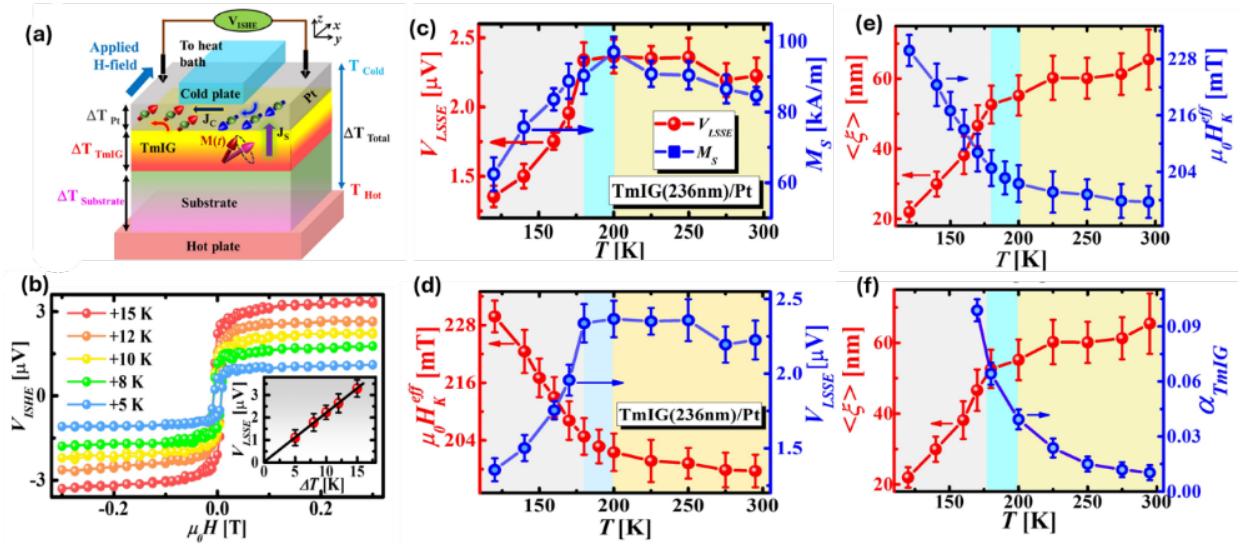

Figure 1: (**a**) Schematic diagram of the experimental set-up for LSSE measurements; (**b**) $V_{LSSE}(H)$ loops for different values of the temperature difference ΔT at a fixed average sample temperature T = 295 K. The inset shows a linear ΔT-dependence of the background-corrected LSSE voltage; (**c**) Temperature dependence of the LSSE voltage (V_{LSSE}) and saturation magnetization (M_s); (**d**) Temperature dependence of the effective magnetic anisotropy field (H_K^{eff}) and the LSSE voltage (V_{LSSE}); (**e**) Temperature dependence of the magnon propagation length ($\langle\xi\rangle$) and the effective magnetic anisotropy field (H_K^{eff}); (**f**) Temperature evolution of $\langle\xi\rangle$ and Gilbert damping constant (α).

Future Plans

These studies lay the foundation for expanding research efforts in the renewal period (2025-2028) of this project to include investigation of exotic physical properties e.g., magnetism, magnetic anisotropy, ANE, AHE, LSSE, FMR, FMR-driven spin pumping (FMR-SP), and spin rectification effect (SRE) in a wide range of novel garnet and ferrite oxides, helimagnets, and their heterostructures with emerging 2D materials, among Heusler alloys, altermagnets and others. Our focus will emphasize the role of the magnetic proximity effect (MPE) in driving new phenomena and inducing novel functionalities in magnetic bilayer systems, which is critical for optimizing spintronic device performance. Building on our previous studies [1,2], which explored the effects of reduced dimensionality, strain, chemical doping, compensation temperature, spin reorientation temperature on spin transport, and thermo-spin transport in garnet systems, including $Y_3Fe_5O_{12}$ (YIG), $Gd_3Fe_5O_{12}$ (GdIG), and $Tm_3Fe_5O_{12}$ (TmIG), we will now investigate MPE and interface-related effects across the ordering temperatures in novel heterostructures composed of these REIG films and emerging 2D materials, such as YIG/2D-*M*/Pt, TmIG/2D-*M*/Pt, and GdIG/2D-*M*/Pt, with *M* = Gr, hBN, TMD, and α-$RuCl_3$. A comprehensive understanding of these effects will be key to developing new materials and discovering new functionalities for high-performance spintronic devices. In addition to studying single-phase ferrite systems (Fe_3O_4, $CoFe_2O_4$, $NiFe_2O_4$), we will explore phase-tunable iron oxide (BPIO: Fe_3O_4 and α-Fe_2O_3) films [3] as model systems to investigate the effects of phase coexistence, competing interactions, and phase transitions on interfacial magnetic coupling and the MPE.

Furthermore, we will examine how these factors influence spin transport and thermo-spin transport in iron oxide/2D-*M* systems. MnP, a novel helical magnetic system exhibiting an exotic magnetic phase diagram [4], will be explored as a substrate for growing functional materials like Fe, FeO, and Fe_3O_4. This will allow us to study the effects of interfacial coupling, MPE, and the Verwey transition on ferromagnetic and helimagnetic behaviors, GMR, and spin transport in MnP nanostructured films. Stacking MnP films with 2D magnets (e.g., V-doped WSe_2) will also be

explored to understand impacts of the 2D magnet on ferromagnetic and helimagnetic orderings and magneto-transport within the same MnP system.

We will also conduct comprehensive magnetic, spin transport, and thermo-spin transport studies on emergent Heusler alloys (e.g., CoFeMnGe, CoFeMnSi, CoFeCrAl, and CuNiCrAl), high-entropy alloys (HEAs) such as CoCrFeNiGa, as well as recently discovered altermagnetic systems (e.g., RuO_2 and MnTe). Other novel 2D vdW magnets (e.g., Fe_3GeTe_2, Fe_5GeTe_2) and exotic systems such as $Co_3Sn_2S_2$ - a topological Kagome magnet and Mn_2RhSn - a magnetic topological insulator that share common and distinct magnetic properties will also be investigated. These studies aim to provide new insights into the magnetic ground states, magnetic anisotropy, phase evolution, spin dynamics, and spin transport in these systems. Our research over the next three years will be focused on exploring and understanding the physics of interface magnetism, spin transport, and thermo-spin transport in the novel electron-correlated magnetic systems and heterostructures, which could broadly impact the development of spintronic devices and quantum computing technology.

References

1. A. Chanda, C. Holzmann, M. Albrecht, E.R. Rosenberg, C.A. Ross, M.H. Phan, and H. Srikanth, *Temperature evolution of magnon propagation length in $Tm_3Fe_5O_{12}$ thin films: Roles of magnetic anisotropy and Gilbert damping*, ACS Nano **18**, 7223 (2024).
2. A. Chanda, C. Holzmann, N. Schulz, J. Seyd, M. Albrecht, M.H. Phan, and H. Srikanth, *Scaling of the thermally induced sign inversion of longitudinal spin Seebeck effect in a compensated ferrimagnet: Role of magnetic anisotropy*, Advanced Functional Materials **32**, 2109170 (2021).
3. A. Chanda, D. DeTellem, Y.T.H. Pham, J.E. Shoup, A.T. Duong, R. Das, S.L. Cho, D.V. Voronine, M. Tuan Trinh, D.A. Arena, S. Witanachchi, H. Srikanth, and M.H. Phan, *Spin Seebeck effect in iron oxide thin films: Effects of phase transition, phase coexistence, and surface magnetism*, ACS Applied Materials and Interfaces **14**, 13468 (2022).
4. R.P. Madhogaria, C.M. Hung, B. Muchharla, A.T. Duong, R. Das, P.T. Huy, S.L. Cho, S. Witanachchi, H. Srikanth, and M.H. Phan, *Strain-modulated helimagnetism and magnetic phase diagram in highly crystalline MnP nanorod thin films*, Physical Review B **103**, 184423 (2021).

Publications

1. N. Mudiyanselage, D. Detellem, A. Chanda, A.T. Duong, T.E. Hsieh, J. Frisch, M. Bär, R. Madhogaria, S. Mozaffari, H. Arachchige, D. Mandrus, H. Srikanth, S. Witanachchi, and M.H. Phan, *Discovery of Giant Positive Magnetoresistance in Proximity to Helimagnetic Order in Manganese Phosphide Nanostructured Films*, ACS Applied Materials and Interfaces 2025 (published online: doi/10.1021/acsami.4c21202)
2. A. Chanda, J. Nag, N. Schulz, D. DeTellem, A. Alam, K. G. Suresh, M.H. Phan, and H. Srikanth, *Robust Nernst magneto-thermoelectricity in the topological spin semimetal FeCrRhX (X=Si,Ge)*, Physical Review B **111**, 094416 (2025).
3. A. Chanda, C. Holzmann, M. Albrecht, E.R. Rosenberg, C.A. Ross, M.H. Phan, and H. Srikanth, *Temperature evolution of magnon propagation length in $Tm_3Fe_5O_{12}$ thin films: Roles of magnetic anisotropy and Gilbert damping*, ACS Nano **18**, 7223 (2024).
4. A. Chanda, J. Nag, N. Schulz, A. Alam, K. G. Suresh, M.H. Phan, and H. Srikanth, *Large anomalous Nernst effect and its bipolarity in quaternary equiatomic Heusler alloys CrRuXGe (X = Co and Mn)*, Physical Review B **109**, 224415 (2024).
5. N. Schulz, G. Pantano, D. DeTellem, A. Chanda, E.M. Clements, M. McGuire, A. Markou, C. Felser, D.A. Arena, J. Gayles, M.H. Phan, and H. Srikanth, *Unravelling the Structural Dependency of Weyl nodes in Co_2MnGa*, Physical Review B **110**, 054419 (2024).
6. A. Chanda, C. Holzmann, N. Schulz, D. Stein, M. Albrecht, M.H. Phan, and H. Srikanth, *Thermally generated magnonic spin current in a polycrystalline gadolinium iron garnet thin film with perpendicular magnetic anisotropy*, Journal of Applied Physics **135**, 123901 (2024).

7. N. Schulz, G. Datt, A. Chanda, C.S. Ong, F. Songfrei, O. Eriksson, D. Voronine, T. Sarkar, V. Kamalakar, M.H. Phan, and H. Srikanth, *Surface Termination-Enhanced Magnetism at Nickel Ferrite/2D Nanomaterial Interfaces: Implications for Spintronics*, ACS Applied Nano Materials **6**, 10402 (2023).
8. A. Chanda, C.M. Hung, A.T. Duong, S. Cho, H. Srikanth, and M.H. Phan, *Magnetism and spin-dependent transport phenomena across Verwey and Morin transitions in iron oxide/Pt bilayers*, Journal of Magnetism and Magnetic Materials **568**, 170370 (2023).
9. C.M. Hung, D.T.X. Dang, A. Chanda, D. Detellem, N. Alzahrani, N. Kapuruge, Yen T. H. Pham, M.Z. Liu, D. Zhou, H.R. Gutierrez, D.A. Arena, M. Terrones, S. Witanachchi, L.M. Woods, H. Srikanth, and M.H. Phan, *Enhanced Magnetism and Anomalous Hall Transport through Two-dimensional Tungsten Disulphide Interfaces*, Nanomaterials **13**, 771 (2023).
10. V.O. Jimenez, Y.T.H. Pham, D. Zhou, M.Z. Liu, V. Kalappattil, T. Eggers, K. Hoang, D.L. Duong, M. Terrones, and M.H. Phan, *Transition Metal Dichalcogenides: Making Atomic-Level Magnetism Tunable with Light at Room Temperature*, Advanced Science **11**, 2304792 (2024).

Understanding and Controlling Light and Spin Dynamics in Chiral Hybrid Semiconductors

Lina Quan, Virginia Polytechnic Institute and State University

Keywords: Low-dimensional semiconductor, Hybrid perovskites, Chirality, Spintronics, Spin dynamics

Research Scope

Semiconductor spintronics aims to advance the evolution of next generation low-power electronics, information processing, communication and storage. In order for spintronic devices to fulfill the demands for high-speed, high-density and low-power electronic components, the innovations in materials design and processes are essential. The spin generation and manipulation in GaAs is feasible due to a strong spin-orbit coupling (SOC), however, the spin lifetime is relatively short. Whereas in graphene and diamond with weak SOC, longer spin lifetimes are observed. Materials possessing both strong SOC and prolonged spin lifetimes represent an ideal yet rare category for spintronic applications, offering an exciting prospect for the development of unconventional semiconductors. To fill this gap, this project will be subdivided into two tasks: (1) advancing new chiral hybrid organic inorganic semiconductor (HOIS) with tailored chiroptical properties, and (2) subsequently obtaining optical control and manipulation of spin dynamics without the need for an external magnetic field through ultrafast spectroscopy measurements. Achieving the objectives of this project requires a strong synergy between materials design and synthesis using a solution-processable approach and advanced characterization of optical and spin dynamics in the materials.

Recent Progress

Goal 1: Synthesis of hybrid single crystals and thin-films to study the impact of dielectric environment on excitonic properties.

The chiral HOISs often crystallize into low-dimensional structures due to the need to introduce chiral organic molecules. As a result, the charge conductivity is often reported to be low. However, to increase the functionality of chiral HOISs for spintronic or spin-optoelectronic applications, it is necessary to improve the charge conductivity. Additionally, low-dimensional HOISs often exhibit a large E_b at room temperature due to the small dielectric constant of organic molecules, making it difficult for excitons to form free carriers via thermal activation.[1] We hypothesize that adjusting the mismatch in dielectric constants between the organic and inorganic layers, along with varying the distance of the inorganic layer, could allow us to effectively control the E_b. Building on this exciting previous knowledge, we proposed to introduce chiral organic amines containing a hydroxy group with a relatively short linear carbon chain to further modify exciton properties.

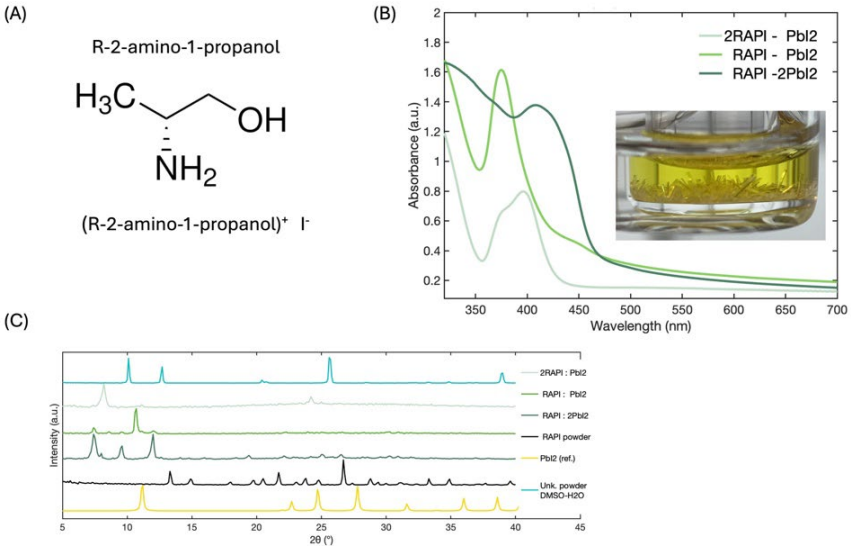

Figure 1. A) Chemical structure of the R-2-amino-1-propanol (RAP) ligand. B) Absorption spectrum of hybrid RAP-PbI2 structure with varied ratio. (inset – photo of synthesized single crystals. C) PXRD spectrum for the crystal made from varied ligand to PbI2 ratio.

We initially utilized R-2-amino-1-propanol (RAP), protonating it to form an iodide-based salt as a ligand for the self-assembly of lead iodide (PbI_2) in both thin-film and single-crystal forms. For thin-film synthesis, we optimized the precursor ratio, achieving a broad absorption feature (Figure 1B). PXRD measurements confirmed the formation of new hybrid structures through the self-assembly of PbI_2 with RAPI ligands (Figure 1C). We will be performing E_b measurement using temperature dependent absorption and PL measurement and extract the E_b in eV.

Goal 2: Impact of mixed chirality and chiral doping strategy in spin-relaxation process of HOISs.

To enhance the degree of polarization, we propose a strategy involving mixed chirality and chiral doping on chiral HOIS. This approach aims to increase polarization by introducing additional distortion and enhancing the DP (inversion symmetry) spin-relaxation mechanisms. Additionally, doping with extra chiral molecules could act as a passivation agent, reducing surface defects and potentially boosting polarization by suppressing EY spin-relaxation mechanisms. To validate this hypothesis, we investigated the impact of adding a chiral cation (THFA = R-tetrahydrofurfurylamine) to a chiral HOIS such as R-MBA_2PbI_4 known for its poor chiroptical activity.

We performed room-temperature spin lifetime measurements across various mixed cation ratios and found that when the ratio of R-MBA to R-THFA was 3:1, the spin lifetime exceeded 35 ps—five times longer than when THFA was the sole chiral ligand. To further investigate the spin polarization (degree of polarized exciton at excited state) mechanisms, we conducted biexciton spin-polarization measurements at temperatures as low as 2.5 K. We observed that the spin polarization ratio for the R-MBA:R-THFA (3:1) sample increased from 8% at room temperature to over 50% at 2.5 K. This finding suggests that the mixed cation strategy significantly influences both the generation of spin-polarized excitons and spin lifetime.

Goal 3: Control the spin-dynamics through spin-injection mechanisms in HOIS heterojunction.

The most promising category of HOIS for spintronic applications would be chiral bulk perovskites due to its low exciton binding energy and excellent charge transport. However, bulk perovskites face a challenge due to the incompatibility with chiral organic cations, constrained by the tolerance factor which dictates size mismatch. To address this limitation, we propose employing a spin-injection scheme to introduce an additional spin degree of freedom in bulk perovskites without relying on external magnetic fields. We hypothesize the spin-filtering and injection process will be feasible from low-dimensional chiral HOIS with large optical bandgap to the 3D perovskites with lower optical bandgap through compositional tuning between chiral organic amines and cesium cations.

We used quasi-2D chiral thin films as a model system to measure excited-state spin polarization and lifetime as an initial step toward validating our approach. Interestingly, beyond the carrier relaxation dynamics of the two phases (2D and 3D) in the quasi-2D sample—corresponding to absorption at 500 nm and 700 nm—we observed strong oscillations superimposed on the carrier dynamics. These oscillations were particularly pronounced in the spectral region corresponding to the absorption of both excitonic phases (2D and 3D).

We identified these oscillations as signatures of coherent phonons generated via resonant impulsive stimulated Raman scattering induced by a femtosecond laser. When the laser pulse duration is significantly shorter than the period of Raman-active low-frequency vibrations, the Raman interaction generates an impulsive force on the lattice, driving its coherent motion. By performing a Fourier transform of the oscillation period, we determined that the frequency ranges from 0.5 to 2 THz, which we associate with angular distortions of the inorganic octahedral framework (Figure 2).

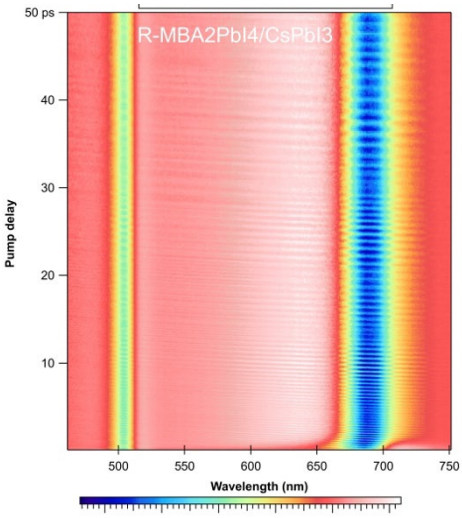

Figure 2. Spin-resolved pump-probe data from 2D/3D perovskite heterostructure at room temperature.

Based on these initial measurements, we hypothesize that chiral phonon modes generated in the 2D chiral perovskite (R-MBA$_2$PbI$_4$) propagate through the 2D/3D interface, leading to strong chiral phonon oscillations in the 3D CsPbI$_3$ perovskite. We believe the chiral phonon transfer take place within a semiconductor heterostructure, which may provide insight into spin transfer processes from high-bandgap chiral components to lower-bandgap non-chiral components.

Future Plans

We will continue to study the chiral induced optical and spin dynamics in HOIS. For more details: we aim to **(1)** diverse the chiral HOIS structures and systematically investigate the impact of dielectric confinement and the effect of inorganic coordination environment to the chiroptical properties and optical control of spin-dynamics; **(2)** employing circularly polarized non-linear optical measurements to enable us to mitigate the effects of defect-induced processes and accurately examine spin-polarization chiroptical activities—a challenging task with conventional photoluminescence approaches; and **(3)** investigate optically accessed spin dynamics in chiral/non-chiral heterojunctions through ultrafast spin-resolved pump-probe spectroscopy to study the spin-filtering mechanisms.

Goal 1: Building on our preliminary research from Year 1, we plan to investigate how exciton binding energy (E_b) influences the chiroptical and spin-dynamic properties of chiral hybrid organic-inorganic semiconductors (HOISs). Using newly synthesized materials, we will perform circular dichroism (CD) and circularly polarized photoluminescence (CPL) measurements to evaluate the effect of exciton binding energy on chirality-transfer-induced chiroptical responses, specifically the dissymmetry factors (g_{CD} and g_{CPL}). To further explore exciton dissociation and free carrier generation, we will employ ultrafast transient absorption and/or reflection spectroscopy. These measurements will allow us to compare the excited-state carrier dynamics of HOISs with high and low E_b. We hypothesize that materials with lower exciton binding energy will exhibit enhanced exciton dissociation at room temperature, promoting the formation of free carriers.

Goal 2: We will continue our investigation of optically induced spin polarization and spin dynamics in chiral HOISs by systematically varying their composition through surface doping and passivation strategies. This approach will help us isolate and understand the contributions of different spin relaxation mechanisms. For instance, the Elliott–Yafet (EY) mechanism is sensitive to impurities and grain boundaries in thin films; the D'yakonov–Perel (DP) mechanism dominates in materials

lacking inversion symmetry; and the Bir–Aronov–Pikus (BAP) mechanism arises from electron–hole exchange interactions. To probe these effects, we will primarily utilize ultrafast spin-resolved pump-probe spectroscopy with circularly polarized pump and probe configurations.

Goal 3: Building on our initial observation of chiral phonon transfer from chiral to non-chiral HOIS, we will continue to investigate the underlying mechanisms of phonon transfer at the interface between two semiconductor heterostructures. We will conduct a systematic study to explore the relationship between chiral phonon transfer and optically induced spin generation and transfer across various types of heterostructures. By integrating spin-resolved pump-probe spectroscopy with theoretical insights into chiral phonon behavior, we aim to address critical knowledge gaps regarding the influence of chiral phonons on spin relaxation mechanisms in chiral HOIS.

References

1. Cheng, B.; Li, T.-Y.; Maity, P.; Wei, P.-C.; Nordlund, D.; Ho, K.-T.; Lien, D.-H.; Lin, C.-H.; Liang, R.-Z.; Miao, X., *Extremely reduced dielectric confinement in two-dimensional hybrid perovskites with large polar organics.* Communications Physics 2018, ***1*** (1), 80.

Publications

1. J. Kim, S. Ghosh, N. Smith, S. Liu, Y. Dou, C. Slebodnick, G. Khodaparast, J. Qian, L. Quan, *Synthetic control of water-stable hybrid perovskitoid semiconductors,* Advanced Materials 2024, **2406274**.

Building a Workforce in Nanomaterial Characterization and Solid-State Synthesis

PI: Sheena Reeves[1] Co-PI(s): Sunil Karna[1], Gururaj Neelgund[1], Jason Gardner[2], Thomas Ward[2]

1: Prairie View A&M University, Prairie View, TX 77446

2: Oak Ridge National Laboratory, Oak Ridge, TN 37830

Keywords: nanocomposites, solid-state synthesis, magnetic, characterization

Research Scope

Fundamental research in nanomaterial characterization and solid-state chemistry (NCSC) is important for developing foundational knowledge of the unique properties of nanomaterials. This knowledge serves as a basis for new theories and models which describe or predict nanoparticle behavior and interactions. Nanoparticle characterization helps to meet regulatory requirements and facilitates the development of safe and effective nanoparticle-based products. The basic understanding of solid-state chemistry will assist in training a workforce with the necessary background who can contribute to innovations in high performance nanomaterials and crystals such as semiconductors and insulators. The research scope includes research projects in four main areas of 1) non-centrosymmetric magnetic materials, 2) chiral magnetic oxides, 3) graphene and graphene-oxide metal ferrite nanocomposites, and 4) metal oxide nanocomposites.

Recent Progress

Non-centrosymmetric and centrosymmetric magnetic materials. $Ba_3V_2O_8$ (Barium Vanadate) is a non-centrosymmetric oxide material that belongs to the family of vanadates, providing a fascinating platform for studying the intricate interplay between structural, electronic, and magnetic properties. We have recently synthesized a high-quality polycrystalline sample of $Ba_3V_2O_8$, which crystallizes in the trigonal crystal system with the *R3m* space group. X-ray diffraction analysis confirms the phase purity of the sample. Detailed magnetic and transport measurements are planned for this summer at Oak Ridge National Laboratory (ORNL). In a separate project, we have synthesized a centrosymmetric material, $Li_2Ni_2TeO_6$, which crystallizes in an orthorhombic structure. Detailed magnetic measurements have already been performed in collaboration with our ORNL partners. Magnetic susceptibility data (Fig. 1) indicate that $Li_2Ni_2TeO_6$ undergoes magnetic ordering below approximately 75 K. A broad hysteresis is observed around 5 K, which diminishes and disappears by 80 K, suggesting that $Li_2Ni_2TeO_6$ exhibits ferromagnetic ordering below ~75 K. Neutron diffraction measurements are scheduled for this summer at ORNL, as beam time has been recently approved.

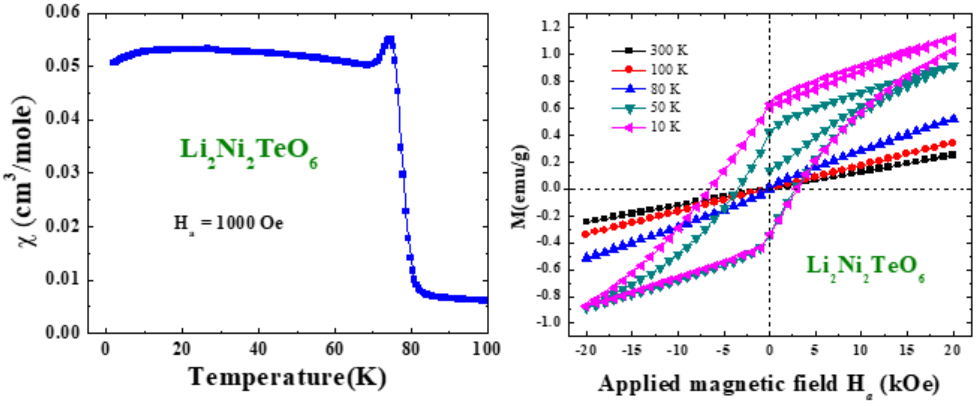

Fig. 1: Graph of the magnetic susceptibility of $Li_2Ni_2TeO_6$

Graphene and graphene-oxide metal ferrite nanocomposites. The preparation of graphene oxide (GO) has been achieved by using the following modified Hummers and Offeman method. Graphite powder (4g, <20 μm, Aldrich) was added to 160 mL concentrated H_2SO_4 and stirred for 1 hour under ice-cooling conditions. Then, 60 mL of fuming HNO3 was slowly added and stirred into the mixture for 30 minutes. To this, 20g of $KMnO_4$ was gradually added with stirring, and the resulting mixture was cooled at room temperature for 12 hours, followed by 600 mL DI water. After stirring the mixture for 30 minutes, 120 mL of H_2O_2 (30%) was slowly added, which turned the color of the reaction mixture to bright yellow. The resulting mixture was then centrifuged and washed with 1:10 HCl in water solution to remove metal ions. Further, the mixture was washed with DI water until the acids were removed entirely, and thus, a dark-yellow colored GO was obtained, which was dried under a vacuum at 40 °C for 12 hours. The drying process of GO was carried out at a lower temperature to avoid its deoxygenation.

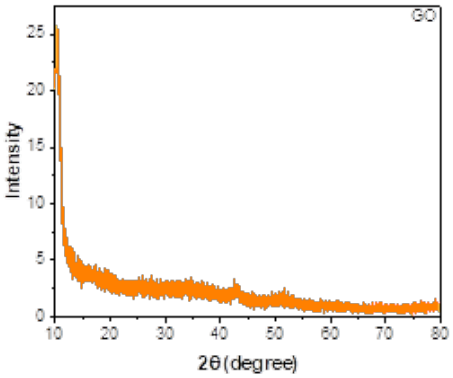

Fig. 2: XRD of graphene oxide.

To create nanocomposites, we preformed a deposition of $CoFe_2O_4$ nanoparticles over the surface of GO nanosheets. To prepare the *GO-$CoFe_2O_4$,* 500 mg of GO was dispersed in 25 mL of DI water by sonification. Next, a solution of 1 mmol of $CoCl_2$ in 25 mL of DI water was added to the mixture and stirred at room temperature for 15 minutes. To this mix, 2 mmol of $FeCl_3$ was added in 25 mL of DI water and stirred at room temperature for 15 minutes. Then, 5 mmol of NaOH in 25 mL of DI water was added to the mixture and stirred for 15 minutes. The obtained mixture was transferred into a Teflon-coated autoclave and heated at 180° C for 18 hours. The GO-$CuFe_2O_4$ nanocomposite was separated by centrifugation and purified by washing with DI water and ethanol.

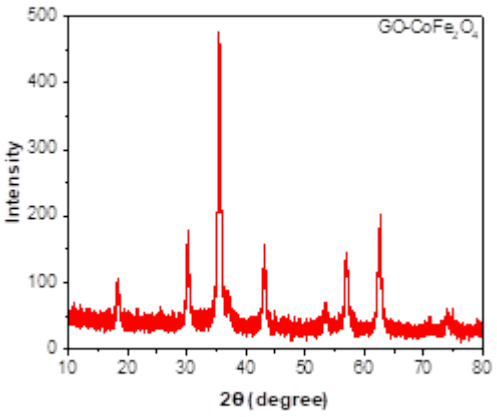

Fig. 3: XRD of GO-$CoFe_2O_4$.

The powder XRD of GO (Fig. 2) displayed the high intensity peak at 10.5° due to (001) plane of GO that corresponds to the typical major oxygen-containing structure [1]. The low intensity peak appeared at 42.7° is related to (100) plane and it indicates the presence of hexagonal carbon structure. In Fig. 3, the XRD of $CoFe_2O_4$ exhibited well resolved peaks at 18.2°, 30.7°, 35.4°, 43.1°, 53.9°, 57.1°, 62.6°, and 75.5° related to the (111), (220), (311), (400), (422), (511), (440), and (533) crystal planes of $CoFe_2O_4$, respectively (JCPDS card: 22-1086) [2].

Metal oxide nanocomposite synthesis. Metal oxides are utilized in many capacities including the development of sensors or biosensors, the creation of catalysts, and the remediation of soil. In terms of metal oxide-based nanoparticles, the synthesis method as well as the materials used during the synthesis process are a major focus as these selections impact the field of environmental sustainability**.** The initial research focus was the solid-state combustion synthesis of lithium tantalate ($LiTaO_3$) polycrystalline nanoparticles. To synthesis this material, lithium carbonate (Li_2CO_3) and lithium acetate ($LiCH_3CO_2$) were selected as precursors for a comparative study with tantalum oxide (Ta_2O_5) used as tantalum supply. Urea was selected as the fuel source. To optimize lithium tantalate synthesis, four parameters were varied – lithium precursor, reaction temperature, reaction time, and urea/precursor ratio.

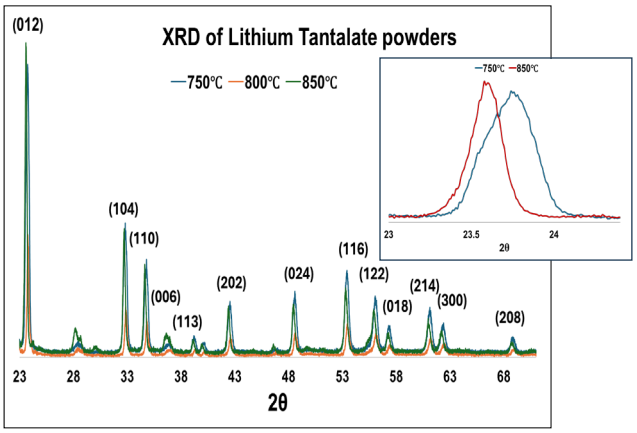

Fig.4 XRD of $LiTaO_3$.

Near stochiometric $LiTaO_3$ was successfully synthesized using solid state combustion method at a much lower temperatures as compared to typical solid-state synthesis temperature. No significant peak shift in XRD (Fig. 4) was observed with changing synthesis temperature even though slight narrowing of peak is observed which may indicate the formation of a larger crystalline size with additional temperature increase. In Fig. 5, DSC analysis shows two very distinctive peaks at 134 and 375˚C which are related to the endothermic reaction to convert the reactants to $LiTaO_3$. The peaks in Raman spectra (Fig. 6) has origin in various modes optical phonon vibrations. The peak around 141.7 $cm^{-}1$ is related to the composition of the material which is an E mode of phonon vibration. [3,4] The variation in urea-to-lithium precursor ratios revealed noticeable trends in particle morphology, size, and crystallinity based on spectroscopy and XRD results. As the fuel content increased in Fig. 7, combustion reactions became more vigorous, promoting better dispersion and energy distribution during synthesis.

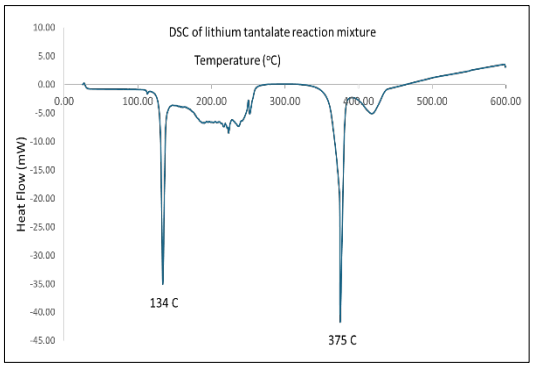

Fig.5 DSC of $LiTaO_3$.

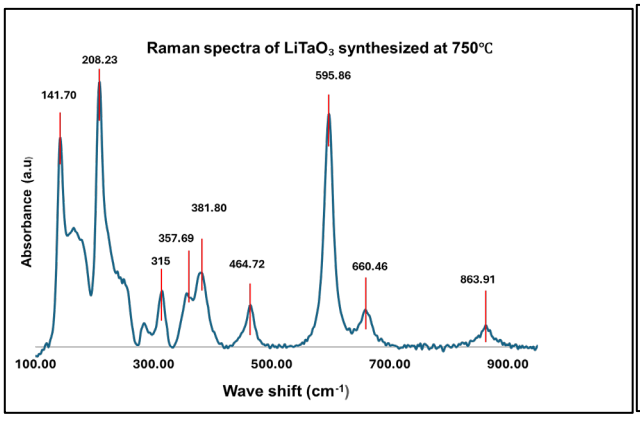

Fig.6 Raman spectra of $LiTaO_3$.

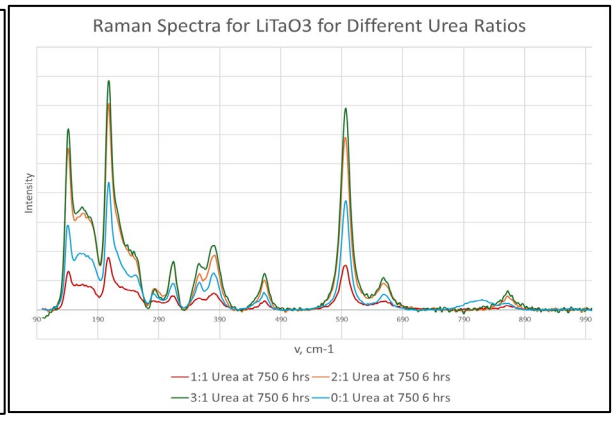

Fig.7 Effect of Urea Feed Ratio on $LiTaO_3$.

Future Plans

Future plans include 1) neutron diffraction measurements of magnetic and metal oxide materials, 2) additional synthesis and characterization of GO nanocomposites, and 3) synthesis of lithium tantalate using recycled lithium precursors, and 4) doping lithium tantalate with rare earth metals and other metal oxides.

References

1) G.M. Neelgund, A. Oki, S. Bandara, L. Carson, Photothermal effect and cytotoxicity of CuS nanoflowers deposited over folic acid conjugated nanographene oxid, J. Mater. Chem. B, **9,** 1792 (2021).
2) O. Gormez, E. Yakar, B. Gozmen, B. Kayan, A. Khataee, $CoFe_2O_4$ nanoparticles decorated onto graphene oxide and graphitic carbon nitride layers as a separable catalyst for ultrasound-assisted photocatalytic degradation of Bisphenol-A, Chemosphere, **288,** 132663 (2022).
3) Y. Zhu, S. Lin, Y. Liu, D. Ma and B. Wang, *Efficient Synthesis of Stoichiometric Lithium Tantalate Powder by a Solid-State Combustion Rout*e, Materials and Manufacturing Processes, **30:11**,1342-1347 (2015).
4) L. Shi , Y. Kong ,W. Yan , J. Sun, S. Chen, L. Zhang , W. Zhang , H. Liu , X. Li , X. Xie , D. Zhao, L. Sun, Z. Wang , J. Xua, and G. Zhang, *Determination of the composition of lithium tantalate by means of Raman and OH− absorption measurements,* Materials Chemistry and Physics, **95,** 229-234 (2006)

Spin-Dependent Quantum Phenomena in Heterostructures

Jing Shi, Department of Physics & Astronomy, University of California, Riverside

Keywords: spin transport in heterostructures, ferromagnet/heavy metal interface, antiferromagnet/2D quantum material interface, easy-plane magnetic films

Research Scope

This research project targets the exploration of spin transport and novel spin-dependent phenomena at interfaces within engineered spin heterostructures. We will investigate systems composed of magnetic insulator thin films (ferrimagnetic $Y_3Fe_5O_{12}$ (YIG); antiferromagnetic Cr_2O_3, α-Fe_2O_3) interfaced with heavy metals (Pt) or 2D quantum materials exhibiting broken mirror symmetry (e.g., Weyl semimetals 1T-WTe_2, 1T-$TaIrTe_4$).

A primary focus is understanding the efficient spin-charge interconversion across these interfaces, particularly the interplay between electronic spin currents generated via the spin Hall effect in the heavy metal/2D layers and magnonic spin currents within the magnetic insulators. We will also study magnon diffusion dynamics in the magnetic insulators. Furthermore, a key objective involves leveraging the unique properties of mirror symmetry-broken 2D quantum materials for local injection and detection of out-of-plane spin polarization, aiming to generate and probe the spin superfluid state—a particularly interesting quantum phenomenon—in 2D easy-plane magnetic systems, especially antiferromagnetic films where the dipolar interaction is weak.

To achieve these goals, high-quality epitaxial magnetic insulator thin films with desired magnetic properties (e.g., easy-plane magnetic anisotropy, low damping) will be synthesized using our established in-house pulsed laser deposition systems, complemented by exfoliation and transfer techniques for 2D materials, both developed in previous BES award periods. An integrated approach involving comprehensive material characterization (e.g., crystallinity, magnetic anisotropy, Dzyaloshinskii-Moriya interaction, exchange interaction) will provide crucial feedback for synthesis optimization. Nanofabrication processes will be employed to create tailored device structures for detailed investigations using techniques such as magnetotransport, spin Seebeck effect measurements, and nonlocal spin transport studies. These experimental efforts will be closely integrated with theoretical collaborations to provide deeper insights.

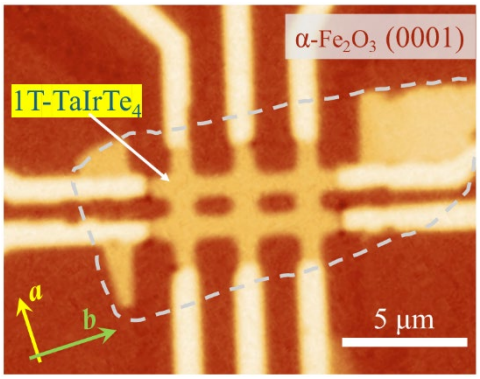

Fig. 1. Image of an etched 1T-phase $TaIrTe_4$ Hall bar devices on atomically flat easy-plane α-Fe_2O_3 film grown by PLD. $TaIrTe_4$ is a Weyl semimetal with broken mirror symmetry along the *a*-direction in the *ab*-plane. Longitudinal and Hall resistances can be measured with current passing in two orthogonal directions respectively. When a magnetic field rotates the Néel vector in the film plane, negative SMR is observed.

Recent Progress

Epitaxial Antiferromagnetic Thin Film Growth. Using in-house pulsed laser deposition (PLD) systems, we have achieved high-quality ultrathin films of Cr_2O_3 and α-Fe_2O_3 with atomic-level flatness and desired magnetic properties. By optimizing parameters such as laser power, repetition rate, substrate temperature, and O_2/O_3 pressure, we have established precise control over film quality, enabling systematic studies of antiferromagnetic (AFM) properties and providing needed magnetic component for constructing various spin heterostructures.

Morin Temperature Tuning and Anisotropic Field Suppression in α-Fe_2O_3. We have demonstrated tunable Morin temperatures (0–280 K) in epitaxial α-Fe_2O_3 films by varying film thickness, a significant advancement over the fixed 260 K in bulk crystals (R1). This tunability reflects transitions between high-temperature easy-plane and low-temperature easy-axis phases. In α-Fe_2O_3/Pt heterostructures, we investigated magnetic field suppression of the Morin temperature, revealing anisotropic behavior driven by the Dzyaloshinskii-Moriya (DM) interaction. The magnetic anisotropy energy density depends on the field orientation relative to the DM vector, allowing us to quantify DM interaction strength, which remains invariant across four orders of magnitude in thickness. This experimental-theoretical collaboration yielded a publication in *Physical Review Materials* (P1), advancing our understanding of DM interaction in AFM systems.

Antiferromagnetic Néel Vector Reversal. While external magnetic fields alone cannot reverse the AFM Néel vector, the DM-induced spin canting in bulk α-Fe_2O_3 crystal generates a net magnetic moment that couples to the field via Zeeman interaction. This coupling, combined with the chiral relationship between the canted moment and Néel vector, enables magnetic field-induced Néel vector reversal, which we demonstrated in our recent experiments using magneto-transport in α-Fe_2O_3/Pt heterostructures. Intriguingly, in Cr_2O_3/Pt heterostructures, we observed similar Néel vector reversal driven by a magnetic field alone, revealing a similar chiral relationship but here due to interfacial DM interaction (R2). This discovery complements our prior work on magnetoelectric switching in Cr_2O_3 (P2) and opens new avenues for Néel vector manipulation. Two manuscripts on field-induced Néel vector reversal in α-Fe_2O_3 and Cr_2O_3 are under preparation.

Spin Disorder Effects on Antiferromagnetic Magnon Transport. We explored the impact of controlled spin disorder on magnon transport in homoepitaxial Cr_2O_3 films grown on Cr_2O_3 bulk crystals. Using the spin Seebeck effect, we characterized spin-flop transition widths, identifying point defects (likely oxygen vacancies) as sources of spin disorder that scatter magnons from the underlying crystal. This pioneering study of spin disorder's effect on diffusive magnon transport resulted in a manuscript under review at *Physical Review Applied* (P3), offering insights into magnon dynamics for spintronic device design.

Spin Transport in Easy-Plane α-Fe_2O_3/$TaIrTe_4$ Heterostructures. In (0001)-oriented α-Fe_2O_3 films, the easy-plane Néel vector rotation produces negative spin Hall magnetoresistance (SMR) in heterostructures detected by heavy metals such as Pt and Ta. We replaced the heavy metals with exfoliated $TaIrTe_4$, a Weyl semimetal, forming α-Fe_2O_3/$TaIrTe_4$ heterostructures. Nanofabricated Hall devices (Figure 1) exhibited stable negative SMR, confirming high-quality interfaces essential for efficient spin injection. Magnetoresistance measurements with rotating fields in zx- and zy-planes revealed two-fold oscillations linked to out-of-plane spin polarization (R3), caused by broken mirror symmetry in $TaIrTe_4$. This is a critical step toward realizing spin superfluid states in AFM systems (R4). A manuscript is in preparation, and we are extending this work to out-of-plane spin injection in (111)-oriented YIG, an easy-plane ferrimagnet as demonstrated recently by us, using $TaIrTe_4$.

2D Ferromagnets and van der Waals Heterostructures. We investigated 2D ferromagnets (Fe_3GeTe_2, $Fe_5Ge_2Te_2$, $Cr_2Ge_2Te_6$, Fe_3GaTe_2), focusing on the layer-number dependence of anomalous Hall conductivity in the Fe-Ge-Te family. Down to a few layers, we found that the anomalous Hall and longitudinal conductivities follow a universal scaling law for 3D poorly conducting ferromagnetic metals, as reported in *Applied Physics Letters* (P4). Additionally, building on our prior work (R5) demonstrating spin-polarized quantum spin Hall edge states in monolayer-WTe_2/$Cr_2Ge_2Te_6$ heterostructures (exhibiting an anomalous Nernst effect), we are developing a WSe_2/graphene/$Cr_2Ge_2Te_6$ heterostructure to induce the quantum anomalous Hall effect. In our recent work in graphene/$Cr_2Ge_2Te_6$ devices, Shubnikov-de Haas oscillations revealed sizable spin splitting due to interfacial exchange interactions, with ongoing efforts to complete the full stack.

Future Plans

Our next research goal is to create and manipulate novel quantum states, such as spin superfluid and quantum anomalous Hall states, in spin heterostructures. The following tasks outline our research roadmap:

1. **Out-of-Plane Spin Injection into Easy-Plane Magnets:** We will optimize α-Fe_2O_3 and YIG thin films and interfaces with Weyl semimetal injectors (e.g., $TaIrTe_4$) to achieve robust injection of out-of-plane spin polarization. Using spin Hall magnetoresistance and second-harmonic Hall effects, we will quantify spin polarization and torque efficiency, iteratively improving material synthesis and interface quality to enable spin superfluid states in both magnetic films.

2. **Long-Distance Spin Transport in Easy-Plane Systems:** In nonlocal spin transport devices, we will study the spatial decay of out-of-plane spin polarization in easy-plane magnetic films, investigating the effects of engineered defects and spin disorder on long-range magnonic spin transport. This will enhance our understanding of spin dynamics in antiferromagnetic systems with spin disorder.

3. **Efficient Néel Vector Detection and Manipulation:** We will explore topological insulators (e.g., Bi_2Te_3) and Weyl semimetals (e.g., WTe_2, $TaIrTe_4$) as alternatives to heavy metals with larger anomalous Hall angles for sensitive Néel vector detection. Optimized fabrication methods will ensure high-quality interfaces to enhance Néel vector manipulation via spin-orbit torques, and we will systematically study magnetoelectric effects and interfacial DM interaction to manipulate Néel vector.

4. **Advancing van der Waals Heterostructures for Quantum Anomalous Hall Effect:** We will address fabrication challenges in graphene/WSe_2/$Cr_2Ge_2Te_6$ heterostructures to demonstrate the quantum anomalous Hall effect. Emphasis will be placed on maintaining pristine interfaces to maximize spin-orbit and exchange interactions which lead to robust quantum anomalous Hall effect.

References

R1. F. J. Morin, *Magnetic susceptibility of α-Fe_2O_3 and α-Fe_2O_3 with added titanium*, Phys. Rev. **78**, 819 (1950).

R2. Md. Rakibul Karim Akanda, In Jun Park, and Roger K. Lake**,** *Interfacial Dzyaloshinskii-Moriya interaction of antiferromagnetic materials.* Phys. Rev. B 102, 224414 (2020).

R3. Y. Zhang, Hongjun Xu, Ke Jia, Guibin Lan, Zhiheng Huang, Bin He, Congli, Qiming Shao, Yizhan Wang, Mingkun Zhao, Tianyi Ma, Jing Dong, Chenyang Guo, Chen Cheng, Jiafeng Feng, Caihua Wan, Hongxiang Wei, Youguo Shi, Guangyu Zhang, Xiufeng Han, and Guoqiang Yu, *Room temperature field-free switching of perpendicular magnetization through spin-orbit torque originating from low-symmetry type II Weyl semimetal.* Sci. Adv. **9**, eadg9819 (2023).

R4. S. Takei, B. I. Halperin, A. Yacoby, and Y. Tserkovnyak, *Superfluid spin transport through antiferromagnetic insulators.* Phys. Rev. B **90**, 094408 (2014).

R5. Junxue Li, Mina Rashetnia, Mark Lohmann, Jahyun Koo, Youming Xu, Xiao Zhang, Kenji Watanabe, Takashi Taniguchi, Shuang Jia, Xi Chen, Binghai Yan, Yongtao Cui, and Jing Shi, *Proximity-magnetized quantum spin Hall insulator: monolayer 1T' WTe_2/$Cr_2Ge_2Te_6$.* Nat. Comm. **13**, 5134 (2022).

Publications

P1. Haoyu Liu, Hantao Zhang, Josiah Keagy, Qinwu Gao, Letian Li, Junxue Li, Ran Cheng, and Jing Shi, *Anisotropic field suppression of Morin transition temperature in epitaxially grown hematite thin films.* Phys. Rev. Materi. **9**, 034410 (2025). DOI: 10.1103/PhysRevMaterials.9.034410.

P2. Wei-Cheng Liao, Haoyu Liu, Weilun Tan, Josiah Keagy, Jia-mou Chen, and Jing Shi, *Electrical Detection of Single-Domain Néel Vector Reorientation across the Spin-Flop Transition in Cr_2O_3 Crystals*. Nano Letters (under review).

P3. Josiah Keagy, Haoyu Liu, Junyu Tang, Weilun Tan, Wei Yuan, Sumukh Mahesh, Ran Cheng, and Jing Shi, *Disorder-Induced Suppression of Antiferromagnetic Magnon Transport in Cr_2O_3*. Phys. Rev. Appl. (under review).

P4. Mohammed Alghamdi, Palani R. Jothi, Wei-Cheng Liao, Sinisa Coh, Xianqing Lin, Boniface P. T. Fokwa, and Jing Shi, *Layer-dependence study of two-dimensional, ferromagnets: Fe_3GeTe_2 and $Fe_5Ge_2Te_2$*. Appl. Phys. Lett. **124**, 192404 (2024). DOI:10.1063/5.0207209.

P5. David Mayes, Farima Farahmand, Maxwell Grossnickle, Mark Lohmann, Mohammed Aldosary, Junxue Li, Vivek Aji, Jing Shi, Justin C. W. Song, and Nathaniel M. Gabor, *Mapping the intrinsic photocurrent streamlines through micromagnetic heterostructure devices*. PNAS **120**, e2221815120 (2023). DOI: 10.1073/pnas.2221815120.

Stimuli-Responsive Materials from Mesoscale Self-Assembly of Plasmonic and Quantum Nanoparticles

Ivan I. Smalyukh, University of Colorado at Boulder

Self-identify keywords: mesostructured materials, nanoparticles, colloids, self-assembly, optical properties.

Research Scope

This project focuses on understanding and control of self-assembly of anisotropic organic molecules and metal and semiconductor nanoparticles at the mesoscale, as well as on novel material behavior arising from their ordered self-organization and alignment. The design and realization of physical properties in these composites are based on the following three strategies: **(1)** discovery of new condensed matter phases of hybrid molecular-colloidal systems enriched by diversity of colloidal particle's geometric shapes, surface charging and boundary conditions for molecular alignment; **(2)** topology of continuous & singular field configurations in the molecular-colloidal systems; **(3)** effective medium behavior and plasmon-exciton interactions in colloidal assemblies formed by different types of nanoparticles co-assembled at mesoscopic scales. The main objective of this project's activities is to explore self-organization of pre-engineered anisotropic functional units into colloidal composites with ordered mesoscopic structures that can be tuned and switched by weak external stimuli, such as light and low-voltage electric fields. Tunable composite materials with interesting physical behavior are designed through integrating unique properties of solid nanostructures with the facile responses of soft matter to weak external stimuli. The fundamental studies of interactions and ordering of nanoparticles reveal underpinning physical mechanisms that guide mesoscale morphology and ultimately determine material properties of the self-assembled composites. Mesoscale self-assembly of anisotropic nanoparticles dispersed in responsive liquid crystalline host media is used to enable new composites with properties controlled by applying fields, changing temperature, and using other external stimuli. The focus is on fundamental understanding and control of nanoscale self-assembly and alignment of metal and semiconductor nanoparticles that enable new material behavior arising from orientationally and positionally ordered self-organization of anisotropic molecules and nanoparticles into tunable long-range structures. Electrical realignment of the liquid crystal host, like that used in displays, allows for rearrangement and reorientation of anisotropic nanoparticles, leading to an unprecedented control over self-assembled nanostructures and to dramatic changes in the material's emergent properties. The effective-medium optical properties are characterized and correlated with the hierarchical structure and composition of self-assembled configurations, as well as with plasmon-excition and other interactions separately studied at the level of individual nanoparticles. Within the project, experiments are conducted in parallel with analytical and numerical modeling of interactions and effective-medium optical properties, providing important insights. We explore how ensuing novel composite materials can be used to control transmission and directional scattering of light, as needed for applications in smart windows, displays and electro-optic devices. The research in this project broadly advances our knowledge of the nanoscale self-organization phenomena and the ensuing physical behavior, transcending the traditional disciplinary boundaries of physics, chemistry, engineering, and materials science.

Recent Progress

Recent progress in this our research project includes the demonstration emergent orthorhombic biaxiality in the nanocolloidal chiral nematics (*Nature Comm.* **15***, 9941 (2024)*) [1], characterization of dynamics of nemato-elastic multipoles (*PNAS* **121**, e2322710121 (2024)) [2], facile topological soliton (toron) re-configuration (*Scientific Reports* **15***, 2684 (2025)*) [3], and nanoparticle-induced symmetry breaking at mesoscale (*Phys. Rev. E* **111**, 045410 (2025)), among others, all demonstrating

new physical behavior in nanoparticle and molecular assemblies. Due to space constraints, we only describe the recent research findings that recently appeared in *Nature Communications* [1], where we demostrated the pre-designed metamaterial-like behavior by utilizing nanoparticle assembly in a chiral liquid crystal host medium.

We have developed unexpected states of matter that feature biaxial orientational order of colloidal supercritical fluids and gases formed by sparse rodlike or disclike nanoparticles (Fig. 1) [1]. Colloidal rods with perpendicular surface boundary conditions exhibit a strong biaxial symmetry breaking when doped into conventional chiral nematic fluids. Minimization of free energy prompts these particles to orient perpendicular to the local molecular director and the helical axis, thereby imparting biaxiality on the hybrid molecular-colloidal system. The ensuing phase diagram features colloidal gas and liquid and supercritical colloidal fluid states with long-range biaxial orientational symmetry, as supported by analytical and numerical modeling at all hierarchical levels of ordering (Fig. 2). Unlike for nonchiral hybrid systems, dispersions in chiral nematic hosts display biaxial orientational order at vanishing colloid volume fractions, promising both technological and fundamental research utility [1].

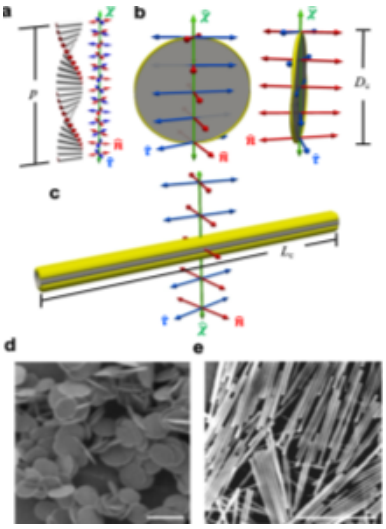

Fig. 1: Chiral hybrid liquid crystals. a Helical structure of a chiral nematic with helical pitch length p, with cylinders representing molecules and colored axes depicting the orthogonal cholesteric frame: molecular director (red), helical axis/director (green), and the third axis/director (blue) orthogonal to both. **b**, **c** Visualizations of a homeotropic (tending to orient perpendicular to the colloidal particle's surface) colloidal disk (**b**) and rod (**c**) immersed in a chiral LC at their equilibrium orientations. Colloidal particles are depicted in gray, and the yellow contours mark a director deviation of 0.67° (**b**) and 0.3° (**c**), respectively, of the numerically energy-relaxed LC structures from the ideal helical state indicated by the colored double arrows. For all simulations the anchoring at the colloid surface is homeotropic with strength $W_0 = 10^{-4}\mathrm{Jm}^{-2}$ (see "Methods" section). Typical disk diameter $D_c = 1$ μm and rod length $L_c = 1.7$ μm are more than one order of magnitude smaller than the pitch $p = 30$ μm of the chiral host LC. **d**, **e** TEM of synthesized disks and SEM of rods, scale bars 2 μm.

The most striking example of the observed emergent biaxiality is found for rods that tend to orient perpendicular to the local molecular director, imparting hierarchical biaxiality at molecular, colloidal, and structural levels of the hybrid colloid-molecular system (Fig. 2) [1]. At the colloidal subsystem level, a generic phase diagram spanning the colloid concentration, temperature, and chirality strength unexpectedly features colloidal gas and liquid states, both with an orthorhombic long-range orientational order interplaying with that of the chiral nematic host. Colloidal liquid-gas phase coexistence terminates in a gas-liquid type critical point located at a well-defined chiral strength of a molecular host (Fig. 2e, f).

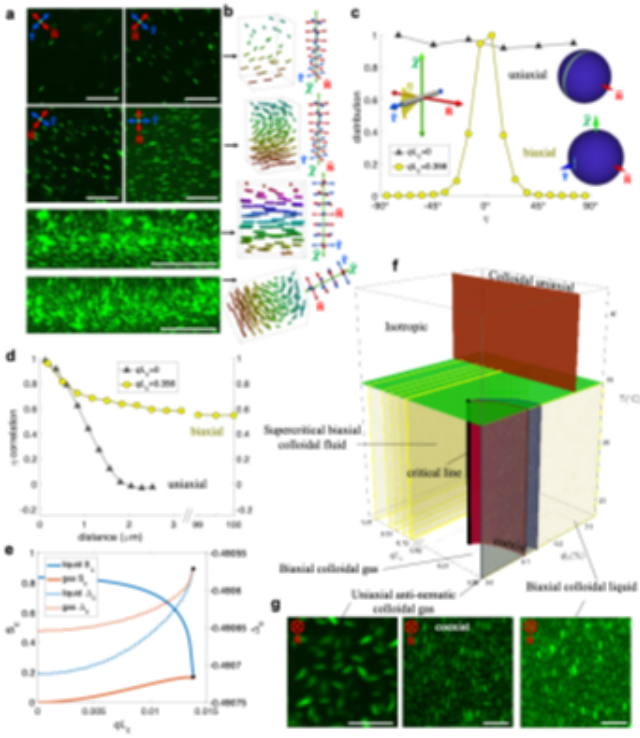

Fig. 2: Supercritical biaxial colloidal fluid. a Cross-sectional micrographs of chiral hybrid liquid crystal samples with colloidal rods rendered green. Images of helical arrangements of rods obtained for oblique viewpoints are shown at the bottom. Scale bars are 10 µm, pitch $p = 30$ µm and rod length $L_c = 1.7$ µm. **b** Schematic presentation of the supercritical biaxial colloidal fluids in (**a**) with rods colored by their orientations. The right-side insets show corresponding co-rotating frames. **c** Distributions of colloidal angles η, defined as the angle in - plane (left inset), measured for low-concentration rod dispersions in nematic (black triangle) or cholesteric (yellow circle), with $q = 2\pi/p$ being the wavenumber associated with molecular chirality. The corresponding orientation distributions of rods in the cholesteric frame are shown as insets on the right side. Colloidal particle concentration $\phi_c \ll 0.1\%$. **d** Corresponding rod angle η correlation function (1 for perfectly aligned and 0 for uncorrelated, see "Results" section) measured for the same pair of samples as in **c**, showing robust long-range correlations of colloidal orientations in cholesteric hosts at $qL_c = 0.356$. **e**, **f** colloidal S_c and Δ_c order parameters, quantifying the orientational order with respect to for coexisting phases of rod dispersions with perpendicular boundary conditions within the chiral LC host. The plots in (**e**) are order parameters quantified along the phase boundaries colored similarly in (**f**), up to the critical molecular chirality ($qL_c \approx 0.014$, marked black) beyond which the biaxial colloidal liquid and gas phases are no longer distinguishable. Temperature T, colloidal volume fraction ϕ_c, and scaled molecular chirality $qL_c = 2\pi L_c/p$. Our experiments have been performed for parameters corresponding to the yellow planes with $qL_c = 0$–1.07 and $\phi_c = 0$–0.35%. **g** Images of samples at $qL_c = 0$ showing an anti-nematic colloidal gas, gas-liquid coexistence, and a biaxial colloidal liquid phase, respectively. Scale bars are 5 µm.

Unlike the previously studied case of hybrid molecular-colloidal biaxial phases, we observed multi-level biaxial symmetry-breaking at ultralow colloidal content where colloid-colloid interactions are negligible. We uncovered a highly unconventional scenario in which the hybrid molecular-colloidal nature of the LC mixture along with the chirality of the molecular host generates strongly biaxial orientation order resulting in long-range ordered biaxial colloidal supercritical fluid states. Unlike in non-chiral hybrid molecular-colloidal LCs, where biaxial order emerges only at modest to high volume fractions of the anisotropic colloidal particles, above a uniaxial-biaxial transition critical concentration, the orientational probability distribution of colloidal inclusions immersed in chiral nematic hosts are unavoidably biaxial even at vanishingly low particle volume fractions [1], which yields new types of nanoparticle assembly.

Future Plans

Within the next year of this project, the focus will continue to be on developing stimuli-responsive materials. Our results [1,2] within the project pave the way towards controlled biaxial order in mesostructured matter. By harnessing the interplay of chiral and biaxial symmetries, future research efforts will be directed along the following emergent avenues. At larger colloidal concentrations a richer phenomenology could be expected and explored due to the more prominent roles expected to be played by steric, electrostatic or defect-mediated colloid-colloid interactions further enriching the surface anchoring and elastic forces discussed here. Besides the emergent symmetry breaking, we will also apply electric or magnetic fields to reconfigure either molecular or colloidal sub-systems, or

both, to achieve even lower externally induced symmetries, for instance, corresponding to triclinic or monoclinic point groups. Finally, by realizing topological solitons in the molecular-colloidal hybrid system with nontrivial chirality and biaxiality, we will probe the stability of topological structures for various low-symmetry order parameter spaces. While ferromagnetic colloidal particle dispersions have already provided insight into the possibility of formation of solitons in polar chiral liquid crystals, this study will be now extended to symmetries differing from nonpolar and polar uniaxial liquid crystals by exploring multi-dimensional solitonic structures corresponding to the SO(3)/D2 order parameter space. Our mesostructured designs will combine properties of solid nanostructures (quantum dots and plasmonic nanoparticles) and facile responses of soft matter, along with emergent new behavior enabled by various aspects of topology in the order parameter fields. Using LC materials and its mixtures doped with magnetically monodomain colloidal platelets, PI will explore topological transformations between different phases. Other nanoparticles will include mesoporous silica nanorods and nanoplatelets recently successfully synthesized on our group, which appear to be ideal for exploring the phase behavior. In-depth studies will reveal how mesoscale self-organization, which can yield centimeter-large mono-crystals of colloidal nanoparticles with tunable center-to-center separations, leads to new physical behavior and material properties arising from a combination of unique properties of nanoparticles and structural organization at nanometer to macroscopic scales. Effective medium properties of pre-engineered metamaterials will be studied. By exploiting unique properties of solid nanostructures, PI intends to develop a new breed of composites with novel physical behavior, pre-engineered properties, and facile response to external fields. For example, PI's preliminary studies already show that mesostructured composites made of perovskite quantum nanoparticles dispersed in thermotropic nematics can exhibit ultra-strong responses to light and electric fields; this work will be now systematically extended to different particle sizes and geometric shapes, including chiral host media for nanoparticle assembly.

Publications within the last 2 years (DE-SC0019293):

1. J.-S. Wu, M.T. Lzaro, H. Mundoor, H. H. Wensink & I. I. Smalyukh. Emergent biaxiality in chiral hybrid liquid crystals. *Nature Comm.* **15**, 9941 (2024).
2. J.-S. Wu, R.A. Valenzuela, M.J. Bowick and I.I. Smalyukh. Topological Rigidity and Non-Abelian Defect Junctions in Chiral Nematic Systems with Effective Biaxial Symmetry. *Phys. Rev. X* **15**, 021036 (2025).
3. B. Senyuk, J-S. Wu and I. I. Smalyukh. Out-of-equilibrium interactions and collective locomotion of colloidal spheres with squirming of nematoelastic multipoles. *PNAS* **121**, e2322710121 (2024).
4. G.N. C. Amaral, H. Zhao, M. Sedahmed, T. Campante, I.I. Smalyukh, M. Tasinkevych, M. M. Telo daGama & R. C. V. Coelho. Liquid crystal torons in Poiseuille-like flows. *Scientific Reports* **15**, 2684 (2025).
5. J.-S. Wu, M. T. Lázaro, S. Ghosh, H. Mundoor, H. H. Wensink and I.I. Smalyukh. Unavoidable multilevel biaxial symmetry breaking in chiral hybrid liquid crystals. *Phys. Rev. E* **111**, 045410 (2025)
6. C. Meng, J.-S. Wu, Z. Kos, J. Dunkel, C. Nisoli and I. I. Smalyukh. Emergent dimer-model topological order and quasi-particle excitations: Combinatorial vortex lattices, *Phys. Rev. X* **15**, XW10857 (2025).
7. C. L. Bassani, I.I. Smalyukh *et al.* Nanoparticle Assemblies: Current Advances and Open Problems. *ACS Nano* **18**, 14791-14840 (2024).
8. B.P. Radka, T. Lee, I. I. Smalyukh, T. J. White. The association of structural chirality and liquid crystal anchoring in stabilized cholesteric liquid crystals. *Soft Matter* **20**, 1815-1823 (2024).
9. C. Meng, J.-S. Wu, and I. I. Smalyukh. Topological steering of light by nematic vortices and analogy to cosmic strings. *Nature Materials* **22**, 64-72 (2023).
10. H. Zhao, J.-S. B. Tai, J.-S. Wu, and I. I. Smalyukh. Liquid crystal defect structures with Möbius strip topology. *Nature Physics* **19**, 451–459 (2023).

Phase Transitions and Physical Behaviors in Metastable Multicaloric Materials

Shane Stadler, Louisiana State University, Department of Physics and Astronomy
Naushad Ali and Saikat Talapatra, Southern Illinois University, School of Physics

KEYWORDS: magnetocaloric materials, magnetostructural phase transitions, metastable phase generation, multicaloric properties, solid-state refrigeration, high-pressure synthesis

Research Scope

The objective of this project is to discover and explore new solid-state caloric materials, and to understand the origins of their physical behaviors including magnetocaloric effects, barocaloric effects, and transport properties. We explore new materials that exhibit magnetic or magnetostructural transitions near room temperature that form as a result of doping, thermal quenching, hydrostatic pressure (during measurement), and the application of pressure during synthesis, leading to metastable magnetostructural phases.

Recent Progress

A central goal of this project is to investigate magnetostructural behaviors in transition-metal-based compounds and study the related magnetocaloric and barocaloric properties. Materials exhibiting these phenomena are sought for future applications in solid-state cooling technologies operating from cryogenic to room temperatures. More specifically, we look to control, or induce, coupled magnetostructural transitions in materials near room temperature by, in addition to applying standard elemental substitution or doping techniques, creating metastable phases through thermal quenching or by employing high pressure during synthesis. The strategy of synthesizing materials under high pressure was hatched from the observed effects of applied hydrostatic pressure during measurement (i.e., not during synthesis) on the magnetic and structural phases in some systems. For example, applied hydrostatic pressure can reversibly shift magnetostructural transitions, or even cause them to form by forcing structural and magnetic transitions to coincide in temperature.[1] This process can result in large magnetocaloric or barocaloric effects (or both) but are temporary behaviors since the transitions return to their normal (standard pressure) temperatures when the hydrostatic pressure is removed. For barocaloric materials, the recovery of the initial state upon pressure release is required. However, a permanent shift and coupling of transitions are sought in the case of magnetocaloric materials.

In order to create a permanent, coupled magnetostructural transition, or to tune an existing one to occur near room temperature, elemental substitutions can be made in parent compounds that undergo separate (uncoupled) magnetic and structural transitions, forcing them to couple, such as that observed in the Cu-substituted magnetocaloric Heusler alloy, $Ni_2Mn_{1-x}Cu_xGa$.[2] In some cases, this strategy can dilute the magnetic species, and therefore reduce the effectiveness of the alloy as a magnetocaloric material.

As stated above, a strategy to *permanently* to shift, or induce, a magnetostructural transition in a ferromagnetic parent compound that undergoes structural and magnetic transitions (sometimes separated by hundreds of Kelvin) without changing the elemental composition is to generate a metastable phase by employing either thermal quenching or high-pressure synthesis. Such processes permanently alter the behaviors of the phase transitions and physical properties of the materials. An example in which this occurs is in the thermal quenching of Mn*TX* alloys, where *T* = Ni, Co, or Fe and *X* = Si or Ge. Mn*TX* alloys have been of great interest for solid-state cooling since they have been shown to exhibit large magnetocaloric effects (MCEs) and barocaloric effects (BCEs), and sometimes *both*.[1] In this comprehensive study, we have utilized high-pressure synthesis, thermal quenching, hydrostatic pressure (during measurement), atomic substitution, or combinations of these to generate metastable phases and couple magnetostructural transitions in the Mn*TX* systems MnCoGe, MnNiGe, and $Mn_{1-x}Co_xNiGe$.

In the case of MnCoGe, we employed high-pressure synthesis and studied its effects on the phase transitions (structural and magnetic) and associated magnetocaloric properties.[3] To ensure the starting materials were identical for each synthesis process, a large source sample was first melted multiple times and annealed under vacuum at 1100 °C for 12 h and then slowly cooled over 24 h. This source sample was then broken up into smaller portions to be used for variable synthesis conditions including slow-cooled and quenched from (all from 800 °C), labeled as SC_0 and RC_0. "SC" and "RC" in the labels stand for "slow-cooled" and "rapidly cooled," respectively. Thermal processing under high pressure was carried out using a cubic multi-anvil apparatus by Rockland Corp. The samples were annealed under pressures of 0, 1.2, 2.2, 3.5, and 6.0 GPa, labeled as RC_0, RC_1.2, RC_2.2, RC_3.5, and RC_6.0, respectively.

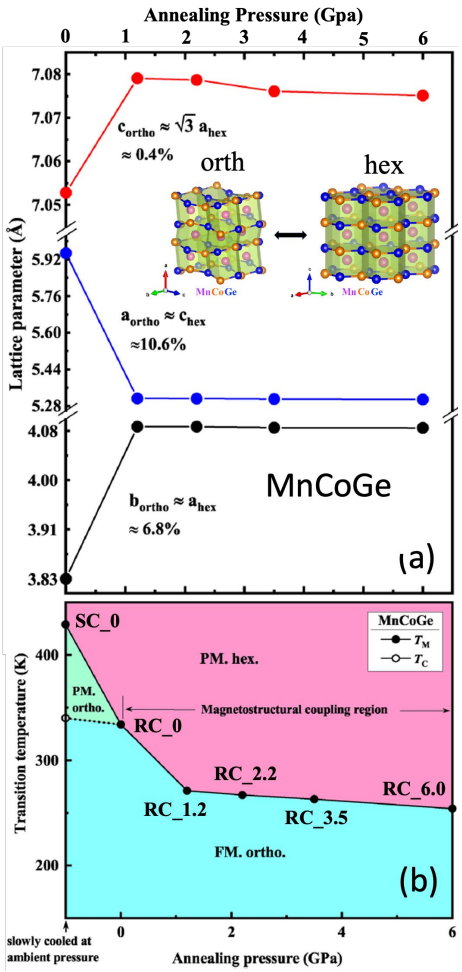

Fig. 1. (a) The room-temperature lattice parameters of MnCoGe determined from powder XRD at the indicated synthesis pressures (x-axis). The inset shows the structure change from the low-temperature TiNiSi orthorhombic to high-temperature Ni_2In hexagonal phases across the transition. **(b)** A magnetostructural phase diagram as a function of annealing pressure and temperature. Sample labels are described in text.

Figure 1(a) shows the room temperature lattice parameters calculated from x-ray diffraction data as a function of annealing pressure. Figure 2 displays the magnetization versus temperature and heat flow curves. As revealed in the heat flow curve (upper right corner of Fig. 2), the slow-cooled MnCoGe (SC_0) undergoes a structural transition from an orthorhombic to hexagonal phase at T_M = 450 K, and a ferromagnetic (FM)

transition at T_C = 350 K (i.e., they are uncoupled). The rapidly-cooled sample RC_0, however, is coupled at 350 K. The effects of high pressure are clearly observed in the curves for samples RC_0 through RC_6.0, i.e., the magnetostructural transition (MST) continually shifts to lower temperature and remains coupled. In the case of RC_1.2, the MST occurs at room temperature at which the magnetic entropy change (see the inset of Fig. 2) reaches 12 J/kgK for a field change of 7 T. A T-P magnetostructural phase diagram is shown in Fig. 1 (b) where the MST coupling region is seen to span an interval of about 80 K, including room temperature.

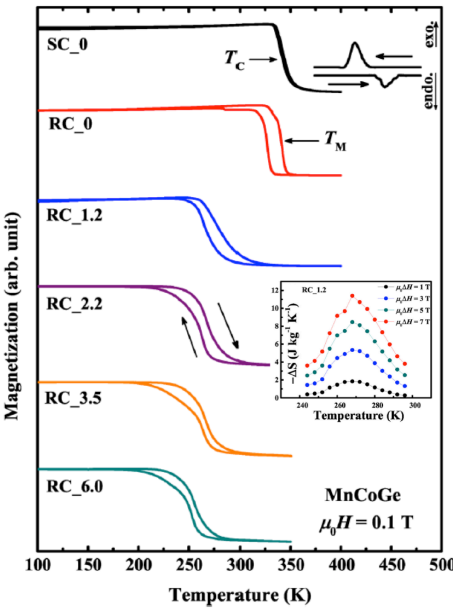

Fig 2. Magnetization as a function of temperature for slow-cooled (SC_0) and rapidly cooled samples at atmospheric pressure (RC_0) and at indicated pressures (RC_x.x) in GPA. Inset: magnetic entropy across the MST of RC_1.2.

It is interesting to compare this study on MnCoGe to another on the closely related Mn*TX* system, MnNiGe.[4] When this compound is annealed and slow-cooled, it undergoes a structural transition at T_M=474 K and a magnetic transition from a paramagnetic to spiral antiferromagnetic state at 350 K. We investigated the effects of thermal quenching and applied hydrostatic pressure (during measurement) on the transitions, both of which had the effect of decreasing the structural transition temperature and eventually coupling the transitions as seen in Fig. 3(a), where it clear that the structural transition shifts to lower temperature as the quenching temperature increases and couples just below 350 K for the sample quenched from 1200 ºC (i.e., AQ1200). Note in the same figure that the sample quenched at 1100 ºC (AQ1100) does not fully couple. However, this sample can be made to temporarily couple with the application of a hydrostatic pressure of about 9 kbar as seen in Fig. 3(b), where it couples at room temperature. This illustrates the effects of applying two concurrent methods to couple transitions in systems that normally do not exhibit magnetostructural transitions: i.e., quenching followed by the application of hydrostatic pressure in this case.

Finally, a third study combined atomic substitution and high-pressure synthesis to couple magnetic and structural transitions in Co-doped MnNiGe, i.e., $Mn_{1-x}Co_xNiGe$ (x = 0.05. and 0.08).[5] For x = 0.08, high pressure annealing at P = 3.5 GPa followed by rapid cooling resulted in a coupled transition at 240 K with a magnetic entropy change of –80 J/kgK, and the combination of varying the doping level and synthesis pressure allowed for a tuning of the transitions from above room temperature to 240 K.

These three projects illuminate some of the underlying physics of magnetostructural transitions and illustrate the utility of combinations of tactics: HP synthesis, quenching, hydrostatic pressure, and doping.

Future Plans

Our future projects include investigating four topic areas. The first topic is the synthesis and exploration of recently theoretically predicted all-*d*-Heuslers for both magnetocaloric effects and permanent magnets.[6] The second area is in Mn*TX* alloys, where the usual *T* and *X* elements are *T* = Ni, Co, or Fe and *X* = Si or Ge. In addition to these, however, we will study new materials theoretically predicted in a high-throughput theory work that identified new materials in this family for solid-state caloric properties and other energy applications.[7] In a third project, we will explore the physical behaviors of Mn_3XC-based alloys (synthesized through ball milling) that undergo magnetostructural transitions using two strategies: isoelectronic substitution for Ga, and doping on the Mn site. Finally, in the fourth project we will investigate the magnetocaloric properties of Cr_xTe_y-based 2-D van der Waals ferromagnets.

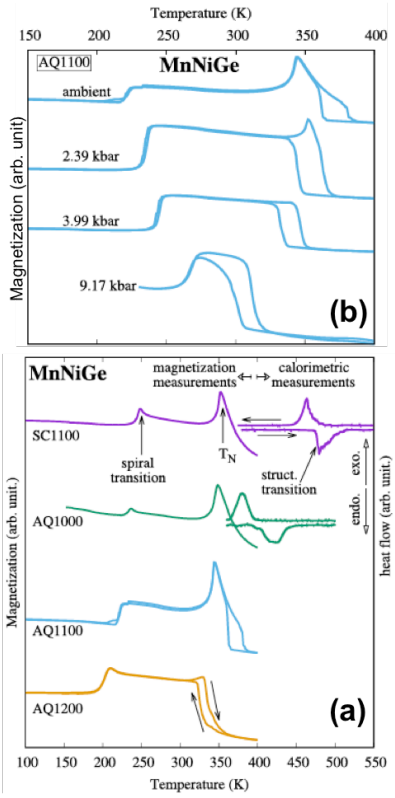

Fig. 3 (a) The magnetization of MnNiGe as a function of temperature and quenching temperature (i.e., SC1100 was slow-cooled from 1100 °C, and AQ1000 was quenched from 1000 °C, etc.). (b) The magnetization of sample AQ1100 as a function of applied hydrostatic pressure.

References

[1] T. Samanta, D.L. Lepkowski, A. Saleheen, A. Shankar, J. Prestigiacomo, I. Dubenko, A. Quetz, I. W. H. Oswald, G. T. McCandless, J. Y. Chan, P. W. Adams, D. P. Young, N. Ali, and S. Stadler, *Hydrostatic pressure-induced modifications of structural transitions lead to large enhancements of magnetocaloric effects in MnNiSi-based systems,* Phys. Rev. B **91**, 020401(R) (2015).

[2] S. Stadler, M. Khan, J. Mitchell, N. Ali, A. M. Gomes, I. Dubenko, A. Y. Takeuchi, and A. P. Guimarães *Magnetocaloric properties of* $Ni_2Mn_{1-x}Cu_xGa$, Appl. Phys. Lett. **88**, 192511 (2006).

[3] T. P. Chhetri, J-H. Chen, D. P. Young, I. Dubenko, S. Talapatra, N. Ali, and S. Stadler, *The effects of high-pressure annealing on magnetostructural transitions and magnetoresponsive properties in stoichiometric MnCoGe,* J. Appl. Phys. **135**, 215101 (2024)

[4] J-H. Chen, T. P. Chhetri, A. T, Grant, X. Bai, Q. Zhang, C-K. Chang, D. P. Young, I. Dubenko, S. Talapatra, N. Ali, and S. Stadler, *Controlling phase transitions in MnNiGe using thermal quenching and hydrostatic pressure*, J. Phys. D: Appl. Phys. **57** (2024) 205003

[5] T. P. Chhetri, J.-H. Chen, A. T. Grant ; D. P. Young, I. Dubenko, S. Talapatra, N. Ali, and S. Stadler, *Enhanced magnetocaloric effects in metastable phases of* $Mn_{1-x}Co_xNiGe$ *generated through thermal quenching and high-pressure annealing*, J. Appl. Phys. **133**, 065104 (2023)

[6] N. M. Fortunato, X. Li, S. Schönecker, R. Xie, A. Taubel, F. Scheibel, I. Opahle, O. Gutfleisch, and H. Zhang, *High-Throughput Screening of All-d-Metal Heusler Alloys for Magnetocaloric Applications*, Chem Mater. **36**, 6765 (2024)

[7] N. M. Fortunato, A. Taubel, A. Marmodoro, L. Pfeuffer, I. Ophale, H. Ebert, O. Gutfleisch, and H. Zhang, *High-Throughput Design of Magnetocaloric Materials for Energy Applications: MM′X alloys*, Adv. Sci. **10**, 2206772 (2023)

Publications

A. Oli, I. Dubenko, A. Granovsky, R. Razhabov, M. Hill, Yu. Koshkid'ko, S. Stadler, N. Ali, and S. Talapatra, *Effects of carbon substitution on magnetic properties and magnetocaloric effects in* $Mn_{65-x}Ga_{17}C_{18+x}$ *compounds*, J. Alloy Cmpds. **1017,** 179036 (2025)
[doi.org/10.1016/j.jallcom.2025.179036]

J-H. Chen, T. P. Chhetri, A. T, Grant, X. Bai, Q. Zhang, C-K. Chang, D. P. Young, I. Dubenko, S. Talapatra, N. Ali, and S. Stadler, *Controlling phase transitions in MnNiGe using thermal quenching and hydrostatic pressure*, J. Phys. D: Appl. Phys. **57** (2024) 205003 [doi.org/10.1088/1361-6463/ad297f]

T. P. Chhetri, J-H. Chen, D. P. Young, I. Dubenko, S. Talapatra, N. Ali, and S. Stadler, *The effects of high-pressure annealing on magnetostructural transitions and magnetoresponsive properties in stoichiometric MnCoGe,* J. Appl. Phys. **135**, 215101 (2024) [doi: 10.1063/5.0204371]

I. Dubenko, A. Oli, J. Duncan, A. Granovsky, R. Razhabov, M. Hill, Yu Koshkid'ko, S. Stadler, S. Talapatra, and N. Ali, *Magnetic properties of B doped Mn-Ga-C based alloys*, J. Magn. Magn. Mater. **595**, 171505 (2024) [doi.org/10.1016/j.jmmm.2023.171505]

J.-H. Chen, T. P. Chhetri, N. Wrobel, X. Bai, D. P. Young, I. Dubenko, S. Talapatra, N. Ali, S. Stadler, *Phase transitions in the Co-doped Heusler alloy* $Ni_2Mn_{1-x}Co_xGa$, J. Appl. Phys. **136**, 233901 (2024) [doi.org/10.1063/5.0226767]

T. P. Chhetri, J.-H. Chen, A. T. Grant ; D. P. Young, I. Dubenko, S. Talapatra, N. Ali, and S. Stadler, *Enhanced magnetocaloric effects in metastable phases of* $Mn_{1-x}Co_xNiGe$ *generated through thermal quenching and high-pressure annealing*, J. Appl. Phys. **133**, 065104 (2023) [doi.org/10.1063/5.0129401]

*One other publication has been submitted for publication and two others are in preparation.

Spin Functionality at Interfaces through Complex Oxide Heteroepitaxy

PI: Yuri Suzuki
Department of Applied Physics, Stanford University

Keywords: spin current, low magnetic loss, complex oxide thin films

Research Scope

The main research objective of our program is to develop a new class of low damping complex oxide thin films and heterostructures with perpendicular magnetic anisotropy (PMA) for isotropic spin wave excitation and propagation in the plane of the film combined with efficient spin wave control. Our focus has been on low damping ferro(i)magnetic insulators (FMI) which efficiently supports spin current without charge flow that gives rise to power dissipation. We have brought our materials expertise in atomic scale synthesis of complex oxide thin films and heterostructures and our recent discovery of spinel ferrite thin films with low magnetic damping: (i) to develop an understanding of the key factors that govern spin current behavior – generation, propagation and modulation and (ii) to demonstrate the role of epitaxial strain and composition on the isotropic and efficient excitation of spin waves. More specifically, we have chosen to study low damping spinel ferrite thin films based on L=0 Fe^{3+} cations placed \ in $Li_{0.5}(Al,Fe)_{2.5}O_4$ thin films and heterostructures. We have interfaced these films with strongly spin-orbit coupled layers in heterostructures to study spin-orbit torque switching and spin-to-charge interconversion.

Recent Progress

Highlights of recent work include (i) the compositional study of lithium aluminum ferrite $Li_{0.5}(Al,Fe)_{2.5}O_4$ films with extremely low damping and in-plane to perpendicular magnetic anisotropy, (ii) demonstration of spin-orbit torque switching in spinel ferrite films based heterostructures with a heavy metal and (iii) efficient spin current transport at interfaces with and without interfacial disorder. Additional highlights include (i) demonstration of emergent anti-ferromagnetism in ultra-thin $LaNiO_3$ films, (ii) emergent ferromagnetism in (111) $CaMnO_3/CaRuO_3$ superlattices and magnetotransport in Cr_2O_3 films.

Ultra-Low-Loss Epitaxial Spinel Ferrite Films with Magnetic Anisotropy Tuned by Epitaxial Strain. [i,ii,iii] We have demonstrated ultra-thin FMIs with PMA in the form of epitaxial $Li_{0.5}AlFe_{1.5}O_4$ films on $MgGa_2O_4$ substrates. They support the manipulation and isotropic propagation of spin waves in the absence of dissipative charge currents, providing a new paradigm for energy efficient spin-based computing and memory. More recently, we have explored the role of epitaxial strain and chemical doping in the performance of lithium ferrite thin films with respect to spin wave generation, propagation and control. Careful aluminum doping of lithium ferrite has shown that we can systematically modify the magnitude of

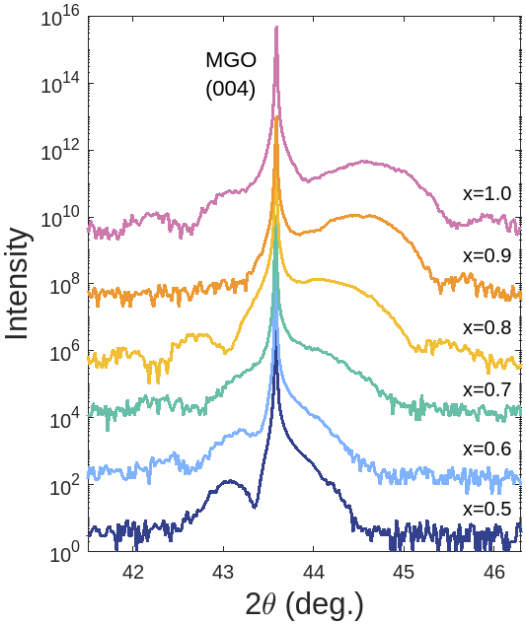

Figure 1. X-ray diffraction spectra of $Li_{0.5}(Al,Fe)_{2.5}O_4$ films on (001) $MgGa_2O_4$ substrates shows a range of aluminum doping.

epitaxial tensile strain in the films. Figure 1 shows x-ray diffraction spectra of a series of $Li_{0.5}(Al_xFe_{2.5-x})O_4$ (LAFO) films on $MgGa_2O_4$ substrates. The epitaxial strain correlates with the degree of Al substitution that shrinks the overall lattice parameter of the spinel ferrite. Al^{3+} substitution for Fe^{3+} ions also suppresses the saturation magnetization (Figure 2(a)) while maintaining excellent epitaxy and crystalline quality. Magnetic anisotropy also varies from in-plane in x=0.5 to out-of-plane in x=1.0 (Figure 2(b)). Ferromagnetic resonance measurements of these films confirm the evolving magnetic anisotropy and also show low magnetic damping from 1.5 - 10 x 10^{-4}. Our studies indicate that magnetic damping reaches a minimum when the magnetic anisotropy is minimized. All of these films form excellent interfaces with adjacent spin-to-charge conversion layers. To date, studies of FMI thin films with low damping and PMA have largely focused on garnet structure ferrite films [1-5]. However they suffer from difficulty in integrating with materials other than garnet structure materials, high deposition temperatures, high external field requirements and a magnetic dead layer at the film-substrate interface due to interdiffusion.

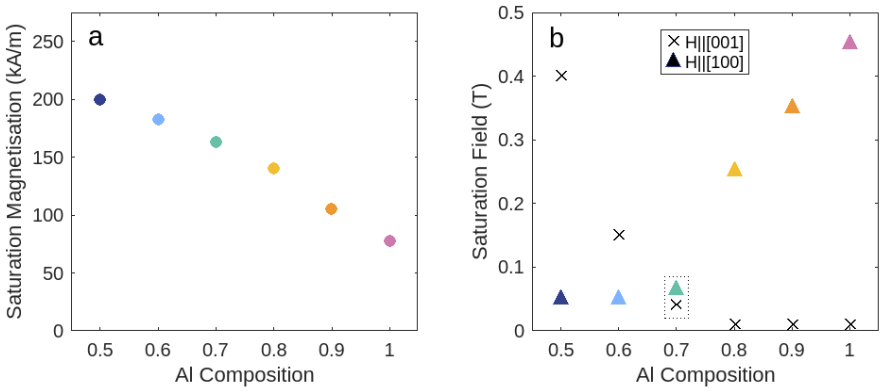

Figure 2. (a) Saturation magnetization of $Li_{0.5}Al_xFe_{2.5-x}O_4$ films on (001) $MgGa_2O_4$ substrates for a range of x values at room temperature; (b) saturation field shows in-plane to out-of-plane magnetic anisotropy.

Spin-Orbit Torque Switching of Lithium Aluminum Ferrite Thin Films. [i] Efficient switching of the magnetic state of our spin wave material with an electrical current is a key accomplishment for their incorporation into applications. To this end, spin-orbit torque switching of ferromagnets via an adjacent spin-to-charge conversion layer has been extensively studied. The analysis is complicated by current shunting through the ferromagnet if it is a metal. But in the case of FMI, the analysis is straightforward. We have demonstrated spin-orbit torque switching in LAFO/Pt bilayers where Pt is the spin-to-charge conversion layer. In contrast to the garnet/Pt bilayers, our spinel/Pt bilayers can be grown epitaxially and therefore improve the interface quality. Figure 3 shows how we can demonstrate the switching of the magnetic state of the LAFO film by monitoring the Hall resistance in the Pt layer which exhibits an anomalous Hall signal due to its proximity to the LAFO. An in-plane helper field is needed to break the symmetry of the switching. The larger the helper field is the smaller critical current density needed in the Pt layer. These values of the critical current density are an order of magnitude or more smaller than demonstrated in other systems.

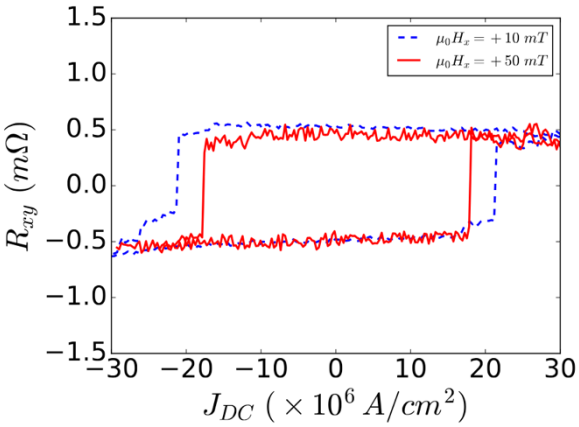

Figure 3. Hall resistance measured as a function of electrical current through the Pt layer in a LAFO/Pt bilayer is indicative of the magnetic state of the LAFO layer. A larger in-plane helper field reduces the critical current density for switching.

(111) Lithium Aluminum Ferrite Thin Films.[ix] In order to achieve more isotropic spin wave propagation in the plane of the film, we focused on the synthesis of (111) oriented LAFO films on

(111) $MgAl_2O_4$ substrates. We realized smooth epitaxial films with bulk saturation magnetization values. Damping values were consistently higher than their (001) counterparts, albeit with lower magnetic anisotropy. The low magnetic anisotropy is confirmed both by static SQUID magnetometry as well as ferromagnetic resonance measurements. Static and dynamic magnetic properties are found to be isotropic in the in-plane directions.

Emergent Antiferromagnetism in Ultra-thin (111) $LaNiO_3$ Films. [v] Another major accomplishment has been the discovery of emergent antiferromagnetic order in ultra-thin metallic (111) $LaNiO_3$ films. This discovery is surprising given that $LaNiO_3$ exhibits metallic, paramagnetic behavior at all temperatures in the bulk. We stabilize AFM ground states in ultra-thin films of (111) $LaNiO_3$ with both insulating and metallic behavior depending on thickness. In metallic films, a nonlinear, hysteretic anomalous Hall effect (AHE) emerges with temperature-dependence indicating multiple complex long-range magnetic orders. Using low energy muon spin resonance, we directly probe the magnetic fields within (111) $LaNiO_3$, revealing that the entire film is magnetically ordered below T = 50 K. Theoretical calculations are consistent with these results, indicating that distortions induced by (111) epitaxy stabilize AFM in (111) $LaNiO_3$, highlighting a new approach to stabilizing novel AFM states in complex oxides.

Emergent Ferromagnetism in (111) $CaRuO_3/CaMnO_3$ superlattices. [vi,vii] Our success in stabilizing the (111) orientation perovskite films on single crystal substrates has led us to stabilize (111) $CaRuO_3/CaMnO_3$ superlattices that exhibit emergent ferromagnetism in not only $CaMnO_3$ but also $CaRuO_3$ – both of which are not ferromagnetic in the bulk. In the bulk, $CaRuO_3$ is a paramagnetic metal and $CaMnO_3$ is an antiferromagnetic insulator. But when the two materials are brought together in an atomically precise superlattice, double exchange interactions among interfacial Mn ions, mediated by the adjacent itinerant $CaRuO_3$ layer at the $CaRuO_3/CaMnO_3$ interface give rise to strong interfacial ferromagnetism. The (111) interface and associated epitaxial strains provide for symmetries that maximizes emergent interfacial moments and therefore exchange interactions. This picture is supported by *ab initio* calculations and structural and magnetic depth profiles extracted using polarized neutron reflectometry. STEM measurements and x-ray reflectivity reveal sharp interfaces. Together the structural and magnetic evidence points to a new materials phase space for low dimensional ferromagnetism driven by charge transfer and strain symmetry.

Orientation Dependence of Epitaxial Cr_2O_3 Films. [viii] We explored antiferromagnetism in Cr_2O_3 thin films through magnetotransport measurements in an adjacent heavy metal layer. Depending on the substrate orientation (m-plane, a-plane, and c-plane), we found a nontrivial temperature dependence of the sign of the magnetoresistance in a series of Cr_2O_3/Pt bilayers on Al_2O_3 substrates, pointing to the complex interplay between the exchange and anisotropy energies that varies with orientation. This work demonstrates the importance of considering the competition between antiferromagnetic exchange and magnetic anisotropy when storing information in the spin state of an antiferromagnetic insulator.

Future Plans

Our current and future plans include spin wave characterization in LAFO thin films via non-local transport measurements and spin torque ferromagnetic resonance (STFMR) measurements. Preliminary STFMR measurements are already underway for the range of different LAFO compositions described above. We will address the challenge of modulating, even amplifying, spin waves through a series of electrical gates. We have already developed fabrication techniques to accurately define nanostructures in these spin wave materials and will incorporate nanofabrication to suppress nonlinear effects in spin wave propagation.

References

1. Jianbo Fu, Muxin Hua, Xin Wen, Minzhu Xue, Shilei Ding, Meng Wang, Pu Yu, Sunquan Liu, Jingzhi Han; Changsheng Wang, Honglin Du, Yingchang Yang and Jinbo Yang, "Epitaxial growth of YsFe5O12 thin films with perpendicular magnetic anisotropy," Appl. Phys. Lett. **110** 202403 (2017).
2. C.N. Wu, C.C. Tseng, Y.T. Fanchiang, C.K. Cheng, K.Y. Lin, S.L. Yeh, S.R. Yang, C.T. Wu, T. Liu, M. Wu, M. Hong, J. Kwo, "High quality thulium iron garnet films with tunable perpendicular magnetic anisotropy by off-axis sputtering – correlation between magnetic properties and films strin," Sci. Rep. **8** 11087 (2018).
3. O. Ciubotariu, A. Semisalova, K. Lenz, and M. Albrecht, "Strain-induced perpendicular magnetic anisotropy and Gilbert damping of $Tm_3Fe_5O_{12}$ thin films," Scientific Reports **9** 17474 (2019).
4. J. Ding, C. Liu, Y. Zhang, U. Erugu, Z. Quan, R. Yu, E. McCollum, S. Mo, S. Yang, H. Ding, X. Xu, J. Tang, X. Yang, and M. Wu, "Nanometer-thick yttrium iron garnet films with perpendicular anisotropy and low damping," Physical Review Applied **14** 014017 (2020).
5. L. Soumah, N. Beaulieu, L. Qassym, C. Carrétéro, E. Jacquet, R. Lebourgeois, J. Ben Youssef, P. Bortolotti, V. Cros, and A. Anane, "Ultra-low damping insulating magnetic thin films get perpendicular," Nature Communications **9** 3355 (2018).

Publications

i. Xin Yu Zheng, Sanyum Channa, Lauren Riddiford, Jacob J. Wisser, Krishnamurthy Mahalingam, Cynthia Bowers, Michael McConney, Alpha T. N'Diaye, Egecan Cogulu, Zbigniew Galazka, Andrew D. Kent, Yuri Suzuki, "Ultra-thin lithium aluminate spinel ferrite films with perpendicular magnetic anisotropy and low damping," *Nature Communications* **14** 4918 (2023).

ii. Daisy O'Mahoney, Sanyum Channa, Xin Yu Zheng, Arturas Vailionis, Padraic Shafer, Alpha N'Diaye, Christoph Klewe, Yuri Suzuki, "Aluminum substitution in low damping epitaxial lithium ferrite films," *Applied Physics Letters* **123** 172405 (2023).

iii. Haowen Ren, Xin Yu Zheng, Sanyum Channa, Guanzhong Wu, Daisy A. O'Mahoney, Yuri Suzuki, and Andrew D. Kent, "Hybrid spin Hall nano-oscillators based on ferromagnetic metal/ferrimagnetic insulator heterostructures," *Nature Communications* **14** 1406 (2023).

iv. Daisy O'Mahoney, Sanyum Channa, Xin Yu Zheng, Yuri Suzuki, "Tuning Magnetic Anisotropy in Aluminum Doped Lithium Ferrite Films," in preparation (2025).

v. Margaret M. Kane, Purnima P. Balakrishnan, Alexander J. Grutter, P. Quarterman, Michael R. Fitzsimmons, Timothy R. Charlton, Apurva Mehta, Megan Holtz, Andrew Herzing, Andreas Suter, Okan Koeksal, Rossitza Pentcheva, Yuri Suzuki, "Evidence for antiferromagnetic order in metallic (111)-oriented $LaNiO_3$ thin films," *Physical Review Materials* **8** 124406 (2024).

vi. Margaret Kane, Churna Bhandari, Megan Holtz, Purnima Balakrishnan, Alexander J. Grutter, Michael Fitzsimmons, Chao Yao Yang, Sashi Satpathy, Durga Paudyal, Yuri Suzuki, "Emergent ferromagnetism in $CaRuO_3/CaMnO_3$ (111)-oriented superlattices," *Nano Letters* **24** 2567-2573 (2024).

vii. Di Yi, Aihua Tang, Margaret M. Kane, Liubin Xu, Zhiying Cheng, Christoph Klewe, Alpha T. N'Diaye, Padraic Shafer, Pu Yu, Rong Yu, Haixuan Xu, Yuanhua Lin, Cewen Nan and Yuri Suzuki, ¨Enhanced ferromagnetism in atomically thin oxides achieved by interfacial reconstruction," *Advanced Functional Materials* 2313294:1-8 (2024).

viii. Jacob J. Wisser, Fen Xue, Shan X, Wang, Yuri Suzuki, "The role of magnetic anisotropy in the magnetoresistance of Cr_2O_3/Al_2O_3 thin film antiferromagnets," *AIP Advances* **14** 035018 (2024).

ix. Lerato Takana, Sanyum Channa, Xin Yu Zhaeng, Daisy O'Mahoney, Arturas Vailionis, Padraic Shafer, Alpha T. N'Diaye, Christoph Klewe, Yuri Suzuki, "Low Damping (111) Oriented Lithium Aluminum Ferrite Thin Films for Spin Wave Applications," submitted to *Applied Physics Letters* (2025).

x. Sanyum Channa, Houssam Sabri, Xin Yu Zheng, Tian-Yue Chen, Haowen Ren, Qiuchen Wu, Yuntian Li, Zbigniew Galazka, Ian R. Fisher, Xia Hong, Andrew D. Kent, Jiadong Zang, Yuri Suzuki, "Signatures of Fluctuation Driven Magnetic Topology in Pt/Ferromagnetic Insulator Bilayers," under review at *Physical Review Letters* (2025).

Universal effect of ammonia pressure on synthesis of colloidal metal nitrides in molten salts

Dmitri V. Talapin

Department of Chemistry, James Franck Institute, and Pritzker School of Molecular Engineering, University of Chicago, Chicago, IL 60637, USA

Keywords: Material Synthesis, Metal Nitrides, Gallium Nitride, Quantum Dots, Nanocrystals

Research Scope

Metal nitrides represent a large class of materials with extensive applications in optoelectronics, energy, and healthcare technologies. For example, GaN and related nitride semiconductors are key materials for solid-state lighting and high-power electronics; TiN and other early transition metal nitrides (TMNs) are widely used in wear-resistant alloys, tool coatings, catalysts and medical implants. Strong metal–nitrogen bonds grant nitrides structural rigidity as well as chemical and thermal stability. However, the covalency of metal-nitrogen bonds necessitates high temperatures to synthesize crystalline metal nitrides. Common synthetic routes include high-temperature solid-state nitridation, crystal growth in supercritical ammonia, molecular-beam epitaxy (MBE), reactive sputtering, and chemical vapor deposition (CVD). The solution synthesis of colloidal nitride nanocrystals (NCs) is rare and particularly challenging because commonly used solvents and surfactants decompose at temperatures far below those required for crystallization of most metal nitrides. Here we report a general approach to solution synthesis of colloidal metal nitride NCs by reacting metal halides and ammonia in molten inorganic salts at elevated pressures. Successful syntheses of colloidal TiN, VN, GaN, NbN, Mo_2N, Ta_3N_5, and W_2N NCs are demonstrated. These NCs expand the scope of solution-processable technologically important materials.

Recent Progress

In recent years, significant progress has been made with synthesizing functional materials in the form of colloidal NCs that combine solution processability, size-dependent optical properties of semiconductor quantum dots (QDs) and plasmonic materials, and high surface-to-volume ratios important for catalytic applications.[1] Previously, some nitride nanoparticles have been synthesized by solid-state nitridation of oxides, laser ablation or plasma methods, but these approaches offer only a limited ability to control phase purity, particle size and dispersibility in solvents. In contrast, solution-synthesized colloidal nitride NCs have the potential to combine the unique material properties of nitrides with the scalability and tunability of colloidal systems. Despite this promise, solution syntheses of nitride NCs have seen only limited success especially when compared to well-established colloidal materials such as CdSe and InP. Some successful examples include thermodynamically metastable and/or barely stable late transition metal nitrides such as Ni_3N, Cu_3N,

Cu_3PdN and Zn_3N_2.[2] The synthetic difficulty of nitride NCs can be illustratively explained by comparing the standard enthalpies of formation for TiN (-265.8 kJ/mol) and InP (-88.7 kJ/mol) phases – this stark thermodynamic difference is a direct result of the high strength and covalent nature of metal-nitrogen bonds. The growth of a defect-free crystalline lattice generally requires microreversibility of elemental steps to eliminate occasional structural defects. Synthesizing refractory materials with strong bonds typically requires high temperatures to access this microreversibility. However, for colloidal synthesis, maximal temperatures are limited by the thermal stability of the solvents and surfactants used, which is below ~400 °C for organic compounds. Alternatively, molten inorganic salts have been recently introduced as a medium to provide high-temperature colloidal stability of NCs and thus enable the synthesis of previously inaccessible Group III phosphide, arsenide, and antimonide NCs.[3] Along parallel lines, it has been shown that molten salts can also facilitate the formation of nanocrystalline powders of boride, carbide and nitride phases. This motivates our investigations into the use of molten salts to similarly generate colloidal nitride NCs.

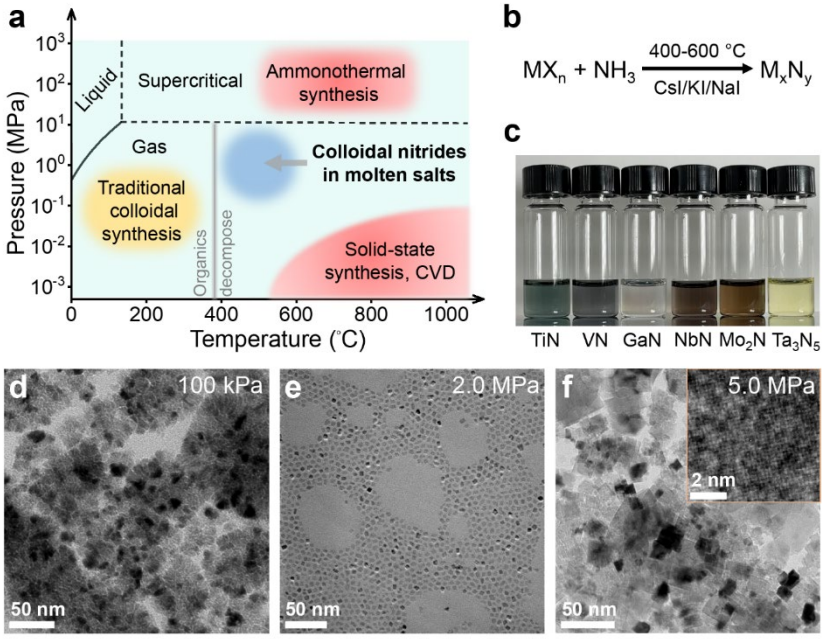

Figure 1. Effect of NH3 pressure on morphology of metal nitrides synthesized in molten inorganic salts. (a) Parameter space accessible for molten salt colloidal nitrides (marked as blue region) compared with traditional colloidal synthesis of nanocrystals (NCs), ammonothermal synthesis, CVD, and solid-state syntheses of nitride crystals and films. (b) Reactions used for synthesis of nitride NCs. (c) Photograph of colloidal solutions of different metal nitride NCs synthesized under conditions marked as the blue region in panel (a). All NCs are capped with oleate/oleylamine ligands and dispersed in toluene. (d-f) TEM images of VN products synthesized using 0.1, 2.0, and 5.0 MPa NH_3 pressure, respectively.

Metal nitrides are often synthesized by utilizing ammonia as a convenient and inexpensive nitrogen source. The phase diagram of ammonia is shown in **Fig. 1a**, superimposed on typical conditions used in different nitride synthesis methods. Thus, CVD synthesis of GaN and other nitrides typically requires temperatures exceeding 500 °C,[4] while the ammonothermal growth of bulk GaN crystals is carried out around 600 °C and 200 MPa in supercritical ammonia[5]. We therefore hypothesized that using elevated pressures of ammonia in molten salt syntheses might be a viable path to nitride NCs. In this study, we find that many metal nitrides can be synthesized in form of colloidal NCs at 425-

600 °C by applying ammonia pressure of 1-5 MPa (**Fig. 1a**). This high-temperature elevated-pressure synthetic space is inaccessible for traditional solution synthesis in organic solvents and has not been previously explored by colloidal chemists.

In a typical synthesis (**Fig. 1b**), we used Lewis-basic alkali metal halides as solvents that simultaneously provide high-temperature stability, high solubility of metal halide precursors (TiI_4, VCl_3, Ga_2I_4, $NbCl_5$, *etc.*), and support the colloidal stability of nucleated nitride NCs. High-pressure NH_3 was injected into the reactor, and the temperature was maintained for 5 min. The reaction was then cooled down to room temperature, and the products were retrieved from the salt matrix with methanol which dissolved the alkali and ammonium halides. Stable colloidal solutions were obtained by subsequent dispersion of the nitride NCs in non-polar organic solvents such as toluene with the addition of oleic acid and oleylamine as surface ligands (**Fig. 1c**).

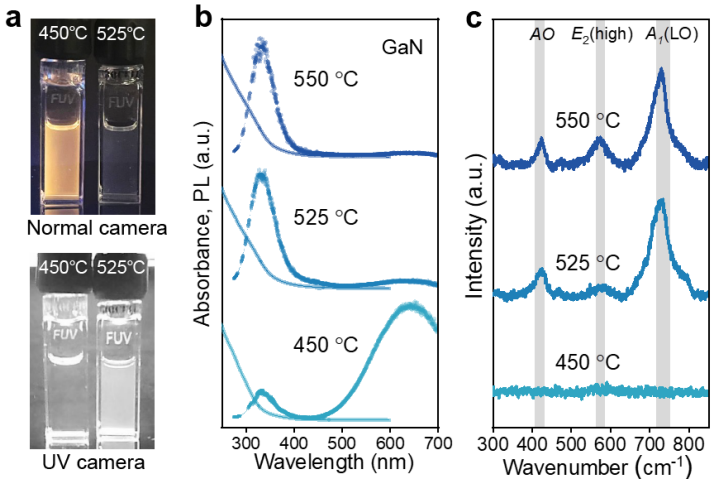

Figure 2. Emissive properties of colloidal GaN nanocrystals. (a) Photographs of colloidal GaN NCs synthesized at 450°C and 525°C, dispersed in methylcyclohexane and illuminated with UV light (254 nm). The photographs capture (top) visible 400 nm – 700 nm emission and (bottom) UV 290 nm – 400 nm emission. **(b)** Absorption (solid line) and room-temperature PL spectra (dots) of colloidal GaN NCs synthesized at 450°C, 525°C and 550°C. The left branch of PL was fit to a Gaussian function (dash line). **(c)** Raman spectra of colloidal GaN NCs with reference GaN Raman modes as grey lines.

The ammonia pressure, together with the reaction temperature, are key parameters for controlling the reaction products. For example, the reaction of VCl_3 with NH_3 at 500 °C yields three distinctive outcomes depending on the ammonia partial pressure. At 100 kPa, nanocrystalline cubic-phase VN powder consisting of sintered grains. When the NH_3 pressure is increased to 2.0 MPa, we observe the formation of discrete and monodisperse VN NCs. These VN NCs form stable colloidal solutions in toluene. Further increasing the NH_3 pressure to 5.0 MPa results in an increase of size of the VN crystalline domains (**Fig. 1f**) and this trend continues with increasing NH_3 pressure, ultimately preventing the formation of stable colloidal dispersions. A very similar NH_3 pressure dependence was observed for GaN. This synthetic approach to colloidal metal nitrides is surprisingly universal – multiple binary (TiN, VN, GaN, NbN, Mo_2N, Ta_3N_5, W_2N) and ternary (*e.g.*, $Ti_{1-x}V_xN$) nitrides successfully nucleate and grow as discrete colloidal NCs (**Fig. 1c**) within the pressure and temperature region highlighted with blue in **Fig. 1a**.

The metal nitrides represent technologically important semiconductors (GaN), superconductors (NbN), and plasmonic materials (TiN, VN). By exploring synthetic conditions previously inaccessible for colloidal NCs, we aim to access materials with novel properties. For example, extensive studies of GaN synthesized by CVD and MBE methods have revealed a strong relation between growth temperature and luminescence – a growth or annealing temperature above 700 °C was required for observing a strong band-edge photoluminescence (PL) in GaN films, while the materials synthesized at lower temperatures showed trap emission because of mid-gap states introduced by gallium and nitrogen vacancies[4]. A similar behavior was observed for colloidal GaN NCs synthesized in this study – all samples synthesized below 500 °C showed broad yellow-red emission from trap states, however, starting from about 525 °C, GaN NCs showed predominantly

band-edge ultraviolet PL (**Fig. 2a,b**). The transition from trap- to band-edge emission shows no obvious correlation with TEM and XRD data, but the Raman spectra clearly correlate with the emergence of band-edge PL (**Fig. 2c**). Samples synthesized at 525 °C and above have well-defined A_1(LO) and E_2(high) GaN phonon modes and corresponding overtone peaks closely resembling the Raman spectrum of CVD-grown GaN. In contrast, GaN NCs synthesized below 500 °C show very weak and broadened Raman peaks, characteristic of disorder associated with vacancy defects in analogy with GaN grown by MBE or CVD at low temperatures.[4]

Future Plans

This work just scratches the surface of colloidal nitrides that can be synthesized in molten inorganic salts. Our results have demonstrated a general route toward colloidal metal nitride NCs using molten halide salts and ammonia, where NH_3 pressure allows controlling the reaction product morphology by stabilizing colloidal nitride NCs against aggregation and sintering. Naturally, we anticipate the emergence of colloidal nitride QDs for optoelectronic applications, backed by the prominence of GaN semiconductor family. Beyond the nitrides, further development of synthetic methodology towards colloidal NCs of other refractory materials with covalent bonds would be highly desired.

References

1. García de Arquer, F. P. et al. Semiconductor quantum dots: Technological progress and future challenges. *Science* **373**, eaaz8541 (2021).
2. Parvizian, M. & De Roo, J. Precursor chemistry of metal nitride nanocrystals. *Nanoscale* **13**, 18865-18882 (2021).
3. Ondry, J. et al. Reductive pathways in molten inorganic salts enable colloidal synthesis of III-V semiconductor nanocrystals. *Science* **386**, 401-407 (2024).
4. Yu, K. M. et al. Effects of native defects on properties of low-temperature grown, non-stoichiometric gallium nitride. *J. Phys. D: Appl. Phys.* **48**, 385101 (2015).
5. Hashimoto, T. et al. A GaN bulk crystal with improved structural quality grown by the ammonothermal method. *Nat. Mater.* **6**, 568-571 (2007).

Publication

R. Lin, V. Khokhar, N. Jiang, W. Cho, Z. Zhou, D. Wang, J. C. Ondry, Z. Mi, J. Cassidy, A. M. Hinkle, J. S. Anderson, R. D. Schaller, D.-e. Jiang, D. V. Talapin. Universal effect of ammonia pressure on synthesis of colloidal metal nitrides in molten salts. *Submitted* (2025).

Excitons in Low-Dimensional Perovskites

William A. Tisdale – Massachusetts Institute of Technology

Keywords: perovskite, exciton, transport, 2D, quantum dot, superlattice, spectroscopy

Program Scope

The goal of this continuing research effort is to obtain a deeper understanding of strongly bound excitonic states in low-dimensional halide perovskites, and to understand how the behavior of excitons in perovskite materials is affected by materials composition, structure, size, and dimensionality. During the current funding period, we focus our attention on the movement of excitons among low-dimensional building blocks in perovskite nanocrystal superlattices and mixed-dimensional heterostructures. Efforts will be devoted both to the fabrication of well-defined heterostructures and the investigation of exciton physics in those systems. Key experimental techniques include high-magnetic-field spectroscopy, angle- and polarization-dependent emission (photoluminescence) and absorption spectroscopy, and temperature-dependent femtosecond time-resolved superresolution emission microscopy. The research program is executed by a highly collaborative and international research team, including unfunded collaborators who bring expertise in materials synthesis, spectroscopy, theory, and computation.

Recent Progress

All-perovskite multicomponent nanocrystal superlattices. Nanocrystal superlattices (NC SLs) have long been sought as promising metamaterials, with nanoscale-engineered properties arising from collective and synergistic effects among the constituent building blocks. Lead halide perovskite (LHP) NCs come across as outstanding candidates for SL design, as they demonstrate collective light emission, known as superfluorescence, in single- and multicomponent SLs. Thus far, LHP NCs have only been assembled in single-component SLs or coassembled with dielectric NC building blocks acting solely as spacers between luminescent NCs. Here, we report the formation of multicomponent LHP NC-only SLs, i.e., using only $CsPbBr_3$ NCs of different sizes as building blocks. The structural diversity of the obtained SLs encompasses the ABO_6, ABO_3, and NaCl structure types, all of which contain orientationally and positionally locked NCs. For the selected model system, the ABO_6-type SL, we observed efficient NC coupling and Förster-like energy transfer from strongly confined 5.3 nm $CsPbBr_3$ NCs to weakly confined 17.6 nm $CsPbBr_3$ NCs, along with characteristic superfluorescence features at cryogenic temperatures. Spatiotemporal exciton dynamics measurements reveal that binary SLs exhibit enhanced exciton diffusivity compared to single-component NC assemblies across the entire temperature range (from 5 to 298 K). The observed coherent and incoherent NC coupling and

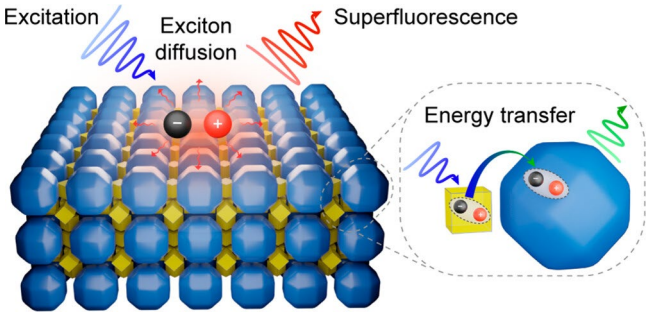

Figure 1. ABO_6-type $CsPbBr_3$-$CsPbBr_3$ superlattice comprising 5.3 and 17.6 nm $CsPbBr_3$ nanocrystals. The superlattices exhibit enhanced exciton transport and superfluorescence emission from coherently coupled nanocrystals. *Published work from this award* (Sekh *et al.*, ***ACS Nano*** (2024)).

controllable excitonic transport within the solid NC SLs hold promise for applications in quantum optoelectronic devices.

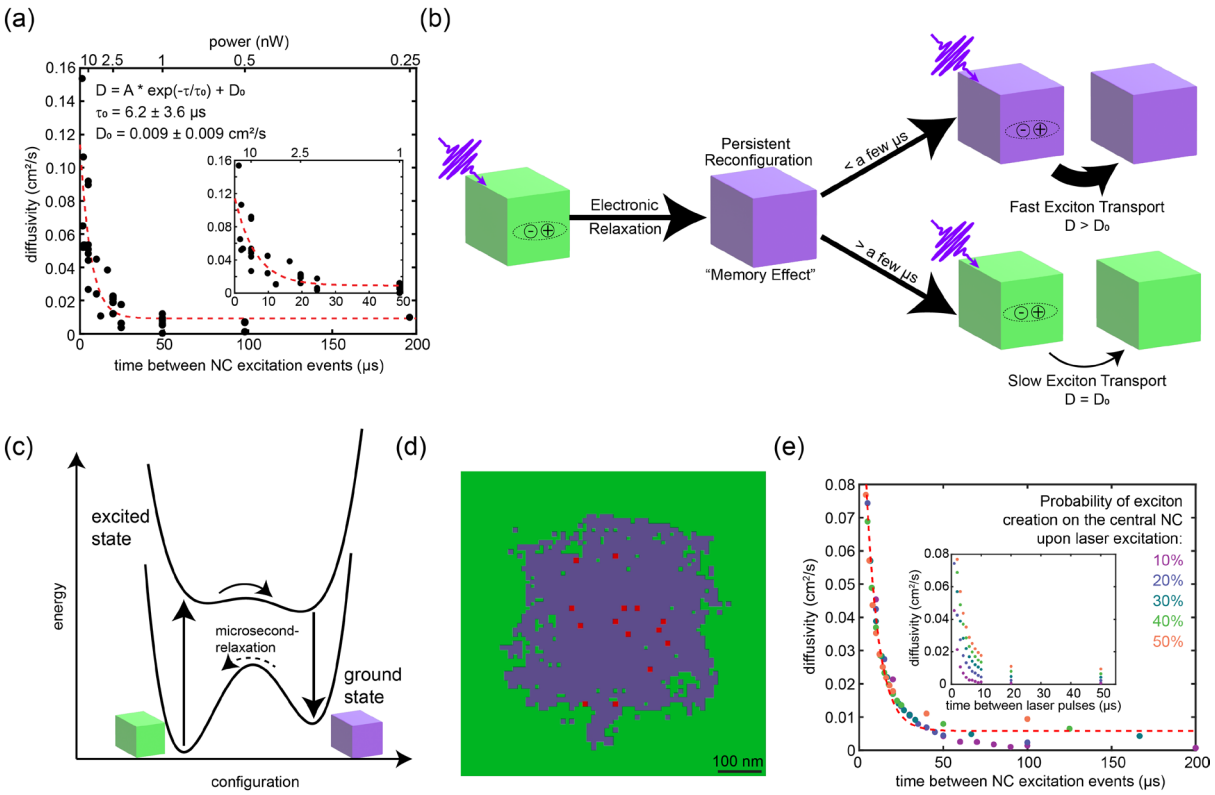

Figure 2. *Persistent enhancement of exciton diffusivity*. (a) Experimentally measured diffusivity relaxation curve. Exciton diffusivity of $CsPbBr_3$ NCs with OLA/OA ligands as a function of time between NC excitation events. (b) Schematic illustration of the excitation memory effect leading to persistent enhancement of exciton diffusivity. (c) Potential energy surface description of the phenomenon illustrated in panel (b). Black curves indicate the electronic excited state and electronic ground state of the NCs. (d) Snapshot of a kinetic Monte Carlo (KMC) simulation of exciton transport in a 2D NC array, which includes excitation memory effects. (e) KMC simulation results plotted as a function of time between NC excitation events, showing consistency with the experimentally measured phenomenon. *Published work from this award* (Shcherbakov-Wu *et al.*, ***Science Advances*** (2024)).

Persistent enhancement of exciton diffusivity in $CsPbBr_3$ nanocrystal solids. In semiconductors, exciton or charge carrier diffusivity is typically described as an inherent material property. Here, we show that the transport of excitons (i.e., bound electron-hole pairs) in $CsPbBr_3$ perovskite nanocrystals (NCs) depends markedly on how recently those NCs were occupied by a previous exciton. Using fluence- and repetition-rate-dependent transient photoluminescence microscopy, we visualize the effect of excitation frequency on exciton transport in $CsPbBr_3$ NC solids. Surprisingly, we observe a striking dependence of the apparent exciton diffusivity on excitation laser power that does not arise from nonlinear exciton-exciton interactions nor from thermal heating of the sample. We interpret our observations with a model in which excitons cause NCs to undergo a transition to a metastable configuration that admits faster exciton transport by roughly an order of magnitude. This metastable configuration persists for ~microseconds at room temperature, and does not depend on the identity of surface ligands or presence of an oxide shell, suggesting that it is an intrinsic response of the perovskite lattice to electronic excitation. The exciton diffusivity observed here (>0.15 cm^2/s) is considerably higher than that observed in other NC systems on similar timescales, revealing unusually

strong excitonic coupling in a NC material. The finding of a persistent enhancement in excitonic coupling between NCs may help explain other extraordinary photophysical behaviors observed in $CsPbBr_3$ NC arrays, such as superfluorescence. Additionally, faster exciton diffusivity under higher photoexcitation intensity is likely to provide practical insights for optoelectronic device engineering.

Future Plans

A key focus for the coming year is visualization of exciton and charge carrier transport in 2D and 3D halide perovskites. Using funds from this award we have purchased a Montana Instruments Cryostation Microscope, which enables high stability optical microscopy at cryogenic temperatures. Using spatially resolved transient photoluminescence, we will study exciton and carrier diffusivity in single crystal and thin film (polycrystalline) perovskite materials as a function of temperature. A key goal is to probe the mechanism of transport and assess the potential interplay between polaron formation and exciton and carrier diffusivity.

10 Most Relevant Publications (citing support from this award over the past 2 years)

1. "Discovery of enhanced lattice dynamics in a single-layered hybrid perovskite"
   Z. Zhang, J. Zhang, Z.-J. Liu, N.S. Dahod, W. Paritmongkol, N. Brown, A. Stollmann, W.S. Lee, Y.-C. Chien, Z. Dai, K.A. Nelson, W.A. Tisdale, A.M. Rappe, E. Baldini
   Science Adv. 9, eadg4417 (2023).
2. "Exciton Fine Structure in 2D Perovskites: The Out-of-Plane Excitonic State"
   K. Posmyk, M. Dyksik, A. Surrente, D.K. Maude, N. Zawadzka, A. Babiński, M.R. Molas, W. Paritmongkol, M. Mączka, W.A. Tisdale, P. Plochocka, M. Baranowski
   Adv. Opt. Mater. 2300877 (2023).
3. "All-Perovskite Multicomponent Nanocrystal Superlattices"
   T. Sekh, I. Cherniukh, E. Kobiyama, T. Sheehan, A. Manoli, C. Zhu, M. Athanasiou, M. Sergides, O. Ortikova, M. Rossell, F. Bertolotti, A. Guagliardi, N. Masciocchi, R. Erni, A. Othonos, G. Itskos, W.A. Tisdale, T. Stöferle, G. Raino, M. Bodnarchuk, M. Kovalenko
   ACS Nano 18, 8423-8436 (2024).
4. "Coherent Exciton-Lattice Dynamics in a 2D Metal Organochalcogenolate Semiconductor"
   E.R. Powers, W. Paritmongkol, D.C. Yost, W.S. Lee, J.C. Grossman, W.A. Tisdale;
   Matter 7, 1-19 (2024).
5. "Persistent Enhancement of Exciton Diffusivity in $CsPbBr_3$ Nanocrystal Solids"
   W. Shcherbakov-Wu, S. Saris, T. Sheehan, N.N. Wong, E.R. Powers, F. Krieg, M.V. Kovalenko, A.P. Willard, W.A. Tisdale; ***Science Advances*** 10, eadj2630 (2024).
6. "Bright Excitonic Fine Structure in Metal Halide Perovskites: From 2D to Bulk"
   K. Posmyk, N. Zawadzka, L. Kipczak, M. Dyksik, A. Surrente, D. Maude, T. Kazimierczuk, A. Babiński, M. Molas, W. Bumrungsan, C. Chooseng, W. Paritmongkol, W.A. Tisdale, M. Baranowski, P. Plochocka; ***J. Am. Chem. Soc.*** 146, 4687-4694 (2024).
7. "Vibrational Fermi Resonance in Atomically Thin Black Phosphorous"
   N. Mao, S. Huang, L.G. Pimenta Martins, H. Yan, X. Ling, L. Liang, J. Kong, W.A. Tisdale; ***Nano Letters*** 10.1021/acs.nanolett.4c03592 (2024).
8. "Twisted Perovskite Layers Come Together"
   W.A. Tisdale; ***Nature Materials*** 23, 1155-1156 (2024).
9. "Triplet Exciton Sensitization of Silicon Mediated by Defect States in Hafnium Oxynitride"
   N. Nagaya, A. Alexiu, C.F. Perkinson, O.M. Nix, D. Koh, M.G. Bawendi, W.A. Tisdale, T. Van Voorhis, M.A. Baldo; ***Adv. Mater.*** 2415110 (2024).
10. "Exciton Transport in Perovskite Materials"
    T.J. Sheehan, S. Saris, W.A. Tisdale; ***Adv. Mater.*** 2415757 (2024).

Uncovering and surmounting loss mechanisms in light emitters

Chris G. Van de Walle, University of California, Santa Barbara

Keywords: first-principles calculations, recombination mechanisms, nonradiative recombination, nitride semiconductors, halide perovskites

Research Scope

The aim of this project is twofold: to develop reliable first-principles methodologies for calculating loss mechanisms in optoelectronic devices, and to apply them to technologically important materials. A main focus over the past two years has been to explain defect-assisted nonradiative recombination in semiconductors with bandgaps larger than ~2.5 eV, in which the traditionally invoked multiphonon emission (MPE) mechanism becomes ineffective. We have addressed this by developing a first-principles methodology that allows rigorous calculations of recombination rates based on trap-assisted Auger-Meitner (TAAM) recombination (**Figure 1**).

The application of this methodology to nitride semiconductors, the key materials for solid-state lighting, indicates that inclusion of TAAM processes can enhance nonradiative recombination rates by orders of magnitude, thus explaining how defects and impurities contribute to efficiency loss in wider-bandgap materials—a particularly important issue for ultraviolet light emitters.

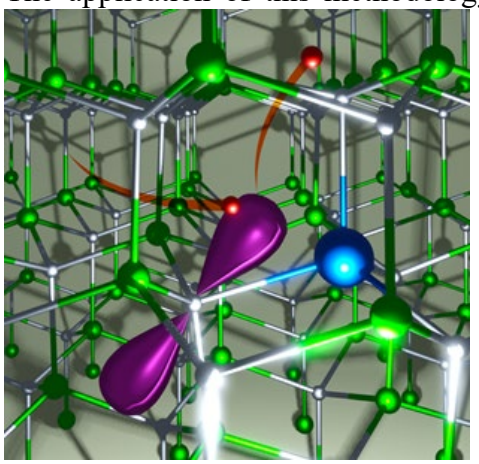

Figure 1. Concept illustration depicting the TAAM process at a Ca substitutional impurity in a GaN crystal. An incoming electron (red) gets trapped in a localized state (purple), and its energy is transferred to another electron.

We have also continued our work on halide perovskites, materials that excel in photovoltaics and are being considered for light emitting diodes (LEDs), but for which a fundamental understanding of defect physics has been lacking. We obtained important results on the role of iodine vacancies, on the trade-off between toxicity (due to Pb) and efficiency, and on impact of strain.

Our overall goal is to generate the fundamental knowledge that is essential for improving efficiencies, and to provide guidelines for overcoming the limitations.

Recent Progress

Methodology

Defect-assisted nonradiative recombination limits the efficiency of optoelectronic devices, and past first-principles calculations were successful in elucidating the fundamental processes in solid-state light emitters emitting at green and longer wavelengths. However, the traditional mechanism based on multiphonon emission (MPE) [R1] fails to account for sources of loss in wider-band-gap materials emitting in the blue or ultraviolet. We resolved this puzzle by taking into account trap-assisted Auger-Meitner (TAAM) recombination.

Instead of releasing energy in the form of phonons, in a TAAM process the electron transfers its energy to another electron that gets kicked up to a higher energy state (**Figure 2**). Such a mechanism is conventionally referred to as the Auger effect, after Pierre Auger who reported it in 1923. It has been noted, however, that Lise Meitner had already described the same phenomenon in 1922, hence the renaming [R2].

We have developed a first-principles methodology to determine the TAAM recombination rate for defects and impurities in semiconductors. As a test case, we focused on a calcium substitutional impurity in InGaN (**Figure 1**), where inclusion of TAAM results in recombination rates orders of magnitude larger than the recombination rate governed by MPE alone. Our paper was published in *Physical Review Letters* [P3].

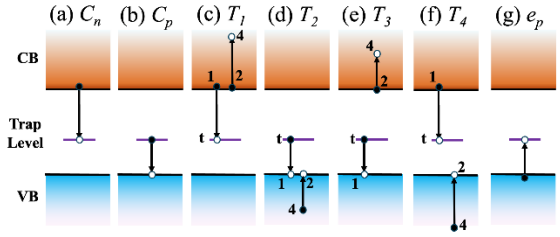

Figure 2. Schematic diagram of trap-assisted recombination processes: (a),(b): electron and hole capture, either radiatively or nonradiatively via MPE; (c)-(f): TAAM processes; (g): hole emission.

Efficiency of nitride light emitters

Inclusion of TAAM processes provides an explanation for why defect-assisted recombination is detrimental to semiconductors with bandgaps wider than about 2.5 eV—for which consideration of MPE alone would lead to the conclusion that defects do not cause efficiency loss.

Our computational formalism is general and can be applied to any defect or impurity in any semiconducting or insulating material. Carbon is a particularly worrisome contaminant, not just in nitrides but in all (opto)electronic materials, since it is abundantly present during synthesis and processing of materials. Indeed, metal-organic chemical vapor deposition (MOCVD), which is the most widely used growth technique for nitrides, is performed with metal-organic sources for the cations, leading to unintentional carbon incorporation. As shown in **Figure 3**, we explicitly calculated the rates of MPE, radiative, and TAAM recombination. The results show that carbon can lead to sizeable nonradiative recombination.

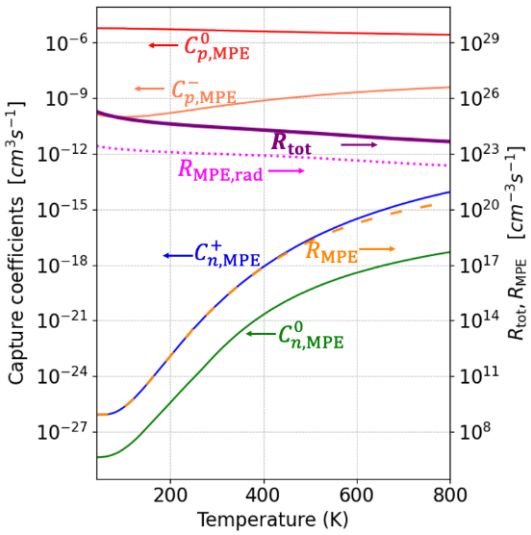

Figure 3. Calculated recombination rate as a function of temperature for C concentration 10^{17} cm^{-3} and injected carrier concentration 10^{18} cm^{-3}. R_{tot} includes MPE, radiative and all TAAM processes, while R_{MPE} includes only MPE processes, and $R_{\mathrm{MPE,rad}}$ includes MPE and radiative processes.

In addition, we performed an analysis as a function of carrier density, including the previously neglected effect of thermal emission. This allowed us to identify the regimes where radiative recombination (carbon gives rise to yellow luminescence) and hole emission would be observable [R3].

In addition to these key results on recombination processes, we have continued investigating other aspects that affect efficiency, including band-to-band AM recombination [P6] and impact of impurities on doping [P9]. Doping is a particular problem for ultraviolet light emitters, and polarization doping [R4] has received attention as an attractive alternative. In previous DOE-supported work [R5] we pointed out that calculations of polarization fields in nitride semiconductors suffered from two serious errors. It is only more recently that these concerns have been taken seriously by researchers in the field, particularly due to the discovery of ferroelectricity in nitride alloys, which highlights the need for adopting the formalism outlined in Ref. [R5]. We have continued our investigations of polarization fields in nitrides in order to elucidate their role in carrier generation [P2] and applications in novel nitrides [P8].

Loss mechanisms in halide perovskites

Halide perovskites, such as methylammonium lead iodide $MAPbI_3$, are highly promising materials for efficient solar cells and light emitters. Despite the remarkable success, the fundamental mechanisms that are responsible for the high efficiency are still vigorously debated. We have continued to make substantial progress in understanding and quantifying the role of point defects in halide perovskites. The halide perovskites have been frequently cited as being "defect tolerant." Our work firmly established that these materials are equally prone to defect-assisted nonradiative recombination as conventional semiconductors. Rigorous evaluation of capture coefficients based on configuration coordinate diagrams calculated with a hybrid functional and including spin-orbit coupling is essential. A *Perspective* paper was published in the *Journal of Applied Physics* [R6].

One defect that has been widely invoked is the iodine vacancy (V_I). We examined this proposition by performing rigorous calculations of V_I in $CsPbI_3$, $CsSnI_3$, and $CsGeI_3$. Our results show that V_I does not have any transition levels in the bandgap in $CsPbI_3$; it does introduce levels in $CsSnI_3$ and $CsGeI_3$, but our computed capture coefficients demonstrate that it has a negligible impact on nonradiative recombination. Our study thus shifts the focus toward identifying and mitigating actual recombination centers in order to further improve the optoelectronic performance. A paper was published in *PRX Energy* [P1].

Toxicity remains one of the major challenges that prevent Pb-based halide perovskites from widespread utilization. Ideally, non-toxic alternatives (e.g., based on Sn) can be identified while still maintaining superior power conversion efficiency. In the spirit of systematic studies of point defects, we set out to investigate halogen interstitials, which are strong recombination centers in $CsPbI_3$ [R7]. We found that due to the band offset between $CsSnI_3$ and $CsPbI_3$, the dominant recombination center changes from the iodine interstitial in $CsPbI_3$ to an iodine antisite in $CsSnI_3$. The latter is an even stronger nonradiative recombination center than the iodine interstitial. The existence of such a highly efficient recombination center constitutes an intrinsic limitation on the performance of Sn-based halide perovskites. Our study thus implies that there is a trade-off between toxicity and efficiency when switching from Pb-based to Sn-based perovskite solar cells. A paper has been published in *Angewandte Chemie* [P10].

We also completed a study of the impact of strain on band structure of halide perovskites, in collaboration with experimentalists. The results produced three key insights into the nature of the band-edge electronic states and their impact on charge-carrier dynamics: (i) the bandgap energy in the bulk is lower compared to the surface; (ii) the Rashba-type band splitting is larger in the bulk compared to the surface; and (iii) fast radiative recombination occurs in the bulk from carrier funneling and strong one-photon transitions even from the extrema of Rashba-split bands. Carriers diffuse away from trap-rich surface states and recombine efficiently within the bulk (**Figure 4**) despite the significant band splitting that has been argued to inhibit efficient radiative recombination. The paper was published in *PRX Energy* [P7].

Future Plans

In terms of methodology, we plan to extend the TAAM formalism to cases where there are multiple bound states in the bandgap, and make the software for TAAM recombination publicly available. For nitride light emitters, we are investigating transition-metal impurities as nonradiative recombination centers, and the role of AM or TAAM processes in degradation of UV light emitters. We also plan to investigate the impact of TAAM on efficiency loss in halide perovskites.

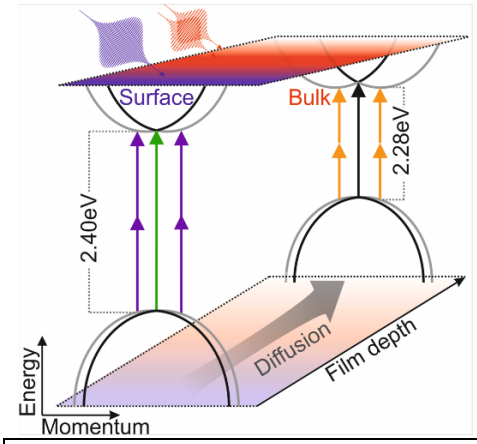

Figure 4. Energy alignment of observed optical transitions, showing carrier diffusion from surface to bulk in $MAPbBr_3$ films [P7].

References

R1. C. H. Henry and D. V. Lang, *Nonradiative capture and recombination by multiphonon emission in GaAs and GaP*, Phys. Rev. B **15**, 989 (1977). [doi: 10.1103/PhysRevB.15.989]

R2. D. Matsakis, A. Coster, B. Laster, and R. Sime, *A renaming proposal: 'The Auger-Meitner effect"*, Phys. Today **72**, 10 (2019). [doi: 10.1063/PT.3.4281]

R3. F. Zhao, H. Guan, M. Turiansky, and C. G. Van de Walle, *Carbon in GaN as a non-radiative recombination center*. [doi: 10.48550/arXiv.2502.13350]

R4. D. Jena *et al*., *Realization of wide electron slabs by polarization bulk doping in graded III–V nitride semiconductor alloys*, Appl. Phys. Lett. **81**, 4395 (2002). [doi: 10.1063/1.1526161]

R5. C. E. Dreyer, A. Janotti, C. G. Van de Walle, and D. Vanderbilt, *Correct implementation of polarization constants in wurtzite materials and impact on III-nitrides*", Phys. Rev. X **6**, 021038 (2016). [10.1103/PhysRevX.6.021038]

R6. X. Zhang, M. E. Turiansky, J.-X. Shen, and C. G. Van de Walle, *Defect tolerance in halide perovskites: A first-principles perspective*, J. Appl. Phys. **131**, 090901 (2022). [doi: 10.1063/5.0083686]

R7. X. Zhang, M. E. Turiansky, and C. G. Van de Walle, *All-inorganic halide perovskites as candidates for efficient solar cell*, Cell Rep. Phys. Sci. **2**, 100604 (2021). [doi: 10.1016/j.xcrp.2021.100604]

Two-year Publication List

P1. J. Zhang, X. Zhang, M. E. Turiansky, and C. G. Van de Walle, *Defect tolerance in halide perovskites: A first-principles perspective*, PRX Energy **2**, 013008 (2023). [doi: 10.1103/PRXEnergy.2.013008]

P2. S. H. Yoo, M. Todorova, J. Neugebauer, and C. G. Van de Walle, *Microscopic origin of polarization charges at GaN/(Al,Ga)N interfaces*, Phys. Rev. Appl. **19**, 064037 (2023). [doi: 10.1103/PhysRevApplied.19.064037]

P3. F. Zhao, M. E. Turiansky, A. Alkauskas, and C. G. Van de Walle, *Trap-assisted Auger-Meitner recombination from first principles*, Phys. Rev. Lett. **131**, 056402 (2023). [doi: 10.1103/PhysRevLett.131.056402]

P4. X. Zhang, M. E. Turiansky, L. Razinkovas, M. Maciaszek, P. Broqvist, Q. Yan, J. L. Lyons, C. E. Dreyer, D. Wickramaratne, Á. Gali, A. Pasquarello, and C. G. Van de Walle, *First-principles calculations of defects and electron-phonon interactions: Seminal contributions of Audrius Alkauskas to the understanding of recombination processes*, J. Appl. Phys. **135**, 150901 (2024). [doi: 10.1063/5.0205525]

P5. S. Lal, J. Lu, B. J. Thibeault, M. H. Wong, C. G. Van de Walle, S. P. DenBaars, and U. K. Mishra, *Trap Passivation for Reducing On-Resistance and Saturation Voltage in Wafer-Bonded InGaAs-channel/GaN-Drain Vertical FETs*, IEEE Trans. Electron Dev. **71**, 1702 (2024). [doi: 10.1109/TED.2024.3355379]

P6. N. Pant, K. Bushick, A. McAllister, W. Lee, Chris G. Van de Walle, and E. Kioupakis, *Carrier confinement and alloy disorder exacerbate Auger-Meitner recombination in AlGaN ultraviolet light-emitting diodes*, Appl. Phys. Lett. **125**, 021109 (2024). [doi: 10.1063/5.0208840]

P7. S. A. Bourelle, X. Zhang, S. Feldmann, B. Zhang, A. Mathieson, L. Eyre, H. Abolins, T. Winkler, C. G. Van de Walle, and F. Deschler, *Energy Level Gradients from Surface to Bulk in Hybrid Metal-Halide Perovskite Thin Films*, PRX Energy **3**, 033001 (2024). [doi: 10.1103/PRXEnergy.3.033001]

P8. A. J. E. Rowberg, S. Mu, and C. G. Van de Walle, *Point defects and doping in wurtzite LaN*, Phys. Rev. B **110**, 205206 (2024). [doi: 10.1103/PhysRevB.110.205206]

P9. Q. Yan, J. L. Lyons, L. Gordon, and C. G. Van de Walle, *Oxygen impurities in AlN and their impact on optical absorption,* Appl. Phys. Lett. **126**, 062106 (2025). [10.1063/5.0234655]

P10. X. Zhang, J.-X. Shen, M. E. Turiansky, and C. G. Van de Walle, *Trade-off between toxicity and efficiency in tin versus lead based halide perovskites*, Angew. Chem. Int. Ed. **64**, e202500557 (2025). [10.1002/anie.202500557]

Optical, Electrical and Magnetic Studies of Hybrid Organic-Inorganic Perovskites

Zeev Valy Vardeny, Physics & Astronomy Department, University of Utah

Keywords: Hybrid organic inorganic perovskites, cw and picosecond transient optical studies, magneto circular dichroism, Rashba exciton, Landé g-factor

Research Scope

This is an experimental effort focused on the fundamental science of hybrid organic/inorganic halide perovskite (HOIP) semiconductors. Through optical, electrical and magneto-optical studies of pristine 3D hybrid perovskites, Cs-based halide perovskites and 2D HOIP compounds, we investigate a number of fundamental scientific questions with important ramifications on potential applications of these materials. In particular, we address key aspects associated with the strong spin orbit coupling (SOC) in these compounds that may lead to Rashba-splitting in their continuum bands and influence the exciton fine structure [1].

Recent Progress

(i) Transient and cw magneto-optical studies of $MAPbBr_3$ crystals, films and LEDs

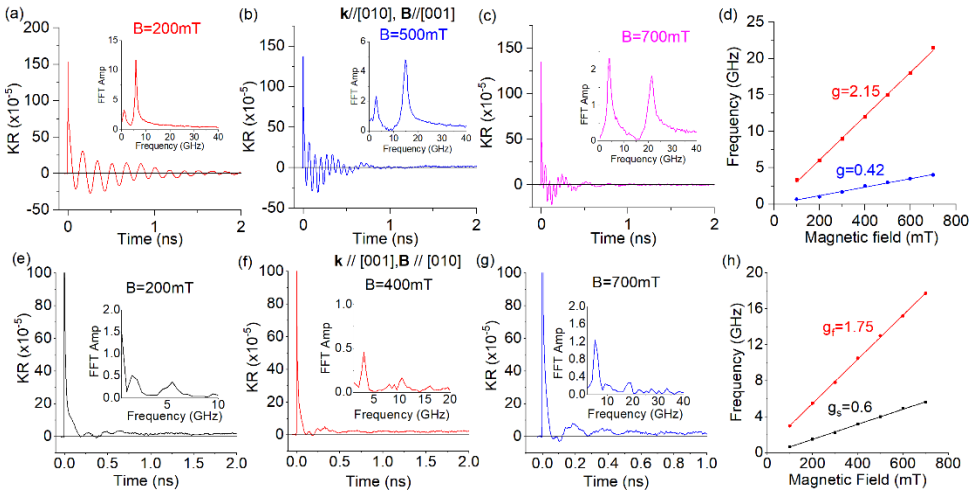

Figure 1: Transient photoinduced quantum beatings in $MAPbBr_3$ single crystal excited at 405 nm measured at various magnetic field strengths at 4 K. Magnetic field dependence of the transient Kerr Rotation dynamics measured on (010) facet with **B** directed along [001] (a-d); and on (001) facet with **B** along [010] (e-h), using probe beam at 552 nm. The insets show the corresponding FFT spectra with two FFT peaks for the fast (electron) and slow (hole) oscillatory frequencies, respectively. (d) and (h) The fast and slow QB frequencies vs *B* and the anisotropy of the obtained electron and hole Landé g-factors [2].

Picosecond time resolved and cw magneto optical methods were used for studying the spin-related properties of excitons and photocarriers in methyl-ammonium lead bromide ($MAPbBr_3$) thin film, single crystal and light emitting diodes (LED), focusing on the Landé g-values of these species [2]. Using the transient circularly polarized photoinduced quantum beatings (QB) under an applied magnetic field, **B** in $MAPbBr_3$ *single crystal,* we obtained the anisotropic Landé g-values of electrons for **B** field along [010] and [001]: g_e along 001 = 2.15 and g_e along 010 = 1.75, and for holes $|g_h|$ along 001 = 0.42 and $|g_h|$ along 010 = 0.60. We also used the magnetic circular dichroism method for measuring the bright excitons' g-value, $g_{ex}=g_e+g_h = 2.24$. From these two types of measurements we conclude that $g_h > 0$ in $MAPbBr_3$. This conclusion was corroborated by measuring the magneto-electroluminescence response of $MAPbBr_3$ based LED.

This work has been published in Phys. Rev. B 109, 014316 (2024)[Ref. 2].

(ii) Provisional Patent in the field of Quantum Information Science. We have achieved control of the photoinduced electron Larmor frequency in the transient pump-probe quantum beatings in HOIP

films via a third cw or pulsed circularly polarized laser beam, which strongly polarizes the nuclear spins of these materials. This led to an invention that was submitted to the UofU patent office in 2023. In 2024 it has been decided to go to the next phase and submit a provisional patent in the field of *Quantum Information Science*; **QUANTUM BITS AND FAST SWITCHES BASED ON HYBRID ORGANIC INORGANIC PEROVSKITES**

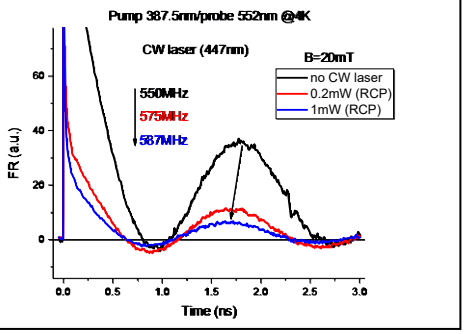

Figure 2: The influence of the photoinduced CW Overhauser magnetic field that is generated by the nuclear spin polarization, on the transient quantum beating measured by pump-probe transient photoinduced Kerr effect associated with the electrons' Larmor frequency in $MAPbBr_3$ crystal measured at 4K [2]. This demonstration has led to a patent disclosure in 2023 in the field of 'quantum bits'.

(iii) Thermalization and spin relaxation dynamics of localized photocarriers in the band tails of nanocrystalline $MAPbBr_3$ films

We have studied the spin properties of localized photocarriers in the band tails (BT) of polycrystalline $MAPbBr_3$ films having nanometer crystal size, using circularly polarized photoluminescence (PL) induced by magnetic field up to 17.5 T at cryogenic temperatures, as well as time-of-flight (TOF) transient photocurrent [3]. The absorption spectrum of these films reveals BT states caused by structural and energetic disorder, having a relatively large Urbach edge of 25 meV. This is corroborated by dispersive transport of photogenerated electrons and holes observed via TOF photocurrent, where the photocarriers thermalize with time more deeply into the BT states giving rise to time dependent mobility. Consequently, the PL emission spectrum in these films originates from radiative recombination of the localized electron and hole pairs in the BT states. Upon applying a magnetic field in the Faraday configuration, field induced circular polarized PL has been observed, from which an effective Landé g-factor of the localized e-h pairs, $g_{e\text{-}h}$, was extracted to be 2.5±0.2; in good agreement with the g-factor of free excitons measured using magnetic circular dichroism spectroscopy. In addition, we also found that the spin relaxation time for the e-h pairs in the BT states is ~ 26 ns at 5K, and ~ 10 ns at 80K indicating that nanocrystalline $MAPbBr_3$ films could be a good candidate for applications in spintronics and quantum information science.

This work has been published in ACS Photonics, 11, 4588–4596. October 18, 2024 [Ref. 3].

Figure 3. False color 2D contour plot of the field induced PL circular polarization spectrum, $P_c(B_z,T,E)$, at (a) various cryochamber temperatures at B_z = -17.5 T, and (c) various B_z at cryochamber temperature T = 5K. (b) P_c of the LE band (black squares) and HE band (red circles) as a function of the cryochamber temperature T, at B_z = -17.5 T. The inset shows the sample temperature, Θ at different chamber temperatures T. (d) P_c of the HE and LE bands as a function of B_z, at T = 5K. The lines thru the data points are fits [3] from which we obtained the Landé g-value of the excitons [3].

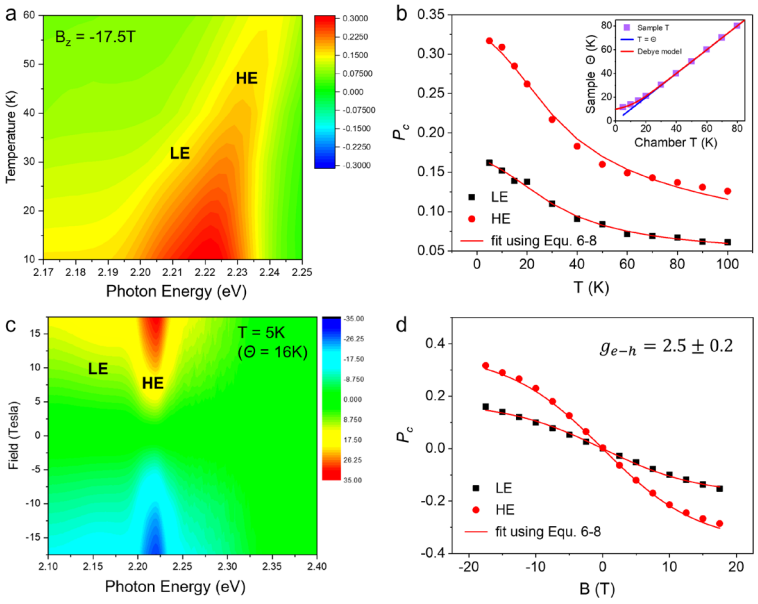

(iv) Landé g-factor spectroscopy of photoexcitations in two-dimensional HOIP films

Figure 4. Magnetic circular dichroism (MCD) spectra of 2D-PEPI film measured at two field polarities of B=415 mT at 3K that are related with various excitons. (a) The three zero-crossings (marked by green ellipses) associated with the free exciton (EX1) and its phonon replicas, EX2 and EX3, respectively. (b) The zero-crossing associated with the trapped exciton, EX_T. (c) MCD spectra of the interband (IB) transition related with the 2D continuum that peaks at the optical bandgap, E_g. (d) The Zeeman splitting energy extracted from the MCD spectra vs. the field B, from which the Landé g-factor of the various excitons are obtained (see text below).

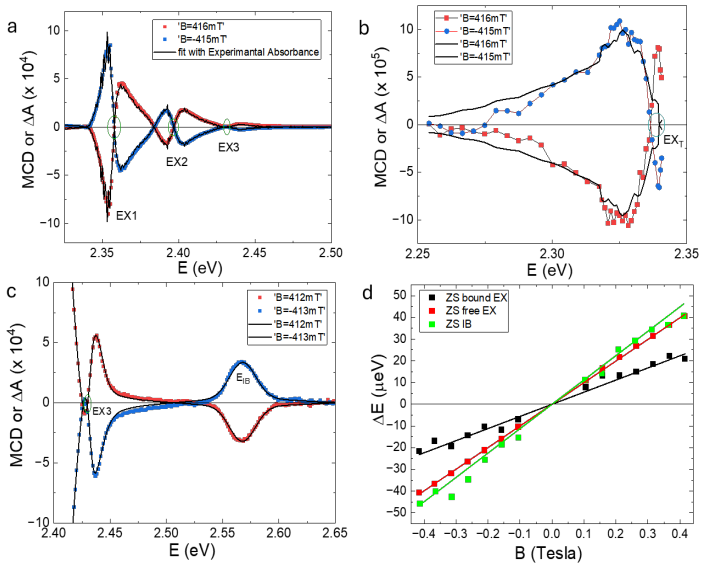

We have studied the Landé g-factor in two-dimensional phenethylammonium lead iodide (2D-PEPI) films using magneto-circular dichroism (MCD) at magnetic field (<0.5 T), complemented by a variety of cw spectroscopies that includes absorption, steady-state photoluminescence (PL), and electroabsorption. These methods enabled a detailed analysis of the g-factors associated with various excitons in this compound, including trapped excitons (EX_t), free excitons (EX), and interband (IB) loosely bound electron-hole pairs. Our MCD analysis reveals a distribution of g-factors across the absorption spectrum of 2D-PEPI (see Fig. 4). At T=3K, we measured g_{EXt} = 1.0±0.2, g_{EX}=1.72±0.03, and g_{IB}=2.0±0.2. The various obtained g-values may be used as a new 'g-value spectroscopy' tool for identifying various photoexcitations in HOIP semiconductors. Notably, we observed a strong negative temperature dependence of g_{IB}, which aligns with a recent model based on 'many-body' interaction. We have also observed in PEPI a 'soft' phase transition at ~150K, which arises from thermal disturbances that induce local structural disorder.

This work has been written and will be submitted shortly.

Future Plans

Our future plan may be divided into two different avenues. Since the present DOE grant would end in August 2025 we will continue to study the optical and magneto-optical properties of 2D HOIP with emphasize on chiral compounds. We have preliminary data on MCD spectroscopy of chiral 2D MBA, which is a prototype chiral HOIP. These results would probably be the basis of another publication in 2025. We have also started to measure circularly polarized Raman scattering of the chiral MBA compounds for studying 'chiral phonons' in these materials. We hope that these studies would be the basis of an additional support period funded by the DOE BES program in the near future.

References

1. H. Lu, Z. V. Vardeny, and M. Beard, *Control of Light, Spin, and Charge with Chiral-Metal-Halide Semiconductor Hybrids*, Nature Reviews Chemistry **6**, 470 (2022).

2. U. N. Huynh, R. Bodin, X. Pan, P. Bailey, H. Liu, S. McGill, D. Semenov, P. C. Sercel, and Z. V Vardeny, *Magneto-optical studies of hybrid organic/inorganic perovskite: The case of methyl-ammonium-lead-bromide*, Phys, Rev. B **109**, 014316 (2024).

3. C. Zhang, P. Bailey, S. Zhang, U. Huynh, X. Jiang, S. McGill, D. Semenov, and Z. V. Vardeny, *Thermalization and spin relaxation dynamics of localized photocarriers in the band tails of nanocrystalline $MAPbBr_3$ films*, ACS Photonics 11, 4588 (2024).

Publications

1. C. Zhang, X. Jiang, P. C. Sercel, H. Lu, M. C. Beard, S. McGill, D. Semenov, and Z. V. Vardeny, *Dark Exciton in 2D Hybrid Halide Perovskite Films Revealed by Magneto-Photoluminescence at High Magnetic Field,* Advanced Optical Materials, 02300436 (2023).

2. X. Li, S. Zhang, X. Zhang, Z. V. Vardeny, and F. Liu, *Topological nodal-point superconductivity in two-dimensional ferroelectric hybrid perovskites*, Nano Letter 24, 2705 (2024).

3. X. Pan, D. R. Khanal, O. Kwon, and Z. V. Vardeny, *Magneto-Optical Studies of Organic Electroluminescent Materials Having Fast Reverse Intersystem Crossing*, Phys. Rev. Applied **21**, 034057 (2024).

4. I. Brown, M. Sheffield, H. H. Walpitage, Y. Yao, Y. Li, and Z. V. Vardeny, "Electric Field Effects in Hybrid Perovskites Studied via Picosecond Kerr Microscopy", *ACS Applied Materials and interfaces*, **16**, 31696−31702 (2024).

5. U. N. Huynh, R. Bodin, X. Pan, P. Bailey, H. Liu, S. McGill, D. Semenov, P. C. Sercel, and Z. V Vardeny, *Magneto-optical studies of hybrid organic/inorganic perovskite: The case of methyl-ammonium-lead-bromide*, Phys, Rev. B **109**, 014316 (2024).

6. C. Zhang, P. Bailey, S. Zhang, U. Huynh, X. Jiang, S. McGill, D. Semenov, and Z. V. Vardeny, *Thermalization and spin relaxation dynamics of localized photocarriers in the band tails of nanocrystalline $MAPbBr_3$ films*, ACS Photonics 11, 4588 (2024).

7. E. Lafalce, R. Bodin, B. W. Larson, J. Hao, Md. A. Haque, U. Huynh, J. L. Blackburn, and Z. V. Vardeny, *Optical Studies of Doped Two-dimensional Lead Halide Perovskites: Evidence for Rashba-Split Branches in the Conduction Band*, *ACS Nano*, 18, 18299 (2024).

8. I. Brown, R. Bodin, U. Huynh, P. C. Sercel, S. McGill, D. Semenov, and Z. V. Vardeny, *Nonlinear Magnetic Field Dependence of Quantum Beats in $FAPbI_3$*, Jour. of Physical Chemistry C 129, 5973 (2025).

Nanocrystal-Based Diodes for Solar to Electric Energy Conversion

David H. Waldeck, University of Pittsburgh, Pittsburgh, PA 15260; Ron Naaman, Department of Chemical and Biological Physics, Weizmann Institute, Rehovot, Israel; David N. Beratan, Department of Chemistry, Duke University, Durham, NC 27708

Keywords: spin-filtered currents, quantum dots, circular dichroism, chiral imprinting, triplet energy transfer

Research Scope

This project explores design features that promote efficient charge transfer in nanoparticle-based materials which form by self-assembly. The symmetry breaking that arises in chiral molecules and nanostructures manifests in unusual electronic and magnetic properties, e.g., spin-filtered electron currents at room temperature. Our team is building upon these earlier discoveries in an effort to elucidate how a chiral nanostructured material's architecture and chiro-optical properties can be designed to promote efficient charge and spin transfer. We are proceeding along two major thrusts.

- Thrust 1 activities are elucidating the differences between the transport of an electron's spin and that of its charge through chiral quantum dots (QDs) and QD networks. We have begun by examining spin-filtered currents in QDs and QD films as a function of their electronic chirality, as measured by circular dichroism spectroscopy.
- Thrust 2 is developing methods to synthesize and study chiral nanoparticles that are doped with metal ions (d- and f-block) to examine how the chiral symmetry breaking can be exploited to impart spin-filtering properties and circularly-polarized luminescence properties to the materials

Our interdisciplinary team consists of researchers at the University of Pittsburgh, Duke University, and the Weizmann Institute of Science.

Recent Progress

Over the past year we have examined the correlation between circular dichroism spectra and the role of chiral-induced spin selectivity (CISS) in energy transfer, electron transport, and circularly-polarized luminescence.

Chiral imprinting. III-V quantum dots are attractive alternatives to those based on chalcogenides because of their wide and tunable range of band gaps and their potential for eliminating heavy metals with indium or gallium. Circular dichroism and circularly-polarized photoluminescence have not yet been demonstrated in these materials. We are investigating strategies to imprint chirality on indium phosphide QDs, an archetypal member of this family. In this ongoing investigation, we are focus on optimizing the ligand exchange process in order to boost both CD and photoluminescence intensity. Subsequent studies on optimized systems will determine the dissymmetry factor in circularly-polarized photoluminescence and in the spin-dependent electron currents, using mc-AFM and/or FET devices with magnetic contacts.

Chiral-induced spin selectivity to manipulate triplet energy transfer processes. To study CISS-induced modulation of triplet energy transfer (TET) rates, we constructed systems comprising molecular triplet acceptors (TAs) bound to the surfaces of quantum dot (QD) donors, and we inferred TET rates from the photoluminescence (PL) decay kinetics of the donor measured by time-correlated single photon counting (TCSPC). Repeatable differences between TET rates when the donor is excited with left- and right-handed circularly polarized light, that reverse when the handedness of the system is flipped, should provide compelling evidence for this effect. To enforce consistent directionality of the exciton spin polarization and the direction of TET necessary for CISS to manifest, we assembled the donor-acceptor systems onto the surfaces of large (~1 μm) SiO_2 microbeads so that TAs predominantly attach only to the side of the QD donors struck by the TCSPC excitation pulses. In our previous report, we investigated systems in which CdS@ZnS core@shell quantum dots (on which chirality can be imprinted) served as the donor and found that their PL quenches significantly

in the presence of achiral triplet accepting molecules based on anthracene and pyrene chromophores, and subsequent efforts have been directed towards optimizing related systems. TCSPC measurements on these QD-TA systems assembled onto SiO_2 microbeads have not displayed a consistent response of donor fluorescence decay kinetics to the polarization of the emission. We suspect that while triplet energy transfer appears to be occurring, it is relatively slow compared with the spin depolarization time of the photoexcited electron (~1 ns), negating any effect that CISS would have.

Spin filtering in quantum dot assemblies. This work explores structure-property relationship development for chiral quantum dot assemblies in order to identify attributes of CISS-based phenomena. Through a series of studies on quantum dot (QD) films in which we can systematically tune the strength of their 'electronic chirality', as measured by the circular dichroism (CD) strength of the chiral CdSe QD's first exciton transition, we have examined how the film's propensity to transmit pure spin currents and to spin filter charge currents changes with the QD's CD transition strength. The experiments show that both pure spin transport and spin-polarized charge transport correlate with the CD strength, Δε, of the chiral QDs lowest energy exciton band, supporting the use of CD as a predictor for spin-dependent transport measurements. The spin-dependent charge current follows a sigmoid shape with Δε for its magnitude and is enantiospecific, i.e., its sign depends on the enantiomorph of the material. The pure spin current increases linearly with $|\Delta\varepsilon|$ and arises from the chirality, or helicity, along the transport direction, but is not enantiospecific. These experimental observations can be rationalized by a chirality-induced unconventional spin-orbit coupling model, which offers a new perspective on the role of chiral symmetry and the electric field associated with the charge motion on the CISS effect. This work was performed in collaboration with Prof. Dali Sun of North Carolina State University. Additional studies are exploring the effects of chiral ligands on carrier transport in quantum dot solids.

Chiro-optical and spin filtering properties of doped chiral semiconductor materials. We are investigating how chiral materials, namely *R*- and S-1-(1-naphthyl) ethylammonium lead bromide (*R*- and *S*-NEA)$_2$PbBr$_4$ perovskite 2D films, can be used to promote circularly-polarized luminescence (CPL) from lanthanide dopants. Two main strategies are being explored: 1) direct substitution into the perovskite lattice and 2) as a tetrakis-*β*-diketonate complex (EuL$_4$) that intercalates between the perovskite sheets. Successful sensitization of Eu^{3+} is observed for both doping mechanisms, i.e. fluorescence spectra of 2.5% Eu @ (*R*-NEA)$_2$PbBr$_4$ (blue) and (S-NEA)$_2$PbBr$_4$ (green) perovskite thin films and 5%EuL$_4$ @ (*R*-NEA)$_2$PbBr$_4$ (black) and (S-NEA)$_2$PbBr$_4$ (red) perovskite thin films. Clear differences in the CPL become manifest, a broad CPL signature is observed for direct substitution; however, CPL is observed at each transition when the perovskite is doped with the Eu complex and suggests different mechanisms for sensitization. We posit that the octahedral crystal field of the perovskite leads to symmetry constraints on the Eu^{3+} electric dipole transitions and therefore limits the observable transitions in the CPL spectra. Conversely, for the EuL$_4$ dopants, we hypothesize that host-guest interactions dominate; i.e., the perovskite's chiral organic ligands organize the ligand shell of EuL$_4$ in a chiral manner and is responsible for generating the CPL. Ongoing control experiments are focused on verifying these suppositions.

Theoretical studies of chiral imprinting. Past studies of chiral imprinting focused on detailed atomistic quantum chemical modeling of adsorbates on perovskites nanocrystals and nanoplatelets. These studies are producing an appealing qualitative picture of how adsorbate distributions can influence the CD signatures of these structures. However, the studies are costly in terms of computational time, and the large size of the structures makes the challenge of energy minimization intractable. As such, one can explore plausibility argument, but it is difficult to bring the analysis to a more rigorous point of providing specific design principles. Some of the earliest imprinting studies of our team (dating to 2006) resorted to an empirical quantum chemical approach, sacrificing

chemical detail while capturing coarse-grained structure function relationships. With a new graduate student, the Beratan group is deploying free electron, effective mass, and tight-binding methods to explore how the gross features of nanoparticle shape and composition influence the circular dichroism response of achiral nanostructures to chiral imprinting. These methods will be used in collaboration with experimental studies to develop strategies to control the circular dichroism of nanostructures and the spin polarization response. Related studies focus on symmetry breaking in achiral structures that are induced upon circularly polarized excitation.

Future Plans

- We are working to optimize the chiral imprinting on quantum dots; we plan to examine their spin filtering properties using mc-AFM measurements and their performance for circularly-polarized luminescence.
- We will continue and complete the project investigating the role of CISS on triplet energy transfer.
- We will examine how CISS affects spin and electron transport through quantum dot networks whose chiral features are controlled through ligand and nanoparticle design. These studies will use the platform which we have developed in our labs and will use a commercial PPMS instrument, now available at the University of Pittsburgh.
- We will examine the correlation between the chiroptical response and the spin-filtering performance of doped quantum dots. We will prepare doped chiral nanoparticles and examine how imprinting chirality can affect the spin-filtering and circularly-polarized luminescence involving the dopant levels. We will measure the spin-filtering performance using mc-AFM and the FET structures; and we will measure the CPL and CD spectra.
- We will continue and complete the project in which we are introducing chiral elements into semiconductor nanomaterials to promote circularly polarized luminescence. The outcomes of this effort will guide the next steps in promoting circular polarized luminescence of semiconductor materials.
- We will continue the theoretical studies of chiral imprinting on nanoparticles of various shapes and compositions to understand how the CD response may be maximized.
- We will continue quantum dynamical studies of how achiral chromophores that are photoexcited by circularly polarized light may relax to structures with a preferred handedness.

Publications

A. Vadakkayil, W. A. Dunlap-Shohl, M. Joy, B. P. Bloom, and D. H. Waldeck, *Improved catalyst performance for the oxygen evolution reaction under a chiral bias,* ACS Catalysis **14,** 17303−17309 (2024).

N. Tabassum, B. Bloom, G.H. Debnath, and D.H. Waldeck, *Factors influencing the chiral imprinting in perovskite nanoparticles,* Nanoscale **16**, 22120 – 22127 (2024).

R. Naaman and D. H. Waldeck, *What can CISS teach us about electron transfer?* J. Phys. Chem. Lett. **15,** 11002−11006(2024).

J.J. Philip, G.H. Debnath, D.H. Waldeck, and R.G. Balakrishna, *Halide exchange mediated cation exchange facilitates room temperature co-doping of d-and f-block elements in cesium lead halide perovskite nanoparticles,* Nanoscale **16**, 9558-9569 (2024).

B.P. Bloom, Z. Chen, H. Lu, and D.H. Waldeck, *A chemical perspective on the chiral induced spin selectivity effect,* National Science Review **11,** nwae212 (2024) .

R. Sun, Z. Wang, B. P. Bloom, A. H. Comstock, C. Yang, A. McConnell, C. Clever, M. Molitoris, D. Lamont, Z.-H. Cheng, Z Yuan, W. Zhang, A. Hoffmann, J. Liu, D. H. Waldeck, and D. Sun, *Colossal anisotropic absorption of spin currents induced by chirality,* Science Advances **10**, eadn3240 (2024).

B. P. Bloom, Y. Paltiel, R. Naaman, and D. H. Waldeck, *Chiral induced spin selectivity,* Chem. Rev. **124,** 1950–1991 (2024).

M. Bhar, N. Bhunia, G. H. Debnath, D.H. Waldeck, and P. Mukherjee, *Optical properties of semiconductor nanoparticles doped with 3d and 4f block elements,* Chem. Phys. Rev. **5,** 011306 (2024) .

W. A. Dunlap-Shohl, N. Tabassum, P. Zhang, E. Shiby, D. N. Beratan, and D. H. Waldeck, *Electron-donating functional groups strengthen ligand-induced chiral imprinting on $CsPbBr_3$ quantum dots,* Scientific Reports **14,** 336 (2024).
D. K. Bhowmick, N. Yuran, M. Fadeev, S. Yochelis, Y. Paltiel, and R. Naaman, *Chiral metal coating to enhance water electrolysis,* Energy Fuels **39**, 764−770 (2025).

Light-Matter Quantum Control: Coherence and Dynamics

Principal investigator: Jigang Wang
Co-investigators: Zhe Fei, Liang, Luo, Yongxin Yao
Materials Science and Engineering Division, Ames National Laboratory, Ames, IA 50011

Keywords: Coherent control, topological materials, spintronics, non-equilibrium dynamics, ultrafast optics

Research Scope

We aim to significantly advance the understanding and control of quantum dynamics and quantum transport processes mediated by coherence. We seek to optimize the initial pathways of photoenergy conversion and photocurrent transport—even in systems with impurities, grain boundaries, and complex microstructures by harnessing quantum coherence and non-equilibrium dynamics. Achieving nearly dissipationless current has far-reaching implications across topological electronics, spintronics, and photovoltaics, paving the way for next-generation microelectronics and quantum functional systems. Our approach involves characterizing the temporal, spatial, and energetic evolution of electronic, vibrational, and quantum geometric properties, as well as collective modes. We focus on materials that exhibit exceptional spin and charge coherence, symmetry, and chirality. We will uncover cross-cutting principles that govern coherent nonlinear coupling, enhanced photocurrent generation, and robust transport in topological, magnetic, and photovoltaic materials. This interdisciplinary effort brings together experimentalists—specializing in ultrafast and terahertz spectroscopy and nano-imaging—and theorists with expertise in out-of-equilibrium simulations. Our research directly supports the DOE Transformative Opportunities in *Harnessing Coherence in Light and Matter* and *Exploiting Transformative Advances in Imaging Capabilities across Multiple Scales*.

Recent Progress

- **Ultrafast Chirality Switching in a Correlated CDW-Weyl Semimetal**

We demonstrate that fluence-dependent photocurrents enable controlled transitions within topological semimetal $(TaSe_4)_2I$, shifting it sequentially from a polaronic state to a charge density wave (CDW) state, and ultimately to a concealed Weyl phase. The manipulation of chirality in correlated topological states through ultrafast photoexcitations represents a new control concept inaccessible via conventional experimental techniques like DC transports and static-state spectroscopic measurements.

Paper reference [1]: ***Nature Communications,*** 15, 785 (2024).

- **Coherent transfer of lattice entropy via extreme nonlinear phononics in photovoltaic perovskites**

This work addresses a long-standing hypothesis that unique entropy transfer pathways are fundamental to the remarkable optoelectronic properties of metal halide perovskites. We revealed a bidirectional and coherent transfer of lattice entropy, facilitated by the immense anharmonicity of organic cations and inorganic lattice quantized motions. These findings have significant implications for the coherent nonlinear control of perovskites in optoelectronics and energy conversion, particularly for achieving operations at terahertz frequencies.

Paper reference [2]: ***PRX Energy,*** 3, 023009 (2024).

- **Extreme terahertz frequency magnon multiplication**

The concept of magnonic multiplication stands as one of the most tantalizing yet enigmatic frontiers in the pursuit of THz nonlinear magnonics. We demonstrated exceptionally high-order terahertz nonlinear magnonics utilizing resonant excitation of collective spin wave modes with long-lasting quantum coherence that persists well after the laser pulses. The distinct magnon multiplication peaks demonstrate a "super" resolution tomography of long-lived interacting magnon quantum coherences.

Paper reference [3]: ***Nature Communications,*** 15, 3214 (2024).

- **Quantum dynamics simulations of coherent phonon-induced carriers pumping**

First-principles quantum dynamics simulations of a laser-driven $ZrTe_5$ system predict dynamical carrier density evolution consistent with experiments. The success of predictive nonequilibrium simulations highlights an opportunity to theoretically design protocols to dynamically control materials properties.

Paper reference [4] : ***Communications Physics,*** 6 (297) (2023).

Future Plans

- **Coherent control of topological correlated states of matter**

We will detect and control Landau-quantized Dirac fermions and axion collective modes through terahertz (THz) two-dimensional coherent spectroscopy (2DCS). The presence of topological conical bands gives rise to unique high-order harmonic generation and multi-wave mixing peaks in the 2DCS spectra that are absent in Landau systems with conventional parabolic bands.

- **Achieve light-induced phononic exitonic insulator phase transitions**

We will provide distinguishing evidence of dynamic exitonic insulator periodically driven by phonons. Coherent control of this new state of excitonic matter will be achieved using THz pulse pair excitations.

- **Harness THz near-fields to achieve real-space visualization of quantum spin Hall States**

We will detect conductive chiral edge modes associated with dissipationless current-carrying chiral edge in real space using magnetic cryogenic scanning near-field spectroscopy. We will search for light-induced Fermi arcs by THz nano-imaging of topological plasmons.

- **Theoretical modeling of the coherent responses and quantum dynamics by computing multi-order correlation functions and time-frequency spectra.**

We will simulate new features from measured quantum dynamics, nonlinear phononics and photocurrent transport. We will perform the 2D THz spectra simulations using time-dependent density functional theory and quantum kinetic density matrix theory.

References

1. B. Cheng, D. Cheng, T. Jiang, W. Xia, B. Song, M. Mootz, L. Luo, I.E. Perakis, Y. Yao, Y. Guo, J. Wang, o-Author, *Chirality manipulation of ultrafast phase switchings in a correlated CDW-Weyl semimetal*, Nature Communications, **15**, 785 (2024).
2. Z. Liu, Y. Shi, T. Jiang, L. Luo, C. Huang, M. Mootz, Z. Song, Y. Yan, Y. Yao, J. Zhao, J. Wang, *Coherent Transfer of Lattice Entropy via Extreme Nonlinear Phononics in Metal Halide Perovskites,* PRX Energy, **3**, 023009 (2024).
3. C. Huang, L. Luo, M. Mootz, J. Shang, P. Man, L. Su, I. E. Perakis, Y. X. Yao, A. Wu & J. Wang, *Extreme terahertz magnon multiplication induced by resonant magnetic pulse pairs,* Nature Communications, **15**, 3214 (2024).
4. Tao Jiang, Peter P. Orth, Liang Luo, Lin-Lin Wang, Feng Zhang, Cai-Zhuang Wang, Jin Zhao, Kai-Ming Ho, Jigang Wang & Yong-Xin Yao, *Ab-initio Simulations of Coherent Phonon-Induced Pumping of Carriers in $ZrTe_5$*, Communication Physics, 6, 297 (2023).

Publications

1. B. Q. Song, J. D. H. Smith, T. Jiang, Y. X. Yao, J. Wang, "Quantum geometry embedded in unitarity of evolution: Revealing its impacts as geometric oscillation and dephasing in spin resonance and crystal bands", Phys. Rev. B., **111**, 144305 (2025)
2. L. Luo*, B. Song*, Genda Gu, Martin Mootz, Yongxin Yao, Ilias E. Perakis, Qiang Li, and Jigang Wang, *Symmetry instability induced by topological phase transitions,* Phys. Rev. B., **111**, 075151 (2025) *equal contribution
3. B. Cheng, D. Cheng, T. Jiang, W. Xia, B. Song, M. Mootz, L. Luo, I.E. Perakis, Y. Yao, Y. Guo, J. Wang, *Chirality manipulation of ultrafast phase switchings in a correlated CDW-Weyl semimetal*, Nature Communications, **15,** 785 (2024). https://doi.org/10.1038/s41467-024-45036-1
4. Z. Liu, Y. Shi, T. Jiang, L. Luo, C. Huang, M. Mootz, Z. Song, Y. Yan, Y. Yao, J. Zhao, J. Wang, *Coherent Transfer of Lattice Entropy via Extreme Nonlinear Phononics in Metal Halide Perovskites*, PRX Energy, **3**, 023009 (2024).
5. B. Cheng, D. Cheng, K. Lee, L. Luo, Z. Chen, Y. Lee, B.Y. Wang, M. Mootz, I.E. Perakis, Z.-X. Shen, H.Y. Hwang, J. Wang, *Evidence for d-wave superconductivity of infinite-layer nickelates from low-energy electrodynamics*, Nature Materials **23**, 775 (2024).

6. C. Huang, L. Luo, M. Mootz, J. Shang, P. Man, L. Su, I.E. Perakis, Y.X. Yao, A. Wu, J. Wang, Extreme Terahertz Magnon Multiplication Induced by Resonant Magnetic Pulse Pairs, Nature Communications, **15**, 3214 (2024). https://doi.org/10.1038/s41467-024-47471-6
7. R.H.J. Kim, A.K. Pathak, J.-M. Park, M. Imran, S.J. Haeuser, Z. Fei, Y. Mudryk, T. Koschny, J. Wang, "Nano-compositional imaging of the lanthanum 2 silicide system at THz wavelengths," Optics Express, **32** (2), 2356-2363 (2024).
8. B.Q. Song, J.D.H. Smith, L. Luo, J. Wang, *Quantum Liouville theorem based on Haar measure*, Physical Review B, 109,144301 (2024). https://doi.org/10.1103/PhysRevB.109.144301
9. T. Jiang, P. P. Orth, L. Luo, L.-L. Wang, F. Zhang, C.-Z. Wang, J. Zhao, K.-M. Ho, J. Wang, Y.-X. Yao, *Ab-Initio Simulations of Coherent Phonon-Induced Pumping of Carriers in Zirconium Pentatelluride*, Communications Physics, 6 (297) (2023). https://doi.org/10.1038/s42005-023-01415-6
10. L. Luo, D. Cheng, C. Huang, X. Yang, C. Vaswani, M. Mootz, Y. Yao, X. Liu, M. Dobrowolska, J.K. Furdyna, I.E. Perakis, J. Wang, "Room temperature persisting surface charge carriers driven by intense terahertz electric fields in a topological insulator Bi2Se3," APL Materials, 11, 121119 (2023). https://doi.org/10.1063/5.0181223

Explore Nonlinear Response Induced by Berry Curvature in Layered Topological Semimetals

Ying Wang, University of Wisconsin-Madison

Keywords: Nonlinear Hall effect, Weyl semimetal, structural-property relationship, RF light matter interaction

Research Scope

The aim of this project is to investigate the quantum geometrical properties and its associated energy-efficient nonlinear electrodynamics in emergent layered topological semimetals. Emerging topological semimetals offer a unique platform for exploring nonlinear quantum phenomena rooted in the geometric properties of electronic wavefunctions. In particular, type-II Weyl semimetals such as WTe_2 and $TaIrTe_4$ exhibit a striking nonlinear Hall effect (NLHE) in the absence of magnetic fields, originating from the diverging Berry curvature near tilted Weyl nodes[1–3]. Each chiral Weyl point acts as a monopole of Berry curvature—an effective magnetic field in momentum space—which imparts anomalous transverse velocities to charge carriers under an applied electric field. This effect manifests as a second-order nonlinear response characterized by a transverse DC current $j_a(\omega-\omega)\ or\ j_a(2\omega) \propto \chi_{abc}E_b(\omega)E_c(\omega)+\cdots$ where $a,b,c \in (x,y,z)$, E_b, E_c are alternating electric field and χ_{abc} is nonlinear conductivity tensor tied to the Berry curvature dipole[4,5] (see in Fig 1). While NLHE has been demonstrated under low-frequency AC fields (<1 kHz), it is unknown how well this mechanism can persist in the higher frequency region including radiofrequency, which is essential for practical energy harvest applications. Second, even under low-frequency conditions, the intrinsic and extrinsic factors controlling this nonlinearity are not well understood as reported rectification efficiencies vary widely. This project aims to address both challenges by experimentally probing the frequency-dependent NLHE arising from Berry curvature dipole and identifying the microscopic parameters that govern the strength of this quantum-geometric response. Insights from this work will not only deepen the understanding of the fundamental relationship among electrodynamics, lattice symmetry and Berry curvature but also pave the way for novel nonlinear optoelectronic devices rooted in quantum geometry.

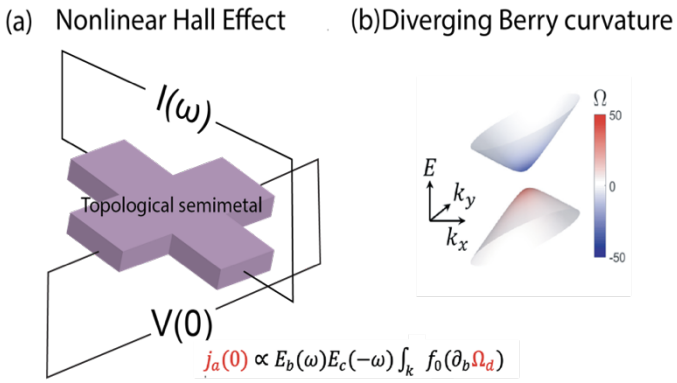

Fig 1. Nonlinear Hall effect in topological semimetals, converting alternating longitudinal current $I(\omega)$ to transverse direct current $V(0)\ or\ V(2\omega)$. Such effect is determined by diverging Berry curvature Ω in momentum space, which is highlighted in red and blue.

Recent Progress

1. A giant nonlinear response arises from the interplay of topology and strong correlation

The interplay between strong electronic correlations and band topology is a fertile ground for discovering emergent quantum phases and transitions, such as the fractional quantum spin Hall effect and topological superconductivity. While nonlinear electrical responses can sensitively probe both symmetry and topology, their role in systems where topology coexists with electron correlation remains largely unexplored. Here, we report a giant nonlinear Hall response in the few-layer topological semimetal $TaIrTe_4$, arising from the interplay between topological band structure and a correlated charge density wave (CDW) state. In the Fig 2, below critical temperature Tc~60K and critical current Ic~20 μA, we discover a new state which greatly enhanace the nonlinearity in $TaIrTe_4$. This correlated phase (state II) is identified through the emergence of a Raman amplitude mode, enhanced second harmonic generation, and nonlinear symmetry analysis (see in Fig 3). The combination of nonlinear transport and optical measurements also points out such CDW is one-dimensional along the Ta chain. First-principles calculations reveal that the CDW induces a redistribution of Berry curvature and Berry curvature dipole, which underlies the enhanced nonlinearity. Our findings demonstrate that the coupling between topology and strong correlations can give rise to unconventional nonlinear transport and establish electrical nonlinearity as a powerful probe for accessing complex quantum phase diagrams in correlated topological materials. Moreover, its recorded-high nonlinear susceptibility at both cryogenic and room temperature also makes it competitive for nonlinear device development, such as energy harvesters and RF detectors.

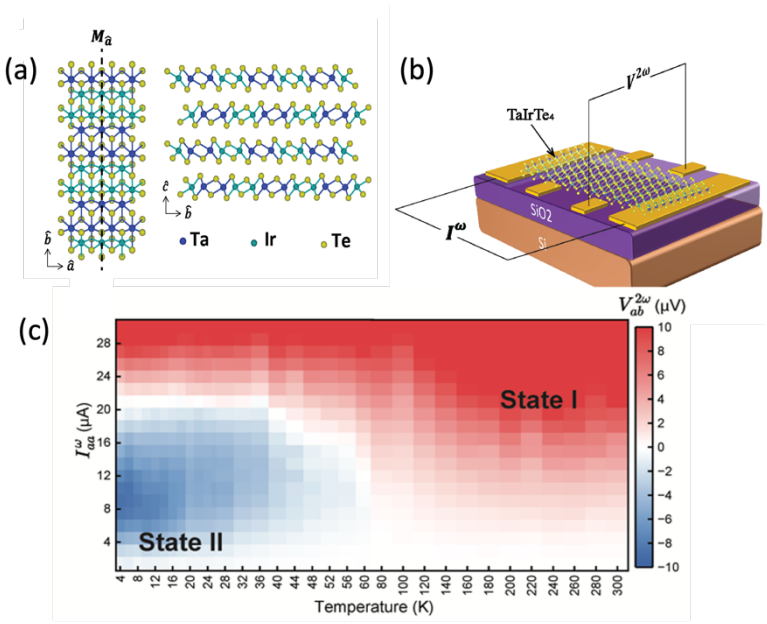

Fig 2. nonlinear Hall measurement in TaIrTe4 (a) crystal structure of TaIrTe4 (b) NLH device schematics (c) a new state II largely enhances nonlinear response below critical temperature Tc~60K and critical current Ic~20 μA.

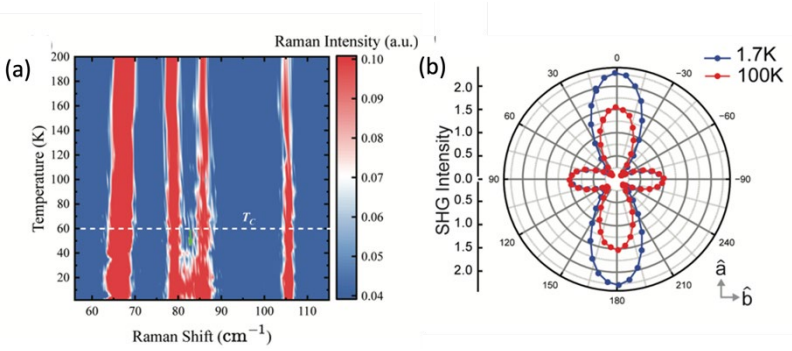

Fig 3. (a) The rising of a new peak at ~83 cm^{-1} emerging below 60 K indicates the amplitude mode in the CDW phase. (b) Polarized SHG patterns of TaIrTe4 at 1.7 K with enhanced anisotropy along a axis supports the 1D nature of the CDW phase.

2. Nonlinear response in THz region arises from Berry curvature dipole in Weyl semimetal $TaIrTe_4$

Realizing the full potential of THz technologies requires a deeper understanding of light–matter interactions at ultrafast timescales and strong coupling regimes. Here, we demonstrate that the nonlinear Hall effect (NLHE)—traditionally explored at low frequencies—can serve as a new fundamental mechanism for THz optoelectronic response in the 2D correlated topological semimetal $TaIrTe_4$ (see in Fig 4). This finding establishes NLHE as an intrinsic, symmetry-protected process that can operate across the ultrabroadband THz range (0.1–10 THz), with its strength directly tied to the underlying electronic band structure and Berry curvature dipole. We also find that Berry curvature dipole, strongly related to the strong correlation state in this material can be controlled electrically. Therefore, through electrostatic gating, we modulate the electron correlation strength and Berry curvature dipole, which demonstrates a dramatic enhancement of performance with large zero-bias responsivity ($R \sim 18$ A/W) and high sensitivity (NEP ~ 0.05 $pW/Hz^{1/2}$) and picosecond-scale response times. Combined with first-principles calculations, the mechanism can be understood by the picture that the electron correlation in 2D TaIrTe4 induces substantial band renormalization with abundant band crossings and inversions around the Fermi level, which leads to drastic changes in the Berry curvature and density of states, and greatly enhanced NHE. By building upon the strong THz light-matter interaction and large gate tunability of few-layer $TaIrTe_4$, our work not only advances the understanding of THz nonlinear electrodynamics in 2D correlated topological semimetals, but also paves the way for developing high-performance intelligent THz sensing technology.

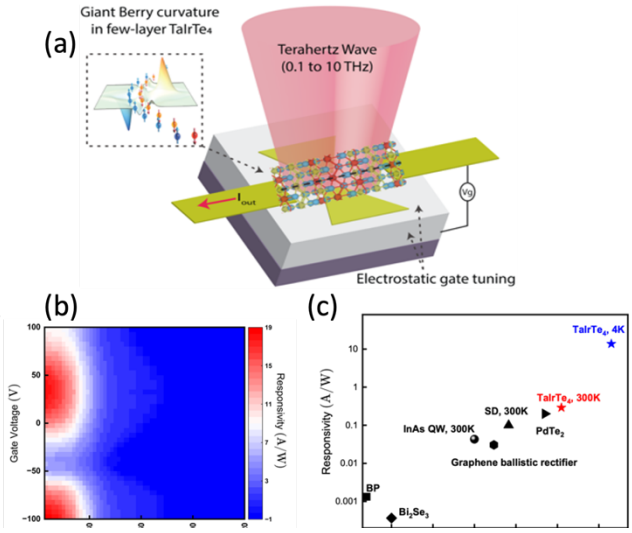

Fig 4. (a) Schematics for THz sensing mechanism based on Berry curvature. (b)THz responsivity as a function of gate bias and temperature. the hot spot of responsivity responses to the emergency of strong correlated states. (c) THz sensing performance comparison among electronic-type THz detectors.

Future Plan

A key direction of our future research is to uncover the fundamental mechanisms by which external perturbations—such as strain—modulate the Berry curvature dipole and their determined nonlinear electrodynamics in topological semimetals. Since the Berry curvature is a geometric property of the electronic band structure, it is highly sensitive to lattice symmetry, electronic degeneracies, and band topology. Strain can break or lower crystal symmetry, shift Weyl node positions, and reshape the energy landscape, all of which may dramatically alter the Berry curvature distribution[6,7]. To realize this, we will combine in-situ strain tuning via piezoelectric platforms and

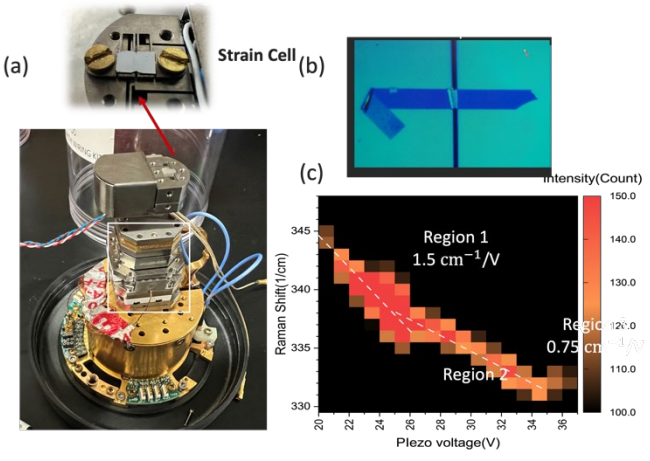

Fig 5. Strain cell enables in-situ strain control in target flakes. (a) strain cell coupled into cryostat in our lab (b) 2D flake in a gap substrate whose strain can be controlled by strain cell (c) In-situ Raman spectroscopy characterize strain level in the flake.

strain characterization via Raman spectroscopy (see in Fig 5). We will measure nonlinear Hall and nonlinear electrodynamic response under variable conditions. By correlating these controlled perturbations with changes in nonlinear response, supported by first-principles calculations, we aim to establish a quantitative framework linking material imperfections and symmetry breaking to quantum geometric responses. This work will provide deep insights into nonlinear phenomena arising from Berry curvature in topological systems and lay the foundation for advance the design of next-generation, symmetry-engineered quantum materials.

References

1. J. Xiao, Y. Wang, H. Wang, C.D. Pemmaraju, S. Wang, P. Muscher, E.J. Sie, C.M. Nyby, T.P. Devereaux, X. Qian, X. Zhang, and A.M. Lindenberg, *Berry curvature memory through electrically driven stacking transitions,* Nat Phys **16** (10), (2020).
2. Q. Ma, S.Y. Xu, H. Shen, D. MacNeill, V. Fatemi, T.R. Chang, A.M. Mier Valdivia, S. Wu, Z. Du, C.H. Hsu, S. Fang, Q.D. Gibson, K. Watanabe, T. Taniguchi, R.J. Cava, E. Kaxiras, H.Z. Lu, H. Lin, L. Fu, N. Gedik, and P. Jarillo-Herrero, *Observation of the nonlinear Hall effect under time-reversal-symmetric conditions,* Nature **565** (7739), (2019).
3. K. Kang, T. Li, E. Sohn, J. Shan, and K.F. Mak, *Nonlinear anomalous Hall effect in few-layer WTe 2*, Nat Mater **18**(4), (2019).
4. I. Sodemann, and L. Fu, *Quantum Nonlinear Hall Effect Induced by Berry Curvature Dipole in Time-Reversal Invariant Materials*, Phys Rev Lett **115** (21), (2015).
5. Z.Z. Du, H.Z. Lu, and X.C. Xie, *Nonlinear Hall effects*, Nature Reviews Physics **3**(11), (2021).
6. Z. Dai, L. Liu, and Z. Zhang, *Strain Engineering of 2D Materials: Issues and Opportunities at the Interface,* Advanced Materials **31**(45), (2019).
7. Z. Peng, X. Chen, Y. Fan, D.J. Srolovitz, and D. Lei, *Strain engineering of 2D semiconductors and graphene: from strain fields to band-structure tuning and photonic applications*, Light Sci Appl **9** (1), (2020).

Publications

1. Carter Fox, Yulu Mao, Xiang Zhang, Ying Wang, Jun Xiao, *Stacking Order Engineering of Two-Dimensional Materials and Device Applications*, Chemical Reviews **124**, 1862-1898 (2024).
2. Tairan Xi, Haotian Jiang, Jiangxu Li, Yangchen He, Yuchen Gu, Carter Fox, Louis Primeau, Yulu Mao, Jack Rollins, Takashi Taniguchi, Kenji Watanabe, Daniel van der Weide, Daniel Rhodes, Yang Zhang, Ying Wang*, Jun Xiao*, *Strong nonlinear electrodynamics in 2D correlated topological semimetal $TaIrTe_4$ for high-performance THz sensing*, Nature Electronics, in press, 2025
3. Haotian Jiang, Tairan Xi, Jiangxu Li, Yangchen He, Hongrui Ma, Yulu Mao, Takashi Taniguchi, Kenji Watanabe, Daniel Rhodes, Yang Zhang, Jun Xiao, Ying Wang, *Probing interplay of topological properties and electron correlation in atomically thin TaIrTe4 via nonlinear Hall effect,* Nature Communications, under review, 2025

Fundamentals of Semiconductor Nanowires

Peidong Yang, Department of Chemistry, UC Berkeley; Materials Sciences Division, Lawrence Berkeley National Laboratory
Stephen R. Leone, Department of Chemistry, UC Berkeley; Materials Sciences Division, Lawrence Berkeley National Laboratory
Eran Rabani, Department of Chemistry, UC Berkeley; Materials Sciences Division, Lawrence Berkeley National Laboratory
David T. Limmer, Department of Chemistry, UC Berkeley; Materials Sciences Division, Lawrence Berkeley National Laboratory
Mary C. Scott, Department of Chemistry, UC Berkeley; Materials Sciences Division, Lawrence Berkeley National Laboratory

Keywords: Semiconductor nanowires, Optical properties, Phase transition, Structural dynamics.

Program Scope

The properties of semiconducting nanowires (NWs) are governed by a rich interplay of dimensionality, bonding characteristics, and emergent nanoscale phenomena. This program integrates atomically precise synthesis (spanning from molecularly thin to mesoscale dimensions), state-of-the-art electron microscopy, ultrafast XUV spectroscopy, and advanced theoretical modeling. Our goal is to develop a fundamental understanding of structure-property relationships in low-dimensional semiconductor NWs, paving the way for next-generation nanotechnologies in energy, photonics, and quantum applications.

Recent Progress

1. Molecular scale supramolecular assembly: The $[MX_6]^{n-}$ (M = Pb^{2+}, Te^{4+}, Sn^{4+} etc.; X = Cl^-, Br^-, I^-) metal halide ionic octahedral units are the fundamental building blocks and functional units in metal halide perovskites. Aiming to construct molecular one-dimensional (1D) wire structures, significant efforts have focused on the rational design and precise control of the assembly process. Incorporating five or more different types of metal halide octahedra creates a system with heterogeneous energy landscape, increasing the configurational entropy of the system, which then enhances the entropy of mixing, and in turn lowers the Gibbs free energy of formation, favoring the stabilization of a single-phase high-entropy system. Taking advantage of the low cohesive energy and solution processability of halide perovskites, we synthesized high-entropy metal halide perovskite single crystals by incorporating five to six different $[MX_6]^{2-}$ octahedra into a single-phase structure at as low as room temperature (**Figure 1a**). Selected compositions exhibit notable photoluminescence (PL) and tunability in optical properties.[1] To enhance design flexibility, supramolecular cations are introduced as counter cations to assemble metal halide octahedra, yielding a family of dumbbell-shaped (crown ether@A)$_2$M(IV)X$_6$ (crown ether = 18-Crown-6 (18C6), 21-Crown-7 (21C7); A = Cs^+, Rb^+, K^+; M = Te^{4+}, Sn^{4+}, Se^{4+}, Ir^{4+}, Pt^{4+}, Zr^{4+}, Ce^{4+}; X = Cl^-, Br^-, I^-) structural units in solution, which can be further packed into various three-dimensional crystal structures (**Figure 1b**).[2] The composition (18C6@K)$_2$HfBr$_6$ exhibits blue emission with a near-unity

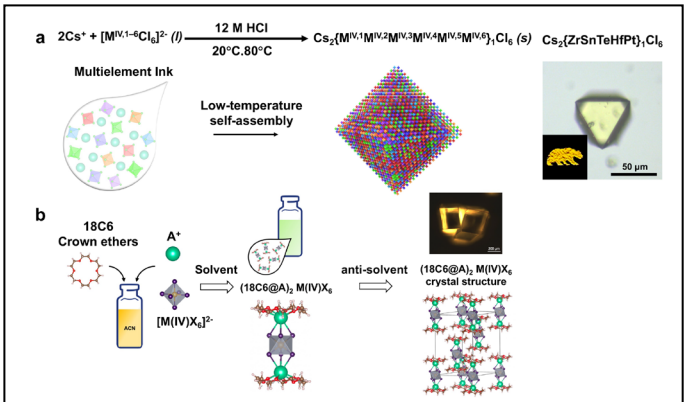

Figure 1. (a) Self-assembly of $[MCl_6]^{2-}$ octahedra and Cs^+ cations to form high entropy halide perovskite single crystals. (b) The supramolecular assembly strategy from $[M(IV)X_6]^{2-}$ octahedron to (18C6@A)$_2$M(IV)X$_6$.

photoluminescence quantum yield (PLQY) of 96.2 ± 1.2%, far surpassing K_2HfBr_6 (PLQY = 12.79%).[3] And another composition $(18C6@K)_2ZrCl_4Br_2$ demonstrates green emission with a PLQY of 82.7 ± 0.9% (**Figure 2**). We also showed that the supramolecular approach is very promising in solution processability.[3] The $(18C6@K)_2HfBr_6$/PS-DCM ink maintains a high PLQY of over 90%. Upon simple drop casting of the ink, a uniform and highly emissive (over 80% PLQY) $(18C6@K)_2HfBr_6$/PS thin film can be obtained for display applications. These advancements represent significant progress toward precisely synthesizing desired structures with outstanding optoelectronic properties, thereby establishing a foundational platform for the subsequent pursuit of molecular wire architectures.

2. Nanoscale halide perovskite nanowires: The optoelectronic properties of semiconducting materials exhibit pronounced size dependence at the nanoscale because of quantum and dielectric confinement, relevant for device applications. Our spectroscopic results revealed that exciton diffusion along the NW length facilitates nonradiative recombination by enabling excitons to reach trap states beyond their initial generation site.[4] This effect is particularly pronounced in weakly confined (>7 nm-thick) NWs, where increased exciton diffusion length correlates with reduced PLQY.[4] Conversely, in the strongly confined regime (<7 nm thickness), enhanced radiative recombination rates mitigate the impact of exciton diffusion, enabling near-unity PLQY despite the presence of trap states (**Figure 3**).[4] Notably, 2.4 nm-thick $CsPbBr_3$ NWs exhibited near-unity PLQY while emitting blue photons at a rate 3.8 times faster than conventional $CsPbBr_3$ QDs without a loss of efficiency.[76] Theoretical insights into the excitonic behavior $CsPbBr_3$ NCs have been critical in understanding the mechanisms that govern PLQY and recombination dynamics. We have developed and applied Path-Integral methods to reveal the role of lattice fluctuations in modulating excitonic properties for bulk materials, 2D materials, and nanocrystals. Additionally, the strong spin-orbit coupling inherent to lead halide perovskites has driven the development of relativistic pseudopotentials tailored for nanocrystals at experimentally relevant sizes. Using an atomistic semi-empirical pseudopotential framework that explicitly incorporates nonlocal angular momentum effects, we have computed excited-state properties and radiative recombination rates in 1D $CsPbX_3$, providing crucial theoretical support for interpreting experimental photodynamics. A key finding is that strongly confined 1D perovskites enjoy an enhancement to the radiative rate due to increased oscillator strength, granting them faster radiative rates than their zero-dimensional analogs.[4] This same trend was verified in 2D perovskites through Path-Integral Monte Carlo and a variational theory. Specifically, as a function of increasing quantum well thickness, there is a competition between dielectric screening from the heterogeneous dielectric environment and the polarization generated from the inorganic lattice. This work sets design principles for obtaining optically efficient $CsPbX_3$, which can help inform the design of optoelectronic devices, as well as highlight previously unexplored structural degrees of freedom to engineer the excited state dynamics of semiconductors.

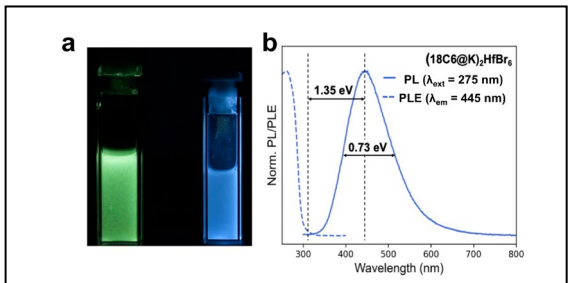

Figure 2. (a) Blue and green emission from $(18C6@K)_2HfBr_6$/polymer and $(18C6@K)_2ZrCl_4Br_2$/polymer inks (b) PL and PL excitation (PLE) spectra of $(18C6@K)_2HfBr_6$ powders with 275 nm excitation.

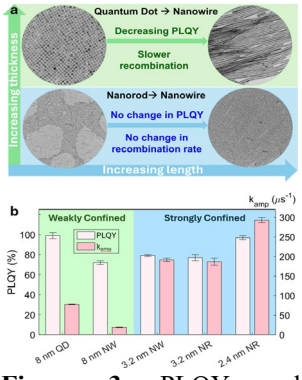

Figure 3. PLQY and recombination rate with NC size and morphology.

3. Mesoscopic perovskite nanowires: Previous studies have identified $CsGeX_3$ (X = Br, I) as a multifunctional material system. Subsequent investigations of epitaxial $CsGeX_3$ nanowire arrays grown on mica substrates via vapor-phase deposition revealed tunable PL from 591 to 712 nm, alongside with room-temperature ferroelectricity, highlighting their potential for next-generation optoelectronic and ferroelectric device applications.

In parallel with the investigations of halide perovskite nanowires, we are transitioning our mesoscopic efforts toward chalcogenide perovskite nanowires. Chalcogenide perovskites have a general chemical formula of AMX_3 (A = Ba^{2+}, Sr^{2+}, B = Zr^{4+}, Hf^{4+}, and X = S^{2-}, Se^{2-}, and Te^{2-}) and exhibit both ionic and covalent bonding characteristics, offering a largely unexplored yet promising avenue for next-generation materials research. These materials present enhanced stability against environmental degradation, higher tunability in electronic and optical properties, and more robust structural integrity, which could lead to breakthroughs in long-term energy and electronic applications. Their mixed bonding nature enables unique phase behaviors and reconfigurable lattices, providing a versatile platform for discovering new emergent phenomena in nanowires. We recently reported the first work on synthesizing the single-crystalline chalcogenide perovskite nanowires (NWs) of mesoscopic scale.[5] In this work, we synthesized the AMS_3 (A = Ba, Sr; M = Zr, Hf) NWs on sapphire substrates via a one-step chemical vapor transport (CVT) process in a sealed quartz ampoule, as shown in **Figure 4**. These NWs have a thickness of approximately 100 nanometers, which can be tuned by adjusting the growth duration and temperature. Comprehensive structural characterizations confirmed their single crystallinity and structural rigidity, especially under prolonged exposure to 300 kV electron beam.

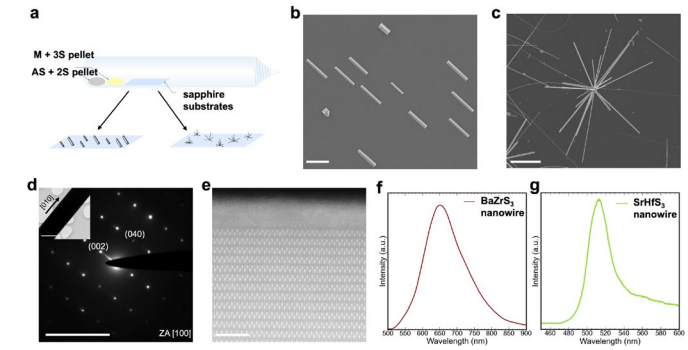

Figure 4. (a) Illustration of the NW synthesis setup. SEM image of (b) $BaZrS_3$ NWs (scale bar: 10 μm) and (c) $SrHfS_3$ NWs (scale bar: 20 μm). (d) Electron diffraction pattern of a $SrHfS_3$ NW (scale bar: 10 1/nm) (inset image: 1 μm). (e) HAADF-STEM image of a $SrHfS_3$ NW (scale bar: 2 nm). Steady-state PL spectra of (f) $BaZrS_3$ (λ_{ex} = 375 nm) and $SrHfS_3$ NWs (λ_{ex} = 400 nm) at room temperature.

Sulfide-based compositions exhibit direct and tunable bandgap of 1.6 eV to 2.4 eV in the visible region, indicating their potential as semiconducting materials for display applications and LEDs. Confocal microscopy and PL spectroscopy were employed to probe chalcogenide perovskite NW's optical properties. The $BaZrS_3$ NWs are expected to have a bandgap of 1.7-1.9 eV, whereas the $SrHfS_3$ NWs have a bandgap of around 2.3-2.4 eV. We observed red and green emissions from $BaZrS_3$ and $SrHfS_3$ NWs, respectively, indicating the material's tunability in emission by varying compositions and their potential for optoelectronic applications. The PL intensity, however, is weaker than the halide perovskite counterparts, mostly due to their intrinsic predominantly harmonic vibrational dynamics and a large number of defects acting as nonradiative recombination centers. The weak emission could be and has been shown to be effectively enhanced via rational defect control in synthesis, highlighting the need for future optimization efforts. The PL lifetime was also probed by Fluorescence Lifetime Imaging Microscopy (FLIM), and their decay profile is fitted by a biexponential model. The longer lifetime components for both $BaZrS_3$ and $SrHfS_3$ NWs are on the nanosecond timescale, comparable to those of halide perovskite NWs. Together, these findings establish a foundation for exploring and tailoring chalcogenide perovskite NWs' structural and optical properties for advanced photonic and electronic devices.

Future Plans

Looking forward, this program will establish a comprehensive framework for semiconductor nanowire studies by integrating rational design and precise synthesis, multimodal electron microscopy, ultrafast spectroscopy, and advanced simulation. We will expand synthetic capabilities to access single-unit-cell and molecular wire systems and explore their size-dependent excitonic and phase transition behaviors. Our efforts will leverage the latest instrumentation, such as 4D-STEM, XUV, and visible transient absorption spectroscopy, to directly visualize structural dynamics at the atomic scale and correlate them with optoelectronic properties. Theoretical efforts will continue to develop predictive models for exciton-phonon coupling and atomistic electronic structure methods for chiroptical responses in complex nanomaterials to further elucidate their structure-property relationships. Collectively, this program will illuminate the fundamental principles governing the emergent physics of 1D semiconductors.

References

1. M. C. Folgueras, Y. Jiang, J. Jin, and P. Yang, *High-Entropy Halide Perovskite Single Crystals Stabilized by Mild Chemistry*, Nature 621, 282-288 (2023).
2. C. Zhu, J. Jin, M. Gao, A. M. Oddo, M. C. Folgueras, Y. Zhang, C.-K. Lin, and P. Yang, *Supramolecular Assembly of Halide Perovskite Building Blocks*, J. Am. Chem. Soc. 144, 12450-12458 (2022).
3. C. Zhu, J. Jin, Z. Wang, Z. Xu, M. C. Folgueras, Y. Jiang, C. B. Uzundal, H. K. Le, F. Wang, and X. Zheng, *Supramolecular Assembly of Blue and Green Halide Perovskites with near-Unity Photoluminescence*, Science 383, 86-93 (2024).
4. A. M. Oddo, D. Chabeda, J. Basu, M. Arnold, C. Song, E. Rabani, and P. Yang, *Exploring the Structural Origins of Optically Efficient One-Dimensional Lead Halide Perovskite Nanostructures*, J. Am. Chem. Soc. 147, 10466-10474 (2025).
5. Y. Jiang, H. K. D. Le, L. Verbitsky, H. DeVyldere, A. M. Oddo, B. Pan, H.-g. Song, C. Zhu, H. Zhu, M. C. Scott, and P. Yang, *Emissive Chalcogenide Perovskite Nanowires*, Nano Lett., **ASAP** (2025).

Publications

1. A. M. Oddo, D. Chabeda, J. Basu, M. Arnold, C. Song, E. Rabani, and P. Yang, *Exploring the Structural Origins of Optically Efficient One-Dimensional Lead Halide Perovskite Nanostructures*, J. Am. Chem. Soc. **147**, 4800-4810 (2025).
2. R. Rana and D. T. Limmer, *On the Interplay of Electronic and Lattice Screening on Exciton Binding in Two-Dimensional Lead Halide Perovskites*, Nano Lett. **25**, 4727-4733 (2025).
3. J. R. Adelman, H. Laurell, L. Drescher, H. K. D. Le, P. Yang, and S. R. Leone, *Coherently Coupled Carrier and Phonon Dynamics in Elemental Tellurium Probed by Few-Femtosecond Core-Level Transient Absorption*, arXiv:2411.09035 (2024).
4. D. Chabeda, S. Gee, and E. Rabani, *Ligand-Induced Size-Dependent Circular Dichroism in Quantum Dots*, J. Phys. Chem. Lett. **15**, 7863-7869 (2024).
5. Y. Park, R. Rana, D. Chabeda, E. Rabani, and D. T. Limmer, *Theoretical Insights into the Role of Lattice Fluctuations on the Excited Behavior of Lead Halide Perovskites*, arXiv:2409.15632 (2024).
6. C. Zhu, J. Jin, Z. Wang, Z. Xu, M. C. Folgueras, Y. Jiang, C. B. Uzundal, H. K. D. Le, F. Wang, X. Zheng, and P. Yang, *Supramolecular Assembly of Blue and Green Halide Perovskites with near-Unity Photoluminescence*, Science **383**, 86-93 (2024).
7. H. K. D. Le, Y. Zhang, P. Behera, A. Vailionis, A. Phang, R. M. Brinn, and P. Yang, *Room-Temperature Ferroelectric Epitaxial Nanowire Arrays with Photoluminescence*, Nano Lett. **24**, 5189-5196 (2024).
8. A. M. Oddo, M. Arnold, and P. Yang, *The Surface Chemistry of Colloidal Lead Halide Perovskite Nanowires*, J. Chem. Phys. **160**, 144701 (2024).
9. D. Weinberg, Y. Park, D. T. Limmer, and E. Rabani, *Size-Dependent Lattice Symmetry Breaking Determines the Exciton Fine Structure of Perovskite Nanocrystals*, Nano Lett. **23**, 4997-5003 (2023).
10. M. Gao, Y. Park, J. Jin, P.-C. Chen, H. Devyldere, Y. Yang, C. Song, Z. Lin, Q. Zhao, M. Siron, M. C. Scott, D. T. Limmer, and P. Yang, *Direct Observation of Transient Structural Dynamics of Atomically Thin Halide Perovskite Nanowires*, J. Am. Chem. Soc. **145**, 4800-4807 (2023).

Quantum Metamaterials

Jiefei Zhang, Jonathan C. Marcks, Nazar Delegan, Benjamin Pingault, Stephan Hruszkewycz, F. Joseph Heremans, David D. Awschalom
Materials Science Division, Argonne National Laboratory, Lemont, IL 60439

Keywords: Quantum Materials, Spin Qubits, Spin coherence, Spin-spin interaction, Spin-bath interaction

Research Scope

Technologies based on the manipulation of spins, photons, charges, and phonons in solid-state platforms are key for revolutionary spin defect-based quantum technologies with applications in computation, sensing, and communication [1]. The quantum metamaterials FWP in the Materials Science Division (MSD) at Argonne National Laboratory builds on our continued effort to understand the fundamental properties of defect-host interactions and the development of new materials platforms and systems tailored to specific quantum applications. We continue to build on our previously demonstrated synthesis capabilities of ultrathin diamond membranes and novel, dopant-confined overgrowth to explore spin-bath dynamics within diamond [2,3]. We focus on the design of new spin qubit systems guided by first-principles calculations in silicon carbide and rare-earth oxide [4,5] and with various form factors to understand spin dynamics and the effect of surfaces/interfaces. This tandem fundamental materials synthesis-spin physics approach leverages new crystallographic orientations and materials, spin bath dimensionalities, and the unique techniques and capabilities of Argonne through MSD collaborations with the Synchrotron Radiation Studies, Selective Interface Synthesis, and Functional Nanoscale Materials FWPs, along with collaborations with the Midwest Integrated Center for Computational Materials (MICCoM) on new defect designs. Furthermore, we leverage unique Argonne facilities including the Advanced Photon Source for X-ray imaging, along with the Q-NEXT Quantum Center facilities and Center for Nanoscale Materials for nanofabrication, defect creation and localization, and spin characterization measurements.

Recent Progress

We continue to explore the complex interactions between spin-qubit systems and their local spin-baths. In the recent two years, we have made significant progress in understanding the NV (nitrogen vacancy) center spin-bath dynamics, exploring guided materials synthesis approaches for understanding the decoherence of qubits in low dimensional spin baths [2]. We have leveraged such knowledge and demonstrated a unique way of using the NV center in diamond to study the spin and charge dynamics of isolated “dark” spins (P1 center, substitutional nitrogen atoms) as potential quantum registers, or for improvement of NV center control and stabilization [3].

Additionally, we continue to understand spin relaxation and spin decoherence mechanisms of telecom-emitting qubits in wide bandgap semiconductors, such as Vanadium in silicon carbide and Erbium (Er) in Ceria (CeO_2). We study phonon mechanisms limiting the spin relaxation (T_1) of vanadium spins in 4H and 6H silicon carbide through temperature dependent hole-burning measurements and identify the role of symmetry in affecting phonon coupling, providing long T_1 with site-specific values ranging from 57.1 ms to 27.9 s (Fig. 1(a)) [4]. Besides Vanadium, we also explore Erbium ions due to their telecom C-band emission. We have focused on Erbium in CeO_2 as a telecom qubit platform in a naturally near-nuclear spin free host. The optical and spin properties of the Er transition including optical T_1 (decay), T_2 (dephasing), homogeneous linewidth and spin T_1 and T_2 have been explored at 4 K [5], along with ongoing work at sub-kelvin temperatures that points to the promise of long spin T_2 up to 180 µs (Fig. 1(b)), with dynamical decoupling sequences decoupling the spins from the spectral diffusion mechanism. This, combined with the long spin T_1 of ~ 120 ms highlights the potential of such new platforms as memory/nodes for quantum networks. Building on our progress exploring Er:CeO_2 as a telecom qubit platform in a naturally near-nuclear spin free host, we continue to explore the effects of the form factor of the host crystal on various qubit properties through the study of Er spins in CeO_2 nanocrystals.

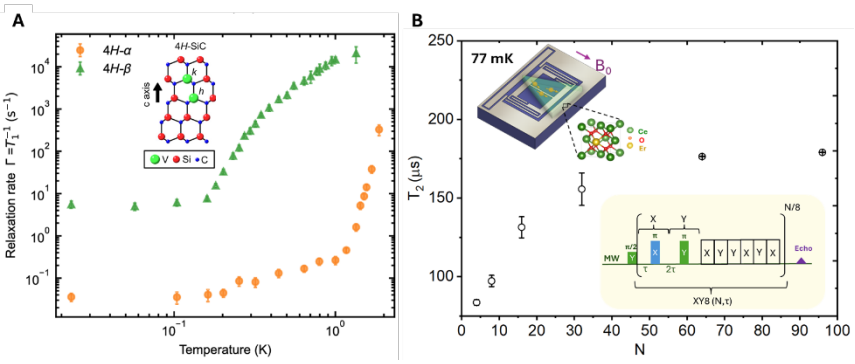

Figure 1. (a) spin relaxation of Vanadium in SiC with different site symmetry at 4K showing T_1 up to tens of second. (b) Ongoing work exploring spin coherence of a telecom qubit system based on Er: CeO_2 thin film, showing T_2 up to 180 µs.

Future Plans

Our future plans build directly on our ongoing efforts. In terms of diamond materials growth, we are actively pursuing tailored crystallographic facets (e.g. diamond growth on (111)) for deterministically localized and synthesized NV- toward studies of local control of defects and nuclear spin bath dimensionality and spin chains. We are also building a new collaborative effort within the MSD division at Argonne including continued efforts in understanding the interaction of spins with interfaces and surfaces through specially synthesized NV sensor arrays and the analytic ALD techniques developed in the *Selective Interface Synthesis* FWP. These low nucleation ALD techniques allow for extreme surface selectivity, enabling novel understanding of the surface chemical state as well as better understanding of *in-situ* termination and passivation. Continuing our broader exploration of novel solid-state defect systems, we will continue our efforts on Er in epitaxially grown Ceria films (Fig. 1(b)),Vanadium in SiC (4H and 6H SiC), extension of Vanadium and other defects to 3C-SiC, as well as isotopically purified SiC baths, and the interaction of the inversion-symmetric group-IV centers in diamond as it relates to understanding the complex interplay between the qubit and host materials. This work will be done in close collaboration with the theory and computational materials group via MSD and MICCoM to better understand how to predict optical and spin coherence properties in new materials and identify coherence mechanisms limiting current materials. These are important for understanding the fundamental limits of electron and nuclear spin coherence, the use of nuclear spins as quantum registers, as well as exploring spin-charge, spin-phonon, and spin-strain interactions to help better design suitable quantum materials for targeted quantum applications.

References

1. G. Wolfowicz, F. J. Heremans, C. P. Anderson, S. Kanai, H. Seo, A. Gali, G. Galli, and D. D. Awschalom, *Quantum guidelines for solid-state spin defects*, Nat. Rev. Mater. **6**, 906–925 (2021).
2. J. C. Marcks, M. Onizhuk, N. Delegan, Y.-X. Wang, M. Fukami, M. Watts, A. Clerk, F. J. Heremans, G. Galli, and D. D. Awschalom, *Guiding diamond spin qubit growth with computational methods*, Phys. Rev. Mater. **8**, 026204 (2024).
3. J. C. Marcks, M. Onizhuk, Y.-X. Wang, Y. Zhu, Y. Jin, B. S. Soloway, M. Fukami, N. Delegan, F. J. Heremans, A. A. Clerk, G. Galli, D. D. Awschalom, *Quantum spin probe of single charge dynamics*, Phys. Rev. Lett. **133**, 130802 (2024).
4. J. Ahn, C. Wicker, N. Bitner, M. T Solomon, B. Tissot, G. Burkard, A. M Dibos, J. Zhang, F. J. Heremans, D. D. Awschalom, *Extended spin relaxation times of optically addressed vanadium defects in silicon carbide at telecommunication frequencies*, Phys. Rev. Appl. **22**, 044078 (2024).
5. J. Zhang, G. D. Grant, I. Masiulionis, M. T. Solomon, J. C. Marcks, J. K. Bindra, J. Niklas, A. M. Dibos, O. G. Poluektov, F. J. Heremans, S. Guha, D. D. Awschalom, *Optical and spin coherence of Er spin qubits in epitaxial cerium dioxide on silicon*, npj Quantum Inf. **10**, 119 (2024).

Publications

1. S. Maddali, T. D. Frazer, N. Delegan, K.J. Harmon, S.E. Sullivan, M. Allain, W. Cha, A. Dibos, I. Poudyal, S. Kandel, Y. S. G Nashed, F. J. Heremans, H. You, Y. Cao, S. O. Hruszkewycz, *Concurrent multi-peak Bragg coherent x-ray diffraction imaging of 3D nanocrystal lattice displacement via global optimization*, npj Comput. Mater. **9**, 77 (2023).
2. J. C. Jones, N. Delegan, F. J. Heremans, A. B. F. Martinson, *Nucleation dependence of atomic layer deposition on diamond surface termination*, Carbon **213**, 118276 (2023).
3. M. Fukami, J. C. Marcks, D. R. Candido, L. R. Weiss, B. Soloway, S. E. Sullivan, N. Delegan, F. J. Heremans, M. E. Flatte, D. D. Awschalom, *Magnon-mediated qubit coupling determined via dissipation measurements*, Proc. Natl. Acad. Sci. **121**, e2313754120 (2024).
4. J. C. Marcks, M. Onizhuk, N. Delegan, Y.-X. Wang, M. Fukami, M. Watts, A. Clerk, F. J. Heremans, G. Galli, and D. D. Awschalom, *Guiding diamond spin qubit growth with computational methods*, Phys. Rev. Mater. **8**, 026204 (2024).
5. J. C. Marcks, M. Onizhuk, Y.-X. Wang, Y. Zhu, Y. Jin, B. S. Soloway, M. Fukami, N. Delegan, F. J. Heremans, A. A. Clerk, G. Galli, D. D. Awschalom, *Quantum spin probe of single charge dynamics*, Phys. Rev. Lett. **133**, 130802 (2024).
6. J. Ahn, C. Wicker, N. Bitner, M. T Solomon, B. Tissot, G. Burkard, A. M Dibos, J. Zhang, F. J. Heremans, D. D. Awschalom, *Extended spin relaxation times of optically addressed vanadium defects in silicon carbide at telecommunication frequencies*, Phys. Rev. Appl. **22**, 044078 (2024).
7. J. Zhang, G. D. Grant, I. Masiulionis, M. T. Solomon, J. C. Marcks, J. K. Bindra, J. Niklas, A. M. Dibos, O. G. Poluektov, F. J. Heremans, S. Guha, D. D. Awschalom, *Optical and spin coherence of Er spin qubits in epitaxial cerium dioxide on silicon*, npj Quantum Inf. **10**, 119 (2024).
8. J. Wong, M. Onizhuk, J. Nagura, A. S. Thind, J. K. Bindra, C. Wicker, G. D. Grant, Y. Zhang, J. Niklas, O. G. Poluektov, S. Guha, R. F. Klie, J. Zhang, G. Galli, F. J. Heremans, D. D. Awschalom, A. P. Alivisatos, *Coherent Erbium Spin Defects in Colloidal Nanocrystal Hosts*, ACS Nano **18**, 19110-19123 (2024).
9. M. Kawahara, Y. Abe, K. Takano, F. J. Heremans, J. Ishihara, S. E. Sullivan, C. Vorwerk, V. Somjit, C. P. Anderson, G. Wolfowicz, M. Kohda, S. Fukami, G. Galli, D. D. Awschalom, H. Ohno, S. Kanai. *Polarization-dependent photoluminescence of Ce-implanted MgO and $MgAl_2O_4$*, Appl. Phys. Express **17** 072004 (2024).
10. X. Zhang, Y. Wang, H. Bae, T. K. M. Graham, N. Delegan, Z. Wang, K. Watanabe, T. Taniguchi, M. Jung, F. Tafti, D. D. Awschalom, F. J. Heremans, B. Yan, and B. B. Zhou, *Optically Enhanced Magnetization by Exciton Recombination in Atomically Thin $CrCl_3$*, Phys. Rev. Mater. **8**, 104402 (2024).

Microscopic understanding of growth, substrate engineering, and proximity coupling in two-dimensional organic/inorganic hybrid systems

Pengpeng Zhang, Department of Physics and Astronomy, Michigan State University

Keywords: Heterostructures, surface and interface, Kagome, thin film materials.

Research Scope

The rapid advances in materials synthesis and processing have enabled the growth of two-dimensional (2D) thin film materials of various crystalline symmetry and chemical composition. For these 2D materials, the substrate effects are essential. Interfacial charge transfer, electrostatic screening, orbital or electronic reconstruction could all impact the properties of 2D materials. Furthermore, rich physical and chemical behaviors may emerge in heterostructures of 2D materials owing to the interfacial processes and proximity coupling. The overarching goal of the program is to establish microscopic understanding of heterostructures and heterointerfaces in organic/inorganic hybrid systems that exhibit correlated and topological properties. The synergistic efforts on hybrid heterostructure design, along with the heterointerface control, are anticipated to lead to unprecedented advances in the tunability of 2D quantum materials and deep understanding of interfacial physics.

Recent Progress

1) Distance-dependent evolution of surface flat bands in Kagome-honeycomb lateral heterostructures in FeSn

Among various condensed matter systems, Kagome lattices have been quickly emerging as one of the most important platforms for studying correlated and toplogical electronic states.[1] In the Kagome lattice, atoms are arranged into a two-dimensional network comprising hexagons interspersed with triangles. Using a simple tight-binding model with nearest-neighbor electron hoping, a band structure with three distinct features, namely flat bands (FBs), van Hove singularities, and a Dirac point is produced in ideal Kagome lattices.[2] FBs are resulted from the destructive interference of electron wave functions, which confines electrons within the hexagons of the lattice in real space. Localized electrons experience strong electron-electron interaction, leading to correlation phenomena and potentially charge, magnetic, and superconductivity instabilities. How the variety of phenomena created by the Kagome band structure interwine, cooperate, or energetically compete is a broad topic that inspires intense interest in the condensed matter community.

Recently, the Kagome metal FeSn has attracted significant research attention. Compared to its binary T_mX_n compounds, the Fe_3Sn Kagome planes are spatially isolated from each other by the intercalation of Sn_2 honeycomb layers, making the FeSn compound closest to the two-dimensional limit. Complementary to the bulk studies, epitaixla FeSn films grown on a substrate, $SrTiO_3$ (STO) (111), were shown to exhibit surface flat bands that can potentially be integrated into heterostructures for various device applications.[3]

We recently demonstrated a novel Kagome-honeycomb lateral heterostructures of Fe_3Sn/Sn_2 in FeSn thin films grown by molecular beam epitaxy, and reported the profound electronic implications of the lateral heterostructures.[4] Our scanning tunneling spectroscopy (STS) results revealed three distinct density of states peaks on the Fe_3Sn-terminated surface. Those located at about -0.2 and 0.1 eV can be assigned to the surface flat bands of the Kagome lattice with 3*d* orbital character, as confirmed by the density functional theory (DFT) calculations, whereas the peak at -0.05 eV may originate from the parabolic band by gapping out of a dispersive band of FeSn. In addition, we determined the bonding motif between the Fe_3Sn- and Sn_2- terminated surface at the lateral heterointerface. More notably, we discovered an unusual long-range effect of the lateral heterointerface, where the surface flat bands are suppressed near the lateral heterointerfce but recovered at a distance that depends on

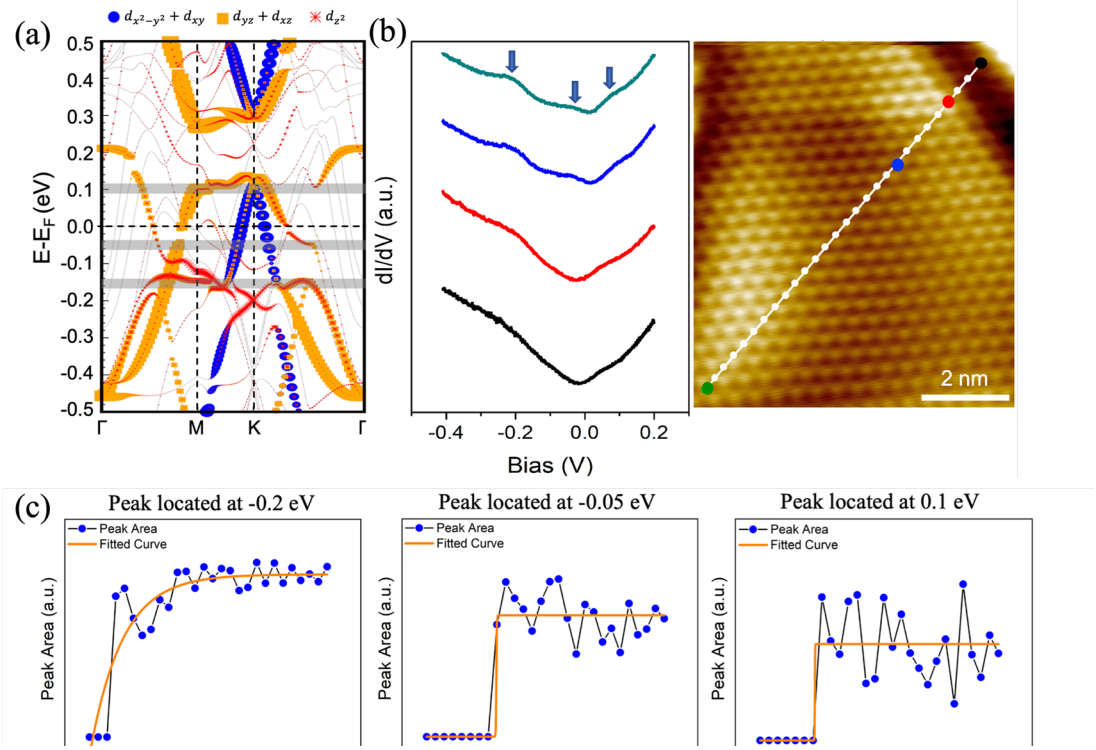

Figure 1. (a) Orbital projected band structure and density of states of the Fe_3Sn Kagome layer calculated by DFT. The highlighted gray regions represent the energies at which the peaks occur, corresponding to the arrows in (b). The density of states features at ~ -0.2 eV and 0.1 eV originate from the surface flat bands. (b) The line STS spectra taken along the white trace in the STM image from the heterointerface (black dot) into the Kagome surface area (green dot). Heterointerface boundary suppresses the electronic structure and surface flat bands of the Kagome surface (black curve). At locations far away from the boundary, the characteristic peaks of the Kagome surface are recovered (green curve). Along the path, the different peaks emerge at the different distances from the boundary. (c) Areas of the peaks located at ~-0.2 eV, -0.05 eV, and 0.1 eV vs. distance from the heterointerface boundary extracted from the STS line spectra. Solid orange curves are the fittings. The results unambiguously reveal long-range heterointerface effects on the electronic structures of the Kagome surface. The "coupling" length to the heterointerface is ~ 1.3 nm for the peak at -0.2 eV, while for the peaks located at -0.05 eV and 0.1 eV, this length is about 2.8 nm and 2.2 nm, respectively, determined by the orbital character of the density of states peaks.

the orbital character of the state, as evidenced by STS line spectroscopy and DFT calculations. Our findings elucidate the impact of lateral heterointerfaces on the electronic behavior of the Kagome lattice, potentially providing a tool for engineering the electronic properties of FeSn to facilitate the development of future electronic and spintronic devices.

2) Evidence of second charge-density-wave in two-dimensional $DyTe_3$ and its impact on magneto-transport properties

Charge density waves (CDWs) are macroscopic quantum states defined by periodic modulations in electronic charge density coupled with lattice distortions. Despite significant research efforts, the evolution of electromagnetic transport properties in the presence of CDWs remains largely unexplored. Quasi-two-dimensional van der Waals layered crystals exhibiting CDW formation represent a broader class of materials with intriguing physical properties. Among these, the lanthanide tritellurides RTe_3, where R denotes rare-earth elements, have emerged as a versatile platform for exploring CDW behaviors.[5]

The lighter rare-earth element based RTe_3 (R = La - Gd) compounds exhibit a single unidirectional,

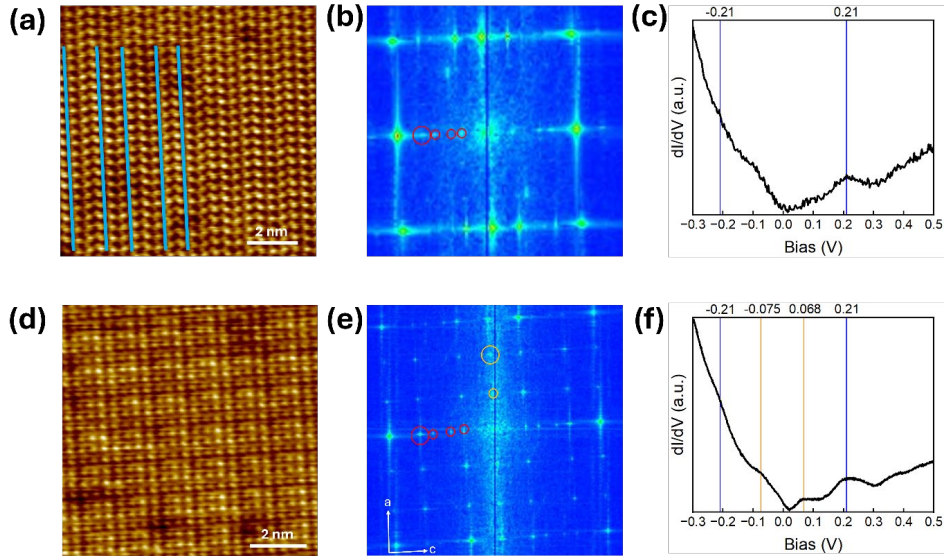

Figure 2. (a-c) STM data at 77K. (a) Morphology scan displaying the incommensurate first CDW phase (Vs = -0.05V, It= 300pA) along the light blue lines. (b) Fast Fourier Transform (FFT) of the image in (a) exhibiting the four CDW_1 peaks at 2/7, 3/7, 4/7, and 5/7 highlighted in red circles. (c) Average STS spectrum of 25 individual curves taken on different spots on the bulk sample away from defects (Vs = -0.5V, It = 50pA). Vertical blue lines represent the gap for the first CDW. (d-f) STM data at 4.5 K. (d) Morphology scan displaying both the incommensurate first CDW phase (running horizontally across the image) and commensurate second CDW phase (running vertically across the image) (Vs = 0.5V, It = 50pA). (e) FFT of the image in (d) clearly showing all the peaks in (b) plus the 1/3 and 2/3 spots for CDW_2 , highlighted by the yellow circles. (f) Average STS spectrum of 6 individual curves taken on different spots on the bulk sample away from defects (Vs = 0.35V, It = 100pA). The blue lines correspond to the same gap as in (c). The orange lines represent the CDW_2 gap.

incommensurate CDW with a wave vector ($q_1 \sim 2/7\ c^*$ with $c^* = 2\pi/c$) oriented along the *c*-axis, denoted as CDW_1. In contrast, RTe_3 compounds with heavier elements (e.g., Ho, Er, Tm) display an additional secondary CDW at lower temperatures, termed as CDW_2 which is characterized by a wave vector ($q_2 \sim 1/3\ a^*$ with $a^* = 2\pi/a$) along the *a*-axis that is orthogonal to the CDW_1 wave vector q_1. Nonetheless, the presence of a low-temperature CDW_2 phase in $DyTe_3$ remains contentious. While a soft phonon mode, which is often associated with the emergence of CDW order, is observed for CDW_1 in $DyTe_3$, it is notably absent for the frequency at which CDW_2 would appear. Similarly, the CDW_1 phase in $DyTe_3$ is evident from a resistivity dip, but no corresponding strong feature has been observed for the CDW_2 phase.

In our recent study, we present the compelling evidence of the low-temperature CDW_2 phase in $DyTe_3$ through STM/STS measurements. And we show that $DyTe_3$ exhibits drastically enhanced magnetoresistance and multiple band driven non-linear Hall effect below the CDW_2 phase transition, which are ascribed to the Fermi surface reconstruction associated with the CDW_2 order. These findings suggest that Fermi surface reconstruction plays a key role in driving the CDW_2 phase transition and highlight the impact of the CDW_2 phase on electromagnetic properties of RTe_3.

Future Plans

Kagome lattice has been realized in a wide range of materials. We are interested in exploring the interplay among different electronic states in these materials. In MBE-grown FeSn thin films, correlated behaviors are expected when the flat band is brought even closer to the Fermi energy via doping, epitaxial strain, etc. Meanwhile, two-dimensional metal organic framework, based on the versatility of its framework structure, could offer a tailorable template with physical properties by design. We have demonstrated long-ranged ordered Kagome metal-dicyanoanthracene lattice on surfaces and will focus the future studies on examining the properties of the complex organic/inorganic hybrid system, particularly those driven by interfacial phenomena.

References

1. J. X. Yin, B. Lian, and M. Z. Hasan, *Toplogical Kagome Magnets and Superconductors*, Nature **612**, 647 (2022).
2. Y. Wang, H. Wu, G. T. McCandless, J. Y. Chan, and M. N. Ali, *Quantum States and Interwining Phases in Kagome Materials*, Nature Reviews Physics **5**, 635 (2023).
3. M. Han, H. Inoue, S. Fang, C. John, L. Ye, M. K. Chan, D. Graf, T. Suzuki, M. P. Ghimire, W. J. Co, E. Kaxiras, and J. G. Checkelsky, *Evidence of Two-Dimemsional Flat Band at the Surface of Antiferromagnetic Kagome Metal FeSn*, Nature Communications **12**, 5345 (2021).
4. T. A. Pham, S. Kang, Y. Ozbek, M. Yoon, and P. P. Zhang, *Distance-Dependent Evolution of Electronic States in Kagome-Honeycomb Lateral Heterostructures in FeSn*, ACS Nano **18**, 8768 (2024).
5. V. Brouet, W. L. Yang, X. J. Zhou, Z. Hussain, R. G. Moore, R. He, D. H. Lu, Z. X. Shen, J. Laverock, S. B. Dugdale, N. Ru, and I. R. Risher, *Angle-Resolved Photoemission Study of the Evolution of Band Structure and Charge Density Wave Properties in RTe_3 (R=Y, La, Ce, Sm, Gd, Tb, and Dy)*, Physical Review B **77**, 235104 (2008).

Publications

1. X. Dong, T. A. Pham, C. Xu, Y. He, W. Lai, X. Ke, and P. P. Zhang, *Growth and Electronic Properties of $SnSe_2$ Films on Reconstructed, (111)-Oriented $SrTiO_3$ Substrates*, The Journal of Physical Chemistry C **127**, 16732 (2023).
2. T. A. Pham, S. Kang, Y. Ozbek, M. Yoon, and P. P. Zhang, *Distance-Dependent Evolution of Electronic States in Kagome-Honeycomb Lateral Heterostructures in FeSn*, ACS Nano **18**, 8768 (2024).
3. D. Ni, X. Xu, Z. Zhu, Y. Ozbek, V. M. Tronl, C. Yang, X. Yang, A. Louat, C. Cacho, N. P. Ong, P. P. Zhang, T. Valla, and R. J. Cava, *Indium-Doped Crystals of $SnSe_2$*, The Journal of Physical Chemistry C **128**, 11054 (2024).
4. S. Gupta, O. O. Emmanuel, Y. Ozbek, M. Xu, W. Xie, P. P. Zhang, abd X. Ke, *Giant Nernst Angle in Self-Intercalated van der Waals Magnet $Cr1_{.25}Te_2$,* Materials Today Physics **50**, 101627 (2025).
5. S. Gupta, Y. Ozbek, O. O. Emmanuel, M. Bostock, J. Kowalski, P. P. Zhang, and X. Ke, *Compelling Eveidence of Second Charge-Density-Wave in Two-Dimensional $DyTe_3$ and Its Impacts on Magneto-Transport Properties*, Under Review (2025).

Partial coherence and elliptical polarization of thermal radiation

Principle Investigator: Zhuomin Zhang
George W. Woodruff School of Mechanical Engineering
Georgia Institute of Technology, Atlanta, GA 30332

Keywords: Degree of polarization, metasurfaces, polarimetry, spatial coherence, thermal emission.

Program Scope

The study of polarized light or radiation has extensive applications in remote sensing, astronomy, and surface and materials characterization. The spatial coherence and degree of polarization are very important for understanding of the electromagnetic field characteristics in the vicinity of thermal sources. Recently, researchers have demonstrated that nonreciprocal materials may break the conventional interpretation of Kirchhoff's law, resulting in unexpected radiative energy transfer in terms of directionality and magnitude. Furthermore, spin angular momentum becomes important with anisotropic metamaterials and chiral metasurfaces.

This project aims at (1) performing a comprehensive analysis of the 3 ×3 coherence matrices for bianisotropic multilayers and patterned metasurfaces and for individual micro/nanostructures, with or without temperature uniformity; and (2) fabricating metasurfaces with varying geometric parameters and experimentally characterizing their thermal emission with corresponding polarization states (linear, circular, and elliptical). Fluctuational electrodynamics will be employed to model the cross-spectral density tensors considering both reciprocal and nonreciprocal materials. Emphasis will be placed on the off-diagonal elements as they are more relevant to circular polarization, which has not been extensively studied in the past. Spectral polarimetry and partial Mueller matrix ellipsometry measurements will be performed to characterize the bilayer grating metasurfaces in the infrared region for the realization of polarization controllability.

This study will result in a better understanding of thermal radiation in both the near field and far field for metasurfaces and micro/nanostructures composed of anisotropic and nonreciprocal materials. The success of this project will demonstrate a simpler and easy-to-fabricate design for full polarization control of far-field thermal emissions.

Recent Progress

Mueller matrices relate the Stokes parameters of the incident and emerging light, providing useful information about the radiative properties and other characteristics of the medium. Determining all elements of the 4×4 Mueller matrix requires complete polarimetry, which is often challenging to perform. Partial polarimetry, on the other hand, uses simpler optical components in generating and/or analyzing states of polarization, thereby measuring only a subset of the Mueller matrix. However, it may be possible to determine the full Mueller matrix under specific symmetry conditions. A symmetry classification scheme allows categorizing the Mueller matrix of materials [1]. It is shown that the symmetry of the Mueller matrix is directly determined from the information of symmetries of the sample's optical properties. Numerical calculations of various measurement scenarios, structures, and materials (with or without Lorentz reciprocity) are carried out to validate the methodology. Multilayer structures and nonplanar diffraction gratings, with or without reciprocity, are analyzed to illustrate the capability and limitation. This study sheds light on the

relationships between the Mueller matrix and the symmetries of structures, outlining a symmetry classification scheme to predict the pattern of Mueller matrix, that is applicable to both reciprocal and nonreciprocal materials.

Tailoring optical and radiative properties has attracted significant attention recently due to its importance in advanced energy systems, nanophotonics, electro-optics, and nanomanufacturing. Metamaterials with micro- and nanostructures exhibit exotic radiative properties with tunability across the spectrum, direction, and polarization. Structures made from anisotropic or nanostructured materials have shown polarization-selective absorption bands in the mid-infrared. Characterizing the optical and radiative properties of such materials is crucial for both fundamental research and the development of practical applications. Ellipsometry has been used for decades to characterize the optical properties of materials. However, due to the limitations of optical components such as compensators, most conventional ellipsometers have a narrow operational bandwidth and are restricted to the visible or near-infrared spectral range. Nevertheless, the mid-infrared region from about 2.5 μm to 25 μm covers strong vibrational transitions of many molecules and the atmospheric transmission windows. Furthermore, the development of thermal photonics, including chiral, nonreciprocal, and anisotropic metamaterials, has increased the demand for broadband mid-infrared spectroscopic ellipsometry to accurately characterize these materials. Recently, a broadband mid-infrared ellipsometer, operating from 2 to 15 μm, was built and tested to measure 12 elements of the Mueller matrix [2]. The performance of the ellipsometer was evaluated using nanostructured materials, including a 1D grating and a chiral F-shaped metasurface. The measurement results compared well to those obtained from rigorous-coupled-wave analysis (RCWA) and finite-difference time-domain (FDTD) simulations.

Following the previous study [3], we have modified and optimized the design of a double-layer twisted-grating thermal emitter to demonstrate coherent thermal emission, as shown in Fig. 1(a). The device enables linear polarization control in the mid-infrared region with a peak wavelength at 5.17 μm (TE) and 5.4 μm (TM) for normal direction. By modifying the twist rotation angle β of the top grating against the bottom grating, the polarization state of the emitted light can switch from to circular polarization at similar wavelengths, as shown in Fig. 1(b). The designed emitter can be divided into three parts: The top grating serves as a waveplate to create circularly polarized light when rotated. The bottom grating is an effective anisotropic material formed by a so-called Damascene pattern (alternating pattern) of amorphous Si (a-Si) and Cu, which supports magnetic polaritons for one of the linear polarization states. The Al ground plane functions as a reflector to eliminate transmission.

To analyze the device's performance, the spectral absorptance of the device under normal incidence is first computed using RCWA for the aligned state and Lumerical FDTD for the 45°-rotated state. The emissivity of the device is equal the absorptance according to Kirchhoff's law. Nearly 100% emissivity for TE and 95% for TM polarizations can be achieved at 5.17 μm and 5.4 μm respectively. Such a strong emittance is caused by the excitation of magnetic polariton mode on the bottom grating [4], though further investigation is needed to identify the resonance effect for TE waves. The difference between the emissivity of TM and TE waves at these wavelengths creates strong polarized thermal emission. In the case of circular polarization, the top grating is rotated by 45 ° to introduce a phase delay, and the corresponding relative emission dichroism, $RED = \frac{|\epsilon_+ - \epsilon_-|}{\epsilon_+ + \epsilon_-}$, is 68% at 5.1 μm (RCP dominates) and 75% at 5.4 μm (LCP dominates).

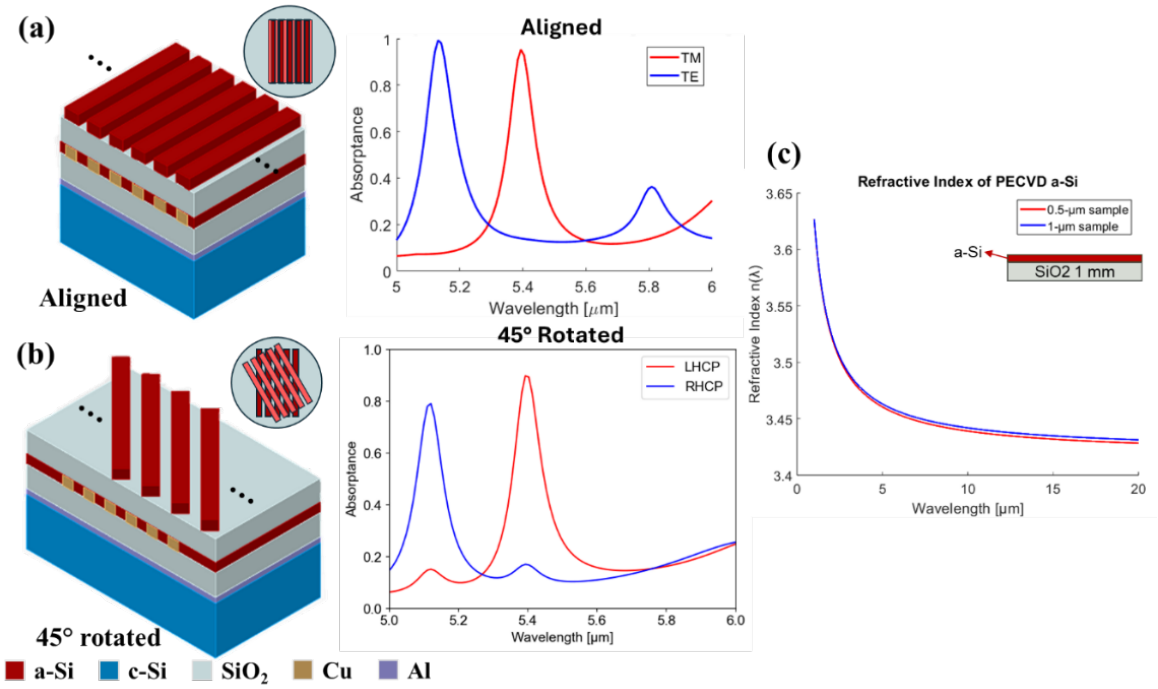

Fig. 1. (a) Perspective view and top view (inset) of the twisted grating at its aligned state, with the predicted absorptance spectra. (b) Perspective view and top view of the 45°-twisted rotation between the gratings, with the predicted absorptance spectra. (c) Measured refractive index of a-Si.

The a-Si in the proposed design is deposited using PECVD in Georgia Tech's cleanroom. Hydrogen bonds can form (a-Si:H) during the process and change the optical constants of the deposited thin layer [5]. To accurately model the optical constant of a-Si to be used for the present study, measurements were performed using FTIR spectrometer to obtain the absorptance spectrum of two SiO_2 discs coated with a-Si, with a nominal thickness of 0.5 μm and 1 μm. The experimental data were fitted with a thin-thick film model [4] to obtain corresponding parameters in the refractive index function of the a-Si. The result as shown in Fig. 1(c) suggests that the PEVCD-deposited a-Si has a refractive index of 3.45 at 5 μm with negligible loss, which implies the existence of a-Si:H.

The fabrication of the twisted gratings contains the steps shown in Fig. 2. The first layer of aluminum is deposited with e-beam evaporation, followed by layers of SiO_2 and a-Si deposited by PECVD. After lithography patterning, a-Si is etched (as shown by the SEM image on the bottom-left of Fig. 2), and trenches are formed by inductively coupled plasma (ICP) etching. To realize the desired Damascene pattern, the trenches are filled by copper deposited using e-beam evaporation. The deposition time is precisely controlled to fill the gap to the same level as the top of the a-Si layer, and excessive metal can be released and removed along with the photoresist. The remaining process repeats the previous steps, including very similar thin-film deposition and patterning. The sample fabrication is currently in progress and the fabricated samples will be characterized by combining infrared emissometry and ellipsometry, along with theoretical calculations to fully understand the resonance mechanisms.

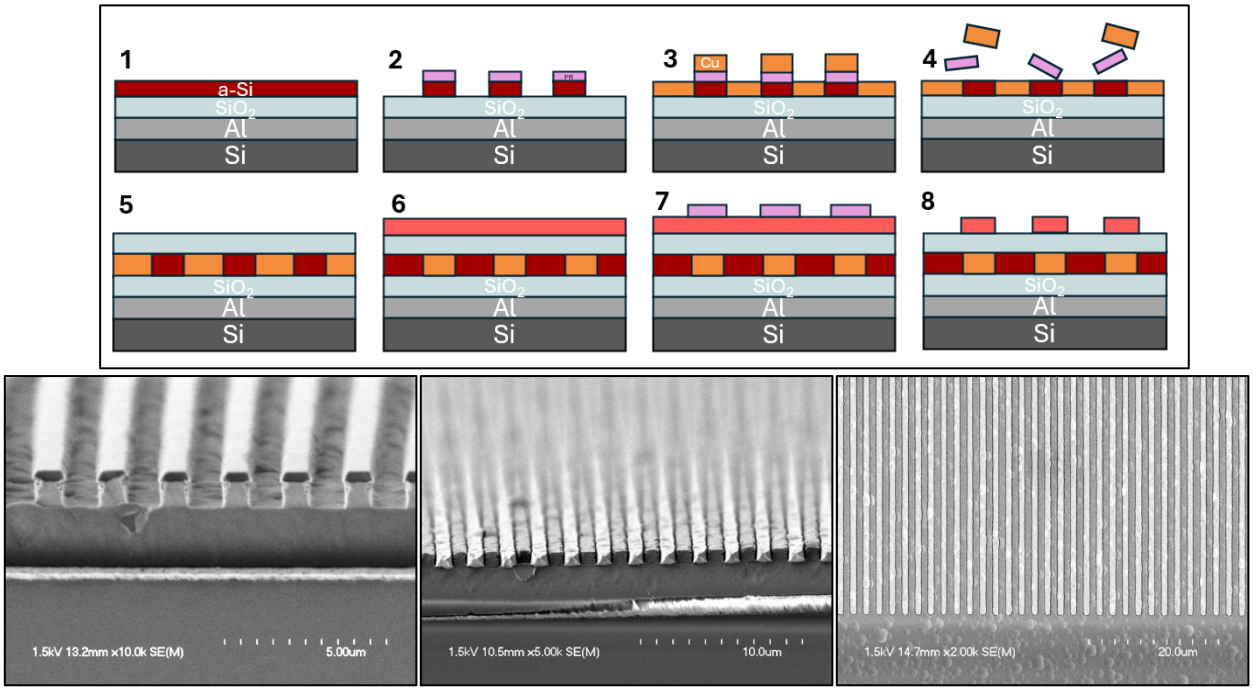

Fig. 2. Top: Fabrication procedure (process step 1-8) of the device. Bottom: Cross-sectional SEM image of the grating after step 2, the ICP etching on a-Si (left); the profile after step 4, e-beam Cu trench filling and etching (middle); top view of the Damascene pattern (right).

Future Plans

We will perform a theoretical investigation on the degree of coherence and polarization of multilayered structures as well as nanostructures. Further studies will also be conducted based on field coherence calculations, aiming to reveal its relation to spin angular momentum. Work will continue to fabricate the twisted grating and demonstrate infrared circular polarization control. Meanwhile, additional efforts will focus on improving the quality of the fabricated device, including achieving precise geometric dimensions, less surface defect, and complete trench filling. Experiments for characterizing the performance of the device, including using in-house ellipsometry based on FTIR to measure the different polarization states, will also be elaborately designed. Further study on how different design parameters, such as geometric dimensions of the device, affects the performance, will also be carried out along with a further exploration of plasmonic mode excitation.

References

1. C. Yang, W. Cai, and Z.M. Zhang, Mueller Matrix Symmetry for Both Reciprocal and Nonreciprocal Metamaterials, *J. Quant. Spectrosc. Radiat. Transfer*, vol. 329, p. 109190 (2024).
2. C. Yang, X. Wang, Z. Jacob, W. Cai, and Z.M. Zhang, Determination of Mid-Infrared Optical Properties of Complex Media Using Partial Mueller Matrix Ellipsometry, *Rev. Sci. Instrum.*, vol. 96, p. 023905 (2025).
3. C. Yang, W. Cai, and Z.M. Zhang, Tailoring Full-Stokes Thermal Emission from Twisted-Gratings Structures, *Nanophotonics*, vol. 13, pp. 803–811 (2024).
4. Z.M. Zhang, *Nano/Microscale Heat Transfer*, 2nd edn., Springer Nature, Switzerland (2020).
5. H. Piller, Silicon (Amorphous) (a-Si), in E.D. Palik (ed.), *Handbook of Optical Constants of Solids*, Vol. I, Academic Press, San Diego, pp. 571–586 (1997).

Publications 2023-2025 (with support by the DOE-BES Grant DE-SC0018369)

1. Yang, C. Bohm, P., Cai, W., and Zhang, Z.M., 2023, "Fluctuational Electrodynamics and Thermal Emission," Chapter 3, pp. 43-67. In ***Light, Plasmonics and Particles***, edited by M.P. Mengüç and M. Francoeur, Elsevier. https://doi.org/10.1016/B978-0-323-99901-4.00010-X

2. Bohm, P., Yang, C., Menon, A.K., and Zhang, Z.M., 2024, "Thermophotovoltaic emitter design with a hyper-heuristic custom optimizer enabled by deep learning surrogates," *Energy*, Vol 291, p. 130424. https://doi.org/10.1016/j.energy.2024.130424

3. Yang, C., Cai, W., and Zhang, Z.M., 2024, "Mueller Matrix Symmetry for Both Reciprocal and Nonreciprocal Metamaterials," *Journal of Quantitative Spectroscopy and Radiative Transfer*, Vol. 329, p. 109190. https://doi.org/10.1016/j.jqsrt.2024.109190

4. Yang, C., Wang, X., Jacob, Z., Cai, W., and Zhang, Z.M., 2025, "Determination of Mid-Infrared Optical Properties of Complex Media Using Partial Mueller Matrix Ellipsometry," *Review of Scientific Instrument*, Vol. 96, p. 023905. https://doi.org/10.1063/5.0250280

5. Zhang, Z.M., Bohm, P., and Menon, A.K., 2025, "Entropic Analysis of the Maximum Output Power of Thermoradiative Cells," *ASME Journal of Heat and Mass Transfer*, Vol. 147, p. 052801. https://doi.org/10.1115/1.4067342

Electron Transfer in Heterostructures based on Two-Dimensional Materials

Hui Zhao, University of Kansas, Lawrence, Kansas

Keywords: two-dimensional material, van der Waals heterostructure, charge transfer, semiconductor, photocarrier dynamics

Research Scope

Two-dimensional (2D) materials offer a new avenue for fabricating van der Waals multilayer heterostructures, with the potential to transform material discovery. A central challenge in this approach is to understand and control interlayer electron transfer, a fundamental process for integrating individual layers and harnessing emergent properties for electronic and optoelectronic applications. Building on recent progress in interlayer charge transfer in heterobilayers, this program aims to generate experimental insights that advance the fundamental understanding of electron transfer—including both charge and energy transfer—in van der Waals multilayer structures. The research is organized into three thrusts. Thrust 1 expands the material library for fabricating heterostructures with novel electron transfer characteristics. Thrust 2 investigates electron transfer through thin barriers within van der Waals multilayers. Thrust 3 explores the influence of electric fields on electron transfer. Leveraging the insights from these efforts, we aim to develop strategies to enhance the optoelectronic performance of graphene through its integration with other layered materials.

Recent Progress

We expanded the material library for fabricating 2D heterostructures by investigating electron transfer in 2D materials with diverse crystalline structures and electronic phases. As one example, we studied α-$RuCl_3$, [1] a Mott insulator with potential applications as a Kitaev material.

In our first step, we studied its photocarrier dynamics. It has been reported that α-$RuCl_3$ can host Mott-Hubbard excitons (MHEs). [2] We performed transient absorption microscopy measurements with 3.10-eV and 1.55-eV pump and probe pulses, respectively. Time-resolved differential reflectance [Fig. 1(b)] reveals an MHE lifetime of 720 ps, which is independent of pump fluence. In the spatially resolved measurements, the probe laser spot was scanned across the pump spot while recording the time-resolved differential reflectance [Fig. 1(a)]. Several examples of the measured spatial profiles are shown in Fig. 1(c), along with their Gaussian fits (curves). The extracted variance of the profiles is plotted as a function of probe delay in Fig. 1(d). A linear fit (red line) yields a diffusion coefficient of 0.13 cm^2/s. Furthermore, the diffusion length of 160 nm,

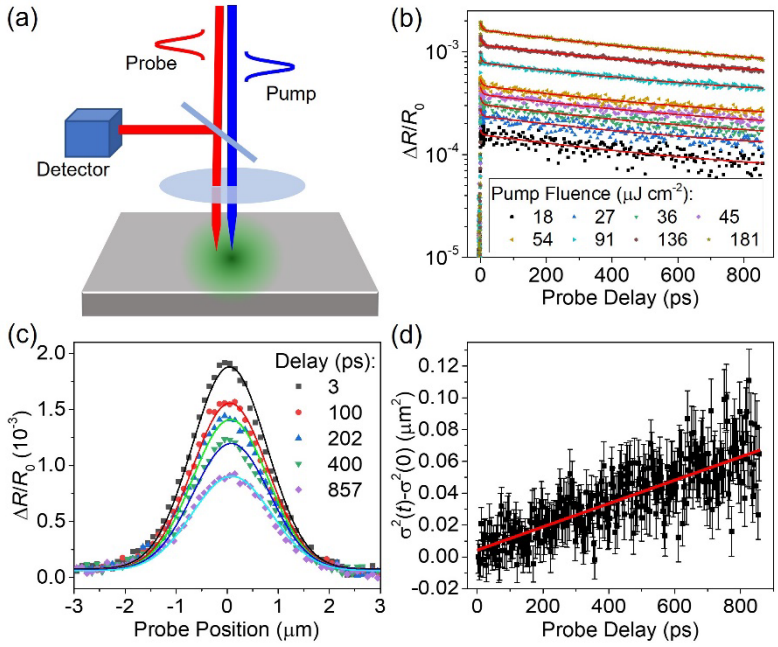

Fig. 1: (a) Schematic of the transient absorption microscopy setup. (b) Differential reflectance under various pump fluences. (c) Spatial profiles of the differential reflectance at selected probe delays, along with fits. (d) Variance of the profile as a function of probe delay.

calculated from the diffusion coefficient and lifetime, is much longer than the unit cell of α-$RuCl_3$, revealing the mobile nature of these MHEs.

To test the feasibility of integrating α-$RuCl_3$ with 2D semiconductors, we studied a heterostructure formed by α-$RuCl_3$ and a WSe_2 monolayer. As shown in Fig. 2(a), WSe_2 and α-$RuCl_3$ form a type-III band alignment, in which the conduction band (CB) minimum of WSe_2 lies below the valence band (VB) maximum of α-$RuCl_3$. Upon contact, electrons transfer from the CB of WSe_2 to the VB of α-$RuCl_3$, resulting in heavy hole doping of WSe_2. Time-resolved differential reflectance, which is proportional to the photocarrier density in WSe_2, indicates that these holes suppress exciton formation and reduce the carrier lifetime to approximately 0.5 ps in the heterostructure, as shown in

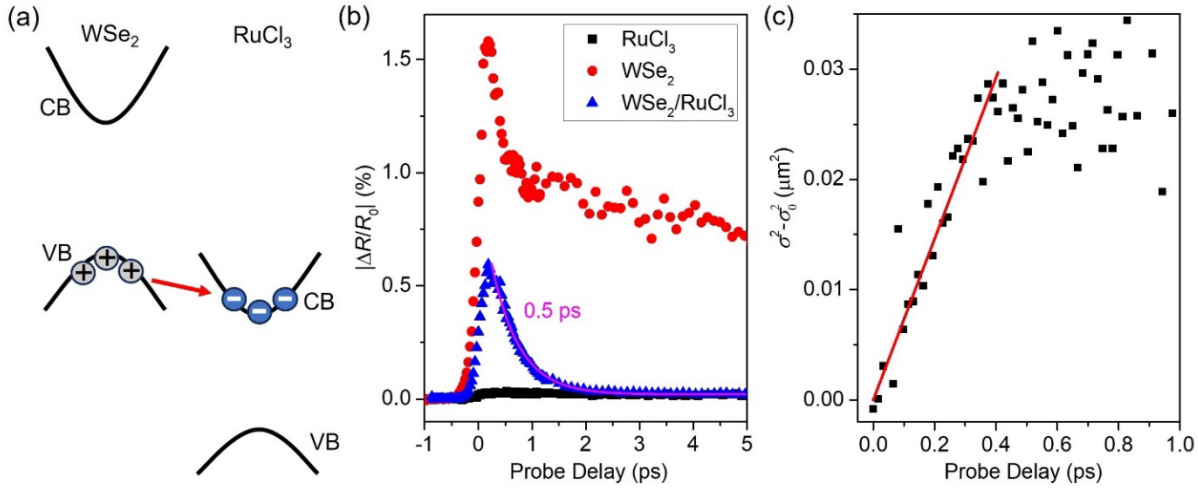

Fig. 2: (a) Band alignment illustrating hole doping of WSe_2 by α-$RuCl_3$. (b) Time-resolved differential reflectance showing reduced carrier lifetime in the WSe_2/α-$RuCl_3$ heterostructure. (c) Transient absorption microscopy measurement showing an increase in the spatial profile variance over time. A linear fit (red line) yields a diffusion coefficient of 370 cm^2/s.

Fig. 2(b). Further transient absorption microscopy measurements [Fig. 2(c)] reveal a carrier diffusion coefficient of 370 cm^2/s, corresponding to a mobility on the order of 10^4 $cm^2/V{\cdot}s$. [3] These results demonstrate that hole-doped WSe_2 via α-$RuCl_3$ is a promising material for ultrafast optoelectronic applications.

Building on our previous progress in understanding electron transfer in 2D heterostructures, we developed strategies to improve the optoelectronic performance of graphene. While graphene possesses many novel properties, its application in optoelectronics is limited by two key challenges.

First, photocarriers in graphene tend to form tightly bound neutral excitons, which hinder the generation of free carriers. Second, the photocarrier lifetime in graphene is extremely short—on the order of a few picoseconds—thereby limiting its efficiency in energy conversion.

We used band alignment to control the layer-specific distribution of photoexcited electrons and holes in graphene-based heterostructures. A four-layer heterostructure was designed and fabricated, as shown in Fig. 3(a). The key feature of this design is the type-II interface between MoS_2 and $MoSe_2$, which facilitates charge separation, is sandwiched between two type-I interfaces with graphene. The band offsets drive interlayer electron and hole transfer, as indicated by the arrows, resulting in net electron and hole populations in the bottom and top graphene layers, respectively. This spatial separation of charge carriers leads to a prolonged carrier lifetime.

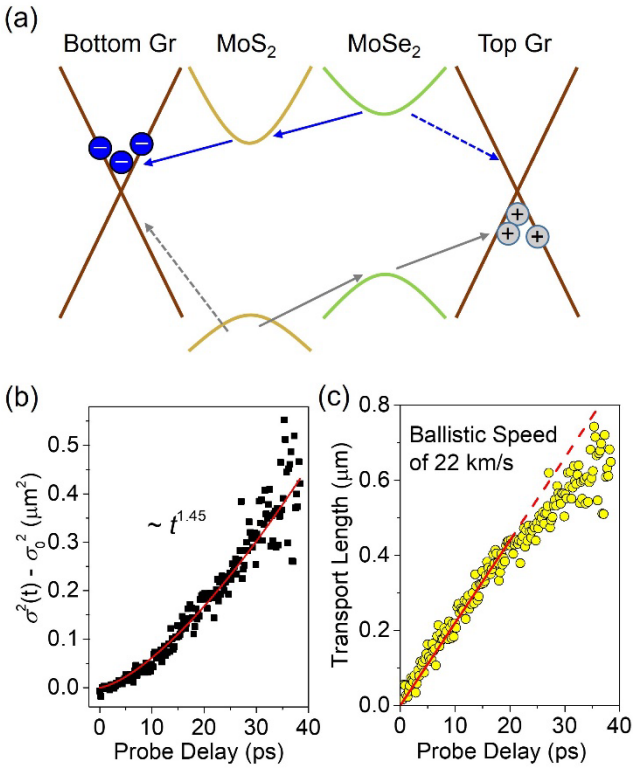

Fig. 3: (a) Band alignment and charge transfer in a graphene-based heterostructure. (b) Superlinear increase in the spatial profile variance, indicating quasi-ballistic electron transport in the bottom graphene layer. (c) Extracted ballistic transport length as a function of probe delay.

We performed transient absorption microscopy measurements to monitor the spatiotemporal dynamics of electrons in the bottom graphene layer. As shown in Fig. 3(b), the variance increases superlinearly with time, following a power-law dependence of 1.45, clearly indicating quasi-ballistic electron transport. Figure 3(c) shows the extracted transport length as a function of probe delay. We observed ballistic electron transport in the bottom graphene layer over 20 ps at room temperature, with a ballistic velocity of 22 km/s. [4]

As a second example, we studied a heterostructure formed by graphene and a monolayer Janus WSSe, as shown in Fig. 4(a). Due to its lattice asymmetry, the Janus WSSe monolayer possesses an intrinsic out-of-plane electric field. We hypothesized that this field could facilitate electron transfer from WSSe to graphene while suppressing hole transfer. [5] In our transient absorption measurements, we excited electrons and holes in WSSe using a 3.02-eV pump pulse. A 0.83-eV probe was then used to selectively monitor the carrier density in graphene. As shown in Fig. 4(b), the signal from the graphene monolayer decays within a few

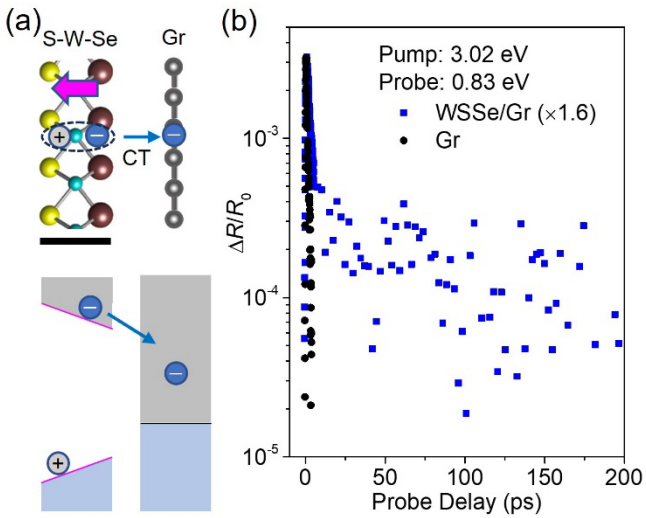

Fig. 4: (a) Schematic showing the electric field of Janus WSSe (pink arrow) prevents hole transfer from WSSe to graphene. (b) Differential reflectance comparison reveals the long-lived signal component in the heterostructure.

picoseconds, consistent with its ultrashort carrier lifetime. In contrast, the signal from the heterostructure exhibits a long-lived component, indicating the presence of carriers in graphene with lifetimes on the order of several hundred picoseconds. This result confirms our hypothesis of net charge transfer from WSSe to graphene.

We also studied graphene-based hybrid heterostructure of Gr/TiOPc/PTCDI. We observed efficient charge transfer between both interfaces. We found that electrons in graphene and holes in PTCDI form interlayer excitons. Efficient charge transfer and interlayer exciton format across organic-inorganic interfaces are important for developing hybrid heterostructures, taking advantage of novel properties of organic semiconductors. [6]

Future Plans

In the next reporting period, we will focus on optimizing the structure and material selection of graphene-based van der Waals multilayer heterostructures. Building on our previous results—where we demonstrated ballistic charge carriers and confirmed the role of electric fields in regulating charge transfer—we will investigate interlayer charge transfer in five-layer heterostructures incorporating dedicated layers for light absorption, charge transfer, and charge accumulation. Additionally, we will explore 3R-stacked transition metal dichalcogenide bilayers and organic monolayer semiconductors with intrinsic dipole moments as means to modulate interlayer charge transfer. We will also examine the integration of α-$RuCl_3$ and other quantum materials with 2D semiconductors to optimize charge transfer and photodoping performance.

References

1. A. Banerjee, C. A. Bridges, J.-Q. Yan, A. A. Aczel, L. Li, M. B. Stone, G. E. Granroth, M. D. Lumsden, Y. Yiu, J. Knolle, S. Bhattacharjee, D. L. Kovrizhin, R. Moessner, D. A. Tennant, D. G. Mandrus, and S. E. Nagler, *Proximate Kitaev Quantum Spin Liquid Behaviour in a Honeycomb Magnet* ", Nat. Mater. **15**, 733–740 (2016).

2. D. Nevola, A. Bataller, A. Kumar, S. Sridhar, J. Frick, S. O'Donnell, H. Ade, P. A. Maggard, A. F. Kemper. K. Gundogdu, and D. B. Dougherty, *Timescales of Excited State Relaxation in α–$RuCl_3$ Observed by Time-Resolved Two-Photon Photoemission Spectroscopy*, Phys. Rev. B **103**, 245105 (2021).

3. T. Zheng, E. Low, N. Rafizadeh, K. S. Burch, and H. Zhao, *Ultrafast and Highly Mobile Photocarriers in Monolayer WSe_2 Doped by α-$RuCl_3$*, Nano Letters **25**, 4054–4059 (2025).

4. R. J. Scott, P. Valencia-Acuna, and H. Zhao, *Spatiotemporal Observation of Quasi-Ballistic Transport of Electrons in Graphene*, ACS Nano **17**, 25368-25376 (2023).

5. T. Zheng, Y.-C. Lin, N. Rafizadeh, D. B. Geohegan, Z. Ni, K. Xiao, and H. Zhao, *Janus monolayers for ultrafast and directional charge transfer in transition metal dichalcogenide heterostructures*. ACS Nano **16**, 4197–4205 (2022).

6. R. J. Scott, N. Fuller, A. Sadanandan; P. Valencia-Acuna, W.-L. Chan, Q. Zhou, and H. Zhao, *Long-Lived Charge-Transfer Excitons in a Graphene-PTCDI-TiOPc Trilayer Heterostructure*, Journal of Physical Chemistry C **129**, 6882–6889 (2025).

Publications

1. T. Zheng, E. Low, N. Rafizadeh, K. S. Burch, and H. Zhao, *Ultrafast and Highly Mobile Photocarriers in Monolayer WSe_2 Doped by α-$RuCl_3$*, Nano Letters **25**, 4054–4059 (2025).

2. R. J. Scott, N. Fuller, A. Sadanandan; P. Valencia-Acuna, W.-L. Chan, Q. Zhou, and H. Zhao, *Long-Lived Charge-Transfer Excitons in a Graphene-PTCDI-TiOPc Trilayer Heterostructure*, Journal of Physical Chemistry C **129**, 6882–6889 (2025).

3. F. Ren, D. He, X. Zhang, G. Li, X. Liu, J. Wang, K. Zhao, J. He, Y. Wang, and H. Zhao, *Charge Transfer in Transition Metal Dichalcogenide Alloy Heterostructures*, Applied Physics Letters **126**, 072101 (2025).

4. N. Rafizadeh, G. Agunbiade, R. J. Scott, M. Vieux, and H. Zhao, *Type-I and Type-II Interfaces in a $MoSe_2/WS_2$ van der Waals Heterostructure*, Applied Physics Letters **126**, 042103 (2025).

5. N. Fuller, F. Rudayni, S. Amos, K. Rijal, S. A. Maroufian, P. Valencia-Acuna, H. Zhao, H. Peelaers, Q. Zhou, W.-L. Chan, *Modulation of Electrostatic Potential in 2D Crystal Engineered by an Array of Alternating Molecular Dipoles*, Nano Letters **24**, 10258–10264 (2024).

6. X. Liu. Y. Wang, X. Zhang, G. Li F. Ren, J. Wang, K. Zhao, J. He, D. He, T. Zheng, and H. Zhao, *Effect of Ground State Charge Transfer on Photoexcited Charge Transfer in Transition Metal Dichalcogenide Heterostructures*, Applied Physics Letters **125**, 121109 (2024).

7. T. Zheng, X. Zhao, F. Yang, J. Song, W. Zhao, H. Zhao, and Z. Nie, *Effective Modulation of Interlayer Excitons in WSe_2/WS_2 Heterostructures by Plasmon-Exciton Interaction*, ACS Photonics **11**, 580-585 (2024).

8. G. Agunbiade, N. Rafizadeh, R. J. Scott, and H. Zhao, *Transient Absorption Measurements of Excitonic Dynamics in 3R-MoS_2*, Physical Review B **109**, 035410 (2024).
9. R. J. Scott, P. Valencia-Acuna, and H. Zhao, *Spatiotemporal Observation of Quasi-Ballistic Transport of Electrons in Graphene*, ACS Nano **17**, 25368-25376 (2023).
10. P. Valencia-Acuna, S. Amos, H. Peelaers, and H. Zhao, *Energy-Valley-Dependent Charge Transfer in Few-Layer Transition Metal Dichalcogenide Heterostructures*, Physical Review B **108**, 085302 (2023).

Author Index

Participant List

Name	Organization
Akanksha Krishnakumar Menon	Georgia Institute of Technology
Alathea Davies	University of Wyoming
Alexander Cerjan	Sandia National Laboratories
Ali Javey	Lawrence Berkeley National Lab
Anand Bhattacharya	Argonne National Laboratory
Ananya Renuka Balakrishna	University of California, Santa Barbara
Andrew Schwartz	U.S. Department of Energy - Basic Energy Sciences
Anthony Rice	National Renewable Energy Laboratory
Athena Sefat	U.S. Department of Energy
Aura Gimm	U.S. Department of Energy - Basic Energy Sciences
Chia-Ling Chien	Johns Hopkins University
Chih-Chieh Chiang	Johns Hopkins University
Chris Fecko	U.S. Department of Energy - Basic Energy Sciences
Chris Van de Walle	University of California, Santa Barbara
Chunhui (Rita) Du	Georgia Institute of Technology
Craig Henderson	U.S. Department of Energy - Basic Energy Sciences
Dali Sun	North Carolina State University
Daniel Nikiforov	University of Utah
Daryl Chrzan	University of California, Berkeley
David Beratan	Duke University
David Cahill	University of Illinois
Demetrios Christodoulides	University of Southern California
Dillon Fong	Argonne National Laboratory
Dmitri Kilin	North Dakota State University
Dmitri Talapin	University of Chicago
E. Dan Dahlberg	University of Minnesota, Minneapolis
Fatima Toor	The University of Iowa
Fazel Tafti	Boston College
Geoffroy Hautier	Dartmouth
Hadiseh Alaeian	Purdue University
Hanan Dery	University of Rochester
Hayk Harutyunyan	Emory University
Helen Kerch	U.S. Department of Energy - Basic Energy Sciences
Hui Zhao	The University of Kansas
Igal Brener	Sandia National Laboratories

Ivan Smalyukh	University of Colorado Boulder
Janice Musfeldt	University of Tennessee
Jennifer Roizen	U.S. Department of Energy - Basic Energy Sciences
Jiefei Zhang	Argonne National Laboratory
Jigang Wang	Ames National Laboratory
Jin-Sheng Wu	University of Colorado, Boulder
Jing Shi	University of California, Riverside
Jinsong Huang	University of North Carolina at Chapel Hill
Joel Ager	Lawrence Berkeley National Laboratory
Joshua Cohn	University of Miami
Kenan Gundogdu	North Carolina State University
Kenneth Burch	Boston College
Kirstin Alberi	National Renewable Energy Laboratory
Krzysztof Gofryk	Idaho National Laboratory
Kun Wang	University of Miami
Leah Bergman	University of Idaho
Lina Quan	Virginia Tech
Mahmoud Asmar	Kennesaw State University
Manh-Huong Phan	University of South Florida
Masaru Kuno	University of Notre Dame
Matthew McCluskey	Washington State University
Matthias Graf	U.S. Department of Energy - Basic Energy Sciences
Michael Crommie	University of California, Berkeley
Michael Flatté	University of Iowa
Mikhail Zamkov	Bowling Green State University
Mohamed Nawwar	Ohio State University
Mona Jarrahi	University of California, Los Angeles
Morgan Stefik	University of South Carolina
Moungi Bawendi	Massachusetts Institute of Technology
Nancy Sandler	Ohio University
Noel Giebink	University of Michigan
Patrick El Khoury	U.S. Department of Energy
Peidong Yang	University of California, Berkeley
Pengpeng Zhang	Michigan State University
Prashant Kamat	University of Notre Dame
Purusottam Jena	Virginia Commonwealth University

Raktim Sarma	Sandia National Laboratories
Raymond Orbach	The University of Texas at Austin
Sage Bauers	National Renewable Energy Laboratory
Samaresh Guchhait	Howard University
Sarah Watzman	University of Cincinnati
Saw Wai Hla	Argonne National Laboratory
Scott Barnett	Northwestern University
Seth Ariel Tongay	Arizona State University
Shane Stadler	Louisiana State University
Shanhui Fan	Stanford University
Shawn Chen	U.S. Department of Energy - Basic Energy Sciences
Sheena Reeves	Prairie View A&M University
Svetlana Kilina	North Dakota State University
Takeshi Egami	University of Tennessee
Thomas Koschny	Ames National Laboratory
Tim Mewes	U.S. Department of Energy - Basic Energy Sciences
Timothy Kidd	U.S. Department of Energy
Tom Autrey	Pacific Northwest National Laboratory
Vadym Apalkov	Georgia State University
Vitaly Podzorov	Rutgers University
William Tisdale	Massachusetts Institute of Technology
William Tumas	National Renewable Energy Lab
Xiaoqin Li	University of Texas at Austin
Xiaoyang Zhu	Columbia University
Xuanyu Long	University of Utah
Yaroslav Mudryk	Ames National Laboratory
Ying Wang	University of Wisconsin-Madison
Yiying Wu	The Ohio State University
Yuri Suzuki	Stanford University
Zbynek Novotny	Pacific Northwest National Laboratory
Zhuomin Zhang	Georgia Institute of Technology
Zubin Jacob	Purdue University